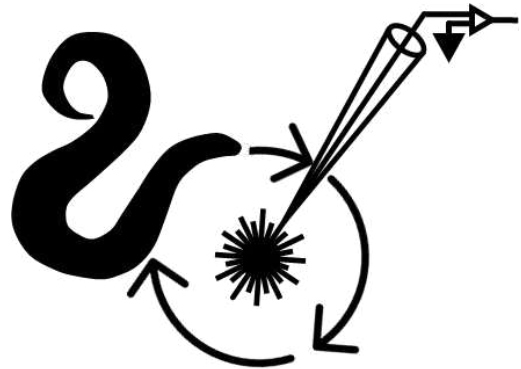Amelie Bergs

From optical perturbation to true control: All-optical voltage clamp in live animals

Thesis

for the award of the degree of
Doctor of Natural Sciences

presented to
the Faculty of Biochemistry, Chemistry
and Pharmacy of Goethe University Frankfurt

Accepted as a thesis by the Faculty of Biochemistry, Chemistry and Pharmacy of Goethe University Frankfurt

Dean: Prof. Dr. Clemens Glaubitz
Reviewer: Prof. Dr. Alexander Gottschalk, Prof. Dr. Clemens Glaubitz

Date of the oral defense: _____07.05.2024_____

Acknowledgements

Contents

Abbreviations

Units, dimension symbols and prefixes

Å	Angstrom
I	Electric current
Hz	Hertz
m	Meter
s	Second
V	Voltage

Acronyms and definitions

Ace2	From *Acetabularia acetabulum*
ACRs	Anion channelrhodopsins
Arch	Archaerhodopsin-3
Archer1	Arch with enhanced radiance
Archon	Based on Arch
ASAPs	Accelerated Sensor of Action Potentials
ATP	Adenosintriphosphat
BiPOLES	Bidirectional Pair of Opsins for Light-induced Excitation and Silencing
BLAST	Basic Local Alignment Search Tool
BWMs	Body wall muscles
C. elegans	*Caenorhabditis elegans*
CatCh	Calcium translocating channelrhodopsin
CCRs	Cation channelrhodopsins
CheRiff	From *Scherffelia*
ChloCs	Chloride-conducting ChRs
ChR	Channelrhodopsin
ChRmine	Red-shifted channel rhodopsin
DMAR	Dimethylaminoretinal
eFRET	Electrochromic fluorescence resonance energy transfer
egl	Egg-laying defective
EMCCD	Electron-multiplying charge-coupled device
EPGs	Electropharyngeograms
FACS	Fluorescence-activated cell scanning
FlicR	Fluorescent indicator for voltage imaging red
FLinChR	Full-length inversion of ChR

g.o.f.	Gain of function
GECIs	Genetically encoded calcium indicators
GEVIs	Genetically encoded voltage indicators
HTS	High-throughput screening
I-controller	Integral-controller
KCRs	Kalium channelrhodopsins
LiEp	Light-induced electrophysiology
MD	Molecular dynamics
Mermaid	Membrane-potential reporter made of ascidian and dual coral fluorescent proteins
MNs	Motor neurons
NpHR	Halorhodopsin
ODC	Optical dynamic clamp
OVC	Optogenetic voltage clamp
paQuasAr3	Photoactivated QuasAr3
PID	Proportional-integral-derivative
PROPS	Proteorhodopsin optical proton sensor
QuasAr	Quality superior to Arch
ReaChR	Red-activatable ChR
RSB	Retinal Schiff base
sCMOS	Scientific Complementary Metal–Oxide–Semiconductor
SFO	Step-function opsin
SNR	Signal-to-noise ratio
somArchon	Soma-targeted Archon
TMHs	Transmembrane helices
Unc	Uncoordinated
VARNAM	'Hue' in Sanskrit
VChR1	*Volvox* channelrhodopsin-1
VNC	Ventral nerve cord
VSD	Voltage-sensitive domain

Abstract

This dissertation constitutes a series of successive research papers, starting with the characterization of various optogenetic tools up to the establishment of purely optical electrophysiology in living animals.

Optogenetics has revolutionized neurobiology as it allows stimulation of excitable cells with exceptionally high spatiotemporal resolution. To cope with the increasing complexity of research issues and accompanying demands on experimental design, the broadening of the optogenetic toolbox is indispensable. Therefore, one goal was to establish a wide variety of novel rhodopsin-based actuators and characterize them, among others, with respect to their spectral properties, kinetics, and efficacy using behavioral experiments in *Caenorhabditis elegans*. During these studies, the applicability of highly potent de- and hyperpolarizers with adapted spectral properties, altered ion specificity, strongly slowed off-kinetics, and inverted functionality was successfully demonstrated. Inhibitory anion channelrhodopsins (ACRs) stood out, filling the gap of long-sought equivalent hyperpolarizing tools, and could be convincingly applied in a tandem configuration combined with the red-shifted depolarizer Chrimson for bidirectional stimulation (Bidirectional Pair of Opsins for Light-induced Excitation and Silencing, BiPOLES). A parallel study aimed to compare various rhodopsin-based genetically encoded voltage indicators (GEVIs) in the worm: In addition to electrochromic FRET-based GEVIs that use lower excitation intensity, QuasAr2 was particularly convincing in terms of voltage sensitivity and photostability in *C. elegans*. However, classical optogenetic approaches are quite static and only allow perturbation of neural activity. Therefore, QuasAr2 and BiPOLES were combined in a closed-loop feedback control system to implement the first proof-of-concept all-optical voltage clamp to date, termed the optogenetic voltage clamp (OVC). Here, an I-controller generates feedback of light wavelengths to bidirectionally stimulate BiPOLES and keep QuasAr's fluorescence at a desired level. The OVC was established in body wall muscles and various types of neurons in *C. elegans* and transferred to rat hippocampal slice culture. In the worm, it allowed to assess altered cellular physiology of mutants and Ca^{2+}-channel characteristics as well as dynamical clamping of distinct action potentials and associated behavior.

Ultimately, the optogenetic actuators and sensors implemented in the course of this cumulative work enabled to synergistically combine the advantages of imaging- and electrode-based techniques, thus providing the basis for noninvasive, optical electrophysiology in behaving animals.

Deutsche Zusammenfassung[1]

Die Entwicklung der Optogenetik revolutionierte die Neurobiologie, indem sie durch den Einsatz lichtempfindlicher Ionenkanäle (Rhodopsine) eine zeitlich und räumlich höchst präzise Ansteuerung von erregbaren Zellen ermöglicht. Sie kommt damit dem Hauptanliegen der Neurowissenschaften nach, die kausalen Zusammenhänge zwischen neuronaler Aktivität und den daraus resultierenden Verhaltensmustern aufzuklären[1,2]. Um diese Verbindungen zu identifizieren, bietet das optogenetische Repertoire sowohl Aktuatoren für die Modulation elektrischer Aktivität als auch Proteinsensoren, die diese Aktivitätsdynamik durch Veränderung ihrer Fluoreszenz verlässlich wiedergeben und eine Aufzeichnung ermöglichen. Alle im Rahmen dieses Forschungsvorhabens implementierten, entwickelten oder kombinierten Werkzeuge sind Rhodopsin-basierte Proteine, welche u. a. hinsichtlich ihrer Ionenselektivität, Kinetik, Leitfähigkeit und/oder spektralen Eigenschaften variieren. Jene Vielfalt an Charakteristika erlaubt einen maßgeschneiderten Einsatz für spezifische Fragestellungen. Einhergehend mit der jeweiligen Versuchsplanung, gewinnen diese jedoch immer weiter an Komplexität. Daher besteht ein großes Interesse, die bestehende optogenetische Toolbox zu erweitern – sei es durch gezieltes Protein-Engineering oder der Isolation neuer, natürlicher Varianten. Klassische optogenetische Experimente beschränken sich in der Regel auf ein einzelnes optogenetisches Tool, um die Aktivität der Zelle zu stimulieren oder zu inhibieren. Dieser Versuchsaufbau ruft jedoch lediglich eine Störung der Aktivität hervor, da der umschließende neuronale Schaltkreis nicht daran gehindert wird, durch Anpassung seinerseits, Einfluss auf die betreffende Zelle zu nehmen. Echte Kontrolle und Steuerung wird erst durch ein Rückkopplungssystem (Closed-Loop Feedback Control) erreicht, wie es beispielsweise bei der elektrophysiologischen Spannungsklemme (Voltage Clamp) zum Einsatz kommt[3,4]. Geringer Durchsatz, hohe Invasivität und technischer Anspruch limitieren jedoch die Anwendbarkeit der Spannungsklemme, vor allem im Hinblick auf kleine Modellorganismen wie *C. elegans*[5–7]. Hier geht die Patch-Clamp Technik mit einer aufwändigen Sezierung einher, was die Messung auf wenige Minuten begrenzt und folglich als nicht vollständig physiologisch angesehen werden kann. Sie ist zudem nicht im frei beweglichen Tier anwendbar. Die optische Umsetzung der Spannungsklemme bedarf zweier gegenläufiger optogenetischer Werkzeuge für bidirektionale Steuerung in Kombination mit einem dritten für die Aufzeichnung des Membranpotentials[8]. Ein solches Projekt verdeutlicht

---

[1] German summary

die Anforderungen an die Vielfalt des Werkzeugkastens: Es wird nicht nur ein ebenbürtig leistungsfähiges und hocheffizientes Aktuatorenpaar benötigt, sondern auch insgesamt drei spektral unabhängig ansteuerbare Rhodopsine.

Diese Dissertation besteht daher aus einer Reihe von aufeinander aufbauenden Forschungsarbeiten, beginnend mit der Charakterisierung einer breiten Palette von de- und hyperpolarisierenden Werkzeugen, insbesondere der hocheffizienten hyperpolarisierenden Anionenkanalrhodopsine (ACRs) und des bidirektionalen Tandemproteins BiPOLES, bestehend aus ACR2 und dem Depolarisator Chrimson in *C. elegans*[9-14]. In einer weiteren Studie wurden mehrere genetisch kodierte Spannungsindikatoren (GEVIs) auf Rhodopsinbasis für die Verwendung in *C. elegans* implementiert und hinsichtlich ihrer Spannungsempfindlichkeit und Gesamtleistung bewertet[15,16]. Auf der Grundlage der Ergebnisse dieser ersten Studien wurden geeignete Werkzeuge, nämlich BiPOLES für die Aktivierung und QuasAr2 für die Spannungsaufzeichnung, ausgewählt und in ein Live- und Closed-Loop-Feedback-Kontrollsystem eingebettet. Dieses System zielt darauf ab, die Nichtinvasivität von Bildgebungsmethoden mit den Kontrolleigenschaften der klassischen Spannungsklemme zu vereinen, woraus die optogenetische Spannungsklemme oder kurz OVC entstand[8]. Im Folgenden werden die Ergebnisse zusammenfassend in deutscher Sprache aufgeführt.

In einer initialen Studie wurde eine Vielfalt an neuen optogenetischen Werkzeugen in *C. elegans* vergleichend getestet und charakterisiert[9]. Mittels Verhaltens-Assays, die auf der durch Lichtstimulation veränderten Körperlänge und dem beeinträchtigten Schwimmverhalten der Tiere aufbauen, konnten wesentliche Eigenschaften, wie etwa Aktionsspektren, Kinetik, repetitive Stimulierbarkeit und Gesamtleistung abgeleitet werden. Sogenannte Step-Function Opsine, bei denen Mutationen im zentralen DC-Gate vorgenommen wurden (Aminosäuren D156 und C128)[17], zeigten eine maßgeblich verlangsamte Schließkinetik, was durch die Expression in den Körperwandmuskeln zu minuten- bis stundenlang anhaltender Muskelkontraktion führte. Getestet wurden die <u>Ch</u>annel<u>r</u>hodopsin-2 (ChR-2) Mutanten ChR2(C128S;H134R), QUINT: ChR2(C128S;L132C;H134R;D156A; T159C), sowie die XXL-Mutante[18] ChR2(H134R;D156C). Neben erhöhter Stabilität bei Unterbrechung der Retinal- (ATR)-Supplementierung im Vergleich zur vormals getesteten Einzelmutante ChR2(C128S)[19], konnten Verbesserungen in der repetitiven Stimulierbarkeit festgestellt werden. Auf Seiten der hyperpolarisierenden Werkzeuge wurden Varianten der durch Protein-Engineering generierten Chlorid-leitenden Channelrhodopsine (ChloCs)[20] und natürlich isolierte Anionenkanalrhodopsine (ACRs)[21] evaluiert, sowie bei Letzteren die homologen Step-Function Mutationen eingeführt. Hierbei konnten vor allem ACR1 und ACR2 überzeugen, wobei die erzielten Effekte, die der ChloCs um ein Vielfaches übertrumpften. Die gemessenen Photoströme waren zudem 10-mal stärker als bei der herkömmlich eingesetzten Ionenpumpe Halorhodopsin. Die zu den Kationenkanalrhodopsinen homologen Step-

Function Mutationen konnten bei den ACRs eine verlangsamte Kinetik hervorrufen, blieben jedoch hinter den zuvor analysierten Kationenkanalrhodopsinen zurück. Die Lichtsensitivität der XXL-Mutante sowie der ACRs konnte die der in *C. elegans* meistverwendeten ChR2 Variante ChR2(H134R) um das bis zu 120-fache übertreffen. Eine nachfolgende Studie erweiterte das optogenetische Repertoire abermals mit der Implementierung eines artifiziell invertierten ChR2[10]. Die topologische Invertierung erfolgte mittels der Fusion einer ChR Variante (ChR2(E123T;H134R;T159C)) an die verkürzte Transmembranhelix von Neurexin-1 beta und der Einführung positiv geladener Aminosäuren in der Linkerregion. Es resultierte ein hyperpolarisierendes Tool (Full-length-inverted-channelrhodopsin-2/FLInChR), das entgegen seines Ausgangsproteins nicht mehr als Kanal, sondern als rotverschobene, lichtaktivierbare Ionenpumpe agierte. Zudem lieferte die Herangehensweise der topologischen Invertierung Einblick in Struktur-Funktions-Zusammenhänge von Rhodopsinen. Wie die zuvor aufgeführten optogenetischen Tools, wurde auch FLInChR über Körperlängenmessung unter Lichtstimulation in *C. elegans* implementiert und charakterisiert. Da für manche Versuchsanordnungen, gerade im Hinblick auf die Umsetzung rein optischer Elektrophysiologie, mehr als ein einzelnes Werkzeug von Nöten ist, wurde in einer weiteren Studie ein bidirektional agierendes Tandemprotein entwickelt[11]. BiPOLES wurde aus dem Hyperpolarisierer ACR2 und dem Depolarisierer Chrimson zusammengesetzt, wodurch ihre geringe spektrale Überlappung eine spezifische und weitestgehend unabhängige Stimulation mit zwei Lichtwellenlängen ermöglicht. Zudem weisen sie eine ähnliche Effizienz sowie hohe Sensitivität auf und konnten erfolgreich in gleich mehreren Modellorganismen etabliert werden.

Die hier aufgeführten Studien zur Erweiterung der optogenetischen Toolbox umfassten nicht nur optogenetische Aktuatoren (de- und hyperpolarisierende Werkzeuge), sondern auch die Etablierung verschiedenster genetisch kodierter Spannungssensoren (GEVIs) in *C. elegans*[15]. Diese unterteilten sich in eFRET- (electrochromic FRET-) basierte Sensoren[22] und solche, bei denen die spannungsabhängige Fluoreszenz des Kofaktors Retinal direkt ausgelesen wird. Messungen mit den eFRET GEVIs MacQ-mCitrine und QuasAr-mOrange benötigten weitaus geringere Anregungsintensitäten und konnten mittels simultaner elektrophysiologischer „sharp electrode" Messungen im Pharynx kalibriert werden. Der Austausch von ATR gegen das Analogon Dimethylaminoretinal (DMAR) hatte eine um 250-fach erhöhte Helligkeit der Fluoreszenz zu Folge. Die von Archaerhodopsin abgeleiteten GEVIs Arch(D95N), QuasAr2 und Archon wurden in Körperwandmuskeln und den RIM-Neuronen exprimiert. Die Anregung mittels eines roten Lasers erlaubte die Beobachtung der Spannungsdynamik und von Aktionspotentialen in diesen Geweben sowie der durch koexprimiertes ChR2 oder ACR2 hervorgerufenen De- oder Hyperpolarisation. Weiterhin konnten im Pharynx durch den Einsatz der GEVIs sowohl Unterschiede in der Muskeldepolarisation einer Ca^{2+}-Kanal Mutante im Vergleich zum Wildtyp aufgedeckt als

auch eine rein optische Ableitung von kompartmentalisierten Repolarisationsevents durchgeführt werden (optisches Elektopharyngeogramm).

Basierend auf den zuvor aufgeführten Publikationen konnten die geeignetsten Werkzeuge für direkte Anwendungen im Wurm, sowie zur Methodenentwicklung in Bezug auf rein optische Elektrophysiologie ausgewählt werden. So konnte das zuvor etablierte ACR1 im Zusammenspiel mit Calcium-Imaging dazu beitragen, die Rolle von AS-Motoneuronen im Bewegungsablauf von *C. elegans* aufzuklären[14]. Der Einsatz von ebenfalls zuvor etablierten Spannungssensoren half dabei, Teilaspekte jener Maschinerie zu untersuchen, die für die synaptische Vesikelfusion in *C. elegans* verantwortlich sind[16]. Den größten Einfluss hatten die Studien zur Etablierung neuer optogenetischer Werkzeuge jedoch auf die Entwicklung der optogenetischen Spannungsklemme[8]. Durch die Kombination von BiPOLES mit QuasAr2, dem Spannungssensor, der am besten in der vorausgegangenen Studie abschnitt, waren die molekularen Grundlagen zur Etablierung der OVC gesetzt. Dabei war es wichtig, den Sensor mit der größten Spannungsempfindlichkeit zu wählen, um mögliche unerwünschte Bewegungsartefakte zu kompensieren, da die Rückkopplungssteuerung empfindlich auf kleine Änderungen des Membranpotenzials reagiert. Die spannungsabhängige Fluoreszenz des Proteins wird bei der OVC-Technologie über eine empfindliche (sCMOS- oder EMCCD-) Kamera aufgezeichnet, die Grauwerte in einen Regelalgorithmus einspeist, der aus einem Integralregler und einem Entscheidungsbaum-Algorithmus besteht: Der vorgewählte Fluoreszenz-Haltewert wird mit dem tatsächlichen Fluoreszenzniveau zu jedem Zeitpunkt verglichen. Auf der Grundlage der daraus resultierenden Abweichung wird die Wellenlänge eines Monochromators angepasst und im Hinblick auf die Größe der Abweichung verstärkt, wodurch die Fluoreszenz in engen Grenzen gehalten wird. Das Vorzeichen der Abweichung zu jedem Zeitpunkt bestimmt, ob die Wellenlänge erhöht oder verringert wird. Dies wird durch den Entscheidungsbaum-Algorithmus verarbeitet und basiert auf den Spezifikationen der verwendeten optogenetischen Werkzeuge. Darüber hinaus wird eine vorangehende Kalibrierungsphase jeder OVC-Aufnahme genutzt, um das Bleichverhalten von QuasAr2 abzuschätzen, wobei die tatsächlichen Fluoreszenzwerte für die Dauer der Messung in Echtzeit geschätzt werden. Das Tandemprotein BiPOLES wird nun genutzt, um eine Wellenlängenrückkopplung an die betreffende Zelle zu übertragen und ihr Membranpotenzial auf einem gewünschten Niveau zu halten. Aufgrund der geringen spektralen Überlappung von ACR2 und Chrimson und übereinstimmenden Photostromamplituden, ist die Verwendung von BiPOLES prädestiniert für eine rein optische und bidirektionale Lenkung des Membranpotentials, die eine unabhängige, zweifarbige Aktivitätsmodulation ermöglicht. Obwohl sie vergleichbare Absorptionsmaxima aufweisen, wird die spektrale Überlagerung zwischen QuasAr2 und Chrimson durch die Anwendung einer kompensierenden Wellenlänge zu Beginn jeder Messung überbrückt. Darüber hinaus garantiert der Tandemcharakter von BiPOLES ein festes 1:1-Verhältnis der Expressionsniveaus der beiden Aktuatoren und überwindet anfängliche Leistungsprobleme

bei unausgewogener getrennter Expression. Die Kalibrierung des OVC-Systems erfolgte durch gleichzeitige Patch-Clamp-Aufzeichnungen, die die Feedback-Wellenlänge mit den Strömen und die Fluoreszenzwerte mit der Membranspannung in Beziehung setzten und den durch die OVC zugänglichen Spannungsbereich aufzeigten. Dies ermöglichte es unter anderem, die Beziehungen zwischen optischer Wellenlänge-Fluoreszenz- in echte Strom-Spannungs-Beziehungen (I-V) zu übersetzen. Auf diese Weise ermöglicht die OVC die Evaluierung veränderter Zellphysiologie in Mutanten in ähnlicher Weise wie ihr elektrophysiologisches Gegenstück. Auch die Untersuchung der veränderten Eigenschaften einer Ca^{2+}-Kanal-Mutante konnte mittels durch OVC-Messungen gewonnenen optischen I-V-Kurven durchgeführt werden. Der Umfang der OVC-Software ermöglichte außerdem die dynamische Unterdrückung einzelner Aktionspotentiale, die Einstellung des gewünschten Fluoreszenzlevels während der Messung, sowie die Verwendung der OVC-Komponenten als optisches Pendant zur Current-Clamp-Methode.

Zusammenfassend ermöglichte die hier aufgeführte Serie an Publikationen zur Erweiterung des optogenetischen Repertoires die Entwicklung des ersten Grundsatzbeweises einer rein optischen Spannungsklemme. Diese ebnet den Weg für echte optogenetische Kontrolle in sich frei verhaltenden Tieren wie *C. elegans*. Zudem ist eine dynamische Responsivität auch im Hinblick auf künftige therapeutische Anwendungen von Vorteil, z. B. bei der akuten Kontrolle von Krampfanfällen oder bei der adaptiven Tiefenhirnstimulation, da sie eine Anpassung der Therapie an die Bedürfnisse des Patienten erlauben könnte.

1. Introduction

1.1   Objectives and motivation

The major objective of this dissertation was to broaden the applicability and scope of the optogenetic toolbox and, ultimately, to implement an in vivo all-optical adaptation of the electrophysiological voltage clamp. Therefore, novel rhodopsin-based optogenetic tools were first implemented and characterized in the model organism *Caenorhabditis elegans* and then evaluated for their suitability in purely optical electrophysiology.

One major issue in neuroscience is to relate the activity of neurons of interest with the behavior they drive, i.e., the causal basis of neuronal computation and behavior[1,2]. To identify those connections, techniques for both, targeted control with high spatiotemporal resolution and methods that allow recording of neural activity are required[23,24]. Rhodopsin-based optogenetic tools vary among others in terms of ion selectivity, kinetics, conductivity, and spectral properties[17,20,21,25–28]. This allows to select custom-fit tools for specific experiments from a wide range of options. As applications successively gain in complexity, there is an ongoing need for further optimization and adaptation of existing or isolation of novel natural occurring rhodopsins. Standard optogenetic experiments traditionally involve a single optogenetic tool, expressed in an excitable cell of interest, to stimulate or inhibit the cell's activity by light. However, this type of experiment allows only a perturbation of neuronal activity and no true control, since the enclosing circuit is still able to adapt, and to exert an influence on the neuron under investigation. To exclude those undesired modulations, the membrane voltage must be held at a pre-selected level, which is the general principle of the voltage clamp technique in electrophysiology[3,4]. Nevertheless, standard electrophysiology is limited by its invasiveness and technical demand[5–7]. Optical adaptation of this technique requires two opposing optogenetic tools for bidirectional stimulation of voltage dynamics along with a third one for voltage recording[8]. Such a project illustrates the requirements made on the variety of the toolbox: Not only an equally performing and highly efficient actuation pair is needed, but also a total of three spectrally independent controllable rhodopsins.

Therefore, this dissertation displays a series of consecutive research efforts (**Fig. 1**), starting from the characterization of a broad range of de- and hyperpolarizing tools, especially the highly efficient hyperpolarizing anion channelrhodopsins (ACRs) and the bidirectional tandem protein BiPOLES (**Movie 1**), consisting of ACR2 and the depolarizer Chrimson in *C. elegans*[9–14]. A further study involved the implementation of several rhodopsin-based genetically encoded voltage indicators (GEVIs) for use in *C. elegans* and evaluation regarding their voltage sensitivity and overall performance[15,16]. Based on the findings of these initial studies, appropriate tools – namely BiPOLES for actuation and QuasAr2 for voltage recording (**Movie 2**) – were selected and embedded in a live and closed-loop feedback control system aiming to synergize the non-invasiveness of imaging methods with the control capabilities of traditional voltage clamp recordings – the optogenetic voltage clamp (OVC)[8]. The OVC was established in various muscular and neuronal tissues of the worm and in rat hippocampal organotypic slices. In *C. elegans*, it was optimized to provide insight into the nature and influence of mutations in proteins affecting neuronal excitability and synaptic transmission, allowing to deduce purely optical I-V relationships as well as dynamical suppression of action potentials (APs) and associated behaviors (**Movie 3**).
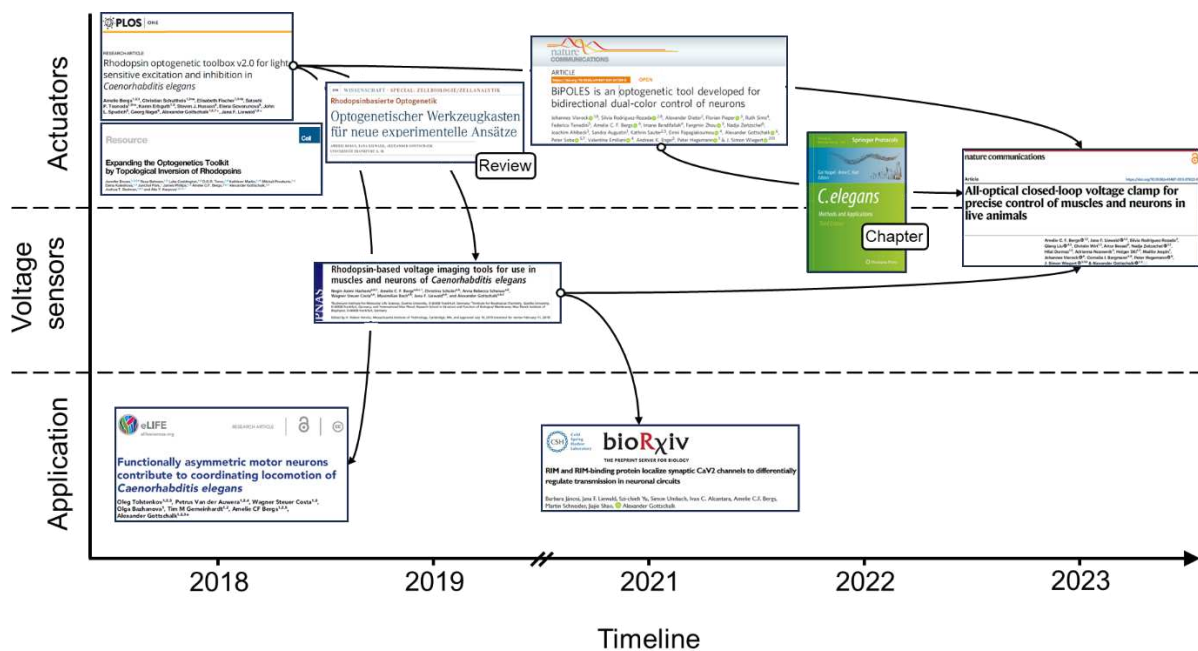

Figure 1. Timeline of publications in the scope of this dissertation[8–16]. Publications are listed according to their year of publication and content (optogenetic actuators, voltage sensors, application in *C. elegans*). Arrows indicate which publications are based on each other (first submission of OVC paper in 2021).

1.2   Expanding the optogenetic toolbox: Microbial rhodopsins to stimulate and record neural activity

Optogenetics has revolutionized neurobiology as it allows targeted control over neural function with high spatiotemporal precision[29-32]. The method employs light to selectively target genetically modified excitable cells, expressing light-sensing ion channels, transporters, or enzymes[29,33]. In contrast to these benefits, previously used microelectrodes were strongly lacking cell specificity and led to substantial damage in model animals. Further to that, the multicomponent character of the first light-based applications limited temporal resolution and specificity, both being central aspects when investigating neural activity[33]. This long-awaited approach of turning individual cells sensitive to light, while leaving others unaffected, eventually led to the development of optogenetics[33].

Depending on the scientific interest, researchers can now select from a wide range of specialized tools (**Fig. 2**).
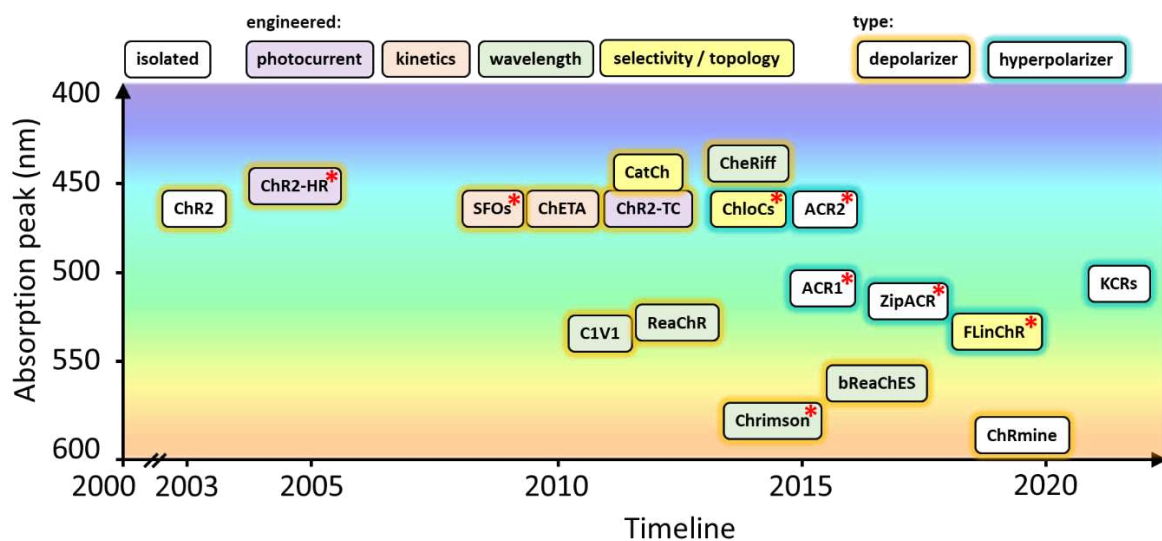
Figure 2. Overview of some of the most relevant channelrhodopsin-based tools listed by their initial description and spectral properties. Color coding further subdivides the tools shown by de- or hyperpolarizing characteristics (orange or blue outline respectively) and the purpose of the genetic manipulation (purple: enhanced photocurrents, red: modified kinetics, green: shift in absorption spectra, and yellow: ion selectivity resp. channel topology). * Tools covered by this project.

Combining methods from optics and genetics, the technology allows activation, inhibition, and observation of electrical activity and can be applied in both, cell culture and freely behaving animal models. Within the last two decades, numerous optogenetic tools have been isolated, engineered, and optimized to meet experimental demands with increasing precision[32]. Most significant among these tools are microbial opsins, on which the present work is based. Considering the nervous system as a highly complex (chemo-) electrical

circuit, those light-activatable ion pumps and channels allow a precise switching of specifically targeted excitable cells, such as neurons or groups of neurons, by modulating their membrane potential. Further, some of these rhodopsin-based proteins – GEVIs – can be utilized to sense and translate voltage dynamics into observable changes of their fluorescence yield[22,34–40].

The following chapters discuss the functionality and versatility of rhodopsin-based optogenetic tools and shed light on the extent to which the tools addressed are suitable for the ultimate goal of all-optical electrophysiology.

1.3   Optogenetic tools for de- and hyperpolarization

All domains of life developed mechanisms to sense electromagnetic radiation, which allows them to adapt to their environment. In this regard, organisms evolved phototaxis as a mechanism to respond with directed locomotory movement to light stimuli, where investigation led to the discovery of the cation channelrhodopsins[41–43]. Contrary to animal opsins (visual pigments) of higher eukaryotes (type II), that act as G protein-coupled receptors, channelrhodopsins belong to the superfamily of microbial opsins (type I), that are considered here, and function as light-dependent ion channels[44]. Next to ion channels, this protein family also includes proton and ion pumps. All types comprise seven transmembrane helices (TMHs)[44,45]. Their co-factor retinal, which serves as the actual photon sensor of the holoprotein, binds covalently to TMH 7 via a lysine residue resulting in a protonated Schiff base. Upon absorption of a photon, retinal undergoes isomerization from *all-trans* to *13-cis* configuration, which in turn induces a conformational change of the protein, leading to channel opening and passive ion transport over the membrane or active, vectorial ion transport via pumping activity[46].

Channelrhodopsin-2 and Halorhodopsin are two of the most frequently used rhodopsin-based optogenetic tools to date, providing both de- and hyperpolarizing currents, i.e., activation and inhibition, respectively. For more complex problems, however, many factors are decisive: the kinetics of the tool used, the spectral properties or the absorption maximum, the conductivity, membrane expression, and finally the ion selectivity[32]. In addition, there are limitations in the applicability of some tools, which can result from a lack of effectiveness or photosensitivity as well as from phototoxicity if long-term stimulation is required. It becomes even clearer when considering the present project: The specifications for the combination of several rhodopsins, as was necessary in the development of the OVC, require spectral compatibility, equal efficiency of the two opposing actuators, and sufficiently fast kinetics of all three tools. This highlights the need to search for novel naturally occurring rhodopsins with properties different to those

already established as well as to optimize and model new artificial tools with specifications tailored to specific needs.

1.4   Cation channelrhodopsins, anion channelrhodopsins, and engineered variants

The first discovered and the most widely used rhodopsin-based optogenetic tool to date is channelrhodopsin-2 (ChR2). It is a light-gated ion channel which, next to channelrhodopsin-1, serves as a sensory photoreceptor in the unicellular green algae *Chlamydomonas reinhardtii*[47,48]. As introduced above, a light-induced isomerization of the co-factor retinal – an aldehyde derivative of vitamin A – from *all-trans* to *13-cis* configuration, leads to a conformational change and the opening of the channel pore by 6 Å. When activated by light, especially at its absorption maximum of around 470 nm, ChR2 non-specifically conducts protons and cations into the cytoplasm of the cell, which causes a depolarization of the plasma membrane[46].

To understand the functional properties of ChR2 and both its naturally occurring and engineered relatives, the photocycle mechanism and involved – usually highly conserved – key residues must be considered. Light absorption of retinal initiates a photocycle with spectroscopically distinctive intermediates, which differ in the electrostatic environment of retinal, the protein's conformation as well as the protonation states of involved residues, and manifest spectrally shifted compared to the dark state[49–51]: First, upon blue light excitation of the dark state D_{470}, the accompanying retinal isomerization leads to the red-shifted intermediate P_{500}. Subsequently, a proton transfer from the protonated retinal Schiff base (RSB) to a counter-ion complex occurs and results in the intermediate P_{390}. After reprotonation of the RSB, P_{390} is followed by P_{520}. Late P_{390} and P_{520} intermediates were found to contribute to the ion conductance of the open state. As the last and non-conducting intermediate, P_{480} succeeds after channel closing. Eventually and with a time constant of around 40 s, the initial dark state D_{470} is recovered. In ChR2 and related proteins, point mutations near the retinal binding pocket alter the biophysical properties of the presented photocycle. This results in a variety of optimized tools, which is discussed below. These modulations target both, optimization of existing and creating entirely new tools with (strongly) deviating or even opposite characteristics. In the present project, novel cation channelrhodopsins (CCRs) were tested in the nematode *C. elegans* that differ from the wild type with regard to kinetics, light sensitivity, and ion specificity as well as in topology and spectral properties which were generated by targeted mutagenesis[9–11]. Moreover, natural ACRs and engineered derivatives were characterized that fill the gap of equivalently efficient optogenetic tools for hyperpolarization[9].

15

A key characteristic of channelrhodopsins is their kinetics, determining the temporal precision of optogenetic manipulation. For wild type channelrhodopsin, the channel opening time constant is in the sub-millisecond time scale (t_{on}) – fast enough to avoid any limitations on the control of neuronal activity[52]. In contrast, off-kinetics are significantly slower, as channels that have entered the photocycle also pass through it completely. Regarding the establishment of the OVC, this relatively slow channel closing was less detrimental, because the tools used enable active counteraction and compensate for lagging photocurrents. In general, however, and especially for fast spiking mammalian neurons, modulations to shorten t_{off} constants are desirable: Mutations of the residue E123 ("ChETA" variants), which stabilize the protonated RSB as part of the counter ion complex, decrease closing kinetics to around 4 ms[26]. Although tools with fast off-kinetics are desirable, there is a tradeoff with respect to light sensitivity, which behaves inversely proportional[53].

Hence, if temporal resolution is of lower priority for a given experimental setup, it might appear more useful to modulate the overall excitability. So-called step-function opsins (SFOs) are the reagents of choice, when a more naturalistic spike pattern is desired, or experiments would suffer from phototoxicity upon otherwise continuous illumination during long-term stimulation[17-19]. Here, point mutations of the TMH 3/4 interaction at the DC-gate – an assumed hydrogen bond between residues Cys-128 (thiol group) and Asp-156 (carbonyl oxygen) – lead to extensively prolonged open lifetimes of the channel pore of up to six logarithmic units. Moreover, for some SFOs, red-shifted excitation of the conducting open state shortcuts the photocycle and results in channel closure through recovery of the retinal's dark conformation. This provides a step-like switching option and – to some extent – preserves temporal resolution[17]. Since SFOs integrate photons over their prolonged open lifetime, they provide an exceptional high light sensitivity, as channels accumulate in the conductive state[53]. While the initially described SFO variants ChR2(C128S) and ChR2(C128T) pass into persistent desensitization states subsequent to channel closing and rely on continuous ATR supplementation in *C. elegans*, variants with combined point mutations tested as part of this project (e.g., ChR2-XXL), bypassed several of these shortcomings: They demonstrated higher off-ATR excitability, performed better in repetitive assays, and showed the slowest closing kinetics of all ChR2 variants identified or engineered so far[9].

In addition to temporal precision, spectral properties and color tuning are central in optogenetic tool development[54]. Experiments that require deeper tissue penetration benefit from alternative red-shifted rhodopsins with less light scattering that complement the conventional blue light excitable ChRs. Further, for multiplexing of various tools in combinatorial control applications, both blue- and red-shifted ChRs with narrow absorption bands are required to avoid potential optical crosstalk. Next to the

development of chimeric rhodopsins like C1V1 or VChR1-based ReaChR (not tested within the scope of this project) that combine helices from ChR1 and VChR1 and exhibit red-shifted absorption maxima, natural spectrally shifted ChR variants like Chrimson were isolated[27,28,55]. Optimized by evolution, these natural ChRs bypass shortcomings of engineered variants with targeted point mutations at the retinal binding pocket, that usually suffer from reduced photocurrent amplitudes or slowed kinetics[54]. With an absorption maximum at 590 nm, Chrimson is optimally suited to be combined with a blue-light activatable tool, e.g., to either independently stimulate two different subsets of neurons or to allow independently targetable de- and hyperpolarization within the same cell, as it was realized in the OVC approach (discussed below: Chapter 1.8)[8,11].

In addition to CCRs, hyperpolarizing rhodopsin-based tools are also utilized in optogenetic research. Here, NpHR (halorhodopsin), derived from the archaeon *Natronomonas pharaonic*, acts as a yellow light-driven chloride pump and is one of the most commonly used inhibitory rhodopsins[56,57]. Upon light stimulation this rhodopsin exhibits pumping activity and transports negatively charged chloride ions into the cytoplasm, thus NpHR-expressing cells become hyperpolarized. Further to chloride-selective pumps, optogenetics also employs light-triggered H^{+}-pumps for optical inhibition experiments (e.g., archaerhodopsin (Arch) from *Halorubrum sodomense* and Mac from *Leptosphaeria maculans*), where hyperpolarization is induced via an extrusion of protons[58].

The use of rhodopsin pumps for optical inhibition is, however, limited by the nature of active transport, since only one ion is transported per photocycle, and photon capture is the rate-limiting step in in vivo applications. When used for long-term experiments, continuous light stimulation is inevitable to maintain NpHR activity, thus resulting in potential phototoxic effects. This is complicated by the fact that point mutations which affect the photocycle to increase light sensitivity (as discussed above for CCRs) are not available for ion pumps[59]. The advantage of ion pumps to transport ions actively and independently of the reversal potential of the respective cell is also opposed by the fact that they might hyperpolarize cells far beyond physiological conditions, which may result in unstable, abnormal gradients. As gradients vary according to cell type or pathological state, passive ion flux via a channel-based tool is preferable, since it mimics neural inhibition in a more physiologically precise and realistic manner[20,60,61]. Here, anion channelrhodopsins (ACRs) fill the gap of equally efficient hyperpolarizing and highly conductive channel-based tools: Based on a BLAST (Basic Local Alignment Search Tool) search in the cryptophyte *Guillardia theta*, researchers identified a multitude of proteins, showing sequence similarity to type I microbial opsins, while two of them functioned as light-activatable chloride channels with strict anion selectivity (Anion Channelrhodopsin 1 (GtACR1) and Anion Channelrhodopsin 2 (GtACR2))[21]. With ACRs, scientists now not only

have equivalent hyperpolarizing tools at their fingertips, but these tools actually outperform ChR2 in terms of plateau currents by six- to eight-fold. While ACR1 exhibits larger plateau currents and is maximally activated at 515 nm, ACR2 provides faster kinetics at a similar absorption maximum as compared to ChR2. In an additional screening study, two further ACRs – ZipACR (from *Proteomonas sulcate*) and RapACR (from *Rhodomonas salina,* not tested within the scope of this project) – revealed significantly faster closing kinetics and even higher photocurrents, enabling spike inhibition of up to 100 Hz[62,63]. As ACRs are a thousand times more light-sensitive than existing hyperpolarizers and display the highest conductance among all channelrhodopsins known so far, ACRs are a coequal tool in the field of inhibitors for optogenetic applications.

In addition to the discovery of natural ACRs, there have also been some efforts to invert the ion selectivity of ChR2 through site-directed mutagenesis and convert it into a hyperpolarizing tool[20,60]. The selectivity of ChR2 is based on various glutamate and lysine residues in TMH 2, where protons and cations are guided through the water-filled channel pore. Within this central selectivity filter, and in close proximity to the RSB, substitution of residue Glu-90 turned wild type ChR2 from an unspecific cation channel into a hyperpolarizing chloride conducting ChR (ChloC)[20]. This residue determines ion selectivity as it changes its protonation state during the photocycle[64]: Within the central gate, E90 is deprotonated and builds a hydrogen bond with N258, which in turn forms one with S63[20]. Irregularities of water distribution around E90 hinted at the central gate functioning as a hydrophobic barrier in the closed state[46]. Elimination and weakening of hydrogen bonds between helices 1 and 7 through the substitution of Glu-90 resulted in the formation of a larger channel cavity and thus high chloride affinity[20]. The introduction of additional point mutations within the DC gate (see above, XXL mutation) improved the conductivity and operational light sensitivity of the tool and enabled light-driven hyperpolarization in the worm[9,18]. Markedly, engineered chloride channels as ChloC or iC++ show some similarity to naturally evolved ACRs in predicted pore electrostatics, suggesting a general and consistent pattern for ion selectivity. Therefore, engineered chloride-conducting ChRs provide valuable insights into structure-function relationships, despite falling short of their natural counterparts, the ACRs[62]. A further approach to transform wildtype ChR2 into a hyperpolarizing tool aimed at the overall protein structure by inverting its topology[10]. This was accomplished by fusion to an additional TMH, a signal sequence and positively charged residues within the linker region. The resulting protein FLInChR (Full Length Inverted Channelrhodopsin) acts as a non-specific cation pump with a significantly red-shifted absorption maximum.

1.5   Opsin genetically encoded voltage indicators

Besides actuation of neural activity, the recording of voltage dynamics is crucial for neuroscience research. Although traditional electrophysiology provides the highest sensitivity and temporal resolution, it is spatially limited and imposes major technical effort, especially when it comes to applications in live animals, while the technical barrier further rises when several neurons are to be examined simultaneously[5–7]. Optical techniques, however, enable to display neural dynamics across spatial scales, e.g., from dendritic spines up to whole circuits of interacting neurons in a contactless manner, yet with reasonable temporal precision[35]. A multitude of genetically encoded sensors have been developed to bridge restrictions of voltage- or calcium-sensitive dyes, that suffer among others from poor and unspecific localization and limited applicability for long-term experiments[65]. The most well-established sensors are genetically encoded calcium indicators (GECIs), providing high spectral diversity that allows for multiplexing in combinatorial optogenetic approaches, several thousand-fold increase of fluorescence signals upon calcium binding, while some even allow detection of single action potentials[66–68]. However, GECIs fall short to display precise spiking dynamics, subthreshold signals, or high-frequency action potentials[39]. Since depolarization is not necessarily associated with calcium increase and calcium imaging provides only an indirect measure of electrical activity, it is generally not appropriate for any type of neuron[69]. Finally, and most critically with respect to the goal of optical voltage clamping, calcium imaging does not reflect hyperpolarization, as calcium levels do not usually fall below basal cytosolic concentration.

This is where GEVIs come in: Using rational design and directed evolution, researchers developed so-called genetically encoded voltage indicators[22,34,35,37,39,70,71]. These proteins sense membrane potential in genetically targeted cells and translate relative changes in voltage into an optically observable, fluorescent output with sub-millisecond timing precision – about an order of magnitude faster compared to GECIs[71]. Besides VSD- (voltage-sensitive domain-) based indicators like Mermaid, ArcLight, ASAPs, and FlicR, consisting of a VSD and a fluorescent protein, there are voltage indicators based on microbial opsins, which are covered by this research work and discussed in the following[72,73].

The first generation rhodopsin-based voltage sensors were PROPS (proteorhodopsin optical proton sensor) and Arch (archaerhodopsin-3), two light-driven outward proton-pumps[34,74]. The latter, from which most of the opsin GEVIs originate, was isolated from the archaeon *Halorubrum sodomense*, that uses it to harvest solar energy to establish a proton motive force for driving ATP synthesis. In addition to its use as a neural silencer, Arch and related proteins provide a dim voltage-dependent fluorescence that

depends on the protonation state of the RSB[75]. Rhodopsin-based proton pumps such as Arch transfer cytoplasmic protons from the proton donor residue towards the proton acceptor residue and from the proton release site further to the outside of the cell (**Figure 3 A**). This is driven by light absorption and ATR isomerization to the *13-cis* configuration, while the RSB is transiently protonated[40]. For the usage as a voltage sensor, the proton acceptor site is mutated to block the main path for the transfer of protons from the RSB to avoid any photocurrent (Arch(D95N)) and shifts the pK_a of the RSB to sense membrane voltage in a physiological range[76]. Voltage sensitivity is based on membrane potential changes, which modify the protonation equilibrium between the RSB, the proton donor site, and the cell cytoplasm[77]. Subsequent to initiation of the photocycle by a primary photon, membrane voltage modulates a proton-transfer equilibrium between two photocycle intermediates (**Figure 3 B**): The M state characterized by a protonated donor residue (D106) and the N state, where the RSB is protonated. Fluorescence results from the transition of N to Q via a second photon, followed by electronic excitation of Q, by a third one[40,77].
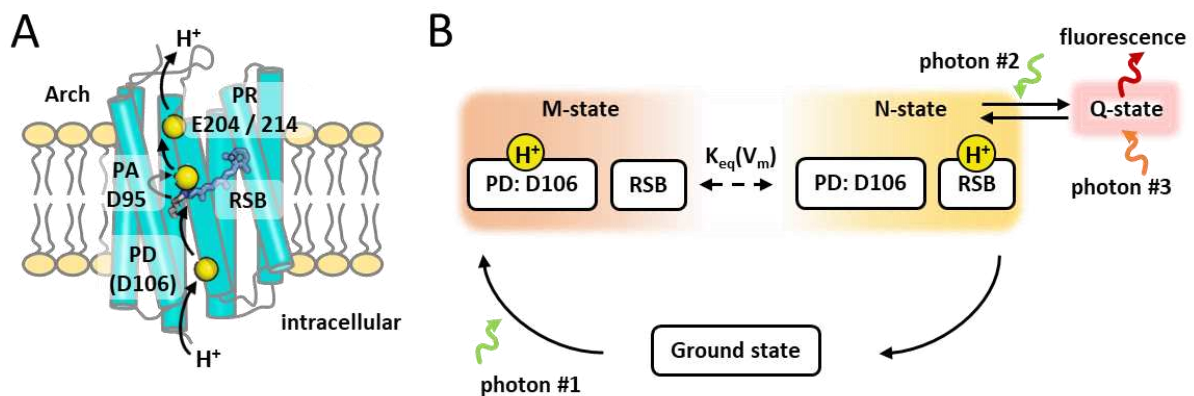

Figure 3. Mechanism of membrane voltage-dependent fluorescence of Arch. (A) Theoretical mechanism of proton transport. Protons are depicted as yellow spheres, proton donor (PD), proton acceptor (PA), and proton release (PR) sites are highlighted. **(B)** Scheme of Arch's voltage sensitivity and fluorescence. Figure prepared by the author according to [40,77].

Molecular dynamics simulations of Arch indicate that residue R92, a homologue of R82 in Bacteriorhodopsin, is the key residue for sensing membrane voltage[75]. This residue switches between inward and outward orientations with respect to membrane voltage[78]. At negative voltage, R92 points towards the protonated RSB and interacts with the negatively charged counterion D95, while at positive voltages it is pointed at the outside of the cell and builds up salt bridges with the proton release site E204 and E214; it directs water molecules away from the protonated RSB and the overall hydrogen bond network is rearranged[75]. The fluorescence intensity is determined by the interaction of the protonated RSB and its counterions (D95 and D222)[75]. Mutations at D95 reflect the protonated state of the counterion, modulating among others the excited-state lifetime, voltage sensitivity

peak absorption wavelength, and pK_a of the RSB and retains D222 as the sole counterion, which in turn rearranges the hydrogen bond connectivity and water content at the active site[34,35,75].

Starting from the prototype Arch(D95N), several further point mutations have been introduced to improve overall brightness, kinetics, and voltage sensitivity (**Figure 4**): Variants QuasAr1 (quality superior to Arch; P60S, T80S, D95H, D106H and F161V) and QuasAr2 (D95Q instead of D95H) showed 10 to 19 times enhanced quantum yields (8×10^{-3} and 4×10^{-3} respectively), exhibited the desired linear voltage-fluorescence dependence, and up to 1.5 times improved voltage sensitivity (90 % $\Delta F/F_0$ per 100 mV in HEK cells and slightly lower sensitivity of 78 % $\Delta F/F_0$ in *C. elegans*[15]) relative to the pump-dead Arch(D95N) mutant[35]. The two constructs differ with respect to the substitution of residue D95 at the protonated RSB counterion position, granting higher quantum yields for QuasAr1 or voltage sensitivity for QuasAr2. In contrast to Arch(D95N), the step response of which was characterized by a 41 ms time constant, variant QuasAr1 showed orders of magnitudes faster step responses, while QuasAr2 provided superior voltage sensitivity, although with slower kinetics and lower absolute brightness[35]. A further screen resulted in the variant Archon with 13 point mutations, exhibiting improved localization, signal-to-noise ratio (SNR), response speed, brightness, and photostability compared to wild-type Arch, but reduced voltage sensitivity compared to QuasAr2 (43 % $\Delta F/F_0$ per 100 mV)[37]. Since larger $\Delta F/F_0$ values are more suitable to precisely detect APs, which is accompanied by an improved SNR, for many experimental questions, a slower sensor is preferable compared to a faster one, albeit with lower sensitivity[79].

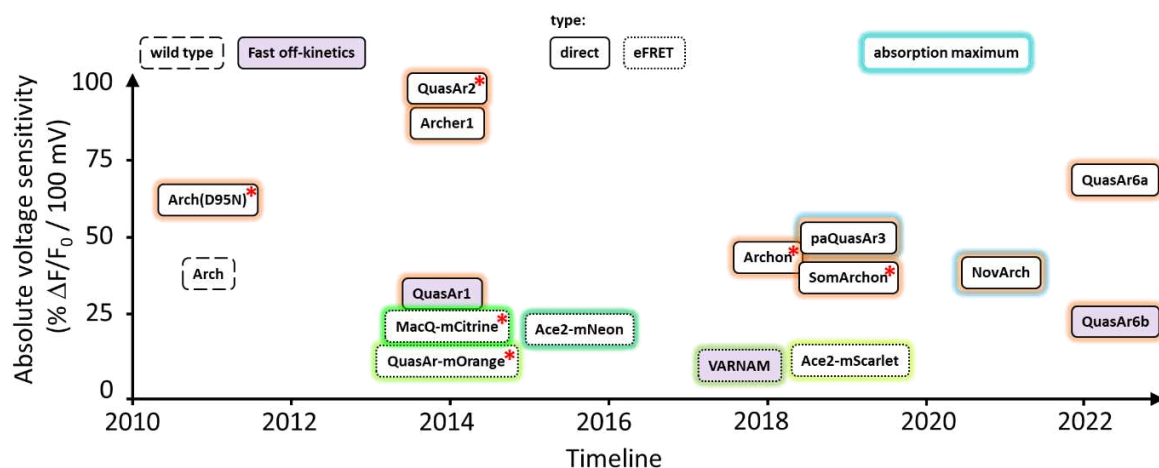**Figure 4. Overview of some of the most relevant rhodopsin-based GEVIs listed by their initial description and voltage sensitivity.** Color coding further subdivides the tools shown by direct readout (fluorophore: retinal) or eFRET sensors (fluorophore: FP; continuous or dotted outline respectively) and absorption maxima. Tools with fast kinetics are highlighted in purple. * Tools covered by this project.

Since rhodopsin-based GEVIs are based on ion pumps, they have not evolved high quantum yields but are rather optimized for ion transport. Therefore, these indicators show a very dim absolute fluorescence, usually orders of magnitude lower than that of fluorescent proteins of the GFP family. To improve brightness levels, fluorescent proteins were fused C-terminally to rhodopsin-based GEVIs, resulting in so-called electrochromic fluorescence resonance energy transfer (eFRET) GEVIs[22,70,80,81]. This is possible, since microbial rhodopsins exhibit absorption spectra that overlap with emission spectra of a variety of fluorescent proteins. Upon depolarization, the retinal absorption non-radiatively quenches the fluorescence of the fused fluorescent protein which is analyzed instead of the dim fluorescence of the rhodopsin as such[22,70]. Here, changes in membrane potential shift the absorption spectrum of retinal and thus modulate FRET efficiency. Possibly, there are also slight voltage-induced conformational changes, which then change the relative orientation of the fluorescent protein to the retinal and consequently the efficiency of quenching process[70]. The eFRET principle is advantageous because orders of magnitude higher intensities are required for direct excitation of voltage-dependent fluorescence. Though showing an improved quantum yield, the overall voltage sensitivity is, however, decreased in eFRET sensors due to the low energy transfer efficiency between large fluorescent proteins and the retinal chromophore[82]. Due to the quenching process, eFRET sensors usually show an inverted voltage dependence. In this regard, an engineering approach resulted in additional positive-going eFRET sensors[77]. eFRET sensors comprise fusions of eGFP, mCitrine, mOrange or mRuby with either Mac, a light-driven proton pump (from *Leptosphaeria maculans*), or QuasAr2, revealing slightly slower kinetics and significantly reduced voltage sensitivity compared to direct readout[22,80]. Latest eFRET reporters involve Ace rhodopsin (from *Acetabularia acetabulum*) as a quencher for mNeonGreen or mRuby (VARNAM, absorption maximum at 565 nm), improving kinetic properties and extending options for multiplexing applications[81,83].

Due to the reduced voltage sensitivities, the lower photostability and the blue-shifted absorption maxima of eFRET sensors, the OVC approach employs a pure rhodopsin GEVI.

1.6   Closed-loop optogenetics

Most applications in optogenetics act in open-loop configuration, as the output of the experiment exerts no influence on any further control action. Neural activity is altered, and the resulting outcome is evaluated subsequent to the experiment (**Figure 5 A**). However, to keep a steady operating status, to avoid disturbances, and to compensate for model uncertainties most engineering but also biological systems rely on feedback control that can control the states of highly complex and dynamical systems. In this regard, closed-loop

systems depend on an error signal – the difference between the desired and the observed output[84,85]. This signal is processed and then used as a feedback to allow a responsive adaptation of the control variable. In this regard, a thermostat without a feedback regulation would be subject to high variability and uncertainty. The same applies to simple, open-loop optogenetic perturbation experiments.
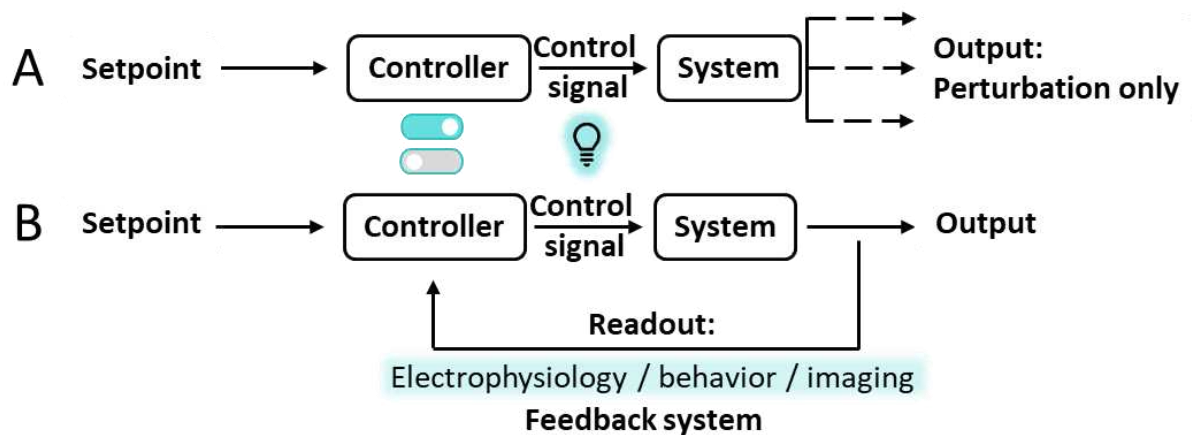

Figure 5. Open- vs. closed-loop optogenetics. (A) Open-loop optogenetic experiments achieve only perturbation of the system, since the control signal is independent of the output variable. Therefore, the stimulus is static and triggered effects on the system are subject to high variability. **(B)** Control signals are modulated online with respect to the output variable. Feedback occurs via readout of either electrophysiologically or optically derived data or based on macroscopic behavior.

Optogenetic stimulation based on simultaneously observed dynamics enables causal investigation of neural circuits, as both effective timing and tailored magnitude of control intervention are crucial for detecting causal relationships[86]. The same principle underlies the common electrophysiological approach of the voltage clamp, where it is used to uncouple the measured membrane potential and assess current-voltage dependencies of voltage-gated ion channels. In closed-loop optogenetics the feedback is automatically generated with real time decisions by electrophysiological, behavioral, or purely optical imaging-based readouts (**Figure 5 B**). Further and in contrast to open-loop approaches, feedback-based systems allow more corrective compensation of variable expression levels[86].

Crucial for the quality of the optogenetic feedback approach are system identification, observability, and controllability[87,88]. Since neuronal activity and circuit plasticity are highly complicated, nonlinear, and nonstationary, while dynamically operating in millisecond timescales on top, it is challenging to build a mathematical model as a basis for the control algorithm[86]. Therefore, concepts like iterative parameter tuning for PID (proportional-integral-derivative) control allow to approximate a system definition (black box system identification) without directly modeling explicit system equations beforehand[89].

Next, controllability and observability are decisive to select optimal control strategies. Controllability accounts for the possibility to force the system into a desired bandwidth of states by using an appropriate control signal[90]. The selection of optogenetic actuators and light intensity and/or wavelength as control signal has a high impact on how controllable the system works: The characteristics of the tools used define the dynamic range and temporal resolution of membrane potential modulation as well as potential spectral crosstalk among the actuators themselves. In short, controllability defines whether desired patterns of neuronal activity or behavior can be triggered with the tools implemented[86]. Observability, however, is related to the sensor of the control system and how accurate the state of the system can be observed[88]. As for controllability, limiting optical crosstalk and kinetics are crucial. Moreover, light scattering and signal-to-noise ratio across an appropriate dynamic range are essential for the quality of the feedback system.

All in all, fully optical, closed-loop optogenetics may provide a testbed for basic-science to assess both neural plasticity and a more nuanced tuning of light stimulus inputs.

1.7   Optical electrophysiology: State of the art

Electrophysiological recordings such as whole-cell patch clamp measurements are the methods of choice to evaluate the electrical characteristics of excitable cells and tissues, comprising both observation of membrane voltage and electric current and manipulation of electrical activity. Ongoing advances in optogenetics and microscopic techniques, however, may take electrophysiology to a completely new level, by combining genetically encoded voltage indicators with optogenetic actuators resulting in purely optical electrophysiology[23]. In this regard, no approach other than optogenetics has combined the synergistic advantages of high spatiotemporal resolution, specificity, and ease of application. To date, there are many approaches pursuing this goal, among others by either unidirectional steering via a single optogenetic tool and GEVI-based observation of neural activity or bidirectional modulation but electrode-based readout, in open- or closed-loop configuration (**Figure 6**)[35,36,91–93]. The requirements for optogenetic tools to be used are high: Narrow absorption bands and appropriate spectral separation to minimize spectral crosstalk, high photostability to allow long-term modulation and monitoring, fast kinetics to precisely track and manipulate electrical activity, as well as matching efficiency to allow multiplexing of actuators.

Noteworthy is the so-called (i)-Optopatch method, for which either the specifically engineered, blue-shifted depolarizer ChR CheRiff or the hyperpolarizer ACR2 (inhibitory-Optopatch) were combined with the GEVI QuasAr2[35,36]. By using Optopatch, researchers were able to characterize APs in dendritic spines, synaptic transmission, and highly

temporally resolved details of action potential propagation, as well as simultaneous spiking of multiple neurons of a circuit[35]. The method is now commercially used in high-throughput screening of neurons[94]. A further approach – optoclamp – employs ChR2 and NpHR in a bidirectional closed-loop setup and extracellular microelectrode arrays for readout. The technique clamps spiking activity of neuron populations, but not membrane potential, to selected levels over long time periods of up to days[91]. A further technique called light-induced electrophysiology (LiEp) involves both bidirectional optogenetic modulation, using ChR2 and ArchT, and GEVI-based voltage readout with QuasAr1. However, no closed-loop feedback control was implemented for this system[92]. LiEp was demonstrated to report on dose-dependent drug interactions and served as screening platform to study voltage-gated calcium channels. Last, an closed-loop optical dynamic clamp (ODC) employed ArchT as optogenetic actuator to imitate potassium currents in immature cardiomyocytes as a drug screening platform, but still relied on electrode-based voltage readout[93].
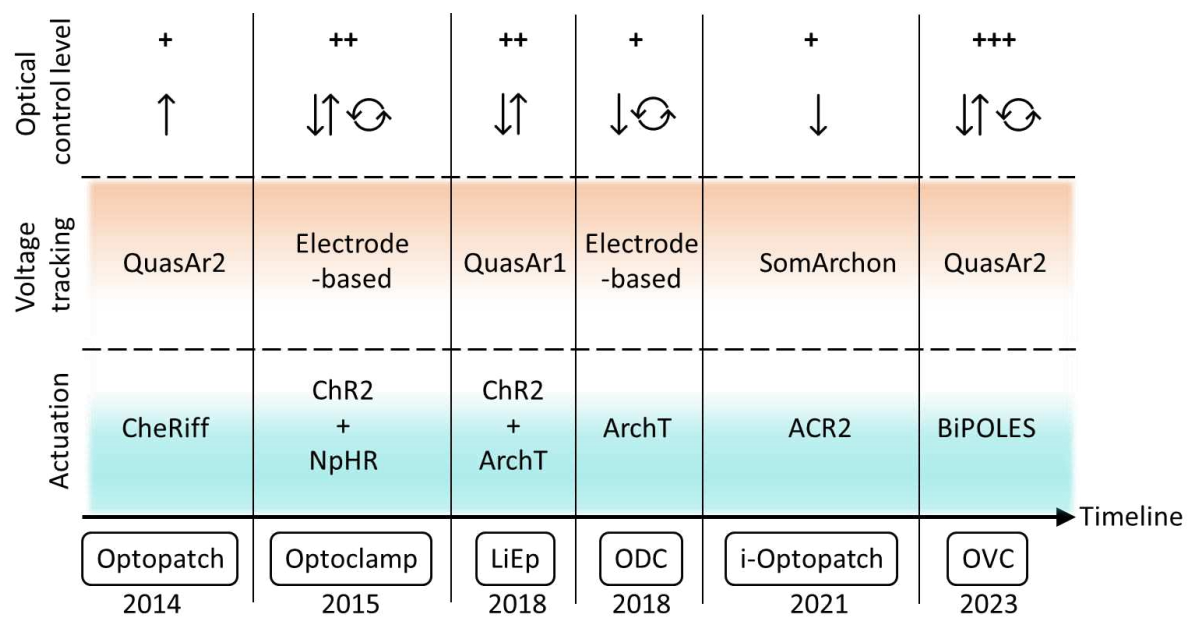
Figure 6. Methods of (all-)optical electrophysiology listed in chronological order of their first description. The technologies are specified according to the choice of actuation and voltage tracking tools and then evaluated in terms of the level of pure optical control achieved. One + was scored each for the use of a GEVI instead of an electrode-based approach, the use of two counteracting tools instead of unidirectional modulation (indicated by one or two arrows; directed up- and downwards for de- and hyperpolarizing respectively), and lastly for the presence of real-time feedback control (indicated by cycle symbol).

All methods presented feature certain basic building blocks that are indispensable for achieving the overall goal of an all-optical voltage clamp: A combination of bidirectional actuators, a voltage sensor that is also genetically encoded, and a closed-loop feedback system that ultimately provides true control over the cell of interest. None of the aforementioned techniques, however, meets all three requirements simultaneously. First,

a system employing two opposing optogenetic tools and a GEVI with no feedback control, allows bidirectional steering, but it is still limited to static optical perturbation only, since the enclosing circuit can adapt quickly. Second, a system involving a feedback control mechanism but only one optogenetic tool, falls short in terms of temporal resolution, as the opposing direction is not subject to any temporally precise control and is limited in its dynamic range. Third, systems that meet the criteria of bidirectionality and feedback control, but are still dependent on electrodes, cannot be considered as true optical electrophysiology in the strict sense. The OVC is the first proof-of-concept methodology to combine all required elements of optical voltage clamping[8].

1.8   All-optical adaptation of the electrophysiological voltage clamp

Originally developed by Hodgkin, Huxley, and Katz, the voltage clamp technique paved the way for neurophysiological research[4,95]. Adapted from engineering control theory and signal processing, its central logic involves closed-loop feedback control as an instrument for system characterization[96]. Biological systems are highly complex and inevitably subject to internal feedback mechanisms (e.g., parameters dependent on activity history, time-variance), are often based on non-linear components, and system output is subject to stochastic processes. This results in dynamic instabilities, mirrored by intricate trajectories of observable system outputs[96]. By introducing the voltage clamp technique, this kind of highly complex output was stabilized through feedback control. Here, the stabilized membrane voltage simplified the observation of membrane conductances, where the feedback current allowed to model the underlying system[96]. Unlike conventional experiments or open-loop approaches like the current clamp method, this control approach strictly determines the system's output, while it records the required input signal and thus compensates for non-linearity and time variance.

While the classical approach of electrophysiology provides superior temporal resolution and thus information content, it is restricted by its invasiveness, specificity, and technical demand. Therefore, a desirable achievement would be to synergistically combine the advantages of both approaches by incorporating suitable optical elements that take the function of the electrodes and be integrated into an adapted all-optical feedback control system (OVC)[8]. Whereas the classical voltage clamp uses the membrane potential amplifier to detect the membrane voltage, the OVC makes use of the GEVI QuasAr2 (**Figure 7 A**), that performed best in a preceding comparative study (see above: Chapter 1.5)[8,15]. Here, it was important to choose the sensor with the greatest voltage sensitivity to compensate for possible unwanted motion artifacts, since the feedback control reacts sensitively to small changes in membrane potential. The protein's voltage-dependent fluorescence is recorded

via a sensitive (sCMOS or EMCCD) camera that feeds grey values into a control algorithm, consisting of an I(integral)-controller and a decision tree algorithm[8]: The preselected holding fluorescence value ($\Delta F/F_{0\ holding}$) is compared to the actual fluorescence level at each timepoint. Based on this deviation, the wavelength of a monochromator is adapted and amplified with respect to the deviation size, clamping the fluorescence into tight margins. The sign of the error at each timepoint determines whether the wavelength is increased or decreased. This is processed by the decision tree algorithm and based on specifications of the optogenetic tools used. Moreover, a preceding calibration phase of each OVC recording is used to estimate QuasAr2's bleaching behavior, precisely reproducing the actual fluorescence values online for the duration of the measurement.

Similar to the role of the current passing electrode (**Figure 8 A**), the OVC employs the bidirectional tandem protein BiPOLES (**Figure 8 B**) to transmit wavelength feedback to the cell of interest and hold its membrane potential at a desired level[8,11].
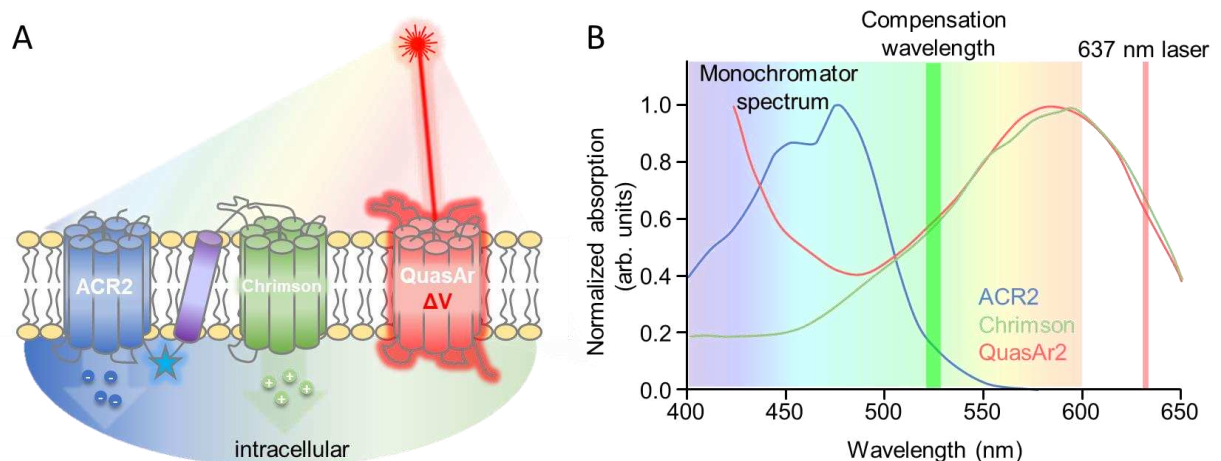

Figure 7. Molecular OVC components and their spectral properties. (A) The OVC[8] involves two counteracting optogenetic tools (BiPOLES – consisting of the hyperpolarizer ACR2 and the depolarizer Chrimson) for bidirectional modulation of the membrane potential as well as a voltage sensor (QuasAr2). QuasAr2's voltage-dependent fluorescence is stimulated via a 637 nm laser and BiPOLES activity is modulated over a wavelength spectrum from 400 to 600 nm via a monochromatic light source. Blue star: mCerulean. **(B)** Absorption spectra of all components[21,28,35]. Wavelengths of the light sources used as specified.

BiPOLES consists of the two equally efficient optogenetic tools Chrimson and ACR2, functioning counteractively as de- and hyperpolarizer, respectively (**Figure 7 A**, single tools are described in underline chapter 1.4)[11]. As it shows only minor spectral overlap (**Figure 7 B**) and matching photocurrent amplitudes, this tool combination is predestined to be used for purely optical and bidirectional tuning of membrane potential, allowing independent, dual-color activity modulation. Even though sharing comparable absorption maxima (**Figure 7 B**), optical crosstalk between QuasAr2 and Chrimson is bridged by the application of a compensatory wavelength at the beginning of each measurement[8].

Further, the tandem character of BiPOLES guarantees a fixed 1:1 ratio of expression levels of the two actuators and overcomes initial performance issues with unbalanced separate expression.
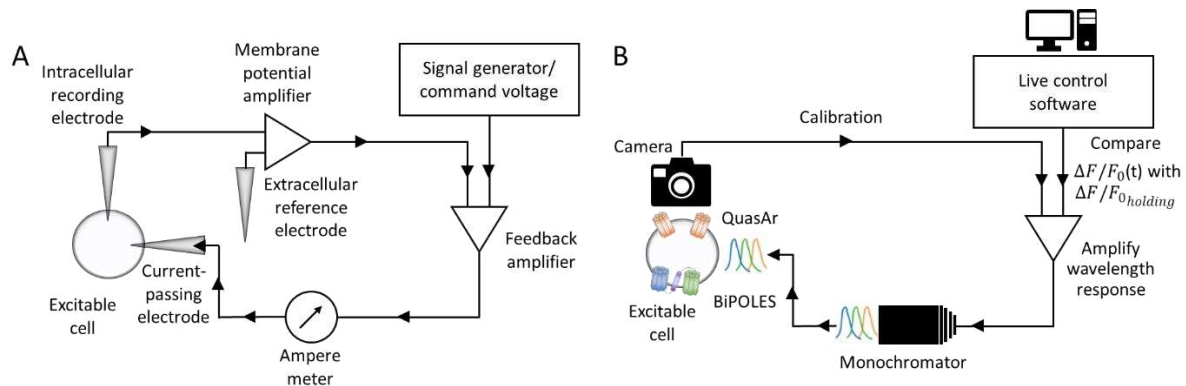

Figure 8. Electrophysiological vs. optical approach of the voltage clamp technique. **(A)** Electrophysiology: The voltage clamp operates by a negative feedback mechanism. The membrane voltage is detected by the membrane potential amplifier and passed on to the feedback amplifier. The feedback amplifier calculates the error between the observed membrane voltage and the command voltage that is determined by the signal generator and is set prior to the experiment. Finally, the signal is amplified and fed back to the cell of interest via the current passing electrode (scheme generated by author according to online media: https://tinyurl.com/bdfvh7ra). **(B)** All-optical adaption of the voltage clamp (OVC approach[8]): The function of the electrodes is adopted by optical elements. A sensitive camera records the fluorescence of the GEVI QuasAr2, while a live control software processes incoming grey values, calculates error signals, and adapts the output variable wavelength accordingly. Eventually, feedback of light is generated and sent back to the optogenetic actuation pair BiPOLES to keep the membrane potential at a desired level.

Calibration of the OVC system is provided by simultaneous patch clamp recordings that relate feedback wavelength to currents and fluorescence levels to membrane voltage and demonstrates the accessible voltage range[8]. Among others, this allowed to translate optical wavelength/fluorescence relations into real current/voltage (I-V) relationships. This way, the OVC enables the assessment of altered cell physiology similar to its electrophysiological counterpart. The range of the OVC software further allows to dynamically suppress distinct action potentials (**Movie 3**), to adjust the desired fluorescence level live during the measurement (**Movie 4**), as well as to use the OVC components as an optical current clamp.

1.9   *C. elegans* as a testbed for all-optical electrophysiology

Caenorhabditis elegans is a non-parasitic, free-living nematode, occurring in soil, compost piles, or rotten fruit of temperate climate zones, measuring about 1 mm in size[97,98]. Various unique features make *C. elegans* one of the most broadly studied model animals in the scientific fields of developmental-, cell- and – since it belongs to the simplest animal species

with a nervous system – neurobiology. With its well-defined nervous system and fixed number of neurons the worm is predestined for neuroscientific research, but it is its transparency and thin body that make it a perfect fit for optogenetics[99]. Not only is its connectome completely described, but it was even the first multicellular organism with a fully sequenced genome, which enables researchers to study causal connections in neural circuitry and to straightforwardly achieve genetic modifications[100,101]. Low cost of cultivation and uncomplicated maintenance as well as the option for long-term preservation contribute decisively to its immense popularity in basic research[98].

The simple anatomy of the worm comprises a mouth, a pharynx, intestine, and gonads (**Figure 9 A**). The typical sinusoidal locomotion pattern is orchestrated by four longitudinal bands of body wall muscles (BWMs) along the dorsal and ventral sides of the nematode, that are innervated by excitatory cholinergic and inhibitory GABAergic motor neurons. Interestingly, the connection between muscles and neurons is established by the muscle cell itself via membranous projections, called muscle arms. The nervous system mainly consists of major and minor ventral and dorsal nerve cords, respectively, and a brain-like central ganglion (nerve ring) at the head part (**Figure 9 B**)[98].
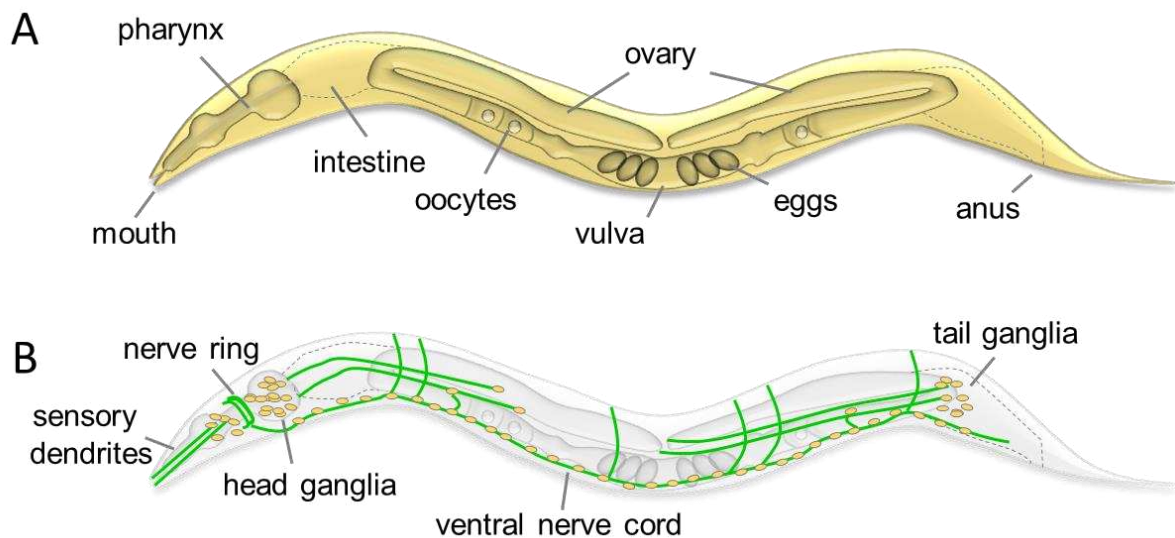
Figure 9. Anatomy of *C. elegans*. (A) General anatomy. **(B)** Nervous system. Figure by the author according to [102,103].

For the characterization of new optogenetic tools, expression in BWMs is advisable, since muscle cells are large and easily accessible, hence allowing readily evaluable behavioral experiments and patch clamp recordings[99]. Similarly, expression in cholinergic neurons allows straightforward execution of behavioral experiments due to direct innervation of BWMs. By analyzing the body length or swimming behavior of the animals upon light stimulation, conclusions can be drawn about the strength of the related photocurrent, the kinetics, and action spectra of the respective tool[9,99]. Activation of a depolarizing tool

causes contraction of the BMWs, accompanied by a reduction of the body length, whereas a hyperpolarizing tool has the opposite effect. The swimming frequency decreases or stops entirely under the influence of light-induced activation of ChR2 and its derivatives in BWMs and represents a very sensitive readout. By expressing optogenetic actuators in the pharynx, the pumping behavior can be actively paced and easily tracked macroscopically[104,105]. Also, the expression of voltage sensors can be easily implemented in the aforementioned tissues: Due to their size, the expression of GEVIs reaches high brightness and the relative changes of fluorescence can be observed clearly[15].

Also, for the establishment of the optogenetic voltage clamp in the living animal, *C. elegans* proved to be an ideal testbed[8]: Both pharyngeal and body wall muscles fire significantly slower action potentials compared to mammalian cells and even neurons exhibit exceptionally slow gradual or – in some cases – action potentials[8,15,106–108]. This feature allows the OVC to dynamically track and suppress individual action potentials, while running at a comparably slow maximal sampling rate of 100 Hz with its current molecular and computational components[8]. Further, the resting potential of *C. elegans*' BWMs is sufficiently distant to the reversal potentials of the ions, which are conducted by the applied optogenetic tools, allowing the tandem protein to effectively steer membrane potential bidirectionally[108].

In addition to the characterization of new tools and the development of all-optical electrophysiology, another focus of this research was on direct application to address specific questions in *C. elegans*. By using the tools presented here – both single expression and expression in combination with voltage sensors (e.g., in the context of OVC application) – inferences could be made about ion channel function (voltage-gated calcium channel: *egl-19* mutant[8,15]), altered cell physiology of different mutants (neurotransmission mutants: *unc-13*[8] and *rimb-1*[16]), and the function of specific neurons (enteric motor neuron DVB[8], motor- and interneurons of the locomotion circuit: AS motorneurons[14] and RIM interneurons[15]).

2. Publications

2.1   Summaries of publications and respective author contributions

All-optical closed-loop voltage clamp for precise control of muscles and neurons in live animals

In this study[8], two opposing optogenetic tools for de- and hyperpolarization (BiPOLES) were combined with a genetically encoded voltage indicator (QuasAr2). Embedded in a live, closed-loop feedback control system, this novel, purely optical approach (optogenetic voltage clamp – OVC) allowed reliable, bidirectional control of QuasAr2's voltage-dependent fluorescence, thus clamping target cells to desired potentials. The OVC was established in various muscular and neural tissues of *C. elegans* and then transferred to rat hippocampal organotypic slice culture. In the worm, this technique allowed generation of all-optical I-V-relationships, when calibrated to electrically recorded membrane voltages and currents. This way, the OVC reported on altered cell physiology and ion channel properties in mutants. Further, it allowed to dynamically clamp distinct action potentials in the DVB neuron and pharyngeal muscle. The OVC is a proof-of-concept method, combining the control capabilities of electrophysiological recordings with the non-invasive character of imaging and clear the way for true all-optical control in behaving animals.

The author contributed to the conceptualization of the project and was responsible for performing all OVC measurements, coding the software, creating all graphs and figures, and the writing of the original manuscript draft (**Table 1**).

Table 1. List of figures and detailed breakdown of the author's contribution. Publication: "All-optical closed-loop voltage clamp for precise control of muscles and neurons in live animals"[8].

# Figure	Description	Author's contribution
1	Components, setup, and functionality of the OVC	Panels **A-H**
2	Bi-directional optical clamping and calibration of membrane voltage and currents in BWMs	Panels **A-L** (patch clamp recordings by Jana Liewald)

3	Assessing altered cell physiology in mutants affecting synaptic transmission and ion channels, using the OVC	Panels **A, B, G-M**
4	Bi-directional clamping of voltage-dependent fluorescence in *C. elegans* neurons	Panels **A-G**
5	Establishing the OVC in rat hippocampal pyramidal neurons	Panels **A-H** (in cooperation with Silvia Rodriguez-Rozada)
6	All-optical clamping of APs in pharyngeal muscle	Panels **A-G**
7	All-optical clamping of APs in the enteric motor neuron DVB	Panels **A-D**
E.D. 1	Setup of the OVC software and control parameters	Panels **A-H**
E.D. 2	Implementation of a PID controller with Kalman filter	Panels **A-F** (cooperation with Artur Bessel)
E.D. 3	Unidirectional steering of membrane voltage	Panels **A-G**
E.D. 4	Testing different combinations of depolarizing and hyperpolarizing actuators	Panels **A-E**
E.D. 5	BiPOLES activation by 637 nm laser light and calibration wavelength have no adverse effects on muscle function and locomotion	Panels **A-I** (C-E in cooperation with Christin Wirt)
E.D. 6	Performance assessment, and long-term action of the OVC	Panels **A-L**
E.D. 7	Simultaneous patch clamp and fluorescence measurement, normal membrane voltage behavior in BiPOLES-activated BWMs, no progressive error following calibration phase	Panels **A-K** (patch clamp recordings by Jana Liewald)
E.D. 8	Optical pseudo-I/V curve measurements	Panels **A-E**
E.D. 9	Software for 'optical current clamp', and software for 'on-the-run' live voltage adjustment	Panels **A-J**
E.D. 10	Voltage imaging and OVC measurements in pharyngeal muscle and the motor neuron DVB	Panels **A-G**

Microbial Rhodopsin Optogenetic Tools: Application for Analyses of Synaptic Transmission and of Neuronal Network Activity in Behavior

This book chapter[13] sheds light on the variety of rhodopsin-based optogenetic tools, recent advances of their application in *C. elegans,* and guidelines for experimental procedure design. Among others, it discusses the use of rhodopsin-based nucleotidyl cyclases and genetically encoded voltage or calcium sensors, as well as combinatory approaches with further actuators, e.g., cGMP-gated cation channel TAX-2/TAX-4 or excitatory tools for upstream neuronal stimulation respectively. The author contributed the text passages on step-function opsins, ACRs, and GEVIs (**Table 2**).

Table 2. List of figures and detailed breakdown of the author's contribution. Book chapter: "Microbial Rhodopsin Optogenetic Tools: Application for Analyses of Synaptic Transmission and of Neuronal Network Activity in Behavior"[13].

# Figure	Description	Author's contribution
1	Photocycle of Channelrhodopsin	-
2	Genetically encoded voltage sensors based on microbial rhodopsins	Figure prepared by author
3	Cyclase rhodopsin-based two-component optogenetic systems for de- and hyperpolarization	-

BiPOLES is an optogenetic tool developed for bidirectional dual-color control of neurons

In this study[11], a novel optogenetic tandem tool was developed, consisting of the hyperpolarizer ACR2 and the depolarizer Chrimson. Based on their minor spectral overlap, equal efficiency, and high sensitivity, this tool configuration allowed dual color, bidirectional stimulation with single- or two-photon excitation in various model animals.

The author contributed behavioral BiPOLES measurements on bidirectional control of body length in *C. elegans*, providing data on maximum behavioral effects at absorption maxima of Chrimson and ACR2 and across a whole color spectrum of 400 to 640 nm (**Table 3**).

Table 3. List of figures and detailed breakdown of the author's contribution. Publication: "BiPOLES is an optogenetic tool developed for bidirectional dual-color control of neurons"[11].

# Figure	Description	Author's contribution
1	Development of BiPOLES and biophysical characterization	-
2	Expression and functional characterization of BiPOLES and somBiPOLES in hippocampal neurons	-
3	somBiPOLES allows potent dual-color spiking and silencing of the same neurons using red and blue light, respectively	-
4	Applications of BiPOLES: bidirectional control of neuronal activity, optical voltage tuning, and independent dual-color excitation of two distinct neuronal populations	-
5	Bidirectional control of neuronal activity with somBiPOLES using dual-color two-photon holography	-
6	BiPOLES allows bidirectional modulation of neuronal activity in *C. elegans* and *D. melanogaster*	Panel **A-B**

7	BiPOLES and somBiPOLES allow bidirectional modulation of neuronal activity in mice and ferrets	-
E.D. 1	Biophysical characterization of different ACR CCR tandem constructs	-
E.D. 2	Comparison of BiPOLES to established bidirectional optogenetic tools in HEK293 cells	-
E.D. 3	Biophysical characterization of BiPOLES and differential expression of BiPOLES and somBiPOLES in CA1 pyramidal neurons	-
E.D. 4	Characterization of Chrimson mediated currents and spiking in CA1 pyramidal cells.	-
E.D. 5	Quantification of som Gt ACR2 mediated photocurrents in CA1 pyramidal cells	-
E.D. 6	Basic neuronal parameters of WT, BiPOLES and somBiPOLES expressing CA1 pyramidal cells.	-
E.D. 7	Optical spiking parameters for BiPOLES and somBiPOLES	-
E.D. 8	Characterization of bidirectional optogenetic manipulat ion of neuronal 138 activity with eNPAC2.0	-
E.D. 9	CheRiff exhibits optical excitation restricted to the blue spectrum	-
E.D. 10	Design of the dual laser 2 photon holography setup	-
E.D. 11	Virally expressed CaMKII somBiPOLES enables bidirectional control of activity in projection neurons	-
E.D. 12	BiPOLES and controls in *C. elegans* and *D. melanogaster*	Panels **A-B**
E.D. 13	somBiPOLES controls in LC neurons	-
E.D. 14	Monte Carlo simulation of light propagation in the mouse brain to estimate somBiPOLES performance in vivo	-
E.D. 15	Virally expressed mDlx BiPOLES enables bidirectional control of GABAergic neuronal activity.	-

RIM and RIM-binding protein localize synaptic CaV2 channels to differentially regulate transmission in neuronal circuits

Next to SNARE complexes that anchor synaptic vesicles to the plasma membrane and prepare vesicle fusion, voltage-gated Ca^{2+} channels are kept solid by a complex of RIM and RIM-binding proteins, being part of the dense projection in *C. elegans*. This study[16] reports on aspects of this machinery responsible for synaptic vesicle fusion in *C. elegans.* It characterizes phenotypes of *rimb-1* mutants and interactions with the CaV2 VGCC α-subunit at neuromuscular junctions in cholinergic and GABAergic neurons, via behavioral,

imaging-based, and electrophysiological experiments, while assessing the ultrastructural level by electron microscopy. As a result, *rimb-1* deletion mutants displayed mild behavioral phenotype with impaired cholinergic transmission, while *unc-10* mutants lacking RIM, as well as *unc-10; rimb-1* double mutants showed much more pronounced deficits. Voltage imaging of *rimb-1* animals revealed reduced depolarization in response to cholinergic stimulation with ChR2, pointing at a delay and impairment in vesicle release.

The author contributed with comparative voltage imaging experiments of wild type and *rimb-1* mutant animals (**Table 4**).

Table 4. List of figures and detailed breakdown of the author's contribution. Publication: "RIM and RIM-binding protein localize synaptic CaV2 channels to differentially regulate transmission in neuronal circuits"[16].

# Figure	Description	Author's contribution
1	UNC-10/RIM and RIMB-1/RIM-binding protein affect UNC-2/CaV2 function in *C. elegans* (motor) neurons.	-
2	*rimb-1* mutants exhibit defective cholinergic transmission, locomotion and muscle activation	-
3	*rimb-1* and *unc-10*/RIM mutants exhibit increased and reduced cholinergic transmission at the NMJ	-
4	Parameters of evoked transmission reveal delayed postsynaptic current onset in *rimb-1* mutants	Panel **G**
5	Lack of RIMB-1 reduces transmission from GABAergic motor neurons.	-
6	Lack of GABAergic transmission reverts increased cholinergic transmission in *rimb-1* mutants	-
7	Electron microscopy analysis of photostimulated cholinergic *rimb-1* synapses	-
8	Untethering the CaV2 VGCC alters synaptic transmission, exacerbated by *rimb-1* deletion	-
9	Acute photodegradation of the CaV2 β-subunit CCB-1 affects behavior and reduces synaptic transmission	-
10	CaV2/UNC-2 channels are reduced at synapses in *rimb-1* mutants and after acute photodegradation of the CCB-1 β-subunit	-
E.D. 1	Comparing two *rimb-1* alleles	-
E.D. 2	*rimb-1* mutants have no post-synaptic defect in muscular nAChRs, and normal muscle excitability.	-
E.D. 3	GABAergic transmission at the NMJ in *rimb-1* mutants	-
E.D. 4	*rimb-1* defects in evoked NMJ transmission at -10 mV	-

E.D. 5	Repeated 2 Hz stimulation of cholinergic and GABAergic synapses reveals no effect on depression or facilitation	-
E.D. 6	Ultrastructural parameters of *rimb-1* mutant synapses	-
E.D. 7	Differential effects of untethering and deleting CaV2/UNC-2 VGCCs on induced behavior and basal synaptic transmission	-

Rhodopsin-based voltage imaging tools for use in muscles and neurons of *Caenorhabditis elegans*

In this study[15], various genetically encoded voltage indicators were implemented and characterized in *C. elegans*, namely Arch(D95N), Archon, QuasAr2, MacQ-mCitrine, and QuasAr-mOrange. The sensors reported on voltage dynamics, including action potentials, in BWMs, the pharynx, and RIM neurons and mirrored ChR2- or ACR2-mediated de- or hyperpolarization respectively. Dim ATR fluorescence could be boosted by 250-fold using the retinal analog dimethylaminoretinal (DMAR). In the pharynx, simultaneous sharp electrode recordings confirmed optical derived observations and analysis of optical recordings allowed the generation of all-optical electropharyngeograms (EPGs), visualizing compartmentalized repolarization events.

The author was responsible for voltage imaging experiments in BWMs and RIM neurons with QuasAr2 and Archon, as well as for combined optogenetic stimulation with ChR2 or ACR2 in BWMs (**Table 5**).

Table 5. List of figures and detailed breakdown of the author's contribution. Publication: "Rhodopsin-based voltage imaging tools for use in muscles and neurons of *Caenorhabditis elegans*"[15].

# Figure	Description	Author's contribution
1	Expression of rhodopsin voltage sensors in *C. elegans* muscle cells.	Panel **A**
2	Rhodopsin sensors detect intrinsic voltage changes in muscles and neurons	Panels **C, D, F-L**
3	Electrical and voltage-sensor signals in BWMs, induced by optogenetic manipulation of cholinergic MNs	Panels **A-I**
4	Arch(D95N) and eFRET voltage-sensor signals quantified in PMs during pumping	-
5	Pharyngeal AP and pump parameters quantified by automated analysis in WT and L-type VGCC g.o.f. mutants	-
6	Pharyngeal AP repolarization occurs in a spatiotemporally compartmentalized fashion	Panel **B** scheme
E.D. 1	Summary of individual and mean voltage fluorescence traces for various rhodopsin	Panels **A-J**

	voltage sensors expressed in BWMs	
E.D. 2	Neuronal activity can be observed by Ca^{2+}- and QuasAr voltage imaging	Panels **B, C**
E.D. 3	Comparison of voltage traces recorded using rhodopsin and eFRET voltage sensors, as well as by sharp electrodes in the pharynx during pump trains in single animals, and across animals	-
E.D. 4	Voltage and pump signal rise and decay times, automatically determined for pharyngeal APs and pump events measured with rhodopsin and eFRET sensors	-
E.D. 5	Comparison of voltage and pump parameters measured in mutants and in response to nemadipine-A (NemA) in the pharynx	-
E.D. 6	Comparison of simultaneous EPG and MacQ-mCitrine fluorescence measurements in presence and absence of ATR	-

Optogenetischer Werkzeugkasten für neue experimentelle Ansätze

This review article[12] briefly outlines the development of optogenetics and describes several newly discovered rhodopsins (including ACRs) and targeted engineered variants (including SFOs and FLInChR). In addition, the article discusses several behavioral assays in *C. elegans* and the extent to which expanding the toolbox is helping to address increasingly complex questions and experimental requirements.

The author wrote the original draft and prepared all figures of this review article (**Table 6**).

Table 6. List of figures and detailed breakdown of the author's contribution. Review article: "Optogenetischer Werkzeugkasten für neue experimentelle Ansätze"[12].

# Figure	Description	Author's contribution
1	Rhodopsinbasierte Optogenetik	Panels **A-C**
2	FLInChR (full-length inversion of ChR)	Panels **A-D**
3	Optogenetik in *Caenorhabditis elegans*	Panels **A-C**

Expanding the Optogenetics Toolkit by Topological Inversion of Rhodopsins

In this study[10], a novel hyperpolarizing tool was engineered by topological inversion of ChR2. This was accomplished via the fusion of ChR2(E123T;H134R;T159C) to the truncated transmembrane helix of Neurexin-1 beta, retaining its signal sequence. In

contrast to its template protein, Full-length-inverted-channelrhodopsin-2 (FLInChR) works as cation pump with a red-shifted absorption maximum.

The author contributed with behavioral body length measurements in *C. elegans*, providing data on maximum effects at the absorption maximum of FLInChR (**Table 7**).

Table 7. List of figures and detailed breakdown of the author's contribution. Publication: "Expanding the Optogenetics Toolkit by Topological Inversion of Rhodopsins"[10].

# Figure	Description	Author's contribution
1	A Molecular Engineering Approach to Topological Inversion of Rhodopsins	
2	Opsin Inversion Generates Novel Functionality	
3	Opsin Inversion Is Compatible with Regular Ionic Flux	
4	FLInChR Mediates Efficient Suppression of Spiking	
5	FLInChR Is an Effective Light-Dependent Ihibitor for Circuit Dissection	
E.D. 1	Inverted ChR ET/TC Displays Robust Intracellular Trafficking	
E.D. 2	Inversion Is Robust to the Choice of N-Terminal Linker Domain	
E.D. 3	FLInChR Mediates Efficient Suppression of Spiking in Cortical Neurons	
E.D. 4	FLInChR-Mediated Photocurrent Shows Moderate Desensitization	
E.D. 5	FLInChR-Mediated Hyperpolarization of Body Wall Muscles Induces Body Elongations in *C. Elegans*	Panels **A, B**

Functionally asymmetric motor neurons contribute to coordinating locomotion of *Caenorhabditis elegans*

This study[14] assessed the role of AS motor neurons (MNs) in the ventral nerve cord (VNC) locomotor circuit of *C. elegans*. In contrast to typical cholinergic VNC MNs that orchestrate undulatory movement by innervating opposing muscles, AS MNs stand out due to asymmetric innervation of muscles and other MNs. Making use of optogenetic tools in behavioral assays and calcium imaging in both immobilized and freely moving animals, their function to coordinate dorsoventral undulation as part of anterior-posterior wave propagation was observed. Further, AS MNs were found to integrate signals within forward and backward movement and to be functionally linked to premotor interneurons via gap junctions.

The author contributed the implementation of ACR1 in *C. elegans* (**Table 8**).

Table 8. List of figures and detailed breakdown of the author's contribution. Publication: "Functionally asymmetric motor neurons contribute to coordinating locomotion of *Caenorhabditis elegans*"[14].

# Figure	Description	Author's contribution
1	Specific photodepolarization of AS MNs via ChR2 leads to body contraction, increased bending angles and reduced speed in freely moving *C. elegans*	-
2	Photodepolarization of AS MNs causes transient activation of dorsal and simultaneous inhibition of ventral BWMs, and a dorsal bias in freely crawling animals	-
3	Optogenetic ablation and chronic hyperpolarization of AS MNs disrupts the locomotion pattern	-
4	Acute optogenetic hyperpolarization of AS MNs ceases locomotion, causes disinhibition of ventral BWM via GABAergic VD MNs, and blocks propagation of the locomotion body wave	-
5	AS MNs show oscillatory Ca2+activity in moving animals	-
6	Reciprocal and asymmetric mutual activation of AS MNs and forward and reverse PINs, AVB and AVA	-
7	Models summarizing findings of this work	-
E.D. 1	Expression of ChR2 can be restricted to AS MNs	-
E.D. 2	Local AS neuron activation affects body length	-
E.D. 3	Specific photodepolarization of AS MNs via Chrimson leads to body contraction, increased bending angles and reduced speed in freely moving *C. elegans*	-
E.D. 4	Optogenetic inactivation and HisCl1-induced hyperpolarization of AS MNs affects locomotion speed and bending angles	-
E.D. 5	Local stimulation of AS MNs in different body segments	-
E.D. 6	AS MNs are simultaneously activated by photostimulation of the AVA and AVB PINs	-

Rhodopsin optogenetic toolbox v2.0 for light-sensitive excitation and inhibition in *Caenorhabditis elegans*

In this study[9], a variety of new naturally occurring and engineered optogenetic tools for de- and hyperpolarization were implemented and characterized in *C. elegans*. Regarding long-term stimulation, the ChR2 variants Quint and ChR2-XXL provided muscle activation

in the minute to hour range, responded with exceptional light sensitivity, and allowed repetitive activation. For hyperpolarization, the anion channelrhodopsins ACR1 and ACR2 demonstrated strong behavioral effects, as well as fast kinetics and large photocurrents.

The author contributed to the conceptualization of the project and writing of the original manuscript draft and was responsible for performing most of the behavioral measurements (**Table 9**).

Table 9. List of figures and detailed breakdown of the author's contribution. Publication: "Rhodopsin optogenetic toolbox v2.0 for light-sensitive excitation and inhibition in *Caenorhabditis elegans*"[9].

# Figure	Description	Author's contribution
1	ChR2 variants expressed in body-wall muscle cells localize to membranes	Part of the fluorescence micrographs
2	ChR2 variants expressed in body-wall muscle cells enable prolonged depolarization and body contractions	Panels **A-F**
3	ACRs mediate strong hyperpolarization and body elongation	Panels **A-K**
4	ACR1 and ACR2 mediate large photocurrents and hyperpolarization in patch clamped BWMs	-
5	Evaluation of de- and hyperpolarizers characterized in this paper	Panels **A, B**
E.D. 1	ChR2 variants expressed in body-wall muscle cells	-
E.D. 2	Description of behavioral assays in *C. elegans* expressing de- or hyperpolarizing rhodopsin-based tools in body-wall muscle cells	Figure prepared by author
E.D. 3	ChR2 variants expressed in body-wall muscle cells induce body contractions depending on the light intensity used	Panel **B**
E.D. 4	Quint induces body contractions over a broad wavelength spectrum	Panels **A-C**
E.D. 5	ACR variants induce body elongations depending on the used light intensity	Panels **A-H, J, K**
E.D. 6	Membrane potential shift following ACR-mediated hyperpolarization may indicate action of Cl^- efflux pumps	-

2.2   All-optical closed-loop voltage clamp for precise control of muscles and neurons in live animals

The following pages contain the published version of the research article "All-optical closed-loop voltage clamp for precise control of muscles and neurons in live animals"[8]. Material from: Bergs, A.C.F., Liewald, J.F., Rodriguez-Rozada, S. *et al.* All-optical closed-loop voltage clamp for precise control of muscles and neurons in live animals. *Nat Commun* **14**, 1939 (2023). https://doi.org/10.1038/s41467-023-37622-6. Reproduced with permission from Springer Nature.

All-optical closed-loop voltage clamp for precise control of muscles and neurons in live animals

Amelie C. F. Bergs [1,2], Jana F. Liewald [1,2], Silvia Rodriguez-Rozada[3], Qiang Liu [4,5], Christin Wirt[1,2], Artur Bessel[6], Nadja Zeitzschel [1,2], Hilal Durmaz[1,2], Adrianna Nozownik[3], Holger Dill[1,2], Maëlle Jospin[7], Johannes Vierock [8], Cornelia I. Bargmann[4,9], Peter Hegemann [8], J. Simon Wiegert [3,10] & Alexander Gottschalk [1,2]

Excitable cells can be stimulated or inhibited by optogenetics. Since optogenetic actuation regimes are often static, neurons and circuits can quickly adapt, allowing perturbation, but not true control. Hence, we established an optogenetic voltage-clamp (OVC). The voltage-indicator QuasAr2 provides information for fast, closed-loop optical feedback to the bidirectional optogenetic actuator BiPOLES. Voltage-dependent fluorescence is held within tight margins, thus clamping the cell to distinct potentials. We established the OVC in muscles and neurons of *Caenorhabditis elegans*, and transferred it to rat hippocampal neurons in slice culture. Fluorescence signals were calibrated to electrically measured potentials, and wavelengths to currents, enabling to determine optical I/V-relationships. The OVC reports on homeostatically altered cellular physiology in mutants and on Ca^{2+}-channel properties, and can dynamically clamp spiking in *C. elegans*. Combining non-invasive imaging with control capabilities of electrophysiology, the OVC facilitates high-throughput, contact-less electrophysiology in individual cells and paves the way for true optogenetic control in behaving animals.

Identifying connections between distinct neurons and their contribution to driving behavior is a central issue in neuroscience[1,2]. To explore such relations, methods to record and concurrently regulate neural activity are needed[3]. Also, high-throughput screening approaches in excitable cell physiology require application of such methods. Diverse approaches to control or observe excitable cell function are in use. Patch-clamp electrophysiology provides superior temporal accuracy

and sensitivity, but is limited by its invasiveness[4–6]. Ca^{2+} imaging, applicable in intact living organisms, enables integrating cell physiology and behavioral output[7–9]. However, due to sensor Ca^{2+} buffering and the non-linear correlation of cytosolic Ca^{2+} concentration and membrane voltage, this technique suffers from comparably low temporal resolution, and fails to resolve subthreshold voltage transients or high-frequency action potentials (APs). Further, since Ca^{2+}

[1]Buchmann Institute for Molecular Life Sciences, Goethe University, Max-von-Laue-Strasse 15, 60438 Frankfurt, Germany. [2]Institute of Biophysical Chemistry, Goethe University, Max-von-Laue-Strasse 9, 60438 Frankfurt, Germany. [3]Research Group Synaptic Wiring and Information Processing, Center for Molecular Neurobiology Hamburg, University Medical Center Hamburg-Eppendorf, 20251 Hamburg, Germany. [4]Lulu and Anthony Wang Laboratory of Neural Circuits and Behavior, The Rockefeller University, New York, NY 10065, USA. [5]Department of Neuroscience, City University of Hong Kong, Tat Chee Avenue, Kowloon Tong, Hong Kong, China. [6]Independent Researcher, Melatener Strasse 93, 52074 Aachen, Germany. [7]Université Claude Bernard Lyon 1, Institut Neuro-MyoGène, 8 Avenue Rockefeller, 69008 Lyon, France. [8]Institute for Biology, Experimental Biophysics, Humboldt University, 10115 Berlin, Germany. [9]Chan Zuckerberg Initiative, Palo Alto, CA, USA. [10]Medical Faculty Mannheim, University of Heidelberg, Ludolf-Krehl-Strasse 13-17, 68167 Mannheim, Germany. ✉e-mail: a.gottschalk@em.uni-frankfurt.de

concentration does not fall below basal cytosolic levels in most neurons, Ca^{2+} imaging is unsuited to reveal synaptic inhibition. Instead, membrane potential can be imaged via genetically encoded voltage indicators (GEVIs), e.g., rhodopsin-based GEVIs, among others[10–17]. The fluorescence of retinal, embedded in rhodopsins, reliably monitors voltage dynamics at millisecond timescales. Since rhodopsin-based GEVIs emit near-infrared light, they can be multiplexed with optogenetic actuators of membrane currents, to selectively photostimulate or inhibit activity of excitable cells with high spatiotemporal precision[18–20]. In the "(i)-Optopatch" approach, the blue-light activated channelrhodopsin (ChR) CheRiff was used together with the voltage indicator QuasAr2, allowing to unidirectionally steer and observe, but not to fully control neuronal activity[11,12,21]. An optical dynamic clamp (ODC) used archaerhodopsin to mimic K^+ currents, absent in immature cardiomyocytes, in closed loop with electrophysiological feedback[22]. Bidirectional optical modulation and readout of voltage was implemented as light-induced electrophysiology (LiEp) for drug screening, however, without a feedback loop[23]. A bidirectional approach with feedback—"optoclamp"—used ChR2 and halorhodopsin (NpHR) as actuators and extracellular microelectrode arrays instead of GEVIs[24]. This approach clamped average firing rates in neuronal ensembles, following indirect voltage readout.

True all-optical control over excitable cell activity with closed-loop feedback, as in voltage-clamp electrophysiology, should combine two opposing optogenetic actuators for de- and hyperpolarization, as well as a GEVI. Such a system could respond to intrinsic changes in membrane potential. It would also prevent inconsistent activity levels arising from cell-to-cell variation in optogenetic tool expression levels. These are usually not taken into account, particularly when static stimulation patterns are used, while a feedback system could increase stimulation until the desired activity is reached. The system should synergize the non-invasive character of imaging methods with the control capabilities of electrophysiology.

Here, we established an optogenetic voltage-clamp (OVC) in *Caenorhabditis elegans* and explored its use in rat hippocampal organotypic slices. The OVC uses QuasAr2 for voltage read-out[11,20], and BiPOLES, a tandem protein comprising the depolarizer Chrimson and the hyperpolarizer *Gt*ACR2, stimulated by orange and blue light, respectively, for actuation[19,25–28]. Spectral separation and their balanced 1:1 expression in BiPOLES enabled gradual transitions from depolarized to hyperpolarized states, and vice versa. QuasAr2 fluorescence was sampled at a rate of up to 100 Hz, and this information was used to compute a feedback of wavelength-adapted light signals transmitted to BiPOLES, in closed-loop, thus keeping the voltage-dependent fluorescence at a desired level. We characterized the system in body-wall muscle cells (BWMs), as well as in cholinergic and GABAergic motor neurons. Simultaneous measurements allowed calibrating fluorescent signals to actual membrane voltages, and passively presented wavelength pulses to currents. In *unc-13* mutants, the OVC readily detected altered excitability of muscle, as a response to the reduced presynaptic input. In *egl-19* VGCC gain-of-function (g.o.f.) mutants, an optical I/V-relationship of the mutated channel could be obtained, comparing well to electrophysiological measurements. In rodent neurons, the OVC also modulated fluorescence and voltage, yet with a smaller range, due to the resting potential being close to Cl^- reversal potential. Last, in spontaneously active tissues, i.e., pharyngeal muscle and the motor neuron DVB[29–32], the OVC could dynamically follow and counteract native APs, and suppress associated behaviors.

Results

Reading GEVI fluorescence to steer optogenetic actuators with light feedback in closed-loop

An OVC should measure voltage-dependent fluorescence of an excitable cell, e.g., via a rhodopsin-GEVI[10,11], and provide adjusted light-feedback to optogenetic actuators of membrane voltage, e.g.,

cation- and anion-selective rhodopsin channels[19,28,33,34] (Fig. 1A). The OVC needs to work in closed-loop, to quickly counteract intrinsic activity. We first implemented suitable hard- and software (Fig. 1B and Supplementary Code 1): To excite fluorescence of rhodopsin GEVIs (e.g., QuasAr2, emitting in the far-red)[10,11], we expanded a 637 nm laser to cover 0.025 mm^2. GEVI fluorescence of a region of interest (ROI) is monitored by a camera, and compared to a target value (Fig. 1C and Supplementary Fig. 1A–C). Light feedback is sent to the sample from a monochromator, whose wavelength limits can be pre-selected to match the chosen hyperpolarizing and depolarizing optogenetic tools' maximal activation, and that can adjust wavelength at 100 µs and 0.1 nm temporal and spectral resolution, respectively.

Communication between camera and monochromator is provided by a custom-written script in Beanshell (part of µManager interface[35]), processing incoming gray values into relative changes of fluorescence ($\Delta F/F_0$) (Fig. 1C, Supplementary Fig. 1A–C, and Supplementary Code 1). We initially performed step response experiments in open loop configuration and found the system to require barely 20 ms to reach the desired OVC step-input of ±5% $\Delta F/F_0$ (see below), which we conclude to approximate the system's time constant (Supplementary Fig. 1D). Due to excitation of QuasAr with a laser, 10 ms exposure sufficed to collect ca. 1,800,000 photons per ROI per frame. Hence, the shot-noise floor is as low as ca. 0.08% of the total signal power (Supplementary Table 1). Since GEVIs exhibit photobleaching, $\Delta F/F_0$ values would gradually deviate from actual voltage levels. Thus, for each recording, an initial calibration phase is used to calculate correction parameters (Supplementary Fig. 1E, F). Once the system can access bleach-corrected $\Delta F/F_0$ values, it feeds them into a decision tree algorithm (Supplementary Fig. 1A), where they are compared to a desired holding $\Delta F/F_0$ value. Deviation between target and actual $\Delta F/F_0$ determines the wavelength change of the monochromator (I(ntegral)-controller). To increase control stability, a selectable tolerance range was defined (in most cases ±1%), in which the actual value is allowed to fluctuate around the target $\Delta F/F_0$. Once this tolerance range is reached, the control variable wavelength is not further changed. An alternative algorithm, using a PID controller[36] and Kalman filter[37] for sensor smoothing, did not increase overall system performance (see "Methods"; Supplementary Fig. 2).

Combining single actuators with QuasAr2 for unidirectional steering of membrane voltage

First, we expressed QuasAr2 in *C. elegans* body wall muscles (BWMs). Expression levels were very uniform across and within strains, ensuring equal OVC activity in different genetic backgrounds (Supplementary Fig. 1G). 20 s calibration under 637 nm laser light sufficed to estimate photobleaching parameters. 300 µW/mm^2 blue light or presenting the full spectrum (400 to 600 nm) caused no additional bleaching and did not affect QuasAr2 fluorescence (Supplementary Fig. 1E, F, H). Thus, monochromator light did not influence bleaching-corrected fluorescence and estimated membrane voltages. Initially, to test the feedback loop, we assessed different actuators and configurations. First, *Chlamydomonas reinhardtii* ChR2(H134R) or *Guillardia theta* anion channelrhodopsin *Gt*ACR2 were expressed in cholinergic motor neurons (Supplementary Fig. 3A). This allowed manipulating muscle voltage indirectly via light-induced (de-)activation of motor neurons, and to adjust QuasAr2 fluorescence to values between +20 and −15% $\Delta F/F_0$, respectively (Supplementary Fig. 3B–D). However, fluorescence (i.e., voltage) returned to baseline only by intrinsic membrane potential relaxation (Supplementary Fig. 3D–G), thus limiting temporal resolution. The time required to reach the tolerance range of the target $\Delta F/F_0$ value was termed "transition time". For ChR2, fluorescence reached the target range after 150 ± 12.7 ms and relaxed within 678 ± 148.9 ms (254 ± 20.4 ms and 239.5 ± 29.9 ms, respectively, for *Gt*ACR2). Next, we
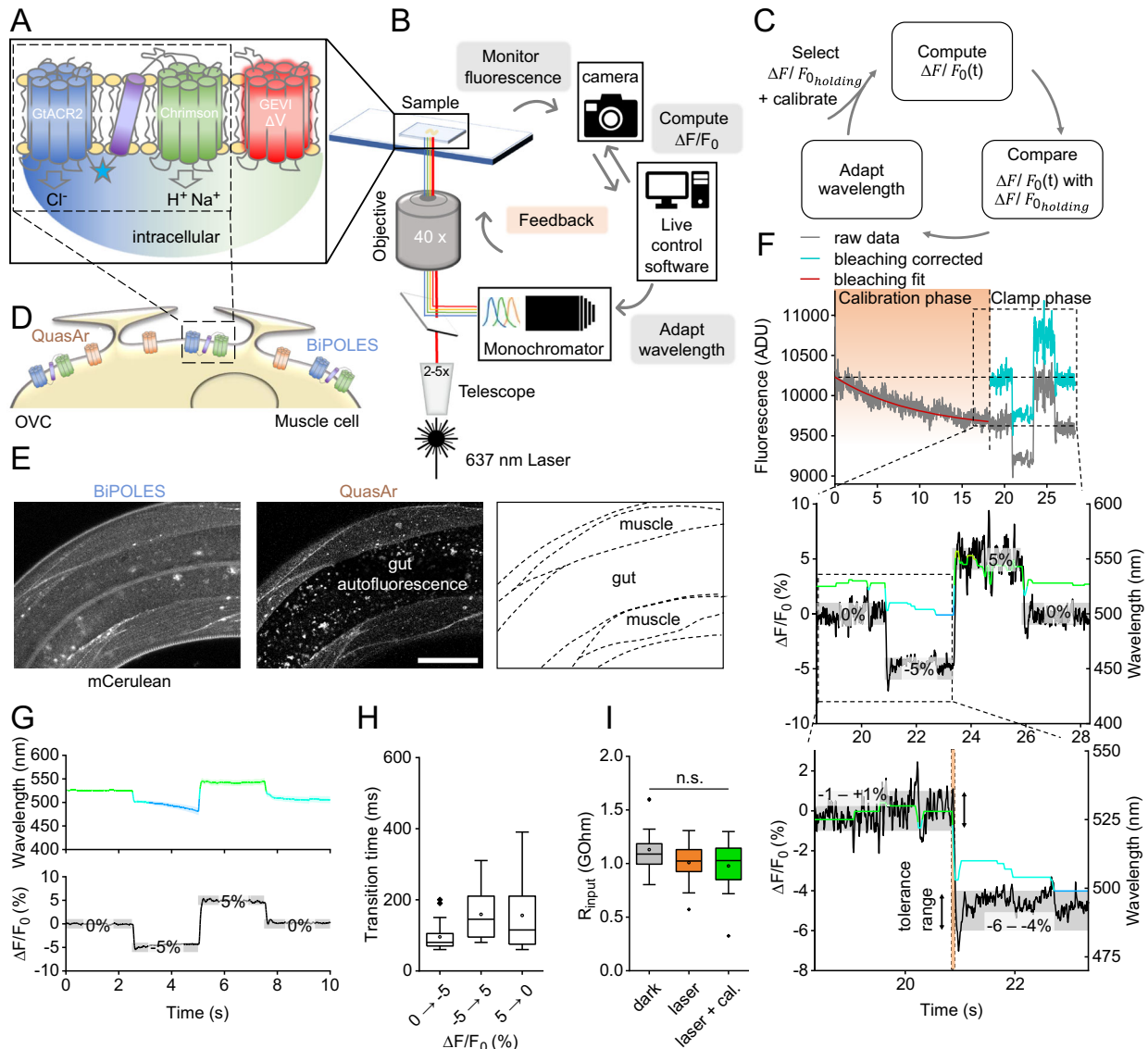
Fig. 1 | Components, setup, and functionality of the OVC. A Molecular OVC components: Two counteracting optogenetic actuators for de- and hyperpolarization (GtACR2, Chrimson; blue star: mCerulean), and a voltage indicator. **B** Hardware setup and communication: Membrane voltage is monitored via a fast and sensitive (sCMOS or EMCCD) camera; gray values are processed by live control software (Supplementary Code 1). Based on the difference to the set holding value, a feedback of light from a monochromator is sent to the optogenetic actuators. **C** OVC feedback mechanism: After selection of clamping parameters and calibration for bleaching correction, $\Delta F/F_0$ is calculated and compared with the set value, to adapt the wavelength accordingly, in closed-loop. **D** OVC (QuasAr2 and BiPOLES) in BWMs. **E** Confocal fluorescence z-projection. BiPOLES (mCerulean) and QuasAr2 in BWM membranes, scheme (dashed lines represent muscle plasma membranes). Scale bar, 50 μm. Representative image (from $n = 22$). **F** OVC four-step protocol (0, −5, 5, and again 0% $\Delta F/F_0$) in BWMs; insets and below: close-up. Wavelength shown in the respective color, holding values and tolerance range (gray boxes) are indicated for each step. Orange shade in lower panel: transition period to reach tolerance range. ADU: analog-to-digital units. **G** Upper panel: Overlay of mean (±S.E.M.) wavelength and (lower panel) fluorescence traces ($n = 24$; holding values: 0, −5, 5, 0% $\Delta F/F_0$). **H** Times required for the indicated 5 and 10% $\Delta F/F_0$ transitions ($n = 24$). **I** Membrane resistance of BWM cells, before ($n = 13$), and during 637 nm laser illumination (orange, $n = 13$), and during laser + calibration light (green, $n = 12$). One-way ANOVA with Bonferroni correction (laser/dark: $p = 0.65$; laser+cal./dark: $p = 0.39$; laser+cal./laser: $p = 1$). In **H**, **I**, box plots (median, 25th–75th quartiles); open dot: mean; whiskers: 1.5× IQR. n−numbers refer to independent biological replicates (animals) (**G**–**I**). Source data are provided as a Source data file.

assessed combinations of spectrally distinct, opposing actuator pairs, like ChR2 (470 nm) and *Gt*ACR1 (515 nm), or *Natronomonas pharaonis* halorhodopsin NpHR (590 nm). Optogenetic de- or hyperpolarization of cholinergic motor neurons affects muscle activation and evokes body contraction or elongation[33,38] (Supplementary Fig. 4A–D). Yet, one actuator was typically outperformed by the other, impeding precise control of membrane potential. Likely, separate expression led to variable relative amounts of the tools. We thus resorted to 1:1 expression via BiPOLES.

BiPOLES enables bidirectional voltage-clamping in *C. elegans* muscle

The tandem protein BiPOLES combines de- and hyperpolarizers Chrimson and GtACR2 (590 and 470 nm, respectively), linked as one sequence[27] (Fig. 1A). BiPOLES activation with a 400−600 nm ramp evoked robust bidirectional effects on body length (Supplementary Fig. 4E). We co-expressed BiPOLES and QuasAr2 in BWMs (Fig. 1D, E). Low levels of BiPOLES were found at the plasma membrane (PM) and in few intracellular aggregates, while QuasAr2 localized mainly to the PM.

As QuasAr2 excitation (637 nm) causes some activation of Chrimson (their spectra overlap[26,39]; Supplementary Fig. 5A), we needed to counteract its effects via GtACR2, by compensatory light from the monochromator. The wavelength was adjusted until −5 and 5% $\Delta F/F_0$ could be maintained for ca. 5 s. Additional assays ensured that compensatory light reinstates normal function: In animals expressing the OVC in BWMs or cholinergic neurons, 637 nm laser light diminished motor behavior. However, compensatory light restored body length and swimming behavior (Supplementary Fig. 5B–E and Supplementary Movie 1), and BWMs expressing the OVC showed voltage fluctuations comparable to animals expressing QuasAr2 only (Supplementary Fig. 5F–H). 637 nm laser light did not fully activate Chrimson, as it could be further excited by 590 nm (300 μW/mm²) light, increasing QuasAr2 fluorescence by 2.3% (Supplementary Fig. 5I). After bleaching correction, prior to each individual experiment (R^2 of the exponential fit was always >0.8, in most cases even >0.95; Supplementary Fig. 6A), the OVC generated incremental changes in wavelength that closely followed the fluctuating fluorescence signals (i.e., membrane voltage; Fig. 1F), as soon as the tolerance range for holding $\Delta F/F_0$ was exceeded. Cells were reliably and quickly (Supplementary Fig. 6B, C), clamped to holding values between −5 and 5% $\Delta F/F_0$ (Fig. 1F, G; Supplementary Fig. 6D). Due to the bidirectionality and live feedback, the BiPOLES-OVC acted significantly faster than when using single actuators, particularly for the return towards resting potential: Transition times were only 147.7 ± 25.5 ms (5→0%) and 88.0 ± 5.7 ms (−5→0%) for BiPOLES, compared to 678.6 ± 148.9 ms for ChR2 and 239.5 ± 29.9 ms for GtACR2 (Fig. 1H and Supplementary Figs. 3G and 6C–E). The transition time depended on the system's sampling rate: At 40 Hz sampling rate, the transition times were significantly larger, since the I-controller then applies fewer control signals to the system within a given period (Supplementary Fig. 6E). Evaluation of all control events (of 11 randomly selected experiments) demonstrated that almost 50% of those events were completed (i.e., $\Delta F/F_0$ back in tolerance) within 20-30 ms. These events where associated with smaller control deviations (Supplementary Fig. 6F). Analysis of the system's accuracy showed that the control deviation was within ±1% (corresponding to the selected tolerance range) at 84% of all time points, and 50% occurred even within ±0.5% (Supplementary Fig. 6G). An analysis of the time-dependent accuracy of the control error (root mean square of the deviation; r.m.s.d.) confirmed stability, apart from the periods of the transition time (Supplementary Fig. 6H). The OVC allowed continuous bidirectional clamping for extended periods (Supplementary Fig. 6I–L). Once the closed-loop control was interrupted, membrane voltage approached baseline and higher fluorescence fluctuations were observed (1.87 ± 0.1 vs. 0.78 ± 0.05% $\Delta F/F_0$ during −5% clamping; 1.89 ± 0.14% $\Delta F/F_0$ for animals expressing only QuasAr; Supplementary Fig. 5F–H). Importantly, the cell could also be actively steered back to the initial fluorescence level by the OVC (Fig. 1F, G).

Calibrating QuasAr2 fluorescence and membrane potential in BWMs

To calibrate the OVC system and determine the actually accessible voltage range, we measured voltage and fluorescence simultaneously (Supplementary Fig. 7A). Concurrent laser (637 nm) and compensation illumination (520 nm) did not significantly alter membrane resistance (Fig. 1I), or APs, that could be observed by fluorescence and patch-clamp simultaneously (Fig. 2A and Supplementary Fig. 7B, C). The dual illumination also did not alter membrane potential; however, adding 470 nm light could hyperpolarize the cell by about 16 mV (Supplementary Fig. 7D). Small voltage fluctuations, likely representing EPSPs, were similar in dark and light conditions by amplitude and frequency (Supplementary Fig. 7E–G). Thus, BiPOLES activation, despite the open channels, did not lead to general shunting of membrane potential in *C. elegans* muscle. In simultaneous electrophysiology and optical OVC

experiments, induced fluorescence changes (−3 to +3% $\Delta F/F_0$, and returning back to 0% $\Delta F/F_0$) modulated voltage by ca. −7 to +8 mV (Fig. 2B–E), i.e., ca. 15 mV range per 6% $\Delta F/F_0$ (24 mV per 10% $\Delta F/F_0$; given the linear fluorescence-voltage relation of QuasAr2; ref. 11). Note, a smaller $\Delta F/F_0$ range was chosen to facilitate patch-clamp measurements; briefer optical clamp periods (400 ms instead of 2 s) allowed accessing broader voltage ranges (see below). We verified the fidelity of the OVC by assessing whether the initially deduced calibration function may cause progressive errors during the voltage clamp phase. Correlating induced $\Delta F/F_0$ traces to evoked membrane potentials revealed no (increasing) deviation of actual voltages from OVC-imposed trajectories (Supplementary Fig. 7H–K).

Measuring all-optical I/V relationships

The OVC allowed reliable optical voltage clamping. We wondered if we could also use it to acquire all-optical I/V relationships. To this end, we devised a different software "pseudo I/V curve" (Supplementary Fig. 8A and Supplementary Code 1), which can consecutively present different $\Delta F/F_0$ clamp steps. First, we performed optical experiments, relating different $\Delta F/F_0$ clamp values (= voltage equivalent) to observed wavelengths (= current equivalent), required to achieve the respective fluorescence steps (Fig. 2F, G). These purely optical experiments (in intact animals) showed that a range of at least ±10% $\Delta F/F_0$ can be achieved with wavelengths of ca. 470–585 nm, different to the simultaneous OVC/patch-clamp experiments (Fig. 2H and Supplementary Fig. 8B). As an inverse control, we presented wavelengths and achieved a congruent output $\Delta F/F_0$ level (Supplementary Fig. 8C, D). Next, we calibrated the $\Delta F/F_0$ steps to actual voltages, and the wavelengths to actual currents. We again carried out simultaneous OVC/patch-clamp experiments and examined membrane voltage as a function of the preset clamp fluorescence (Fig. 2I). Individual steps were shortened to 400 ms, which allowed covering a range of ±5% $\Delta F/F_0$. The voltages determined and the range covered corresponded to those of the ±3% $\Delta F/F_0$ measurements using the 'standard' OVC protocol, i.e., ca. 22 mV (−40 to −18 mV) for ±5% $\Delta F/F_0$ (Fig. 2J). Likewise, we determined membrane currents (at −24 mV, i.e., BWM resting potential), induced by step changes in applied wavelengths (Fig. 2K). BiPOLES mediated currents in a total range of ~190 pA, running almost linearly between 420 and 580 nm (Fig. 2L). Linear regression estimations allowed relating membrane voltages to $\Delta F/F_0$ and currents to wavelengths, and to identify calibration parameters (Fig. 2J, L; "Methods"). Significance levels for the coefficients were <0.001, indicating high precision. Thus, averaged optical data can be converted to voltage and currents.

Demonstrating homeostatic changes in muscle excitability using the OVC

We explored the utility of the OVC to assess divergent cell physiology. *unc-13(n2813)* mutants lack an essential synaptic vesicle priming factor[40] and thus exhibit largely reduced postsynaptic currents upon ChR2-stimulation of motor neurons[41]. Yet, *unc-13* and other neurotransmission mutants showed enhanced muscle contraction when BWMs were directly photostimulated. We hypothesized that muscles homeostatically change their excitability. To explore if the OVC can detect this, we induced a +5% $\Delta F/F_0$ depolarization step: In *unc-13(n2813)* mutants, the OVC required significantly blue-shifted light (i.e., less Chrimson activation) to induce the same level of depolarization as in wild type (534.2 ± 2.8 vs. 550.4 ± 3.1 nm; Fig. 3A, B). Muscles in *unc-13* animals may exhibit higher excitability to balance the lower excitatory input they receive. Though no significant change in membrane resistance was observed (Fig. 3C), the amplitude of induced voltage increases was higher in *unc-13* mutants when we injected current ramps (Fig. 3D–F). Similarly, APs measured by voltage imaging were significantly increased by amplitude and duration (Fig. 3G, H, J). Thus,
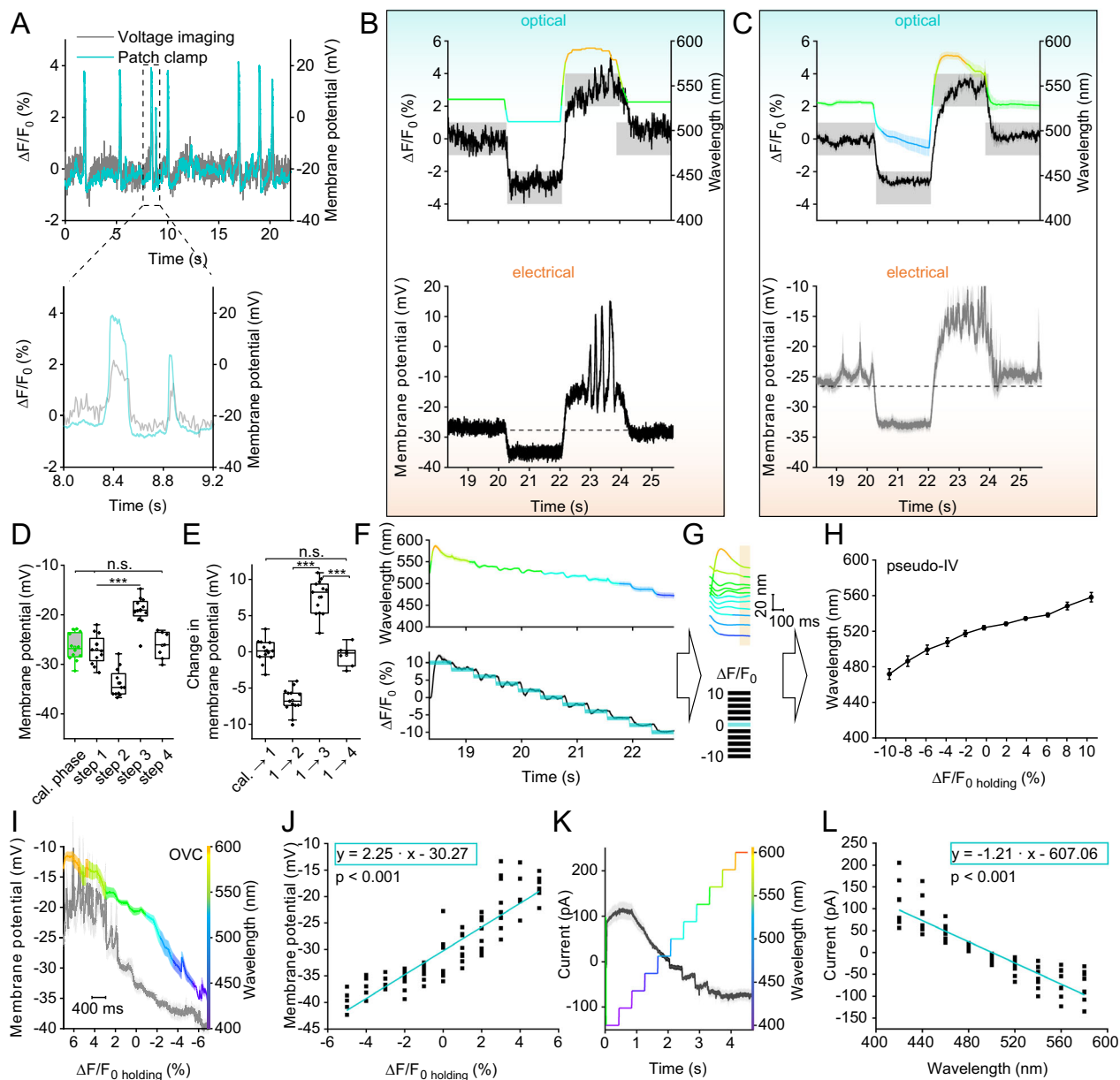
Fig. 2 | Bi-directional optical clamping and calibration of membrane voltage and currents in BWMs. A APs in simultaneous patch-clamp/fluorescence recordings during OVC calibration (637 nm laser + calibration wavelength). Inset: close-up. **B** Simultaneous patch-clamp/fluorescence recording, OVC four-step protocol (0, −3, 3, 0% $\Delta F/F_0$). Upper: Fluorescence recording, wavelength adaptation and tolerance ranges indicated. Lower: Corresponding patch-clamp voltage recording. **C** Overlay of mean (± S.E.M.) wavelength, fluorescence (upper) and voltage traces (lower; $n = 12$) as in **B**. **D** Statistics of data in **C**; absolute voltages of transitions during simultaneous OVC measurements ($n = 12, 12, 12, 12, 7$ for cal., steps 1, 2, 3, 4; $p = 1, 1, 1, 4.1E-6, 1.6E-7, 4.5E-16$ for cal/step 1, cal/step 4, step 1/step 4, step 1/step 2, step 1/step 3, step 2/step 3). **E** Voltage modulation for respective steps of OVC protocol in **D** ($n = 12, 12, 12, 7$ for cal→step 1, step 1→step 2, step 1→step 3, step1→step 4; and p = 7.51E-11, 1.04E-21, 1.13E-10, 1 for cal→step1/step 1→step 2, step 1→step2/ step1→step3, step1→step3/step1→step 4, cal→step1/ step 1→step 4). **F** Distinct $\Delta F/F_0$ steps, presented by the OVC (lower: blue shades, tolerance ranges; black trace, actual $\Delta F/F_0$ mean ± S.E.M.), and the required wavelengths (upper: mean ± S.E.M. nm; $n = 19$). **G, H** Determining wavelengths (≙ currents) at the end (orange shade) of each $\Delta F/F_0$ clamp step (≙ voltage) to deduce pseudo-I/V relation ($n = 19$). **I, J** Simultaneous OVC/electrophysiology experiment, setting $\Delta F/F_0$ clamp-steps, measuring resulting membrane potentials, to determine calibration regression (membrane potential/$\Delta F/F_0$; 5, 4, −3%: $n = 7$; 3, 2, 1, 0, −1%: $n = 9$; −2%: $n = 8$; −4%: $n = 6$; −5%: $n = 5$; mean ± S.E.M. (**I**)). **K, L** Voltage clamp (−24 mV) measurement of currents resulting from wavelength steps, to determine calibration regression (current/wavelength, $n = 8$, mean ± S.E.M. (**K**)). White heteroscedasticity test in (**J, L**, $p < 0.0001$). One-way ANOVA, Bonferroni correction (**D, E**), ***$p \le 0.001$, box plots (median, 25th–75th quartiles); open dot: mean; whiskers: 1.5× IQR. n refers to biological replicates (**C–L**). Source data are provided as a Source data file.

in response to a lack of presynaptic input, ion channels shaping muscle APs, i.e., voltage-gated Ca^{2+} (EGL-19) and K^+-channels (SLO-2, SHK-1)[42,43], may undergo homeostatic changes to enable the observed higher muscle excitability.

egl-19 g.o.f. mutants were shown to mediate larger currents and slowed inactivation[20,44]. We analyzed APs in the *n2368* allele using

voltage imaging (Fig. 3I, J), which revealed larger APs of longer duration than in wild type. We compared the two genotypes by generating an optical I/V-curve. In the ± 5% range (i.e., ca. −40 to −18 mV; Fig. 2I, J), *egl-19* mutants and wild type animals were similar below 0% $\Delta F/F_0$ (-resting potential) but diverged significantly once positive $\Delta F/F_0$ clamp values were reached (i.e., −28 *vs.* −20 mV;
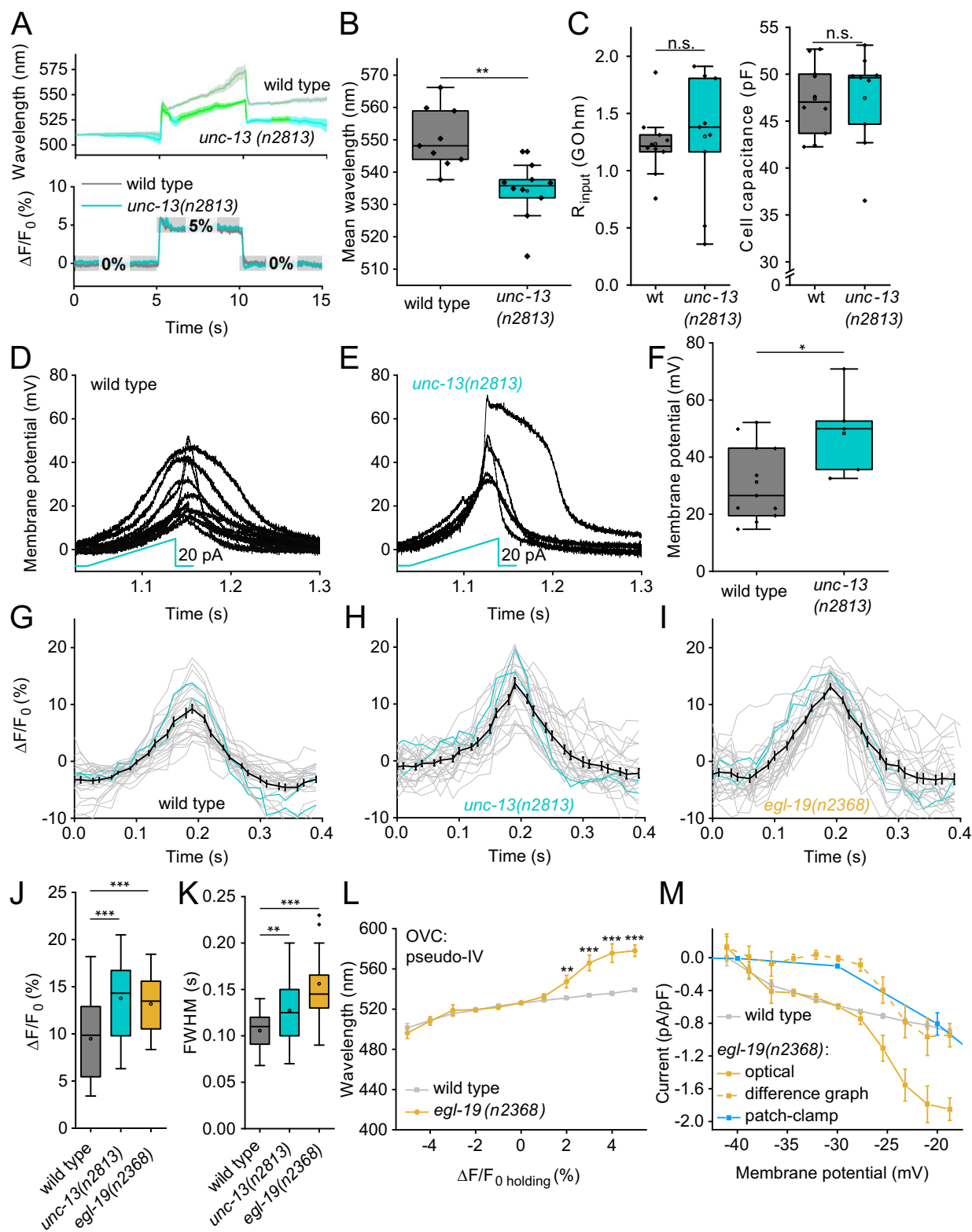
Fig. 3L and Supplementary Fig. 8E). Since we cannot block K^+ channels in intact worms, we calculated the difference of wild type and mutant data to extract the additional $n2368$-mediated Ca^{2+} currents (Fig. 3M). Our optically derived data, corrected for mean membrane capacitance, compared well to electrophysiological data[44] (again, difference of wild type and $egl-19$ mutants; Fig. 3M). Thus, EGL-19 g.o.f. channels open at less depolarized membrane potential, compared to wild type EGL-19.

Optogenetic current-clamp and live OVC

Our approach enables to achieve an "optogenetic current-clamp". We wrote according software that allows to present continuous or pulsed wavelength ramps, or a single light pulse of the selected wavelength, while $\Delta F/F_0$ is recorded live (Supplementary Fig. 9A and Supplementary Code 1). This way, similar to earlier unidirectional approaches[11,12], we could induce and record APs (or inhibitory potentials) in BWMs in all-optical experiments (Supplementary Fig. 9B, C). To further extend

Fig. 3 | Assessing altered cell physiology in mutants affecting synaptic transmission and ion channels, using the OVC. A *unc-13(n2813)* mutant and wild type animals were subjected to OVC depolarization, to +5% $\Delta F/F_0$. Mean wavelength traces (± S.E.M.), wild type: *n* = 9, *unc-13(n2813)*: *n* = 10. **B** Mean wavelength required during the depolarization step to hold +5% $\Delta F/F_0$ (*p* = 0.0012, *n*−numbers as in **A**). **C** Membrane resistance was analyzed in wild type and *unc-13* mutant muscles. wild type: *n* = 10, *unc-13(n2813)*: *n* = 9. **D, E** Current ramps (0-20 pA over 100 ms; cyan) were injected into wild type and *unc-13* mutant muscles and the induced voltage increases were aligned to the peak (*p* = 0.74). wild type: *n* = 11, *unc-13(n2813)*: *n* = 5. **F** Group data of induced voltage increases in **D, E** (*p* = 0.04, *n*−numbers as in **D, E**). **G–I** Optical recordings of spontaneous APs in wild type animals, *unc-13(n2813)* and *egl-19(n2368)* mutants. Overlay of single (each two are highlighted in cyan) and mean (± S.E.M.) traces. wild type: *n* = 6, 27 APs analyzed; *unc-13(n2813)*: *n* = 5, 26 APs analyzed, *egl-19(n2368)*: *n* = 7, 28 APs analyzed. **J, K** Statistical analysis of peak AP amplitude (wt/*unc-13*: *p* = 8.27E-4, wt/*egl-19 p* = 3.04E-4) and AP duration (at FWHM; wt/*unc-13*: *p* = 0.0082, wt/*egl-19 p* = 1.53E-6) of data in **G–I**. *n*−numbers as in **G–I**. **L** All-optical *I/V*-relationship (mean ± S.E.M.) obtained in wild type (*n* = 17) and *egl-19(n2368)* mutants (*n* = 14) (2% *p* = 0.018, 3% *p* = 9.36E-9, 4% *p* = 7.26E-10, 5% *p* = 7.92E-9). **M** Data in **L** were transformed to *I/V*-relations (mean ± S.E.M.), using calibrations in Fig. 2J, L. The currents were normalized using capacitance measured in patch-clamped muscle cells (analogous to Fig. 1I). Data obtained for wild type (gray, *n* = 17) was deduced from *egl-19* data (yellow, *n* = 14), generating a difference curve (dashed, yellow), and compared to difference data obtained by electrophysiology[44] (*n* = 16) in wild type and *egl-19(n2368)* mutants (blue). Two-sided *t* test with Bonferroni correction in (**B, C, F, J, K**). ***p* ≤ 0.001, **p* ≤ 0.01, *p* ≤ 0.05 and box plots (median, 25th–75th quartiles); open dot: mean; whiskers: 1.5× IQR. *n*−numbers refer to independent biological replicates (animals) (**A–M**). Source data are provided as a Source data file.

the applicability of the OVC, we wanted to enable the researcher to respond to observations and to dynamically adapt clamping parameters. We thus wrote software "on-the-run" allowing to select holding $\Delta F/F_0$ values during a running acquisition (Supplementary Fig. 9D and Supplementary Code 1). The software provides a live status update, whether the OVC system is on hold, adapting or if it has reached its limits (Supplementary Fig. 9E, F and Supplementary Movie 2). Using this tool, we could show that the OVC remained responsive to frequently changing live selected clamping values up to several minutes (Supplementary Fig. 9G, H).

Establishing the OVC in cholinergic and GABAergic motor neurons

We tested if the OVC works also in *C. elegans* neurons. Cholinergic and GABAergic motor neurons are small (ca. 2–3 μm cell body, BWMs ca. 50 μm) and exhibit low absolute fluorescence. Both mCerulean (BiPOLES) and QuasAr2 fluorescence were observed in respective ganglia, including the anterior nerve ring and ventral nerve cord (Fig. 4A, B). Calibration parameters could be adopted from muscle experiments (Fig. 4C). The OVC could readily clamp neuronal voltage-dependent fluorescence between −5 and 5% $\Delta F/F_0$ (Fig. 4C–G), and also adaptive experiments were possible (Supplementary Fig. 9I, J).

Establishing the OVC in mammalian neurons

Rodent neurons are larger, more hyperpolarized cells and display faster AP kinetics than *C. elegans* muscles and neurons. Since such cells are relevant to studies of human-like neurophysiology, we explored the utility of the OVC in rat hippocampal pyramidal neurons (organotypic slice culture; Fig. 5A), expressing QuasAr2 and soma-targeted (som)BiPOLES. After bleaching calibration (Fig. 5B), optical clamping could be achieved between ±3% $\Delta F/F_0$ (Fig. 5B, C) with the OVC protocol as used in *C. elegans*. Importantly, in the absence of somBiPOLES, monochromator light did not lead to modulation of QuasAr2 fluorescence (Fig. 5D), while electrically evoked potential shifts (100 mV depolarization step, from −74.5 mV to +25.5 mV holding voltage) caused clear increases of QuasAr2 fluorescence (ca. 21% $\Delta F/F_0$; Fig. 5E). In cells expressing QuasAr2 and somBiPOLES, the ±3% $\Delta F/F_0$ OVC protocol caused hyperpolarizing and depolarizing potential jumps (ca. −4 mV and +3 mV, respectively; Fig. 5F, G). These were small, compared to earlier experiments using somBiPOLES, where 595 nm light application caused depolarization of up to 30 mV, while 400 nm light clamped cells to the Cl⁻ reversal potential[27]. Possibly, due to the more negative resting potential in mammalian neurons compared to *C. elegans* cells, 637 nm activation of Chrimson causes stronger effects, and thus the OVC triggers more compensatory GtACR2 currents. When we expressed somBiPOLES only, 637 nm laser light depolarized hippocampal neurons (via Chrimson) by ca. 21.5 mV, which could be partially counteracted by GtACR2 activation using 530 nm compensation light (Fig. 5H). However, due to the high conductance of GtACR2, shunting effects likely prevented further optical hyper- or depolarization. Thus,

in mammalian neurons, the OVC works with a limited range, likely due to different voltage and ion conditions in the resting state, and probably due to higher relative expression levels, as compared to *C. elegans*.

Dynamic suppression of APs in pharyngeal muscle

Thus far, we imposed fixed voltage steps to cells. To see if the OVC can dynamically counteract spontaneous activity, as opposed to shunting hyperpolarization, we turned to a periodically active muscular pump, the *C. elegans* pharynx (Fig. 6A).

This feeding organ exhibits periodic, ca. 4 Hz APs[20]. Closing of the grinder, a structure used to crush bacteria, was forced by activation of *Gt*ACR2 (400 nm), and could be observed by QuasAr2 fluorescence (Supplementary Fig. 10A). Illumination with only the 637 nm laser caused grinder opening. The OVC could clamp the pharynx statically between −5 and 5% $\Delta F/F_0$ (Supplementary Fig. 10B–D), and dynamically follow its activity to keep it at 0% $\Delta F/F_0$ (Fig. 6B, C and Supplementary Movie 3). Optically observed APs showed a rise time constant of around 15 ms and duration of ca. 150 ms (at full-width-half-maximum (FWHM))[20]. To clamp these APs dynamically, i.e., to counteract de- and repolarization phases quickly enough, we set the OVC software parameters to respond with more pronounced wavelength changes to a given fluorescence change (increased integral gain; "Methods," Eq. 6), and reduced the tolerance range to ± 0.005%. During calibration, APs showed 26.0 ± 1.6% $\Delta F/F_0$ mean amplitude and 118.7 ± 7.3 ms duration at FWHM (Fig. 6B, C, E, F). Upon clamping, all subsequent attempts to spike were dynamically counteracted and almost completely suppressed (Fig. 6B–F). Clamping was rapid: APs occurring at clamping onset were shortened by 65%, while the OVC traversed the full wavelength spectrum within 20 ms (Fig. 6D). Signal amplitude was significantly reduced to ca. 5 ± 0.7% (Fig. 6E, F), as was its duration (to 83.14 ± 8.8 ms at FWHM). The greatly reduced voltage signals also resulted in the suppression of pump events (Fig. 6G). This finding supports the effectiveness of OVC-mediated AP suppression. As shown above in BWMs, APs, associated with the opening of the grinder, could be elicited using the current clamp mode (Supplementary Fig. 10E, F).

Dynamic clamping of APs in the GABAergic motor neuron DVB

C. elegans exhibits a rhythmic motor program to move and expel gut contents[29–32]. Expulsion muscle contraction is regulated by an intestinal pacemaker and by GABAergic motor neurons DVB and AVL (Fig. 7A). Ca²⁺ imaging of DVB[45] revealed activity reminiscent of APs, thus far observed in only few *C. elegans* neurons[46]. DVB voltage imaging showed APs (7.7 ± 1% $\Delta F/F_0$, 500 ± 60 ms at FWHM) at regular time intervals of 40-50 s, that were followed by posterior body contraction (Fig. 7B). Using parameters as for the pharynx, DVB APs were clamped to significantly reduced amplitude and duration (Fig. 7C, D and see Supplementary Fig. 10G for single trace). DVB allowed calibrating the neuronal OVC by patch-clamp electrophysiology[47]: resting potential was −49.0 ± 8.9 mV (Fig. 7E, F), and increasing current steps (1 pA)
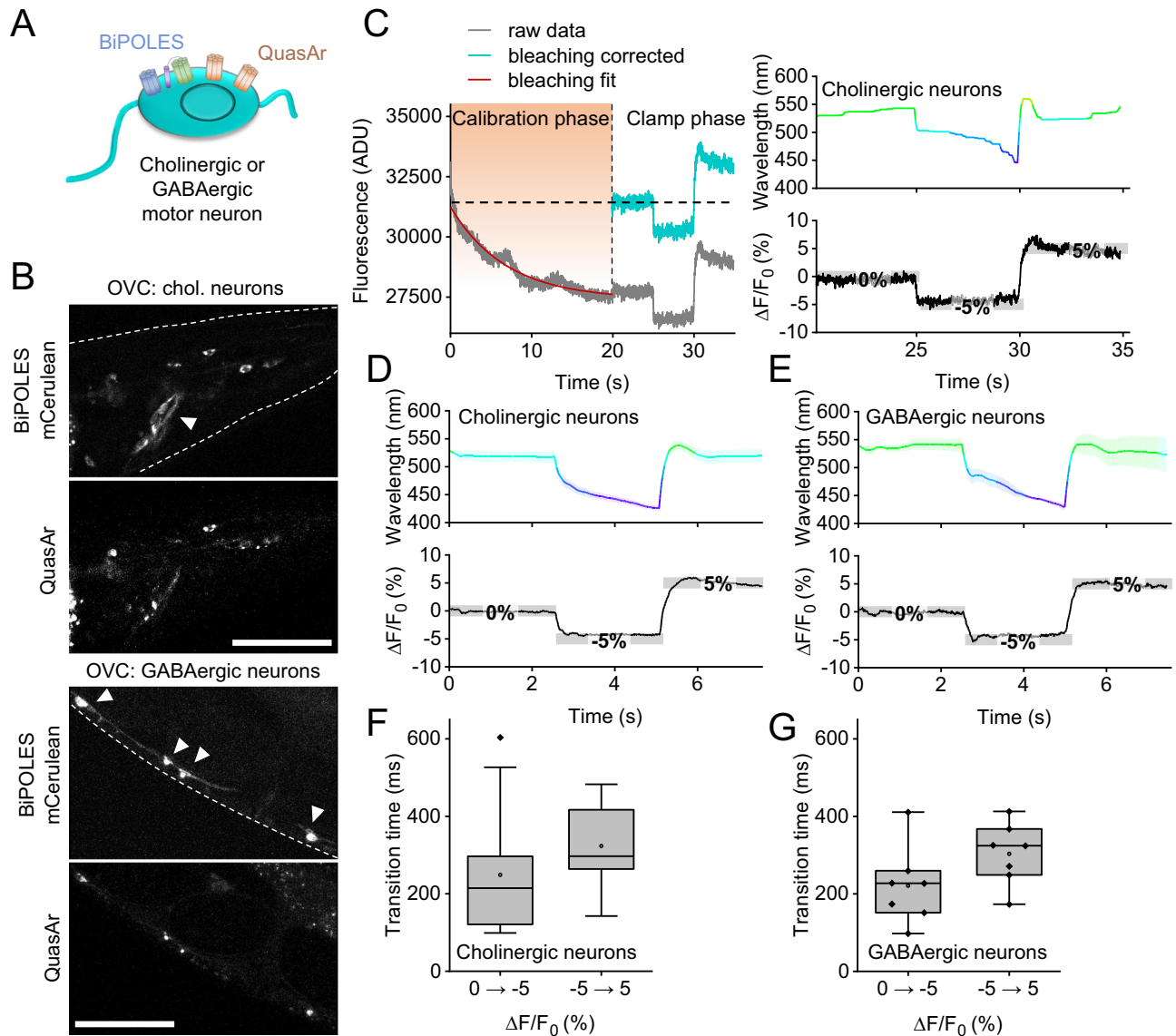
Fig. 4 | Bi-directional clamping of voltage-dependent fluorescence in *C. elegans* neurons. A OVC in cholinergic or GABAergic neurons. **B** Confocal fluorescence z-projections of BiPOLES (mCerulean) and QuasAr2 expression. Arrowheads: Neuronal cell bodies. Scale bars: 50 μm. Representative image (from $n = 11$ (cholinergic) or 16 (GABAergic neurons)). **C** OVC protocol (holding values 0, −5, 5% $\Delta F/F_0$) in cholinergic neurons, single recording. **D**, **E** Mean (±S.E.M.) traces of the OVC in cholinergic (**D**; $n = 14$), or GABAergic (**E**, $n = 7$) neurons, respectively, holding values: 0, −5, 5% $\Delta F/F_0$. **F**, **G** Transition times for 5 and 10% $\Delta F/F_0$ steps (**F**: cholinergic, **G**: GABAergic neurons, n−numbers as in **D**, **E**); box plots (median, 25th–75th quartiles), open dot: mean, whiskers: 1.5× IQR. n−numbers refer to independent biological replicates (animals) (**D**–**G**). Source data are provided as a Source data file.

evoked APs (−23.4 mV threshold, depolarization to 26.3 mV, 359 ms duration (FWHM), −38.5 mV after-hyperpolarization; n = 5; Fig. 7F). DVB AP amplitude thus is ca. 50 mV. Although fluorescence baseline may be altered by the 637 nm laser and Chrimson activation, this did not evoke APs. Thus, the QuasAr2 signal in DVB, i.e., 7.7% $\Delta F/F_0$ for an AP, corresponds to ca. 50 mV (calculating from threshold, or up to 75 mV, from resting potential).

Discussion

Here, we established the first, to our knowledge, all-optical voltage-clamp approach to date. We demonstrated its performance in various excitable cell types in intact animals (*C. elegans*) and tested it in mammalian hippocampal neurons. In *C. elegans*, the OVC allowed reliable clamping of voltage in two muscular organs and three neuron types via QuasAr2 fluorescence read-out and bidirectional optogenetic actuation *via* BiPOLES. The OVC could further detect the altered postsynaptic excitability of *unc-13* mutants, a

homeostatic response to reduced presynaptic input, and allowed deducing all-optical I/V-relationships that provided insight into altered functionality of the L-type VGCC EGL-19 in a g.o.f. mutant, matching electrophysiological data. Using the OVC, we did not only control resting membrane potential, but could also dynamically clamp spontaneous rhythmic activity and APs in pharyngeal muscle and in the motor neuron DVB.

The OVC operates at sampling rates up to 100 Hz on a typical PC with moderate computing power. This orchestrates the communication between camera and monochromator, while in parallel running image acquisition and providing live computation of bleaching-corrected $\Delta F/F_0$ values, fed into a decision tree and Integral-control algorithm. An alternative algorithm with PID controller and Kalman filter showed similar performance. While the OVC at present is slower than standard patch-clamp electrophysiology, it is not necessarily less sensitive or accurate, within the range of experimental variation, and given variations imposed by dissection required for electrophysiology.
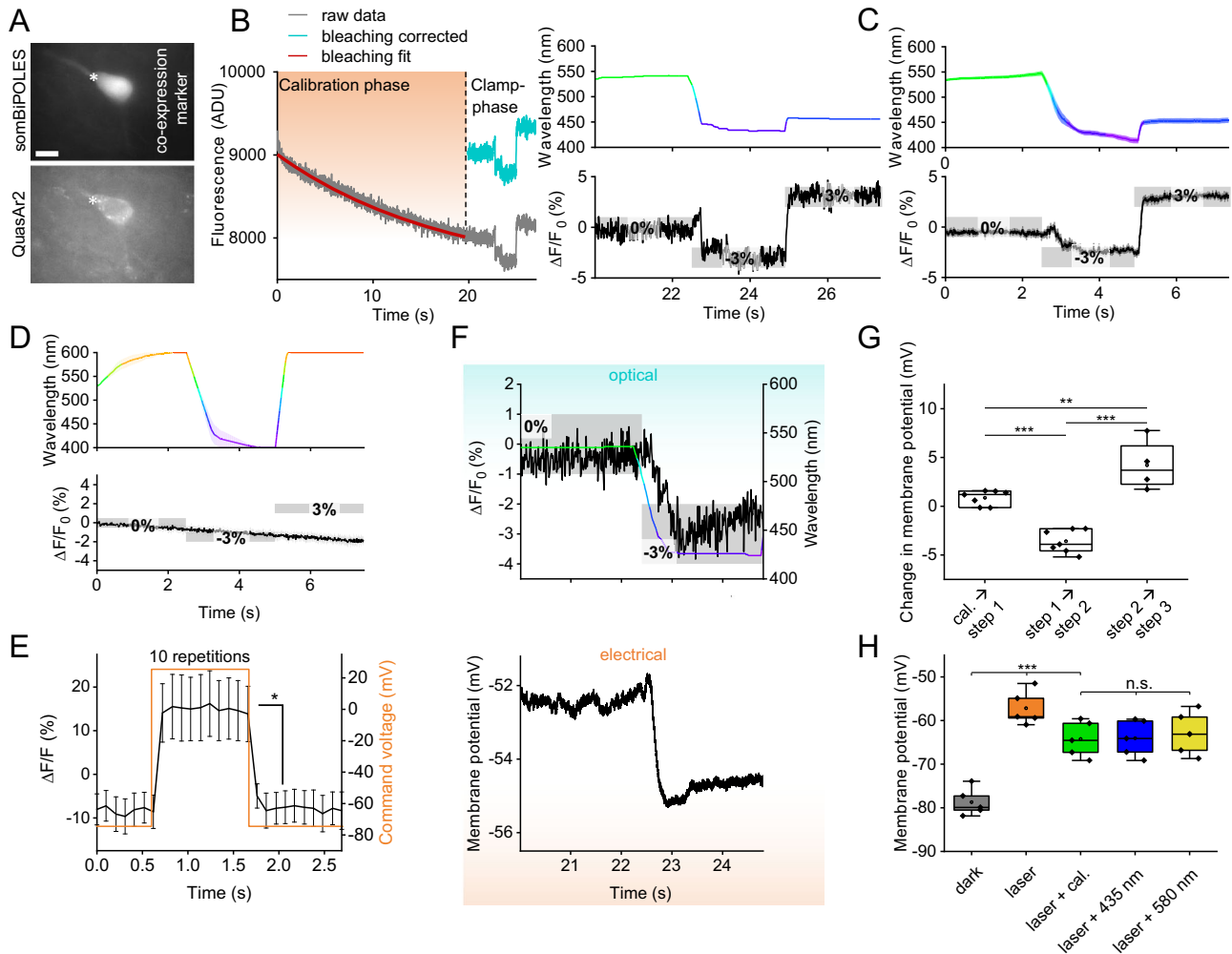
Fig. 5 | Establishing the OVC in rat hippocampal pyramidal neurons.
A Fluorescence micrographs of somBiPOLES (CFP co-expression marker) and
QuasAr2 expression in a neuron (asterisk). Scale bar: 10 μm. Representative image
(from $n = 3$). **B** OVC three-step protocol (0, −3 and 3% $\Delta F/F_0$). Right: Wavelength
shown in the respective color (upper), holding values and tolerance range (gray
boxes, lower panel) are indicated for each step. Left: Orange shade marks transi-
tion/calibration period to reach tolerance range. **C** Overlay of mean (±S.E.M.)
wavelength (upper panel) and fluorescence traces (lower panel; $n = 12$; holding
values: 0, −3, 3% $\Delta F/F_0$). **D** Average fluorescence data (lower panel) for cells
expressing QuasAr2 only, while the OVC attempts to run a 0, −3, 3% $\Delta F/F_0$ protocol
($n = 5$; upper panel: Monochromator wavelength). **E** QuasAr2 fluorescence during
electrically evoked 100 mV depolarization step, from −74.5 mV to +25.5 mV holding
voltage ($n = 3$, 10 steps analyzed per cell, $p = 0.046$). **F** Simultaneous patch-clamp

(voltage, lower panel) and fluorescence recording (upper panel) with indicated
wavelength adaptation and tolerance ranges. **G** Statistical analysis of voltage
modulation between transition events during simultaneous patch clamp/OVC
measurements (step 1 → step 2/cal. → step 1: p = 1.62E-4; step 1 → step 3/cal. → step 1:
$p = 0.00578$; step 1 → step 3/step 1 → step 2: $p = 2.96E-6$; cal. → step 1: $n = 7$, step 1 →
step 2: $n = 7$, step 1 → step 3: $n = 4$). **H** Modulation of membrane voltage in cells
expressing somBiPOLES only, in response to different light application, as indicated
(laser/dark: $p = 7.07E-7$; laser + cal./dark: $p = 1.97E-4$; $n = 5$). Two-sided t test with
Bonferroni correction in **E**. One-way ANOVA with Bonferroni correction in **G**, **H**.
***$p \le 0.001$, **$p \le 0.01$, *$p \le 0.05$. In **G**, **H**, box plots (median, 25th−75th quartiles);
open dot: mean; whiskers: 1.5× IQR. n−numbers refer to independent biological
replicates (animals) (**C**−**E**, **G**, **H**). Source data are provided as a Source data file.

The OVC outperforms electrophysiology in terms of non-invasiveness,
throughput and ease of application.

Though activation of Chrimson by QuasAr2 excitation light
evoked currents, this effect could be counterbalanced in *C. elegans* by
the bidirectionality of BiPOLES, using compensating GtACR2 activa-
tion. Despite this low level opening of BiPOLES channels, no significant
effects on membrane resistance or membrane potential were
observed, intrinsic neuronal activity and cellular excitability were
normal, muscles fired regular APs, locomotion behavior was unaltered,
and also spontaneous activity in pharyngeal muscle or the DVB neuron
were unaffected.

The voltage range covered by the OVC differed between muscles
and neurons: 10% $\Delta F/F_0$ change corresponded to about 22 mV in
BWMs, and to about 65 mV in DVB. Differences in membrane potential
and AP amplitude depend on the different ion channels and gradients

present in the two cell types, and input resistance. The different range
of $\Delta F/F_0$ fluorescence of QuasAr2 in muscles and neurons may also
correspond to different levels of QuasAr2 protein in plasma membrane
vs. intracellular membranes of the two cell types. Fluorescence from
the latter would not contribute to voltage-dependent $\Delta F/F_0$, while it
would increase overall fluorescence at rest.

BiPOLES mediated currents in a range of approx. 190 pA,
comparable to common optogenetic tools[33,34,48], but falling behind
the effects of individually expressed ACR2[19]. In terms of accuracy
and in line with previous patch-clamp measurements in BWMs, the
examined (patched) cells show a normal distribution in resting
potential (ca. −23 to −27 mV), which remains unchanged during the
calibration phase. Since our system is based on relative changes in
fluorescence, which originate from slightly varying resting poten-
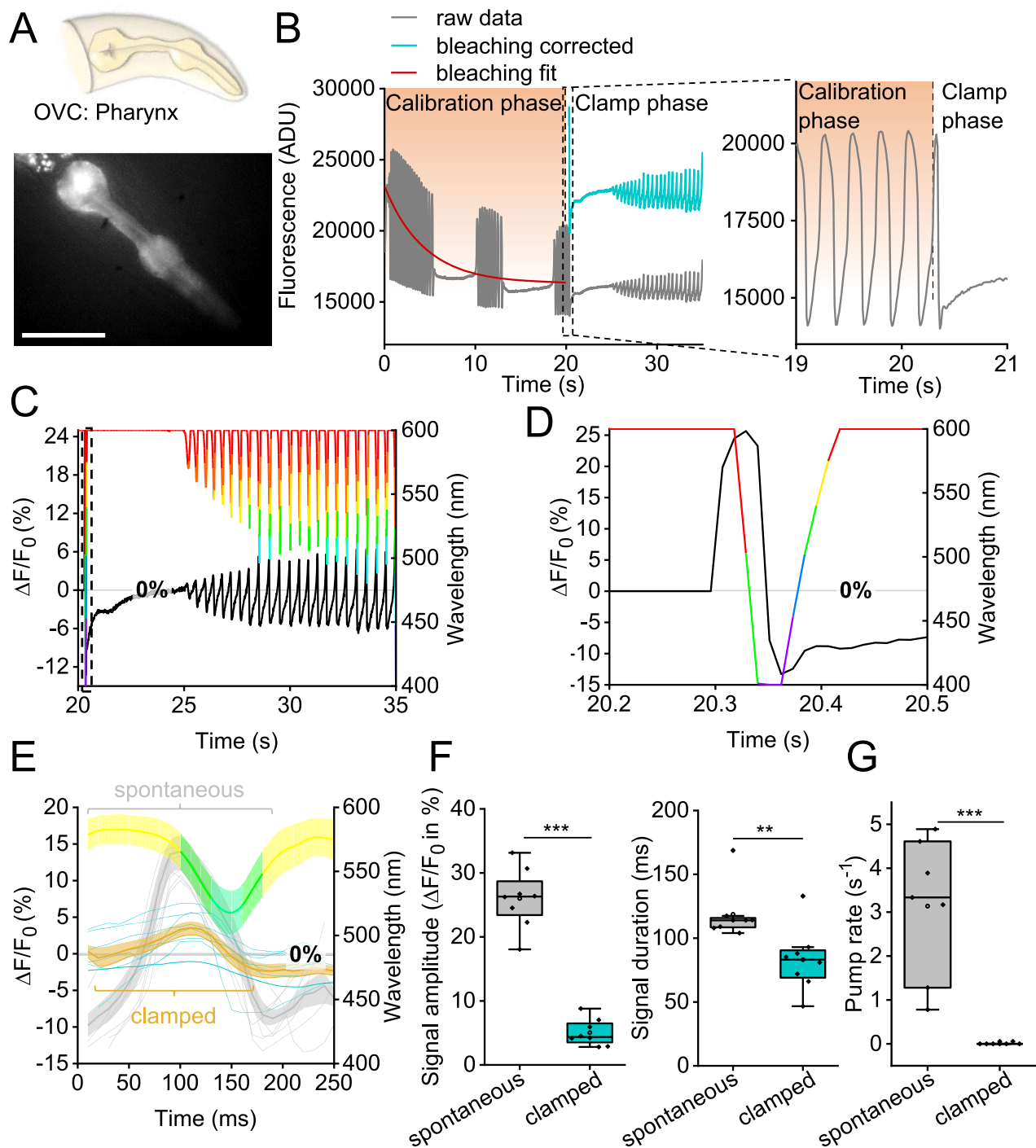tials, set clamp values may be subject to small variations. The OVC is

Fig. 6 | All-optical clamping of APs in pharyngeal muscle. A The pharynx, a muscular pump used for feeding, expressing BiPOLES and QuasAr2 (fluorescence, representative image (from $n = 8$)). Scale bar is 50 μm. **B–D** OVC experiment in pharyngeal muscle, holding fluorescence at 0% $\Delta F/F_0$ and suppressing APs. **B** Original trace, calibration and clamping. Inset: close-up of boxed region, transition calibration to clamp phase. ADU: analog-to-digital units. **C** Overlay: wavelength and $\Delta F/F_0$ traces during clamp phase. **D** Close-up of box in **C**: OVC counteracting first AP during clamp phase. **E** Aligned traces of spontaneous (light gray, $n = 8$ animals, 5 APs each) and clamped (blue) pharyngeal fluorescence signals. Mean

wavelength chosen by the system shown in respective color. **F** Statistics of data in **E** and additional APs ($n = 8$ animals, 10 APs each; amplitude $p = 1.45\text{E-8}$, duration $p = 0.0078$), fluorescence voltage signal amplitude and duration at FWHM. **G** Pumping, observed visually, was suppressed by dynamic OVC clamping ($n = 7$; $p = 2.028\text{E-4}$). In **F, G**: box plots (median, 25th–75th quartiles), open dot: mean, whiskers: 1.5× IQR. In **F, G**, two-sided t test with Bonferroni correction. ***$p \leq 0.001$, **$p \leq 0.01$. n refers to biological replicates (**E–G**). Source data are provided as a Source data file.

not a one-to-one replacement for electrophysiology: Membrane potential is mapped as a relative change using fluorescence, thus requiring calibration measurements to deduce absolute values. The rhodopsins used are not as persistent as a patch-clamp electrode

and limited by the cells' reversal potentials for the respective ions. However, in the range of physiological voltage fluctuations in the respective cell type, the OVC is robust and enables generating data with the advantages of a purely optical, contact-less system. This
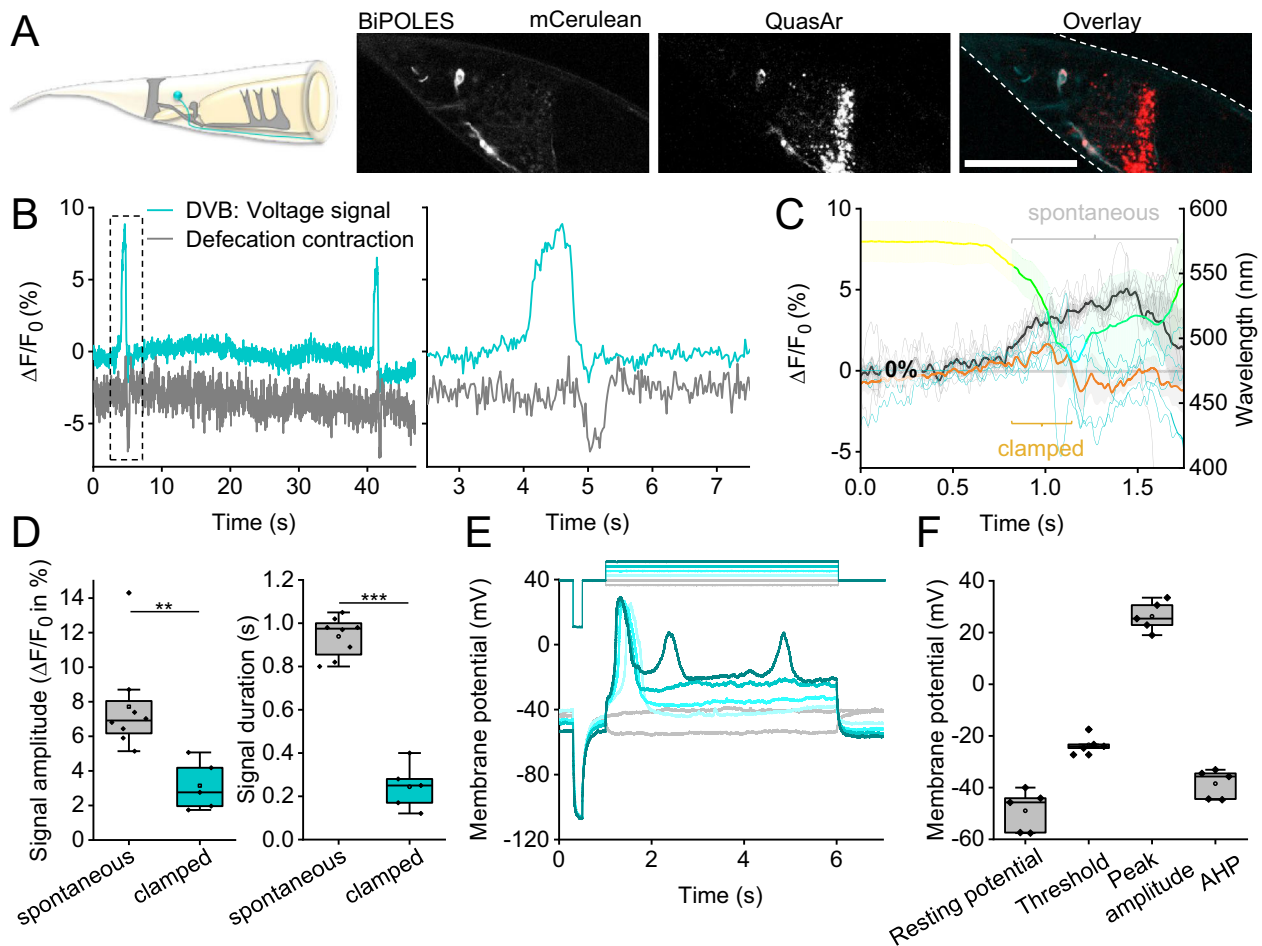
Fig. 7 | All-optical clamping of APs in the enteric motor neuron DVB.
A GABAergic motor neuron DVB (cyan), innervating enteric muscles (gray, upper panel). Below: confocal z-projection, BiPOLES and QuasAr2 in DVB, and overlay; scale bar: 50 μm. **B** Voltage fluorescence signals, spontaneous APs in DVB (blue trace). Expulsion muscle contraction, deduced from DVB movement (gray trace). Right panel: Close-up of boxed region. **C** Overlay of spontaneous (light gray traces, $n = 8$; mean: black) and clamped (blue traces, $n = 5$; mean: orange) DVB voltage signals. Mean wavelength set by OVC shown in respective color. **D** Statistics of data in **C**, mean voltage fluorescence signal amplitude and total duration (amplitude

$p = 0.0073$, duration $p = 7.97E\text{-}8$). **E** Current clamp recordings ($n = 5$, lower panel) of DVB in dissected animals, following indicated (upper panel) hyperpolarizing (gray) and depolarizing (cyan) current injection (1 pA steps). **F** Group data of **E**: resting potential, threshold, peak amplitude, duration at FWHM, and after-hyperpolarization (AHP). In **D**, **F**: box plots (median, 25th–75th quartiles), open dot: mean, whiskers: 1.5× IQR. In **D**, two-sided t test with Bonferroni correction. ***$p \leq 0.001$, **$p \leq 0.01$. n refers to biological replicates (**C**–**F**). Source data are provided as a Source data file.

enables acquiring I/V-relationships, and to some extent (since without feedback), current clamp.

In mammalian neurons, optical voltage control was currently limited to a few mV. This was likely due to the resting potential being close to the Cl⁻-reversal potential, but possibly also due to BiPOLES expression levels, as imaging light affected membrane conductance. Thus, in comparison to *C. elegans*, more activation of GtACR2 is required to counteract Chrimson-based depolarization, causing membrane leak. Minimizing the optical crosstalk of voltage sensor and BiPOLES is especially important in mammalian neurons. Further red-shifted voltage sensors and blue-shifted BiPOLES variants are thus required for future OVC experiments. Light-driven ion pumps, provided they become as powerful as the channels used, could be a future alternative.

The speed of the OVC, characterized by transition times of about 90–150 ms for the relevant induced $\Delta F/F_0$ steps, is currently limited by the software that operates at a maximum sampling rate of 100 Hz. The software currently runs within μManager on a PC. Running the software on an integrated circuit, like a field programmable gate array, and using small ROIs, may enable faster sampling rates up to 1 kHz. The goal would be to identify the optimal sampling rate, thus bringing the

transition time closer to the open loop system time constant of approx. 20 ms (50 Hz system frequency) and optimize control quality. In general, sampling rates should exceed the system frequency by at least a factor greater than 2, but ideally by 6–20 (ca. 300–1000 Hz)[49,50]. The optimal sampling rate is not exclusively dependent on that system frequency, but is also limited by the necessary computing time of the processor and the photon count at shorter exposure times. Considering the high photon count at 10 ms exposure, and assuming a linear relation of exposure time and photon count, we expect that the latter will still be sufficient at theoretical sampling rates of up to 1 kHz (assuming 185,000 captured photons, accuracy <0.4%; Supplementary Table 1). In addition, alternative, or even future optogenetic tools with faster kinetics might overcome the ultimate speed limitation imposed by the OVC's current tool combination and inherent system frequency. Here a 10x faster variant of Chrimson[25,26], and the 20x faster ZipACR were described[49]. That rhodopsin channels show some inactivation during prolonged illumination is not a concern, because the OVC feedback loop can counteract progressive inactivation of BiPOLES components, at least until one of those would desensitize completely. We observed no problems in measurements lasting up to three minutes.

The OVC detected altered muscular excitability in *C. elegans unc-13* mutants, likely caused by changes in ion channel physiology, and it could directly confirm altered channel excitability and currents through a g.o.f. variant of the EGL-19 VGCC. This shows that the OVC represents an approach to enable all-optical, contact-less high-throughput screening applications, e.g., of compound libraries targeted at ion channels. Testing its use in mammalian cell types other than neurons, where such ion channels can be expressed individually, and where the resting membrane potential is less depending on the Cl⁻ gradient, will facilitate this approach.

The establishment of the OVC paves the way for all-optical control of individual neurons in freely behaving transparent animals like *C. elegans*. Accuracy of fluorescence quantification (and thus OVC feedback) requires the cell to remain in focus, which can be achieved with the OVC, while it is impossible to keep a patch-clamp electrode physically attached to such a small animal. Using the OVC on neurons controlling behavior will allow fine-tuning of behavioral aspects, and enable understanding how activity of the individual cell regulates them. Online behavioral analysis (e.g., extent of body bending, locomotion velocity), may be used for feedback to the neuron such that behavior can be dynamically controlled.

Transferring the OVC to other model organisms may require modifications depending on the respective cellular properties. Extending electrophysiology applications, and provided the monochromator light is projected via a digital micromirror device, the OVC should enable efficient space clamp, as well as dynamic local clamping in neuronal processes. The OVC software is universally applicable, as it can be adapted to other GEVI-optogenetic actuator combinations. The OVC broadens applicability of optogenetics as it allows modulation in closed-loop, to better adapt to the variable activity patterns found in living organisms. Dynamic responsiveness is also advantageous with regard to future therapeutic applications, for example in acute control of seizures[51], or in adaptive deep brain stimulation, as it would allow adjusting the therapy to the need of the patient[52].

Methods

Transgenic *C. elegans* strains

C. elegans were cultivated at room temperature (21 °C) on nematode growth medium (NGM) plates, seeded with *E. coli* OP50-1 strain[41]. The following strains were used or generated, and are available upon request: **ZX2476**: *zxEx1139[pmyo-3::QuasAr2; pmyo-2::CFP]*, **ZX2482**: *zxEx1145[pmyo-3::QuasAr2; pmyo-2::CFP]; zxIs5[punc-17::ChR2(H134R)::yfp;lin-15 +]*, **ZX2483**: *zxEx1146[punc-17::ACR2::eYFP; pmyo-3::QuasAr2; pelt-2::GFP]*, **ZX2586**: *zxEx1228[punc-17::GtACR2::mCerulean::βHK::Chrimson; pelt-2::GFP]*, **ZX2714**: *zxEx1250[punc-17::GtACR2::mCerulean::βHK::Chrimson; pmyo-3::QuasAr2; pelt-2::GFP]*, **ZX2753**: *zxEx1266[pmyo-3::GtACR2::mCerulean::βHK::Chrimson; pmyo-3::QuasAr2; pmyo-2::CFP]*, **ZX2755**: *zxEx1268[punc-47::QuasAr2::GFP; pmyo-2::CFP]*, **ZX2826**: *zxEx1282[pmyo-2::QuasAr2; pmyo-2::GtACR2::mCerulean::βHK::Chrimson; pmyo-3::CFP]*, **ZX2827**: *zxEx1283[punc-17::GtACR2::mCerulean::βHK::Chrimson; punc-17::QuasAr2; pelt-2::GFP]*, **ZX2828**: *zxEx1284[punc-47::QuasAr2::GFP; punc-47::GtACR2::mCerulean::βHK::Chrimson; pmyo-2::CFP]*, **ZX2876**: *zxIs139[pmyo-3::GtACR2::mCerulean::βHK::Chrimson; pmyo-3::QuasAr2; pmyo-2::CFP]*, **ZX2935**: *unc-13(n2813); zxIs139[pmyo-3::GtACR2::mCerulean::βHK::Chrimson; pmyo-3::QuasAr2; pmyo-2::CFP]*; **ZX3074**: *egl-19(2368); zxIs139[pmyo-3::GtACR2::mCerulean::bHK::Chrimson; pmyo-3::QuasAr; pmyo-2::CFP]*. These strains are available upon request from A. Gottschalk.

Molecular biology

Plasmids pAB4 (p*unc-17*::ACR2::eYFP), pAB16 (p*myo-3*::QuasAr; Addgene plasmid #130272), pAB17 (p*unc-17*::QuasAr), pAB23 (p*tdc-1s*::QuasAr::GFP) and pNH12 (p*myo-2*::MacQ::mCitrine) were described earlier[19,20]. **pAB26 (p*unc-17*::GtACR2::mCerulean::βHK::Chrimson)** was generated by Gibson Assembly based on RM#348p (*unc-17*; a gift from J. Rand) and pAAV-hSyn-BiPOLES-mCerulean (Addgene plasmid #154944), using *Nhe*I and primers 5′-attttcaggaggacccttggATGGCATCACAGGTCGTC-3′ and 5′-ataccatggtaccgtcgacgTCACACTGTGTCCTCGTC-3′. **pAB27 (p*myo-3*::GtACR2::mCerulean::βHK::Chrimson)** was generated *via* Gibson Assembly based on pDD96.52 (p*myo-3*, Addgene plasmid #1608) and pAAV-hSyn-BiPOLES-mCerulean, using *Bam*HI and primers 5′-actagatccatctagagATGGCATCACAGGTCGTC-3′ and 5′-ttggccaatcccgggCACTGTGTCCTCGTCCTC-3′. **pAB28 (p*unc-47*::QuasAr::GFP)** was generated by Gibson Assembly based on pMSM08 (p*unc-47*::eGFP::MmBoNTB) and pAB23 (p*tdc-1s*::QuasAr::GFP), using *Xma*I, *Msc*I and primers 5′-ttacagcaccggtggattggATGGTAAGTATCGCTCTG-3′ and 5′-ttctacgaatgctcctaggcCTATTTGTATAGTTCATCCATGC-3′. **pAB29 (p*myo-2*::QuasAr)** was generated by Gibson Assembly based on pNH12 (p*myo-2*::MacQ::mCitrine) and pAB16 (p*myo-3*::QuasAr), using primers 5′-caccgagtgaGAAGAGCAGGATCACCAG-3′, 5′-tgcagagcgatacttaccatCCCCGAGGGTTAAAATGAAAAG-3′, 5′-ATGGTAAGTATCGCTCTGCAG-3′ and 5′-cctgctcttctcaCTCGGTGTCGCCCAGAATAG-3′. **pAB30 (p*myo-2*::GtACR2::mCerulean::bHK::Chrimson)** was generated by Gibson Assembly based on pNH12 (p*myo-2*::MacQ::mCitrine) and pAAV-hSyn-BiPOLES-mCerulean, using *Bam*HI, *Hind*III and primers 5′-ggacgaggacacagtgtgaaAAGAGCAGGATCACCAGC-3′ and 5′-agacgacctgtgatgccatgCCCCGAGGGTTAAAATGAAAAG-3′. **pAB31 (p*unc-47*::GtACR2::mCerulean::bHK::Chrimson)** was made by Gibson Assembly based on pAB28 (p*unc-47*::QuasAr::GFP) and pAAV-hSyn-BiPOLES-mCerulean, using *Age*I, *Eco*RI and primers 5′-acatttatttcattacagcaATGGCATCACAGGTCGTC-3′ and 5′-agcgaccggcgctcagttggTCACACTGTGTCCTCGTC-3′. These plasmids available upon request from A. Gottschalk.

For mammalian neuronal expression, the coding sequence of QuasAr2[53] (Addgene #107705) was cloned together with a trafficking signal (ts: KSRITSEGEYIPLDQIDINV) and an ER-export signal (ER: FCYENEV) from the Kir 2.1 channel[54,55] into an AAV2-backbone behind a human synapsin (hSyn) promoter resulting in **pAAV-QuasAr2-ts-ER**. These plasmids are available upon request from S. Wiegert.

OVC voltage imaging experiments

For voltage imaging experiments, animals were supplemented with all-*trans* retinal (ATR; Sigma-Aldrich, USA): One day prior to experiments, transgenic L4 stage animals were transferred to NGM plates, seeded with OP50 bacterial suspension mixed with ATR (stock in ethanol). To avoid interfering fluorescence of unbound ATR, its concentration was adjusted for each tissue. Final ATR concentrations (mM): BWMs (0.01), pharynx (0.03), cholinergic neurons (0.1), GABAergic neurons (0.005). Animals were immobilized with polystyrene beads (0.1 μm diameter, at 2.5% w/v, Sigma-Aldrich) on 10% agarose pads (in M9 buffer). Voltage-dependent fluorescence of QuasAr2 was excited with a 637 nm red laser (OBIS FP 637LX, Coherent) at 1.8 W/mm² and imaged at 700 nm (700/75 ET Bandpass filter, integrated in Cy5 filter cube, AHF Analysentechnik), while optogenetic actuators (BiPOLES, *Gt*ACR2 or ChR2(H134R)) were activated using a monochromator (Polychrome V, Till Photonics/Thermo Scientific), set to emit light from 400 to 600 nm at 300 μW/mm². Imaging was performed on an inverted microscope (Zeiss Axio Observer Z1), equipped with a ×40 oil immersion objective (Zeiss EC Plan-NEOFLUAR ×40/N.A. 1.3, Oil DIC ∞/0.17), a laser beam splitter (HC BS R594 lambda/2 PV flat, AHF Analysentechnik), a galilean beam expander (BE02-05-A, Thorlabs) and an EMCCD or an sCMOS camera (Evolve 512 Delta, Photometrics, or Kinetix 22, Teledyne). All OVC experiments were performed at up to 100 fps with 10 ms exposure and a binning of 4 × 4 (computer specifications: 24 GB RAM, AMD FX-8150 Octa-core processor (3.6 GHz), NVIDIA GeForce GT 520). To induce pharyngeal pumping, animals were incubated in 3 μl serotonin (20 mM, in M9) for 3 min prior to experiments.

OVC software

The OVC control software was written in Beanshell, the scripting language used by the open source microscopy software μManager v. 1.4.22[35]. Scripts are provided in supplementary information (Supplementary Code 1). Experiments were initiated via the μManager script panel. For support of Polychrome V related commands, a copy of the Java archive file *TILLPolychrome.jar* must be placed into the MMPlugins folder and the dynamic link library file *TILLPolychromeJ.dll* into the Sys32 folder (both provided by Till Photonics). The main OVC software is compatible with all cameras supported by μManager. Before running the software, simple rectangular ROIs (to save computation capacity, Supplementary Fig. 1B) must be selected in the live image mode by using the ROI button in the μManager main window. Once a ROI is selected, the script can be executed via the script panel GUI. An input tab prompts the user to select the OVC- and acquisition parameters. The software allows to define a holding $\Delta F/F_0$ value (in %) and the number of frames for each of the steps (three- or four-step-protocol). One can further select the number of frames for the calibration period, the tolerance range (in %; range in which the actual value may fluctuate around the target $\Delta F/F_0$, and in which limits the control variable wavelength is set to hold), the algebraic sign of the increment factor that decides whether to increase or decrease the wavelength with respect to the current $\Delta F/F_0$, the starting wavelength and the wavelength limits (in nm). The free choice of these parameters ensures that the program can also be used for other and/or future combinations of optogenetic tools with different spectral properties. For acquisition, light intensity of the Polychrome V (in %), exposure time of the camera (in ms) and binning can be selected.

During calibration, acquired gray values are stored in an array and used to evaluate the parameters for the exponential decay function to correct for bleaching of the voltage sensor, live during the clamping phase (Eqs. 1–3; based on the ImageJ Plugin "Correctbleach"[56,57]). At the last time point of the calibration phase, the first 50 bleaching corrected gray values of the recording are used to calculate F_0. Subsequently, bleaching corrected $\Delta F/F_0$ values are calculated at each time point of the clamping phase (Eq. 4). Once the system has access to the bleaching-corrected $\Delta F/F_0$ values, it feeds them into a decision tree algorithm, where they are compared to a desired holding $\Delta F/F_0$ value. Depending on the sign of the difference, it decides, whether to shift the wavelength blue or red (mirrored by the sign of the increment i[k]). Wavelength adaptation occurs *via* an implemented I-controller (integral gain K_I was empirically chosen to fit the desired system-behavior) that maps the "I" dynamics by buffering the manipulated variable (wavelength λ) to compensate for permanent control deviation, which would otherwise occur by using a sole P-controller (Supplementary Fig. 1A). That means that the difference (error) between command and current $\Delta F/F_0$ determines the wavelength change of the monochromator – hence, the current wavelength results from the previous plus the respective wavelength change at each time point (Eqs. 5 and 6). The software comes with a three- or four-step protocol, where among others, the desired holding values (within a tolerance range) and number of frames for each step can be selected by the user (Supplementary Fig. 1C and Supplementary Code 1). The system changes the wavelength only if the tolerance range is exceeded.

$$\text{Exp. offset} = a*e^{-b*\text{frame}} + c \tag{1}$$

$$\text{ratio} = \exp. \text{offset}_0 \div \exp. \text{offset}_{\text{frame}} \tag{2}$$

$$F_{\text{correct}} = F_{\text{frame}}*\text{ratio} \tag{3}$$

$$\Delta F/F_{0\,\text{correct}} = ((F_{\text{correct}} - F_0)/F_0)*100 \tag{4}$$

$$e = |\Delta F/F_{0\,\text{holding}} - \Delta F/F_0| \tag{5}$$

$$\lambda = \lambda_{\text{frame}-1} + K_I*e*i[k] \tag{6}$$

Exp. offset: exponential offset; *a, b, c*: exponential fitting parameters; Ratio: ratio between first and current exponential offset; F_{correct}: Bleaching-corrected gray values; F_{frame}: Gray value of current frame; $\Delta F/F_{0\,\text{correct}}$: Bleaching-corrected relative change in fluorescence; F_0: Resting fluorescence value; *e*: error. λ: wavelength; K_I: integral gain; i[k]: current sign of the control error. Equations 1–3 are based on the ImageJ Plugin "Correctbleach"[56].

When the OVC acquisition is complete, a results text file is given out, and the respective image stack is saved automatically as TIFF file. The results file comprises the selected parameters, the bleach correction function and its quality, the framerate, as well as time, (bleaching corrected-) raw gray- and $\Delta F/F_0$ values, and wavelength traces. In addition, status information (system on hold, adapting, or wavelength limits reached) is recorded for each time point of the clamp phase. For the "on-the-run" mode, an additional control window opens as soon as the measurement starts. Here, the holding $\Delta F/F_0$ values can be selected live, either via a range slider or with help of the keyboard arrow keys, while a live status update is displayed.

In addition, "pseudo I/V curve" software (Supplementary Code 1) is available to clamp relative fluorescence in 11 consecutive steps based on previously selected upper and lower limits, resulting in an output of the average $\Delta F/F_0$ value and associated wavelength achieved for each step (calculated as a mean of the last 25% of each step). An optical wavelength/$\Delta F/F_0$ curve is produced and can be translated into an estimated I/V-diagram using these linear calibration functions (Fig. 2J, L):

linear regression: $y = a + bx + e$, where e is assumed as i.i.d. residuals with mean 0.

Membrane potential as a function of $\Delta F/F_0$ holding (estimate: all observations, $n = 80$, w/o outliers)[a]

Constant	−30.27***
B	2.25***
R^2	0.8

linear regression: $y = a + bx + e$, where e is assumed as i.i.d. residuals with mean 0.

Current as a function of wavelength (estimate: all observations, $n = 72$)[a]

Constant	607.06***
b	−1.21***
R^2	0.8

[a]Estimate with robust (white heteroscedasticity consistent) standard errors.
***Significantly different from 0 at the 1% level.

A further software version involves a PID-controller to adjust the wavelength of the OVC (Supplementary Code 1). At each time point, the new wavelength is calculated by the addition of the output (u) of the PID equation to the calibration wavelength (Eqs. 7–9).

$$e = \Delta F/F_{0\,\text{holding}} - \Delta F/F_0 \tag{7}$$

$$u = K_P * e + K_I * T_a * e_{sum} + K_D * \frac{e - e_{t-1}}{T_a} \qquad (8)$$

$$\lambda = \lambda_0 + u \qquad (9)$$

e: current error; u: output; K_P: proportional gain; K_I: integral gain; K_D: derivative gain; e_{t-1}: previous error; T_a: sampling rate; e_{sum}: summed up error; λ_0: calibration wavelength.

Parameter tuning was performed by applying the Ziegler–Nichols method to empirically tune the P, I, and D control gains for better control performance (Supplementary Fig. 2C). Therefore, K_P was adapted until the system started to oscillate at the critical proportional gain ($K_{P\ crit}$). The oscillation period was noted as T_{crit}. PID coefficients were calculated according to Eqs. 10 and 11:

Ziegler–Nichols parameter tuning

K_P	T_n	T_v
0.6 $K_{P\ crit}$	0.5 T_{crit}	0.12 T_{crit}

K_P: proportional gain; $K_{P\ crit}$: critical proportional gain; T_{crit}: period of oscillation; T_n: integration coefficient; T_v: derivation coefficient[36].

$$K_D = K_P * T_v \qquad (10)$$

$$K_I = K_P * \frac{1}{T_n} \qquad (11)$$

To also achieve a better control performance, a Kalman filter for sensor-signal smoothing was added (Supplementary Fig. 2A). Here, the error covariances of the measurement- and system noise of the Kalman filter were empirically adjusted so that the OVC controller dynamics achieved a desired performance. After initializing the system state with an a priori estimate (variables $\hat{x}_0$: estimated fluorescence at the beginning of the measurement and P_0: estimated error covariance of measured fluorescence vs. estimated fluorescence at the beginning of the measurement), prediction and correction are performed at each time step, alternately propagating the system state in time, and correcting it with new observations (Eqs. 12–17)[58]:

1. Prediction of the fluorescence value and the error covariance:

$$x^*(k+1|k) = \mathbf{A}\hat{x}(k) \qquad (12)$$

$$\mathbf{P}^*(k+1|k) = \mathbf{A}P(k)\mathbf{A}^\top + \mathbf{Q} \qquad (13)$$

k: discrete time step; A: system matrix, was here set to scalar value one (which is sufficient for error smoothing); x^*: predicted fluorescence; P^*: predicted error covariance of the estimate; Q: error covariance of the system noise; P(k): estimated error covariance.

2. Calculation of the Kalman gain:

$$\mathbf{S}(k+1) = \mathbf{H}\mathbf{P}^*(k+1|k)\mathbf{H}^\top + \mathbf{R} \qquad (14)$$

$$\mathbf{K}(k+1) = \mathbf{P}^*(k+1|k)\mathbf{H}^\top \mathbf{S}^{-1}(k+1) \qquad (15)$$

S: auxiliary quantity for determining the Kalman gain; H: system output matrix; R: error covariance matrix of the measurement noise; K: Kalman gain.

3. Correction of the state estimate:

$$\hat{x}(k+1) = x^*(k+1|k) + \mathbf{K}(k+1)\left[z(k+1) - \mathbf{H}x^*(k+1|k)\right] \qquad (16)$$

$z(k+1)$: current measurement; $x^*(k+1,|,k)$: predicted measurement; $\hat{x}(k+1)$: current estimate.

4. Correction of the covariance estimation

$$\mathbf{P}(k+1) = \left[\mathbb{1} - \mathbf{K}(k+1)\mathbf{H}\right]\mathbf{P}^*(k+1|k) \qquad (17)$$

The system matrices A and H were set as constant scalars ($A=1$, $H=1$; constant system dynamics) since this assumption is perfectly sufficient for signal smoothing for the PID controller. Here, the sampling rate is fast enough that the Kalman filter can respond to membrane potential changes occurring in this time period with reasonable estimates.

Another software, "optical current clamp" (Supplementary Code 1) is used for the purely optical adaptation of a current clamp. The experimenter has the choice to set single pulses of certain wavelength and duration or to select step-like or continuous wavelength ramps prior to the experiment. Similar to the main OVC script (Supplementary Code 1), this software provides bleaching correction and live $\Delta F/F_0$ readout.

Quality assessment of the OVC

The predictive accuracy for bleaching correction had R^2 values above 0.95 in most cases, and at least above 0.8 (Supplementary Fig. 6A). Experiments with lower R^2 values were attributable to APs occurring during the calibration phase (e.g., in pharyngeal muscle). As expected, the fraction of system saturation decreased once optogenetic tools for de- and hyperpolarization were simultaneously used, which stresses the importance of a second, opposing actuator (Supplementary Fig. 6B). While for the single-tool approaches, the percentage of system saturation was relatively high with $16.3 \pm 2.8\%$, this relation was significantly reduced for all bidirectional BiPOLES combinations. This was also reflected in the speed of the system, where compared to single-tool combinations, BiPOLES was significantly faster, particularly for driving excited or hyperpolarized states back towards resting potential (Supplementary Fig. 6C).

Electrophysiology in C. elegans

Electrophysiological recordings from body wall muscle cells were conducted in immobilized and dissected adult worms as described previously[41]. Animals were immobilized with Histoacryl L glue (B. Braun Surgical, Spain) and a lateral incision was made to access neuromuscular junctions (NMJs) along the anterior ventral nerve cord. The basement membrane overlying body wall muscles was enzymatically removed by 0.5 mg/ml collagenase for 10 s (C5138, Sigma-Aldrich, Germany). Integrity of BWMs and nerve cord was visually examined via DIC microscopy. Recordings from BWMs were acquired in whole-cell patch-clamp mode at 20-22 °C using an EPC-10 amplifier equipped with Patchmaster software (HEKA, Germany). Voltage clamp experiments were conducted at the given holding potential (e.g., −24 mV). Membrane potentials in body wall muscle cells were recorded in current clamp mode. In regular recordings no additional current pulse was injected. For measurements of input resistance, a current pulse of −20 pA was injected via the Patchmaster software for 1000 ms in five consecutive pulses with 5 s breaks in between the current pulses.

The head stage was connected to a standard HEKA pipette holder for fire-polished borosilicate pipettes (1B100F-4, Worcester Polytechnic Institute, Worcester, MA, USA) of 4-10 MΩ resistance. The extracellular bath solution consisted of 150 mM NaCl, 5 mM KCl, 5 mM $CaCl_2$, 1 mM $MgCl_2$, 10 mM glucose, 5 mM sucrose, and 15 mM HEPES (pH 7.3 with NaOH, ≈330 mOsm). The internal/patch pipette solution consisted of K-gluconate 115 mM, KCl 25 mM, $CaCl_2$ 0.1 mM, $MgCl_2$

5 mM, BAPTA 1 mM, HEPES 10 mM, Na$_2$ATP 5 mM, Na$_2$GTP 0.5 mM, cAMP 0.5 mM, and cGMP 0.5 mM (pH 7.2 with KOH, ≈ 320 mOsm). For some experiments, BAPTA was replaced by EGTA (5 mM).

For light activation a monochromator (Polychrome V, Thermo Scientific) was used, ranging from 400 to 600 nm at 300 µW/mm^2. To create conditions as similar as possible to those for the OVC experiments, additional excitation was performed with a laser at 637 nm. Subsequent analysis and graphing were performed using Patchmaster, and Origin (Originlabs).

Electrophysiological recordings from the DVB neuron were conducted in immobilized and dissected adult worms as described previously[46] with minor modifications. Both dissection and recording were performed at room temperature. Briefly, an animal was immobilized with cyanoacrylate adhesive (Vetbond tissue adhesive; 3 M) along the ventral side of the posterior body on a Sylgard 184-coated (Dow Corning) glass coverslip. A small longitudinal incision was made using a diamond dissecting blade (Type M-DL 72029 L; EMS) in the tail region along the glue line. The cuticle flap was folded back and glued to the coverslip with GLUture Topical Adhesive (Abbott Laboratories), exposing DVB. The coverslip with the dissected preparation was then placed into a custom-made open recording chamber (-1.5 ml volume) and treated with 1 mg/ml collagenase (type IV; Sigma) for -10 s by hand pipetting. The recording chamber was subsequently perfused with the standard extracellular solution using a custom-made gravity-feed perfusion system for -10 ml. The standard pipette solution was (all concentrations in mM): K-gluconate 115; KCl 15; KOH 10; MgCl$_2$ 5; CaCl$_2$ 0.1; Na$_2$ATP 5; NaGTP 0.5; Na-cGMP 0.5; cAMP 0.5; BAPTA 1; Hepes 10; Sucrose 50, with pH adjusted to 7.2, using KOH, osmolarity 320–330 mOsm. The standard extracellular solution was: NaCl 140; NaOH 5; KCl 5; CaCl$_2$ 2; MgCl$_2$ 5; Sucrose 15; Hepes 15; Dextrose 25, with pH adjusted to 7.3, using NaOH, osmolarity 330–340 mOsm. Liquid junction potentials were calculated and corrected before recording. Electrodes with resistance of 20–30 MΩ were made from borosilicate glass (BF100-58-10; Sutter Instruments) using a laser pipette puller (P-2000; Sutter Instruments) and fire-polished with a microforge (MF-830; Narishige). Recordings were performed using single-electrode whole-cell current-clamp (Heka, EPC-10 USB) with two-stage capacitive compensation optimized at rest, and series resistance compensated to 50%.

Preparation of organotypic hippocampal slice cultures and transgene delivery

All procedures were in agreement with the German national animal care guidelines and approved by the independent Hamburg state authority for animal welfare (Behörde für Justiz und Verbraucherschutz). They were performed in accordance with the guidelines of the German Animal Protection Law and the animal welfare officer of the University Medical Center Hamburg-Eppendorf.

Organotypic hippocampal slices were prepared from Wistar rats of both sexes (Jackson-No. 031628) at post-natal days 5–7 as previously described[59]. In brief, dissected hippocampi were cut into 350 µm slices with a tissue chopper and placed on a porous membrane (Millicell CM, Millipore). Cultures were maintained at 37 °C, 5% CO$_2$ in a medium containing 80% MEM (Sigma M7278), 20% heat-inactivated horse serum (Sigma H1138) supplemented with 1 mM L-glutamine, 0.00125% ascorbic acid, 0.01 mg ml^{-1} insulin, 1.44 mM CaCl$_2$, 2 mM MgSO$_4$ and 13 mM D-glucose. No antibiotics were added to the culture medium. Pre-warmed medium was replaced twice per week.

For transgene delivery, organotypic slice cultures were transduced at DIV 3–5 with a recombinant adeno-associated viral vector (rAAV) encoding a soma-targeted version of BiPOLES[27] (AAV9-CaMKII-somBiPOLES-mCerulean, Addgene #154948). The rAAV was locally injected into the CA1 region using a Picospritzer (Parker, Hannafin) by a pressurized air pulse (2 bar, 100 ms) expelling the viral suspension into the slice[60]. During virus transduction, membranes carrying the slices were kept on pre-warmed HEPES-buffered solution. At DIV 14–16,

individual CA1 pyramidal cells in the previously somBiPOLES-transduced slices were transfected by single-cell electroporation[61] with the plasmid pAAV-QuasAr2-ts-ER at a final concentration of 10 ng/µl in K-gluconate-based solution consisting of (in mM): 135 K-gluconate, 10 HEPES, 4 Na$_2$-ATP, 0.4 Na-GTP, 4 MgCl$_2$, 3 ascorbate, 10 Na$_2$-phosphocreatine (pH 7.2). An Axoporator 800 A (Molecular Devices) was used to deliver 50 hyperpolarizing pulses (−12 V, 0.5 ms) at 50 Hz. During electroporation slices were maintained in pre-warmed (37 °C) HEPES-buffered solution (in mM): 145 NaCl, 10 HEPES, 25 D-glucose, 2.5 KCl, 1 MgCl$_2$ and 2 CaCl$_2$ (pH 7.4, sterile filtered). A plasmid encoding hSyn-mCerulean (at 50 ng/µl) was co-electroporated and served as a marker to rapidly identify cells putatively co-expressing QuasAr2 and somBiPOLES under epifluorescence excitation.

OVC voltage imaging and electrophysiology experiments in rat organotypic slices

At DIV 19-21, voltage imaging and/or whole-cell patch-clamp recordings of transfected CA1 pyramidal neurons were performed. Experiments were done at room temperature (21–23 °C) using a BX51WI upright microscope (Olympus) equipped with an EMCCD camera (Evolve 512 Delta, Photometrics), dodt-gradient contrast and a Double IPA integrated patch amplifier controlled with SutterPatch software (Sutter Instrument). QuasAr2 was excited with a 637 nm red laser (OBIS FP 637LX, Coherent) at 0.52 W/mm^2 via a dichroic mirror (660 nm, Edmund Optics) and voltage-dependent fluorescence was detected through the objective LUMPLFLN 60XW (Olympus) and through an emission filter (732/68 nm Bandpass filter, Edmund Optics). somBiPOLES was activated using a monochromator (Polychrome V, Till Photonics/Thermo Scientific), set to emit light from 400 to 600 nm at 1.7 mW/mm^2. Laser and monochromator light were combined using a 605 nm dichroic mirror (Edmund Optics). Irradiance was measured in the object plane with a PM400 power meter equipped with a S130C photodiode sensor (Thorlabs) and divided by the illuminated field of the Olympus LUMPLFLN 60XW objective (0.134 mm^2). As for *C.elegans*, OVC experiments were performed at ≈ 90 fps with 10 ms exposure and a binning of 4 × 4.

For electrophysiology, patch pipettes with a tip resistance of 3-4 MOhm were filled with intracellular solution consisting of (in mM): 135 K-gluconate, 4 MgCl$_2$, 4 Na$_2$-ATP, 0.4 Na-GTP, 10 Na$_2$-phosphocreatine, 3 ascorbate, 0.2 EGTA, and 10 HEPES (pH 7.2). Artificial cerebrospinal fluid (ACSF) consisted of (in mM): 135 NaCl, 2.5 KCl, 2 CaCl$_2$, 1 MgCl$_2$, 10 Na-HEPES, 12.5 D-glucose, 1.25 NaH$_2$PO$_4$ (pH 7.4). Synaptic transmission was blocked by adding 10 µM CPPene, 10 µM NBQX, and 100 µM picrotoxin (Tocris) to the extracellular solution. Measurements were corrected for a liquid junction potential of −14,5 mV. Access resistance of the recorded neurons was continuously monitored and recordings above 30 MΩ were discarded.

Statistical methods

Statistical methods used are described in the figure legends. No sample was measured multiple times, and no samples were excluded from analysis. Statistical analysis was performed in Prism (Version 8.0.2, GraphPad Software, Inc.), OriginPro 2021 (OriginLab Corporation, Northampton, USA), Microsoft Excel 2016, 2019, SutterPatch V2 (Sutter Instruments), MATLAB 2016b, 2019b (Mathworks), Stata 12 ic, or ImageJ v1.53c. No statistical methods were applied to predetermine sample size. However, sample sizes reported here are consistent to data presented in previous publications, and which typically allow distinction of significant differences in the types of experiments used. Throughout, n indicates biological replicates (i.e., animals analyzed), with additional mention of specific data that was analyzed (e.g., action potential number), where appropriate. Data was tested for normality prior to statistical inference. Data is given as means ± SEM, if not otherwise stated. Significance between data sets after paired or two-sided t test or ANOVA, with Bonferroni correction for multiple comparisons, is given as p value (*$p \leq 0.05$; **$p \leq 0.01$; ***$p \leq 0.001$), when not otherwise stated. Group

data are presented as box plots with median (line), 25th–75th quartiles (box), mean (open dot) and whiskers, representing 1.5× inter quartile range (IQR). Single data points are shown for $n \leq 10$, or for outliers. The R^2 coefficient of determination was determined as: $R^2 = 1 - SSE/SSD$ (SSE = sum of the squared errors; SSD = sum of the squared deviations about the mean). The linear regressions were estimated with robust standard errors (White heteroscedasticity consistent).

Reporting summary

Further information on research design is available in the Nature Portfolio Reporting Summary linked to this article.

Data availability

Original data (videos) are available from the authors on request. Source data are provided with this paper.

Code availability

The software/code used for operating the OVC is written in Beanshell, the scripting language used by µManager freeware. Scripts ("OVC_main_script", "OVC_on_the_run_script", "OVC_4_step_script", "OVC_pseudo-IV_script", "optical_current_clamp_script") are available as a zip archive in Supplementary Code 1.

References

1. Bargmann, C. I. & Marder, E. From the connectome to brain function. *Nat. Methods* **10**, 483–490 (2013).
2. Anderson, D. J. Circuit modules linking internal states and social behaviour in flies and mice. *Nat. Rev. Neurosci.* **17**, 692–704 (2016).
3. Rajasethupathy, P., Ferenczi, E. & Deisseroth, K. Targeting neural circuits. *Cell* **165**, 524–534 (2016).
4. Francis, M. M., Mellem, J. E. & Maricq, A. V. Bridging the gap between genes and behavior: recent advances in the electrophysiological analysis of neural function in *Caenorhabditis elegans*. *Trends Neurosci.* **26**, 90–99 (2003).
5. Liu, P., Chen, B. & Wang, Z.-W. GABAergic motor neurons bias locomotor decision-making in C. elegans. *Nat. Commun.* **11**, 5076 (2020).
6. Noguchi, A., Ikegaya, Y. & Matsumoto, N. In vivo whole-cell patch-clamp methods: recent technical progress and future perspectives. *Sensors* **21**, 1448 (2021).
7. Akerboom, J. et al. Genetically encoded calcium indicators for multi-color neural activity imaging and combination with optogenetics. *Front. Mol. Neurosci.* **6**, 2 (2013).
8. Chen, T. W. et al. Ultrasensitive fluorescent proteins for imaging neuronal activity. *Nature* **499**, 295–300 (2013).
9. Lin, M. Z. & Schnitzer, M. J. Genetically encoded indicators of neuronal activity. *Nat. Neurosci.* **19**, 1142–1153 (2016).
10. Kralj, J. M., Douglass, A. D., Hochbaum, D. R., Maclaurin, D. & Cohen, A. E. Optical recording of action potentials in mammalian neurons using a microbial rhodopsin. *Nat. Methods* **9**, 90–95 (2012).
11. Hochbaum, D. R. et al. All-optical electrophysiology in mammalian neurons using engineered microbial rhodopsins. *Nat. Methods* **11**, 825–833 (2014).
12. Fan, L. Z. et al. All-optical electrophysiology reveals the role of lateral inhibition in sensory processing in cortical layer 1. *Cell* **180**, 521.e8–535.e8 (2020).
13. Piatkevich, K. D. et al. A robotic multidimensional directed evolution approach applied to fluorescent voltage reporters. *Nat. Chem. Biol.* **14**, 352–360 (2018).
14. Knopfel, T. & Song, C. Optical voltage imaging in neurons: moving from technology development to practical tool. *Nat. Rev. Neurosci.* **20**, 719–727 (2019).
15. Gong, Y., Wagner, M. J., Zhong Li, J. & Schnitzer, M. J. Imaging neural spiking in brain tissue using FRET-opsin protein voltage sensors. *Nat. Commun.* **5**, 3674 (2014).
16. Gong, Y., Li, J. Z. & Schnitzer, M. J. Enhanced archaerhodopsin fluorescent protein voltage indicators. *PLoS ONE* **8**, e66959 (2013).
17. Maclaurin, D., Venkatachalam, V., Lee, H. & Cohen, A. E. Mechanism of voltage-sensitive fluorescence in a microbial rhodopsin. *Proc. Natl Acad. Sci. USA* **110**, 5939–5944 (2013).
18. Flytzanis, N. C. et al. Archaerhodopsin variants with enhanced voltage-sensitive fluorescence in mammalian and *Caenorhabditis elegans* neurons. *Nat. Commun.* **5**, 4894 (2014).
19. Bergs, A. et al. Rhodopsin optogenetic toolbox v2.0 for light-sensitive excitation and inhibition in *Caenorhabditis elegans*. *PLoS ONE* **13**, e0191802 (2018).
20. Azimi Hashemi, N. et al. Rhodopsin-based voltage imaging tools for use in muscles and neurons of *Caenorhabditis elegans*. *Proc. Natl Acad. Sci. USA* **116**, 17051–17060 (2019).
21. Kannan, M. et al. Fast, in vivo voltage imaging using a red fluorescent indicator. *Nat. Methods* **15**, 1108–1116 (2018).
22. Quach, B., Krogh-Madsen, T., Entcheva, E. & Christini, D. J. Light-activated dynamic clamp using iPSC-derived cardiomyocytes. *Biophys. J.* **115**, 2206–2217 (2018).
23. Streit, J. & Kleinlogel, S. Dynamic all-optical drug screening on cardiac voltage-gated ion channels. *Sci. Rep.* **8**, 1153 (2018).
24. Newman, J. P. et al. Optogenetic feedback control of neural activity. *eLife* **4**, e07192 (2015).
25. Klapoetke, N. C. et al. Independent optical excitation of distinct neural populations. *Nat. Methods* **11**, 338–346 (2014).
26. Oda, K. et al. Crystal structure of the red light-activated channelrhodopsin Chrimson. *Nat. Commun.* **9**, 3949 (2018).
27. Vierock, J. et al. BiPOLES is an optogenetic tool developed for bidirectional dual-color control of neurons. *Nat. Commun.* **12**, 4527 (2021).
28. Govorunova, E. G., Sineshchekov, O. A., Janz, R., Liu, X. & Spudich, J. L. Natural light-gated anion channels: a family of microbial rhodopsins for advanced optogenetics. *Science* **349**, 647–650 (2015).
29. Shtonda, B. & Avery, L. CCA-1, EGL-19 and EXP-2 currents shape action potentials in the *Caenorhabditis elegans* pharynx. *J. Exp. Biol.* **208**, 2177–2190 (2005).
30. Beg, A. A. & Jorgensen, E. M. EXP-1 is an excitatory GABA-gated cation channel. *Nat. Neurosci.* **6**, 1145–1152 (2003).
31. McIntire, S. L., Jorgensen, E., Kaplan, J. & Horvitz, H. R. The GABAergic nervous system of *Caenorhabditis elegans*. *Nature* **364**, 337–341 (1993).
32. Avery, L. & Thomas, J. H. in *C. elegans II* (eds. Riddle, D. L., Blumenthal, T. Meyer, B. J. & Priess, J. R.) Ch. 24 (Cold Spring Harbor, 1997).
33. Zhang, F. et al. Multimodal fast optical interrogation of neural circuitry. *Nature* **446**, 633–639 (2007).
34. Nagel, G. et al. Light activation of channelrhodopsin-2 in excitable cells of *Caenorhabditis elegans* triggers rapid behavioral responses. *Curr. Biol.* **15**, 2279–2284 (2005).
35. Edelstein, A., Amodaj, N., Hoover, K., Vale, R. & Stuurman, N. *Computer Control of Microscopes Using µManager* (Wiley, 2010).
36. Foellinger, O., Doerrscheidt, F. & Klittich, M. *Regelungstechnik* 12th edn (Vde Verlag, 2016).
37. Kalman, R. E. A new approach to linear filtering and prediction problems. *J. Basic Eng.* **82**, 35–45 (1960).
38. Nagel, G. et al. Channelrhodopsins: directly light-gated cation channels. *Biochem. Soc. Trans.* **33**, 863–866 (2005).
39. Zou, P. et al. Bright and fast multicoloured voltage reporters via electrochromic FRET. *Nat. Commun.* **5**, 4625 (2014).
40. Richmond, J. E., Davis, W. S. & Jorgensen, E. M. UNC-13 is required for synaptic vesicle fusion in C. elegans. *Nat. Neurosci.* **2**, 959–964 (1999).
41. Liewald, J. F. et al. Optogenetic analysis of synaptic function. *Nat. Methods* **5**, 895–902 (2008).

42. Liu, P. et al. Genetic dissection of ion currents underlying all-or-none action potentials in *C. elegans* body-wall muscle cells. *J. Physiol.* **589**, 101–117 (2011).

43. Gao, S. & Zhen, M. Action potentials drive body wall muscle contractions in *Caenorhabditis elegans*. *Proc. Natl Acad. Sci. USA* **108**, 2557–2562 (2011).

44. Laine, V., Segor, J. R., Zhan, H., Bessereau, J. L. & Jospin, M. Hyperactivation of L-type voltage-gated Ca^{2+} channels in *Caenorhabditis elegans* striated muscle can result from point mutations in the IS6 or the IIIS4 segment of the alpha1 subunit. *J. Exp. Biol.* **217**, 3805–3814 (2014).

45. Wang, H. & Sieburth, D. PKA controls calcium influx into motor neurons during a rhythmic behavior. *PLoS Genet.* **9**, e1003831 (2013).

46. Liu, Q., Kidd, P. B., Dobosiewicz, M. & Bargmann, C. I. *C. elegans* AWA olfactory neurons fire calcium-mediated all-or-none action potentials. *Cell* **175**, 57.e17–70.e17 (2018).

47. Jiang, J. et al. *C. elegans* enteric motor neurons fire synchronized action potentials underlying the defecation motor program. *Nat. Commun.* **13**, 2783 (2021).

48. Husson, S. J. et al. Microbial light-activatable proton pumps as neuronal inhibitors to functionally dissect neuronal networks in *C. elegans*. *PLoS ONE* **7**, e40937 (2012).

49. Shannon, C. E. Communication in the presence of noise. *Proc. IRE* **37**, 10–21 (1949).

50. Lunze, J. in *Regelungstechnik 2* 435–489 (Springer Berlin, Heidelberg, 2010).

51. Paz, J. T. et al. Closed-loop optogenetic control of thalamus as a tool for interrupting seizures after cortical injury. *Nat. Neurosci.* **16**, 64–70 (2013).

52. Widge, A. S., Malone, D. A. Jr. & Dougherty, D. D. Closing the loop on deep brain stimulation for treatment-resistant depression. *Front. Neurosci.* **12**, 175 (2018).

53. Adam, Y. et al. Voltage imaging and optogenetics reveal behaviour-dependent changes in hippocampal dynamics. *Nature* **569**, 413–417 (2019).

54. Gradinaru, V. et al. Molecular and cellular approaches for diversifying and extending optogenetics. *Cell* **141**, 154–165 (2010).

55. Mahn, M. et al. High-efficiency optogenetic silencing with soma-targeted anion-conducting channelrhodopsins. *Nat. Commun.* **9**, 4125 (2018).

56. Schindelin, J., Rueden, C., Miura, K., Hiner, M. & Tinevez, J.-Y. CorrectBleach: upgrade with exponential fitting method. zenodo. https://doi.org/10.5281/zenodo.58701 (2016).

57. Schindelin, J. et al. Fiji: an open-source platform for biological-image analysis. *Nat. Methods* **9**, 676–682 (2012).

58. Kim, P. *Kalman Filter for Beginners: with MATLAB Examples* 1st edn (CreateSpace Independent Publishing Platform, 2011).

59. Gee, C. E., Ohmert, I., Wiegert, J. S. & Oertner, T. G. Preparation of slice cultures from rodent hippocampus. *Cold Spring Harb. Protoc.* https://doi.org/10.1101/pdb.prot094888 (2017).

60. Wiegert, J. S., Gee, C. E. & Oertner, T. G. Viral vector-based transduction of slice cultures. *Cold Spring Harb. Protoc.* https://doi.org/10.1101/pdb.prot094896 (2017).

61. Wiegert, J. S., Gee, C. E. & Oertner, T. G. Single-cell electroporation of neurons. *Cold Spring Harb. Protoc.* https://doi.org/10.1101/pdb.prot094904 (2017).

Acknowledgements

Author contributions

Conceptualization: A.C.F.B., A.G., J.S.W. Methodology: A.C.F.B., A.B., J.V., P.H., J.S.W. Investigation: A.C.F.B., J.F.L., S.R.-R., Q.L., A.N., C.W., N.Z., H. Durmaz, H. Dill, M.J. Visualization: A.C.F.B., A.G. Funding acquisition: A.G., A.C.F.B., J.S.W., P.H., C.I.B. Project administration: A.G. Supervision: A.G., J.S.W., C.I.B. Writing—original draft: A.C.F.B., A.G. Writing—review and editing: A.C.F.B., A.G., S.R.-R., J.S.W., J.V., C.I.B., P.H.

Funding

Competing interests

A patent application has been filed: Applicants: A.C.F.B., A.G., Goethe University; inventors: Amelie Bergs, Alexander Gottschalk; application number: EP 21162331.9; PCT/EP2022/056030, pending, claims focusing on use of an optogenetic voltage clamp for providing models of neurodegenerative or cardiac diseases and for functional characterization or screening of ion channels and/or drugs that affect ion channels. The remaining authors declare no competing interests.

Additional information

Supplementary information The online version contains supplementary material available at https://doi.org/10.1038/s41467-023-37622-6.

Correspondence and requests for materials should be addressed to Alexander Gottschalk.

Peer review information *Nature Communications* thanks the anonymous reviewers for their contribution to the peer review of this work. Peer reviewer reports are available.

Reprints and permissions information is available at http://www.nature.com/reprints

Publisher's note Springer Nature remains neutral with regard to jurisdictional claims in published maps and institutional affiliations.

All-optical closed-loop voltage clamp for precise control of muscles and neurons in live animals

Amelie C.F. Bergs[1,2], Jana F. Liewald[1,2], Silvia Rodriguez-Rozada[3], Qiang Liu[4, 5], Christin Wirt[1,2], Artur Bessel[6], Nadja Zeitzschel[1,2], Hilal Durmaz[1,2], Adrianna Nozownik[3], Holger Dill[1,2], Maëlle Jospin[7] Johannes Vierock[8], Cornelia I. Bargmann[4,9], Peter Hegemann[8], J. Simon Wiegert[3,10], Alexander Gottschalk[1,2,*]

Affiliations:

[1] Buchmann Institute for Molecular Life Sciences, Goethe University, Max-von-Laue-Strasse 15, D-60438 Frankfurt, Germany.

[2] Institute of Biophysical Chemistry, Goethe University, Max-von-Laue-Strasse 9, D-60438 Frankfurt, Germany.

[3] Research Group Synaptic Wiring and Information Processing, Center for Molecular Neurobiology Hamburg, University Medical Center Hamburg-Eppendorf, D-20251 Hamburg, Germany.

[4] Lulu and Anthony Wang Laboratory of Neural Circuits and Behavior, The Rockefeller University, New York, NY 10065, USA.

[5] Department of Neuroscience, City University of Hong Kong, Tat Chee Avenue, Kowloon Tong, Hong Kong, China.

[6] independent researcher: Melatener Strasse 93, D-52074 Aachen, Germany.

[7] Université Claude Bernard Lyon 1, Institut NeuroMyoGène, 8 avenue Rockefeller, 69008 Lyon, France

[8] Institute for Biology, Experimental Biophysics, Humboldt University, D-10115 Berlin, Germany.

[9] Chan Zuckerberg Initiative, Palo Alto, USA.

[10] Medical Faculty Mannheim, University of Heidelberg, Ludolf-Krehl-Strasse 13-17, D-68167 Mannheim, Germany.
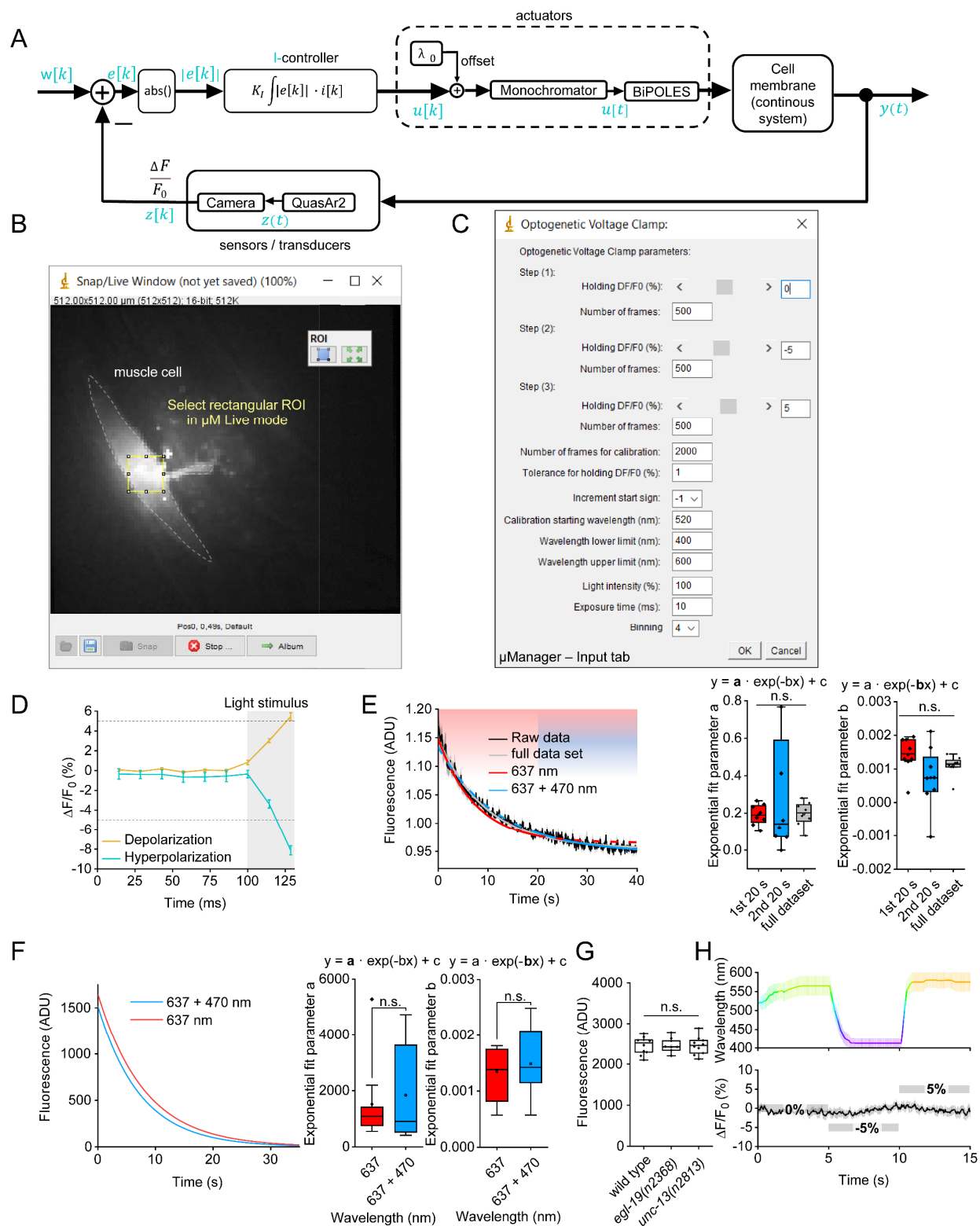
* Corresponding author. Email: a.gottschalk@em.uni-frankfurt.de
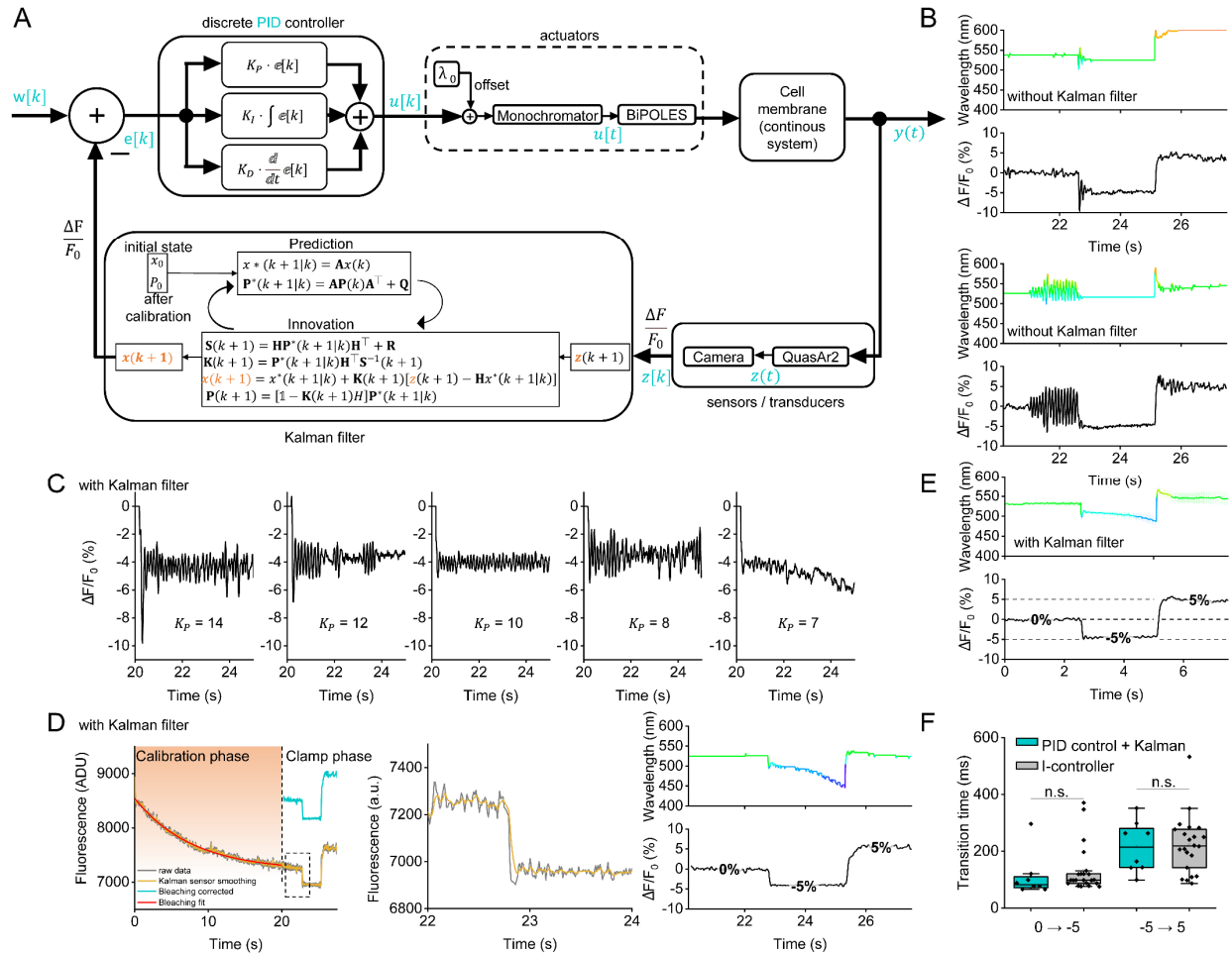
Supplementary data

Supplementary Figures 1-10
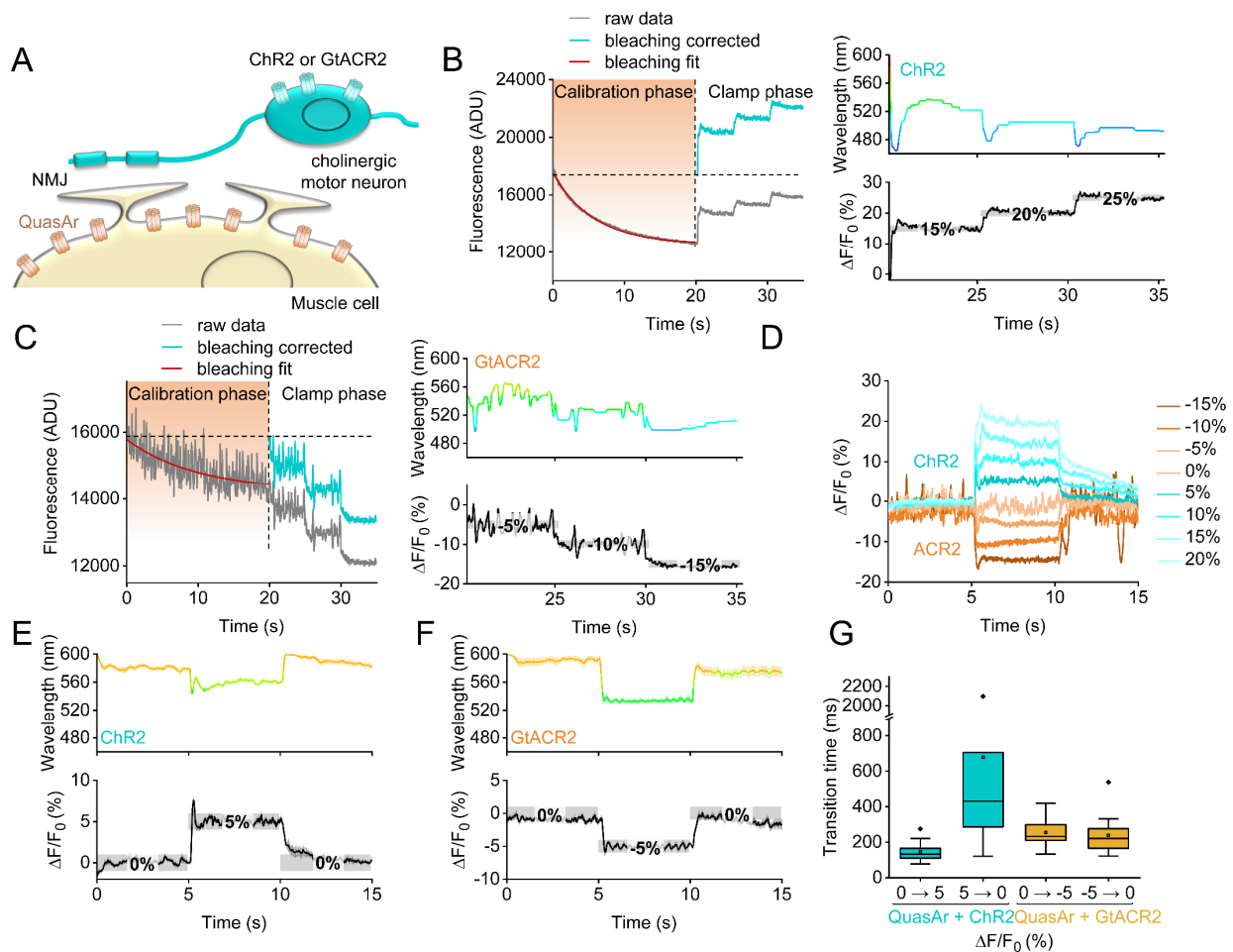
Supplementary Table 1

Supplementary References

1

Supplementary Figure 1. Setup of the OVC software and control parameters. (A) Wiring diagram of I-controller: I-controller generates a digital control value u[k] based on error e[k] for the monochromator, which in turn generates analog light output u[t]. BiPOLES modulates membrane voltage y(t) upon analog light activation that in turn defines QuasAr2's fluorescence z(t) (transduced analog actual value). Fluorescence is monitored via camera and ΔF/F₀ is

calculated (digital actual value). w[k]: Set point. i[k]: current sign of control error e[k]. **(B)** Rectangular ROI selection in µManager "live mode" prior to OVC measurement. **(C)** Input tab of the standard OVC software, implemented in µManager. **(D)** Step response analysis of the open loop system. System was challenged with de- and hyperpolarizing pulses (n=5 and n=8 independent animals, at 580 and 430 nm) to reach desired ±5% $\Delta F/F_0$ (shown is mean ± S.E.M.) and to approximate system time constant τ. **(E)** Left: Bleaching behavior and exponential fits of the fluorescence of QuasAr2 in BWMs, in control animals expressing no actuators (mean ± S.E.M.). Animals were illuminated with the 637 nm laser for the entire duration, and in addition, with 470 nm (300 µW/mm^2) for the last 20 s (n = 8 independent animals). Fits were performed for the first (red) or second 20 sec period (blue), or for the entire duration (grey). Middle and right panel: Statistical analysis of the deduced fit parameters. Parameter a: 1st 20 s / 2nd 20 s: P = 0.29777; 1st 20 s / full data set: P = 0.97414; 2nd 20 s / full data set: P = 0.63254; Parameter B: 1st 20 s / 2nd 20 s: P = 0.09717; 1st 20 s / full data set: P = 1; 2nd 20 s / full data set: P = 0.86977. **(F)** Exponential fits of QuasAr2 fluorescence as in (E) but illuminated with either 637 nm laser (n = 11 independent animals) or 637 nm laser and 470 (300 µW/mm^2) for the entire duration (n = 10 independent animals). Middle and right panels: Statistical analysis of the fit parameters of data in left panel. Parameter a: 637 + 470 / 637: P = 0.62431; Parameter b: 637 + 470 / 637: P = 0.56032. **(G)** Expression levels were assessed in wild type animals, and two different mutant strains expressing the OVC components (all from the same integrated transgene, *zxIs139*), using mean QuasAr fluorescence of comparable ROIs (n = 10, 9, 10 independent animals of the indicated genotypes, wild type, *egl-19(n2368)* and *unc-13(n2813)*). Coefficients of variation were 0.08 (wild type), 0.07 (*egl-19*) and 0.09 (*unc-13*). P values: *egl-19(n2368)* / wild type: 1; *unc-13(n2813)* / wild type: 1; *unc-13(n2813)* / *egl-19(n2368)*: 1. **(H)** Mean ± S.E.M. data for animals expressing only QuasAr2 in BWMs, while the OVC attempts to run a 0, -5, 5 % $\Delta F/F_0$ protocol (n = 8 independent animals). Upper panel: Monochromator wavelength; lower panel: mean fluorescence traces. Statistically significant differences analyzed by One-way ANOVA (in E, G) or two-sided t-test (in F), each with Bonferroni correction. Box plots (median, 25-75th quartiles); open dot: mean; whiskers: 1.5x inter-quartile range (IQR). Source data are provided as a Source Data file.

3

Supplementary Figure 2. Implementation of a PID controller with Kalman filter. (A) Wiring diagram of PID-controller with Kalman filter. Signal flow as in **Supplementary Fig. 1A** with the addition of a Kalman filter. **(B)** Comparison of single OVC experiments with PID control but without Kalman filter. Top: No oscillations. Bottom: With strong oscillations, despite identical parameters, emphasizing the need for a Kalman filter to obtain a stable PID-controller. **(C)** Ziegler-Nichols parameter tuning, with Kalman filter. **(D)** OVC three-step protocol (0, -5 and 5 % $\Delta F/F_0$) in BWMs, insets for close-up. Wavelength shown in the respective color, holding values are indicated for each step, yellow trace represents data processed with Kalman filter for sensor smoothing. Orange shade in left panel: transition period to reach tolerance range. **(E)** Upper panel: Overlay of mean (± S.E.M.) wavelength and (lower panel) fluorescence traces (n=8 independent animals; holding values: 0, -5, 5 % $\Delta F/F_0$). **(F)** Times required for the indicated 5 and 10 % $\Delta F/F_0$ transitions for PID- (plus Kalman filter) and I-controller (n = 8, 22, 8, 22 independent animals for these transitions, respectively: PID control + Kalman, 0 → -5; I-controller, 0 → -5; PID control + Kalman, -5 → 5; I-controller, -5 → 5). Statistically significant differences analyzed by Two-sided t-test with Bonferroni correction. Comparison 0 → -5, P = 0.52321; Comparison -5 → 5, P = 0.85972. Box plots (median, 25-75th quartiles); open dot: mean; whiskers: 1.5x inter-quartile range (IQR). Source data are provided as a Source Data file.

4

62

Supplementary Figure 3. Unidirectional steering of membrane voltage. (A) Cholinergic neurons express either ChR2 or *Gt*ACR2, while QuasAr2 is expressed in BWMs. **(B)** Three-step protocol in ChR2 animals. Left: Raw and bleaching corrected data of calibration (red: exponential fit) and clamping phase. Right panels: Corresponding wavelength and $\Delta F/F_0$ traces. Holding values 15, 20 and 25 % $\Delta F/F_0$; grey shade: tolerance range for each step. **(C)** Three-step (-5, -10 and -15 % $\Delta F/F_0$) protocol in *Gt*ACR2 animals, as in (B). **(D)** Single traces for both strains, 0 %, then -15 to 20 % $\Delta F/F_0$ (in 5% increments), and return to baseline. **(E)** Mean (± S.E.M.) traces (n = 17 independent animals); holding values: 0, 5, 0 % $\Delta F/F_0$, in ChR2 animals. **(F)** As in E, for *Gt*ACR2 animals (n = 14 independent animals; 0, -5, 0 % $\Delta F/F_0$). **(G)** Transition time, respective 5 % $\Delta F/F_0$ steps (n = 17, 17, 14, 13 independent animals for these transitions, respectively: 0 → 5, QuasAr+ChR2; 5 → 0; 0 → -5, QuasAr+ACR2; -5 → 0); box plots (median, 25-75th quartiles); open dot: mean; whiskers: 1.5x inter-quartile range (IQR). Source data are provided as a Source Data file.

5

63
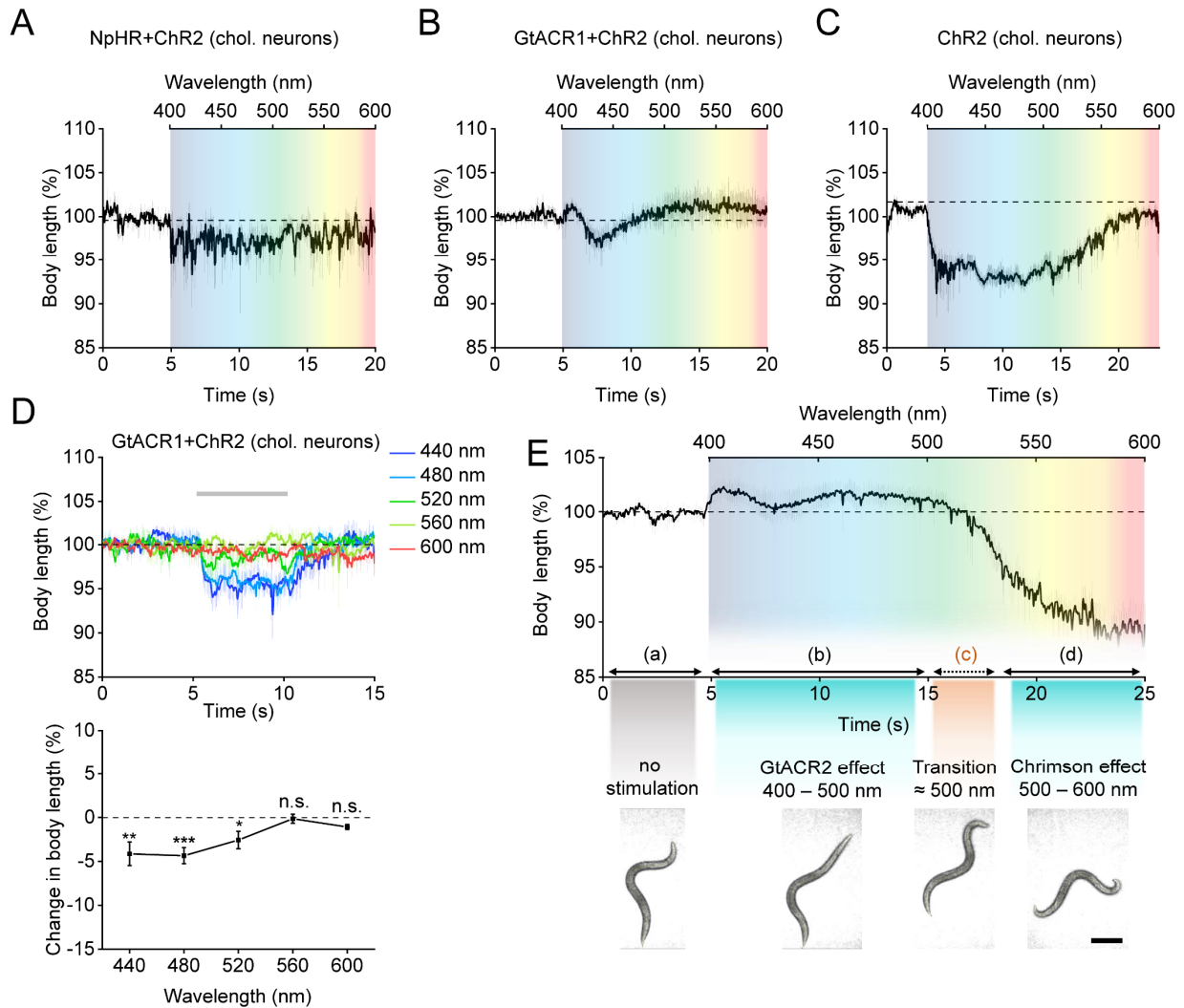
Supplementary Figure 4. Testing different combinations of depolarizing and hyperpolarizing actuators. (A-E) Body length measurements (mean ± S.E.M.) to test functionality of optogenetic actuator combinations, expressed in cholinergic neurons. **(A)** NpHR and ChR2 (n = 8 independent animals; monochromator wavelength ramp from 400 to 600 nm, 300 µW/mm^2). **(B)** *Gt*ACR1 and ChR2 (n = 10 independent animals). **(C)** ChR2-only (n = 8 independent animals). **(D)** *Gt*ACR1 and ChR2. Upper panel: 5 s light pulses, wavelength as indicated, 300 µW/mm^2 (n = 7, 7, 5, 6, 6 independent animals for the following wavelengths, respectively: 440, 480, 520, 560, and 600 nm). Lower panel: Mean (± S.E.M.) body length changes. Statistically significant differences were analyzed by one-way ANOVA with Bonferroni correction (P = 0,008577953; 0,000166674; 0,028628144; 0,476848228; 0,189584323 for the following wavelengths, respectively: 440, 480, 520, 560, and 600 nm). **(E)** Upper panel: Body length measurements of animals expressing BiPOLES in cholinergic neurons (mean ± S.E.M., wavelength ramp 400 - 600 nm, n = 8 independent animals). Below: Representative still images of animals for each phase of the experiment: (a) before light, (b) *Gt*ACR2 effect / muscle relaxation, (c) transition from hyper- to depolarization, (d) Chrimson effect / muscle contraction (scale bar: 200 µm). Source data are provided as a Source Data file.

6
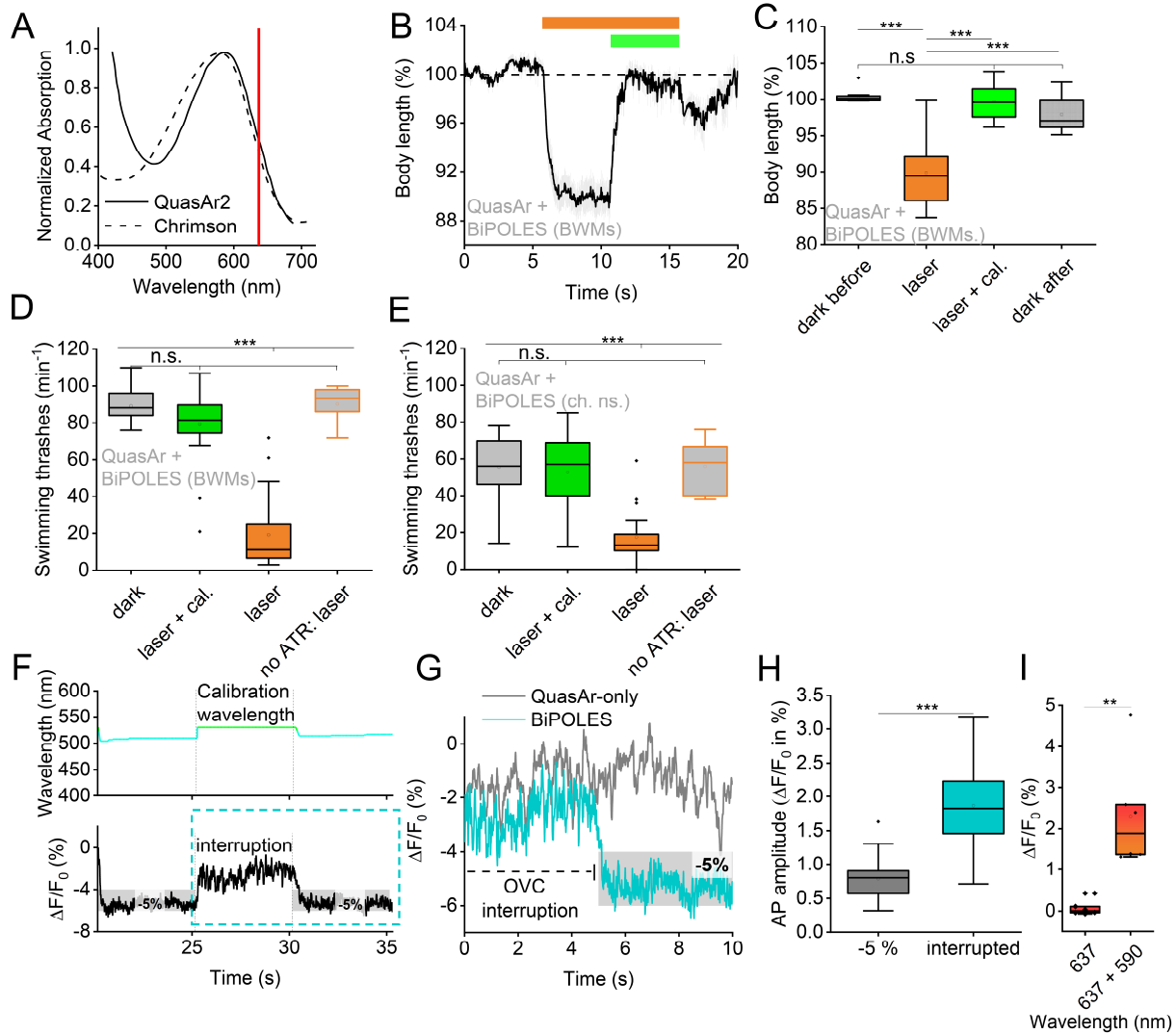
Supplementary Figure 5. BiPOLES activation by 637 nm laser light and calibration wavelength have no adverse effects on muscle function and locomotion. (A) Normalized absorption spectra of Chrimson and QuasAr2[1, 2], laser wavelength used for QuasAr2 imaging is indicated by a red line. **(B)** Body length measurements of animals expressing BiPOLES and Quasar in BWMs (mean ± S.E.M., light pulses: 637 nm laser and 637 nm laser plus calibration wavelength (ca. 521 nm, n = 14 independent animals). **(C)** Statistical analysis of data in (B). laser / dark before: p = 5.94E-13; laser + cal. / dark before: p = 1; laser + cal. / laser: p = 4.41E-12; dark after / dark before: p = 0.156; dark after / laser: p = 2.11E-09; dark after / laser + cal.: p = 0.55. **(D, E)** Analysis of swimming activity of animals expressing BiPOLES and Quasar in BWMs (D, n = 17, 19, 19, 8 independent animals for these conditions: dark, laser + cal., laser, no ATR: laser; statistical significance was: laser / dark: p = 3.16E-19; laser / laser+cal.: p = 3.36E-16; laser / no ATR: laser: p = 1.23E-14; dark / laser+cal.: p = 1; dark / no ATR: laser: p = 1; laser+cal. / no ATR: laser: p = 1) or cholinergic neurons (E, n = 17, 17, 17, 10 independent animals for these conditions: dark, laser + cal., laser, no ATR: laser; statistical significance was: laser / dark: p = 3.82E-07; laser / laser+cal.: p = 2.1E-06; laser / no ATR: laser: p = 7.57E-06; dark / laser+cal.: p = 1; dark / no ATR: laser: p = 1; laser+cal. / no ATR: laser: p = 1). Illumination parameters as in (C), or in the absence of all-*trans* retinal (ATR). **(F)** OVC experiment in BWMs (BiPOLES and QuasAr2) with clamp interruption (protocol: 1) holding value - 5 %, wavelength determined by OVC, 2) interruption at calibration wavelength, 3) holding value - 5 % $\Delta F/F_0$). **(G)** Close-up of (F, lower panel), with comparison to voltage fluorescence activity of

7

65

unstimulated animals expressing only QuasAr2. **(H)** Group data of $\Delta F/F_0$ fluorescence amplitudes of typical, action potential-based fluctuations during -5 % clamping, or during no OVC action (n = 30 independent animals, p=2.69E-13). Box plots (median, 25-75th quartiles); open dot: mean; whiskers: 1.5x inter-quartile range (IQR). **(I)** Mean $\Delta F/F_0$ QuasAr2 signal (n = 6 independent animals, p=0.0023) in BWMs (co-expressed with BiPOLES) in the presence of laser light (637 nm) and additional signal in response to Chrimson excitation light (590 nm). In (C-E, H, I): Statistically significant differences were analyzed by two-sided t-test or One-way ANOVA with Bonferroni correction (***P ≤ 0.001, **P ≤ 0.01, *P ≤ 0.05, and see above for exact values). Box plots (median, 25-75th quartiles); open dot: mean; whiskers: 1.5x inter-quartile range (IQR). Source data are provided as a Source Data file.

8
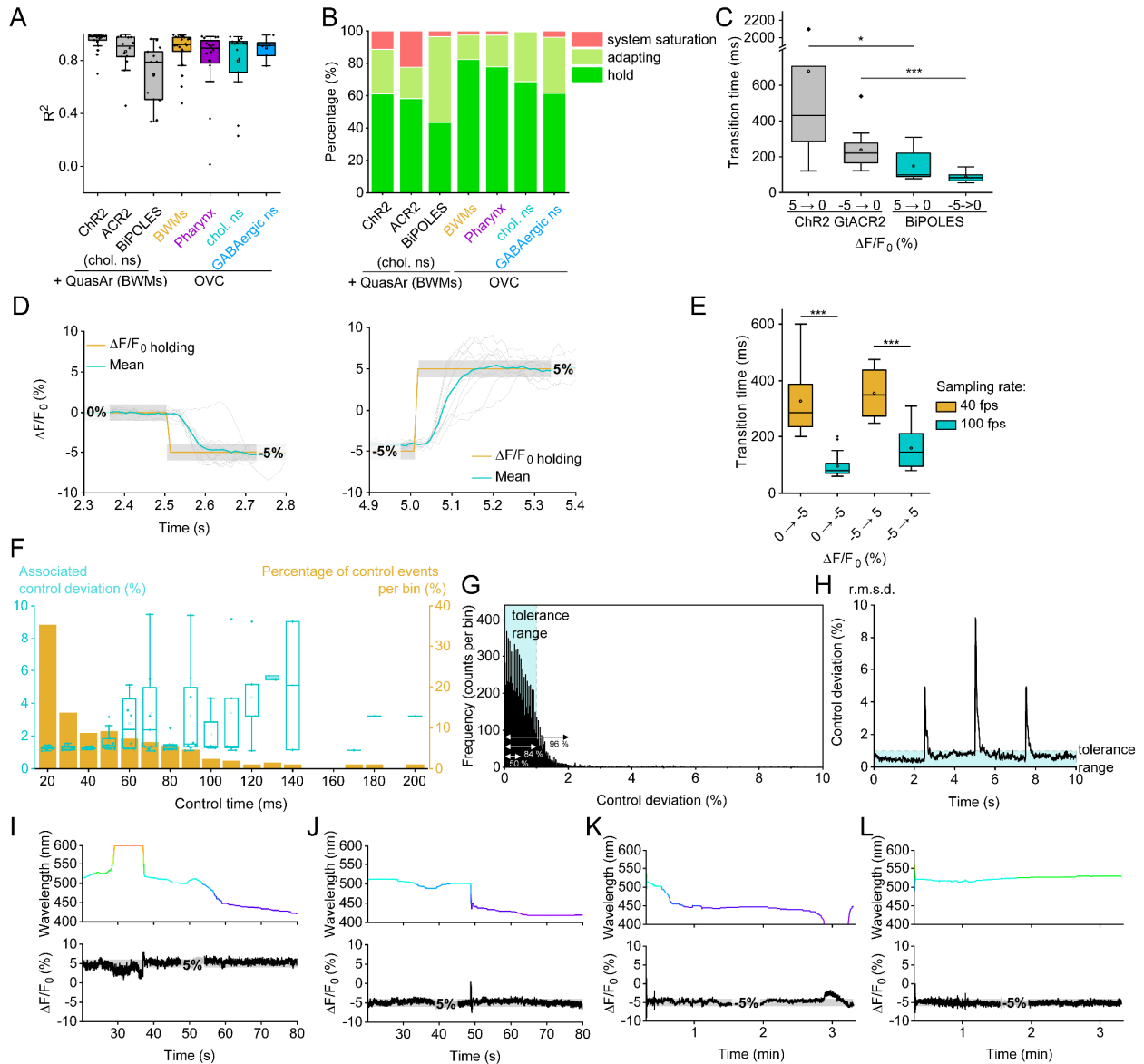
Supplementary Figure 6. Performance assessment, and long-term action of the OVC. (A) Quality of the exponential fit for bleach correction (coefficient of determination, R^2), for the different QuasAr2 / optogenetic actuator combinations, as indicated (n = 17, 14, 13, 22, 16, 14, 7 independent animals of these strains expressing: ChR2, ACR2, BiPOLES, OVC BWMs, OVC Pharynx, OVC chol. ns, OVC GABAergic ns). **(B)** Percentages of the clamping status (hold, adapting, system saturation), for the different QuasAr2 / optogenetic actuator combinations, as indicated (n = 17, 14, 13, 22, 16, 14, 7 independent animals of these strains expressing: ChR2, ACR2, BiPOLES, OVC BWMs, OVC Pharynx, OVC chol. ns, OVC GABAergic ns). **(C)** Summary of OVC speed, reflected by the time needed for a 5 % $\Delta F/F_0$ step for different configurations (single tools, same-cell approach; n = 17, 13, 10, 22 independent animals of these strains and conditions: ChR2, 5 → 0; ACR2, -5 → 0; BiPOLES, 5 → 0; BiPOLES, -5 → 0; statistically significant differences were: comparison: 5 → 0: ChR2 / BiPOLES: p = 0.01229; comparison: -5 → 0: ACR2 / BiPOLES: p = 3.8E-07). **(D)** Magnification of the transitions (left panel: 0 to -5 %, and right panel: -5 to 5% $\Delta F/F_0$) of the 4-step OVC protocol. Single traces are depicted in light grey, mean trace in cyan and $\Delta F/F_0$ holding in orange. **(E)** Comparison of transition times at 40 Hz and 100 Hz sampling rates (n = 8, 24, 8, 24 independent animals; 0 → -5 %: p = 1.38E-8; -5 → 5 %: p

9

67

= 4.13E-7). **(F)** Control events as a function of their duration and respective control deviations, measured in n = 11 independent animals. Orange bar graphs (right y-axis) represent the relative proportion of control events per control duration bin. The blue boxes (left y-axis) assign the respective control deviation that had to be overcome depending on the required control duration. Paired t test, P = 0.2271. **(G)** Histogram representation of all control deviations. Tolerance range is highlighted in blue. **(H)** Root-mean-square deviation of $\Delta F/F_0 - \Delta F/F_{0\,holding\,/\,target}$. Tolerance range is highlighted in blue. **(I-L)** Long-term OVC action, de- and hyperpolarizing steps. Shown are the achieved fluorescence values (lower panels, grey shades are tolerance range of the OVC protocol), and monochromator wavelength required (upper panels). Box plots (median, 25-75th quartiles); open dot: mean; whiskers: 1.5x inter-quartile range (IQR). Statistically significant differences were analyzed (C) by one-way ANOVA with Bonferroni correction (***P ≤ 0.001, *P ≤ 0.05). Source data are provided as a Source Data file.

10
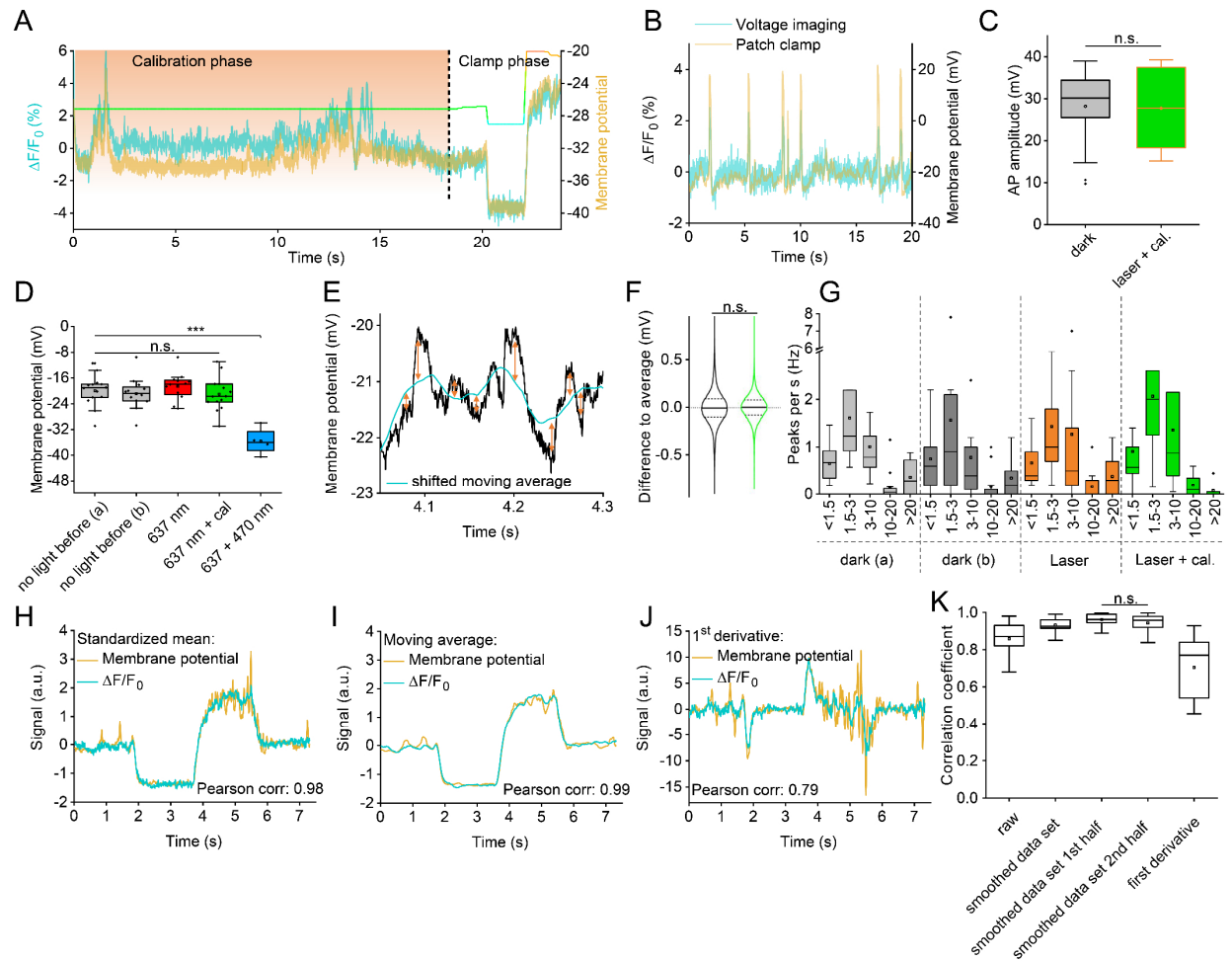
Supplementary Figure 7. Simultaneous patch-clamp and fluorescence measurement, normal membrane voltage behavior in BiPOLES-activated BWMs, no progressive error following calibration phase. (A) Original record of simultaneous voltage and fluorescence measurement during calibration and clamp phase (3 step OVC protocol, -3, +3 % $\Delta F/F_0$). Note the fluorescence trace was subsequently bleaching-corrected for the calibration phase. **(B)** APs in simultaneous patch-clamp and fluorescence recordings during OVC calibration phase (637 nm laser and 521 nm calibration wavelength). **(C)** Statistical analysis of AP amplitude. n = 4 independent animals, 24-27 APs. **(D)** Membrane potential in muscle was measured by patch-clamp under the indicated light conditions in n = 14, 12, 12, 14, 4 independent animals under these conditions: no light before (a), no light before (b), 637 nm, 637 nm + cal, 637 + 470 nm. **(E, F)** Analysis of small, subthreshold voltage fluctuations observed during patch-clamp, without or with 637 nm laser and calibration wavelength. Differences (arrows) of actual peaks to shifted moving average (blue), as a proxy for base line (E), were statistically analyzed in (F). n = 14 independent animals, with ca. 55.000 single data points per measurement. **(G)** Frequency distribution of distinct voltage signals, incl. APs, observed during patch-clamp recordings. Mean number of events (±S.E.M.) per second is shown as a function of peak amplitudes (in mV), for the different illumination conditions, as indicated below. n = 14 independent animals, 3118 peaks. None of the respective amplitude distributions showed significant differences to any other bin. **(H)** Patch-clamp derived membrane voltages (mean, yellow line) were compared to the mean $\Delta F/F_0$ levels (blue line) induced by the OVC during the clamp phase, based on parameters derived in the calibration phase (not shown). **(I)** As in (H), but mean moving averages were analyzed. **(J)** As in (H), but the signal change (1st derivative) was compared. **(K)** Statistical analyses of correlation coefficients

11

determined from data in (H-J; n = 14 independent animals), comparing the first and second halves of the experiments (p = 0.31). Correlation coefficients show high fidelity, typically >0.8. Statistically significant differences (***P ≤ 0.001) were analyzed by one-way ANOVA with Bonferroni correction (in D, F, G, K) or paired, two-sided t-test (in C). Box plots (median, 25-75th quartiles); open dot: mean; whiskers: 1.5x inter-quartile range (IQR). Source data are provided as a Source Data file.
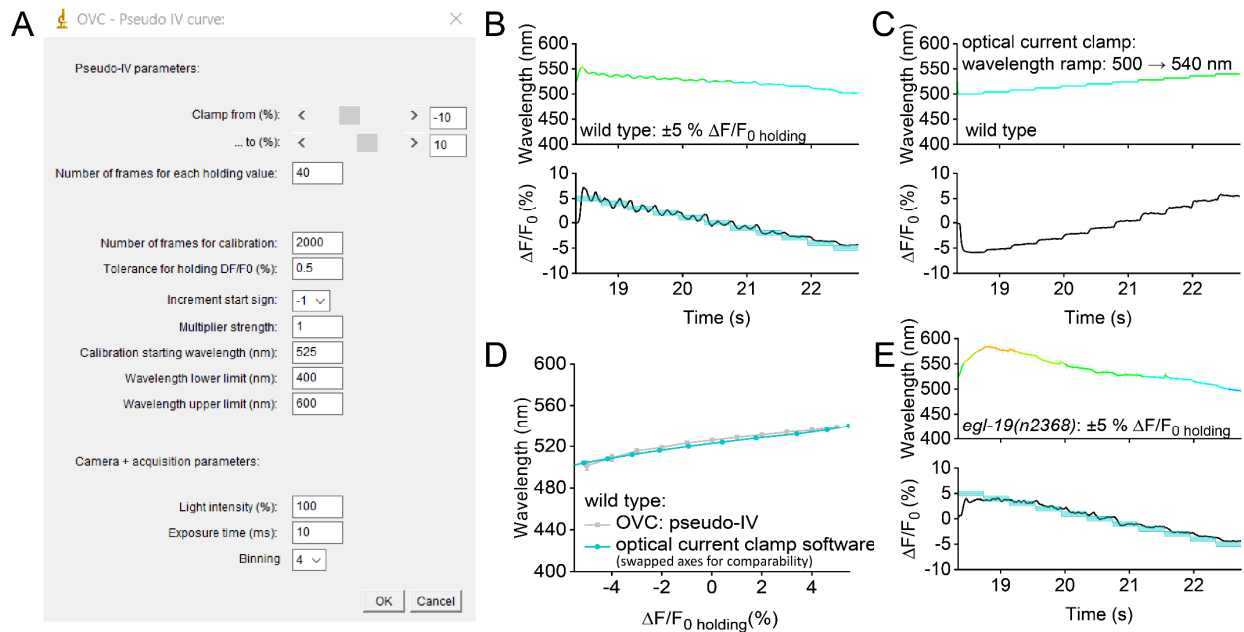
Supplementary Figure 8. Optical pseudo-I/V curve measurements: (A) Input tab of the "pseudo I/V curve" software allowing to run distinct % $\Delta F/F_0$ as clamp values (equivalent to voltages), while recording wavelengths (equivalent to currents). **(B)** Ramping +5 to -5 % $\Delta F/F_0$ (lower panel, mean ±S.E.M.; blue shades: tolerance ranges), while recording wavelengths (upper panel, mean ±S.E.M.; n = 17 independent animals). **(C)** Inverse experiment of (B), single trace, running a wavelength ramp (upper panel) and recording % $\Delta F/F_0$ (lower panel; n = 15 independent animals). **(D)** Comparison of OVC-based pseudo-I/V curve and measurement with the optical current clamp software (see **Supplementary Fig. 9A-C**), demonstrating high fidelity of the OVC control capabilities. **(E)** Measuring optical pseudo-I/V curves for *egl-19(n2368)* mutants, compare to (B) for wild type animals (n = 14 independent animals). Source data are provided as a Source Data file.

13
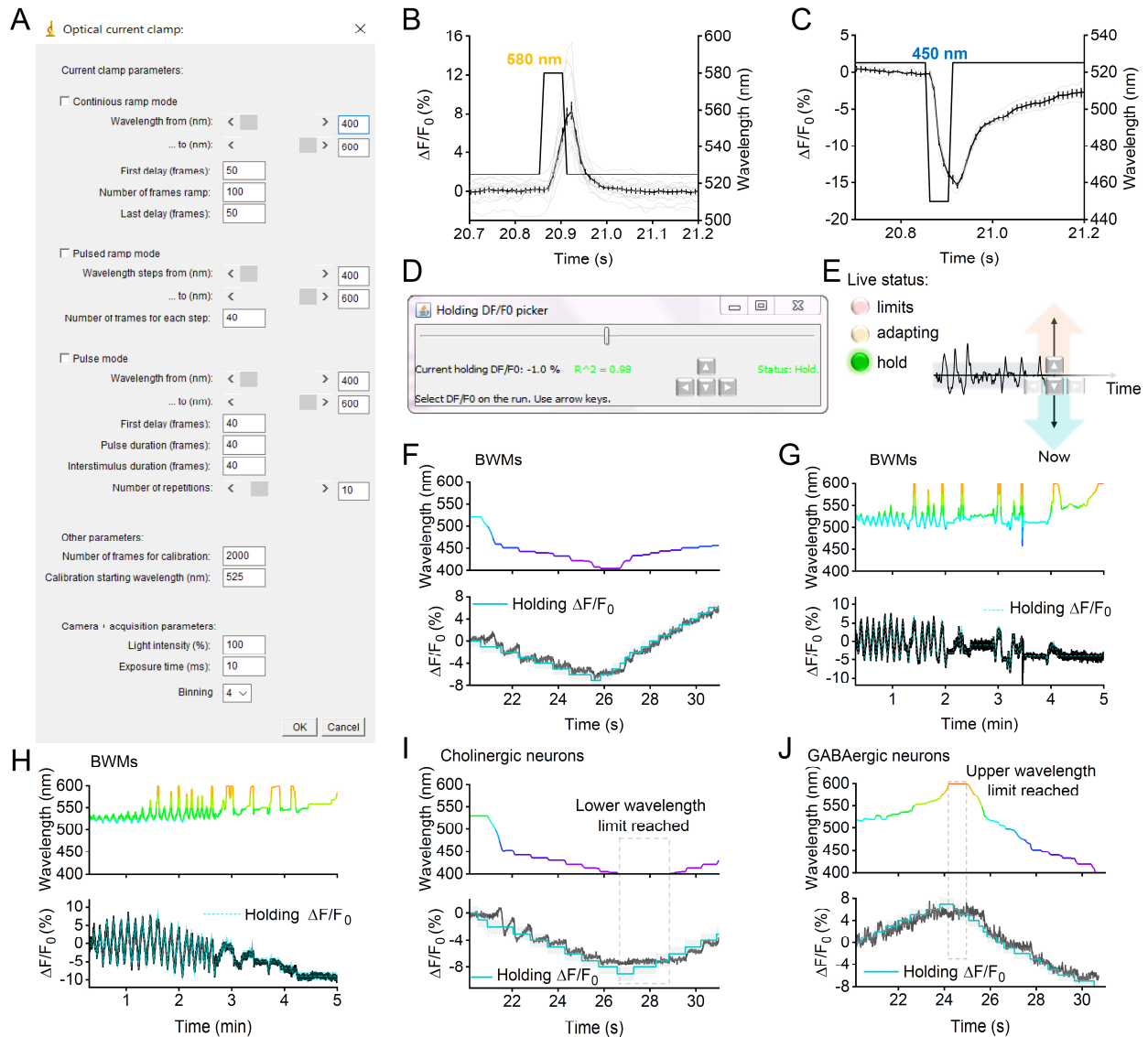
Supplementary Figure 9. Software for 'optical current clamp', and software for 'on-the-run' live voltage adjustment: (A) Software to achieve bidirectional optical current clamping, input tab. **(B, C)** Mean ±S.E.M. % $\Delta F/F_0$, resulting from 100 ms depolarizing (590 nm) step (B, n = 13 independent animals) or from a hyperpolarizing (450 nm) step (C, n = 5 independent animals). **(D-J)** Time-varying OVC live control ('on-the-run'). (D) User interface for software version allowing live control of membrane voltage fluorescence. (E) Scheme: Holding values can be selected using arrow keys. Live status (system on hold, adapting or exceeding limits) is shown, enabling adjustment. (F-H) Example traces of wavelength (upper panels) and holding values as % $\Delta F/F_0$ (lower panels) in BWMs for brief (F) and extended periods (G, H), as well as in cholinergic (I) and GABAergic neurons (J). Source data are provided as a Source Data file.

14
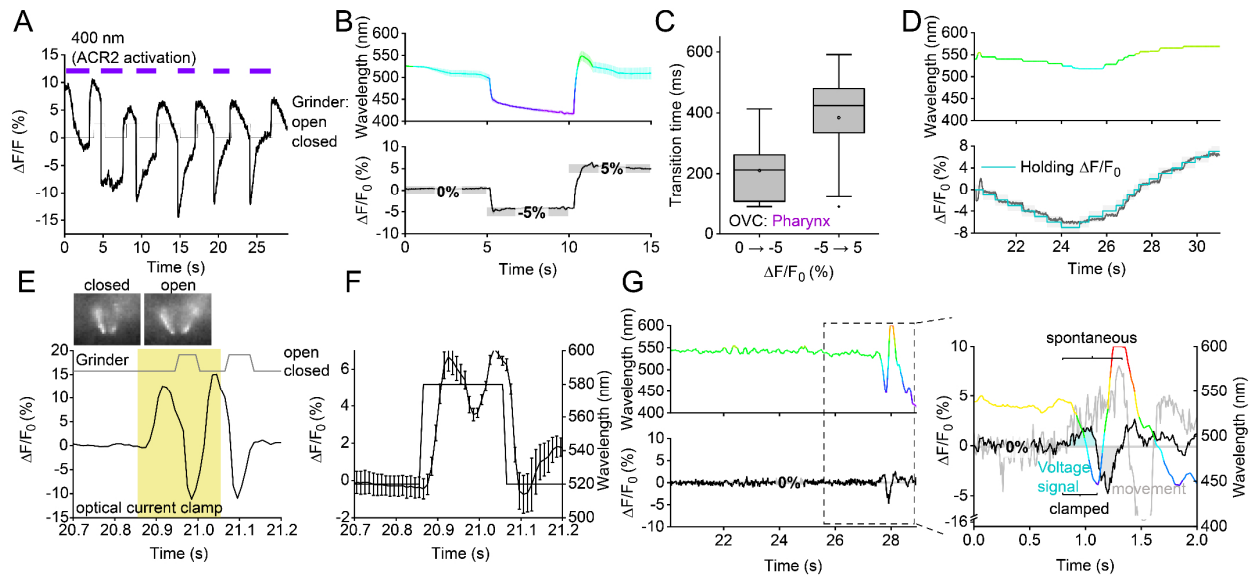
Supplementary Figure 10. Voltage imaging and OVC measurements in pharyngeal muscle and the motor neuron DVB. (A) Voltage imaging and analysis of grinder opening in animals expressing QuasAr2 and BiPOLES in pharyngeal muscle, stimulated with consecutive 400 nm light pulses (300 µW/mm^2). Corresponding open or closed state of the grinder as indicated. **(B)** Mean (± S.E.M.) traces (n = 16 independent animals) of OVC protocol in pharyngeal muscle (0, -5, 5 % ΔF/F$_0$). **(C)** Transition time required by the OVC in the pharynx to execute 5 and 10 % ΔF/F$_0$ steps (n = 16 independent animals). **(D)** "On-the-run"- experiment of OVC in pharyngeal muscle. **(E, F)** 'Optical current clamp' protocol, applied to pharyngeal muscle (yellow shade, depolarization evokes two APs), and assessing QuasAr fluorescence as a readout; single experiment (E), mean (± S.E.M.) fluorescence analysis (n = 9 independent animals, F). **(G)** Example DVB voltage fluorescence (lower panel) and wavelength (upper panel) traces upon suppression of an AP by the OVC. Inset: Close-up and overlay of spontaneous (light gray trace) and clamped (black trace) DVB voltage signal. Monochromator wavelength is presented in the respective color. Voltage signal and movement artefact highlighted in blue and grey, respectively. Box plots (median, 25-75th quartiles); open dot: mean; whiskers: 1.5x inter-quartile range (IQR). Source data are provided as a Source Data file.

15

Supplementary Table 1. Photon count and shot noise limited accuracy of the OVC system.

		per pixel	full ROI
Conversion gain (e$^-$/count)		0.23	
QE at 700 nm		0.87	
Exposure time (s)		0.01	
Mean grey value per pixel (ADU)		19714 ± 1825	
Signal	e$^-$	4534 ± 420	1578198 ± 176770
	photons	5212 ± 482	1814021 ± 203184
Photon shot noise (photons)		70 ± 3	1294 ± 69
Accuracy (%)		1.47 ± 0.05	0.08 ± 0.005

Source data are provided as a Source Data file.

Supplementary References

1. Oda, K. et al. Crystal structure of the red light-activated channelrhodopsin Chrimson. *Nature communications* **9**, 3949 (2018).
2. Zou, P. et al. Bright and fast multicoloured voltage reporters via electrochromic FRET. *Nature communications* **5**, 4625 (2014).

2.3 Microbial Rhodopsin Optogenetic Tools: Application for Analyses of Synaptic Transmission and of Neuronal Network Activity in Behavior

The following pages contain the published version of the book chapter "Microbial Rhodopsin Optogenetic Tools: Application for Analyses of Synaptic Transmission and of Neuronal Network Activity in Behavior"[13]. Material from: Bergs, A., Henss, T., Glock, C., Nagpal, J., Gottschalk, A. (2022). Microbial Rhodopsin Optogenetic Tools: Application for Analyses of Synaptic Transmission and of Neuronal Network Activity in Behavior. In: Haspel, G., Hart, A.C. (eds) C. elegans. *Methods in Molecular Biology*, vol **2468**. Humana, New York, NY. https://doi.org/10.1007/978-1-0716-2181-3_6. Reproduced with permission from Springer Nature.

Chapter 6

Microbial Rhodopsin Optogenetic Tools: Application for Analyses of Synaptic Transmission and of Neuronal Network Activity in Behavior

Amelie Bergs, Thilo Henss, Caspar Glock, Jatin Nagpal, and Alexander Gottschalk

Abstract

Over the past 15 years, optogenetic methods have revolutionized neuroscientific and cell biological research, also in the nematode *Caenorhabditis elegans*. In this chapter, we give an update about current optogenetic tools and methods to address neuronal activity and inhibition, as well as second messenger signaling, based on microbial rhodopsins. We address channelrhodopsins and variants thereof, which conduct cations or anions, for depolarization and hyperpolarization of the membrane potential. Also, we cover ion pumping rhodopsins, like halorhodopsin, Mac, and Arch. A recent addition to rhodopsin-based optogenetics is voltage imaging tools that allow fluorescent readout of membrane voltage (directly, via fluorescence of the rhodopsin chromophore retinal, or indirectly, via electrochromic FRET). Last, we report on a new addition to the optogenetic toolbox, which is rhodopsin guanylyl cyclases, as well as mutated variants with specificity for cyclic AMP. These can be used to regulate intracellular levels of cGMP and cAMP, which are important second messengers in sensory and other neurons. We further show how they can be combined with cyclic nucleotide-gated channels in two-component optogenetics, for depolarization or hyperpolarization of membrane potential. For all tools, we present protocols for straightforward experimentation to address neuronal activation and inhibition, particularly at the neuromuscular junction, and for combined optogenetic actuation and Ca^{2+} imaging. We also provide protocols for usage of rhodopsin guanylyl and adenylyl cyclases. Finally, we list a number of points to consider when designing and conducting rhodopsin-based optogenetic experiments.

Key words Optogenetics, Channelrhodopsin-2, Halorhodopsin, Archaerhodopsin, Mac, Calcium imaging, RCaMP, Electrochromic FRET sensor, Guanylyl cyclase rhodopsin CyclOp, Two-component optogenetics, TAX-2/TAX-4 CNG channel

Amelie Bergs and Thilo Henss contributed equally to this work.

89

1   Introduction

Optogenetics allows analyzing genetic determinants of synaptic transmission at the neuromuscular junction, as well as the causative role of single neurons in the generation of behavior, or their effects on signaling within neuronal circuits. This involves activators and inhibitors, which can be used as single tools, or in combination in different nodes of a neuronal network. Rhodopsin optogenetic tools are most commonly used. Opsins consist of seven transmembrane helices and require the vitamin A-related organic molecule retinal as a cofactor. When retinal is bound, the functional opsins are called rhodopsins. Retinal isomerizes upon the absorption of a photon, thus triggering a conformational change of the protein, which then enters a distinct photocycle [31–33]. Whereas type I rhodopsins combine the two tasks of light-sensation and (passive or active) ion flux across the plasma membrane, type II rhodopsins are G-protein coupled proteins that activate intracellular signal transduction pathways. Channelrhodopsin-2 (ChR2), a blue light-gated cation channel [34, 35], was the first microbial rhodopsin to be used for depolarizing neurons [2] and further to modulate behavior in a living organism [3]. In later studies, the yellow light activated chloride pump Halorhodopsin (NpHR) was used to hyperpolarize neurons [36]. Besides NpHR, archaerhodopsin (Arch) and the fungal rhodopsin Mac [37, 38] have emerged as further inhibitory optogenetic tools. More lately, anion channelrhodopsins, conducting chloride ions, were discovered or engineered in the lab [15, 39–41]. These constitute the most potent inhibitory rhodopsins, though in contrast to NpHR, they enable only shunting inhibition, as they cannot transport Cl^- against a gradient. Also, in neurons or neuronal compartments with inverse Cl^- gradient, these ACRs can be depolarizing [42]. Nowadays, the optogenetic toolbox comprises a wide variety of rhodopsins and variants thereof that are used to directly activate, directly inhibit or to indirectly modulate neurons [5, 15, 43]. We here included a chapter on the more recent additions to the *C. elegans* rhodopsin-based optogenetic toolbox. In addition, we describe the rhodopsin cyclases, which can be used as membrane-bound light-activated enzymes for the generation of cGMP, or, after mutation of the specificity-determining aminoacids, cAMP.

The experimental outcomes of optogenetic manipulations are evident by behavioral, electrical, or optical readouts [8, 44]. Combination of electrical recording and optical stimulation constitutes a powerful way to analyze the functionality of distinct neuronal connections [45, 46], but is less easily applied in *C. elegans*. Here, this methodology is feasible to investigate different mutants with pre- or post-synaptic defects to understand and/or determine their impact on synaptic transmission [47–50]. Optical readouts of

neuronal or network function are mostly obtained by calcium imaging. Genetically encoded calcium indicators (GECIs) permit a cell type specific observation of neuronal activity [51, 52]. However, the spectral overlap between the action spectrum of the optogenetic tool and the excitation spectrum of the GECI complicate this approach [53]. Yet, color-shifted variants of both sensor (like RCaMP; [44, 54, 55]) and actuator (like Chrimson; [56, 57]), enable more all-optical experiments nowadays. A recent addition in this context are the rhodopsin-based voltage imaging tools, which enable imaging of electrical events and can be combined with optogenetic actuation to some extent [27, 28, 30]. These proteins include variants of archaerhodopsin, which show a linearly voltage-dependent dim fluorescence of the retinal chromophore [58, 59] as well as the so-called electrochromic Foerster resonance energy transfer (eFRET) sensors [60–62], which combine archaerhodopsin and a fluorescent protein fused to it, that can transfer energy to the rhodopsin upon depolarization, and thus drops in its own fluorescence (which is more readily observable). Still, many applications of rhodopsins for functional circuit analyses in *C. elegans* lie in the combination of optogenetic actuation and simultaneous analysis of animal behavior [3, 47, 49, 54, 63–73].

2   Materials

2.1   Optogenetic Activation: Depolarizing Membrane Potential

Channelrhodopsin-2 and other microbial rhodopsin-based optogenetic activators enable a spatio-temporally precise control of genetically targeted neurons. This optogenetic activation allows us to study their causative role in generating diverse behaviors.

2.1.1   Channelrhodopsin-2

Channelrhodopsin-2 (ChR2) is a directly light-gated cation channel endogenous to the green alga *Chlamydomonas reinhardtii*, where it is enriched in the so-called eye spot region, mediating phototaxis and photophobic responses [35, 74]. ChR2 requires all-*trans*-retinal (ATR) as a cofactor [75]. This light-absorbing chromophore is embedded within the hydrophobic core of the seven transmembrane (TM) helices, where retinal binds covalently to a conserved lysine residue of TM domain seven by forming a Schiff base [76]. A protonation of the Schiff base shifts the absorption of light into the blue range of the spectrum (around 470 nm). Upon absorption of a photon, retinal isomerizes from the all-*trans* to the 13-*cis* configuration in less than 50 ns and triggers a conformational change of the protein that causes the opening of the channel [34, 35]. This induces an inward rectifying current for different monovalent (e.g. Na^+, K^+, and H^+) and some divalent cations, including (minute amounts of) Ca^{2+}, and in the native

context of a cell, particularly a neuron, thus depolarizes its plasma membrane [2, 3, 35].

The extent of current mediated by ChR2, as compared to other ion channels, is rather small (ca. 40 fS in contrast to ca. 40–60 pS in the case of a nAChR) [77]. In non-spiking neurons of *C. elegans*, all of the current required to activate a neuron has to be provided by ChR2, while in (mammalian) neurons firing action potentials, one "just" needs to reach threshold [11]. This implies that ChR2 expression levels need to be high, such that "strong" promoters should be used. Yet, there are more light-sensitive, conductive / better expressing variants of ChR2 available, that can be used as alternatives (see below).

The light-induced conductive state of ChR2 is part of a photocycle (Fig. 1) that underlies the mechanism of the channel [33]. In the dark, ChR2 is in the ground state D470. After absorption of a blue photon (maximal activation is reached with light of ca. 460 nm; however, as the rhodopsin spectrum is rather broad, light between ca. 350 and ca. 530 nm can activate ChR2), the intermediate state P500 is formed within nanoseconds by the light-induced isomerization of retinal. The following deprotonation of the Schiff base to the extracellular side converts the protein to the P350 state within ca. 25 μs. Reprotonation of the Schiff base from the cytoplasmic side leads to the conducting state P520 [32, 77, 78], which is in a pH-dependent equilibrium with the deprotonated form P390. Upon closing, the channel changes to the intermediate states $P480_a$ and $P480_b$ before it eventually recovers to the ground state after ca. 45 s. In a flash-photolysis (i.e. a "single-photon") experiment, the latter is the rate-limiting step of the photocycle, in which hydrogen bonds of amino acids
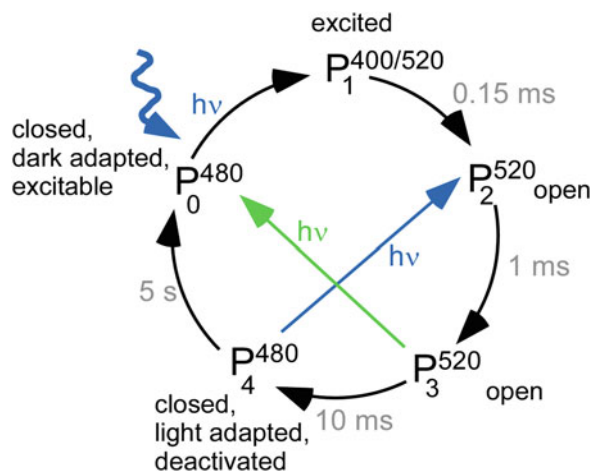

Fig. 1 Photocycle of Channelrhodopsin. Adapted from [32]. Blue light induces the conducting state, but can also short-circuit the light-adapted dark state to the open state. Green light can lead to channel closure

change and backbone rearrangements occur. However, during continuous blue light, $P480_b$ absorbs a photon to be directly converted into the early P500 intermediate, thereby circumventing the ground state D470. Thus, after a brief peak current, involving all available channels, steady state currents occur, as a distinct proportion of channels in the dynamic equilibrium can be converted again to open state after channel closure, i.e. the stationary-state level results from the desensitization of a fraction of channels. The larger the proportion of channels in the light-sensitive state, the more can be opened by light. The shorter the time required for channel closure and reactivation, the more channels can regain a light-sensitive state. From these effects, a higher steady state current will result. This has been achieved by certain mutations, e.g. in the "high efficiency" E123T variant [79]. Upon repeated stimulation, ChR2 exhibits a desensitized state, which leads to reduced initial peak currents in successive trials. Desensitized channels recover in the dark only slowly, with a typical time constant around 5 s, influenced by the extracellular pH and the membrane potential [35, 47]. Once the channel is open, it closes by spontaneous progression through the photocycle. However, channel closure may also be achieved by green light illumination of the P520 state [78]. In sum, size and the kinetic properties of the ChR2 photocurrent are a result of the described photocycle, the ion selectivity and the time constants of activation, deactivation, and inactivation [31].

In comparison to rhodopsins of higher eukaryotes, retinal does not dissociate from its opsin molecule after activation, but thermally reisomerizes to the initial all-*trans* state [80]. Because nematodes do not generate ATR, exogenous ATR has to be added to the bacteria lawn in order to render the channel functional [3]. However, transgenic animals grown without ATR can serve as convenient negative controls for ChR2 experiments in *C. elegans*.

2.1.2   ChR2 Variants with Distinct Functional Properties for Specific Applications

ChR2 is a powerful tool, but there is also room for improvement. Thus, ChR2 variants that enable specific optogenetic applications were engineered by site-directed mutagenesis, yielding channels with altered ion selectivity and conductance, spectral properties or photocycle kinetics. The mutated residues are often near the retinal-binding pocket or in close proximity of the putative pore of the channel. ChR2 with histidine 134 mutated to arginine, ChR2(H134R), shows a two-fold extended open state life time, a two-fold higher Na^+ conductance and a two-fold lower degree of inactivation [3, 81]. Conversely, the mutation of glutamate 123 to threonine, ChR2(E123T), shortens closing kinetics significantly and is thus capable to elicit firing frequencies in neurons with more than 200 Hz [79]. This has also been used to elicit very fast depolarization of neurons for electron microscopy analyses of the

stimulated neuromuscular junction [82]. Mutation of threonine 159 to cysteine, ChR2(T159C), displays up to tenfold enhanced photocurrents, due to higher conductance and/or better plasma membrane trafficking, as well as faster kinetics [83, 84]. The mutation leucine 132 to cysteine, ChR2(L132C), exhibits an enhanced calcium conductance by sixfold [85]. ChR2 was also altered to allow long-term manipulation at low light intensities [86–88]. Here, mutations within the so-called DC-gate (D156 and C128 (e.g. mutated to serine, C128S), step-function-opsins, SFOs) significantly delay the closing of the channel in the dark to several minutes, thus a large proportion of the channels accumulates in the open state. Similar effects were found for the D156A and D156C (ChR2-XXL) mutant as well as the C128S; D156A double mutant [89, 90], while a quintuple ChR2 variant ("QUINT," ChR2(C128S;L132C;H134R;D156A;T159C)) showed the longest persistent depolarization observed in the worm so far (8–10 h following a single blue light pulse) [15]. For low light applications, ChR2-XXL is the reagent of choice, demonstrating significant activation (light-evoked contraction in muscle) at intensities as low as 0.26 $\mu W/mm^2$ [15, 88]. This effectively reduces the light intensity required to achieve activation, and both effects allow stimulating cells in the long term (even for hours) without the need for continuous intense blue light exposure that would be harmful. Alike wild type ChR2, this variant can be turned off by yellow or green light [86, 87]. While handling SFO expressing animals, especially QUINT and ChR2-XXL transgenics, working light should be reduced to a minimum, since even red filters for transmission light are insufficient to circumvent at least minor pre-activation of animals. Hence, after transferring SFO animals to experimental plates, a subsequent recovery period of several minutes in the dark is advisable before starting the experiment.

In general, we find that combining the H134R mutation with the above mentioned mutations improves the function in *C. elegans*, for unknown reasons. Last, variants of ChR have been generated that have altered activation spectral peaks. The chimeric protein C1V1, composed from *Chlamydomonas reinhardtii* ChR1 and *Volvox carteri* ChR1, with two additional mutations, is activated with green light instead of blue light [89, 91]. However, due to the naturally broad absorption band of rhodopsins, it can still respond to blue light, and is furthermore quite light-sensitive. Thus, in order to allow for independent blue and green activation of two distinct neuron populations, with ChR2 and C1V1-ETET, respectively, the highly efficient ChR2(H134R; T159C) double mutant should be used (to allow efficient activation with blue light while not co-activating C1V1), and the relative expression levels of the two proteins need to be carefully titrated [84].

2.2   Optogenetic Inhibition: Hyperpolarizing Membrane Potential

The ability to silence the activity of genetically defined neurons in a temporally precise fashion allows investigating the causative role of the defined neuron cell type in driving the behavior. When used in combination with channelrhodopsins, optogenetic inhibitors enable multimodal optical interrogation of neural circuits [36, 38].

2.2.1   Halorhodopsin

Optical inhibiton of neural activity was first achieved using the yellow light-gated chloride pump Halorhodopsin (NpHR), from the archaeon *Natronomonas pharaonis* [36]. When expressed in *Xenopus* oocytes, it produced vectorial, hyperpolarizing inward currents associated with chloride influx into the cell, with a peak photocurrent observed at 590 nm excitation. Illumination with yellow light potently inhibited action potential firing in cultured hippocampal neurons expressing NpHR. Activation of NpHR in *C. elegans* body wall muscle cells resulted in the extension of the worm's body due to hyperpolarization and relaxation of muscle cells. In contrast to ChR2, which is a channel that is opened by absorption of a photon to allow passage of many ions, NpHR as a pump allows for only one ion to be transported per photocycle. Thus, as is the case for ChR2, though for different reasons, also NpHR requires robust plasma membrane expression. Unfortunately, the protein traffics inefficiently to the plasma membrane in eukaryotes. Hence, molecular engineering of NpHR, comprising of incorporation of ER export and trafficking motifs from mammalian membrane proteins, was performed [92, 93]. However, incorporating these plasma membrane targeting signals in NpHR did not enhance NpHR's ability to photo-inhibit excitable cells in worms as these signals are not conserved in *C. elegans* [38]. Thus, for a strong and robust inhibition, massive over-expression of NpHR is required in worms, such that enough protein makes it into the plasma membrane. This is not always possible, unless a strong promoter is used to drive its expression, which limits the neuronal networks that can be investigated in this ideal model system for optogenetics.

2.2.2   Archaerhodopsin and Mac

As alternative to NpHR for neuronal photoinhibition, light-driven outward-directed proton pumps were discovered or characterized for utilization in optogenetics in an extensive screen of microbial opsins carried out by Chow and colleagues [37]. Archaerhodopsin-3, known as Arch, from *Halorubrum sodomense*, and Mac, from the fungus *Leptosphaeria maculans*, are activated by yellow-green and blue-green wavelengths of light, respectively, and express well on the neural plasma membrane. The magnitude of photocurrents mediated by outward proton flux through Arch and Mac are higher than those with NpHR's chloride influx, making them more potent photo-inhibitors. Both Mac and Arch have been effectively utilized to inhibit excitable cells in *C. elegans* [38, 63]. Using behavioral assays and current recordings from dissected muscle cells expressing

NpHR, Mac or Arch, Husson and colleagues showed that Arch is the most potent hyperpolarizer when illuminated with yellow-green light. Also, the action spectrum of Mac is blue-shifted as compared to NpHR and Arch (primary peaks of their action spectra are 550 nm for Mac, 566 nm for Arch, and 590 nm for NpHR). Using the nociceptive ASH network, they also demonstrated that Mac and Arch can be used to interfere with downstream signaling in networks in which upstream neurons are stimulated by ChR2, using multimodal illumination strategies. A concern with the usage of the proton pumps is the gradual elevation of proton concentration in the extracellular space, which might have deleterious or non-specific effects on the activity of neurons. As the pseudocoelom is well buffered, this may not be a problem.

2.2.3 *Voltage Imaging Tools*

Since Ca^{2+}-imaging often fails to display fast neuronal dynamics, such as action potentials, the dim, but linear, voltage-dependent fluorescence of Archaerhodopsin (Arch) mutants is employed in the emerging field of rhodopsin-based voltage imaging [29, 58, 94]. In addition, voltage imaging also allows to reflect hyperpolarization, which is not the case for Ca^{2+}-imaging. Molecular engineering of the light-driven proton-pump Arch resulted in various mutants that are pump-dead and show an improved brightness and voltage sensitivity [30, 59]. Moreover, eFRET sensors were established, by fusing a fluorescent protein to the sensor (Fig. 2). Here, the bright fluorescence of the fluorescent protein is imaged, which becomes quenched upon depolarization of the membrane voltage,
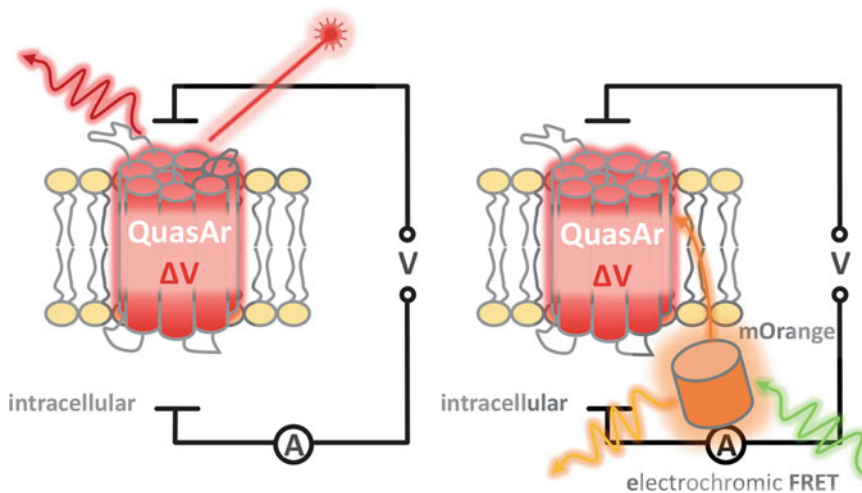

Fig. 2 Genetically encoded voltage sensors based on microbial rhodopsins. (**a**) QuasAr, a mutated version of Archaerhodopsin, can be used as a directly fluorescent voltage sensor, excited by strong 637 nm laser light, however, its fluorescence is dim. (**b**) As a combination (fusion) with fluorescent proteins (like mOrange), sensors like QuasAr (or Arch(D95N) or MacQ) can be used as indirect sensor, that quenches the fluorescence of the XFP during depolarized states, due to electrochromic Foerster Resonance Energy Transfer (eFRET)

thus enhancing the brightness of the imaging tools [28, 62]. As for GECIs, rhodopsin-based voltage indicators can be combined with other, mostly blue light activatable optogenetic actuators such as ChR2 or ACR2 [27, 59, 95].

In a *C. elegans* side-by-side study, the Arch mutant QuasAr [59] performed best and could reliably demonstrate ChR2- and ACR2-evoked de- and hyperpolarization, as well as recording of spontaneous action potentials in muscle cells (~78% $\Delta F/F$ per 100 mV) [27].

2.2.4 Anion Channelrhodopsins (ACRs)	Next to commonly used optogenetic tools like ChR2 and NpHR, there has been great progress in extending the spectrum of available optogenetic actuators, by either molecular engineering of existing or discovery of novel natural rhodopsin variants. For the increasingly complex requirements of applications, new tools differ in conductivity, kinetics, spectral properties, and ion selectivity, whereas the latter defines the tool being either a de- or hyperpolarizer [81, 86–88, 96]. The gap of equally efficient hyperpolarizing tools was closed by the natural Cl^--conducting anion channel rhodopsins (ACR1 and ACR2, derived from *Guillardia theta*) [39]. Prior to that, light-driven ion pumps as NpHR were the agents of choice, however being restricted by active transport, since only one ion is moved per photocycle [36, 38].

In *C. elegans* behavioral experiments, investigating the body length upon light stimulation, expression of ACRs in muscle (p*myo-3* promoter) led to the strongest relaxation effects recorded to date (up to $6.1 \pm 0.4\%$ body elongation), while requiring only very low light intensities (down to 3.6 µW/mm^2) [15]. Despite their high operational light-sensitivity, handling of ACR-expressing animals proved to be possible, as long as red filter foil was used for transferring of the transgenic, ATR-supplied worms (ATR incubation and storage of ATR-supplied animals in aluminum foil). In addition to their high efficiency, ACR1 is about 45 nm red-shifted compared to ACR2, which facilitates a selective stimulation by green light (peak absorption: 515 nm) and a combination with blue light-activated optogenetic tools such as ChR2 (peak absorption: 470 nm). In contrast to that, blue light activatable ACR2 (peak absorption: 470 nm) can be combined with red-shifted ChR variants, like ChRimson.

|	
2.3 Guanylyl Cyclase Rhodopsin (CyclOp)	In 2014, a novel rhodopsin was described in the sweet water alga *Blastocladiella emersonii* [97]. This protein turned out to be a rhodopsin fused to a guanylyl cyclase domain that forms dimers and is activated by blue-green light to catalyze the conversion of GTP to cGMP at high efficiency and very high dynamic range [25, 98]. As could be shown, BeCyclOp is a robust tool in *C. elegans* excitable cells, i.e. muscles and neurons (Fig. 3). In muscles, in combination with the cGMP-gated cation channel
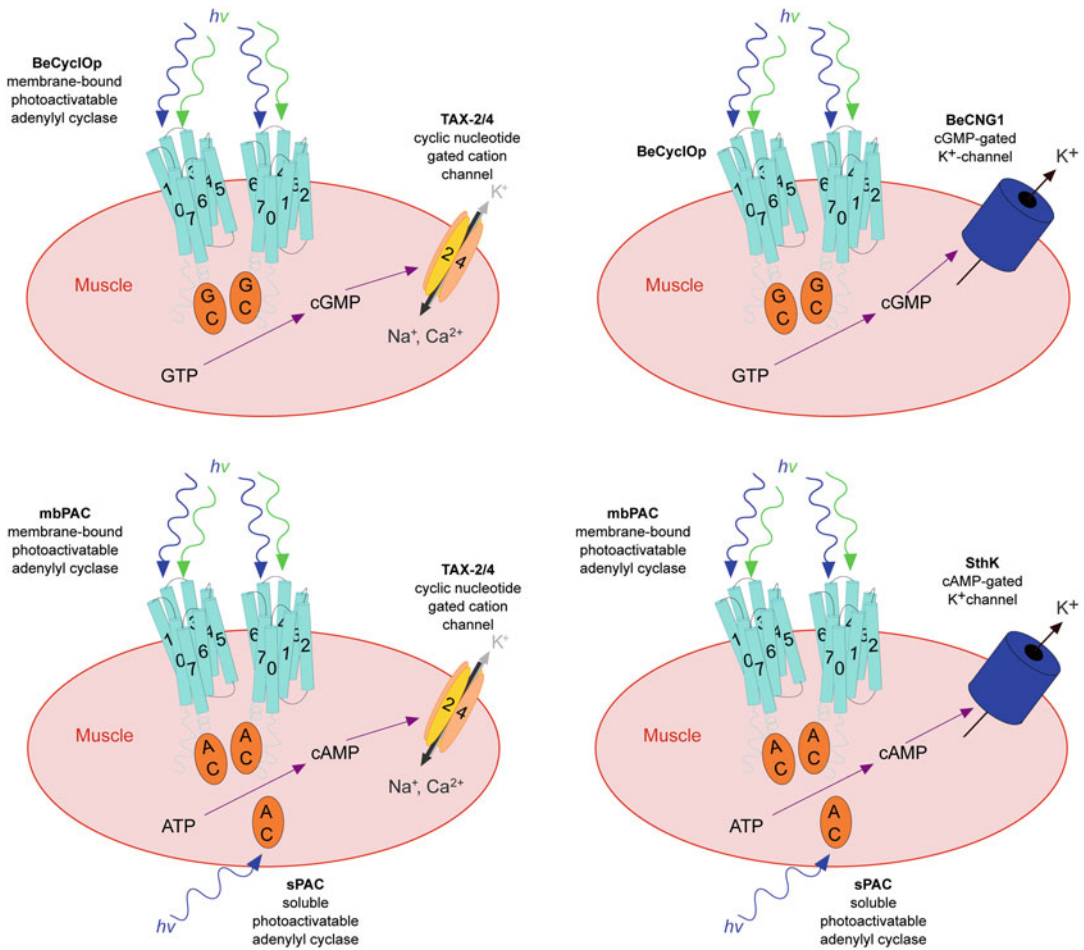
Fig. 3 Cyclase rhodopsin-based two-component optogenetic systems for de- and hyperpolarization. (**a**) Co-expression of BeCyclOp (or CaCyclOp) with the cGMP-activated TAX-2/-4 cation channel effectively causes depolarization by blue-green illumination. (**b**) Co-expression of BeCyclOp with the BeCNG1 K⁺-channel allows driving mild hyperpolarizing currents (**c**) Co-expression of BeCyclOp(A-2x) (or CaCyclOp(A-2x)), i.e. membrane-bound photoactivated adenylyl cyclases (mbPACs), as well as soluble PAC, also allows cAMP-driven gating of the TAX-2/-4 cation channel (even though the channel has much lower affinity for cAMP). (**d**) mbPACs as well as soluble PAC can also be used to trigger outward K⁺-currents via the cAMP-gated K⁺-channel SthK

encoded by TAX-2 and TAX-4 subunits, which have to be co-expressed, as they are not intrinsically present in muscle cells, BeCyclOp robustly causes depolarization upon photoactivation, that is also quite long-lasting, likely due to the low expression of phosphodiesterases in this tissue [25]. In sensory neurons (specifically, BAG neurons that detect oxygen), BeCyclOp photostimulation led to behavioral responses that mimicked photodepolarization by ChR2, i.e. increased locomotion speed. Thus, this rhodopsin is a valuable tool for research in sensory neurons, which often use cGMP as signaling molecule.

Recently [26], we implemented another CyclOp, from *Catenaria anguillulae* (CaCyclOp), as an additional tool for cGMP generation. CaCyclOp exhibits a slower cGMP production rate, but comparably high substrate specificity as BeCyclOp. Thus CaCyclOp may be used for the fine-tuning of cGMP levels in respective cell types. In addition, since no membrane-bound photoactivatable tool for cAMP generation existed, we mutated the specificity-determining amino acids of the cyclase domains, and implemented YFP-BeCyclOp(A-2x) and YFP-CaCyclOp(A-2x). These tools are characterized by high substrate specificity and magnitude of cAMP production.

In cholinergic neurons (p*unc-17* promoter), the membrane-bound PACs and the soluble bPAC evoke similar increases in crawling speed and number of swimming cycles during illumination, however, the membrane-bound PACs induce longer-lasting behavioral changes.

Besides their application as single optogenetic tools, CyclOps can be combined with cyclic nucleotide-gated (CNG) channels, obtaining two-component optogenetic systems for de- and hyperpolarization of excitable cells. To this end, we co-expressed respective CyclOps for cGMP or cAMP creation with the CNG channels TAX-2/-4 (Na$^+$ and Ca^{2+} conductive), and the cAMP- and cGMP-gated K$^+$-channels from *Spirochaeta thermophila* (SthK) and *Blastocladiella emersonii* (BeCNG1), respectively, displaying variable levels of activity, kinetics, and long- or short-lasting effects (*see* **Note 1**). Though these systems for de- and hyperpolarization require expression of 2–3 genes, they represent valuable tools in comparison to single rhodopsin tools due to the amplification of the primary signal (meaning reduced light budget) and K$^+$-conductance.

3 Methods

3.1 Specific Application of Optogenetics to Investigate Synaptic Function

C. elegans is particularly suited to study mechanisms of chemical synaptic transmission. The basic synaptic machinery involved in neurotransmission is conserved from *C. elegans* to mammals. The distinct advantage of working in worms is that most mutants affecting pre- or post-synaptic function are viable, and can be analyzed in adult animals, unlike in mammals. However, the physiological tools used to study synaptic function in worms—pharmacological and behavioral assays, as well as electrophysiological recording of neuronal activity [99–103]—are either slow and tedious or technically challenging. Here, optogenetics offers advantages as it allows non-invasive stimulation in intact moving animals, is repeatable, is specific for stimulation of a neuron type, and causes the release of the neurotransmitter at the synaptic sites only. In 2008, Liewald et al. introduced optogenetic investigation of neurotransmission

(OptIoN), which uses photo-induced electrical activity to affect behavior, or to drive transmission at dissected neuromuscular junctions (NMJ), in a quantitative and time-resolved manner. Selective and repetitive photostimulation of cholinergic or GABAergic neurons can be used to examine mutants for defects in various aspects of synaptic function [47, 49, 50]. Following on, Liu et al. also studied graded synaptic transmission at the NMJ using ChR2-mediated photostimulation [48]. Optogenetic stimulation followed by electron microscopic analysis of the synaptic ultrastructure has also yielded new insights into the maintenance of synaptic vesicle pools and synaptic activity [82, 104]. The basics of conducting an optogenetics experiment in worms are described below.

3.1.1 Expression of Optogenetic Proteins

Optogenetic activators and inhibitors are expressed using appropriate promoters. There are promoters known which can drive expression specifically in many if not all tissues and cell types in *C. elegans*. However, there are a very few promoters that drive expression specifically in only single (pairs of) neuron(s), which is particularly important for applications in this small nervous system, as every single neuron is expected to have a distinct role or even several roles. Thus, for optogenetic manipulation of a single cell or cell type, either combinatorial genetic approaches using intersectional promoter strategies with Cre or FLP recombinases should be used [105–108]. Alternatively, or in combination, patterned illumination with digital micromirror devices (DMDs), LCD projectors, etc. have been employed [53, 63, 64, 109]. The *myo-3* promoter, driving expression in body wall muscle cells, is commonly used to express and assess the efficacy of new optogenetic proteins [3, 36, 38, 84]. This is convenient, as photoactivation or inhibition of muscle cells lead to a straightforward behavioral readout (body contraction or elongation, respectively). Also, muscle cells are relatively more accessible than neurons to electrophysiological characterization of the optogenetic proteins [47, 110]. For dos and don'ts regarding the usage of the different optogenetic tools (*see* **Notes 2** and **3**).

3.1.2 Worm Rearing

Transgenic worms expressing the desired optogenetic protein are cultivated on standard NGM plates and fed with *E. coli* OP50. The microbial rhodopsins require all-*trans*-retinal (ATR) as a cofactor, which has to be exogenously supplied in the OP50 that is fed to the worms [3, 47]. Animals for optogenetic analyses are cultivated on NGM plates with OP50 supplemented with 2.5–5 μM ATR (calculated with respect to the volume of NGM in the culture dish) for one generation at 20 °C in the dark. Typically, 1 μl 100 mM ATR stock solution in EtOH is mixed with 1000 μl of OP50 culture, and 200–300 μl of this mixture are spread onto the top of the NGM plates. Thus, ATR is not mixed into the NGM medium itself. As a control, animals of the same genotype are grown on NGM plates

without ATR. Ca. 18 h prior to experiments, L4 larvae, grown on ATR plates, are placed on fresh ATR plates.

3.1.3   Illumination

1. An epi-fluorescence microscope with a mercury lamp as light source and standard bandpass filters for the desired excitation wavelength can be used to induce a behavioral response in transgenic animals. Optogenetic proteins expressed in *C. elegans* are commonly activated with light intensities in the $0.2–5$ mW/mm^2 range.

2. The precise light intensity needs to be measured, e.g. with a light-meter, where the sensor is placed under the microscope instead of the culture dish, at the focal plane that would be used for worm imaging during the experiment. The diameter of the spot of light can be measured when focused on a piece of paper through a "Neubauer" chamber (used for cell counting, with a μm grating). Of course, it can also be calculated from the specifications of the microscope and objective used.

3. Duration of the light stimulus is set with a computer-controlled shutter. For a typical behavioral response, e.g. from mechanosensory neurons, a 500 ms light pulse is sufficient. For full muscle contraction to be achieved, a 2 s or longer light stimulus should be used.

4. LEDs with the desired wavelength are also commonly used as excitation light sources. Patterned single cell illumination [64, 109], and see above, is another means to provide illumination, even of single neurons in freely moving animals.

3.1.4   Video Analysis

1. The locomotion behavior of the worms on a solid NGM substrate can be quantified and several locomotion parameters like the worm body length, velocity, body bending angles, frequency of turns, etc. can be obtained (for a review of different tracking and behavior analysis systems available for *C. elegans*, *see* [111]).

2. For quantitative analysis of worm body length, consecutive frames (e.g. 30 frames per second) from the captured videos are extracted as individual images. Individual images are converted into binary images (black and white), background subtracted and skeletonized into a single pixel thick backbone. This image processing can be automatized with custom written ImageJ or Matlab scripts [47, 84, 109, 112]. The body length of the worm is recorded as the length of the backbone obtained after skeletonization.

3. Worm length is normalized by the mean length before the light stimulation and followed over hundreds of consecutive video frames. Length chronograms of multiple worms are then averaged and the length profiles of test vs. control strain can be

plotted [47]. For single time points, body length can also be measured "by hand," by drawing a segmented line along the backbone of the animal, e.g. using ImageJ, and determining the length in pixels.

4. For precise annotation of the different aspects of locomotion, different worm-tracking packages based on machine vision tools have been developed by the worm research community [111]. These tracker systems can be combined with optogenetic experiments that require spatially and temporally precise illumination of the worm with various colors of light [63, 64, 109].

3.2 Combining Optogenetic Actuation with Ca^{2+} Imaging

Ca^{2+} imaging provides a non-invasive way to monitor the activity of muscles and neurons in *C. elegans* in close to real time. This can be achieved in fully intact worms, due to the optical transparency of the animal. Different genetically encoded calcium indicators (GECIs) have been designed to visualize and quantify intracellular calcium levels [51, 52, 113–116]. For chemically synthesized Ca^{2+} sensitive dyes, we refer the reader to other reviews; application of such dyes in *C. elegans* is challenging due to the difficulty to get them across the cuticle. Instead, GECIs are preferred to capitalize on the genetic tractability of *C. elegans*. Since GECIs are built entirely from proteins, they may be expressed in targeted cells under a tissue-specific promoter. There are two major classes of GECIs: The FRET-based indicators such as cameleons [51] and Tn-XXL [116], as well as the single fluorophore indicators, such as the GCaMPs and GECOs [52, 113–115, 117].

Cameleons have been extensively used in *C. elegans* to monitor neural activity [118–121]. These GECIs use Förster resonance energy transfer (FRET) to indicate changes in Ca^{2+} concentration [51, 122]. FRET is a distance- and orientation-dependent, radiation-free transfer of energy from donor to acceptor chromophore (e.g. CFP and YFP), which results in the loss and gain of fluorescence of donor and acceptor molecule, respectively. In Cameleons CFP and YFP are connected via calmodulin and the calmodulin-binding peptide M13. When calmodulin binds Ca^{2+} ions, it undergoes a conformational change, binds M13, and thus affects CFP/YFP FRET efficiency. The ratio between YFP and CFP fluorescence serves as a measure for the Ca^{2+} concentration [51, 118], and the ratiometric nature allows to control for focus artifacts of the fluorescent signals, particularly in experiments with freely behaving animals.

The non-FRET Ca^{2+} indicators consist of a single circularly permuted (cp) GFP-variant that is fused to calmodulin at its C-terminus and to M13 at its N-terminus. Binding of Ca^{2+} causes the M13 and calmodulin domains to interact and to alter the environment of the chromophore (exclude water), which changes

the brightness of the indicator [113, 123]. Examples for single fluorophore GECIs are the GCaMPs, originally introduced by Nakai et al. in 2001 [52], and the GECOs [117]. Since then, GCaMPs have been improved continuously by using structure-based mutagenesis, with GCaMP6 as the most recent version [114, 115]. These Ca^{2+} indicators are prone to movement and focus artifacts. Thus, they are usually co-expressed with a reference fluorophore with a non-overlapping fluorescence, which must not alter with calcium concentration [124], to allow distinction of Ca^{2+}-induced vs. focus-dependent fluorescence intensity changes.

The combination of optogenetic modulators with calcium indicators constitutes a powerful approach to study neuronal functionality. However, the overlap of spectral channels is often problematic. ChR2 and CFP, GFP or YFP excitation spectra largely overlap, thus it is virtually impossible to image Cameleons or GCaMPs without concomitantly activating the ChR2-containing cell. One, however, "dirty" approach is to compare stimulating one cell with ChR2 and imaging a linked cell with Cameleon or GCaMP, and to perform this experiment twice, once with, and a second time without ATR. In the case of the ATR-experiment, one will not achieve a stable "baseline" Ca^{2+} trace, however. Another approach is to spatially restrict the actuation and the imaging light, provided that the cells to be imaged and the cell to be activated are spatially distinct from one another. This has recently been achieved by patterned illumination using a DMD-based illumination system in combination with a tracking system [53, 64]. A much less demanding approach is provided by using a spectrally shifted (relative to ChR2) Ca^{2+} indicator, namely RCaMP [44]. RCaMP is based on the red fluorescent protein mRuby. In 2012, Husson and colleagues used RCaMP as an optical readout for the excitation of the forward command neuron PVC by upstream photoactivation of the sensory PVD neuron [54]. Thus, the combination of ChR2 and RCaMP is feasible for the analysis of neuron to neuron and neuron to muscle communications. A similar, actually more potent red fluorescent Ca^{2+} indicator is R-GECO, which is based on the mApple protein [117]. However, R-GECO is not suited for optogenetic applications, as it shows photoconversion/photoactivation in response to blue illumination for concomitant ChR2 stimulation, which leads to a large increase in the red fluorescent signal, irrespective of the Ca^{2+} concentration [44]. A typical experiment combining optogenetic activation with in vivo Ca^{2+} imaging of the induced activity in body wall muscle cells is described below.

1. Animals expressing RCaMP in body wall muscle cells and ChR2 in the neuron of interest (for example, in locomotion command neurons) may be investigated to assess muscular calcium changes during photostimulation of the command neurons (mediated via evoked or inhibited activity of the

motor neurons). One day prior to the experiment, L4 larvae are transferred to either NGM plates seeded with bacteria, and supplemented with 2.5–5 μM ATR (from a 100 mM EtOH stock solution), calculated with respect to the amount of NGM in the culture dish; control animals are transferred to plates without ATR.

2. On the day of the experiment, up to three animals are picked onto a 10% agar pad (w/v, in M9 buffer) and are fully immobilized by using 0.1 μm polystyrene beads [125].

3. RCaMP fluorescence is monitored with a 10× air objective lens on an inverted fluorescence microscope. Two high power light-emitting diodes (LEDs) with the respective wavelengths of 470 nm for ChR2 excitation and 590 nm for RCaMP excitation are used as light sources. A beam splitter couples both LEDs to enable a simultaneous illumination of the specimen, thus allowing the excitation of RCaMP and the photostimulation of ChR2 in parallel. A double bandpass excitation filter permits wavelengths of 479 nm and 585 nm from the illuminator to pass onto a 605 nm beam splitter that reflects the light towards the sample. Eventually, the emitted light is filtered by a 647/57 bandpass barrier filter that allows only wavelengths about 647 nm to pass towards the eye or the detector. In order to run different photostimulation protocols, a Lambda SC Smart Shutter controller (Sutter Instrument Company) can be used to switch the power supply of the 470 nm LED through TTL pulses. Videos are obtained with a CCD camera or a sCMOS camera at a frame rate of 20 fps. Micro-Manager freeware (https://www.micro-manager.org/) can be used to adjust video settings. The exposure time is set to 30 ms and frames are binned to 4×4 pixels. The light power is adjusted to 1 mW/mm^2 at 470 nm.

4. For analysis, the image sequences can be analyzed using ImageJ (http://imagej.nih.gov/ij/). Animals are segmented into regions of interest (ROI) by only circumscribing the RCaMP expressing areas. The mean fluorescence intensity values are calculated for every ROI at every frame. A region outside the animal is chosen as background and subtracted from the mean fluorescence values. The traces for each ROI are normalized:

$$F\text{all} = \frac{(F - F0)}{F0}$$

$F0$ is the mean fluorescence of the first 100 video frames. The increase of the signal due to autofluorescence caused by the photostimulation is circumvented by normalizing the fluorescence values of the illumination period, with $F0$ as the first frame of the illumination.

3.3 Voltage Imaging Using Rhodopsins

Methodically, voltage imaging experiments are conducted similar to RCaMP measurements described above. Due to its dim fluorescence, direct imaging of the (non-eFRET) Archaerhodopsin mutant QuasAr requires activation with a 637 nm laser at 1800 mW/mm^2 and the usage of highly sensitive EMCCD cameras is advisable. Using this configuration, QuasAr enables to monitor voltage dynamics at high frame rates (ca. 150 frames per second (fps), 2-ms exposure) in various tissues, ranging from muscle cells to individual neurons, such as the locomotion interneuron RIM [27]. For combination with optogenetic control (e.g. ChR2 or ACR2), blue light crosstalk by undesired fluorescence of free retinal can be reduced with low ATR concentrations (as low as 0.01 mM) and comparably low excitation intensities of around 300 μW/mm^2. For the use in the pharynx, pumping can be induced by incubation of transgenic animals in 3 μl serotonin (20 mM, in M9 buffer) right before the experiment. Here, automated data analysis (KNIME [126] workflow, available from the authors on request) allows to synchronize pumping events on the behavioral level (identified by the opening of the grinder lumen) with preceding voltage signals recorded via the voltage sensor's fluorescence. To measure the relative change in fluorescence over time ($\Delta F/F_0$), ROIs should cover the entire pharynx, while a smaller ROI can be set onto the grinder structure to track pumping motion (compare Subheading 3.2, **step 4**). Extracted parameters like pump- and voltage signal duration and kinetics enable conclusions about mutant phenotypes compared to the wild type N2. By calculating difference videos, it is even possible to spatially resolve compartmentalized voltage activity in the pharynx, where outcomes are in line with electropharyngeograms (extracellular recordings of pharyngeal electrical activity) [27].

Alternatively, much brighter eFRET sensors can be used to visualize voltage dynamics, e.g. for applications where high intensity laser light is undesired or costly camera equipment is not available. These kind of voltage indicators require conventional excitation light sources like LEDs or HBO or Xenon lamps, with appropriate filter sets (e.g. MacQ-mCitrine: excitation at 472/30 nm with 10 mW/mm^2 and emission at 520/35 nm. QuasAr-mOrange: excitation at 545/30 nm with 30 mW/mm^2 and emission at 610/75 nm). The selection of the indicator therefore depends on the spectral requirements in terms of combination with other actuators as well as hardware configuration and photosensitivity of the experiment.

3.4 Cyclase Rhodopsins and Two-Component Optogenetics

In general, application of CyclOp proteins for cyclic nucleotide monophosphate (cNMP) signaling studies work well [26], if one considers the following experimental details:

1. Usage of a red filter foil for the transfer of transgenic (ATR-cultivated) animals on an experimental plate.

2. Acclimation of these animals for several minutes in dark before starting the experiment.

3. Storage of the ATR-cultivated animals in aluminum foil to avoid pre-exposure to (ambient) light.

4. Application of a red bandpass filter for the transmission light of the microscope.

5. Depending on the cell type in which the respective CyclOp is used, photoactivation may trigger long-lasting effects, depending on the expression levels of phosphodiesterases (PDEs) in the respective tissue.

4   Notes

1. Dos and Don'ts when using CyclOps and CNG channels: To reduce basal activation of CNG channels due to intrinsic cNMP, we recommend to inject <5.5 ng/μl of the respective channel DNA (TAX-2,-4 or SthK) to obtain a low expression level of the channel. In contrast, for BeCNG1 we suggest to work with a high expression level, i.e. the amount of injected DNA should exceed 40 ng/μl, to obtain quantifiable behavioral effects. Also, for the application of the BeCyclOp; BeCNG1 system, a long light pulse >15 s is advised. For use of SthK and the co-expressed PAC in (cholinergic) neurons, the expression levels had to be adjusted, and we recommend to inject <15 ng/μl of the respective PAC DNA (for PACs with low light-induced cAMP production, we suggest to inject >15 ng/μl DNA) and < 5.5 ng/μl of the SthK channel DNA. Here, the amount of injected DNA had to be individually adjusted for the respective systems, since in some cases, it was difficult to get transgenic strains (we occasionally observed transgenic larvae arresting at L1-L2 larvae stages, that did not develop into adults).

2. Dos and Don'ts when using ChR2: As ChR2 is a low-efficiency Na^+ channel, high expression levels need to be achieved. Thus, multicopy extrachromosomal arrays are required, that should be integrated into the genome. In some cases, we observed robust effects only after integration, e.g. for activation of PVD neurons, only 5% of the transgenic animals showed PVD-evoked escape behavior, while after integration, 100% of the animals responded [54]. Single-copy genomic integration, e.g. by MosSCI [127], is thus not suitable to generate optogenetic strains (at least not with ChR2(H134R)).

Of course, as *C. elegans* neurons produce graded potentials, higher blue light intensity also increases the ChR2-mediated effects [48, 49]. However, as *C. elegans* has an intrinsic light response to avoid UV and blue light, mediated by the *lite-1* receptor [128], any optogenetic experiment using ChR2 runs the risk of activating the photoavoidance response in addition to the ChR2-evoked behavioral response. This is particularly true when prolonged (>300–500 ms) photostimulation of the neuron of interest is required to evoke an observable behavioral response. There are two possibilities to distinguish the specific from the non-specific photoresponse: (1) Run the experiment with two groups of animals, one cultivated with, the other without ATR, and compare the behavioral response. This is problematic, however, if the behavior is actually modulated by the photoavoidance. (2) Perform the experiment in a *lite-1(ce314)* mutant background, which largely lacks the photophobic responses. This is to be done with caution, however, as *lite-1* mutants are not wild type, and for example exhibit slowed locomotion, particularly in swimming assays. Generally, as little blue light as necessary to evoke the full response should be used (both with respect to duration and intensity), and more light-sensitive variants of ChR2 can be used (C128S or H134R; T159C, see above), that mediate effects at light intensities that evoke almost no photophobic responses.

All-*trans* retinal itself has some non-specific effects on *C. elegans*, (e.g. animals show slightly deeper body bending with ATR), and too much ATR actually becomes toxic. Thus the concentration of ATR should be kept as low as possible, while still evoking maximal activity. This can be titrated for the specific application. Keep in mind that ATR is prone to oxidation and photo damage, so keep the plates in the dark and do not use them if they are older than 4–5 days.

3. Dos and Don'ts when using inhibitory rhodopsins: As a word of caution, Arch and Mac, possibly due to their enhanced membrane insertion in *C. elegans*, actually can cause toxicity when overexpressed, unlike NpHR. Our observations are that expressing lots of NpHR in body wall muscle (80 ng/μl injected DNA) had no negative effects on viability or muscle physiology, despite the presence of large intracellular protein aggregates. In contrast, similar amounts of Arch and Mac caused animals to be sick and muscle cells to show aberrant membrane protrusions ("blebbing"). This could be avoided by expressing much less (<10 ng/μl injected DNA), while still maintaining more potent inhibition than with NpHR [38].

Also, while yellow light required for NpHR activation does not evoke photophobic responses, and thus can be applied in

wild type animals, the blue-green light wavelengths needed for Arch activation do evoke photophobicity. Thus, such experiments should be done in *lite-1* mutants, particularly if prolonged inhibition is required. Also for photoinhibition experiments, always include controls like the same transgenic animals cultivated without ATR, and perform experiments in wild type, with and without ATR, but with the same light exposure.

References

1. Zemelman BV, Lee GA, Ng M, Miesenbock G (2002) Selective photostimulation of genetically chARGed neurons. Neuron 33(1):15–22

2. Boyden ES, Zhang F, Bamberg E, Nagel G, Deisseroth K (2005) Millisecond-timescale, genetically targeted optical control of neural activity. Nat Neurosci 8(9):1263–1268

3. Nagel G, Brauner M, Liewald JF, Adeishvili N, Bamberg E, Gottschalk A (2005) Light activation of channelrhodopsin-2 in excitable cells of Caenorhabditis elegans triggers rapid behavioral responses. Curr Biol 15(24):2279–2284

4. Zemelman BV, Nesnas N, Lee GA, Miesenbock G (2003) Photochemical gating of heterologous ion channels: remote control over genetically designated populations of neurons. Proc Natl Acad Sci U S A 100(3): 1352–1357

5. Rost BR, Schneider-Warme F, Schmitz D, Hegemann P (2017) Optogenetic tools for subcellular applications in Neuroscience. Neuron 96(3):572–603. https://doi.org/ 10.1016/j.neuron.2017.09.047

6. Fang-Yen C, Alkema MJ, Samuel AD (2015) Illuminating neural circuits and behaviour in Caenorhabditis elegans with optogenetics. Philos Trans R Soc Lond Ser B Biol Sci 370(1677):20140212. https://doi.org/10. 1098/rstb.2014.0212

7. Rein ML, Deussing JM (2012) The optogenetic (r)evolution. Mol Gen Genomics 287(2):95–109. https://doi.org/10.1007/ s00438-011-0663-7

8. Yizhar O, Fenno LE, Davidson TJ, Mogri M, Deisseroth K (2011) Optogenetics in neural systems. Neuron 71(1):9–34. https://doi. org/10.1016/j.neuron.2011.06.004

9. White JG, Southgate E, Thomson JN, Brenner S (1986) The structure of the nervous system of the nematode Caenorhabditis elegans. Philos Trans R Soc Lond Ser B Biol Sci 314(1165):1–340

10. De Bono M, Schafer WR, Gottschalk A (2013) Optogenetic actuation, inhibition, modulation and readout for neuronal networks generating behavior in the nematode Caenorhabditis elegans. In: Hegemann P, Sigrist SJ (eds) Optogenetics. De Gruyter, Berlin

11. Husson SJ, Gottschalk A, Leifer AM (2013) Optogenetic manipulation of neural activity in *C. elegans*: from synapse to circuits and behaviour. Biol Cell 105(6):235–250. https://doi.org/10.1111/boc.201200069

12. Xu X, Kim SK (2011) The early bird catches the worm: new technologies for the Caenorhabditis elegans toolkit. Nat Rev Genet 12(11):793–801. https://doi.org/10.1038/ nrg3050

13. Zhen M, Samuel AD (2015) C. elegans locomotion: small circuits, complex functions. Curr Opin Neurobiol 33:117–126. https:// doi.org/10.1016/j.conb.2015.03.009

14. Steuer Costa W, Liewald J, Gottschalk A (2014) Photoactivated adenylyl Cyclases as Optogenetic modulators of neuronal activity. In: Cambridge S (ed) Photoswitching proteins, Methods in Molecular Biology, vol 1148. Springer, New York, pp 161–175

15. Bergs A, Schultheis C, Fischer E, Tsunoda SP, Erbguth K, Husson SJ, Govorunova E, Spudich JL, Nagel G, Gottschalk A, Liewald JF (2018) Rhodopsin optogenetic toolbox v2.0 for light-sensitive excitation and inhibition in Caenorhabditis elegans. PLoS One 13(2): e0191802. https://doi.org/10.1371/jour nal.pone.0191802

16. Bernal Sierra YA, Rost BR, Pofahl M, Fernandes AM, Kopton RA, Moser S, Holtkamp D, Masala N, Beed P, Tukker JJ, Oldani S, Bönigk W, Kohl P, Baier H, Schneider-Warme F, Hegemann P, Beck H, Seifert R, Schmitz D (2018) Potassium channel-based optogenetic silencing. Nat

Commun 9(1):4611. https://doi.org/10.1038/s41467-018-07038-8

17. Szobota S, Gorostiza P, Del Bene F, Wyart C, Fortin DL, Kolstad KD, Tulyathan O, Volgraf M, Numano R, Aaron HL, Scott EK, Kramer RH, Flannery J, Baier H, Trauner D, Isacoff EY (2007) Remote control of neuronal activity with a light-gated glutamate receptor. Neuron 54(4):535–545

18. Renicke C, Schuster D, Usherenko S, Essen LO, Taxis C (2013) A LOV2 domain-based optogenetic tool to control protein degradation and cellular function. Chem Biol 20(4):619–626. https://doi.org/10.1016/j.chembiol.2013.03.005

19. Hermann A, Liewald JF, Gottschalk A (2015) A photosensitive degron enables acute light-induced protein degradation in the nervous system. Curr Biol 25(17):R749–R750. https://doi.org/10.1016/j.cub.2015.07.040

20. Cosentino C, Alberio L, Gazzarrini S, Aquila M, Romano E, Cermenati S, Zuccolini P, Petersen J, Beltrame M, Van Etten JL, Christie JM, Thiel G, Moroni A (2015) Optogenetics. Engineering of a light-gated potassium channel. Science 348(6235):707–710. https://doi.org/10.1126/science.aaa2787

21. Dagliyan O, Tarnawski M, Chu PH, Shirvanyants D, Schlichting I, Dokholyan NV, Hahn KM (2016) Engineering extrinsic disorder to control protein activity in living cells. Science 354(6318):1441–1444. https://doi.org/10.1126/science.aah3404

22. Harterink M, van Bergeijk P, Allier C, de Haan B, van den Heuvel S, Hoogenraad CC, Kapitein LC (2016) Light-controlled intracellular transport in Caenorhabditis elegans. Curr Biol 26(4):R153–R154. https://doi.org/10.1016/j.cub.2015.12.016

23. Liu Q, Sinnen BL, Boxer EE, Schneider MW, Grybko MJ, Buchta WC, Gibson ES, Wysoczynski CL, Ford CP, Gottschalk A, Aoto J, Tucker CL, Kennedy MJ (2019) A photoactivatable botulinum neurotoxin for inducible control of neurotransmission. Neuron 101(5):863–875 e866. https://doi.org/10.1016/j.neuron.2019.01.002

24. Weissenberger S, Schultheis C, Liewald JF, Erbguth K, Nagel G, Gottschalk A (2011) PACalpha--an optogenetic tool for in vivo manipulation of cellular cAMP levels, neurotransmitter release, and behavior in Caenorhabditis elegans. J Neurochem 116(4):616–625. https://doi.org/10.1111/j.1471-4159.2010.07148.x

25. Gao S, Nagpal J, Schneider MW, Kozjak-Pavlovic V, Nagel G, Gottschalk A (2015) Optogenetic manipulation of cGMP in cells and animals by the tightly light-regulated guanylyl-cyclase opsin CyclOp. Nat Commun 6:8046. https://doi.org/10.1038/ncomms9046

26. Henss T, Nagpal J, Gao S, Scheib U, Pieragnolo A, Hirschhäuser A, Schneider-Warme F, Hegemann P, Nagel G, Gottschalk A (2020) Optogenetic tools for manipulation of cyclic nucleotides, functionally coupled to CNG-channels. Br J Pharmacol. https://doi.org/10.22541/au.160209923.37567730/v1

27. Azimi Hashemi N, Bergs ACF, Schuler C, Scheiwe AR, Steuer Costa W, Bach M, Liewald JF, Gottschalk A (2019) Rhodopsin-based voltage imaging tools for use in muscles and neurons of Caenorhabditis elegans. Proc Natl Acad Sci U S A 116(34):17051–17060. https://doi.org/10.1073/pnas.1902443116

28. Flytzanis NC, Bedbrook CN, Chiu H, Engqvist MK, Xiao C, Chan KY, Sternberg PW, Arnold FH, Gradinaru V (2014) Archaerhodopsin variants with enhanced voltage-sensitive fluorescence in mammalian and Caenorhabditis elegans neurons. Nat Commun 5:4894. https://doi.org/10.1038/ncomms5894

29. Xu Y, Zou P, Cohen AE (2017) Voltage imaging with genetically encoded indicators. Curr Opin Chem Biol 39:1–10. https://doi.org/10.1016/j.cbpa.2017.04.005

30. Piatkevich KD, Jung EE, Straub C, Linghu C, Park D, Suk HJ, Hochbaum DR, Goodwin D, Pnevmatikakis E, Pak N, Kawashima T, Yang CT, Rhoades JL, Shemesh O, Asano S, Yoon YG, Freifeld L, Saulnier JL, Riegler C, Engert F, Hughes T, Drobizhev M, Szabo B, Ahrens MB, Flavell SW, Sabatini BL, Boyden ES (2018) A robotic multidimensional directed evolution approach applied to fluorescent voltage reporters. Nat Chem Biol 14(4):352–360. https://doi.org/10.1038/s41589-018-0004-9

31. Fenno L, Yizhar O, Deisseroth K (2011) The development and application of optogenetics. Annu Rev Neurosci 34:389–412. https://doi.org/10.1146/annurev-neuro-061010-113817

32. Bamann C, Kirsch T, Nagel G, Bamberg E (2008) Spectral characteristics of the photocycle of channelrhodopsin-2 and its implication for channel function. J Mol Biol 375(3):686–694

33. Stehfest K, Hegemann P (2010) Evolution of the channelrhodopsin photocycle model. ChemPhysChem 11(6):1120–1126. https://doi.org/10.1002/cphc.200900980

34. Nagel G, Ollig D, Fuhrmann M, Kateriya S, Musti AM, Bamberg E, Hegemann P (2002) Channelrhodopsin-1: a light-gated proton channel in green algae. Science 296(5577):2395–2398

35. Nagel G, Szellas T, Huhn W, Kateriya S, Adeishvili N, Berthold P, Ollig D, Hegemann P, Bamberg E (2003) Channelrhodopsin-2, a directly light-gated cation-selective membrane channel. Proc Natl Acad Sci U S A 100(24):13940–13945

36. Zhang F, Wang LP, Brauner M, Liewald JF, Kay K, Watzke N, Wood PG, Bamberg E, Nagel G, Gottschalk A, Deisseroth K (2007) Multimodal fast optical interrogation of neural circuitry. Nature 446(7136):633–639

37. Chow BY, Han X, Dobry AS, Qian X, Chuong AS, Li M, Henninger MA, Belfort GM, Lin Y, Monahan PE, Boyden ES (2010) High-performance genetically targetable optical neural silencing by light-driven proton pumps. Nature 463(7277):98–102. https://doi.org/10.1038/nature08652

38. Husson SJ, Liewald JF, Schultheis C, Stirman JN, Lu H, Gottschalk A (2012) Microbial light-Activatable proton pumps as neuronal inhibitors to functionally dissect neuronal networks in C. elegans. PLoS One 7(7):e40937. https://doi.org/10.1371/journal.pone.0040937

39. Govorunova EG, Sineshchekov OA, Janz R, Liu X, Spudich JL (2015) NEUROSCIENCE. Natural light-gated anion channels: a family of microbial rhodopsins for advanced optogenetics. Science 349(6248):647–650. https://doi.org/10.1126/science.aaa7484

40. Wietek J, Wiegert JS, Adeishvili N, Schneider F, Watanabe H, Tsunoda SP, Vogt A, Elstner M, Oertner TG, Hegemann P (2014) Conversion of channelrhodopsin into a light-gated chloride channel. Science 344(6182):409–412. https://doi.org/10.1126/science.1249375

41. Berndt A, Lee SY, Ramakrishnan C, Deisseroth K (2014) Structure-guided transformation of channelrhodopsin into a light-activated chloride channel. Science 344(6182):420–424. https://doi.org/10.1126/science.1252367

42. Mahn M, Prigge M, Ron S, Levy R, Yizhar O (2016) Biophysical constraints of optogenetic inhibition at presynaptic terminals. Nat Neurosci 19(4):554–556. https://doi.org/10.1038/nn.4266

43. Mattis J, Tye KM, Ferenczi EA, Ramakrishnan C, O'Shea DJ, Prakash R, Gunaydin LA, Hyun M, Fenno LE, Gradinaru V, Yizhar O, Deisseroth K (2012) Principles for applying optogenetic tools derived from direct comparative analysis of microbial opsins. Nat Methods 9(2):159–172. https://doi.org/10.1038/Nmeth.1808

44. Akerboom J, Carreras Calderon N, Tian L, Wabnig S, Prigge M, Tolo J, Gordus A, Orger MB, Severi KE, Macklin JJ, Patel R, Pulver SR, Wardill TJ, Fischer E, Schuler C, Chen TW, Sarkisyan KS, Marvin JS, Bargmann CI, Kim DS, Kugler S, Lagnado L, Hegemann P, Gottschalk A, Schreiter ER, Looger LL (2013) Genetically encoded calcium indicators for multi-color neural activity imaging and combination with optogenetics. Front Mol Neurosci 6:2. https://doi.org/10.3389/fnmol.2013.00002

45. Gradinaru V, Thompson KR, Zhang F, Mogri M, Kay K, Schneider MB, Deisseroth K (2007) Targeting and readout strategies for fast optical neural control in vitro and in vivo. J Neurosci 27(52):14231–14238. https://doi.org/10.1523/JNEUROSCI.3578-07.2007

46. Petreanu L, Huber D, Sobczyk A, Svoboda K (2007) Channelrhodopsin-2-assisted circuit mapping of long-range callosal projections. Nat Neurosci 10(5):663–668

47. Liewald JF, Brauner M, Stephens GJ, Bouhours M, Schultheis C, Zhen M, Gottschalk A (2008) Optogenetic analysis of synaptic function. Nat Methods 5(10):895–902

48. Liu Q, Hollopeter G, Jorgensen EM (2009) Graded synaptic transmission at the Caenorhabditis elegans neuromuscular junction. Proc Natl Acad Sci U S A 106(26):10823–10828

49. Schultheis C, Brauner M, Liewald JF, Gottschalk A (2011) Optogenetic analysis of GABAB receptor signaling in Caenorhabditis elegans motor neurons. J Neurophysiol 106(2):817–827. https://doi.org/10.1152/jn.00578.2010

50. Stirman JN, Brauner M, Gottschalk A, Lu H (2010) High-throughput study of synaptic transmission at the neuromuscular junction enabled by optogenetics and microfluidics. J Neurosci Methods 191(1):90–93. https://doi.org/10.1016/j.jneumeth.2010.05.019

51. Miyawaki A, Llopis J, Heim R, McCaffery JM, Adams JA, Ikura M, Tsien RY (1997) Fluorescent indicators for Ca^{2+} based on green fluorescent proteins and calmodulin. Nature

388(6645):882–887. https://doi.org/10.1038/42264

52. Nakai J, Ohkura M, Imoto K (2001) A high signal-to-noise Ca(2+) probe composed of a single green fluorescent protein. Nat Biotechnol 19(2):137–141. https://doi.org/10.1038/84397

53. Guo ZV, Hart AC, Ramanathan S (2009) Optical interrogation of neural circuits in Caenorhabditis elegans. Nat Methods 6(12):891–896. https://doi.org/10.1038/nmeth.1397

54. Husson SJ, Costa WS, Wabnig S, Stirman JN, Watson JD, Spencer WC, Akerboom J, Looger LL, Treinin M, Miller DM 3rd, Lu H, Gottschalk A (2012) Optogenetic analysis of a nociceptor neuron and network reveals ion channels acting downstream of primary sensors. Curr Biol 22:743–752. https://doi.org/10.1016/j.cub.2012.02.066

55. Wabnig S, Liewald JF, Yu SC, Gottschalk A (2015) High-throughput all-optical analysis of synaptic transmission and synaptic vesicle recycling in Caenorhabditis elegans. PLoS One 10(8):e0135584. https://doi.org/10.1371/journal.pone.0135584

56. Tolstenkov O, Van der Auwera P, Steuer Costa W, Bazhanova O, Gemeinhardt TM, Bergs AC, Gottschalk A (2018) Functionally asymmetric motor neurons contribute to coordinating locomotion of Caenorhabditis elegans. eLife 7:e34997. https://doi.org/10.7554/eLife.34997

57. Schild LC, Glauser DA (2015) Dual color neural activation and behavior control with Chrimson and CoChR in Caenorhabditis elegans. Genetics 200(4):1029–1034. https://doi.org/10.1534/genetics.115.177956

58. Kralj JM, Douglass AD, Hochbaum DR, Maclaurin D, Cohen AE (2012) Optical recording of action potentials in mammalian neurons using a microbial rhodopsin. Nat Methods 9(1):90–95. https://doi.org/10.1038/nmeth.1782

59. Hochbaum DR, Zhao Y, Farhi SL, Klapoetke N, Werley CA, Kapoor V, Zou P, Kralj JM, Maclaurin D, Smedemark-Margulies N, Saulnier JL, Boulting GL, Straub C, Cho YK, Melkonian M, Wong GK, Harrison DJ, Murthy VN, Sabatini BL, Boyden ES, Campbell RE, Cohen AE (2014) All-optical electrophysiology in mammalian neurons using engineered microbial rhodopsins. Nat Methods 11(8):825–833. https://doi.org/10.1038/nmeth.3000

60. Zou P, Zhao Y, Douglass AD, Hochbaum DR, Brinks D, Werley CA, Harrison DJ, Campbell RE, Cohen AE (2014) Bright and fast multicoloured voltage reporters via electrochromic FRET. Nat Commun 5:4625. https://doi.org/10.1038/ncomms5625

61. Kannan M, Vasan G, Huang C, Haziza S, Li JZ, Inan H, Schnitzer MJ, Pieribone VA (2018) Fast, in vivo voltage imaging using a red fluorescent indicator. Nat Methods 15(12):1108–1116. https://doi.org/10.1038/s41592-018-0188-7

62. Gong Y, Wagner MJ, Zhong Li J, Schnitzer MJ (2014) Imaging neural spiking in brain tissue using FRET-opsin protein voltage sensors. Nat Commun 5:3674. https://doi.org/10.1038/ncomms4674

63. Stirman JN, Crane MM, Husson SJ, Wabnig S, Schultheis C, Gottschalk A, Lu H (2011) Real-time multimodal optical control of neurons and muscles in freely behaving Caenorhabditis elegans. Nat Methods 8(2):153–158. https://doi.org/10.1038/nmeth.1555

64. Leifer AM, Fang-Yen C, Gershow M, Alkema MJ, Samuel AD (2011) Optogenetic manipulation of neural activity in freely moving Caenorhabditis elegans. Nat Methods 8(2):147–152. https://doi.org/10.1038/nmeth.1554

65. Piggott BJ, Liu J, Feng Z, Wescott SA, Xu XZS (2011) The neural circuits and synaptic mechanisms underlying motor initiation in C. elegans. Cell 147(4):922–933. https://doi.org/10.1016/j.cell.2011.08.053

66. Kocabas A, Shen CH, Guo ZV, Ramanathan S (2012) Controlling interneuron activity in Caenorhabditis elegans to evoke chemotactic behaviour. Nature 490(7419):273–277. https://doi.org/10.1038/nature11431

67. Pirri JK, McPherson AD, Donnelly JL, Francis MM, Alkema MJ (2009) A tyramine-gated chloride channel coordinates distinct motor programs of a Caenorhabditis elegans escape response. Neuron 62(4):526–538

68. Busch KE, Laurent P, Soltesz Z, Murphy RJ, Faivre O, Hedwig B, Thomas M, Smith HL, de Bono M (2012) Tonic signaling from O (2) sensors sets neural circuit activity and behavioral state. Nat Neurosci 15(4):581–591. https://doi.org/10.1038/nn.3061

69. Zimmer M, Gray JM, Pokala N, Chang AJ, Karow DS, Marletta MA, Hudson ML, Morton DB, Chronis N, Bargmann CI (2009) Neurons detect increases and decreases in oxygen levels using distinct guanylate cyclases. Neuron 61(6):865–879

70. Oranth A, Schultheis C, Tolstenkov O, Erbguth K, Nagpal J, Hain D, Brauner M,

Wabnig S, Steuer Costa W, McWhirter RD, Zels S, Palumbos S, Miller III DM, Beets I, Gottschalk A (2018) Food sensation modulates locomotion by dopamine and neuropeptide signaling in a distributed neuronal network. Neuron 100(6):1414–1428 e1410. https://doi.org/10.1016/j.neuron.2018.10.024

71. Steuer Costa W, Van der Auwera P, Glock C, Liewald JF, Bach M, Schuler C, Wabnig S, Oranth A, Masurat F, Bringmann H, Schoofs L, Stelzer EHK, Fischer SC, Gottschalk A (2019) A GABAergic and peptidergic sleep neuron as a locomotion stop neuron with compartmentalized Ca^{2+} dynamics. Nat Commun 10(1):4095. https://doi.org/10.1038/s41467-019-12098-5

72. Lopez-Cruz A, Sordillo A, Pokala N, Liu Q, McGrath PT, Bargmann CI (2019) Parallel multimodal circuits control an innate foraging behavior. Neuron 102(2):407–419 e408. https://doi.org/10.1016/j.neuron.2019.01.053

73. Gordus A, Pokala N, Levy S, Flavell SW, Bargmann CI (2015) Feedback from network states generates variability in a probabilistic olfactory circuit. Cell 161(2):215–227. https://doi.org/10.1016/j.cell.2015.02.018

74. Kateriya S, Nagel G, Bamberg E, Hegemann P (2004) "Vision" in single-celled algae. News Physiol Sci 19:133–137

75. Lawson MA, Zacks DN, Derguini F, Nakanishi K, Spudich JL (1991) Retinal analog restoration of photophobic responses in a blind Chlamydomonas reinhardtii mutant. Evidence for an archaebacterial like chromophore in a eukaryotic rhodopsin. Biophys J 60(6):1490–1498. https://doi.org/10.1016/S0006-3495(91)82184-1

76. Kato HE, Zhang F, Yizhar O, Ramakrishnan C, Nishizawa T, Hirata K, Ito J, Aita Y, Tsukazaki T, Hayashi S, Hegemann P, Maturana AD, Ishitani R, Deisseroth K, Nureki O (2012) Crystal structure of the channelrhodopsin light-gated cation channel. Nature 482(7385):369–374. https://doi.org/10.1038/nature10870

77. Feldbauer K, Zimmermann D, Pintschovius V, Spitz J, Bamann C, Bamberg E (2009) Channelrhodopsin-2 is a leaky proton pump. Proc Natl Acad Sci U S A 106(30):12317–12322. https://doi.org/10.1073/pnas.0905852106

78. Ritter E, Stehfest K, Berndt A, Hegemann P, Bartl FJ (2008) Monitoring light-induced structural changes of Channelrhodopsin-2 by UV-visible and Fourier transform infrared spectroscopy. J Biol Chem 283(50):35033–35041. https://doi.org/10.1074/jbc.M806353200

79. Gunaydin LA, Yizhar O, Berndt A, Sohal VS, Deisseroth K, Hegemann P (2010) Ultrafast optogenetic control. Nat Neurosci 13(3):387–392. https://doi.org/10.1038/nn.2495

80. Haupts U, Tittor J, Bamberg E, Oesterhelt D (1997) General concept for ion translocation by halobacterial retinal proteins: the isomerization/switch/transfer (IST) model. Biochemistry 36(1):2–7. https://doi.org/10.1021/bi962014g

81. Lin JY, Lin MZ, Steinbach P, Tsien RY (2009) Characterization of engineered channelrhodopsin variants with improved properties and kinetics. Biophys J 96(5):1803–1814

82. Watanabe S, Liu Q, Davis MW, Hollopeter G, Thomas N, Jorgensen NB, Jorgensen EM (2013) Ultrafast endocytosis at Caenorhabditis elegans neuromuscular junctions. eLife 2:e00723. https://doi.org/10.7554/eLife.00723

83. Berndt A, Schoenenberger P, Mattis J, Tye KM, Deisseroth K, Hegemann P, Oertner TG (2011) High-efficiency channelrhodopsins for fast neuronal stimulation at low light levels. Proc Natl Acad Sci U S A 108(18):7595–7600. https://doi.org/10.1073/pnas.1017210108

84. Erbguth K, Prigge M, Schneider F, Hegemann P, Gottschalk A (2012) Bimodal activation of different neuron classes with the spectrally red-shifted channelrhodopsin chimera C1V1 in Caenorhabditis elegans. PLoS One 7(10):e46827. https://doi.org/10.1371/journal.pone.0046827

85. Kleinlogel S, Feldbauer K, Dempski RE, Fotis H, Wood PG, Bamann C, Bamberg E (2011) Ultra light-sensitive and fast neuronal activation with the ca(2)+−permeable channelrhodopsin CatCh. Nat Neurosci 14(4):513–518. https://doi.org/10.1038/nn.2776

86. Berndt A, Yizhar O, Gunaydin LA, Hegemann P, Deisseroth K (2009) Bi-stable neural state switches. Nat Neurosci 12(2):229–234. https://doi.org/10.1038/nn.2247

87. Schultheis C, Liewald JF, Bamberg E, Nagel G, Gottschalk A (2011) Optogenetic long-term manipulation of behavior and animal development. PLoS One 6(4):e18766. https://doi.org/10.1371/journal.pone.0018766

88. Dawydow A, Gueta R, Ljaschenko D, Ullrich S, Hermann M, Ehmann N, Gao S, Fiala A, Langenhan T, Nagel G, Kittel RJ (2014) Channelrhodopsin-2-XXL, a powerful optogenetic tool for low-light applications. Proc Natl Acad Sci U S A 111(38): 13972–13977. https://doi.org/10.1073/pnas.1408269111

89. Yizhar O, Fenno LE, Prigge M, Schneider F, Davidson TJ, O'Shea DJ, Sohal VS, Goshen I, Finkelstein J, Paz JT, Stehfest K, Fudim R, Ramakrishnan C, Huguenard JR, Hegemann P, Deisseroth K (2011) Neocortical excitation/inhibition balance in information processing and social dysfunction. Nature 477(7363):171–178. https://doi.org/10.1038/nature10360

90. Bamann C, Gueta R, Kleinlogel S, Nagel G, Bamberg E (2010) Structural guidance of the photocycle of channelrhodopsin-2 by an interhelical hydrogen bond. Biochemistry 49(2):267–278. https://doi.org/10.1021/bi901634p

91. Prigge M, Schneider F, Tsunoda SP, Shilyansky C, Wietek J, Deisseroth K, Hegemann P (2012) Color-tuned channelrhodopsins for multiwavelength optogenetics. J Biol Chem 287(38):31804–31812. https://doi.org/10.1074/jbc.M112.391185

92. Gradinaru V, Thompson KR, Deisseroth K (2008) eNpHR: a Natronomonas halorhodopsin enhanced for optogenetic applications. Brain Cell Biol 36(1–4):129–139. https://doi.org/10.1007/s11068-008-9027-6

93. Gradinaru V, Zhang F, Ramakrishnan C, Mattis J, Prakash R, Diester I, Goshen I, Thompson KR, Deisseroth K (2010) Molecular and cellular approaches for diversifying and extending optogenetics. Cell 141(1): 154–165. https://doi.org/10.1016/j.cell.2010.02.037

94. Lin MZ, Schnitzer MJ (2016) Genetically encoded indicators of neuronal activity. Nat Neurosci 19(9):1142–1153. https://doi.org/10.1038/nn.4359

95. Fan LZ, Kheifets S, Bohm UL, Wu H, Piatkevich KD, Xie ME, Parot V, Ha Y, Evans KE, Boyden ES, Takesian AE, Cohen AE (2020) All-optical electrophysiology reveals the role of lateral inhibition in sensory processing in cortical layer 1. Cell 180(3):521–535 e518. https://doi.org/10.1016/j.cell.2020.01.001

96. Schneider F, Grimm C, Hegemann P (2015) Biophysics of Channelrhodopsin. Annu Rev Biophys 44:167–186. https://doi.org/10.1146/annurev-biophys-060414-034014

97. Avelar GM, Schumacher RI, Zaini PA, Leonard G, Richards TA, Gomes SL (2014) A rhodopsin-guanylyl cyclase gene fusion functions in visual perception in a fungus. Curr Biol 24(11):1234–1240. https://doi.org/10.1016/j.cub.2014.04.009

98. Scheib U, Stehfest K, Gee CE, Korschen HG, Fudim R, Oertner TG, Hegemann P (2015) The rhodopsin-guanylyl cyclase of the aquatic fungus Blastocladiella emersonii enables fast optical control of cGMP signaling. Sci Signal 8(389):rs8. https://doi.org/10.1126/scisignal.aab0611

99. Miller KG, Alfonso A, Nguyen M, Crowell JA, Johnson CD, Rand JB (1996) A genetic selection for Caenorhabditis elegans synaptic transmission mutants. Proc Natl Acad Sci U S A 93(22):12593–12598

100. Richmond J (2005) Synaptic function. WormBook:1–14

101. Richmond JE (2006) Electrophysiological recordings from the neuromuscular junction of *C. elegans*. WormBook:1–8

102. Francis MM, Maricq AV (2006) Electrophysiological analysis of neuronal and muscle function in C. elegans. Methods Mol Biol 351:175–192. https://doi.org/10.1385/1-59745-151-7:175

103. Sieburth D, Ch'ng Q, Dybbs M, Tavazoie M, Kennedy S, Wang D, Dupuy D, Rual JF, Hill DE, Vidal M, Ruvkun G, Kaplan JM (2005) Systematic analysis of genes required for synapse structure and function. Nature 436(7050):510–517. https://doi.org/10.1038/nature03809

104. Kittelmann M, Liewald JF, Hegermann J, Schultheis C, Brauner M, Steuer Costa W, Wabnig S, Eimer S, Gottschalk A (2013) In vivo synaptic recovery following optogenetic hyperstimulation. Proc Natl Acad Sci U S A 110(32):E3007–E3016. https://doi.org/10.1073/pnas.1305679110

105. Davis MW, Morton JJ, Carroll D, Jorgensen EM (2008) Gene activation using FLP recombinase in *C. elegans*. PLoS Genet 4(3): e1000028

106. Macosko EZ, Pokala N, Feinberg EH, Chalasani SH, Butcher RA, Clardy J, Bargmann CI (2009) A hub-and-spoke circuit drives pheromone attraction and social behaviour in C. elegans. Nature 458(7242):1171–1175

107. Schmitt C, Schultheis C, Pokala N, Husson SJ, Liewald JF, Bargmann CI, Gottschalk A (2012) Specific expression of channelrhodopsin-2 in single neurons of Caenorhabditis elegans. PLoS One 7(8):e43164.

https://doi.org/10.1371/journal.pone.0043164

108. Voutev R, Hubbard EJ (2008) A "FLP-out" system for controlled gene expression in Caenorhabditis elegans. Genetics 180(1): 103–119. https://doi.org/10.1534/genetics.108.090274

109. Stirman JN, Crane MM, Husson SJ, Gottschalk A, Lu H (2012) A multispectral optical illumination system with precise spatiotemporal control for the manipulation of optogenetic reagents. Nat Protoc 7(2): 207–220. https://doi.org/10.1038/nprot.2011.433

110. Richmond JE, Jorgensen EM (1999) One GABA and two acetylcholine receptors function at the C. elegans neuromuscular junction. Nat Neurosci 2(9):791–797

111. Husson SH, Steuer Costa W, Schmitt C, Gottschalk A (2012) Keeping track of worm trackers. WormBook:1–17. https://doi.org/10.1895/wormbook.1.150.1

112. Stephens GJ, Johnson-Kerner B, Bialek W, Ryu WS (2008) Dimensionality and dynamics in the behavior of C. elegans. PLoS Comput Biol 4(4):e1000028

113. Baird GS, Zacharias DA, Tsien RY (1999) Circular permutation and receptor insertion within green fluorescent proteins. Proc Natl Acad Sci U S A 96(20):11241–11246

114. Akerboom J, Chen TW, Wardill TJ, Tian L, Marvin JS, Mutlu S, Calderon NC, Esposti F, Borghuis BG, Sun XR, Gordus A, Orger MB, Portugues R, Engert F, Macklin JJ, Filosa A, Aggarwal A, Kerr RA, Takagi R, Kracun S, Shigetomi E, Khakh BS, Baier H, Lagnado L, Wang SS, Bargmann CI, Kimmel BE, Jayaraman V, Svoboda K, Kim DS, Schreiter ER, Looger LL (2012) Optimization of a GCaMP calcium indicator for neural activity imaging. J Neurosci 32(40): 13819–13840. https://doi.org/10.1523/JNEUROSCI.2601-12.2012

115. Tian L, Hires SA, Mao T, Huber D, Chiappe ME, Chalasani SH, Petreanu L, Akerboom J, McKinney SA, Schreiter ER, Bargmann CI, Jayaraman V, Svoboda K, Looger LL (2009) Imaging neural activity in worms, flies and mice with improved GCaMP calcium indicators. Nat Methods 6(12):875–881. https://doi.org/10.1038/nmeth.1398

116. Mank M, Santos AF, Direnberger S, Mrsic-Flogel TD, Hofer SB, Stein V, Hendel T, Reiff DF, Levelt C, Borst A, Bonhoeffer T, Hubener M, Griesbeck O (2008) A genetically encoded calcium indicator for chronic in vivo two-photon imaging. Nat Methods

5(9):805–811. https://doi.org/10.1038/nmeth.1243

117. Zhao Y, Araki S, Wu J, Teramoto T, Chang YF, Nakano M, Abdelfattah AS, Fujiwara M, Ishihara T, Nagai T, Campbell RE (2011) An expanded palette of genetically encoded Ca (2)(+) indicators. Science 333(6051): 1888–1891. https://doi.org/10.1126/science.1208592

118. Kerr R, Lev-Ram V, Baird G, Vincent P, Tsien RY, Schafer WR (2000) Optical imaging of calcium transients in neurons and pharyngeal muscle of C. elegans. Neuron 26(3):583–594

119. Hilliard MA, Apicella AJ, Kerr R, Suzuki H, Bazzicalupo P, Schafer WR (2005) In vivo imaging of C. elegans ASH neurons: cellular response and adaptation to chemical repellents. EMBO J 24(1):63–72

120. Suzuki H, Kerr R, Bianchi L, Frokjaer-Jensen C, Slone D, Xue J, Gerstbrein B, Driscoll M, Schafer WR (2003) In vivo imaging of C. elegans mechanosensory neurons demonstrates a specific role for the MEC-4 channel in the process of gentle touch sensation. Neuron 39(6):1005–1017

121. Suzuki H, Thiele TR, Faumont S, Ezcurra M, Lockery SR, Schafer WR (2008) Functional asymmetry in Caenorhabditis elegans taste neurons and its computational role in chemotaxis. Nature 454(7200):114–117. https://doi.org/10.1038/nature06927

122. Nagai T, Yamada S, Tominaga T, Ichikawa M, Miyawaki A (2004) Expanded dynamic range of fluorescent indicators for Ca(2+) by circularly permuted yellow fluorescent proteins. Proc Natl Acad Sci U S A 101(29): 10554–10559. https://doi.org/10.1073/pnas.0400417101

123. Nagai T, Sawano A, Park ES, Miyawaki A (2001) Circularly permuted green fluorescent proteins engineered to sense Ca2+. Proc Natl Acad Sci U S A 98(6):3197–3202. https://doi.org/10.1073/pnas.051636098

124. Kerr RA, Schafer WR (2006) Intracellular Ca^{2+} imaging in C. elegans. Methods Mol Biol 351:253–264. https://doi.org/10.1385/1-59745-151-7:253

125. Kim E, Sun L, Gabel CV, Fang-Yen C (2013) Long-term imaging of Caenorhabditis elegans using nanoparticle-mediated immobilization. PLoS One 8(1):e53419. https://doi.org/10.1371/journal.pone.0053419

126. Berthold M, Cebron N, Dill F, Gabriel T, Kötter T, Meinl T, Ohl P, Sieb C, Thiel K, Wiswedel B (2008) KNIME: the Konstanz information miner. In: Preisach C, Burkhardt H, Schmidt-Thieme L, Decker R

(eds) Data analysis, machine learning and applications. Studies in classification, data analysis, and knowledge organization. Springer, Berlin Heidelberg, pp 319–326. https://doi.org/10.1007/978-3-540-78246-9_38

127. Frokjaer-Jensen C, Davis MW, Hopkins CE, Newman BJ, Thummel JM, Olesen SP, Grunnet M, Jorgensen EM (2008) Single-copy insertion of transgenes in Caenorhabditis elegans. Nat Genet 40(11):1375–1383

128. Edwards SL, Charlie NK, Milfort MC, Brown BS, Gravlin CN, Knecht JE, Miller KG (2008) A novel molecular solution for ultraviolet light detection in Caenorhabditis elegans. PLoS Biol 6(8):0060198

2.4   BiPOLES is an optogenetic tool developed for bidirectional dual-color control of neurons

The following pages contain the published version of the research article "BiPOLES is an optogenetic tool developed for bidirectional dual-color control of neurons"[11]. Material from: Vierock, J., Rodriguez-Rozada, S., Dieter, A. *et al.* BiPOLES is an optogenetic tool developed for bidirectional dual-color control of neurons. *Nat Commun* **12**, 4527 (2021). https://doi.org/10.1038/s41467-021-24759-5. Reproduced with permission from Springer Nature.

BiPOLES is an optogenetic tool developed for bidirectional dual-color control of neurons

Johannes Vierock [1,8], Silvia Rodriguez-Rozada [2,8], Alexander Dieter[2], Florian Pieper [3], Ruth Sims[4], Federico Tenedini[5], Amelie C. F. Bergs [6], Imane Bendifallah[4], Fangmin Zhou [5], Nadja Zeitzschel[6], Joachim Ahlbeck[3], Sandra Augustin[1], Kathrin Sauter[2,5], Eirini Papagiakoumou [4], Alexander Gottschalk [6], Peter Soba [5,7], Valentina Emiliani [4], Andreas K. Engel[3], Peter Hegemann [1] & J. Simon Wiegert [2✉]

Optogenetic manipulation of neuronal activity through excitatory and inhibitory opsins has become an indispensable experimental strategy in neuroscience research. For many applications bidirectional control of neuronal activity allowing both excitation and inhibition of the same neurons in a single experiment is desired. This requires low spectral overlap between the excitatory and inhibitory opsin, matched photocurrent amplitudes and a fixed expression ratio. Moreover, independent activation of two distinct neuronal populations with different optogenetic actuators is still challenging due to blue-light sensitivity of all opsins. Here we report BiPOLES, an optogenetic tool for potent neuronal excitation and inhibition with light of two different wavelengths. BiPOLES enables sensitive, reliable dual-color neuronal spiking and silencing with single- or two-photon excitation, optical tuning of the membrane voltage, and independent optogenetic control of two neuronal populations using a second, blue-light sensitive opsin. The utility of BiPOLES is demonstrated in worms, flies, mice and ferrets.

[1] Institute for Biology, Experimental Biophysics, Humboldt University Berlin, Berlin, Germany. [2] Research Group Synaptic Wiring and Information Processing, Center for Molecular Neurobiology Hamburg, University Medical Center Hamburg-Eppendorf, Hamburg, Germany. [3] Department of Neurophysiology and Pathophysiology, University Medical Center Hamburg-Eppendorf, Hamburg, Germany. [4] Wavefront-Engineering Microscopy Group, Photonics Department, Institut de la Vision, Sorbonne Université, INSERM, CNRS, Institut de la Vision, Paris, France. [5] Research Group Neuronal Patterning and Connectivity, Center for Molecular Neurobiology Hamburg, University Medical Center Hamburg-Eppendorf, Hamburg, Germany. [6] Buchmann Institute for Molecular Life Sciences and Institute of Biophysical Chemistry, Goethe University, Frankfurt, Germany. [7] LIMES Institute, University of Bonn, Bonn, Germany. [8] These authors contributed equally: Johannes Vierock, Silvia Rodriguez-Rozada. ✉email: simon.wiegert@zmnh.uni-hamburg.de

To prove the necessity and sufficiency of a particular neuronal population for a specific behavior, a cognitive task, or a pathological condition, faithful activation, and inhibition of this population of neurons are required. In principle, optogenetic manipulations allow such interventions. However, excitation and inhibition of the neuronal population of interest are commonly done in separate experiments, where either an excitatory or inhibitory microbial opsin is expressed. Alternatively, if both opsins are co-expressed in the same cells, it is essential to achieve efficient membrane trafficking of both opsins, equal subcellular distributions, and a tightly controlled ratio between excitatory and inhibitory action at the specific wavelengths and membrane potentials, so that neuronal activation and silencing can be controlled precisely and predictably in all transduced cells. Precise co-localization of the two opsins is important when local, subcellular stimulation is required, or when control of individual neurons is intended, for example with two-photon holographic illumination[1]. Meeting these criteria is particularly challenging in vivo, where the optogenetic actuators are either expressed in transgenic lines or from viral vectors that are exogenously transduced. Ideally, both opsins are expressed from the same gene locus or delivered to the target neurons by a single viral vector. Moreover, for expression with fixed stoichiometry, the opsins should be encoded in a single open reading frame (ORF).

Previously, two strategies for stoichiometric expression of an inhibitory and an excitatory opsin from a single ORF were reported using either a gene fusion approach[2] or a 2A ribosomal skip sequence[3,4]. In both cases, a blue-light sensitive cation-conducting channel for excitation was combined with a red-shifted rhodopsin pump for inhibition. The gene fusion approach was used to systematically combine the inhibitory ion pumps halorhodopsin (NpHR), bacteriorhodopsin (BR), or archaerhodopsin (Arch) with a number of channelrhodopsin-2 (ChR2) mutants to generate single tandem-proteins[2]. While this strategy ensured co-localized expression of the inhibitory and excitatory opsins at a one-to-one ratio and provided important mechanistic insights into their relative ion-transport rates, membrane trafficking was not as efficient as with individually expressed opsins, thus limiting the potency of these fusion constructs for reliable control of neuronal activity.

The second strategy employed a 2A ribosomal skip sequence[3] to express the enhanced opsins ChR2(H134R)[5] and eNpHR3.0 as independent proteins at a fixed ratio from the same mRNA[4]. These bicistronic constructs, termed eNPAC, and eNPAC2.0[6], were used for bidirectional control of neuronal activity in various brain regions in mice[6–9]. While membrane trafficking of the individual opsins is more efficient compared to the gene fusion strategy, the expression ratio might still vary from cell to cell. Moreover, subcellular targeted co-localization (e.g., at the soma) is not easily achieved. Finally, functionality is limited in some model organisms such as *D. melanogaster*, since rhodopsin pumps are not efficient in these animals[10,11].

In addition to activation and inhibition of the same neurons, also independent optogenetic activation of two distinct neuronal populations is still challenging. Although two spectrally distinct opsins have been combined previously to spike two distinct sets of neurons[12–15], careful calibration and dosing of blue light were required to avoid activation of the red-shifted opsin. This typically leaves only a narrow spectral and energetic window to activate the blue-light but not the red-light-sensitive rhodopsin. Thus, dual-color control of neurons is particularly challenging in the mammalian brain where irradiance decreases by orders of magnitude over a few millimeters in a wavelength-dependent manner[16,17].

In order to overcome current limitations for bidirectional neuronal manipulations and to facilitate spiking of neuronal populations with orange-red light exclusively, in this work we systematically explore the generation of two-channel fusion proteins that combine red-light activated cation-channels and blue-light activated anion-channels enabling neuronal spiking and inhibition with red and blue light, respectively. With respect to previous bidirectional tools, inversion of the excitatory and inhibitory action spectra restricts depolarization to a narrow, orange-red spectral window since the inhibitory opsin compensates the blue-light-activated currents of the excitatory red-shifted channel. We show that among all tested variants, a combination of *Gt*ACR2[18] and Chrimson[12] termed BiPOLES (for Bidirectional Pair of Opsins for Light-induced Excitation and Silencing) proves most promising and allows (1) potent and reliable blue-light-mediated silencing and red-light-mediated spiking of pyramidal neurons in hippocampal slices; (2) bidirectional control of single neurons with single-photon illumination and two-photon holographic stimulation; (3) dual-color control of two distinct neuronal populations in combination with a second blue-light-sensitive ChR without cross-talk at light intensities spanning multiple orders of magnitude; (4) precise optical tuning of the membrane voltage between the chloride and cation reversal potentials; (5) bidirectional manipulations of neuronal activity in a wide range of invertebrate and vertebrate model organisms including worms, fruit flies, mice, and ferrets.

Results

Engineering of BiPOLES and biophysical characterization in HEK cells. To identify suitable combinations of opsins for potent membrane voltage shunting or depolarization with blue and red light, respectively, we combined the blue-light or green-light sensitive anion-conducting channelrhodopsins (ACRs) Aurora[11], iC++[19], *Gt*ACR1, and *Gt*ACR2[18] with the red-light sensitive cation-conducting channelrhodopsin (CCR) Chrimson[12]; or conversely, the blue-light sensitive *Gt*ACR2 with the red-light sensitive CCRs bReaChES[20], f-Chrimson, vf-Chrimson[21], and ChRmine[22] (Fig. 1a). We fused these opsin-pairs with different linkers, expanding previous rhodopsin fusion strategies[2,23] to obtain optimal expression and membrane targeting. The linkers were composed of the Kir2.1 membrane trafficking signal (TS)[4], different arrangements of a cyan or yellow fluorescent protein, and the transmembrane β helix of the rat gastric H^+/K^+ ATPase (βHK) to maintain the correct membrane topology of both opsins[2] (Fig. 1a).

For a detailed biophysical evaluation, we expressed all ACR-CCR tandems in human embryonic kidney (HEK) cells and recorded blue-light and red-light evoked photocurrents in the presence of a chloride gradient. In all constructs, except the one lacking the βHK-subunit (L3, Fig. 1a), blue-light-activated currents were shifted towards the chloride Nernst potential whereas red-light-activated currents were shifted towards the Nernst potential for protons and sodium (Fig. 1b–d, Supplementary Fig. 1), indicating functional membrane insertion of both channels constituting the tandem constructs. Reversal potentials (Fig. 1d) and photocurrent densities (Fig. 1e) varied strongly for the different tandem variants indicating considerable differences in their wavelength-specific anion/cation conductance ratio and their membrane expression. Photocurrent densities were not only dependent on the identity of the fused channels, but also on the sequence of both opsins in the fusion construct, as well as the employed fusion linker. In contrast to a previous study[2], the optimized linker used in this study did not require a fluorescent protein to preserve the functionality of both channels (L4, Fig. 1a, d, e). Direct comparison of red-light and blue-light evoked photocurrent densities with those of ßHK-Chrimson and *Gt*ACR2 expressed alone indicated that most tandem constructs

105
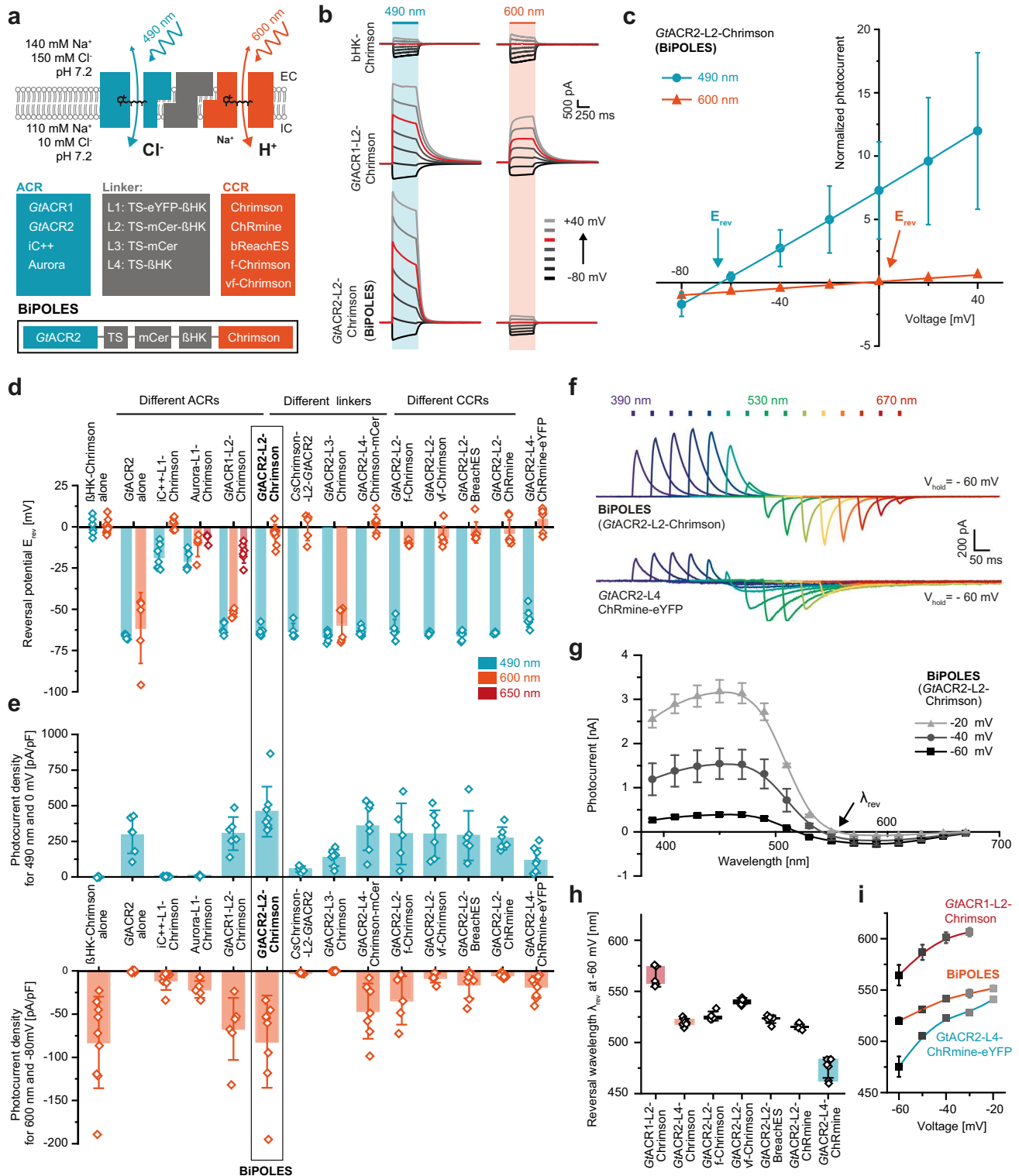
harboring a *Gt*ACR reached similar membrane expression efficacy as the individually expressed channels (Fig. 1e).

At membrane potentials between the Nernst potentials for chloride and protons, blue and red light induced outward and inward currents, respectively, in all *Gt*ACR-fusion constructs. (Fig. 1e–g, Supplementary Fig. 1). The specific wavelength of photocurrent inversion (λ_{rev}) was dependent on the absorption spectra and relative conductance of the employed channels, as

well as on the relative ionic driving forces defined by the membrane voltage and the respective ion gradients (Fig. 1g–i). The red-shift of λ_{rev} for the vf-Chrimson tandem compared to BiPOLES reflects the reduced conductance of this Chrimson mutant (Fig. 1h, Supplementary Fig. 1c), as already previously shown[21,24], whereas the blue-shift of λ_{rev} for the ChRmine tandem with L4 (Fig. 1f, h) is explained by the blue-shifted activation spectrum of ChRmine compared to Chrimson[25] and its

Fig. 1 Development of BiPOLES and biophysical characterization. a Molecular scheme of BiPOLES with the extracellular (EC) and intracellular (IC) ionic conditions used for HEK293-cell recordings. The blue-green-light-activated natural anion channels GtACR1 and GtACR2 or the engineered ChR-chimeras iC++ and Aurora were fused to the red-light-activated cation channels Chrimson, ChRmine, bReaChES, f-Chrimson, or vf-Chrimson by different linker regions consisting of a trafficking signal (ts), a yellow or cyan fluorescent protein (eYFP, mCerulean3) and the βHK transmembrane fragment. The fusion construct termed BiPOLES is indicated by a black frame. **b** Representative photocurrents of βHK-Chrimson-mCerulean (top), GtACR1-ts-mCerulean-βHK-Chrimson (middle) GtACR2-ts-mCerulean-βHK-Chrimson (BiPOLES, bottom) in whole-cell patch-clamp recordings from HEK293 cells at 490 nm and 600 nm illumination. **c** Normalized peak photocurrents of BiPOLES at different membrane voltages evoked at either 490 or 600 nm (see panel **b**, mean ± SD; n = 8 independent cells; normalized to the peak photocurrent at −80 mV and 600 nm illumination). **d** Reversal potential of peak photocurrents during 500-ms illumination with 490, 600, or 650 nm light as shown in **b** (mean ± SD). **e** Peak photocurrent densities for 490 nm and 600 nm excitation at 0 mV (close to the reversal potential of protons and cations) and −80 mV (close to the reversal potential for chloride) measured as shown in **b** (mean ± SD; for both **d** and **e** n = 5 biological independent cells for Aurora-L1-Chrimson, CsChrimson-L2-GtACR2 and GtACR2-L2-f-Chrimson; n = 6 for GtACR2, GtACR1-L2-Chrimson and GtACR2-L2-vf-Chrimson; n = 7 for iC++-L1-Chrimson, GtACR2-L3-Chrimson, GtACR2-L4-Chrimson-mCer, GtACR2-L2-BreachES, and GtACR2-L2-ChRmine; n = 8 for GtACR2-L2-Chrimson and n = 9 for ßHK-Chrimson and GtACR2-L4-ChRmine-ts-eYFP-er). **f** Representative photocurrents of BiPOLES (top) and GtACR2-L4-ChRmine-ts-eYFP-er (bottom) with 10 ms light pulses at indicated wavelengths and equal photon flux at −60 mV. **g** Action spectra of BiPOLES at different membrane voltages (λ_rev = photocurrent reversal wavelength, mean ± SEM, n = 9 independent cells for −60 mV, n = 4 for −40 mV and n = 2 for −20 mV). **h** Photocurrent reversal wavelength λ_rev at −60 mV (mean ± SD, n = 5 independent cells for GtACR1-L2-Chrimson and GtACR2-L2-f-Chrimson, n = 6 for GtACR2-L2-vf-Chrimson and GtACR2-L2-ChRmine, n = 7 for GtACR2-L4-ChRmine-ts-eYFP-er, n = 8 for GtACR2-L2-BreachES and n = 9 for GtACR2-L2-Chrimson). **i** λ_rev of GtACR1-L2-Chrimson, BiPOLES, and GtACR2-L4-ChRmine-TS-eYFP-ER at different membrane voltages (mean ± SD; n = 5 biological independent cells for GtACR1-L2-Chrimson, n = 7 for GtACR2-L4-ChRmine-ts-eYFP-er and n = 9 for GtACR2-L2-Chrimson).

presumably large single-channel conductance. Switching the L4 linker to L2 shifted λ_rev to longer wavelengths for the ChRmine fusion constructs at the expense of ChRmine photocurrents (Fig. 1e, h), pointing to a stronger impact of the protein linker on the ChRmine photocurrent compared to other red-shifted CCRs (Fig. 1e).

Among all tested combinations, GtACR2-L2-Chrimson—from here on termed BiPOLES—was the most promising variant. First, it showed the largest photocurrent densities of all tested fusion constructs (Fig. 1e,f), second, reversal potentials for blue or red light excitation were close to those of individually expressed channels (−64 ± 3 mV and −5 ± 6 mV for BiPOLES compared to −66 ± 2 mV and 0 ± 5 mV of GtACR2 and βHK-Chrimson expressed alone, Fig. 1c, d, Supplementary Fig. 1b) and third, peak activity of the inhibitory anion and excitatory cation current had the largest spectral separation among all tested variants (150 ± 5 nm, Fig. 1f, g). Thus, BiPOLES enables selective activation of large anion and cation currents with spectrally well-separated wavelengths (Fig. 1e). BiPOLES was remarkably better expressed in HEK-cells than the previously reported ChR2-L1-NpHR fusion construct[2] and featured larger photocurrents at −60 mV than the bicistronic construct eNPAC2.0[6] (Supplementary Fig. 2a–c). Moreover, employing an anion channel with high conductance instead of a chloride pump, which transports one charge per absorbed photon and is weak at a negative voltage, yielded chloride currents in BiPOLES expressing cells at irradiances 2 orders of magnitude lower than with eNPAC2.0 (Supplementary Fig. 2d–f). Anion conductance in BiPOLES was sufficiently large to compensate inward currents of Chrimson even at high irradiance, driving the cell back to the chloride Nernst potential, which is close to the resting membrane voltage (Supplementary Fig. 2d–f). We further verified the implementation of an anion-conducting channel by testing whether sufficient blue-light hyperpolarization could be achieved with a rhodopsin pump[26] instead of a channel. Replacing GtACR2 with a blue-light sensitive proton pump led to barely detectable outward currents at the same irradiance due to low ion turnover of the ion pump under the given voltage and ion conditions (Supplementary Fig. 2d, g).

Evaluation of BiPOLES in CA1 pyramidal neurons. Next, we validated BiPOLES as an optogenetic tool for bidirectional control

of neuronal activity. In CA1 pyramidal neurons of rat hippocampal slice cultures, illumination triggered photocurrents with biophysical properties similar to those observed in HEK cells (Fig. 2a, b, Supplementary Fig. 3a–c). We observed membrane-localized BiPOLES expression most strongly in the somatodendritic compartment (Fig. 2c, Supplementary Fig. 3d). However, some fraction of the protein accumulated inside the cell in the periphery of the cell nucleus, indicating sub-optimal membrane trafficking of BiPOLES. To enhance membrane trafficking, we generated a soma-targeted variant (somBiPOLES) by attaching a C-terminal Kv2.1-trafficking sequence[27]. Soma targeting has the additional benefit of avoiding the expression of the construct in axon terminals, where the functionality of BiPOLES might be limited due to an excitatory chloride reversal potential and subsequent depolarizing action of GtACR2[28,29]. somBiPOLES showed strongly improved membrane localization restricted to the cell soma and proximal dendrites with no detectable intracellular accumulations (Fig. 2c, Supplementary Fig. 3d). Compared to BiPOLES, blue-light and red-light mediated photocurrents were enhanced and now similar in magnitude to those in neurons expressing either Chrimson or soma-targeted GtACR2 (somGtACR2), alone (Fig. 2d, Supplementary Fig. 4a, 5a, b). Passive and active membrane parameters of BiPOLES-expressing and somBiPOLES-expressing neurons were similar to non-transduced, wild-type neurons (Supplementary Fig. 6), indicative of good tolerability in neurons.

To verify the confinement of somBiPOLES to the somatodendritic compartment despite the improved expression, we virally transduced area CA3 in hippocampal slice cultures with somBiPOLES and recorded optically evoked EPSCs in postsynaptic CA1 cells. Local illumination with red light in CA3 triggered large excitatory postsynaptic currents (EPSCs), while local red illumination of axon terminals in CA1 (635 nm, 2 pulses of 5 ms, 40 ms ISI, 50 mW mm⁻²), did not trigger synaptic release, indicating the absence of somBiPOLES from axonal terminals (Supplementary Fig. 3e,f). Thus, despite enhanced membrane trafficking, somBiPOLES remained confined to the somatodendritic compartment.

Having shown that somBiPOLES is efficiently expressed in CA1 pyramidal cells, we next systematically benchmarked light-evoked spiking and inhibition parameters for somBiPOLES by direct comparison to Chrimson or somGtACR2 expressed in
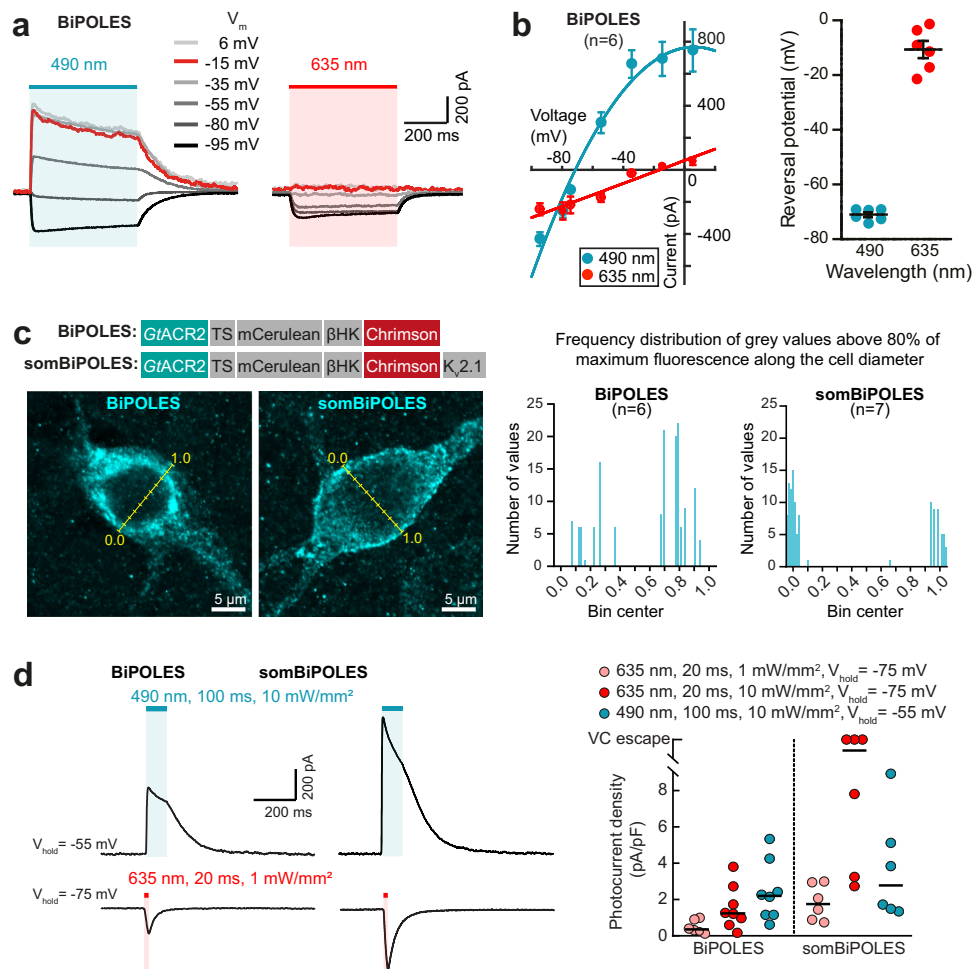
Fig. 2 Expression and functional characterization of BiPOLES and somBiPOLES in hippocampal neurons. a Representative photocurrent traces of BiPOLES in CA1 pyramidal neurons at indicated membrane voltages (V_m: from −95 to +6 mV) upon illumination with 490 or 635 nm (500 ms, 10 mW mm^{-2}). **b** Left: quantification of photocurrent-voltage relationship (symbols: mean ± SEM, $n = 6$ cells, lines: polynomial regression fitting, $R^2 = 0.98$ and 0.94, for 490 and 635 nm, respectively). Right: reversal potential under 490 or 635 nm illumination (black lines: mean ± SEM, $n = 6$ cells). **c** Left: Molecular scheme of BiPOLES and somBiPOLES as used in neurons. Representative maximum-intensity projection images of immunostainings showing expression of BiPOLES or soma-targeted BiPOLES (somBiPOLES) in CA3 pyramidal neurons of organotypic hippocampal slices. Yellow lines indicate the bins used to measure fluorescence intensity along the cell equator. Right: Frequency distribution of gray values above 80% of the maximum fluorescence intensity measured along the cell diameter in BiPOLES-expressing ($n = 6$ cells) and somBiPOLES-expressing CA3 cells ($n = 7$ cells). Note improved trafficking of somBiPOLES to the cell membrane, shown by the preferential distribution of brighter pixels around bins 0.0 and 1.0. **d** Left: Representative photocurrent traces measured in BiPOLES-expressing or somBiPOLES-expressing CA1 pyramidal neurons. Inward cationic photocurrents evoked by a 635 nm light pulse (20 ms, 1 mW mm^{-2}) were recorded at a membrane voltage of −75 mV, and outward anionic photocurrents evoked by a 490 nm light pulse (100 ms, 10 mW mm^{-2}) were recorded at a membrane voltage of −55 mV. Right: Quantification of photocurrent densities evoked under the indicated conditions. Note that photocurrent densities were strongly enhanced for somBiPOLES compared to BiPOLES (black horizontal lines: medians, $n_{BiPOLES} = 8$ cells, $n_{somBiPOLES} = 6$ cells.

hippocampal CA1 pyramidal neurons, respectively (Fig. 3, Supplementary Figs. 4, 5). To compare spiking performance in somBiPOLES or Chrimson expressing CA1 pyramidal cells, we delivered trains of 5-ms blue (470 nm), orange (595 nm), or red (635 nm) light pulses at irradiances ranging from 0.1 to 100 mW mm^{-2}. Action potential (AP) probability in somBiPOLES neurons reached 100% at 0.5 mW mm^{-2} with 595 nm and 10 mW mm^{-2} with 635 nm light, similar to neurons expressing Chrimson alone (Fig. 3b,c). In pyramidal cells, action potentials (APs) could be reliably driven up to 10-20 Hz with somBiPOLES (Supplementary Fig. 7c) similar to Chrimson alone, as shown previously[12]. Delivering the same number of photons in a time range of 1–25 ms did not alter the AP probability, but longer pulses increased sub-threshold depolarization (Supplementary Fig. 7d).

In contrast to orange or red light, blue light did not evoke APs at any irradiance in somBiPOLES neurons due to the activity of the blue-light sensitive anion channel. On the contrary, neurons expressing Chrimson alone reached 100% AP firing probability at 10 mW mm^{-2} with 470 nm (Fig. 3b, c). Using light ramps with gradually increasing irradiance enabled us to precisely determine the AP threshold and to quantitatively compare the spiking efficacy of different excitatory opsins. The irradiance threshold for the first AP was similar for somBiPOLES and Chrimson at 595 nm (0.74 ± 0.06 mW mm^{-2} for somBiPOLES and 0.68 ± 0.05 mW mm^{-2} for Chrimson) reflecting that the functional expression levels were similar. In contrast, blue light triggered APs at 0.95 ± 0.09 mW mm^{-2} in Chrimson expressing cells, but never in somBiPOLES or BiPOLES neurons (Fig. 3d, e, Supplementary Fig. 7a, b). Thus, somBiPOLES enables neuronal excitation
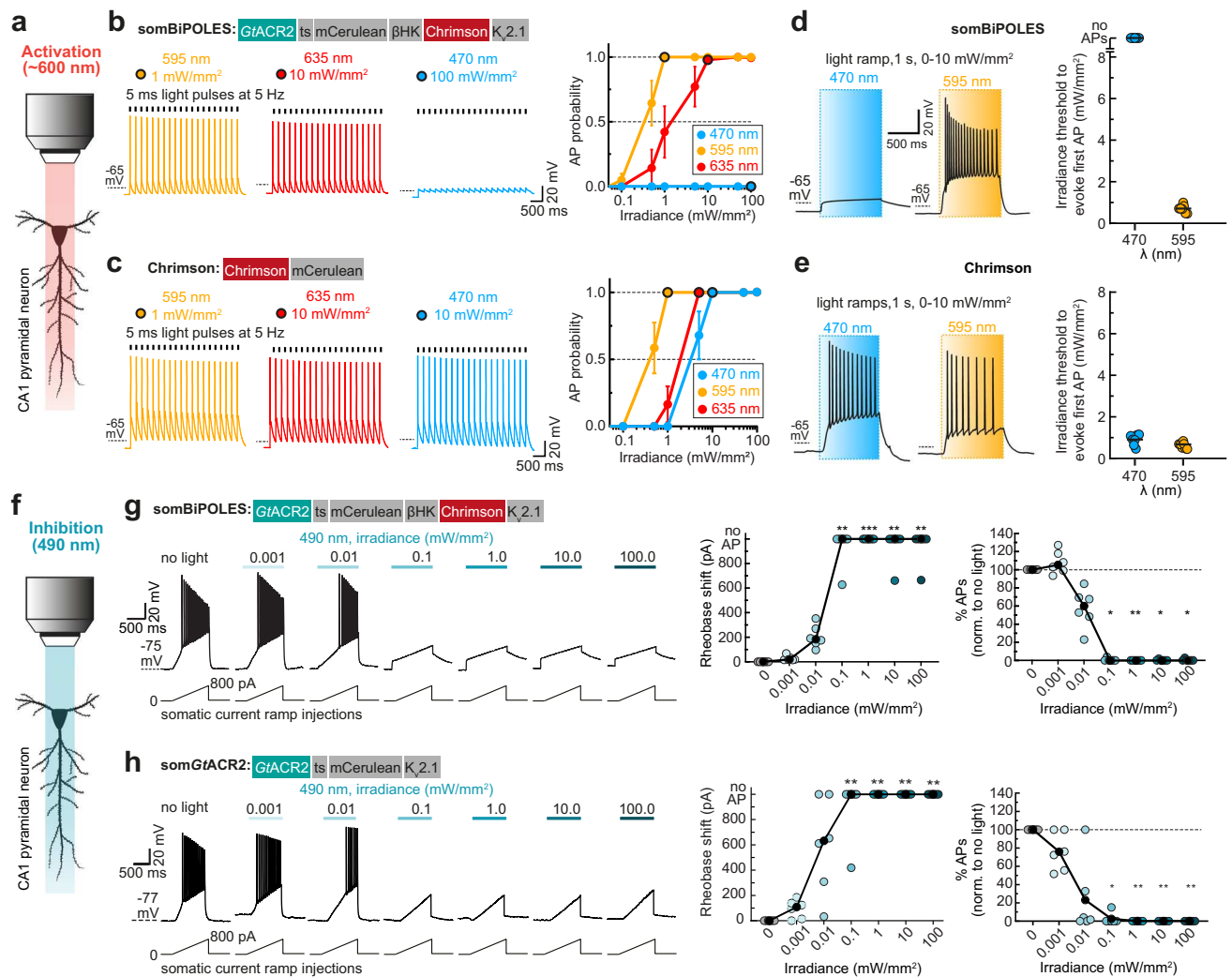
Fig. 3 somBiPOLES allows potent dual-color spiking and silencing of the same neurons using red and blue light, respectively. a Quantification of neuronal excitation with somBiPOLES or Chrimson only. **b** Optical excitation is restricted exclusively to the orange/red spectrum in somBiPOLES-expressing neurons. Left: Example traces of current-clamp (IC) recordings in somBiPOLES-expressing CA1 pyramidal cells to determine light-evoked action potential (AP)-probability at different wavelengths. Right: quantification of light-mediated AP probability at indicated wavelengths and irradiances (symbols correspond to mean ± SEM, $n = 8$ cells). Black outlined circles correspond to irradiance values shown in example traces on the left. **c** Same experiment as shown in **b**, except that CA1 neurons express Chrimson only (symbols correspond to mean ± SEM, $n = 7$ cells) Note blue-light excitation of Chrimson, but not somBiPOLES cells. **d** Light-ramp stimulation to determine the AP threshold irradiance. Left: Representative membrane voltage traces measured in somBiPOLES-expressing CA1 pyramidal neurons. The light was ramped linearly from 0 to 10 mW mm^{-2} over 1s. Right: Quantification of the irradiance threshold at which the first AP was evoked (black horizontal lines: medians, $n = 7$ cells). **e** Same experiment as shown in (**b**), except that CA1 neurons express Chrimson only (black horizontal lines: medians, $n = 7$ cells). The threshold for action potential firing with 595 nm was similar between somBiPOLES-expressing and Chrimson-expressing neurons, while somBiPOLES cells were not sensitive to blue light. **f** Quantification of neuronal silencing with somBiPOLES or somGtACR2 only. **g** somBiPOLES mediates neuronal silencing upon illumination with blue light. Left: Current ramps (from 0–100 to 0–900 pA) were injected into somBiPOLES-expressing CA1 pyramidal cells to induce APs during illumination with blue light at indicated intensities (from 0.001 to 100 mW mm^{-2}). The injected current at the time of the first action potential was defined as the rheobase. Right: Quantification of the rheobase shift and the relative change in the number of ramp-evoked action potentials. Illumination with 490 nm light of increasing intensities activated somBiPOLES-mediated Cl$^-$ currents shifting the rheobase to higher values and shunting action potentials. **h** Same experiment is shown in **g**, except that CA1 neurons express somGtACR2 only. Note similar silencing performance of somBiPOLES and GtACR2. In **h**, **g** black circles correspond to medians, $n_{\text{somBiPOLES}} = 6$ cells, $n_{\text{somGtACR2}} = 6$ cells, one-way Friedman test, *$p < 0.05$, **$p < 0.01$, ***$p < 0.001$.

exclusively within a narrow spectral window restricted to orange-red light, avoiding inadvertent blue-light mediated spiking.

Next, we quantified the silencing capacity of somBiPOLES and compared it to somGtACR2 alone—the most potent opsin for blue-light mediated somatic silencing[28,29]—by measuring the capacity to shift the threshold for electrically evoked APs (i.e., rheobase, see "Methods" section). Both variants similarly shifted the rheobase towards larger currents starting at an irradiance of

0.1 mW mm^{-2} with 490 nm light, leading to a complete block of APs in most cases (Fig. 3g, h). Neuronal silencing was efficient under 490 nm-illumination, even at high irradiances (up to 100 mW mm^{-2}, Fig. 3g), showing that blue light cross-activation of Chrimson in somBiPOLES did not compromise neuronal shunting.

We compared somBiPOLES with eNPAC2.0, the most advanced optogenetic tool currently available for dual-color

excitation and inhibition[4,6,7]. In eNPAC2.0 expressing CA1 pyramidal neurons, depolarizing and hyperpolarizing photocurrents were present under blue and yellow/orange light, respectively (Supplementary Fig. 8a), consistent with its inverted action spectrum compared to BiPOLES (Supplementary Fig. 2). Compared to BiPOLES (Supplementary Fig. 3c) peak photocurrent ratios were more variable between cells (Supplementary Fig. 8a), indicative of different stoichiometries between ChR2(HR) and eNpHR3.0 in different neurons, probably because membrane trafficking and degradation of both opsins occur independently. Moreover, blue-light-evoked spiking with eNPAC2.0 required approx. 10-fold higher irradiance compared to somBiPOLES and did not reach 100% reliability (Supplementary Fig. 8c), which might be explained by cross-activation of eNpHR3.0 under high blue irradiance (see also Supplementary Fig. 2d). Blue-light-triggered APs could not be reliably blocked with concomitant yellow illumination at 10 mW mm^{-2} (Supplementary Fig. 8b). Further on, activation of eNPAC2.0 (i.e., eNpHR3.0) with yellow light (580 nm) caused strong membrane hyperpolarization followed by rebound spikes in some cases (Supplementary Fig. 8d). Finally, and consistent with photocurrent measurements in HEK cells (Supplementary Fig. 2e, f), silencing of electrically evoked APs required 100-fold higher irradiance with eNPAC2.0, compared to somBiPOLES, until a significant rheobase-shift was observed (Supplementary Fig. 8e).

In summary, somBiPOLES is suitable for potent, reliable neuronal activation exclusively with orange-red light and silencing with blue light. somBiPOLES displays similar potency for neuronal excitation and inhibition as Chrimson and somGtACR2 alone.

BiPOLES allows various neuronal manipulations with visible light. We evaluated BiPOLES and somBiPOLES in the context of three distinct neuronal applications: bidirectional control of neuronal activity, optical tuning of the membrane voltage, and independent spiking of two distinct neuronal populations.

We first tested the suitability of BiPOLES and somBiPOLES for all-optical excitation and inhibition of the same neurons (Fig. 4a). Red light pulses (635 nm, 20 ms, 10 mW mm^{-2}) reliably triggered APs in somBiPOLES expressing neurons (Fig. 4b), while APs were triggered only in approx. 50% of BiPOLES expressing neurons under these stimulation conditions (Supplementary Fig. 7e), due to a higher irradiance threshold to evoke APs in those cells (Supplementary Fig. 7a, b). Concomitant blue illumination (490 nm, 10 mW mm^{-2}) for 100 ms reliably blocked red-light evoked APs in all cases. As expected from an anion conducting channel, blue light alone had only a minor impact on the resting membrane voltage, due to the close proximity of the chloride reversal potential to the resting potential of the cell (Fig. 4b, Supplementary Fig. 7e) In contrast, neurons expressing Chrimson alone showed APs both under red and blue illumination (Supplementary Fig. 4b).

Aside from dual-color spiking and inhibition, a major advantage of the fixed 1:1 stoichiometry between an anion and cation channel with different activation spectra in BiPOLES is the ability to precisely tune the ratio between anion-conductance and cation-conductance with light (Fig. 1f,g, Supplementary Fig. 3c). In neurons, this allows to optically tune the membrane voltage between the chloride reversal potential and the action potential threshold (Fig. 4c). Optical membrane voltage tuning was achieved either by a variable ratio of blue and orange light at the absorption peak wavelengths of GtACR2 and Chrimson (Fig. 4d) or by using a single color with fixed irradiance over a wide spectral range (Fig. 4e). Both approaches yielded reliable and reproducible membrane voltage shifts. Starting from the chloride

Nernst potential when only GtACR2 was activated with blue light at 470 nm, the membrane depolarized steadily with an increasing 595/470 nm ratio, eventually passing the action potential threshold (Fig. 4d). Similarly, tuning a single wavelength between 385 nm and 490 nm clamped the cell near the Nernst potential for chloride, while shifting the wavelength peak further towards red led to gradual depolarization, eventually triggering action potentials at 580 nm (Fig. 4e). Depending on the available light source both methods allow precise control of anion and cation fluxes at a fixed ratio and might be applied for locally defined subthreshold membrane depolarization in single neurons or to control the excitability of networks of defined neuronal populations.

Since BiPOLES permits neuronal spiking exclusively within the orange-red light window, it facilitates two-color excitation of genetically distinct but spatially intermingled neuronal populations using a second, blue-light-activated ChR (Fig. 4f). To demonstrate this, we expressed somBiPOLES in CA1 VIP interneurons and CheRiff, a blue-light-sensitive ChR ($\lambda_{max} = 460$ nm)[30] in CA1 pyramidal neurons (Fig. 4g, see "Methods" section for details). Both CA1 and VIP neurons innervate Oriens-Lacunosum-Molecolare (OLM) interneurons. Therefore, exclusive excitation of CA1 pyramidal cells or VIP interneurons is expected to trigger excitatory (EPSCs) and inhibitory (IPSCs) postsynaptic currents, respectively. CheRiff-expressing pyramidal cells were readily spiking upon blue, but not orange-red illumination up to 10 mW mm^{-2} (Fig. 4h, Supplementary Fig. 9). Conversely, as expected, red light evoked APs in somBiPOLES-expressing VIP neurons, while blue light up to 100 mW mm^{-2} did not evoke APs (Fig. 4h). Next, we recorded synaptic inputs from these two populations onto VIP-negative GABAergic neurons in stratum-oriens (Fig. 4i). As expected, blue light triggered EPSCs (CheRiff) and red light triggered IPSCs (somBiPOLES), evident by their respective reversal potentials at 8.8 ± 10.4 mV and -71.4 ± 13.1 mV (Fig. 4i). Thus, somBiPOLES, in combination with the blue-light sensitive CheRiff enabled independent activation of two distinct populations of neurons in the same field of view.

Bidirectional neuronal control using dual-laser two-photon holography. Two-photon holographic excitation enables spatially localized photostimulation of multiple neurons with single-cell resolution in scattering tissue[1]. We evaluated the feasibility of bidirectional control of single neurons by two-photon holographic excitation (Supplementary Fig. 10a) in hippocampal organotypic slices virally transduced with somBiPOLES expressed from a CaMKII promoter. Single-photon excitation confirmed the high potency of somBiPOLES using this expression strategy (Supplementary Fig. 11). The two-photon action spectrum of somBiPOLES was explored by measuring the peak photocurrents (I_p) at a range of holding potentials (-80 to -55 mV) and excitation wavelengths (850 to 1100 nm). Similar to single-photon excitation, blue-shifted wavelengths ($\lambda_{ex} < 980$ nm) generated large photocurrents, apparently dominated by the flow of chloride ions (outward chloride currents below the chloride Nernst potential and inward chloride currents above the chloride Nernst potential, Fig. 5a–c, Supplementary Fig. 10b). Red-shifted wavelengths ($\lambda_{ex} > 980$ nm) generated photocurrents, which appeared to be dominated by the flow of protons and cations across the membrane (inward currents at physiological neuronal membrane potentials, Fig. 5a–c, Supplementary Fig. 10b). Since 920 nm and 1100 nm illumination generated the largest magnitudes of inhibitory and excitatory photocurrents, respectively, these wavelengths were used to evaluate whether the neuronal activity could be reliably suppressed or evoked in neurons expressing
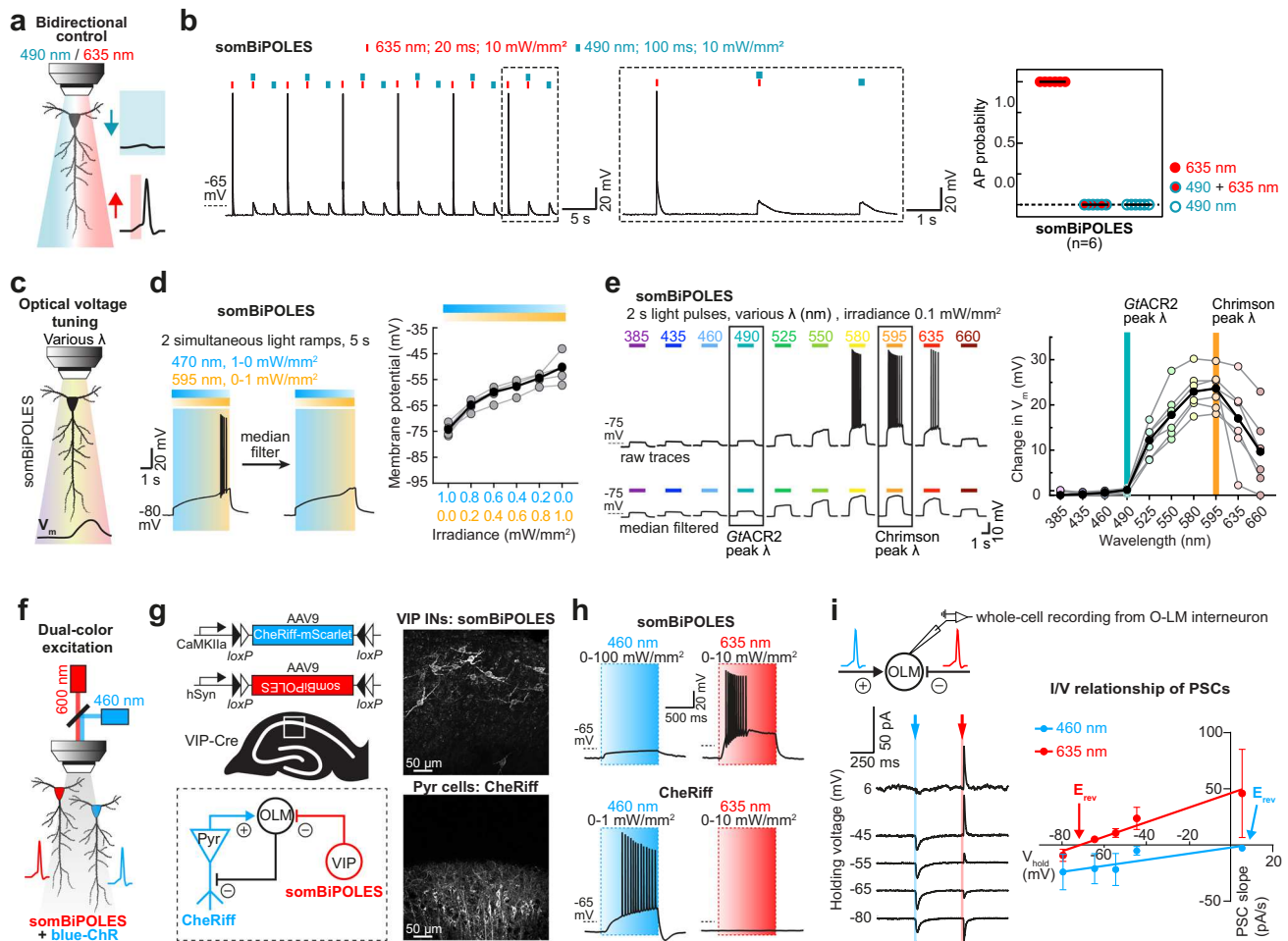
Fig. 4 Applications of BiPOLES: bidirectional control of neuronal activity, optical voltage tuning, and independent dual-color excitation of two distinct neuronal populations. a Schematic drawing illustrating bidirectional control of neurons with blue and red light. **b** Current-clamp characterization of bidirectional optical spiking-control with somBiPOLES. Left: Voltage traces showing red-light-evoked APs, which were blocked by a concomitant blue light pulse. Right: quantification of AP probability under indicated conditions (black horizontal lines: medians, $n = 6$ cells). **c** Schematic drawing illustrating control of membrane voltage with somBiPOLES. **d** Left: Representative membrane voltage traces from a somBiPOLES-expressing CA1 pyramidal cell during simultaneous illumination with 470-nm and 595-nm light ramps of the opposite gradient. Voltage traces were median-filtered to reveal the slow change in membrane voltage during the ramp protocol. Right: Quantification of membrane voltage at different 595/470 nm light ratios (black circles: medians, $n = 5$ cells). **e** Left: Representative membrane voltage traces of somBiPOLES in CA1 pyramidal neurons upon illumination with different wavelengths and equal photon flux. As in **d** voltage traces were median-filtered to eliminate action potentials and reveal the slow changes in membrane voltage during the light protocol. Right: Quantification of membrane potential along the spectrum showing optical voltage tuning at the indicated wavelengths. (black circles: medians, an irradiance of 0.1 mW mm^{-2} was kept constant for all wavelengths, $n = 6$ cells). **f** Schematic drawing illustrating control of 2 neurons expressing either somBiPOLES (red) or a blue-light-sensitive ChR (blue). **g** Left: Cre-On/Cre-Off strategy to achieve mutually exclusive expression of CheRiff-mScarlet in CA1 pyramidal neurons and somBiPOLES in VIP-positive GABAergic neurons. Both cell types innervate OLM interneurons in CA1. Right: Example maximum-intensity projection images of two-photon stacks showing expression of somBiPOLES in VIP-interneurons (top) and CheRiff-mScarlet in the pyramidal layer of CA1 (bottom). **h** IC-recordings demonstrating mutually exclusive spiking of somBiPOLES-expressing and CheRiff-expressing neurons under red or blue illumination. **i** Postsynaptic whole-cell voltage-clamp recordings from an OLM cell at indicated membrane voltages showing EPSCs and IPSCs upon blue-light and red-light pulses, respectively. Right: quantification of blue-light and red-light-evoked PSCs and their reversal potential. Symbols show mean ± SEM, $n_{460\,nm} = 8$ cells, $n_{635\,nm} = 7$ cells, lines: linear regression fit, $R^2 = 0.06$ and 0.20 for a blue and red light, respectively.

somBiPOLES. Action potentials could be reliably evoked using short (5 ms) exposure to 1100 nm light (power density: 0.44 mW/ μm²), with latency (19.9 ± 6.3 ms) and jitter (2.5 ± 1.5 ms) (Fig. 5d, Supplementary Fig. 10c) comparable to literature values for Chrimson[31]. 5 ms pulses were also able to induce high-fidelity trains of APs with frequencies up to 20 Hz (Supplementary Fig. 10d). It is likely that shorter latency and jitter (and consequently higher rates of trains of APs) could be achieved by replacing the stimulation laser with one with optimized pulse

parameters, in particular, higher peak energy[32]. 920 nm excitation effectively inhibited neural activity, increasing the rheobase of AP firing at power densities above 0.1 mW μm^{-2} (Fig. 5e). It further enabled temporally precise elimination of single electrically evoked APs (Supplementary Fig. 10e) and silencing of neuronal activity over sustained (200 ms) periods (Fig. 5f). Finally, we demonstrate two-photon, bidirectional control of neurons by co-incident illumination of appropriately titrated 920 nm and 1100 nm light (Fig. 5g). Thus, somBiPOLES is suitable for dual-color
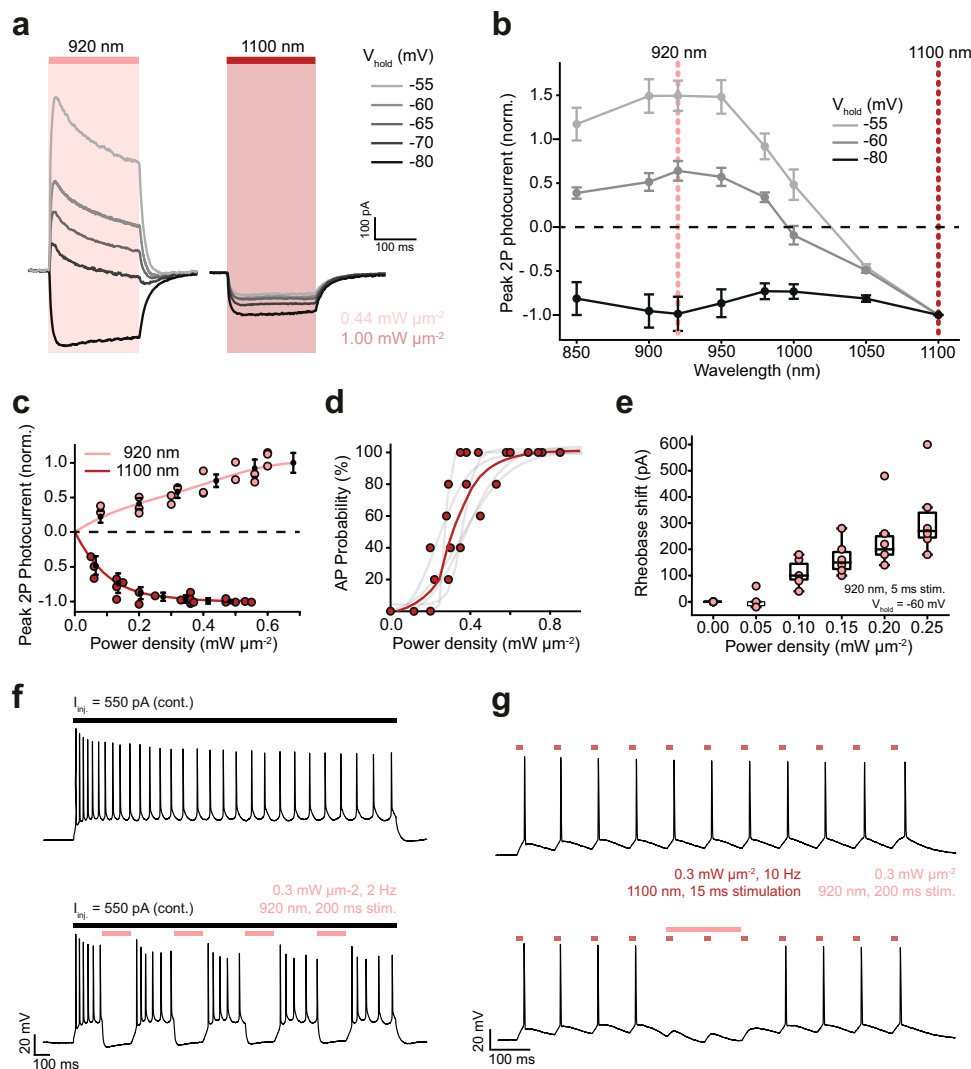
Fig. 5 Bidirectional control of neuronal activity with somBiPOLES using dual-color two-photon holography. a–c Voltage clamp (VC) characterization of somBiPOLES in CA1 pyramidal cells. **a** Representative photocurrent traces at different holding potentials, obtained by continuous 200 ms illumination of 920 and 1100 nm at constant average power density (0.44 and 1.00 mW μm^{-2}). **b** Peak photocurrent as a function of wavelength at different holding potentials (mean ± SEM, $n = 5$). Data acquired with a constant photon flux of 6.77×10^{26} photons s^{1}m^{-2}. Dashed lines indicate 920 and 1100 nm respectively; the wavelengths subsequently utilized for photo-stimulation and inhibition. **c** Peak photocurrent as a function of incident power density at a holding potential of −60 mV (mean ± SEM, 920 nm, $n = 4$; 1100 nm, $n = 5$). **d–g** Current clamp (IC) characterization of somBiPOLES in CA1 pyramidal cells. **d** Probability of photo evoked action potentials under 1100 nm illumination for 5 ms ($n = 5$, red: average, gray: individual trials). **e** Characterization of the efficacy of silencing somBiPOLES expressing neurons under 920-nm illumination by co-injection of current (Box: median, 1st–3rd quartile, whiskers: 1.5x inter quartile range, $n = 5$). **f** Representative voltage traces demonstrating sustained neuronal silencing of neurons by two-photon excitation of somBiPOLES at 920 nm. Upper trace (control): 550 pA current injected (illustrated by the black line), no light. Lower trace: continuous injection of 550 pA current, 0.3 mW μm^{-2}, 920 nm, 2 Hz, 200 ms illumination. **g** Two-photon, bidirectional, control of single neurons demonstrated by co-incident illumination of 920 nm and 1100 nm light. Upper trace: 10 Hz spike train evoked by 15 ms pulses of 1100 nm light. Lower trace: optically induced action potentials shunted using a single, 200 ms pulse of 920 nm light.

two-photon holographic manipulation of neuronal activity with a cellular resolution with standard lasers typically used for two-photon imaging.

Considering the reliable performance of BiPOLES in pyramidal neurons we next tested its applicability in the invertebrate model systems *C. elegans* and *D. melanogaster*, as well as mice and ferrets, representing vertebrate model systems.

Bidirectional control of motor activity in *C. elegans*. We expressed BiPOLES in cholinergic motor neurons of *C. elegans* to optically control body contraction and relaxation. Illumination with

red light resulted in body-wall muscle contraction and effective body shrinkage, consistent with motor neuron activation. Conversely, blue light triggered body extension, indicative of muscle relaxation and thus, cholinergic motor neuron inhibition (Fig. 6b). Maximal body length changes of +3% at 480 nm and −10% at 560–600 nm and reversal of the effect between 480 and 520 nm were consistent with the inhibitory and excitatory action spectrum of BiPOLES (Fig. 6b, Supplementary Fig. 12a). The light effects on body length required functional BiPOLES as the light did not affect body length in the absence of all-*trans*-retinal (ATR, Fig. 6b). Previous strategies for bidirectional motor control in *C. elegans* using ChR2(HR) and NpHR did not show body contraction and elongation in the same
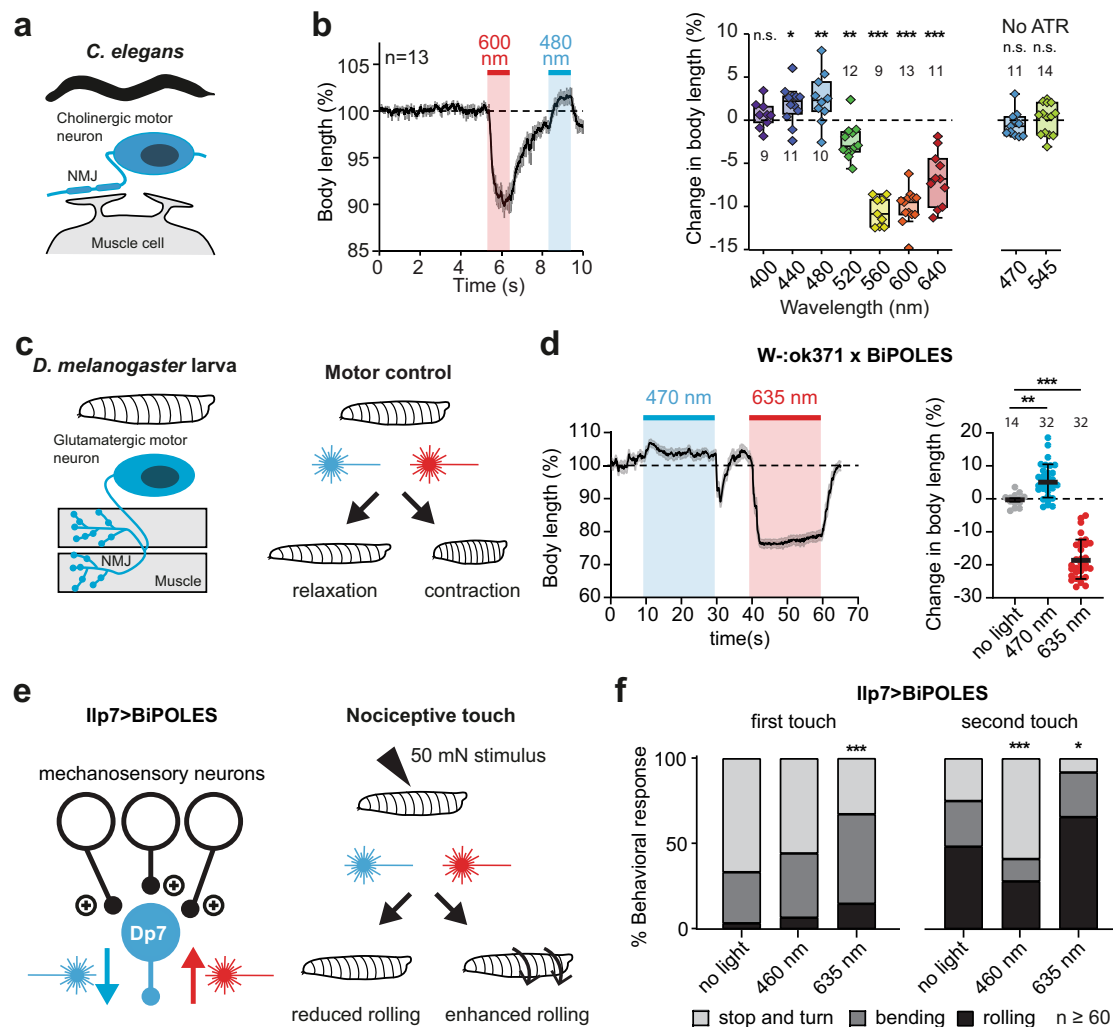
Fig. 6 BiPOLES allows bidirectional modulation of neuronal activity in *C. elegans* and *D. melanogaster*. a BiPOLES expressed in cholinergic neurons of *C. elegans* enables bidirectional control of body contraction and relaxation. Scheme of BiPOLES-expressing cholinergic motor neuron innervating a muscle cell. **b** Left: Temporal dynamics of relative changes in body length upon illumination with 600 and 480 nm light (mean ± SEM, 1.1 mW mm^{-2}, n = 13 animals). Right: Spectral quantification of maximal change in body length, compared is the body length before to during light stimulation (seconds 0–4 vs. seconds 6–9, see Supplementary fig. 12a; Box: median, 1st–3rd quartile, whiskers: 1.5x interquartile range, two-way ANOVA (Sidak's multiple comparisons test), p values: 400 nm (n = 9 animals): 0.99, 440 nm (n = 12): 0.049, 480 nm (n = 10): 0.007, 520 nm (n = 12): 0.002, 560 nm (n = 9): <0.0001, 600 nm (n = 13): <0.0001, 640 nm (n = 11): <0.0001, no ATR 470 nm (n = 11): 0.24, no ATR 545 nm (n = 14): 0.78). Experiments in absence of all-*trans*-retinal were done with 470/40 nm and 545/30 nm bandpass filters. **c** BiPOLES expressed in glutamatergic neurons of *D. melanogaster* larvae enables bidirectional control of body contraction and relaxation. Scheme of BiPOLES-expressing glutamatergic motor neuron innervating muscle fibers. **d** Left: Temporal dynamics of relative changes in body length upon illumination with 470 (17 µW mm^{-2}, n = 32 animals) and 635 nm light (25 µW mm^{-2}, n = 32). Right: Quantification of maximal change in body length (mean ± SEM, no light = 14, 470 nm = 32, 635 nm = 32, **p = 0.0152, ***p = 0.0005, one-way ANOVA with Dunnett's multiple comparisons test). **e** BiPOLES-dependent manipulation of Dp7 neurons in the Drosophila larval brain (Ilp7-Gal4>UAS-BiPOLES) and the resulting change in nociceptive escape behavior following a 50 mN noxious touch. **f** Behavioral response after the first and second mechanical stimulus under blue light (470 nm, 1.7 mW mm^{-2}) or red light (635 nm, 2.5 mW mm^{-2}) illumination compared to no light. n = 61 animals *p = 0.034, ***p = 0.0005 (first touch) and 0.0007 (second touch), X^2-test.

animal[33]. Therefore, we tested this directly with light conditions similar to those used for BiPOLES activation. Excitation with blue light resulted in a 5% body length decrease, while activation of NpHR at its peak wavelength (575 nm) failed to induce significant changes in body length (Supplementary Fig. 12b). Thus, BiPOLES expands the possibilities for bidirectional control of neuronal activity in *C. elegans* beyond what is achievable with currently available tools.

Bidirectional control of motor activity and nociception in *D. melanogaster*. Next, we demonstrate bidirectional control of circuit function and behavior with BiPOLES in *Drosophila*

melanogaster. *Gt*ACR2 and *Cs*Chrimson were previously used in separate experiments to silence and activate neuronal activity, respectively[10]. In contrast, rhodopsin pump functionality is strongly limited in this organism[10,11], and bidirectional control of neuronal activity has not been achieved. We, therefore, expressed BiPOLES in glutamatergic motor neurons of *D. melanogaster* larvae (Fig. 6c). Illumination with blue light led to muscle relaxation and concomitant elongation (Fig. 6d). The change in body length was similar to animals expressing *Gt*ACR2 alone (Supplementary Fig. 12c). Importantly, *Gt*ACR2 activation in BiPOLES overrides blue-light evoked Chrimson activity and

thereby eliminates blue-light excitation of neurons, as observed with *Cs*Chrimson alone (Supplementary Fig. 12c). Conversely, red illumination of BiPOLES expressing larvae triggered robust muscle contraction and corresponding body length reduction (Fig. 6d). Thus, BiPOLES facilitates bidirectional optogenetic control of neuronal activity in *D. melanogaster* which was not achieved previously.

We further tested BiPOLES functionality in a more sophisticated in vivo paradigm expressing it in key modulatory neurons (dorsal pair Ilp7 neurons, Dp7) of the mechanonociceptive circuit. Dp7 neurons naturally exert bidirectional control of the larval escape response to noxious touch depending on their activation level[34] (Fig. 6e). Acute BiPOLES-dependent silencing of Dp7 neurons with blue light strongly decreased the rolling escape (Fig. 6f), consistent with previously shown chronic silencing of these neurons[34]. In turn, red light illumination of the same animals enhanced escape responses upon noxious touch showing that BiPOLES activation in Dp7 neurons can acutely tune their output and thus the corresponding escape response (Fig. 6f). BiPOLES activation in Dp7 neurons showed a similar ability to block or enhance nociceptive behavior as *Gt*ACR2 or *Cs*Chrimson, respectively, while preventing Chrimson-dependent activation with blue light (Supplementary Fig. 12d, e). Taken together, BiPOLES allows robust, acute, and bidirectional manipulation of neuronal output and behavior in *Drosophila melanogaster* in vivo.

All-optical, bidirectional control of pupil size in mice. To further extend the applications of BiPOLES to vertebrates, we generated various conditional and non-conditional viral vectors, in which the expression of the fusion construct is regulated by different promoters (see "Methods" section, Table 1). Using these viral vectors, we sought to test BiPOLES and somBiPOLES in the mammalian brain. To this end, we conditionally expressed somBiPOLES in TH-Cre mice, targeting Cre-expressing neurons in the Locus Coeruleus (LC) (Fig. 7a). Orange illumination (594 nm) through an optical fiber implanted bilaterally above LC reliably triggered transient pupil dilation, indicative of LC-mediated arousal[35] (Fig. 7b–d). Pupil dilation was evident already at 0.7 mW at the fiber tip and gradually increased with increasing light power (Supplementary Fig. 13a). Light-mediated pupil dilation was reverted immediately by additional blue light (473 nm) during the orange-light stimulation or suppressed altogether when blue-light delivery started before orange-light application (Fig. 7b–d), suggesting that orange-light-induced spiking of somBiPOLES-expressing neurons in LC was efficiently shunted. Illumination of the LC in wt-animals did not influence pupil dynamics (Supplementary Fig. 13b). Thus, LC neurons were bidirectionally controlled specifically in somBiPOLES expressing animals.

We estimated the brain volume accessible to reliable activation and inhibition with somBiPOLES using Monte-Carlo simulations of light propagation[16] under the experimental settings used for the LC-manipulations described above (Supplementary Fig. 14). Based on the light parameters required for neuronal excitation and inhibition determined in Fig. 3, and assuming 1 mW of 473 nm and 10 mW of 593 nm at the fiber tip, we estimate that reliable bidirectional control of neuronal activity can be achieved over a distance of >1.5 mm in the axial direction below the fiber tip (Supplementary Fig. 14c).

Manipulation of neocortical excitation/inhibition ratio in ferrets. Finally, we applied BiPOLES to bidirectionally control the excitation/inhibition (E/I) ratio in the mammalian neocortex. Therefore, we generated a viral vector using the minimal *Dlx*

promoter[36] (mDlx) to target GABAergic neurons in the ferret secondary visual cortex (V2). Functional characterization in GABAergic neurons in vitro confirms all-optical spiking and inhibition of GABAergic neurons with mDlx-BiPOLES (Supplementary Fig. 15). Thus, we injected mDlx-BiPOLES in ferret V2 to modulate E/I-ratio during sensory processing (Fig. 7e). Extracellular recordings obtained from linear silicon probes in V2 of isoflurane-anesthetized ferrets provided evidence for modulation of cortical activity by shifts in the E/I ratio (Fig. 7f, g). Blue light led to an increase in baseline activity, consistent with the deactivation of inhibitory, GABAergic neurons (Fig. 7f, g). Activation of GABAergic cells by red light did not further decrease the low cortical baseline activity, but significantly reduced cortical responses triggered by sensory stimuli (Fig. 7f, g). Although effects of blue light on evoked spiking were not significant in the average data, we obtained clear evidence in individual recordings that blue light could enhance late response components (Fig. 7f), confirming a disinhibitory effect. Overall, these data suggest that BiPOLES is efficient in bidirectional control of inhibitory mechanisms, demonstrating its applicability for the control of E/I shifts in the cortical microcircuit in vivo.

Discussion

In summary, BiPOLES is a performance-optimized fusion construct composed of a red-light-activated cation- and a blue-light-activated anion-selective ChR. BiPOLES serves as an optogenetic tool for potent excitation and inhibition of the same neurons with red and blue light, respectively. In addition, it can be applied for exclusive red-light activation of a neuronal subpopulation in multicolor experiments, and for locally defined optical tuning of the membrane voltage between the Nernst potential for chloride and the action potential threshold.

BiPOLES performs reliably in invertebrate and vertebrate model systems, showing potent, bidirectional modulation in the *C. elegans* motor system, the *D. melanogaster* motor and nociceptive systems, and the ferret visual cortex. The addition of the soma-targeting signal from the mammalian potassium channel Kv2.1 yielded somBiPOLES, leading to further enhancement of trafficking to the plasma membrane at the soma and proximal dendrites while avoiding localization to distal dendrites and axons, as previously shown for individually expressed microbial rhodopsins[27–29]. Thus, eliminating the risk of inadvertent blue-light mediated depolarization of axons[28,37] while improving bidirectional optogenetic manipulation of the somatodendritic compartment somBiPOLES is optimized for applications in mammalian systems.

Combining cation and anion channels of overlapping action spectra requires careful consideration of the electrochemical conditions of the neuronal membrane. Since the resting membrane potential is close to the Nernst potential of chloride, anion channels displaying large unitary conductance are needed in order to efficiently shunt depolarizing currents of the red-shifted cation channel, which, in turn, needs to be potent enough to reliably trigger action potentials. Thus, photocurrent amplitudes and spectral sensitivity of the two opsins need to match the aforementioned conditions in order to both reliably silence and drive neuronal activity. If the red-shifted excitatory opsin shows too large, blue-light sensitive photocurrents, it may compromise the silencing capacity of the anion channel. Conversely, if the action spectrum of the blue-light sensitive anion channel extends too far towards longer wavelengths, efficient red-light evoked spiking may get impaired. For the molecular engineering of BiPOLES we focused on a large spectral separation of the anion and the cation conductance. Minimizing the optical cross-talk of both channels favors inhibitory conductance under blue light
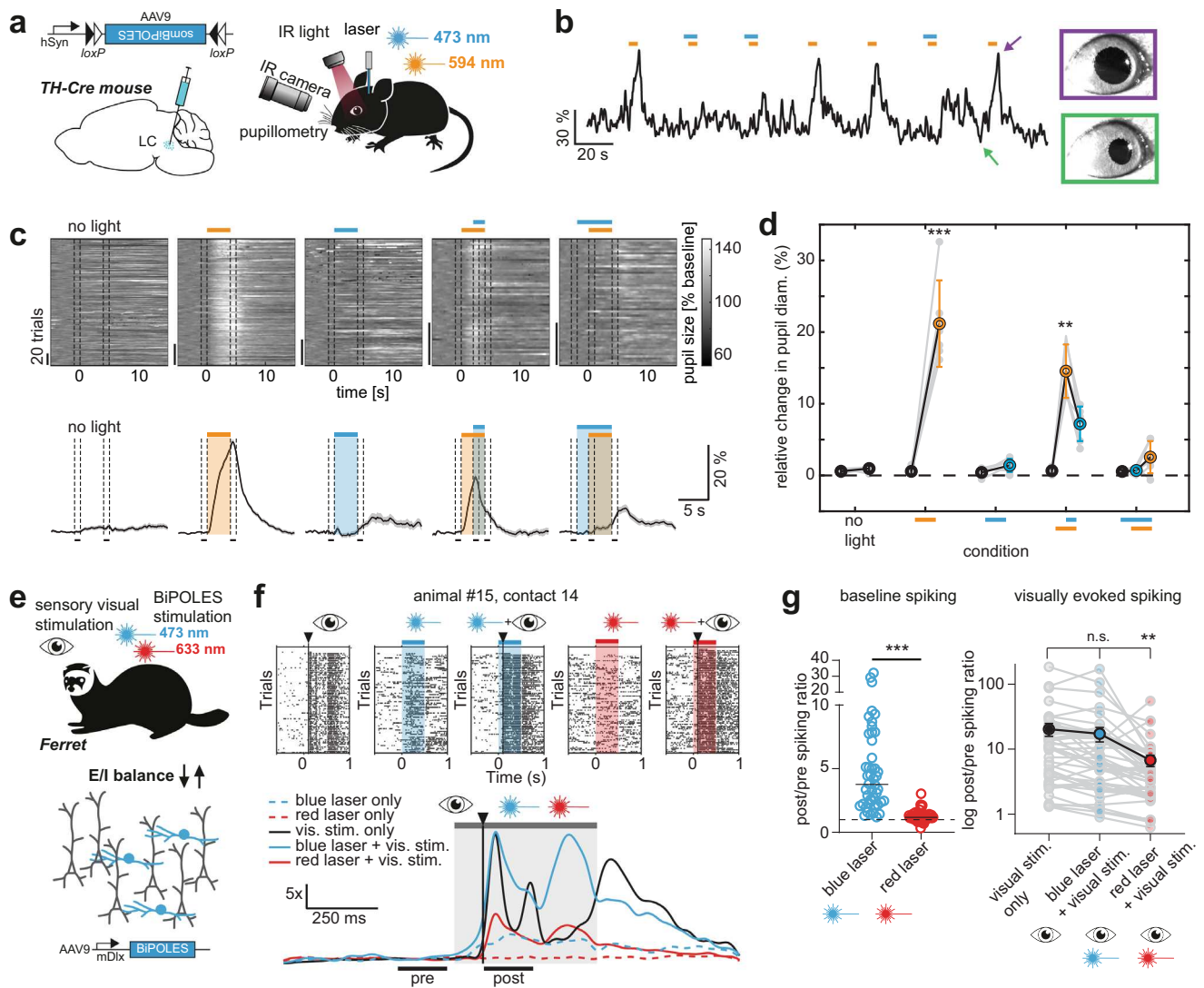
Fig. 7 BiPOLES and somBiPOLES allow bidirectional modulation of neuronal activity in mice and ferrets. a Conditional expression of somBiPOLES in Cre-positive neurons of the TH-Cre mouse to modulate pupil dilation. **b** Relative pupil diameter in single trials. Orange and blue bars indicate the time of illumination with 594 (orange) and 473 nm (blue), respectively. Arrows indicate positions of the two example images of the eye. **c** Quantification of normalized pupil size in one animal under various stimulation conditions for somBiPOLES as indicated. Top: single trials. Bottom: mean ± SEM. Dashed lines show time windows used for quantification in the plot on the right. **d** Quantification of relative pupil size ($n = 6$ mice; One-way analysis of variance; $F = 61.67$, $p = 1.36 \times 10^{-12}$; Tukey's multiple comparison test: $**p = 0.0028$, $***p < 0.0001$). **e** Modulation of GABAergic neurons (blue) in ferret secondary visual cortex (area 18) with mDlx-BiPOLES. Red (633 nm) or blue (473 nm) laser light was used to (de-)activate interneurons with or without a following 10-ms visual flash (white LED; Osram OSLON Compact) to the ferret's right eye. **f** Example neuronal spiking responses at one contact of the linear probe (~700 μm depth) under indicated stimulation conditions Top: Raster-plots of the visual stimulus alone, blue laser (+visual), red laser (+visual) conditions. Bottom: Normalized to 'pre'-phase averaged spike-density plot (sigma = 20 ms) of each indicated condition. Gray area: laser-on epoch; black vertical line: visual stimulus onset. Black horizontal lines indicate the 200 ms pre-stim and post-stim analysis epochs to compute the results in **g**. Note the rate increase after the onset of the blue laser before the onset of the visual stimulus and the reduced answer after red laser illumination. **g** Spike-rate ratio of post vs. pre-laser-stimulus epoch. Left: quantification of laser-mediated impact on baseline spiking rate (no visual stim.). Right: quantification of the spike-rate change of the same units during only visual and laser + visual stimulation ($n = 46$ contacts showing visual responses from 3 animals, $**p = 0.0046$, $***p < 0.0001$).

illumination and increases both the light intensity range and the spectral range that allows exclusive activation of the red-shifted cation channel. Due to the large spectral separation, BiPOLES can be controlled with two simple light sources, such as LEDs, without the requirement of sophisticated spectral control, making its use straightforward. The *Gt*ACR2-L4-ChRmine-construct might be an interesting alternative if spectrally narrow light sources, such as lasers, are available, because it reaches peak depolarizing currents 60 nm blue-shifted compared to BiPOLES. Thus, inhibition and excitation can be achieved with 430–470 nm

and 530–550 nm (Fig. 1f) providing an additional spectral window in the red, that can be used for a third optogenetic actuator or sensor. Finally, a seemingly trivial but equally important advantage of all the tandem systems we present here is their modular architecture allowing easy tailoring of fusion constructs fulfilling specific future experimental requirements.

Noteworthy, BiPOLES does not represent the first optogenetic tool for bidirectional control of neuronal activity. Different combinations of the excitatory blue-light-sensitive ChR2 and orange-light-sensitive inhibitory ion pumps such as NpHR, bR, or

115

Arch3.0 were generated previously[2,4,6]. However, among all these variants, only the combination of ChR2 and NpHR (i.e., eNPAC and eNPAC2.0) was successfully used to address neuroscientific questions in mice[6–9]. BiPOLES will significantly expand the possibilities of bidirectional neuronal manipulations, since, aside from efficient expression in a wide array of different model systems, it also features a number of additional advantages: First, combining two potent channels, rather than a pump and a channel, provides a more balanced ionic flux per absorbed photon for the inhibitory and excitatory rhodopsin. This results in a high operational light sensitivity for both excitation and inhibition by orange and blue light, respectively. In contrast, high irradiance and expression levels are required for the ion pumps that only transport one charge per absorbed photon. Second, due to the use of two channels, BiPOLES-mediated photocurrents do not actively move ions against their gradients, which can cause adverse side-effects[37], but rather fixes the neuronal membrane voltage anywhere between the reversal potential of GtACR2 and Chrimson. The membrane voltage can be tuned depending on the ratio of blue/red light or a single light source tuned to wavelengths between the absorption peaks of GtACR2 and Chrimson. Third, inverting the color of the excitatory and inhibitory opsin, compared to previous tools, restricts optical excitation in BiPOLES-expressing cells exclusively to the orange/red spectrum. The inverted color scheme enables scale-free and mutually exclusive spiking of two neuronal populations in combination with a second, blue-light-sensitive ChR, expressed in the second population of neurons, as the blue-light-activated, inhibitory channel GtACR2 potently shunts Chrimson-mediated, blue-light-activated excitatory photocurrents. Other applications could employ multiplexing with blue-light sensitive cyclases[38] or genetically encoded activity-indicators that require blue light for photoconversion[39,40]. Fourth, compared to the first generation of tandem constructs, BiPOLES was optimized for membrane trafficking and especially the somBiPOLES variant shows strongly improved membrane expression in mammalian neurons, enabling reliable and potent optogenetic spiking and inhibition even in deep brain regions in vivo. One additional reason for the superior membrane expression of BiPOLES compared to other rhodopsin-tandems might be the absence of N-terminal, extracellular cysteine residues, which are involved in disulfide bond formation and thus dimerization in all structurally described ChRs[41–44]. The absence of N-terminal cysteines may avoid heteromeric protein networks and undesired clustering of the fused tandem rhodopsins. Fifth, soma-targeted BiPOLES allows efficient and reliable bidirectional control of neuronal spiking over a wide range of light intensities. This is important for in vivo applications in the mammalian brain, where light scattering and absorption lead to an exponential fall-off of the irradiance over distance[17]. The color scheme in somBiPOLES in combination with the large-conductance of GtACR2 and its absence from axon terminals enables potent and reliable silencing with blue light over a wide range of intensities. Potential cross-activation of Chrimson by high blue light intensities did not compromise neuronal silencing in pyramidal neurons. Similarly, due to the red-shifted absorption of Chrimson, neuronal spiking can be efficiently achieved with orange light. somBiPOLES reliably mediates silencing and activation at modest intensities of blue and orange light far away from the fiber tip, while maintaining its wavelength-specificity under high-intensity irradiance, as typically present directly under the fiber tip. Thus, somBiPOLES holds the potential to manipulate neuronal activity in large brain areas with single-photon illumination (Supplementary Fig. 14c). Finally, a fusion protein of two potent channels with opposite charge selectivity targeted to the somatodendritic compartment and displaying a local one-to-one expression ratio in the plasma

membrane enables temporally precise bidirectional control of neuronal activity at single-cell resolution using two-photon excitation. In contrast to widefield illumination with visible light, two-photon excitation in combination with soma-targeted opsins allows optogenetic control with single-cell resolution[45–47]. Bidirectional optogenetic control in the same cells has not been achieved with two-photon excitation, so far; partially due to the low quantum efficiency of rhodopsin pumps, which limits their two-photon activation. In contrast, the large conductance of the two channels improves their efficacy with respect to the number of transported ions per absorbed photon, and their presence at equal stoichiometry anywhere on the membrane ensures the reliable and reproducible generation of anion currents and/or cation currents, which is particularly important under locally confined two-photon excitation.

In principle, also multicistronic vectors encoding both opsins under a single promoter using either an internal ribosomal entry site (IRES)[48] or a 2A ribosomal skip sequence allow expression of both ion channels at a fixed ratio from a single AAV vector[3,7]. However, with both of these strategies, neither co-localized nor stoichiometric membrane expression of both channels is guaranteed since both channels might get differentially targeted and distributed in the plasma membrane. This may not pose a limitation for experiments that require bidirectional control of large numbers of cells where precise control of a single-cell activity or sub-cellular ion gradients is not so crucial. BiPOLES as a covalently linked fusion protein displays a fixed expression of both opsins at a 1:1 stoichiometry anywhere in the membrane and membrane trafficking or degradation of both opsins occur at identical rates, preserving excitatory and inhibitory currents at a fixed ratio in all expressing cells. A fixed stoichiometry anywhere in the cell membrane is important if local, subcellular activation of the opsins is required, such as during two-photon excitation or when a fixed ratio of cation and anion conductance is desired between different neurons or in particular neuronal compartments, such as single dendrites or dendritic spines.

Notably, BiPOLES employs an anion channel for optogenetic silencing and therefore relies on the extracellular and intracellular chloride concentration. In the case of a depolarized chloride Nernst potential, the opening of the anion channel may produce depolarizing currents, which can trigger action potentials or neurotransmitter release[49]. Unlike for rhodopsin pumps, efficient silencing consequently requires low cytosolic chloride concentrations and is therefore limited in neurons or cellular compartments with a depolarized Nernst potential for chloride, such as immature neurons or axon terminals. Given these caveats, BiPOLES may not be suitable for bidirectional control of developing neurons or presynaptic boutons. In this case, silencing may be more efficient with rhodopsin pumps, despite their own limitations[37,49] or with G-protein coupled rhodopsins[50,51]. As with any optogenetic application, neurophysiological parameters need to be considered by the experimenter, guiding the appropriate choice of the tool suitable to address the specific experimental requirements.

Since BiPOLES can be used to spike or inhibit the same population of mature neurons in vivo, a number of previously inaccessible questions can be addressed. During extracellular recordings, BiPOLES may be useful for optogenetic identification (optotagging) with red light[52] and optogenetic silencing of the same neurons. This will permit verification of the identity of silenced neurons by their spiking profiles. Moreover, in combination with a second, blue-light sensitive ChR, BiPOLES can be used to map local networks of spatially intermingled neurons. For example, expressed in distinct types of molecularly defined GABAergic neurons, connectivity of these neurons to a post-synaptic target cell can be evaluated. Additional applications of

BiPOLES may encompass bidirectional control of engram neurons[53] to test both necessity and sufficiency of a particular set of neurons for memory retrieval or switching the valence of a particular experience by inhibiting or activating the same or even two distinct populations of neuromodulatory neurons. In principle, this could even be achieved with cellular resolution using two-photon holography. Due to its utility for a wide range of research questions, its versatile functionality, and its applicability in numerous model systems, as demonstrated in this study, BiPOLES fills an important gap in the optogenetic toolbox and might become the tool of choice to address a number of yet inaccessible problems in neuroscience.

Methods

Molecular biology. For HEK-cell expression, the coding sequences of Chrimson (KF992060.1), CsChrimson (KJ995863.2) from *Chlamydomonas noctigama*[12], ChRmine from *Rhodomonas lens* although initially attributed to *Tiarina fusus*[22,25] (Addgene #130997), bReaChES[20], iC++ (Addgene #98165)[19], Aurora (Addgene #98217)[11], *Gt*ACR1 (KP171708) and *Gt*ACR2 (KP171709) from *Guillardia theta*[18], as well as the blue-shifted Arch3.0 mutant M128A/S151A/A225T herein described as ArchBlue[26] were cloned together with mCerulean3[54] and a trafficking signal (ts) from the Kir 2.1 channel[4] into a pCDNA3.1 vector containing the original opsin tandem cassette[2] with a linker composed of eYFP and the first 105 N-terminal amino acids of the rat gastric H+/K+-ATPase beta subunit (βHK, NM_012510.2), kindly provided by Sonja Kleinlogel (University of Bern, CH). For direct comparison also the bicistronic tool eNPAC2.0[6]—kindly provided by Karl Deisseroth (Stanford University, CA)—was cloned into the same backbone. Site-directed mutagenesis to introduce the f-Chrimson and vf-Chrimson mutations Y261F, S267M, and K176R[21] was performed using the QuickChange Site-Directed Mutagenesis Kit (Agilent Technologies, Santa Clara, CA) according to the manufacturers' instructions.

For neuronal expression, the insert consisting of *Gt*ACR2-ts-mCerulean3-βHK-Chrimson was cloned into an AAV2-backbone behind human synapsin (hSyn) promoter (pAAV-hSyn-BiPOLES-mCerulean; Addgene #154944). A soma-targeted, membrane-trafficking optimized variant was generated by fusing an additional trafficking signal from the potassium channel Kv2.1[27] to the C-terminus of Chrimson (pAAV-hSyn-somBiPOLES-mCerulean; Addgene #154945). For expression in GABAergic neurons, BiPOLES was cloned into an AAV2-backbone behind the minimal Dlx (mDlx) promoter[36] resulting in pAAV-mDlx-BiPOLES-mCerulean (Addgene #154946). For expression in projection neurons, somBiPOLES was cloned into an AAV2-backbone behind the minimal CaMKII promoter[55] resulting in pAAV-CaMKII-somBiPOLES-mCerulean (Addgene #154948). Double-floxed inverted open reading frame variants of BiPOLES and somBiPOLES were generated by cloning these inserts in antisense direction behind the hSyn promoter, flanked by two loxP and lox2272 sites (hSyn-DIO-BiPOLES-mCerulean, Addgene #154950; hSyn-DIO-somBiPOLES-mCerulean, Addgene #154951). Note that in all constructs the mCerulean3-tag is fused between *Gt*ACR2-ts and βHK-Chrimson and therefore part of BiPOLES. We nonetheless chose to add "mCerulean" to the plasmid names to remind the reader of the presence of a cyan fluorophore in BiPOLES. BiPOLES stands for "<u>Bi</u>directional <u>P</u>air of <u>O</u>psins for <u>L</u>ight-induced <u>E</u>xcitation and <u>S</u>ilencing". Sequences of all primers used for cloning and sequences of DNA inserts used in this study are provided in a separate list (Supplementary Data 1).

Patch-Clamp experiments in HEK293 cells. Fusion constructs were expressed under the control of a CMV-promotor in HEK293 cells that were cultured in Dulbecco's Modified Medium (DMEM) with stable glutamine (Biochrom, Berlin, Germany), supplemented with 10% (v/v) fetal bovine serum (FBS Superior; Biochrom, Berlin, Germany), 1 μM all-*trans*-retinal, and 100 μg ml⁻¹ penicillin/

streptomycin (Biochrom, Berlin, Germany). Cells were seeded on poly-lysine coated glass coverslips at a concentration of 1×10^5 cell ml⁻¹ and transiently transfected using the FuGENE® HD Transfection Reagent (Promega, Madison, WI). two days before measurement.

Patch-clamp experiments were performed in transgene expressing HEK293 cells two days after transfection[56]. Patch pipettes were prepared from borosilicate glass capillaries (G150F-3; Warner Instruments, Hamden, CT) using a P-1000 micropipette puller (Sutter Instruments, Novato, CA) and subsequently fire-polished. Pipette resistance was between 1.2 and 2.5 MΩ. Single fluorescent cells were identified using an Axiovert 100 inverted microscope (Carl Zeiss, Jena, Germany). Monochromatic light (± 7 nm) was provided by a Polychrome V monochromator (TILL Photonics, Planegg, Germany) or by a pE-4000 CoolLED system (CoolLED, Andover, UK) for light titration experiments. Light intensities were attenuated by a motorized neutral density filter wheel (Newport, Irvine, CA) for equal photon flux during action spectra recordings. Light pulses of the Polychrome V were controlled by a VS25 and VCM-D1 shutter system (Vincent Associates, Rochester, NY). Recordings were done with an AxoPatch 200B amplifier (Molecular Devices, Sunnyvale, CA) or an ELV-03XS amplifier (npi Electronics, Tamm, Germany), filtered at 2 kHz, and digitized using a DigiData 1440 A digitizer (Molecular Devices, Sunnyvale, CA) at a sampling rate of 10 kHz. The reference bath electrode was connected to the bath solution via a 140 mM NaCl agar bridge. Bath solutions contained 140 mM NaCl, 1 mM KCl, 1 mM CsCl, 2 mM $CaCl_2$, 2 mM $MgCl_2$ and 10 mM HEPES at pH$_e$ 7.2 (with glucose added up to 310 mOsm). Pipette solution contained 110 mM NaGluconate, 1 mM KCl, 1 mM CsCl, 2 mM $CaCl_2$, 2 mM $MgCl_2$, 10 mM EGTA and 10 mM HEPES at pH$_i$ 7.2 (glucose added up to 290 mOsm). All light intensities were measured in the object plane using a P9710 optometer (Gigahertz-Optik, Türkenfeld, Germany) and normalized to the water Plan-Apochromat ×40/1.0 differential interference contrast (DIC) objective illuminated field (0.066 mm²). The irradiance was 2.7 mW mm⁻² at 650 nm, 3.5 mW mm⁻² at 600 nm, 4.2 mW mm⁻² at 530 nm, 5.7 mW mm⁻² at 490 nm, and 5.2 mW mm⁻² at 450 nm. All electrical recordings were controlled by the pCLAMP™ software (Molecular Devices, Sunnyvale, CA). All whole-cell recordings had a membrane resistance of at least 500 MΩ (usual >1 GΩ) and an access resistance below 10 MΩ.

Preparation of organotypic hippocampal slice cultures. All procedures were in agreement with the German national animal care guidelines and approved by the independent Hamburg state authority for animal welfare (Behörde für Justiz und Verbraucherschutz). They were performed in accordance with the guidelines of the German Animal Protection Law and the animal welfare officer of the University Medical Center Hamburg-Eppendorf.

Organotypic hippocampal slices were prepared from Wistar rats or VIP-IRES-Cre mice of both sexes (Jackson-No. 031628) at post-natal days 5–7[57]. Dissected hippocampi were cut into 350 μm slices with a tissue chopper and placed on a porous membrane (Millicell CM, Millipore). Cultures were maintained at 37 °C, 5% CO_2 in a medium containing 80% MEM (Sigma M7278), 20% heat-inactivated horse serum (Sigma H1138) supplemented with 1 mM L-glutamine, 0.00125% ascorbic acid, 0.01 mg ml⁻¹ insulin, 1.44 mM $CaCl_2$, 2 mM $MgSO_4$ and 13 mM D-glucose. No antibiotics were added to the culture medium.

Transgene delivery for single-photon experiments. For transgene delivery in organotypic slices, individual CA1 pyramidal cells were transfected by single-cell electroporation[58] between DIV 14–16. Except for pAAV-hSyn-eNPAC2.0, which was used at a final concentration of 20 ng μl⁻¹, all other plasmids, namely pAAV-hSyn-BiPOLES-mCerulean, pAAV-hSyn-somBiPOLES-mCerulean, pAAV-hSyn-Chrimson-mCerulean, and pAAV-hSyn-som*Gt*ACR2-mCerulean were used at a final concentration of 5 ng μl⁻¹ in K-gluconate-based solution consisting of (in mM): 135 K-gluconate, 10 HEPES, 4 Na₂-ATP, 0.4 Na-GTP, 4 MgCl₂, 3 ascorbate, 10 Na₂-phosphocreatine (pH 7.2). A plasmid encoding hSyn-mKate2 or hSyn-mCerulean (both at 50 ng μl⁻¹) was co-electroporated with the opsin-mCerulean or eNPAC2.0 plasmids, respectively, and served as a morphology marker. An Axoporator 800 A (Molecular Devices) was used to deliver 50 hyperpolarizing

Table 1 List of recombinant adeno-associated viral vectors used for experiments in organotypic hippocampal slices.

Recombinant adeno-associated virus (rAAV2/9)	Titer used for transduction of hippocampal organotypic slice cultures (vg/ml)	Addgene plasmid reference
mDlx-BiPOLES-mCerulean	2.8×10^{13}	154946
hSyn-DIO-BiPOLES-mCerulean	7.0×10^{13}	154950
hSyn-DIO-somBiPOLES-mCerulean	3.4×10^{13}	154951
CaMKIIa(0.4)-somBiPOLES-mCerulean	2.5×10^{13}	154948
CaMKIIa(0.4)-DO-CheRiff-ts-mScarlet-ER	8.15×10^{11}	n.a.
mDlx-H2B-EGFP	2.8×10^{10}	n.a.
CaMKIIa-Cre	3.0×10^{12}	n.a.

Viruses were transduced at the indicated titers. *n.a.*: not applicable.

pulses (−12 V, 0.5 ms) at 50 Hz. During electroporation, slices were maintained in pre-warmed (37 °C) HEPES-buffered solution (in mM): 145 NaCl, 10 HEPES, 25 D-glucose, 2.5 KCl, 1 MgCl$_2$, and 2 CaCl$_2$ (pH 7.4, sterile filtered). In some cases, slice cultures were transduced with recombinant adeno-associated virus (see Table 1 for details) at DIV 3–5[59]. The different rAAVs were locally injected into the CA1 region using a Picospritzer (Parker, Hannafin) by a pressurized air pulse (2 bar, 100 ms) expelling the viral suspension into the slice. During virus transduction, membranes carrying the slices were kept on pre-warmed HEPES-buffered solution.

Preparation of organotypic hippocampal slice cultures for two-photon holographic stimulation of somBiPOLES.
All experimental procedures were conducted in accordance with guidelines from the European Union and institutional guidelines on the care and use of laboratory animals (council directive 2010/63/EU of the European Union). Organotypic hippocampal slices were prepared from mice (Janvier Labs, C57Bl6J) at postnatal day 8 (P8). Hippocampi were sliced into 300 μm thick sections in a cold dissecting medium consisting of GBSS supplemented with 25 mM D-glucose, 10 mM HEPES, 1 mM Na-Pyruvate, 0.5 mM α-tocopherol, 20 nM ascorbic acid, and 0.4% penicillin/streptomycin (5000 U ml^{-1}).

Slices were placed onto a porous membrane (Millicell CM, Millipore) and cultured at 37 °C, 5% CO2 in a medium consisting of 50% Opti-MEM (Fisher 15392402), 25% heat-inactivated horse serum (Fisher 10368902), 24% HBSS, and 1% penicillin/streptomycin (5000 U ml^{-1}). This medium was supplemented with 25 mM D-glucose, 1 mM Na-Pyruvate, 20 nM ascorbic acid, and 0.5 mM α-tocopherol. After three days in-vitro, the medium was replaced with one containing 82% neurobasal-A, 15% heat-inactivated horse serum (Fisher 11570426), 2% B27 supplement (Fisher, 11530536), 1% penicillin/streptomycin (5000 U ml^{-1}), which was supplemented with 0.8 mM L-glutamine, 0.8 mM Na-Pyruvate, 10 nM ascorbic acid and 0.5 mM α-tocopherol. This medium was removed and replaced once every 2-3 days.

Slices were transduced with rAAV9-CaMKII-somBiPOLES-mCerulean at DIV 3 by bulk application of 1 μl of virus (final titer: 2.5 × 10^{13} vg ml^{-1}) per slice. Experiments were performed between DIV 13 and 17.

Slice culture electrophysiology with singe-photon stimulation.
At DIV 19-21, whole-cell patch-clamp recordings of transfected or virus-transduced CA1 pyramidal or GABAergic neurons were performed. Experiments were done at room temperature (21–23 °C) under visual guidance using a BX 51WI microscope (Olympus) equipped with Dodt-gradient contrast and a Double IPA integrated patch amplifier controlled with SutterPatch software (Sutter Instrument, Novato, CA). Patch pipettes with a tip resistance of 3–4 MΩ were filled with an intracellular solution consisting of (in mM): 135 K-gluconate, 4 MgCl$_2$, 4 Na$_2$-ATP, 0.4 Na-GTP, 10 Na$_2$-phosphocreatine, 3 ascorbate, 0.2 EGTA, and 10 HEPES (pH 7.2). Artificial cerebrospinal fluid (ACSF) consisted of (in mM): 135 NaCl, 2.5 KCl, 2 CaCl$_2$, 1 MgCl$_2$, 10 Na-HEPES, 12.5 D-glucose, 1.25 NaH$_2$PO$_4$ (pH 7.4). In experiments where synaptic transmission was blocked, 10 μM CPPene, 10 μM NBQX, and 100 μM picrotoxin (Tocris, Bristol, UK) were added to the recording solution. In experiments analyzing synaptic inputs onto O-LM interneurons, ACSF containing 4 mM CaCl$_2$ and 4 mM MgCl$_2$ was used to reduce the overall excitability. Measurements were corrected for a liquid junction potential of −14,5 mV. Access resistance of the recorded neurons was continuously monitored and recordings above 30 MΩ were discarded. A 16 channel LED light engine (CoolLED pE-4000, Andover, UK) was used for epifluorescence excitation and delivery of light pulses for optogenetic stimulation (ranging from 385 to 635 nm). Irradiance was measured in the object plane with a 1918 R power meter equipped with a calibrated 818 ST2 UV/D detector (Newport, Irvine CA) and divided by the illuminated field of the Olympus LUMPLFLN 60XW objective (0.134 mm^2).

For photocurrent density measurements in voltage-clamp mode CA1 cells expressing BiPOLES, somBiPOLES, Chrimson or somGtACR2 were held at −75 or −55 mV to detect inward (cationic) or outward (anionic) currents elicited by red (635 nm, 20 ms, 1 and 10 mW mm^{-2}) and blue light (490 nm, 100 ms, 10 mW mm^{-2}), respectively. For each cell, the peak photocurrent amplitude (in pA) was divided by the cell membrane capacitance (in pF) which was automatically recorded by the SutterPatch software in voltage-clamp mode (V_{hold} = −75 mV).

In current-clamp experiments holding current was injected to maintain CA1 cells near their resting membrane potential (−75 to −80 mV). To assess the suitability of BiPOLES and somBiPOLES as dual-color neuronal excitation and silencing tools, alternating pulses of red (635 nm, 20 ms, 10 mW mm^{-2}), blue (490 nm, 100 ms, 10 mW mm^{-2}), and a combination of these two (onset of blue light 40 ms before red light) were delivered to elicit and block action potentials. For eNPAC2.0 alternating pulses of blue (470 nm, 20 ms, 10 mW mm^{-2}), yellow (580 nm, 100 ms, 10 mW mm^{-2}), and a combination of these two (onset of yellow light 40 ms before blue light) were used.

In experiments determining the spiking probability of somBiPOLES and Chrimson under illumination with light of different wavelengths (470, 595, and 635 nm), a train of 20 light pulses (5 ms pulse duration) was delivered at 5 Hz. For each wavelength, irradiance values from 0.1 to 100 mW mm^{-2} were used. For comparisons with eNPAC2.0, only light of 470 nm was used, which is the peak activation wavelength of ChR2(HR). AP probability was calculated by dividing the number of light-triggered APs by the total number of light pulses.

To compare the irradiance threshold needed to spike CA1 cells with BiPOLES, somBiPOLES, eNPAC2.0, Chrimson, and CheRiff across different wavelengths, 470, 525, 595, and 635 nm light ramps going from 0 to 10 mW mm^{-2} over 1 s were delivered in current-clamp mode. In the case of BiPOLES and somBiPOLES the blue light ramp went up to 100 mW mm^{-2} to rule out that very high blue-light irradiance might still spike neurons. The irradiance value at the time of the first spike was defined as the irradiance threshold (in mW mm^{-2}) needed to evoke action potential firing.

To measure the ability of BiPOLES, somBiPOLES, and somGtACR2 to shift the rheobase upon blue-light illumination, depolarizing current ramps (from 0–100 to 0–900 pA) were injected into CA1 neurons in the dark and during illumination with 490 nm light at irradiance values ranging from 0.001 to 100 mW mm^{-2}. The injected current at the time of the first spike was defined as the rheobase. The relative change in the number of ramp-evoked APs was calculated counting the total number of APs elicited during the 9 current ramp injections (from 0–100 to 0–900 pA) for each irradiance and normalized to the number of APs elicited in the absence of light. The same experiment was conducted for eNPAC2.0, but using 580 nm light ranging from 0.01 to 100 mW mm^{-2}. Statistical significance was calculated using the Friedman test.

To optically clamp the neuronal membrane potential using somBiPOLES, simultaneous illumination with blue and orange light at varying ratios was used. In current-clamp experiments, 470 and 595 nm light ramps (5 s) of opposite gradients (1 to 0 mW mm^{-2} and 0 to 1 mW mm^{-2}, respectively) were applied. Alternatively, optical clamping of the membrane potential was achieved by tuning a single wavelength between 385 and 660 nm (2 s light pulses, 0.1 mW mm^{-2}). Voltage traces were median-filtered to remove orange/red-light-mediated spikes and reveal the slow change in membrane voltage during illumination.

For independent optogenetic activation of two distinct populations of neurons, organotypic slice cultures from VIP-Cre mice were transduced with two rAAVs: 1, a double-floxed inverted open reading frame (DIO) construct encoding somBiPOLES (hSyn-DIO-somBiPOLES-mCerulean, see Table 1 for details) to target VIP-positive interneurons, and 2, a double-floxed open reading frame (DO) construct encoding CheRiff (hSyn-DO-CheRiff-ts-mScarlet-ER, see Table 1 for details) to target CA1 pyramidal neurons and exclude expression in VIP-positive cells. Synaptic input from these two populations was recorded in VIP-negative stratum-oriens GABAergic neurons (putative O-LM cells). In CA1, O-LM neurons receive innervation both from local CA1 pyramidal neurons and VIP-positive GABAergic neurons[60]. To facilitate the identification of putative GABAergic post-synaptic neurons in stratum oriens, slices were transduced with an additional rAAV encoding mDlx-H2B-EGFP. In the absence of synaptic blockers light-evoked EPSCs and IPSCs were recorded while holding the postsynaptic cell at different membrane potentials (−80, −65, −55, −45, and 6 mV) in whole-cell voltage-clamp mode. A blue (460 nm, 0.03–84.0 mW mm^{-2}) and a red (635 nm, 6.0–97.0 mW mm^{-2}) light pulse were delivered 500 ms apart from each other through a Leica HC FLUOTAR L ×25/0.95 W VISIR objective.

To functionally assess the putative expression of somBiPOLES in the axon terminals of CA3 pyramidal cells, slice cultures were transduced with an rAAV9 encoding for CaMKIIa(0.4)-somBiPOLES-mCerulean (see Table 1 for details). Red-light evoked EPSCs were recorded in postsynaptic CA1 cells during local illumination either in CA3 at the somata (two light pulses of 5 ms delivered 40 ms apart using a fiber-coupled LED (400 μm fiber, 0.39 NA, 625 nm, Thorlabs) controlled by a Mightex Universal 4-Channel LED Driver (1.6 mW at fiber tip), or in CA1 at axon terminals of somBiPOLES-expressing CA3 cells (two light pulses of 5 ms delivered 40 ms apart through the ×60 microscope objective, 635 nm, 50 mW mm^{-2}). Axonal light stimulation was done in the presence of tetrodotoxin (TTX, 1 μM) and 4-aminopyridine (4-AP, 100 μM) to avoid antidromic spiking of CA3 cells.

To determine the high-frequency spiking limit with somBiPOLES, action potentials were triggered in CA1 cells at frequencies ranging from 10 to 100 Hz using 40 light pulses (595 nm, 3 ms pulse width, 10 mW mm^{-2}). AP probability was calculated by dividing the number of light-triggered APs by the total number of light pulses.

To characterize the spectral activation of BiPOLES, eNPAC2.0. and somGtACR2, photocurrents were recorded from CA1 cells in a voltage-clamp mode in response to 500 ms illumination with various wavelengths (from 385 to 660 nm, 10 mW mm^{-2}). BiPOLES-expressing and somGtACR2-expressing cells were held at a membrane voltage of −55 mV, more positive than the chloride Nernst potential, to measure light-mediated outward chloride currents. Photocurrent recordings from eNPAC2.0-expressing cells were done at a holding voltage of −75 mV. For BiPOLES and eNPAC2.0 the photocurrent ratio between excitatory and inhibitory photocurrents was calculated in each cell by diving the amplitude of the photocurrents evoked by 490/595 nm (for BiPOLES) and 460/580 nm (for eNPAC2.0).

Passive and active membrane parameters were measured in somBiPOLES-expressing and non-transduced, wild-type CA1 pyramidal cells. Resting membrane potential, membrane resistance, and capacitance were automatically recorded by the SutterPatch software in voltage-clamp mode (V_{hold} = −75 mV) in response to a voltage test pulse of 100 ms and −5 mV. The number of elicited action potentials were counted in response to a somatic current injection of 300 pA in current-clamp mode (0 pA holding current). For the 1st elicited AP, the voltage threshold, peak, and amplitude were measured.

Slice culture immunohistochemistry and confocal imaging. The subcellular localization of BiPOLES and somBiPOLES in hippocampal neurons was assessed 20 days after virus transduction (rAAV9-hSyn-DIO-BiPOLES-mCerulean + CaMKIIa-Cre, and CaMKIIa(0.4)-somBiPOLES-mCerulean, respectively. See Table 1 for details). Hippocampal organotypic slice cultures were fixed in a solution of 4% (w/v) paraformaldehyde (PFA) in PBS for 30 min at room temperature (RT). Next, slices were washed in PBS (3 × 10 min), blocked for 2 h at RT (10% [v/v] normal goat serum [NGS] in 0.3% [v/v] Triton X-100 containing PBS) and subsequently incubated for 48 h at 4 °C with a primary antibody against GFP to amplify the mCerulean signal (chicken, anti-GFP, Invitrogen, A10262, Lot 1972783) at 1:1000 in carrier solution (2% [v/v] NGS, in 0.3% [v/v] Triton X-100 containing PBS). Following 3 rinses of 10 min with PBS, slices were incubated for 3 h at RT in carrier solution (same as above) with an Alexa Fluor® dye-conjugated secondary antibody (goat, anti-chicken Alexa-488, Invitrogen; A11039, Lot 2079383, 1:1000). Slices were washed again, transferred onto glass slides, and mounted for visualization with Shandon Immu-Mount (Thermo Scientific; 9990402).

Confocal images were acquired using a laser-scanning microscope (Zeiss, LSM 900) equipped with a ×40 oil-immersion objective lens (Zeiss EC Plan-Neofluar ×40/1.3 oil). Excitation/emission filters were appropriately selected for Alexa 488 using the dye selection function of the ZEN software. The image acquisition settings were optimized once and kept constant for all images within an experimental data set. Z-stack images were obtained using a 1 μm z-step at a 1024 × 1024-pixel resolution scanning at 8 μs per pixel. Fiji[61] was used to quantify fluorescence intensity values along a line perpendicular to the cell equator and spanning the cell diameter. For each cell, gray values above 80% of the maximum intensity were distributed in 10 bins according to their location along the line.

Slice culture two-photon imaging. Neurons in organotypic slice cultures (DIV 19-21) were imaged with two-photon microscopy to check for the live expression of hSyn-DIO-somBiPOLES-mCerulean, CaMKIIa(0.4)-DO-CheRiff-ts-mScarlet-ER, mDlx-BiPOLES-mCerulean and CaMKIIa(0.4)-somBiPOLES-mCerulean. The custom-built two-photon imaging setup was based on an Olympus BX-51WI upright microscope upgraded with a multiphoton imaging package (DF-Scope, Sutter Instrument), and controlled by ScanImage 2017b software (Vidrio Technologies). Fluorescence was detected through the objective (Leica HC FLUOTAR L 25x/0.95 W VISIR) and through the oil immersion condenser (numerical aperture 1.4, Olympus) by two pairs of GaAsP photomultiplier tubes (Hamamatsu, H11706-40). Dichroic mirrors (560 DXCR, Chroma Technology) and emission filters (ET525/70m-2P, ET605/70m-2P, Chroma Technology) were used to separate cyan and red fluorescence. Excitation light was blocked by short-pass filters (ET700SP-2P, Chroma Technology). A tunable Ti:Sapphire laser (Chameleon Vision-S, Coherent) was set to 810 nm to excite mCerulean on BiPOLES and somBiPOLES. An Ytterbium-doped 1070-nm pulsed fiber laser (Fidelity-2, Coherent) was used at 1070 nm to excite mScarlet on CheRiff. Maximal intensity projections of z-stacks were generated with Fiji[61].

Electrophysiology for two-photon photostimulation of somBiPOLES. At DIV 13–17, whole-cell patch-clamp recordings of somBiPOLES-infected excitatory neurons were performed at room temperature (21– 23 °C). An upright microscope (Scientifica, SliceScope) was equipped with an infrared (IR) source (Thorlabs, M1050L4), oblique condenser, microscope objective (Nikon, CFI APO NIR, ×40, 0.8 NA), tube lens (Thorlabs, AC508-300-B), and a CMOS camera (Point Grey, CM3-U3-31S4M-CS) to collect IR light transmitted through the sample. Recordings were performed using an amplifier (Molecular Devices, Multiclamp 700B), a digitizer (Molecular Devices, Digidata 1550B) at a sampling rate of 10 kHz and controlled using pCLAMP11 (Molecular Devices). During experimental sessions, slice cultures were perfused with artificial cerebrospinal fluid (ACSF) comprised of 125 mM NaCl, 2.5 mM KCl, 1.5 mM CaCl₂, 1 mM MgCl₂, 26 mM NaHCO₃, 0.3 mM ascorbic acid, 25 mM D-glucose, 1.25 mM NaH₂PO₄. Synaptic transmission was blocked during all experiments by the addition of 1 μM AP5 (Abcam, ab120003), 1 μM NBQX (Abcam, ab120046), and 10 μM picrotoxin (Abcam, ab120315) to the extracellular (recording) solution. Continuous aeration of the recording solution with 95% O₂ and 5% CO₂, resulted in a final pH of 7.4. Patch pipettes with a tip resistance of 4–6 MΩ were filled with an intracellular solution consisting of 135 mM K-gluconate, 4 mM KCl, 4 mM Mg-ATP, 0.3 mM Na-GTP, 10 mM Na₂-phosphocreatine, and 10 mM HEPES (pH 7.35). Only recordings with an access resistance below 30 MΩ were included in the subsequent analysis.

During experiments performed using whole-cell voltage clamp, neurons were held at −60 mV (the average resting potential of neurons in hippocampal organotypic slices). The soma of each patched neuron was precisely positioned in the center of the field of view. When recording the photocurrent as a function of membrane potential (holding potentials: −80, −70, −65, −60, −55 mV), neurons were temporarily held at each holding potential 5 s before and after photostimulation. For data presented in Fig. 5a–d, two-photon photoactivation was performed by continuous, 200 ms, illumination of each patched neuron using a 12-μm-diameter holographic spot (wavelengths: 850, 900, 920, 950, 980, 1000, 1050, 1100 nm), which was precisely positioned in the center of the field of view.

Data presented in Fig. 7d–g was acquired in current-clamp experiments. Where necessary, the current was injected to maintain neurons at the resting membrane potential (−60 mV).

The ability of two-photon holographic excitation to evoke action potentials was first assessed using a protocol consisting of 5, 5 ms pulses of 1100 nm light for power densities ranging between 0.16 and 1.00 mW μm⁻². The latency and jitter of light-evoked action potentials, respectively defined as the mean and standard deviation of the time between the onset of stimulation to the peak of the action potential, were measured using an identical protocol. Trains of light pulses with frequencies between (2–30 Hz) were used to verify that trains of action potentials could be reliably induced using 5 ms 1100 nm illumination.

The potency of two-photon inhibition was evaluated by measuring the rheobase shift induced by 920 nm illumination. The depolarizing current was injected for 5 ms into recorded neurons (from 0 to 1.2 nA in steps of 20 pA). The protocol was stopped when action potentials were observed for 3 consecutive current steps. The rheobase was defined as the amount of current injected to evoke the first of these 3 action potentials. The rheobase shift was measured by repeating the protocol with co-incident, 5 ms, illumination of the neuron with a 920 nm holographic spot (power densities between 0.05 and 0.25 mW μm⁻²). Co-incident trains of light pulses (15 ms) and injected current (10 ms) with frequencies between (2–30 Hz) were used to verify that two-photon inhibition could precisely and reliably eliminate single spikes.

Sustained neuronal silencing by two-photon excitation of somBiPOLES under 920 nm illumination was characterized by continuously injecting current above the rheobase for 1 s. The protocol was repeated with 200 ms co-incident illumination using a 920 nm holographic spot (power densities between 0.05 and 0.3 mW μm⁻²).

Two-photon, bidirectional, control of single neurons was demonstrated by co-incident illumination of titrated 920 nm and 1100 nm light. A 10-Hz train of 15 ms pulses of 1100 nm light was used to evoke a train of action potentials which were shunted using a continuous 200 ms pulse of 920 nm light.

Two-photon photostimulation of somBiPOLES in hippocampal organotypic slices. Two-photon photostimulation was performed using a tunable femtosecond laser (Coherent Discovery, 80 MHz, 100 fs, tuned between 850 and 1100 nm). A schematic diagram of the experimental setup is presented in Supplementary Fig. 10. A telescope formed of two lenses (L1 (Thorlabs, AC508-100-B) and L2 (Thorlabs, AC508-400-B)) expanded the beam onto a Spatial Light Modulator (SLM, Hamamatsu, LCOS 10468-07, 600 × 800 pixels, 20 μm pitch). In the schematic diagram, the reflective SLM is shown as transmissive for illustrative purposes. The SLM, controlled using custom-built software[62], was used to modulate the phase of the beam. Holograms designed to generate 12 μm holographic spots at the focal plane of the microscope were computed using an iterative Gerchberg-Saxton algorithm[63]. The zeroth diffraction order from the SLM was removed using a physical beam block. The modulated field was relayed and de-magnified using a pair of telescopes (formed of lenses L3 (Thorlabs, AC508-750-B), L4 (Thorlabs, AC508-750-B), L5 (Thorlabs, AC508-500-B) and L6 (Thorlabs, AC508-300-B)) to fill the back-aperture of the microscope objective (Nikon, CFI APO NIR, ×40, 0.8 NA) which projected the holograms onto the focal plane. Phase masks were calculated such that holographic spots for the light of different wavelengths overlapped laterally and axially. The anti-reflective coating of the lenses used are optimized for wavelengths 650–1050 nm, and losses incurred at 1100 nm result in the system being power limited at this wavelength. Hence, spectral characterization was performed by normalizing the power density at all wavelengths to the maximum transmitted at 1100 nm. The power incident on the sample plane was adjusted using a high-speed modulator (Thorlabs, OM6NH/M), which was calibrated for each experimental session for each wavelength used, to ensure a photon flux of 6.77 × 10²⁶ photons s⁻¹ m⁻² for all data presented in Fig. 5a. All powers were measured in the object plane using a power meter (Thorlabs, S121C). This experimental configuration was used for all data presented in Fig. 5a, along with all data acquired using 1100 nm illumination. Two-photon inhibition was performed using a femtosecond laser with a fixed wavelength (Spark Alcor, 80 MHz, 100 fs, 920 nm) which was combined with the beam from the tunable laser using a dichroic mirror (Thorlabs, DMLP950R). A liquid crystal variable retarder (Thorlabs, LCC1111-B) and a polarizing beam splitter (Thorlabs, PBS253) were combined to modulate the maximum power of the fixed 920 nm beam independently of that of the tunable laser. The power densities used in each experiment are specified alongside the relevant data in Fig. 5 and Supplementary Fig. 10.

Transgenic *C. elegans* lines and transgenes. The strain ZX417 (zxEx34[punc17::NpHR-ECFP;punc17::CHOP-2(H134R)::eYFP;rol-6]) was generated by injection of plasmid DNA (plasmids prF4 (rol-6d), punc-17::NpHR-eCFP, and punc-17::ChR2 (H134R)-eYFP; each at 80 ng/μl) into the germline of *C. elegans* wild-type hermaphrodites. Transgenic animals were picked from the F1 generation and one line (ZX417) was selected out of several transgenic F2 lines for further experiments[33]. For expression in cholinergic neurons of *C. elegans*, BiPOLES (GtACR2::ts::mCerulean3::βHK::Chrimson) was subcloned into the punc-17 vector RM#348p (a gift from Jim Rand) via Gibson Assembly based on the plasmid CMV_GtACR2_mCerulean_βHK_Chrimson, using the restriction enzyme NheI and the primers ACR2_Chrimson_fwd (5′-atttcaggaggacccttggATGGCATCACAGGTCGTC-3′) and ACR2_Chrimson_rev (5′-ataccatggtaccgtcgacgTCACACTGTGTCCTCGTC-3′), resulting in the construct

119

pAB26. The respective transgenic strain ZX2586 (wild type; *zxEx1228[punc-17::GtACR2::ts::mCerulean3::βHK::Chrimson; pelt-2::GFP]*), was generated via microinjection[64] of both 30 ng μl⁻¹ plasmid and co-marker plasmid DNA p*elt-2*::GFP. Animals were cultivated on nematode growth medium (NGM), seeded with *E. coli* OP-50 strain, in 6 cm Petri dishes. To obtain functional rhodopsins in optogenetic experiments, the OP-50 bacteria were supplemented with all-*trans*-retinal ATR (0.25 μl of a 100 mM stock (in ethanol) mixed with 250 μl OP-50 bacterial suspension).

C. elegans stimulation and behavioral experiments. For body-length measurements, L4 stage transgenic animals were cultivated on ATR plates overnight. Video analysis of light-stimulation protocols provided information on depolarized and hyperpolarized states, based on contracted or relaxed body-wall muscles (BWMs)[65]. Prior to experiments, animals were singled on plain NGM plates to avoid imaging artefacts. They were manually tracked with an Axio Scope.A1 microscope (Zeiss, Germany), using a ×10 objective (Zeiss A-Plan 10x/0,25 Ph1 M27) and a Powershot G9 digital camera (Canon, USA). For light-stimulation of optogenetic tools, transgenic worms were illuminated with 5 s light pulses at 1.1 mW mm⁻² of different wavelengths as indicated in Fig. 6d (monochromatic light source, Polychrome V, Till Photonics or 100 W HBO mercury lamp with 470/40 ET Bandpass or 575/40 ET Bandpass filters, AHF Analysentechnik), controlled via an Arduino-driven shutter (Sutter Instrument, USA). Videos were processed and analyzed using a custom-written MATLAB script[66] (MathWorks, USA). For the analysis of data, the animals' body length was normalized to the recording period prior to illumination.

Transgenic D. melanogaster lines and transgenes. BiPOLES-mCerulean cDNA was cloned via blunt-end ligation into pJFRC7[67]. BILOES was cut with BamHI/HindIII and the vector was cut with NotI/XbaI. A transgenic line inserted into the attP2 site on the 3rd chromosome[68] was generated by phiC31-mediated site-specific transgenesis (FlyORF Injection Service, Zurich, Switzerland). A Gal4 line expressing in glutamatergic neurons including motor neurons (OK371-Gal4[11]) was used for locomotion experiments, a Dp7-expressing line (Ilp7-Gal4[34]) was used for mechanonociception experiments.

Locomotion and mechanonociception assays in D. melanogaster larvae. *D. melanogaster* larvae were staged in darkness on grape agar plates and fed with yeast paste containing 5 mM all-trans-retinal. Third instar larvae (96 h ± 2 h after egg laying) were used for all experiments.

For locomotion and body length analyses, animals were carefully transferred under minimum red light conditions to a 2% agar film on an FTIR (frustrated total internal reflection) based tracking system (FIM, University of Münster)[69]. Five freely moving larvae/trials were video-captured and stimulated with 470 nm (17 μW mm⁻²) or 635 nm (25 μW mm⁻²) light (CoolLED PE4000) for activation of BiPOLES. Animal locomotion was tracked with 10 frames per s for up to 70 s and then body length was analyzed using the FIMtracking software (FIM, University of Münster). For analysis, only animals displaying continuous locomotion before the light stimulus were kept. Larval body length was analyzed over time and was displayed with a 1 s moving average. The body length was normalized to the average of the first 5 s of recording. Relative body length changes during the experiment were then analyzed and plotted.

For mechanonociception, staged larvae were placed on 2% agar plates with a 1 ml water film added. Experiments were performed under minimum light conditions (no activation) with calibrated von-Frey-filaments (50 mN). For activation of BiPOLES, larvae were illuminated during the assay with either 470 nm (17 μW mm⁻²) or 635 nm (25 μW mm⁻²). Larvae were stimulated twice on mid-abdominal segments (a3–a6) within 2 s. Behavioral responses (stop and turning, bending, rolling) were noted, analyzed, and plotted. Staging and experiments were done in a blinded and randomized fashion.

Modulation of noradrenergic neurons in the mouse locus coeruleus

Animals. All procedures were in agreement with the German national animal care guidelines and approved by the Hamburg state authority for animal welfare (Behörde für Justiz und Verbraucherschutz) and the animal welfare officer of the University Medical Center Hamburg-Eppendorf. Experiments were performed on mice of either sex between 2.5 and 4 months of age at the start of the experiment. Mice were obtained from The Jackson Laboratory, bred, and maintained at our own colony (12/12 h light-dark cycle, 22 °C room temperature, ~40% relative humidity, food, and water ad libitum). Transgenic mice expressing Cre recombinase in tyrosine hydroxylase positive neurons (TH-Cre, Stock No: 008601)[70] were injected with a suspension of rAAV2/9 viral particles encoding hSyn-DIO-somBiPOLES to target Cre-expressing neurons in the locus coeruleus. Control experiments were performed in non-injected wild-type littermates.

Virus injection and implantation of optic fibers. General anesthesia and analgesia were achieved by intraperitoneal injections of midazolam/medetomidine/fentanyl (5.0/0.5/0.05 mg kg⁻¹, diluted in NaCl). After confirming anesthesia and analgesia by the absence of the hind limb withdrawal reflex, the scalp of the animal was trimmed and disinfected with Iodide solution (Betaisodona; Mundipharma, Germany). The animal was placed on a heating pad to maintain body temperature,

fixed in a stereotactic frame, and eye ointment (Vidisic; Bausch + Lomb, Germany) was applied to prevent drying of the eyes. To bilaterally access the LC, an incision (~1 cm) was made along the midline of the scalp, the skull was cleaned, and small craniotomies were drilled −5.4 mm posterior and ±1 mm lateral to Bregma. 0.4 μl of virus suspension were injected into each LC (−3.6 mm relative to Bregma) at a speed of ~100–200 nl min⁻¹ using a custom-made air pressure system connected to a glass micropipette. After each injection, the micropipette was left in place for a minimum of 5 min before removal. After virus injection, cannulas housing two ferrule-coupled optical fibers (200 μm core diameter, 0.37 NA, 4 mm length) spaced 2 mm apart (TFC_200/245-0.37_4mm_TS2.0_FLT; Doric Lenses, Canada) were inserted just above the injection site to a depth of −3.5 mm relative to Bregma using a stereotactic micromanipulator. The implant, as well as a headpost for animal fixation during the experiment, were fixed to the roughened skull using cyanoacrylate glue (Pattex; Henkel, Germany) and dental cement (Super Bond C&B; Sun Medical, Japan). The incised skin was glued to the cement to close the wound. Anesthesia was antagonized by intraperitoneally injecting a cocktail of atipamezole/flumazenil/buprenorphine (2.5/0.5/0.1 mg kg⁻¹, diluted in NaCl). Carprofen (4 mg kg⁻¹) was given subcutaneously for additional analgesia and to avoid inflammation. In addition, animals received meloxicam mixed into softened food for 3 days after surgery.

Optogenetic stimulation. Four to six weeks after surgery, mice were habituated to head fixation and placement in a movement-restraining plastic tube for at least one session. Bilateral optogenetic stimulation of LC neurons was achieved by connecting the fiber implant to a 1 × 2 step-index multimode fiber optic coupler (200 μm core diameter, 0.39 NA; TT200SL1A, Thorlabs, Germany) in turn connected to a laser combiner system (LightHUB; Omicron, Germany) housing a 473 nm (LuxX 473-100; Omicron, Germany) and a 594 nm diode laser (Obis 594 nm LS 100 mW; Coherent, Germany) for activation of the *Gt*ACR2 and Chrimson components of somBiPOLES, respectively. Coupling to the implant was achieved with zirconia mating sleeves (SLEEVE_ZR_1.25; Doric lenses, Canada) wrapped with black tape to avoid light emission from the coupling interface. Following a habituation period of ~3 min after placing mice in the setup, stimuli were generated and presented using custom-written MATLAB scripts (MathWorks, Germany) controlling a NI-DAQ-card (PCIe-6323; National Instruments, US) to trigger the lasers via digital input channels. For activation of Chrimson, pulse trains (594 nm, ~10 mW at each fiber end, 20 ms pulse duration, 20 Hz repetition rate) of 4 s duration were presented, while *Gt*ACR2 was activated by continuous illumination (473 nm, ~10 mW at each fiber end) of 2–6 s duration. 30–40 trials of 473 nm pulses, 594 nm pulse trains, and combinations thereof, were presented at an inter-train-interval of 20–30 s in each session.

Data acquisition. A monochrome camera (DMK 33UX249; The Imaging Source, Germany) equipped with a macro objective (TMN 1.0/50; The Imaging Source, Germany) and a 780 nm long-pass filter (FGL780; Thorlabs, Germany) was pointed towards one eye of the mouse. Background illumination was provided with an infrared spotlight (850 nm), while a UV LED (395 nm; Nichia, Japan) was adjusted to maintain pupil dilation of the mouse at a moderate baseline level. Single frames were triggered at 30 Hz by an additional channel of the NI-DAQ-card that controlled optogenetic stimulation, and synchronization was achieved by simultaneous recording of all control voltages and their corresponding timestamps.

Data analysis. Pupil diameter was estimated using a custom-modified, MATLAB-based algorithm developed by McGinley et al.[71]. In short, an intensity threshold was chosen for each recording to roughly separate between pupil (dark) and non-pupil (bright) pixels. For each frame, a circle around the center of mass of putative pupil pixels and with an area equivalent to the number of pupil pixels was then calculated, and putative edge pixels were identified by canny edge detection. Putative edge pixels that were more than 3 pixels away from pixels below the threshold (putative pupil) or outside an area of ±0.25–1.5 times the diameter of the fitted circle were neglected. Using least-squares regression, an ellipse was then fit on the remaining edge pixels, and the diameter of a circle of the equivalent area to this ellipse was taken as the pupil diameter. Noisy frames (e.g., no visible pupil due to blinking or blurry pupil images due to saccades of the animal) were linearly interpolated, and the data was low-passed filtered (<3 Hz; 3rd order Butterworth filter). Pupil data was segmented from 5 s before to 15 s after the onset of each stimulus and normalized to the median pupil diameter of the 5 s preceding the stimulus onset, before individual trials were averaged. Randomly chosen segments of pupil data of the same duration served as a control. The difference in median pupil diameter one second before and after stimulation (as indicated in Fig. 7c) was used to calculate potential changes in pupil diameter for each condition. Statistical significance was calculated using one-way analysis of variance and Tukey's post-hoc multiple comparison tests.

In-vivo recordings from ferret visual cortex. Data were collected from 3 adult female ferrets (*Mustela putorius*). All experiments were approved by the independent Hamburg state authority for animal welfare (Behörde für Justiz und Verbraucherschutz) and were performed in accordance with the guidelines of the German Animal Protection Law and the animal welfare officer of the University Medical Center Hamburg-Eppendorf.

Table 2 Photon flux given as a number of photons s⁻¹ m⁻².

	Irradiance (mW mm⁻²)					
	0.001	0.01	0.1	1	10	100
Wavelength (nm)						
365	1.84E + 18	1.84E + 19	1.84E + 20	1.84E + 21	1.84E + 22	1.84E + 23
385	1.94E + 18	1.94E + 19	1.94E + 20	1.94E + 21	1.94E + 22	1.94E + 23
405	2.04E + 18	2.04E + 19	2.04E + 20	2.04E + 21	2.04E + 22	2.04E + 23
435	2.19E + 18	2.19E + 19	2.19E + 20	2.19E + 21	2.19E + 22	2.19E + 23
460	2.32E + 18	2.32E + 19	2.32E + 20	2.32E + 21	2.32E + 22	2.32E + 23
470	2.37E + 18	2.37E + 19	2.37E + 20	2.37E + 21	2.37E + 22	2.37E + 23
490	2.47E + 18	2.47E + 19	2.47E + 20	2.47E + 21	2.47E + 22	2.47E + 23
525	2.65E + 18	2.65E + 19	2.65E + 20	2.65E + 21	2.65E + 22	2.65E + 23
550	2.77E + 18	2.77E + 19	2.77E + 20	2.77E + 21	2.77E + 22	2.77E + 23
580	2.92E + 18	2.92E + 19	2.92E + 20	2.92E + 21	2.92E + 22	2.92E +;23
595	3E + 18	3E + 19	3E + 20	3E + 21	3E + 22	3E + 23
630	3.18E + 18	3.18E + 19	3.18E + 20	3.18E + 21	3.18E + 22	3.18E + 23
660	3.33E + 18	3.33E + 19	3.33E + 20	3.33E + 21	3.33E + 22	3.33E + 23

For injection of rAAV2/9 viral particles encoding mDlx-BiPOLES-mCerulean (see Table 2) animals were anesthetized with an injection of ketamine (15 mg kg⁻¹), medetomidine (0.02 mg kg⁻¹), midazolam (0.5 mg kg⁻¹) and atropine (0.15 mg kg⁻¹). Subsequently, they were intubated and respiration with a mixture of 70:30 N_2/O_2 and 1–1.5% isoflurane. A cannula was inserted into the femoral vein to deliver a bolus injection of enrofloxacin (15 mg kg⁻¹) and Rimadyl (4 mg kg⁻¹) and, subsequently, continuous infusion of 0.9% NaCl and fentanyl (0.01 mg kg⁻¹ h⁻¹). Body temperature, heart rate, and end-tidal CO_2 were constantly monitored throughout the surgery. Before fixing the animal's head in the stereotaxic frame, a local anesthetic (Lidocaine, 10%) was applied to the external auditory canal. The temporalis muscle was folded back, such that a small craniotomy (ø: 2.5 mm) could be performed over the left posterior cortex and the viral construct was slowly (0.1 µl min⁻¹) injected into the secondary visual cortex (area 18). The excised piece of bone was put back in place and fixed with tissue-safe silicone (Kwikcast; WPI). Also, the temporalis muscle was returned to its physiological position and the skin was closed. After the surgery, the animals received preventive analgesics (Metacam, 0.1 mg) and antibiotics (Enrofloxacin, 15 mg kg⁻¹) for ten days.

After an expression period of at least 4 weeks, recordings of cortical signals were carried out under isoflurane anesthesia. Anesthesia induction and maintenance were similar to the procedures described above, except for a tracheotomy performed to allow for artificial ventilation of the animal over an extended period. The i.v. infusion was supplemented with pancuronium bromide (6 µg kg⁻¹ h⁻¹) to prevent slow ocular drifts. To keep the animal's head in a stable position throughout the placement of recording electrodes and the measurements, a headpost was fixed with screws and dental acrylic to the frontal bone of the head. Again, the temporalis muscle was folded back and a portion of the cranial bone was resected. The dura was removed before introducing an optrode with 32 linearly distributed electrodes (A1x32-15mm-50(100)-177, NeuroNexus Technologies) into the former virus-injection site (area 18). The optrode was manually advanced via a micromanipulator (David Kopf Instruments) under visual inspection until the optic fiber was positioned above the pial surface and the uppermost electrode caught a physiological signal, indicating that it had just entered the cortex.

During electrophysiological recordings, the isoflurane level was maintained at 0.7%. To ensure controlled conditions for sensory stimulation, all experiments were carried out in a dark, sound-attenuated anechoic chamber (Acoustair, Moerkapelle, Netherlands). Visual stimuli were created via an LED placed in front of the animal's eye. In separate blocks, 150 laser stimuli of different colors ('red', 633 nm LuxXplus and 'blue', 473 nm LuxXplus, LightHub-4, Omicron) were applied through the optrode for 500 ms, each, at a variable interval of 2.5–3 s. Randomly, 75 laser stimuli were accompanied by a 10 ms LED flash, starting 100 ms after the respective laser onset. For control, one block of 75 LED flashes alone was presented at comparable interstimulus intervals.

Electrophysiological signals were sampled with an AlphaLab SnR recording system (Alpha Omega Engineering, Nazareth, Israel) or with a self-developed neural recording system based on INTAN digital head-stages (RHD2132, Intantech). Signals recorded from the intracortical laminar probe were band-pass filtered between 0.5 Hz and 7.5 kHz and digitized at 22–44 kHz or 25 kHz, respectively. All analyses of neural data presented in this study were performed offline after the completion of experiments using MATLAB scripts (MathWorks). To extract multiunit spiking activity (MUA) from broadband extracellular recordings, we high-pass filtered signals at 500 Hz and detected spikes at negative threshold (>3.5 SD)[72].

Reporting summary. Further information on research design is available in the Nature Research Reporting Summary linked to this article.

References
1. Chen, I. W., Papagiakoumou, E. & Emiliani, V. Towards circuit optogenetics. *Curr. Opin. Neurobiol.* **50**, 179–189 (2018).
2. Kleinlogel, S. et al. A gene-fusion strategy for stoichiometric and co-localized expression of light-gated membrane proteins. *Nat. Methods* **8**, 1083–1088 (2011).
3. Tang, W. et al. Faithful expression of multiple proteins via 2A-peptide self-processing: a versatile and reliable method for manipulating brain circuits. *J. Neurosci.* **29**, 8621–8629 (2009).
4. Gradinaru, V. et al. Molecular and cellular approaches for diversifying and extending optogenetics. *Cell* **141**, 154–165 (2010).
5. Gradinaru, V. et al. Targeting and readout strategies for fast optical neural control in vitro and in vivo. *J. Neurosci.* **27**, 14231–14238 (2007).
6. Carus-Cadavieco, M. et al. Gamma oscillations organize top-down signalling to hypothalamus and enable food seeking. *Nature* **542**, 232–236 (2017).
7. Rashid, A. J. et al. Competition between engrams influences fear memory formation and recall. *Science* **353**, 383–387 (2016).
8. Vesuna, S. et al. Deep posteromedial cortical rhythm in dissociation. *Nature* **586**, 87–94 (2020).
9. Heikenfeld, C. et al. Prefrontal-subthalamic pathway supports action selection in a spatial working memory task. *Sci. Rep.* **10**, 10497 (2020).
10. Mohammad, F. et al. Optogenetic inhibition of behavior with anion channelrhodopsins. *Nat. Methods* **14**, 271–274 (2017).
11. Wietek, J. et al. Anion-conducting channelrhodopsins with tuned spectra and modified kinetics engineered for optogenetic manipulation of behavior. *Sci. Rep.* **7**, 14957 (2017).
12. Klapoetke, N. C. et al. Independent optical excitation of distinct neural populations. *Nat. Methods* **11**, 338–346 (2014).
13. Yizhar, O. et al. Neocortical excitation/inhibition balance in information processing and social dysfunction. *Nature* **477**, 171–178 (2011).
14. Akerboom, J. et al. Genetically encoded calcium indicators for multi-color neural activity imaging and combination with optogenetics. *Front. Mol. Neurosci.* **6**, 2 (2013).
15. Erbguth, K., Prigge, M., Schneider, F., Hegemann, P. & Gottschalk, A. Bimodal activation of different neuron classes with the spectrally red-shifted channelrhodopsin chimera C1V1 in Caenorhabditis elegans. *PLoS ONE* **7**, e46827 (2012).

121

16. Stujenske, J. M., Spellman, T. & Gordon, J. A. Modeling the spatiotemporal dynamics of light and heat propagation for in vivo optogenetics. *Cell Rep.* **12**, 525–534 (2015).

17. Yizhar, O., Fenno, L. E., Davidson, T. J., Mogri, M. & Deisseroth, K. Optogenetics in neural systems. *Neuron* **71**, 9–34 (2011).

18. Govorunova, E. G., Sineshchekov, O. A., Janz, R., Liu, X. & Spudich, J. L. NEUROSCIENCE. Natural light-gated anion channels: A family of microbial rhodopsins for advanced optogenetics. *Science* **349**, 647–650 (2015).

19. Berndt, A. et al. Structural foundations of optogenetics: determinants of channelrhodopsin ion selectivity. *Proc. Natl Acad. Sci. USA* **113**, 822–829 (2016).

20. Rajasethupathy, P. et al. Projections from neocortex mediate top-down control of memory retrieval. *Nature* **526**, 653–659 (2015).

21. Mager, T. et al. High frequency neural spiking and auditory signaling by ultrafast red-shifted optogenetics. *Nat. Commun.* **9**, 1750 (2018).

22. Marshel, J. H. et al. Cortical layer-specific critical dynamics triggering perception. *Science* **365**, https://doi.org/10.1126/science.aaw5202 (2019).

23. Batabyal, S., Cervenka, G., Ha, J. H., Kim, Y. T. & Mohanty, S. Broad-band activatable white-opsin. *PLoS ONE* **10**, e0136958 (2015).

24. Bansal, H., Gupta, N. & Roy, S. Theoretical analysis of low-power bidirectional optogenetic control of high-frequency neural codes with single spike resolution. *Neuroscience* **449**, 165–188 (2020).

25. Sineshchekov, O. A. et al. Conductance mechanisms of rapidly desensitizing cation channelrhodopsins from cryptophyte algae. *mBio* **11**, https://doi.org/10.1128/mBio.00657-20 (2020).

26. Sudo, Y. et al. A blue-shifted light-driven proton pump for neural silencing. *J. Biol. Chem.* **288**, 20624–20632 (2013).

27. Lim, S. T., Antonucci, D. E., Scannevin, R. H. & Trimmer, J. S. A novel targeting signal for proximal clustering of the Kv2.1 K+ channel in hippocampal neurons. *Neuron* **25**, 385–397 (2000).

28. Mahn, M. et al. High-efficiency optogenetic silencing with soma-targeted anion-conducting channelrhodopsins. *Nat. Commun.* **9**, 4125 (2018).

29. Messier, J. E., Chen, H., Cai, Z. L. & Xue, M. Targeting light-gated chloride channels to neuronal somatodendritic domain reduces their excitatory effect in the axon. *eLife* **7**, https://doi.org/10.7554/eLife.38506 (2018).

30. Hochbaum, D. R. et al. All-optical electrophysiology in mammalian neurons using engineered microbial rhodopsins. *Nat. Methods* **11**, 825–833 (2014).

31. Mardinly, A. R. et al. Precise multimodal optical control of neural ensemble activity. *Nat. Neurosci.* **21**, 881–893 (2018).

32. Ronzitti, E. et al. Submillisecond optogenetic control of neuronal firing with two-photon holographic photoactivation of Chronos. *J. Neurosci.* **37**, 10679–10689 (2017).

33. Zhang, F. et al. Multimodal fast optical interrogation of neural circuitry. *Nature* **446**, 633–639 (2007).

34. Hu, C. et al. Sensory integration and neuromodulatory feedback facilitate Drosophila mechanonociceptive behavior. *Nat. Neurosci.* **20**, 1085–1095 (2017).

35. Breton-Provencher, V. & Sur, M. Active control of arousal by a locus coeruleus GABAergic circuit. *Nat. Neurosci.* **22**, 218–228 (2019).

36. Dimidschstein, J. et al. A viral strategy for targeting and manipulating interneurons across vertebrate species. *Nat. Neurosci.* **19**, 1743–1749 (2016).

37. Mahn, M., Prigge, M., Ron, S., Levy, R. & Yizhar, O. Biophysical constraints of optogenetic inhibition at presynaptic terminals. *Nat. Neurosci.* **19**, 554–556 (2016).

38. Stierl, M. et al. Light modulation of cellular cAMP by a small bacterial photoactivated adenylyl cyclase, bPAC, of the soil bacterium Beggiatoa. *J. Biol. Chem.* **286**, 1181–1188 (2011).

39. Moeyaert, B. et al. Improved methods for marking active neuron populations. *Nat. Commun.* **9**, 4440 (2018).

40. Perez-Alvarez, A. et al. Freeze-frame imaging of synaptic activity using SynTagMA. *Nat. Commun.* **11**, 2464 (2020).

41. Kato, H. E. et al. Crystal structure of the channelrhodopsin light-gated cation channel. *Nature* **482**, 369–374 (2012).

42. Volkov, O. et al. Structural insights into ion conduction by channelrhodopsin 2. *Science* **358**, https://doi.org/10.1126/science.aan8862 (2017).

43. Oda, K. et al. Crystal structure of the red light-activated channelrhodopsin Chrimson. *Nat. Commun.* **9**, 3949 (2018).

44. Kim, Y. S. et al. Crystal structure of the natural anion-conducting channelrhodopsin GtACR1. *Nature* **561**, 343–348 (2018).

45. Baker, C. A., Elyada, Y. M., Parra, A. & Bolton, M. M. Cellular resolution circuit mapping with temporal-focused excitation of soma-targeted channelrhodopsin. *eLife* **5**, https://doi.org/10.7554/eLife.14193 (2016).

46. Forli, A. et al. Two-photon bidirectional control and imaging of neuronal excitability in vivo. *Cell Rep.* **22**, 3087–3098 (2018).

47. Shemesh, O. A. et al. Temporally precise single-cell-resolution optogenetics. *Nat. Neurosci.* **20**, 1796–1806 (2017).

48. Douin, V. et al. Use and comparison of different internal ribosomal entry sites (IRES) in tricistronic retroviral vectors. *BMC Biotechnol.* **4**, 16 (2004).

49. Wiegert, J. S., Mahn, M., Prigge, M., Printz, Y. & Yizhar, O. Silencing neurons: tools, applications, and experimental constraints. *Neuron* **95**, 504–529 (2017).

50. Mahn, M. et al. Efficient optogenetic silencing of neurotransmitter release with a mosquito rhodopsin. *Neuron* **109**, 1621–1635 e1628 (2021).

51. Copits, B. A. et al. A photoswitchable GPCR-based opsin for presynaptic inhibition. *Neuron* https://doi.org/10.1016/j.neuron.2021.04.026 (2021).

52. Lima, S. Q., Hromadka, T., Znamenskiy, P. & Zador, A. M. PINP: a new method of tagging neuronal populations for identification during in vivo electrophysiological recording. *PLoS ONE* **4**, e6099 (2009).

53. Ramirez, S. et al. Creating a false memory in the hippocampus. *Science* **341**, 387–391 (2013).

54. Markwardt, M. L. et al. An improved cerulean fluorescent protein with enhanced brightness and reduced reversible photoswitching. *PLoS ONE* **6**, e17896 (2011).

55. Dittgen, T. et al. Lentivirus-based genetic manipulations of cortical neurons and their optical and electrophysiological monitoring in vivo. *Proc. Natl Acad. Sci. USA* **101**, 18206–18211 (2004).

56. Grimm, C., Vierock, J., Hegemann, P. & Wietek, J. Whole-cell patch-clamp recordings for electrophysiological determination of ion selectivity in Channelrhodopsins. *J. Vis. Exp.* https://doi.org/10.3791/55497 (2017).

57. Gee, C. E., Ohmert, I., Wiegert, J. S. & Oertner, T. G. Preparation of slice cultures from rodent Hippocampus. *Cold Spring Harb. Protoc.* **2017**, pdb prot094888 (2017).

58. Wiegert, J. S., Gee, C. E. & Oertner, T. G. Single-cell electroporation of neurons. *Cold Spring Harb. Protoc.* **2017**, pdb prot094904 (2017).

59. Wiegert, J. S., Gee, C. E. & Oertner, T. G. Viral vector-based transduction of slice cultures. *Cold Spring Harb. Protoc.* **2017**, pdb prot094896 (2017).

60. Booker, S. A. & Vida, I. Morphological diversity and connectivity of hippocampal interneurons. *Cell Tissue Res.* **373**, 619–641 (2018).

61. Schindelin, J. et al. Fiji: an open-source platform for biological-image analysis. *Nat. Methods* **9**, 676–682 (2012).

62. Lutz, C. et al. Holographic photolysis of caged neurotransmitters. *Nat. Methods* **5**, 821–827 (2008).

63. Gerchberg, R. W. & Saxton, W. O. Practical algorithm for determination of phase from image and diffraction plane pictures. *Optik* **35**, 237–+ (1972).

64. Fire, A. Integrative transformation of Caenorhabditis elegans. *Embo J.* **5**, 2673–2680 (1986).

65. Liewald, J. F. et al. Optogenetic analysis of synaptic function. *Nat. Methods* **5**, 895–902 (2008).

66. Stephens, G. J., Johnson-Kerner, B., Bialek, W. & Ryu, W. S. Dimensionality and dynamics in the behavior of C. elegans. *PLoS Comput. Biol.* **4**, e1000028 (2008).

67. Pfeiffer, B. D. et al. Refinement of tools for targeted gene expression in Drosophila. *Genetics* **186**, 735–755 (2010).

68. Groth, A. C., Fish, M., Nusse, R. & Calos, M. P. Construction of transgenic Drosophila by using the site-specific integrase from phage phiC31. *Genetics* **166**, 1775–1782 (2004).

69. Risse, B. et al. FIM, a novel FTIR-based imaging method for high throughput locomotion analysis. *PLoS ONE* **8**, e53963 (2013).

70. Savitt, J. M., Jang, S. S., Mu, W., Dawson, V. L. & Dawson, T. M. Bcl-x is required for proper development of the mouse substantia nigra. *J. Neurosci.* **25**, 6721–6728 (2005).

71. McGinley, M. J., David, S. V. & McCormick, D. A. Cortical membrane potential signature of optimal states for sensory signal detection. *Neuron* **87**, 179–192 (2015).

72. Quiroga, R. Q., Nadasdy, Z. & Ben-Shaul, Y. Unsupervised spike detection and sorting with wavelets and superparamagnetic clustering. *Neural Comput.* **16**, 1661–1687 (2004).

Acknowledgements

Author contributions

Conceptualization: J.V., S.R.R., P.H., J.S.W.; investigation: J.V., S.R.R., A.D., F.P., R.S., F.T., A.C.F.B., I.B., F.Z., N.Z., J.A., S.A., K.S., J.S.W.; data curation: J.V., S.R.R., A.D., F.P.,

Additional information
Supplementary information The online version contains supplementary material available at https://doi.org/10.1038/s41467-021-24759-5.

Correspondence and requests for materials should be addressed to J.S.W.

Peer review information *Nature Communications* thanks Ute Hochgeschwender, Adam Packer and the other, anonymous, reviewer(s) for their contribution to the peer review of this work. Peer reviewer reports are available.

Reprints and permission information is available at http://www.nature.com/reprints

Publisher's note Springer Nature remains neutral with regard to jurisdictional claims in published maps and institutional affiliations.

1 **BiPOLES is an optogenetic tool developed for bidirectional dual-color control of neurons**

2

3 **Supplementary Fig. 1. Biophysical characterization of different ACR-CCR tandem constructs. (a)**
4 Representative photocurrents of ßHK-Chrimson and different tandem constructs as described in Fig.
5 1a. **(b)** Normalized peak photocurrents of ßHK-Chrimson and tandem constructs at different membrane
6 voltages evoked at 450 nm, 490 nm, 530 nm or 600 nm (see panel (a), mean ± SD; n indicates number
7 of independent cells. n = 4 for ßHK-Chrimson; n = 5 for Aurora-L1-Chrimson, *Cs*Chrimson-L2-*Gt*ACR2
8 and *Gt*ACR2-L2-f-Chrimson; n = 6 for *Gt*ACR2, *Gt*ACR1-L2-Chrimson and *Gt*ACR2-L2-vf-Chrimson; n
9 = 7 for iC++-L1-Chrimson, *Gt*ACR2-L3-Chrimson, *Gt*ACR2-L4-Chrimson-mCer, *Gt*ACR2-L2-BreachES
10 and *Gt*ACR2-L2-ChRmine; n = 8 for *Gt*ACR2-L2-Chrimson and n = 9 for *Gt*ACR2-L4-ChRmine-ts-
11 eYFP-er); normalized to the peak photocurrent at -80 mV and 600 nm illumination). **(c)** Representative
12 photocurrents of different ACR-CCR tandems with 10 ms light pulses at indicated wavelengths and
13 equal photon flux at -60 mV. **(d, e)** Action spectra of *Gt*ACR1-L2-Chrimson and *Gt*ACR2-L4-ChRmine-

14 TS-eYFP-ER at different membrane voltages (mean ± SEM, n = 6 for *Gt*ACR1-L2-Chrimson and n = 8

15 for *Gt*ACR2-L4-ChRmine-TS-eYFP-ER). The data presented in this figure are provided in the Source

16 Data file.

17
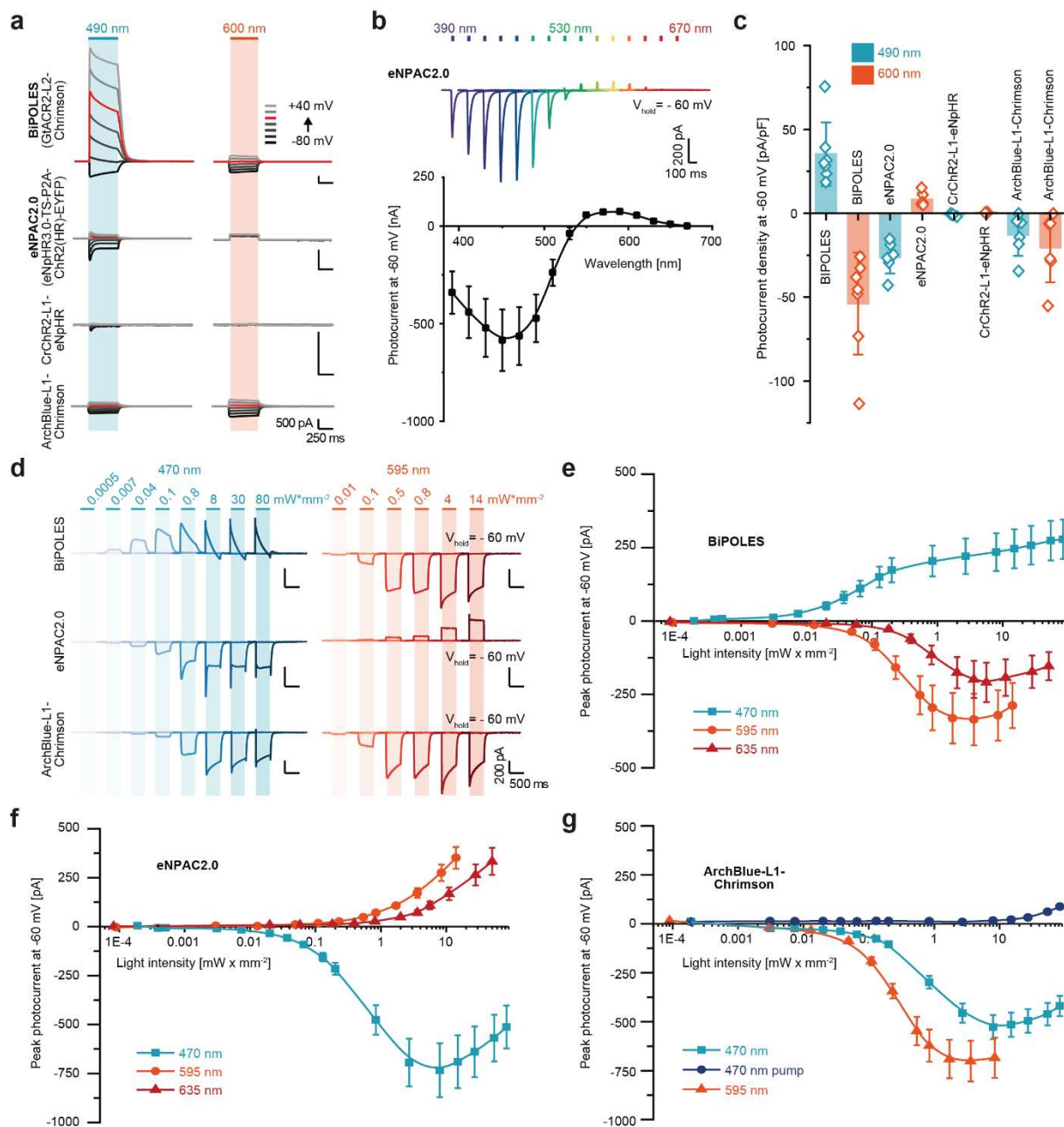
Supplementary Fig. 2. Comparison of BiPOLES to established bidirectional optogenetic tools in HEK293 cells. (a) From top to bottom: representative photocurrents of BiPOLES, eNPAC2.0 (eNpHR3.0-TS-p2A-*Cr*ChR2(H134R)-EYFP), *Cr*ChR2-L1-eNpHR[2] and ArchBlue-L1-Chrimson in whole-cell patch clamp recordings from HEK293 cells at 490 nm and 600 nm illumination. ArchBlue stands for the blue shifted mutant of Arch3.0[26]. **(b)** Top: Representative photocurrents of eNPAC2.0 with 10 ms light pulses at indicated wavelengths and equal photon flux at -60 mV. Bottom: Action spectrum of eNPAC2.0 at -60 mV (mean ± SEM, n = 5). **(c)** Peak photocurrent densities for 490 nm and 600 nm excitation at -60 mV (close to the neuronal resting potential) as shown in (a) (Mean ± SD; n indicates number of independent cells. n = 5 for *Cr*ChR2-L1-NpHR; n = 6 for ArchBlue-L1-Chrimson and eNPAC2.0, n = 7 for BiPOLES). **(d)** Representative photocurrents of BiPOLES (top), eNPAC2.0(middle) and ArchBlue-L1-Chrimson (bottom) at -60 mV and different irradiances and wavelengths. **(e-g)** Peak photocurrents at different irradiances, different excitation wavelength and -60 mV according to (d). (mean ± SEM, n = 4 for ArchBlue-L1-Chrimson and n = 6 for BiPOLES and eNPAC2.0)   6). Pump currents at 470 nm in (g) describe the initial outward currents observed directly after blue light switching in (d). The data presented in this figure are provided in the Source Data file.
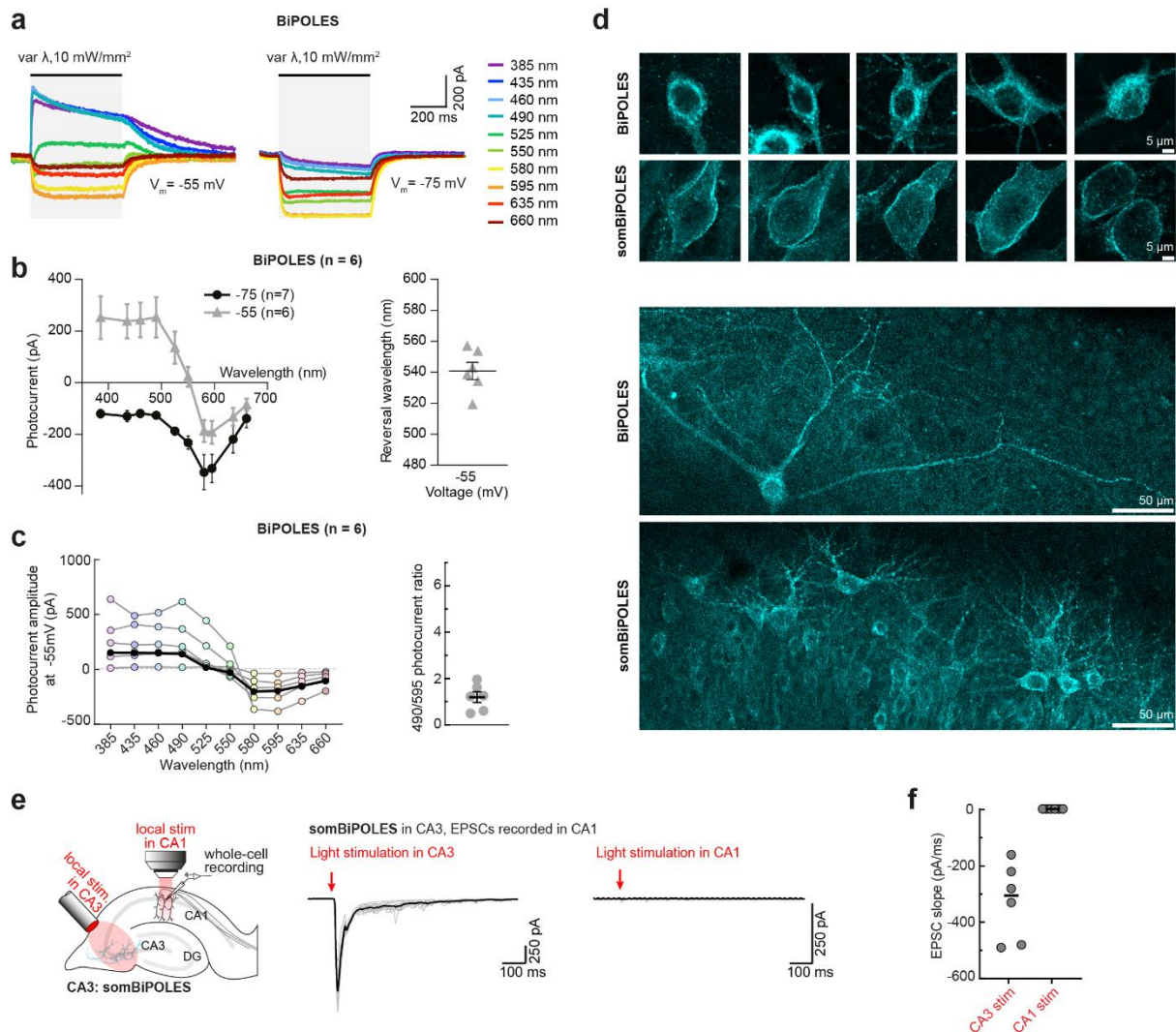
Supplementary Fig. 3. Biophysical characterization of BiPOLES and differential expression of BiPOLES and somBiPOLES in CA1 pyramidal neurons. (a) Representative photocurrent traces of BiPOLES in CA1 pyramidal neurons upon illumination with different wavelengths and equal photon flux at membrane voltages above (left) and below (right) the chloride Nernst potential. **(b)** Left: Quantification of photocurrent amplitude along the spectrum at a membrane voltage of -55 mV (grey) and -75 mV (black). Symbols indicate mean ± SEM and lines are interpolations of data points ($n_{-55\,mV}$ = 6 cells, $n_{-75\,mV}$ = 7 cells). Similar to HEK-cell measurements, inward and outward photocurrents were evoked with 635 nm and 490 nm at a membrane voltage between the chloride and proton Nernst potentials, respectively, indicative of independently evoked Chrimson- and GtACR2-photocurrents. Right: Quantification of photocurrent reversal wavelength at -55 mV (mean ± SEM, n = 6 cells). **(c)** Left: Quantification of photocurrent amplitudes at -55 mV (same data as in (b) but showing individual data points for each wavelength, black circles: medians, n = 6 cells). Right: Ratio of inhibitory (490 nm) over excitatory (595 nm) photocurrents (mean ± SEM, n = 6 cells). Note that, unlike for eNPAC2.0 (Supplementary Fig. 8a) the photocurrent ratio shows little variability between cells, indicating a reproducible stoichiometry of Chrimson and GtACR2 currents. **(d)** Maximum-intensity projections of confocal images showing expression of BiPOLES or soma-targeted BiPOLES (somBiPOLES) in CA3 pyramidal neurons of organotypic hippocampal slices. For each opsin 5 representative neurons from 5 organotypic slices are shown (top rows).. Bottom: lower-magnification example images of CA3 neurons in *stratum oriens* show confinement of somBiPOLES to soma and proximal dendrites. These images were not used for quantitative analysis. CA3 cells were transduced with an AAV9 encoding for either BiPOLES or somBiPOLES and fixed after 20 days. Fluorescence was enhanced by an antibody staining against the fluorophore mCerulean. **(e)** Left: Schematic drawing depicting the experiment used to verify

57 absence of somBiPOLES-expression in axon terminals of CA3 cells. Whole-cell voltage-clamp
58 recordings were done in postsynaptic CA1 cells to determine red-light evoked EPSCs. Illumination was
59 done locally either in CA3 at the somata or in CA1 at axon terminals of somBiPOLES-expressing CA3
60 cells. Axon stimulation was done in the presence of TTX to avoid antidromic spiking of CA3 cells and 4-
61 AP to inhibit K+-mediated fast repolarization. Middle: Example voltage-clamp recordings from CA1 cells
62 upon red-light stimulation in CA3. Right: example voltage-clamp recordings from CA1 cells upon red-
63 light stimulation of axon terminals in CA1. Black lines show average response of 10 repetitions (grey
64 lines). **(f)** Quantification of experiment shown in (e) (black lines: medians, no error bars shown, n = 6
65 cells). The absence of somBiPOLES-mediated EPSCs upon local illumination in CA1, indicates efficient
66 exclusion of somBiPOLES from the axon terminals, despite strong membrane expression in the
67 somatodendritic compartment, which was evident from large EPSCs upon local illumination in CA3. The
68 data presented in this figure are provided in the Source Data file.
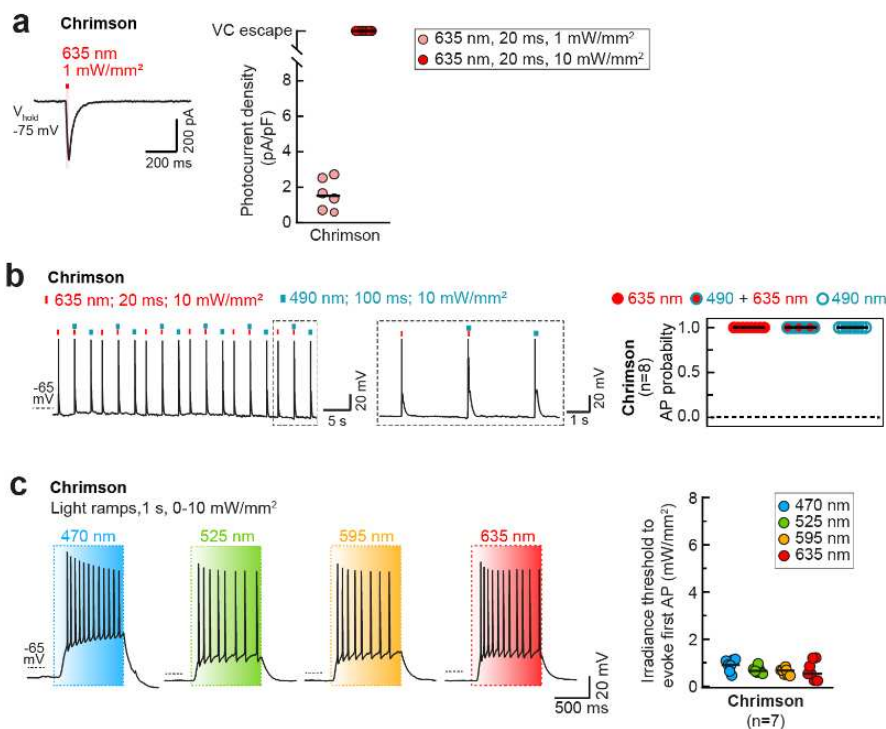
72 **Supplementary Fig. 4. Characterization of Chrimson-mediated currents and spiking in CA1**
73 **pyramidal cells. (a)** Left: Representative photocurrent trace evoked by a 635 nm light pulse (20 ms, 1
74 mW mm^{-2}) recorded in a Chrimson-expressing CA1 pyramidal neuron at a membrane voltage of -75
75 mV. Right: Quantification of photocurrent densities evoked under the indicated conditions (black
76 horizontal lines: medians, n = 6 cells). **(b)** Left: Voltage traces showing red- and blue-light-evoked APs.
77 Right: Quantification of AP probability under indicated conditions (black horizontal lines: medians, n = 8
78 cells). Note that blue light does not elicit APs in somBiPOLES-expressing cells due to *Gt*ACR2-mediated
79 shunting (see Fig. 4b). **(c)** Spectral quantification of the irradiance threshold for AP generation with
80 Chrimson. Left: Representative membrane voltage traces during light ramps at indicated wavelengths
81 with irradiance increasing linearly from 0 to 10 mW mm^{-2}. Right: Quantification of the irradiance threshold
82 at which the first AP was evoked (black horizontal lines: medians, n = 7 cells). Datasets for 470 and 595
83 nm are the same as shown in Fig. 3e. The data presented in this figure are provided in the Source Data
84 file.

86
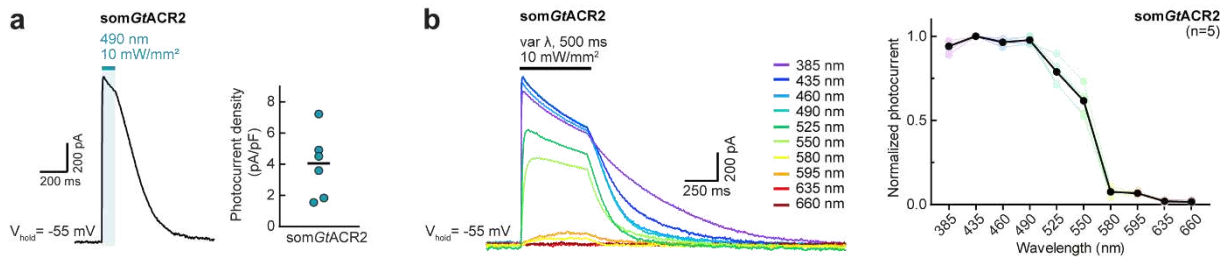
Supplementary Fig. 5. Quantification of som*Gt*ACR2-mediated photocurrents in CA1 pyramidal cells. (a) Left: Representative photocurrent trace evoked by a 490 nm light pulse (100 ms, 10 mW mm^{-2}) recorded in a som*Gt*ACR2-expressing CA1 pyramidal neuron at -55 mV, 20 mV more positive than the chloride Nernst potential. Right: Quantification of photocurrent densities evoked under the indicated conditions (black horizontal lines: medians, n = 6 cells). **(b)** Left: Representative photocurrent traces upon illumination with different wavelengths and equal photon flux at a membrane voltage of -55 mV. Right: Normalized photocurrent amplitude along the spectrum (black circles: medians, n = 5 cells). The data presented in this figure are provided in the Source Data file.
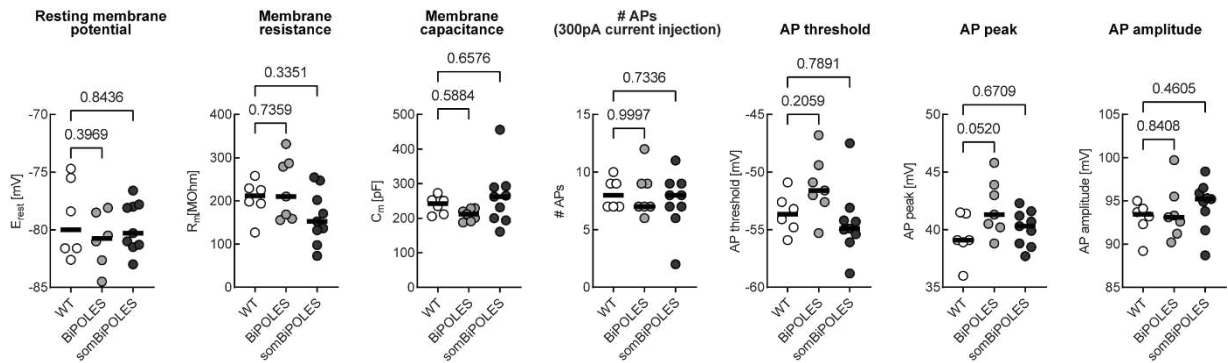
Supplementary Fig. 6: Basic neuronal parameters of WT, BiPOLES- and somBiPOLES-expressing CA1 pyramidal cells. The following parameters were measured to asses cell viability and tolerability of BiPOLES and somBiPOLES: resting membrane potential, membrane resistance, membrane capacitance, number of APs evoked by somatic current injection (300 pA, 500 ms), voltage threshold, peak voltage and AP amplitude of the 1st AP elicited by somatic current injection (black lines: medians, WT n = 6 cells, BiPOLES n = 7 cells, somBiPOLES n = 9 cells, one-way ANOVA, exact P-values are shown). The data presented in this figure and details on the statistical analysis are provided in the Source Data file.
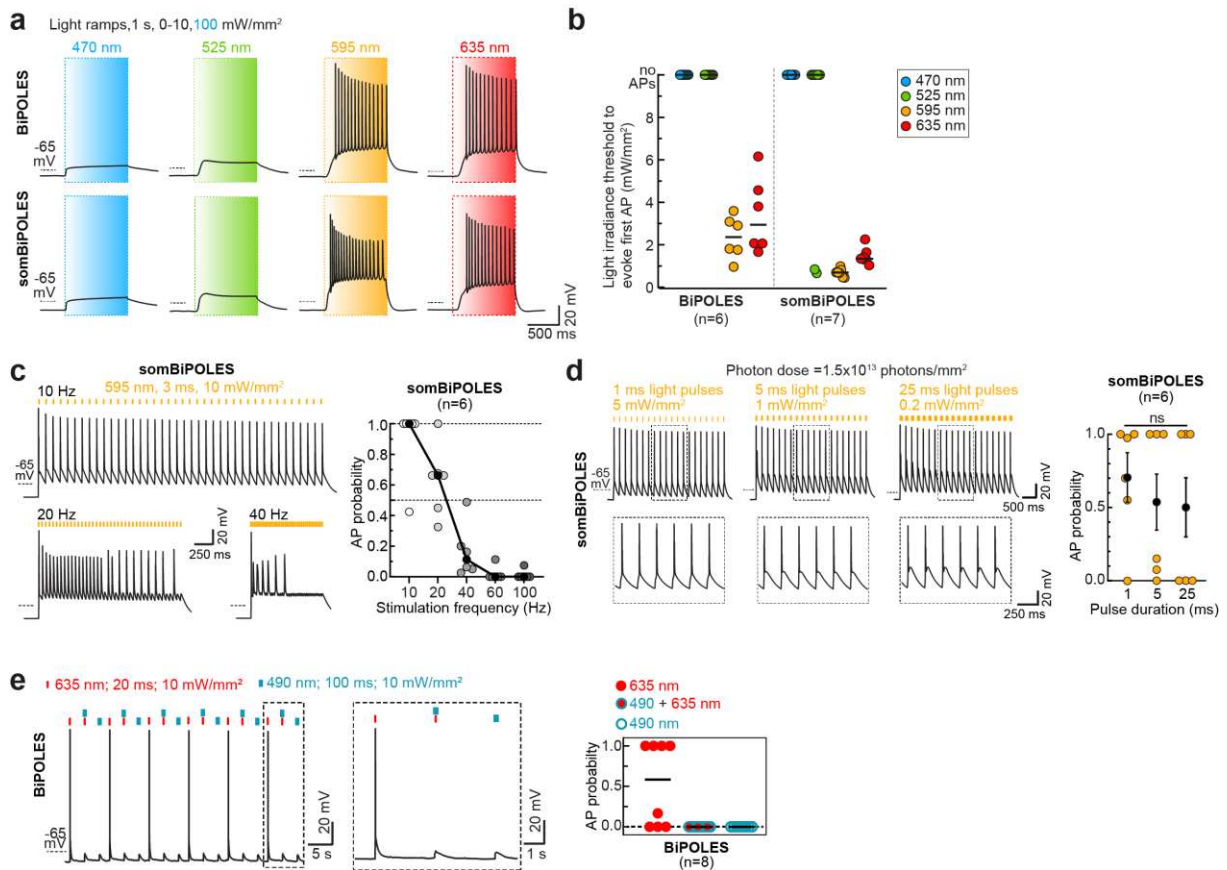
Supplementary Fig. 7. Optical spiking parameters for BiPOLES and somBiPOLES. (a,b) Spectral quantification of action potential threshold for BiPOLES and somBiPOLES. **(a)** Representative membrane voltage traces measured in BiPOLES- (top), or somBiPOLES-expressing CA1 pyramidal neurons (bottom). In IC experiments, light ramps of different wavelengths were applied as indicated. The irradiance was ramped linearly from 0 to 10 mW mm^{-2} over 1 s, except for 470-nm ramps, which were ranging to 100 mW mm^{-2} to rule out the possibility that high-intensity blue light might still evoke action potentials. **(b)** Quantification of the irradiance threshold at which the first action potential was evoked. 470-nm light up to 100 mW mm^{-2} did not evoke action potentials in BiPOLES or somBiPOLES-expressing cells. The irradiance threshold for 595 and 635 nm illumination was lower in somBiPOLES-expressing cells compared to BiPOLES-expressing cells indicating higher light sensitivity in the former (black horizontal lines: medians, $n_{BiPOLES}$ = 6 cells, $n_{somBiPOLES}$ =7 cells). somBiPOLES data for 470 and 595 nm are the same as in Fig. 3d. **(c)** Left: membrane voltage traces at different light-pulse frequencies in CA1 cells expressing somBiPOLES. APs were triggered by 40 pulses (λ = 595 nm, pulse width = 3 ms, 10 mW mm^{-2}). Right: Quantification of AP probability at increasing stimulation frequencies (from 10 to 100 Hz, black circles: medians, n = 6 cells). To determine AP probability, the number of light-triggered APs was divided by the total number of light pulses. **(d)** Left: membrane voltage traces at different light-pulse widths (1, 5 and 25 ms) and irradiances (5, 1, and 0.2 mW mm^{-2}, respectively). In all conditions the photon dose was kept constant at 1.5x10^{13} photons/mm^2. Magnified views of the traces are shown below. Note the different shapes of the sub-threshold membrane voltages evoked by the respective combination of parameters. Right: Quantification of AP probability at indicated light stimulation condition (black circles: mean ± SEM, n = 6 cells). **(e)** All-optical excitation and inhibition with BiPOLES. Current-clamp characterization of bidirectional optical spiking-control with BiPOLES. Left: Voltage traces showing red-light-evoked action potentials (APs), which were blocked by a concomitant blue light pulse. Right: quantification of AP probability under indicated conditions (black horizontal lines: medians, n = 8 cells). The data presented in this figure and details on the statistical analysis are provided in the Source Data file.
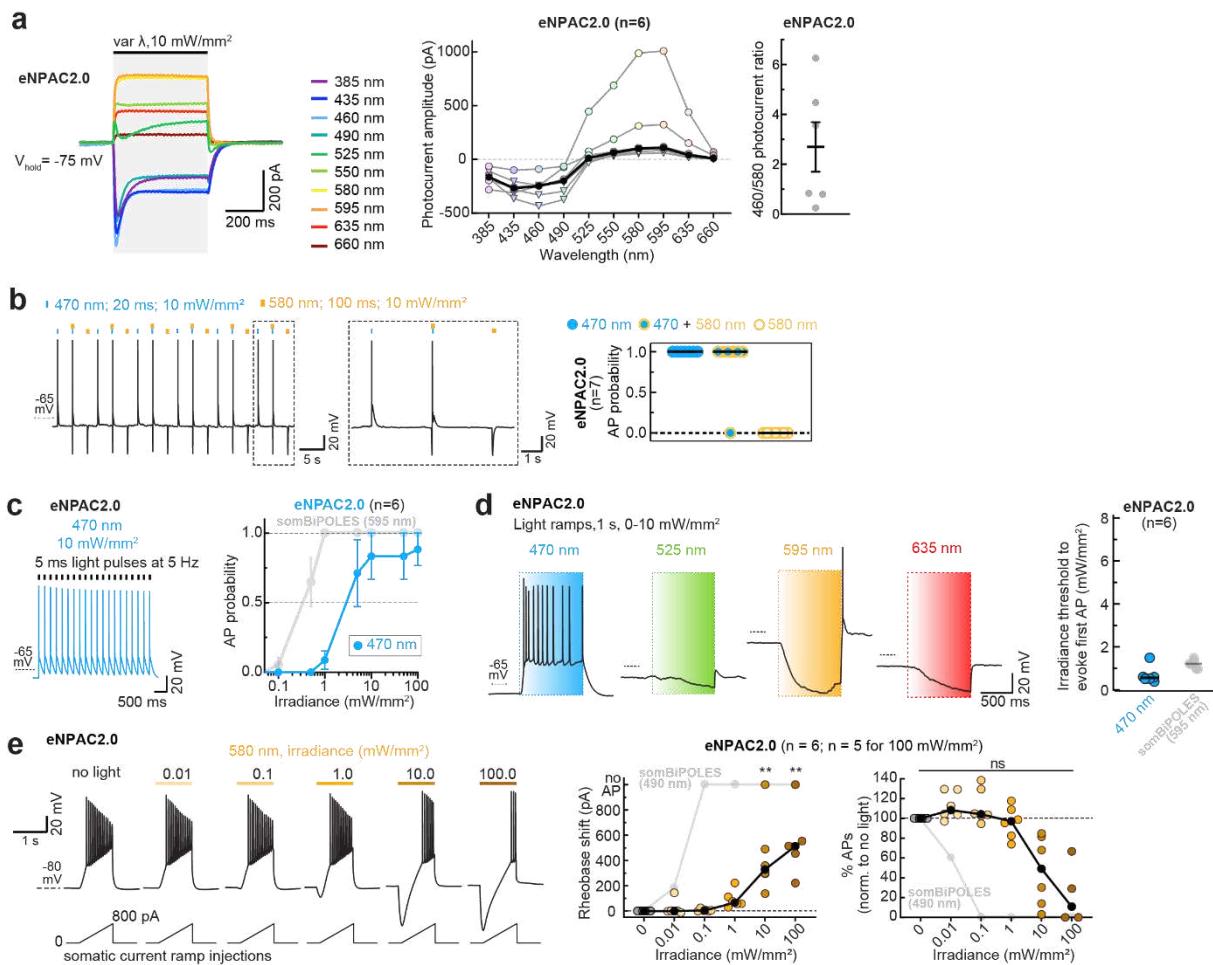
Supplementary Fig. 8. Characterization of bidirectional optogenetic manipulation of neuronal activity with eNPAC2.0. (a) Left: Representative eNPAC2.0 photocurrent traces in CA1 pyramidal neurons upon illumination with different wavelengths and equal photon flux at a membrane voltage of -75 mV. Middle: Quantification of photocurrent amplitude along the spectrum (black circles: medians, colored circles: photocurrents elicited by an irradiance of 10 mW mm^{-2}, colored triangles: photocurrents elicited by an irradiance of 1 mW mm^{-2}, n = 6 cells). Similar to HEK-cell measurements (see Supplementary Fig. 2b), inward and outward photocurrents were evoked with blue and orange light, respectively, indicative of independently evoked ChR2(H134R)- and eNpHR3.0-photocurrents. Right: Quantification of the ratio of excitatory (460 nm) over inhibitory (580 nm) photocurrents (black line: mean ± SEM, n = 6 cells). Note that this ratio is more scattered compared to BiPOLES (see Supplementary Fig. 3c), indicating variability in the stoichiometry of excitatory and inhibitory opsins between cells. This is likely explained by the different expression strategies for eNPAC2.0 (bi-cistronic, p2A construct) and BiPOLES (fusion protein and 1:1 stoichiometric expression of both tandem partners). **(b)** Characterization of all-optical spiking and silencing with eNPAC2.0. Left: Voltage traces showing blue-light-evoked APs, which, under the indicated conditions, could not be blocked by stimulation of eNpHR3.0 with a concomitant yellow light pulse. Yellow light alone led to a hyperpolarization of membrane voltage, indicating chloride loading of the cell by eNpHR3.0. Right: quantification of AP probability under indicated conditions (black horizontal lines: medians, n = 7 cells). **(c)** Left: Example traces of voltage clamp recordings of eNPAC2.0 to determine light-evoked AP probability with 470 nm. Right: quantification of light-mediated AP probability at indicated irradiances (symbols represent mean ± SEM, n = 6 cells). Note that even at an irradiance of 100 mW mm^{-2} not all cells achieved 100% spiking probability. This contrasts with CA1 cells expressing somBiPOLES or Chrimson alone, where 100% spiking probability is achieved with 595-nm light (their peak activation wavelength) at irradiances around 1 mW mm^{-2} (see Fig. 3b,c). **(d)** Spectral quantification of the irradiance threshold for AP generation with

162 eNPAC2.0. Left: Representative membrane voltage traces during light ramps at indicated wavelengths
163 with irradiance increasing linearly from 0 to 10 mW mm^{-2}. Note that a rebound spike was triggered after
164 applying a 595-nm light ramp. Right: Quantification of the irradiance threshold at which the first AP was
165 evoked (black horizontal lines: medians, n = 6 cells). **(e)** eNPAC2.0 mediates neuronal membrane
166 voltage hyperpolarization upon illumination with yellow light. Left: Current ramps (from 0–100 to 0–900
167 pA) were injected into eNPAC2.0-expressing CA1 pyramidal cells to induce APs during illumination with
168 yellow light at indicated intensities (from 0.01 to 100 mW mm^{-2}). Right: Quantification of the rheobase
169 shift and the relative change in the number of ramp-evoked action potentials. The injected current at the
170 time of the first action potential was defined as the rheobase. Illumination with 580 nm light of increasing
171 intensities activated eNpHR3.0-mediated Cl^{-} pumping, which strongly hyperpolarized the membrane
172 voltage, shifting the rheobase to higher values and shunting APs. Note that the ability of eNPAC2.0 to
173 silence neurons is smaller compared to somBiPOLES (see Fig. 3g). eNPAC2.0 required 2 orders of
174 magnitude higher irradiance to achieve a significant shift of the rheobase (black circles: medians, n = 6,
175 one-way Friedman test, *p < 0.05, **p < 0.01, ***p < 0.001). Grey symbols and lines in (c), (d) and (e)
176 are somBiPOLES values from Fig. 3 plotted for comparison. The data presented in this figure and details
177 on the statistical analysis are provided in the Source Data file.

178

179
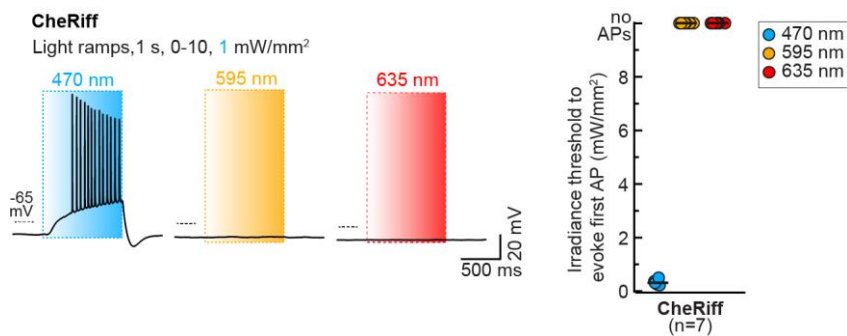
180

181 **Supplementary Fig. 9. CheRiff exhibits optical excitation restricted to the blue spectrum. (a)** Left:
182 Representative membrane voltage traces measured in CheRiff-expressing CA1 pyramidal neurons. In
183 IC experiments, light ramps of different wavelengths were applied as indicated. Light was ramped
184 linearly from 0 to 10 mW mm^{-2} over 1 s. 470-nm ramps were ranging only up to 1 mW mm^{-2}, which was
185 already sufficient to evoke APs. Right: Quantification of the irradiance threshold at which the first AP
186 was evoked. Orange/red light up to 10 mW mm^{-2} did not evoke action potentials in CheRiff-expressing
187 cells (black horizontal lines: medians, n = 7 cells). The data presented in this figure are provided in the
188 Source Data file.

189

190

191
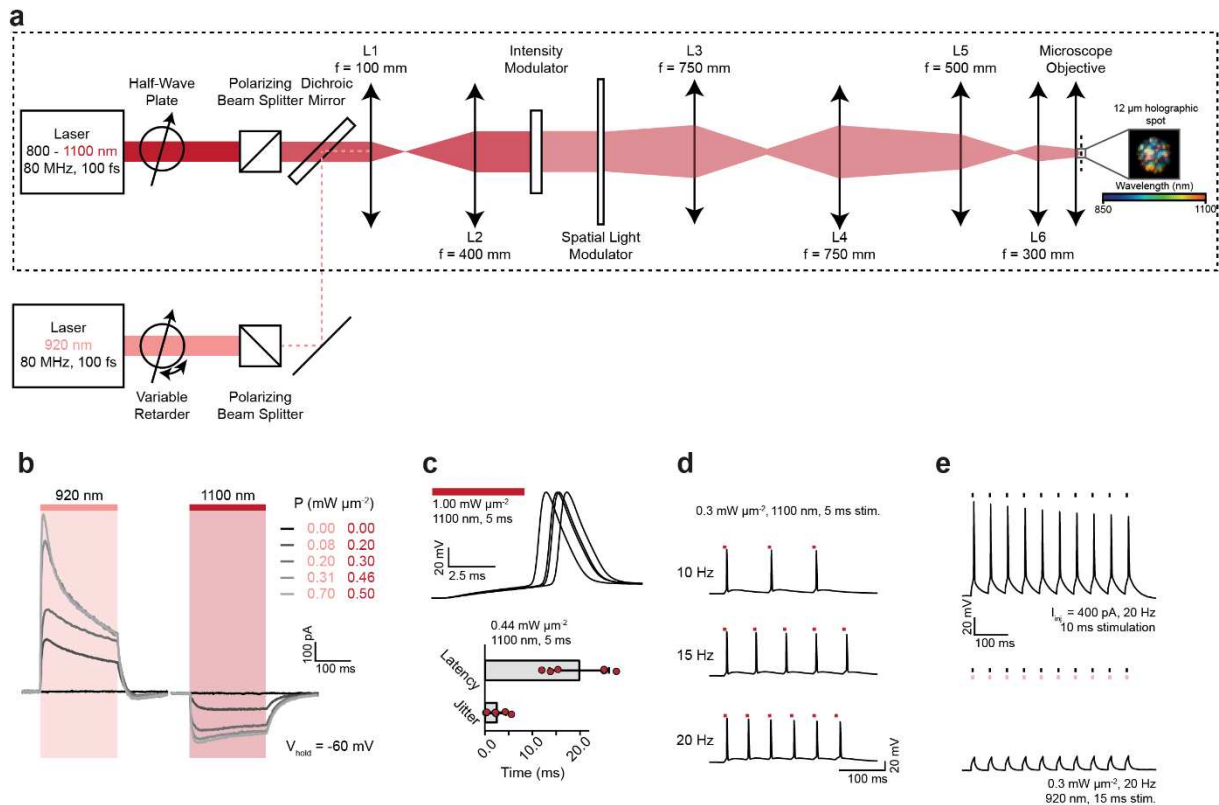
Supplementary Fig. 10. Design of the dual-laser 2-photon holography setup. (a) A schematic diagram of the experimental setup used for two-photon photo-stimulation and inhibition using holography. The optical path indicated by the black, dashed rectangle was used to acquire all data presented in Fig. 5. The system was aligned at the central wavelength (980 nm), but holograms at all wavelengths were co-aligned laterally and axially as demonstrated in the inset. Double-headed arrows are used to illustrate lenses, denoted by L, with focal lengths denoted by f. The reflective Spatial Light Modulator (SLM) is shown as transmissive for illustrative purposes. The photoinhibition beam (920 nm) was combined with the beam from the tunable laser using a dichroic mirror. The precise details of each optical component can be found in the main text. **(b)** Representative photocurrent traces at a range of different average power densities, obtained by continuous 200 ms illumination of 920 and 1100 nm at a holding potential of -60 mV. **(c)** Top: Representative traces of photo-evoked action potentials. Bottom: Mean latency and jitter calculated as the average of 5 trials in different neurons. Error bars represent the standard deviation across trials. **(d)** Representative photo evoked trains of action potentials under 1100-nm illumination at different stimulation frequencies. **(e)** Demonstration of precise elimination of single action potentials using short (15 ms) pulses of 920 nm light. Upper trace (control): electrically induced 20 Hz spike train by 10 ms injection of 400 pA current. Lower trace: suppression of electrically induced action potentials by co-incident illumination of 15 ms pulses of 920 nm light. The data presented in this figure are provided in the Source Data file.

210

133
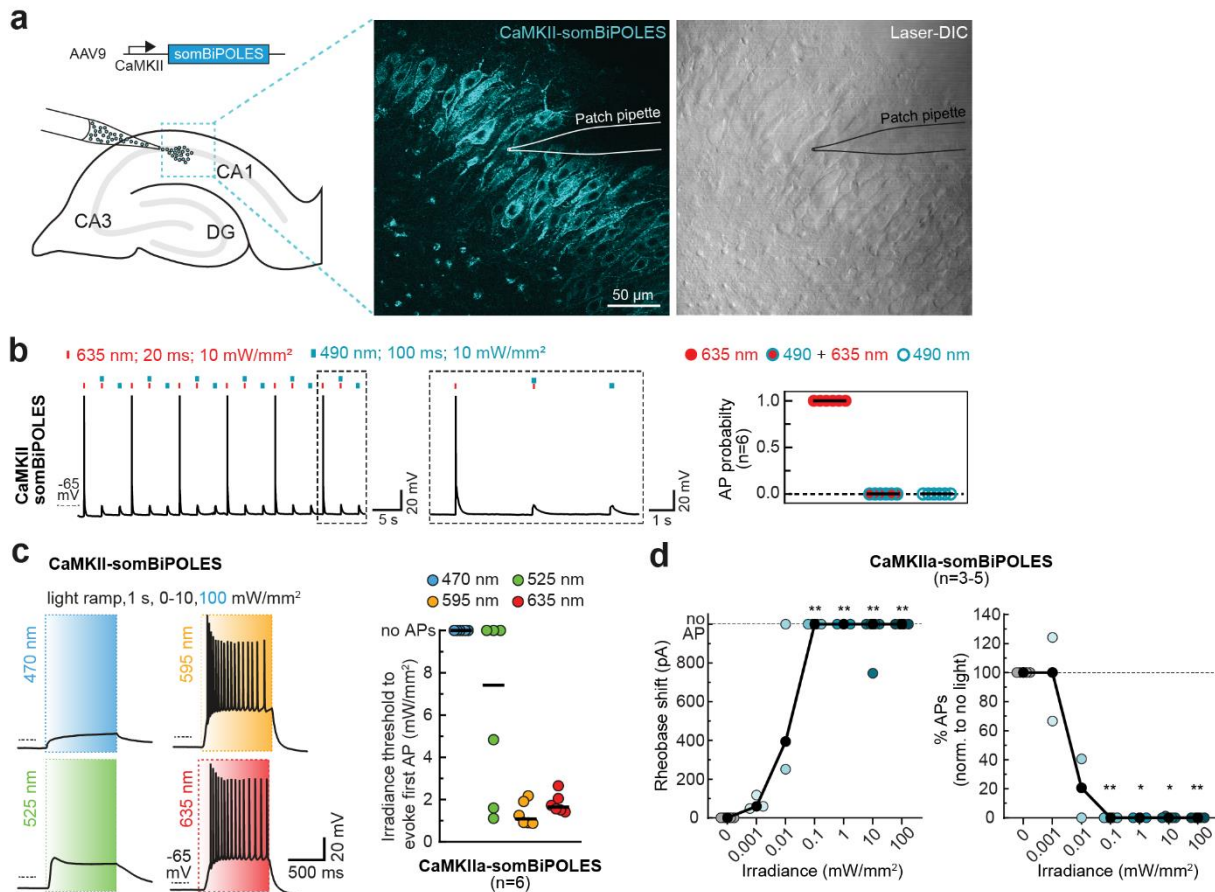
Supplementary Fig. 11. Virally expressed CaMKII-somBiPOLES enables bidirectional control of activity in projection neurons. (a) Viral transduction of CaMKII-somBiPOLES in hippocampal organotypic slice cultures. Right: Single-plane 2-photon fluorescence (cyan) and laser-DIC (gray) example images showing expression of somBiPOLES in pyramidal cells of *stratum pyramidale* and cellular morphology, respectively. The position of the patch pipette is depicted by a drawing of its outline. **(b)** IC characterization of bidirectional optical spiking-control with CaMKII-somBiPOLES. Left: Voltage traces showing red-light-evoked APs, which were blocked by a concomitant blue-light pulse. Blue light alone did not trigger APs. Right: quantification of AP probability under indicated conditions (black horizontal lines: medians, n = 6 cells). **(c)** Left: Representative membrane voltage traces measured in CaMKII-somBiPOLES-expressing pyramidal neurons. In IC experiments, light ramps were applied as indicated. Light was ramped linearly from 0 to 10 mW mm^{-2} over 1 s, except for 470 nm ramps, which were ranging to 100 mW mm^{-2} to rule out the possibility that high-irradiance blue light might still evoke APs. Right: Quantification of the irradiance threshold at which the first AP was evoked (black horizontal lines: medians, n = 6 cells). **(d)** Quantification of CaMKII-somBiPOLES-mediated neuronal silencing. Current ramps (from 0–100 to 0–900 pA) were injected into CaMKII-somBiPOLES-expressing cells to induce APs. The injected current at the time of the first AP was defined as the rheobase. Illumination with blue light of increasing irradiance (from 0.001 to 100 mW mm^{-2}) activated *Gt*ACR2-mediated Cl$^-$ currents shifting the rheobase to higher values (black circles: medians, n = 5 cells (in 3 cells rheobase shift and %APs were measured for all light irradiances, in 1 cell for 0.0 0.1, 10 and 100 mW mm^{-2}; and in 1 cell only for 0.0 and 0.1 mW mm^{-2}) , one-way Kruskal-Wallis test, **p < 0.01, **p < 0.001). The data presented in this figure and details on the statistical analysis are provided in the Source Data file.
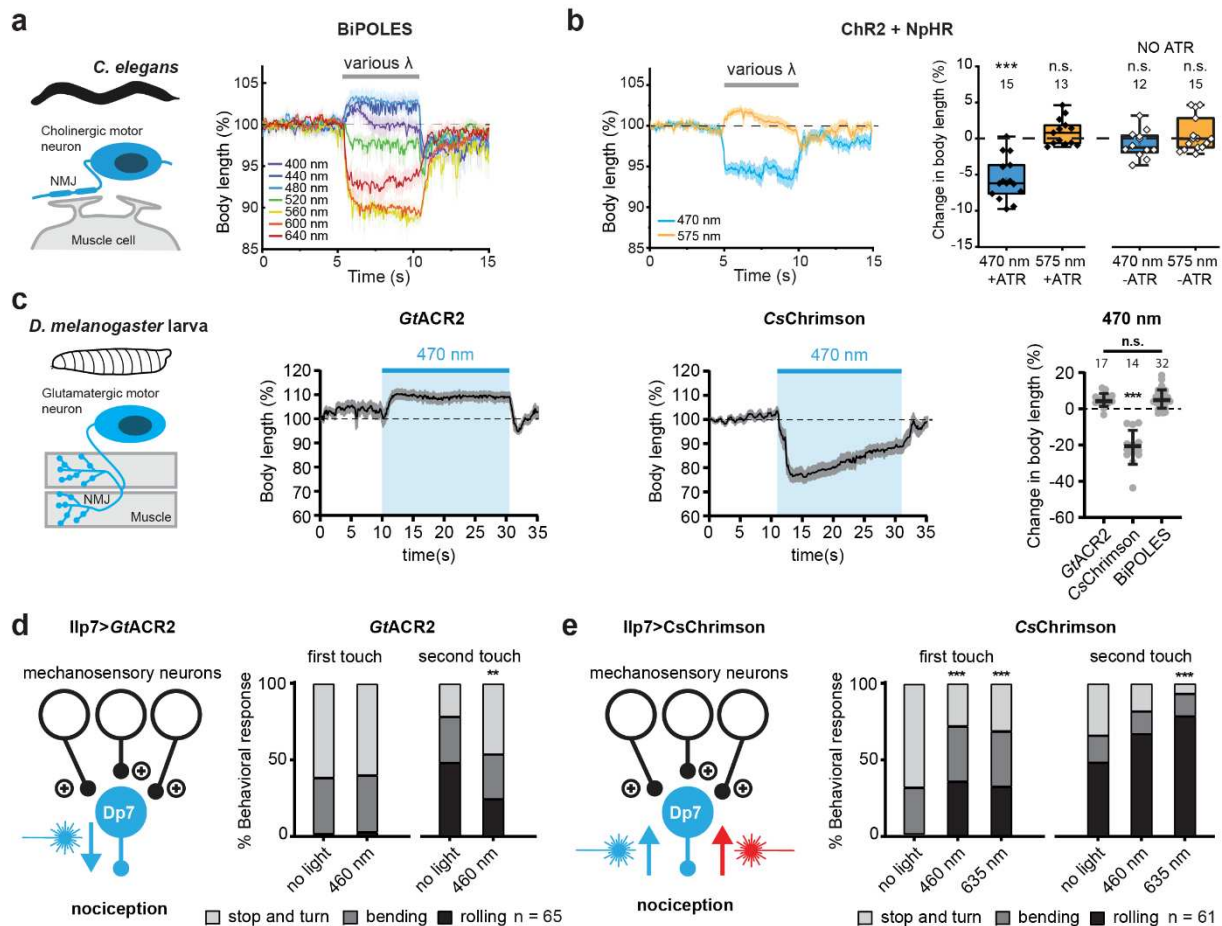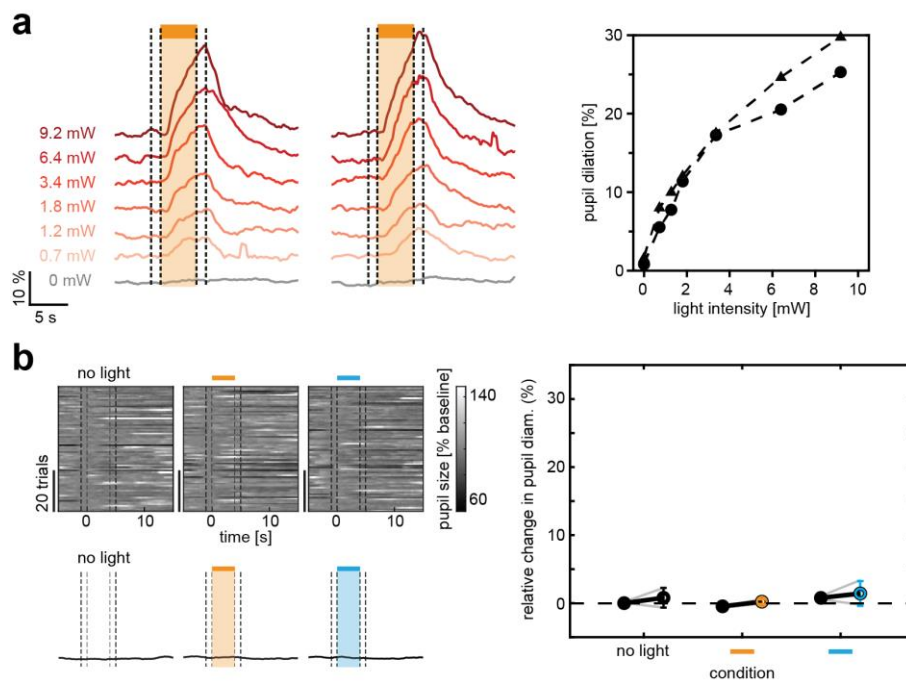
Supplementary Fig. 12. BiPOLES and controls in *C. elegans* and *D. melanogaster*. (a) Precise timing of bidirectional control of cholinergic motor neurons in *C. elegans*. Temporal dynamics of relative changes in body length upon illumination with light at wavelengths ranging from 400 to 640 nm in *C. elegans* expressing BiPOLES in cholinergic motor neurons (mean ± SEM, 1.1 mW mm^{-2}, 400 nm, n = 9; 440 nm, n = 12; 480 nm, n = 10; 520 nm, n = 12; 560 nm, n= 9; 600 nm, n = 13; 640 nm, n = 11). **(b)** Left: temporal dynamics of relative changes in body length upon illumination with light at 470 and 575 nm in *C. elegans* expressing ChR2(HR) and NpHR in cholinergic motor neurons (mean ± SEM, 1.1 mW mm^{-2}, 400 nm, n = 9; 440 nm, n = 12; 480 nm, n = 10; 520 nm, n = 12; 560 nm, n= 9; 600 nm, n = 13; 640 nm, n = 11). Right: quantification of maximal change in body length (Box: median, 1st – 3rd quartile, whiskers: 1.5x inter quartile range, ***p < 0.0001, paired, two-sided t-test, p values of comparisons of the stimulated condition (seconds 6-9 against the non-stimulated condition (seconds 0-4): 470 nm with ATR (n = 15): 6.4E-8, 575 nm with ATR (n = 13): 0.11, 470 nm without ATR (n = 12): 0.21, 575 nm without ATR (n = 15): 0.73. Note that NpHR stimulation did not lead to significant body relaxation. **(c)** *Gt*ACR2 or *Cs*Chrimson expressed alone in glutamatergic neurons of *D. melanogaster* larvae (*OK371-Gal4>UAS-GtACR2* or *UAS-CsChrimson*) result in opposite responses upon blue light stimulation. Schematic of *Gt*ACR2- or *Cs*Chrimson-expressing glutamatergic motor neuron innervating muscle fibers. Middle: Temporal dynamics of relative changes in body length upon illumination with 470 nm light (mean ± SEM, 17 μW/mm^2, n = 32). Right: Quantification of maximal change in body length (mean ± SEM, *Gt*ACR2, n = 17; *Cs*Chrimson, n = 14; BiPOLES, n = 32, ***p < 0.0001). Note that similar to BiPOLES, blue light illumination of animals expressing *Gt*ACR2 alone leads to body relaxation (BiPOLES dataset from Fig. 6d). In contrast, *Cs*Chrimson alone induces body constriction under blue light. **(d)** *Gt*ACR2 expression in Dp7 neurons in *Drosophila* larvae (*Ilp7-Gal4>UAS-GtACR2*) and behavioral response after the first and second mechanical stimulus under blue light (470 nm) compared to no light shows comparable inhibition of rolling as BiPOLES. n = 60 **p = 0.0057, X^2-test. **(e)** *Cs*Chrimson expression in Dp7 neurons (*Ilp7-Gal4>UAS-CsChrimson*) and behavioral response after the first and second mechanical stimulus under blue light (470 nm, 1.7 μmW mm^{-2}) or red light (635 nm, 2.5 μW/mm^2) illumination compared to no light. Note that unlike with BiPOLES, blue light and red light

263 increased rolling responses with *Cs*Chrimson. n = 61, ***p < 0.0001, X^2-test. The data presented in this
264 figure and details on the statistical analysis are provided in the Source Data file.

265

266

Supplementary Fig. 13. somBiPOLES controls in LC neurons. (a) The magnitude of pupil dilation
scales with the red-light irradiance. Quantification of normalized pupil size in two animals under indicated
light powers per fiber (594 nm). Dashed lines show regions used for quantification in the plot on the
right. **(b)** Pupil dilation is not altered by light applied to the LC in fiber-implanted, non-injected wild-type
animals. Quantification of normalized pupil size in one wild-type animal under various stimulation
conditions as indicated. Orange and blue bars indicate time of illumination with 594 (orange) and 473
nm (blue), respectively. Top left: single trials. Bottom left: mean ± SEM. Dashed lines show time points
used for quantification in the plot on the right. Right: quantification of relative pupil size (n = 3 mice; One-
way analysis of variance; F = 0.01, p = 0.99). The data presented in this figure and details on the
statistical analysis are provided in the Source Data file.

277
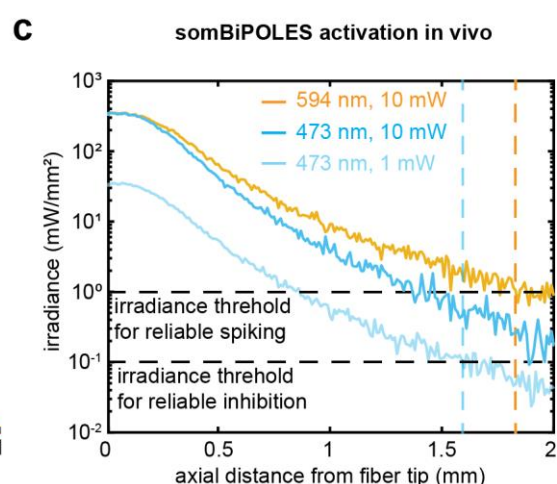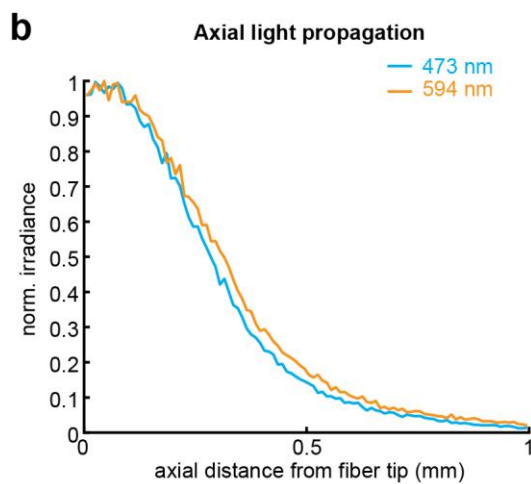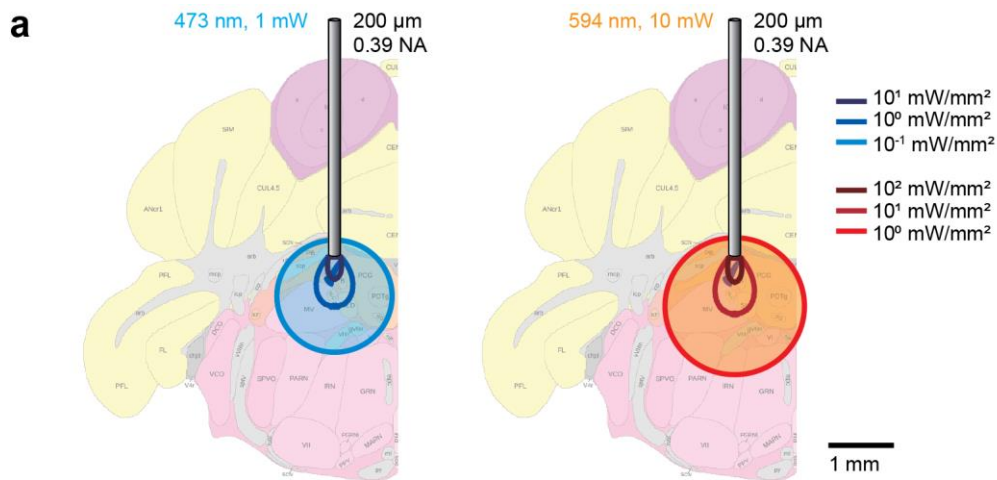
Supplementary Fig. 14. Monte-Carlo simulation of light propagation in the mouse brain to estimate somBiPOLES performance in vivo. **(a)** Simulation of light propagation (473 nm, left and 594 nm, right) from the tip of an optical fiber implanted above Locus Coeruleus in the mouse brain. Contour lines indicate interval of one log unit. **(b)** Simulation of the axial irradiance perpendicular to the fiber tip. Note the minimal differences in attenuation of blue light vs. orange light. **(c)** Estimation of reliable somBiPOLES performance under indicated light conditions. Reliable spiking of neurons can be achieved up to ~1.8 mm away from the fiber tip with 10 mW of 594 nm light. Similarly, efficient shunting of neuronal activity is achieved up to ~1.6 mm from the fiber tip with 1 mW of 473 nm light. The blue and orange irradiance thresholds required for reliable silencing and spiking are derived from Fig. 3. The data presented in this figure are provided in the Source Data file.

290
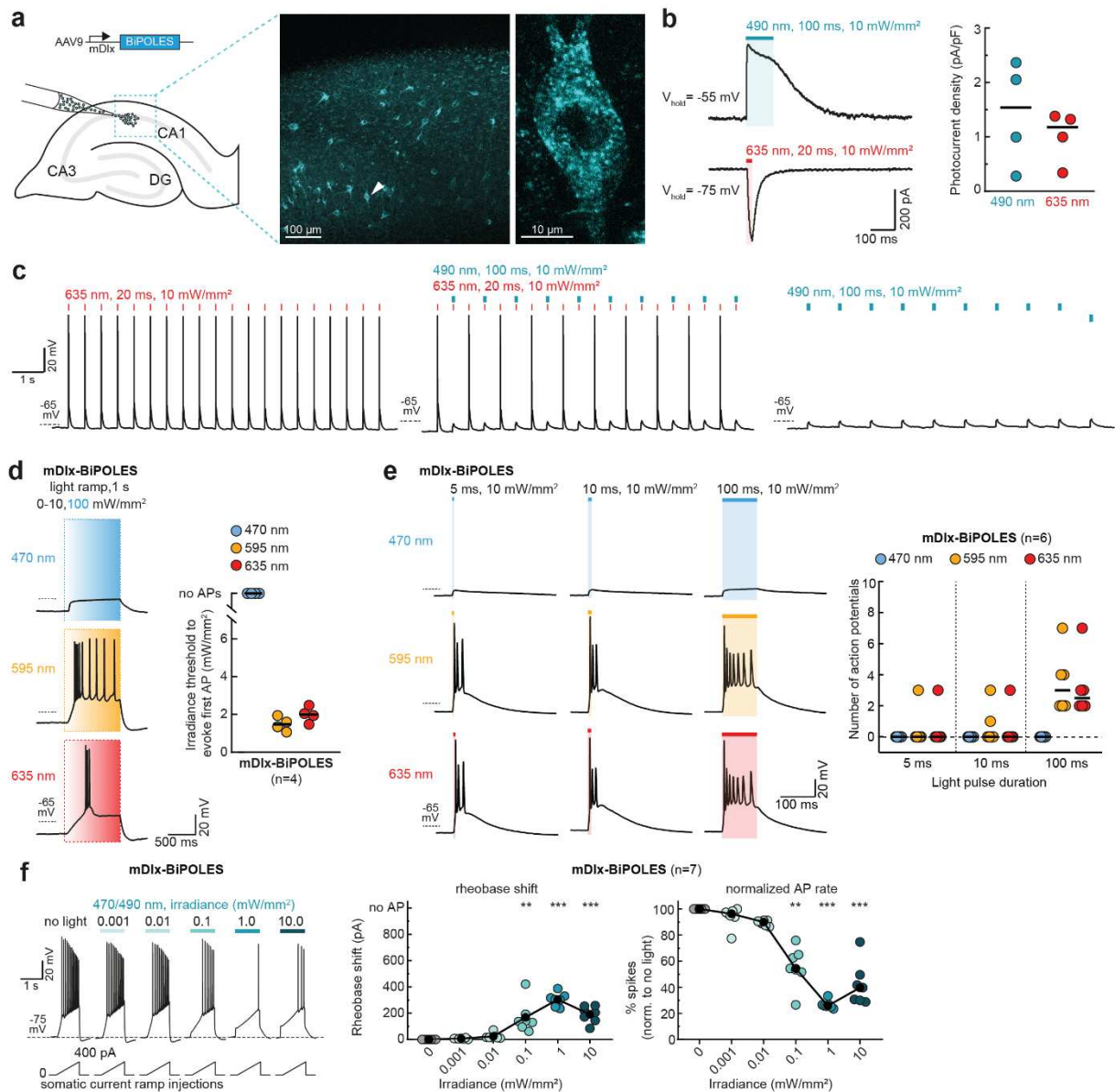
Supplementary Fig. 15. Virally expressed mDlx-BiPOLES enables bidirectional control of GABAergic neuronal activity. (a) Viral transduction of mDlx-BiPOLES in hippocampal organotypic slice cultures. Right: Representative maximum-intensity projection image of a 2-photon stack showing expression of BiPOLES in GABAergic neurons in CA1. Magnified view of a single neuron indicated by white arrowhead is shown on the right. **(b)** Left: Representative photocurrent traces measured in an mDlx-BiPOLES-expressing CA1 GABAergic neuron. Photocurrents evoked by a 490 nm light pulse (100 ms, 10 mW mm^{-2}) were recorded at a membrane voltage of -55 mV and photocurrents evoked by a 635 nm light pulse (20 ms, 10 mW mm^{-2}) were recorded at a membrane voltage of -75 mV. Right: Quantification of photocurrent densities evoked under the indicated conditions (black horizontal lines: medians, n = 4 cells). **(c)** IC characterization of bidirectional optical spiking-control with mDlx-BiPOLES. Voltage traces showing red-light-evoked APs (left), which were blocked by a concomitant blue-light pulse (middle). Blue light alone did not trigger APs (right). **(d)** Left: Representative IC membrane voltage traces measured in mDlx-BiPOLES-expressing neurons. In IC experiments, light ramps were applied as indicated. Irradiance was ramped linearly over 1 s from 0 to 10 mW mm^{-2} or to 100 mW mm^{-2} for 470 nm to rule out the possibility that high-irradiance blue light might still evoke action potentials. Right: Quantification of the irradiance threshold at which the first AP was evoked (black horizontal lines: medians, n = 4 cells) 470-nm light up to 100 mW mm^{-2} did not evoke APs in mDlx-BiPOLES-expressing cells, while 595 and 635 nm light evoked APs at irradiance levels comparable to pyramidal cells expressing BiPOLES (see Supplementary Fig. 7a,b). **(e)** Extended duration of illumination increased the

138

310 probability and number of action potentials. Left: Representative IC membrane voltage traces measured
311 in mDlx-BiPOLES-expressing neurons illuminated as indicated. Right: quantification of the number of
312 action potentials evoked by the different illumination protocols (black horizontal lines: medians, n = 6
313 cells). **(f)** Quantification of mDlx-BiPOLES-mediated neuronal silencing. Current ramps (from 0–100 to
314 0–900 pA) were injected into mDlx-BiPOLES-expressing cells to induce action potentials. The injected
315 current at the time of the first action potential was defined as the rheobase. Illumination with blue light
316 of increasing irradiance (from 0.001 to 10.0 mW mm^{-2}) activated GtACR2-mediated Cl$^-$ currents shifting
317 the rheobase to higher values. Middle: Quantification of the rheobase shift at different light intensities.
318 Right: Relative change in the number of ramp-evoked action potentials upon illumination with blue light
319 at indicated irradiance values (black circles: medians, n = 7 cells, one-way Friedman test, $**p < 0.01$,
320 $***p < 0.001$). The data presented in this figure and details on the statistical analysis are provided in the
321 Source Data file.

322

2.5 RIM and RIM-binding protein localize synaptic CaV2 channels to differentially regulate transmission in neuronal circuits

The following pages contain the preprint version of the research article "RIM and RIM-binding protein localize synaptic CaV2 channels to differentially regulate transmission in neuronal circuits"[16]. Material from: Janosi, B. *et al.* RIM and RIM-binding protein localize synaptic Cav2 channels in a differential manner to regulate transmission in neuronal circuits. *bioRxiv.* doi: https://doi.org/10.1101/2021.02.01.429206 (2021).

RIM and RIM-binding protein localize synaptic CaV2 channels to differentially regulate transmission in neuronal circuits

Barbara Jánosi[1,2,3], Jana F. Liewald[1,2,3], Szi-chieh Yu[1,2,4], Simon Umbach[1,2], Ivan C. Alcantara[1,2,5], Amelie C.F. Bergs[1,2], Martin Schneider[1,2,6], Jiajie Shao[1,2], Alexander Gottschalk[1,2,*]

1 Buchmann Institute for Molecular Life Sciences, Goethe-University, Max-von-Laue-Strasse 15, D-60438 Frankfurt, Germany

2 Department of Biochemistry, Chemistry and Pharmacy, Institute for Biophysical Chemistry, Goethe-University, Max-von-Laue-Strasse 9, D-60438 Frankfurt, Germany

3 these authors contributed equally

4 current address: Princeton Neuroscience Institute, Princeton University, Princeton, NJ 08544, USA

5 current address: National Institute of Diabetes and Digestive and Kidney Disease, National Institutes of Health, Bethesda, MD 20814, USA

6 current address: Max-Planck-Institute for Neurobiology, Department of Genes – Circuits – Behavior, Am Klopferspitz 18, D-82152 Martinsried, Germany

*Correspondence and lead contact: a.gottschalk@em.uni-frankfurt.de

Short title: RIM and RIMB-1 jointly localize the CaV2 VGCC to docked synaptic vesicles

Abstract

At chemical synapses, voltage-gated Ca^{2+}-channels (VGCCs) translate electrical signals into a trigger for synaptic vesicle (SV) fusion. VGCCs and the Ca^{2+} microdomains they elicit must be located precisely to primed SVs, to evoke rapid transmitter release. Localization is mediated by Rab3 interacting molecule (RIM) and RIM-binding proteins (RIM-BPs), which interact and bind to the C-terminus of the CaV2 VGCC α-subunit. We studied this machinery at the mixed cholinergic/GABAergic neuromuscular junction (NMJ) of *Caenorhabditis elegans*. *rimb-1* mutants had mild synaptic defects, through loosening the anchoring of UNC-2/CaV2 and delaying the onset of SV fusion. UNC-10/RIM deletion much more severely affected transmission. Even though postsynaptic depolarization was reduced, *rimb-1* mutants had increased cholinergic (but reduced GABAergic) transmission, to compensate for the delayed release. This did not occur when the excitation-inhibition balance was altered by removing GABA transmission. RIMB-1 thus may differentially regulate transmission in mixed circuits. Untethering the UNC-2/CaV2 channel by removing its C-terminal PDZ ligand exacerbated the *rimb-1* defects, and similar phenotypes resulted from acute degradation of the CaV2 β-subunit CCB-1. Therefore, untethering of the CaV2 complex is as severe as its elimination, yet does not abolish transmission, likely due to compensation by CaV1. Thus, robustness and flexibility of synaptic transmission emerges from VGCC regulation.

Keywords: synaptic vesicle cycle, active zone, RIMB-1, RBP, RIM, voltage gated Ca^{2+} channels, VGCC, CaV1, CaV2, *Caenorhabditis elegans*

1

Introduction

Neurons release chemical signals by fusion of synaptic vesicles (SVs) with the plasma membrane (Brunger et al., 2018; Sudhof, 2013). This process occurs in synaptic terminals, triggered by action potentials that activate voltage gated Ca^{2+} channels (VGCCs), which mediate a rapid, local rise in cytosolic Ca^{2+} (Nanou and Catterall, 2018). This is detected by the Ca^{2+} sensor for synchronous release, synaptotagmin, an intrinsic component of SVs (Sudhof, 2012). Protein complexes intricately organize SVs and P/Q-type VGCCs (CaV2.1 in mammals, UNC-2 in *Caenorhabditis elegans*) in the presynaptic active zone membrane, to ensure an optimal distance for rapid Ca^{2+} sensing (Acuna et al., 2015; Acuna et al., 2016; Han et al., 2011; Held et al., 2020; Hibino et al., 2002; Kaeser et al., 2011; Liu et al., 2011; Wu et al., 2019). While SNARE complexes hold the SV in a configuration ready to catalyze membrane fusion in response to the Ca^{2+} signal, the VGCC, via its C-terminal tail, is held in place by a complex of the RIM (RAB3 interacting molecule) and RIM-binding proteins (RIM-BP). RIM binds to the SV via RAB3 proteins, and to other components of the active zone protein scaffold, termed presynaptic particle web in mammals, cytomatrix of the active zone (CAZ) in *Drosophila*, or dense projection (DP) in *C. elegans* (Ackermann et al., 2015).

In recent years the function of RIMBPs (RIMB-1 in *C. elegans*) was elucidated in mammalian and *Drosophila* neurons (Acuna et al., 2015; Acuna et al., 2016; Brockmann et al., 2019; Brockmann et al., 2020; Liu et al., 2011; Muller et al., 2015). While mice lacking both neuronal RIM-BPs show no alteration in number of hippocampal synapses and evoked release per se, the fidelity of precisely timed coupling of release in response to evoked action potentials is decreased (Acuna et al., 2015). RIM-BPs anchor CaV2 in the vicinity of primed SVs, by binding the VGCC C-terminus, however, they do not affect VGCC function or kinetics. The fly mutant *drbp* shows a more severe phenotype, with reduced Ca^{2+} sensitivity of release, and a defect in presynaptic homeostatic plasticity (Liu et al., 2011; Muller et al., 2015). This is because neurons cannot upregulate their Ca^{2+} influx, an otherwise normal response to the blocking of post-synaptic transmitter receptors (Muller and Davis, 2012). In *Drosophila*, *drbp* is genetically interacting with *rim* during baseline transmission, with similar phenotypes of both mutants, and more severe phenotypes if they are combined. RIM-BP is also affecting SV recycling after extensive synaptic activity (Muller et al., 2015). The synergy of RIM and RIM-BPs is also present in mice, ensuring the anchoring of active zone VGCCs, but affecting also the assembly of the active zone protein scaffold, as well as recruitment of Munc13 proteins, which are essential for SV priming (Acuna et al., 2016; Brockmann et al., 2019; Brockmann et al., 2020). However, in mice, RIM single mutants have a more pronounced defect in recruiting and stabilizing VGCCs at synapses than RIM-BP mutants (Han et al., 2011). In *C. elegans*, RIM deletion alone affects synaptic function more severely than in mice (Koushika et al., 2001). Transgenic overexpression of *C. elegans* GFP::UNC-2 (CaV2) protein can be augmented by overexpressing RIMB-1, and in the *rimb-1*; *unc-10* (RIM) double mutants, as in mice, synaptic abundance of CaV2/UNC-2 channels is reduced (Kushibiki et al., 2019). The molecular interplay of interactions of UNC-10 and RIMB-1 in locating the UNC-2 CaV2 channel has been analyzed in mutants lacking or overexpressing various proteins of the active zone protein scaffold (Oh et al., 2021). However, how RIMB-1 and RIM affect localization of UNC-2 relative to the docked SV is not known in *C. elegans*, and the synaptic ultrastructure of the *rimb-1* mutant is yet to be analyzed. Likewise, it is not clear how absence of RIMB-1 and the likely consequent untethering of UNC-2/CaV2 channels affects synaptic properties and the characteristics of chemical transmission in *C. elegans*.

2

87   The neuromuscular junction (NMJ) of *C. elegans* is thought to be driven by graded, not action
88   potentials (Liu et al., 2009; Schultheis et al., 2011), though recent voltage imaging data suggest
89   that cholinergic neurons may also produce fast, action-potential like activities (Azimi Hashemi
90   et al., 2019). These result from activity of the premotor interneurons that are presynaptic to,
91   and induce burst activity in, cholinergic motor neurons (Liu et al., 2013). The *C. elegans* NMJ
92   is a tripartite synapse comprising cholinergic motor neurons that innervate muscle cells as well
93   as GABAergic motor neurons. The latter project to the respective contralateral (dorso-ventral)
94   side of the body to innervate opposing muscle. This circuitry orchestrates the dorso-ventral
95   undulatory locomotion, and muscles thus integrate activity of both cholinergic and GABAergic
96   inputs. Precise function of synapses in both types of neurons is required to ensure normal
97   excitation-inhibition balance, and this likely involves precise positioning of VGCCs. In fact,
98   cholinergic and GABAergic synapses exhibit a differential requirement of L- and P/Q-type
99   VGCCs (Liu et al., 2018; Tong et al., 2017).
100   Here, we set out to characterize in detail the synaptic phenotypes of *rimb-1* mutants at
101   the behavioral, physiological, and ultrastructural level, and to address molecular details of its
102   interaction with UNC-2/CaV2 channels. Despite reduced postsynaptic depolarization, *rimb-1*
103   mutants had increased, but delayed, cholinergic release, which occurred from SVs that were
104   located distal to the center of the active zone. This homeostatic change was not found when
105   inhibition at the mixed cholinergic/GABAergic NMJ was eliminated genetically. RIMB-1
106   interacts with RIM in localizing the CaV2 channel UNC-2 and we find that progressive de-
107   anchoring of the UNC-2 channel, by C-terminal truncation and/or *rimb-1* mutation, causes
108   phenotypes that resemble its deletion. RIMB-1 may differentially affect UNC-2 channels in
109   different cell types, thus regulating the outcome of circuit function at different levels.
110

Results

RIMB-1 is expressed in cholinergic and GABAergic motor neurons

113   RIMB-1, the single *C. elegans* homolog of vertebrate RIM-BPs, contains three *src*-homology
114   type III (SH3) domains, and three fibronectin type III (FN3) domains (**Fig. 1A**). RIM-BPs bind
115   to proline-rich sequences of RIM (UNC-10) and the CaV2 α1 subunit (UNC-2) via their SH3
116   domains (Hibino et al., 2002; Wu et al., 2019). RIM/UNC-10 further binds to the C-terminal end
117   of CaV2/UNC-2 via its PSD95/Discs large/Zonula occludens (PDZ) domain (Kaeser et al.,
118   2011), thus the three proteins form a tripartite complex (**Fig. 1B**). To verify the expression of
119   *rimb-1* in neurons, specifically at the NMJ, we co-expressed GFP (from the *rimb-1p* promoter,
120   3 kb upstream of the ATG) and mCherry (from the cholinergic neuron specific *unc-17p*
121   promoter; **Fig. 1C**). *rimb-1p*::GFP expressed throughout the nervous system, including motor
122   neurons in the ventral nerve cord, while *unc-17p*::mCherry was observed in a subset of
123   neurons, in which it overlapped with *rimb-1p*::GFP. Thus, *rimb-1* is likely pan-neuronal, and at
124   the NMJ, it is expressed in both cholinergic and GABAergic motor neurons.
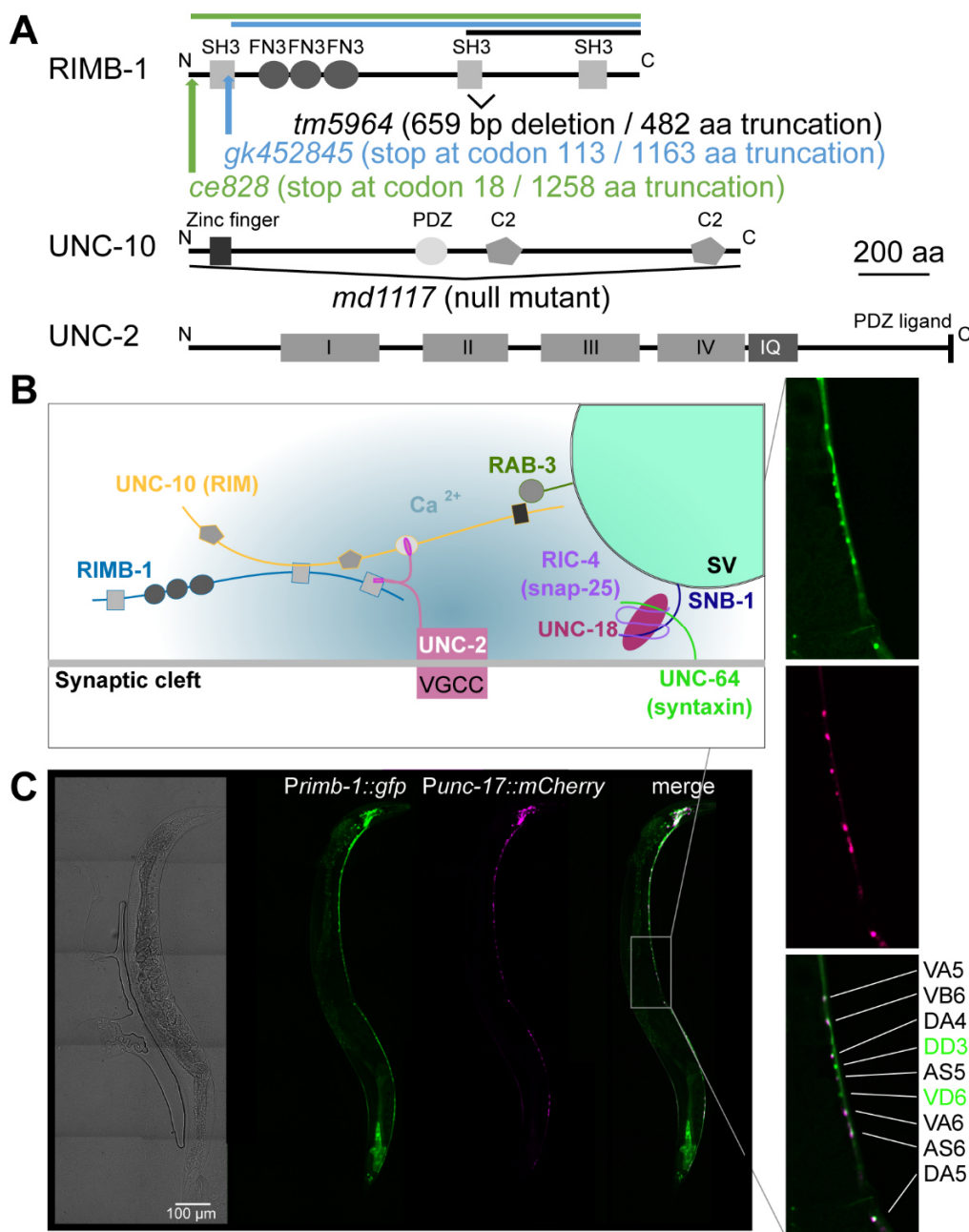
Figure 1: UNC-10/RIM and RIMB-1/RIM-binding protein affect UNC-2/CaV2 function in *C. elegans* (motor) neurons. A) Protein primary structures and sequence features (SH3 – src homology 3; FN3 – fibronectin 3; PDZ – PDZ domain; C2 – Ca^{2+} and phospholipid binding domain; I-IV – VGCC modules; IQ – IQ domain) of RIMB-1, UNC-10/RIM, and UNC-2/CaV2. Deletion sites / regions of alleles used in this work are indicated by bars or brackets. **B)** Arrangement of proteins anchoring the UNC-2 channel in the vicinity of a docked SV. **C)** Brightfield and fluorescence micrographs of an animal expressing GFP from the *rimb-1p* promoter and mCherry from the *unc-17p* promoter (cholinergic neurons). RIMB-1 appears to be pan-neuronal, and in the ventral nerve cord, is expressed in cholinergic (magenta and green) and GABAergic motor neurons (green only). Neuron designations: AS, DA, VA, VB, are cholinergic neurons required for locomotion (D, V: targeting dorsal or ventral partners); DD and VD are dorsally and ventrally innervating GABAergic motor neurons. Scale bar: 100 µm.

rimb-1 mutants exhibit reduced cholinergic transmission

We assessed possible defects in synaptic transmission of *rimb-1* animals. The *rimb-1(tm5964)* mutant has a 659 bp deletion affecting exon 14 and the preceding intron, which likely leads to a frameshift and early stop codon, resulting in a protein that misses the last 482 amino acids (**Fig. 1A**). Whether this represents a null allele is not known. In any case, this allele should

4

144

affect the interaction of RIMB-1 and UNC-10/RIM, since it is mediated by the second SH3 domain (Wang et al., 2000), as well as the interaction with the UNC-2 VGCC, mediated by the third SH3 domain. Additional deletion alleles have been reported: *gk452845* truncates the protein already after amino acid 113, while *ce828* induces an early stop at codon 18 (**Fig. 1A**; Edwards et al., 2018). We compared the *tm5964* and *ce828* alleles. First we assayed cholinergic transmission: Incubation in the acetylcholinesterase inhibitor aldicarb leads to progressive paralysis due to accumulation of acetylcholine (ACh) in the synaptic cleft and muscle hyper-contraction (Mahoney et al., 2006). *rimb-1(tm5964)* animals paralyzed significantly later than wild type controls (**Fig. S1A**), while *ce828* animals essentially paralyzed with the same kinetics as wild type. To further compare these two alleles, we measured swimming and crawling behavior (**Fig. S1B, C**). Here, *ce828* animals were slightly, but significantly impaired, while *tm5964* animals showed a stronger defect. Thus, the *tm5964* allele, which likely retains the N-terminal two thirds of the protein, exhibits a stronger phenotype than the complete deletion of RIMB-1. Also a recent publication reported normal distribution of UNC-2 VGCCs in the *rimb-1(ce828)* mutant (Oh et al., 2021). Possibly, in the absence of RIMB-1, where also other interactions of its N-terminus with unknown partners are absent, and/or due to compensatory changes, the *ce828* animals show near wild type behavior. The *gk452845* allele, retaining 113 amino acids, had a locomotion defect and aldicarb resistance, similar to *tm5964* (Kushibiki et al., 2019). Thus, we used the *tm5964* allele in all experiments.

We compared *rimb-1(tm5964)* mutants to *unc-10(md1117)* animals, as well as *rimb-1; unc-10* double mutants, and wild type controls (**Fig. 2A**). Again, *rimb-1(tm5964)* animals paralyzed significantly later than controls on 2 mM aldicarb, indicating defective ACh release. *unc-10* mutants, as well as *rimb-1; unc-10* animals, were much more compromised, not paralyzing during the time course of the assay, thus emphasizing a very strong reduction of synaptic transmission. Function of post-synaptic nicotinic acetylcholine receptors (nAChRs) was assessed by a similar paralysis assay using an agonist of the main *C. elegans* muscle nAChR: The *rimb-1* mutant was similar to wild type in the levamisole sensitivity assay, in contrast to the nAChR subunit mutant *unc-38* (**Fig. S2A**). Thus, post-synaptic nAChRs are normal in *rimb-1* animals. Second, swimming behavior (**Fig. 2B**) was compromised in *rimb-1* mutants, which showed a significant reduction of the swimming rate, while *unc-10* as well as *rimb-1; unc-10* double mutants were almost paralyzed, with *rimb-1* exacerbating the *unc-10* single mutant phenotype. Third, we assessed cholinergic function by optogenetics. We expressed channelrhodopsin-2 (ChR2) in cholinergic neurons (transgene *zxIs6*) and photostimulated them for 60 s. This causes ACh release, muscle activation, and macroscopic body contraction (Liewald et al., 2008). Body length was measured before, during, and after photostimulation (**Fig. 2C, D**). Wild type animals contracted by about 10 %, *rimb-1* mutants only by about 6 %. *rimb-1; unc-10* double mutants initially shortened like wild type, but showed a significant, progressive reduction in the contraction to about 6 %. This is indicative of synaptic fatigue, possibly due to an SV recycling defect (Kittelmann et al., 2013). *rimb-1* mutants did not behave like typical SV release mutants (e.g., synaptobrevin *snb-1*; **Fig. S2B, C**), because such mutants show increased contraction, due to a compensatory or homeostatic increase in post-synaptic excitability (Liewald et al., 2008). When we directly excited muscles via ChR2 in *snb-1* and *rimb-1* mutants (**Fig. S2D**), *snb-1* mutants contracted more than controls, while *rimb-1* animals behaved like wild type. Thus, the abnormal contraction behavior of *rimb-1* mutants, evoked by ChR2 in cholinergic neurons, must be due to complex synaptic transmission defects that could affect not only SV release, but also recycling, possibly through VGCC signaling. As RIMB-1 is expressed in cholinergic and GABAergic motor neurons, it may affect NMJ transmission through both cell types.

5

189
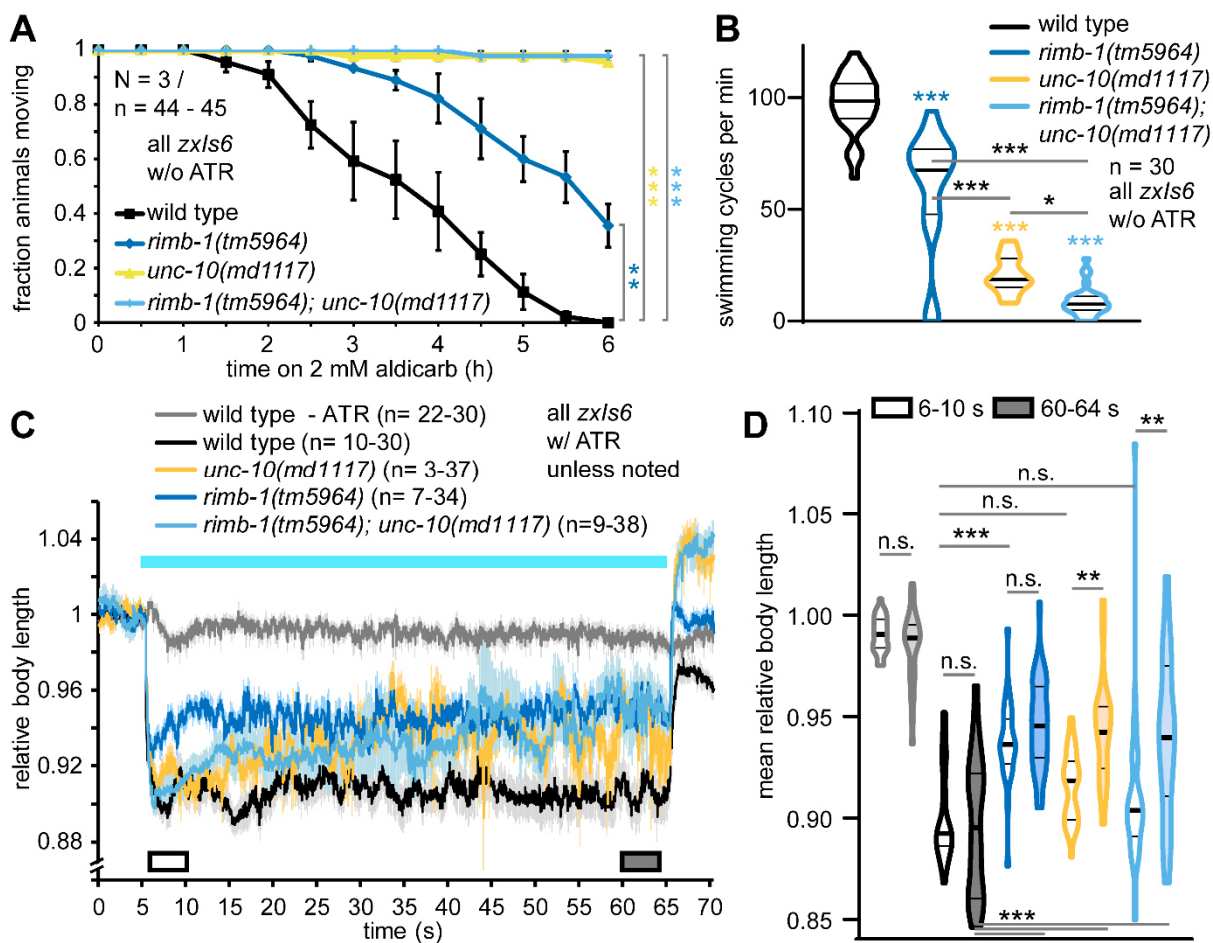
Figure 2: *rimb-1* mutants exhibit defective cholinergic transmission, locomotion and muscle activation. A)
Aldicarb paralysis assay probing cholinergic transmission; progressive paralysis is delayed in mutants. The
indicated genotypes and number of animals were scored and data from 3 experiments averaged at the indicated
time points. Mean ± s.e.m. Log rank test, Bonferroni correction. **B)** Swimming locomotion assay of the indicated
genotypes (n=30 animals each). Animals were left swimming in liquid and their full body thrashes during 1 min were
counted. Data shown as median and 25/75 quartiles (thick and thin lines), min to max. Statistical significance
determined by one-way ANOVA, Bonferroni-corrected. **C)** Photostimulated cholinergic transmission causes muscle
contraction, measured by video microscopy. Relative body length (mean ± s.e.m.) of the indicated number of
animals (note, for some time points, not all animals could be analyzed) of the indicated genotypes, before, during
and after a 1 min photostimulus (blue bar). +/-ATR: presence/absence of all-*trans* retinal, rendering ChR2 functional
(or not). White and grey boxes indicate periods for which statistical comparisons were calculated in **D)** Data in C)
(6-10 and 60-64 s) shown as median and 25/75 quartiles (thick and thin lines), min to max. One-way ANOVA, Tukey
test. In A, B, D: Statistical significance given as *p<0.05; **p<0.01; ***p<0.001.

rimb-1 mutants show delayed, but unexpectedly increased cholinergic ePSCs

To more directly assess transmission in *rimb-1(tm5964)*, *unc-10(md1117)*, and *rimb-1; unc-10*
double mutants, we recorded post-synaptic currents in patch-clamped muscle cells. We
analyzed spontaneous as well as evoked release, before and during repeated optogenetic
stimulation (*via zxls6*; **Fig. 3A**). *unc-10* and *rimb-1; unc-10* animals showed significantly
reduced miniature post-synaptic current (mPSC) frequencies, while mPSC amplitudes were
the same in all genetic backgrounds (**Fig. 3B, C**). Photostimulation evoked large PSCs
(ePSCs); however, compared to wild type, ePSC amplitudes were unexpectedly increased in
rimb-1 mutants (first stimulus; **Fig. 3D, E**), and also remained larger throughout a stimulus train
(0.5 Hz; 2-way ANOVA). In contrast, *unc-10* and *rimb-1; unc-10* animals showed significantly
reduced ePSC amplitudes. The ePSC amplitude increase in *rimb-1* mutants was contradictory

6

214 to the aldicarb and swimming assays as well as the evoked muscle contraction (**Fig. 2**), which
215 were compromised in *rimb-1* mutants.
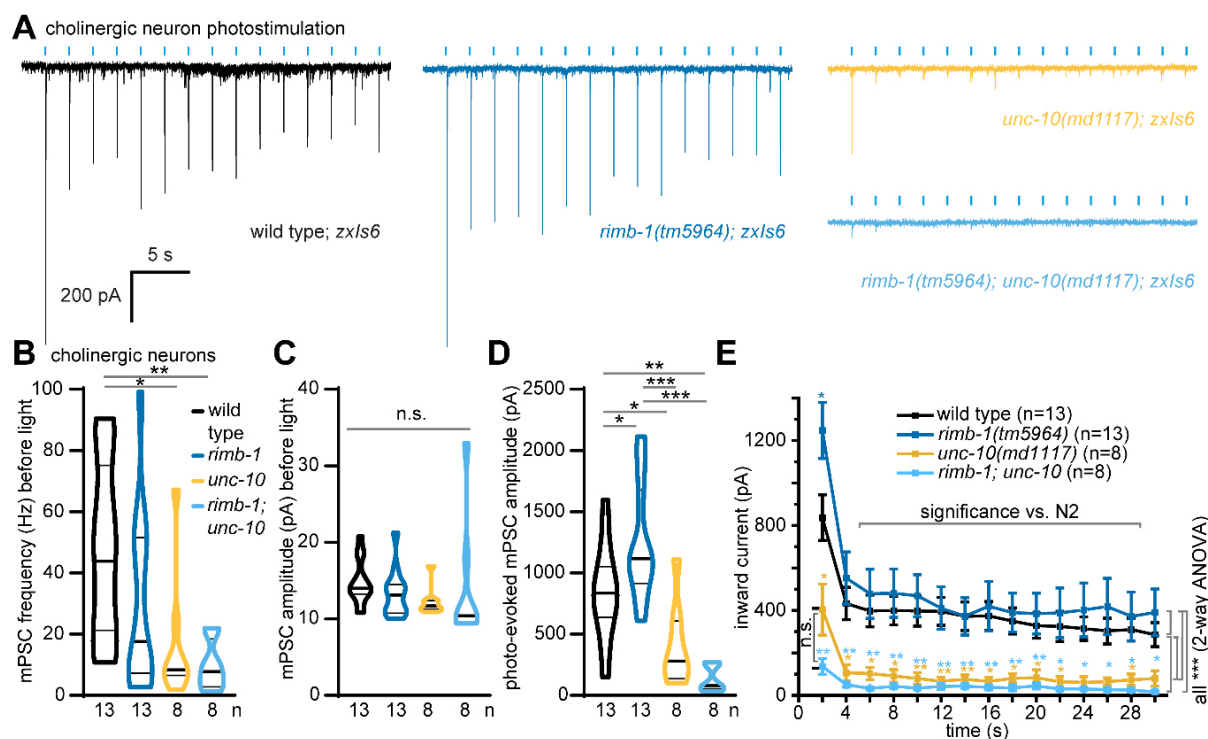
216

217 **Figure 3: *rimb-1* and unc-10/RIM mutants exhibit increased and reduced cholinergic transmission at the**
218 **NMJ. A)** Photo-stimulation of cholinergic motor neurons induces post-synaptic currents. Shown are original records
219 for the indicated genotypes, induced by 0.5 Hz, 10 ms stimuli (blue tick marks) of animals bearing transgene *zxIs6*
220 (ChR2 in cholinergic neurons, expressed from promoter *unc-17p*). **B)** Miniature post-synaptic current (mPSC)
221 frequencies and **C)** amplitudes during 30 s before first light stimulus. Data shown as median and 25/75 quartiles
222 (thick and thin lines), min to max. One-way ANOVA, Kruskall-Wallis test. **D)** Photoevoked post-synaptic current
223 (ePSC) amplitude of the first, and consecutive **E)** photostimuli (mean ± s.e.m.). One-way ANOVA with Tukey test
224 in D, and for individual stimuli in E; two-way ANOVA in E to compare entire datasets. Statistical significance given
225 as *p<0.05; **p<0.01; ***p<0.001.

226 **Delayed current onset determines reduced muscle depolarization in *rimb-1* mutants**
227 Why are ePSCs increased in *rimb-1* mutants, despite the behavioral deficits? To explore
228 possible reasons for this discrepancy, we analyzed parameters of evoked release: amplitude,
229 delay from light pulse onset to peak current (time to peak), rise and decay times, as well as
230 area under the curve (**Fig. 4A-D**). *rimb-1* mutants were delayed in their current onset and time
231 to peak, particularly if combined with the *unc-10* RIM mutant. Quantal content, calculated by
232 dividing the area under the ePSC curve by the mean area under the mPSC peak (**Fig. 4D**),
233 was significantly smaller in the *rimb-1; unc-10* mutants. Both proteins thus contribute to
234 effective synaptic transmission at the *C. elegans* NMJ, likely through jointly anchoring the UNC-
235 2/CaV2 channel to SV release sites. We wondered if the timing of postsynaptic current onset
236 may determine the outcome of muscle activation. *C. elegans* motor neurons produce bursts of
237 transmitter release, which effect muscular action potentials (Liu et al., 2013). Timing of
238 postsynaptic current events thus determines muscle activation and this is likely promoted by
239 RIMB-1. We therefore analyzed the timing of photo-evoked release (**Fig. 4E, F**), looking at the
240 first derivative (slope) of the current rise. These events were occurring 1-2 ms faster in wild
241 type than in *rimb-1* mutants. This faster release in wild type thus must affect more efficient
242 muscle activation, despite the larger currents in *rimb-1* mutants. To directly test this, we
243 employed voltage imaging in muscle (**Fig. 4G**). The archaerhodopsin variant D95N shows

7

244   voltage dependent fluorescence (Azimi Hashemi et al., 2019; Hochbaum et al., 2014; Kralj et
245   al., 2012). Imaging Arch(D95N) before, during, and after 10 s photostimulation of cholinergic
246   neurons revealed largely reduced muscle depolarization in *rimb-1* mutants, in line with the
247   behavioral defects of *rimb-1* animals. Therefore, the summed outcome of fast synchronous SV
248   fusions during evoked release is relevant for acute muscle depolarization, explaining the
249   reduced muscle activation in *rimb-1* mutants, despite larger evoked currents. The latter could
250   represent a homeostatic compensation in the mutant. However, we wondered if an alterntive
251   explanation could be provided by the specific architecture of the *C. elegans* NMJ.
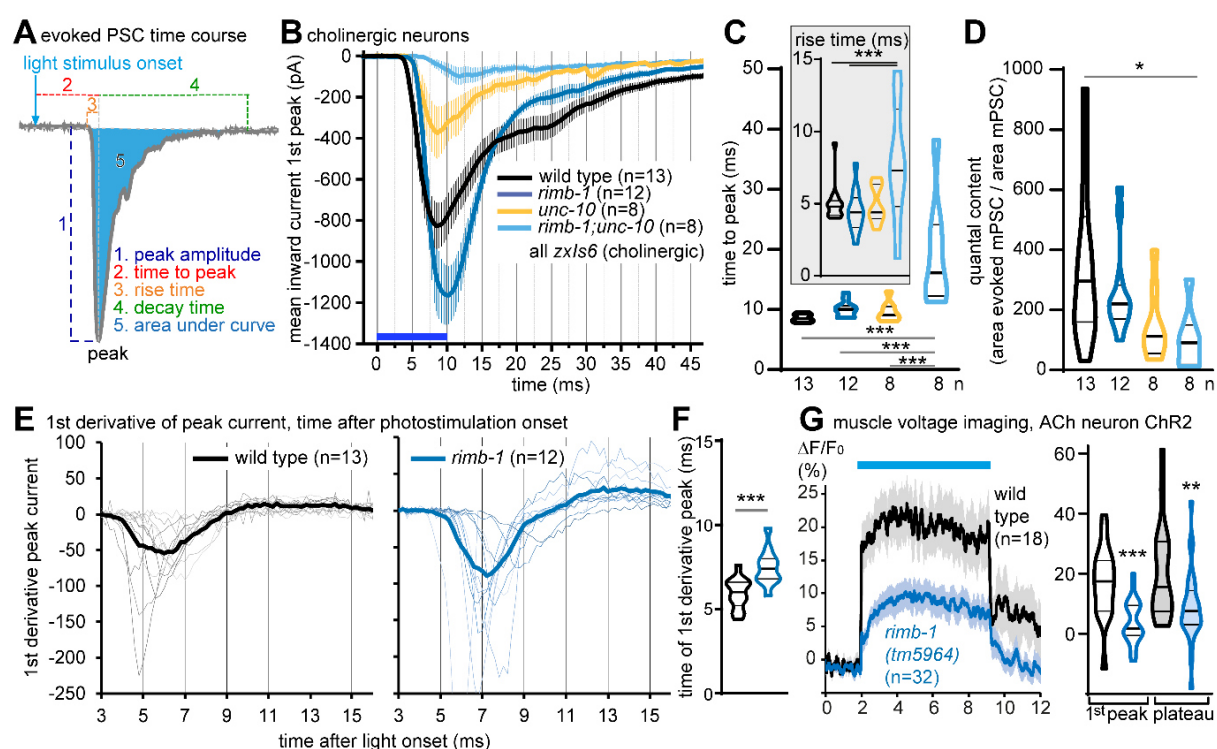
252
253 **Figure 4: Parameters of evoked transmission reveal delayed postsynaptic current onset in *rimb-1* mutants.**
254 **A)** Analysis of ePSC properties, relative to the onset of the light stimulus (blue arrow). 1: peak amplitude; 2: time
255 from light onset to peak; 3: rise time (from current onset to peak); 4: decay time (from peak to baseline); 5: area
256 under the curve (charge transfer). **B)** High-resolution analysis of first light-evoked cholinergic peak current, mean ±
257 s.e.m. **C)** Group data analysis of time to peak and rise time (inset). **D)** Quantal content, calculated as the area under
258 the curve (ePSC) divided by the mPSC area under curve, from data in Fig. 3A. One-way ANOVA and Tukey test in
259 C and Newman-Keuls test in D. **E)** Analysis of photo-evoked current slope (first derivative), to determine onset and
260 peak current rise in individual (thin traces) and mean (thick line) stimulations, in wild type and *rimb-1* mutants. Time
261 following photostimulus onset. **F)** Timing of the largest slope of the evoked currents, shown as median and 25/75
262 quartiles (thick and thin lines), min to max; unpaired t-test. **G)** Voltage imaging of muscle depolarization following
263 cholinergic photostimulation. Muscles express the Arch(D95N) voltage sensor, fluorescence increases during
264 photostimulation (blue bar); compared are wild type and *rimb-1* animals. Group data (peak response, plateau)
265 shown as median and 25/75 quartiles (thick and thin lines), min to max. One-way ANOVA, Tukey test. Statistical
266 significance given as *p<0.05; **p<0.01; ***p<0.001 in C, D, F, G.

267 **GABAergic ePSCs and summed NMJ transmission are reduced in *rimb-1* mutants**
268 *C. elegans* body wall muscles are innervated not only by cholinergic, but also by GABAergic
269 neurons (**Fig. 5A**), facilitating undulatory locomotion. Ventral (dorsal) cholinergic activity thus
270 also evokes concomitant dorsal (ventral) GABAergic inhibition of muscle. Therefore,
271 photostimulation of cholinergic neurons also evokes a GABAergic component. To address
272 RIMB-1 function in GABAergic neurons specifically, we photostimulated them using ChR2
273 expressed from the *unc-47p* promoter (transgenes *zxls3* or *zxls9*; **Fig. 5B, C; S3A, B**). Over
274 all time points, ePSCs were significantly smaller in *rimb-1; zxls3* animals (**Fig. 5C, D**), while at

8

275 the behavioral level, no significant difference to wild type was observed (**Fig. S3A, B**).
276 Normalized GABA ePSCs did not reveal any difference over time (**Fig. S3C**). The time to peak
277 was significantly delayed in *rimb-1* animals (**Fig. 5E, F**), while quantal content was unaltered
278 (**Fig. 5G**). Thus, mutation of *rimb-1* delayed transmission in both cholinergic and GABAergic
279 synapses, while it increased (ACh) or reduced (GABA) peak ePSCs. Therefore, cholinergic
280 and GABAergic synapses may be differentially affected by *rimb-1* mutation. To distinguish this,
281 we recorded spontaneous, as well as cholinergic neuron (*zxIs6*) evoked PSCs at a different
282 holding potential (-10 mV), where GABA induced currents appear as outward (**Fig. S4A**). We
283 observed a trend to reduced mPSC frequency for both ACh and GABA, and unaltered
284 amplitudes (**Fig. S4B, C**). ePSCs were delayed, and smaller in *rimb-1* mutants (**Fig. S4D-H**).
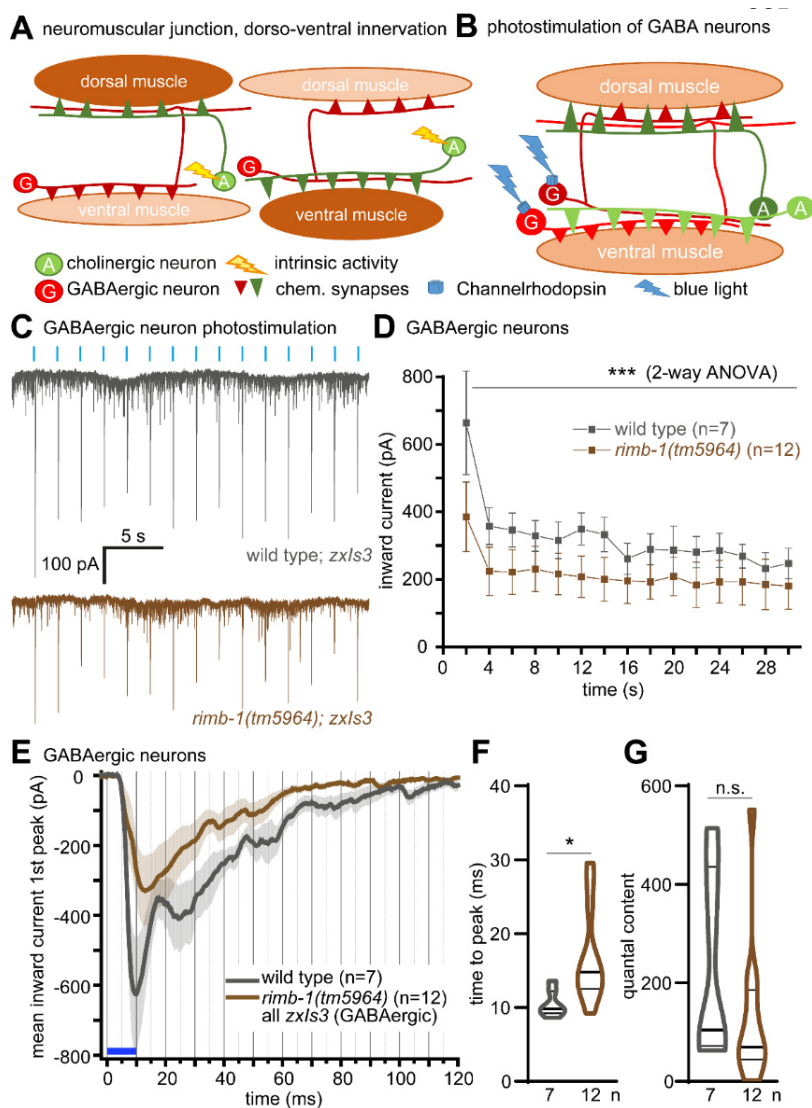

Figure 5: Lack of RIMB-1 reduces transmission from GABAergic motor neurons. A) Organization of the *C. elegans* NMJ: Reciprocal innervation of muscle by cholinergic (A, green) and GABAergic (G, red) neurons, and further contralateral innervation of GABAergic neurons by cholinergic neurons. Dorsal or ventral activity in cholinergic neurons (yellow flashes) causes concomitant GABAergic release and antagonistic inhibition, enabling undulatory locomotion. **B)** Specific optogenetic stimulation of GABAergic neurons (blue flashes). **C)** Animals carrying transgene *zxIs3*, expressing ChR2 in GABAergic neurons (promoter *unc-47p*) were photostimulated (0.5 Hz, 10 ms stimuli; blue tick marks), evoking postsynaptic currents; genotypes as indicated. Note that GABA induced currents appear as inward under the conditions used (-60 mV holding potential, specific pipette and bath solutions, see materials and methods). **D)** Repeated stimulation of GABAergic neurons (*zxIs3*), mean ± s.e.m. amplitudes of consecutive photostimuli. Two-way ANOVA. **E)** High-resolution analysis of first light-evoked GABAergic peak current, mean ± s.e.m. **F)** Group data

320 analysis of time to peak, or quantal content **G)**, calculated as the area under the curve (ePSC) divided by the mPSC
321 area under curve, from data in C. Shown as median and 25/75 quartiles (thick and thin lines), min to max. One-way
322 ANOVA and Tukey test in F and Newman-Keuls test in G. Statistical significance given as *p<0.05; ***p<0.001.

323 This is more in line with a similar role of RIMB-1 in both cholinergic and GABAergic terminals.
324 We wondered if differences in the two synapse types may be more apparent at higher
325 stimulation regimes. Previously, it was shown that cholinergic synapses depress, while
326 GABAergic synapse are facilitated at increased stimulation frequencies (Liewald et al., 2008;
327 Liu et al., 2009). We therefore compared ePSCs during 2 Hz photostimulation in cholinergic
328 (*zxIs6*) and GABAergic (*zxIs9*) neurons, in wild type and *rimb-1* mutants (**Fig. S5A-F**). At this

9

329 stimulus frequency, both cholinergic and GABAergic synapses showed a fast run down during
330 the first 3-4 pulses, and no obvious further depression. Importantly, in *rimb-1* mutants,
331 cholinergic currents were slightly increased, while GABAergic currents were reduced
332 (compared to wild type). Thus, the increased current in cholinergic synapses in *rimb-1* mutants
333 does not originate from an increased activity in concomitantly activated GABAergic synapses.

rimb-1 defects are more pronounced in the absence of GABA transmission

335 To further probe the role of *rimb-1* in GABA transmission at the NMJ, we stimulated cholinergic
336 neurons in *unc-47(e307)* mutants, lacking the vesicular GABA transporter (vGAT), and in *rimb-*
337 *1; unc-47* double mutants. vGAT mutants contracted much more than wild type, since inhibitory
338 transmission is abolished (**Fig. 6A**). In *rimb-1; unc-47* double mutants, the contractions were
339 similar to wild type, i.e. in-between the single mutants. In addition, the double mutants showed
340 a significant, progressive fatigue (i.e. SV recycling phenotype), as observed for *rimb-1* single
341 mutants, though more pronounced. Thus, the lack of GABA transmission emphasizes the role
342 of RIMB-1 in cholinergic transmission and SV recycling. mPSC frequency was significantly
343 reduced in *unc-47* and (by about 80%) in *rimb-1; unc-47* double mutants (**Fig. 6B**), and
344 likewise, mPSC amplitudes were significantly reduced in *rimb-1; unc-47* double mutants (**Fig.**
345 **6C**).

346
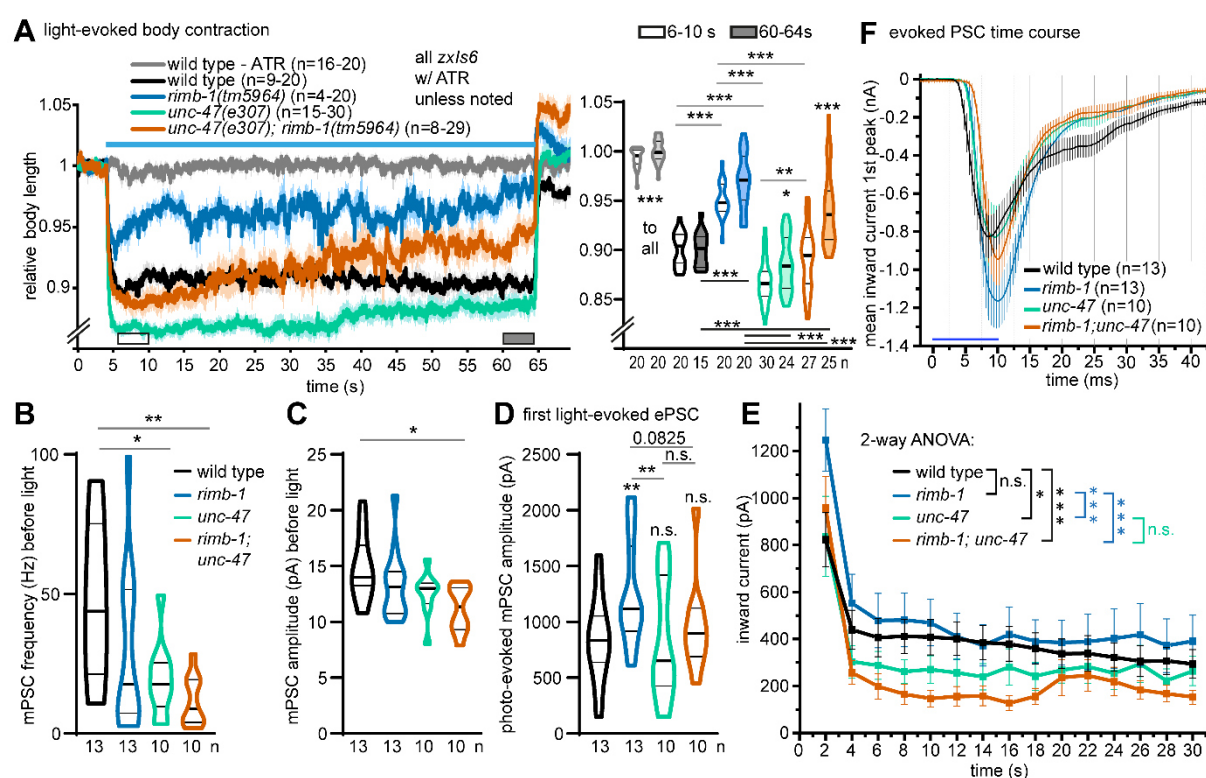
Figure 6: Lack of GABAergic transmission reverts increased cholinergic transmission in *rimb-1* mutants.
348 **A)** Left panel: Body contraction after photostimulation of cholinergic neurons (*zxIs6*). Indicated genotypes and
349 number of animals. Right panel: Group data for the 6-10 / 60-64 s time periods. Significant differences after one-
350 way ANOVA with Tukey test (for same period) and two-way ANOVA with Bonferroni correction (for different time
351 periods). **B)** mPSC frequencies and **C)** amplitudes during 30 s before first light stimulus for the indicated strains
352 expressing ChR2 in cholinergic neurons (*zxIs6*). Data shown as median and 25/75 quartiles (thick and thin lines),
353 min to max. n = number of animals. One-way ANOVA, Tukey test. **D)** Photoevoked PSC amplitude of first and **E)**
354 consecutive photostimuli (mean ± s.e.m.). One-way ANOVA, Tukey test in D; two-way ANOVA with Fisher test in
355 E. **F)** Time-course of ePSCs (first peak; blue bar: light stimulus); mean ± s.e.m. In A-E: Statistical significance given
356 as *p<0.05; **p<0.01; ***p<0.001.

357 When we analyzed photoevoked cholinergic PSCs, we observed no difference for the
358 comparison of wild type and *unc-47* mutants (**Fig. 6D-F**). This indicates that there is no relevant
359 GABA contribution to muscle currents in these experiments, likely due to severing of
360 cholinergic to GABAergic connections during the dissection. However, in the *rimb-1; unc-47*
361 double mutant, the lack of GABA negatively affected the (increased) evoked amplitudes
362 observed in *rimb-1* mutants (**Fig. 6D**): Amplitudes were not significantly different when
363 compared to wild type. We suggest that the increased cholinergic ePSCs in *rimb-1* mutants
364 reflect a homeostatic compensatory response to the temporally imprecise (delayed) cholinergic
365 transmission (**Fig. 2, 4E-G**). In the absence of GABA, since the normal excitation-inhibition
366 balance is disturbed (i.e., only excitation remains), the need for a homeostatic increase in
367 cholinergic transmission in *rimb-1* animals is gone. Therefore, *rimb-1; unc-47* animals show
368 normal evoked responses (**Fig. 6D**). In addition, *rimb-1; unc-47* mutants showed a strong
369 rundown in 0.5 Hz stimulus trains, as in the contraction assay (**Fig. 6A, E, S3D**). Thus,
370 synapses become more vulnerable to SV depletion in the absence of RIMB-1.

371 **RIMB-1 affects the location of SV fusion sites in the active zone**
372 RIMB-1, together with UNC-10/RIM, aligns UNC-2/CaV2 VGCCs with primed SVs, ensuring
373 that upon depolarization, Ca^{2+} microdomains are most effective in triggering SV fusion. Thus,
374 the site of SV fusion, but possibly also the overall arrangement of the active zone (AZ), may
375 be affected in *rimb-1* mutants. The *C. elegans* AZ harbors the dense projection (DP) at its
376 center, where SVs are thought to be recruited for priming. We analyzed the ultrastructure of
377 wild type and *rimb-1* mutant synapses by serial section transmission electron microscopy
378 (TEM) (Kittelmann et al., 2013). 40 nm thin sections of high-pressure frozen (HPF), freeze-
379 substituted and stained samples were analyzed, in resting or photostimulated animals (*zxls6*)
380 (Kittelmann et al., 2013; Steuer Costa et al., 2017; Yu et al., 2018). Following 30 s illumination
381 in animals grown in presence or absence of all-*trans* retinal (ATR; thus rendering ChR2 active
382 or inactive), total SVs, docked SVs, dense core vesicles (DCVs), and recycling-induced large
383 vesicles (LVs) were quantified (**Fig. 7A-E**). Total SVs were slightly, but significantly reduced in
384 *rimb-1* synapses, and photostimulation led to a more pronounced decrease in SV numbers in
385 *rimb-1* mutants compared to wild type (**Fig. 7B**). This is surprising, since given the reduced
386 fidelity of transmission in *rimb-1* mutants, one would expect reduced release and higher
387 numbers of (docked) SVs. Possibly RIMB-1 is also required for SV docking. Indeed, there were
388 significantly less docked SVs in *rimb-1* synapses, before and after photostimulation (**Fig. 7C**).
389 DCV numbers were not affected by *rimb-1* or photostimulation (**Fig. 7D**; note DCV release in
390 cholinergic neurons requires an increase in cAMP; Steuer Costa et al., 2017). Large vesicles,
391 i.e. endosomes induced by photostimulation, were significantly increased in wild type
392 photostimulated animals, but not in *rimb-1* synapses (**Fig. 7E**), in line with the reduced overall
393 synaptic activity observed in behavioral experiments. DP size was not significantly different in
394 wild type vs. *rimb-1* mutants, as it is in mammalian synapses (**Fig. S6A**; Acuna et al., 2016).
395   Next, we analyzed the occurrence of docked SVs along the active zone membrane, i.e.
396 their distribution relative to the DP (**Fig. 7F**). In non-stimulated synapses, docked SVs were
397 most frequently found in close proximity to the DP, i.e. within 33 nm, and this leveled off to
398 baseline between 132 and 165 nm distal to the DP. *rimb-1* mutants contained significantly
399 fewer docked SVs in the 33 nm bin, but did not differ from wild type at other distances. This
400 indicated that docked SVs distributed more distally in *rimb-1* mutants, possibly because SV
401 tethering with the UNC-10/RIM scaffold is compromised (evident also from a cumulative
402 distribution analysis; **Fig. S6B**). Upon photostimulation, wild type synapses fused SVs most
403 effectively in close proximity to the DP, while in *rimb-1* mutants this occurred more distal to the
404 DP (**Fig. 5F inset, Fig. S6B**). This is in line with putative mislocalization of UNC-2 VGCCs in

11

405 *rimb-1* mutants, e.g. more distal to the DP, where SVs may experience a higher Ca^{2+}
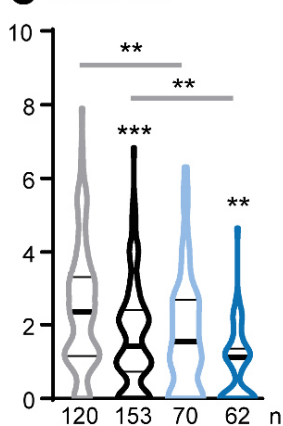406 concentration than at the DP.
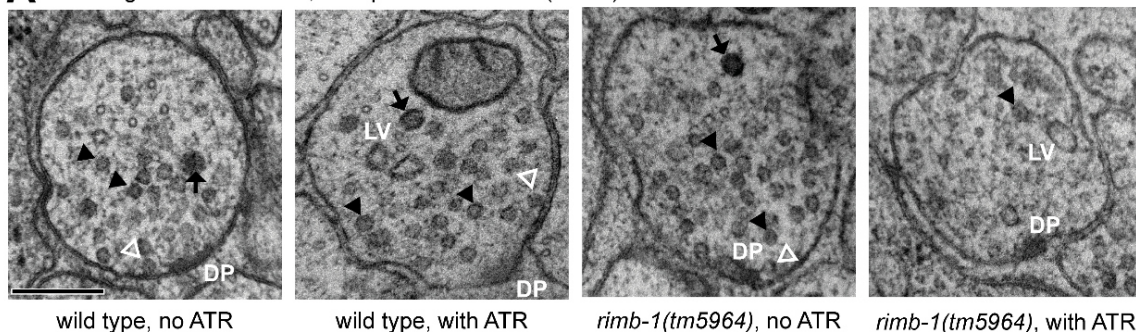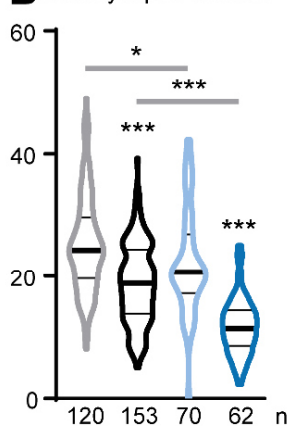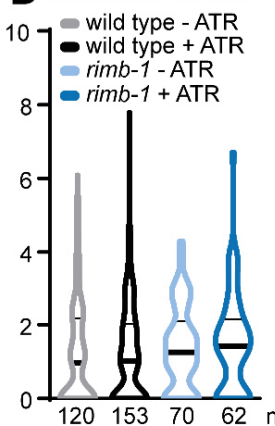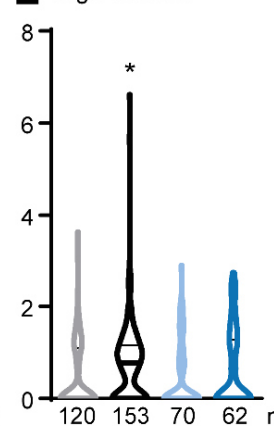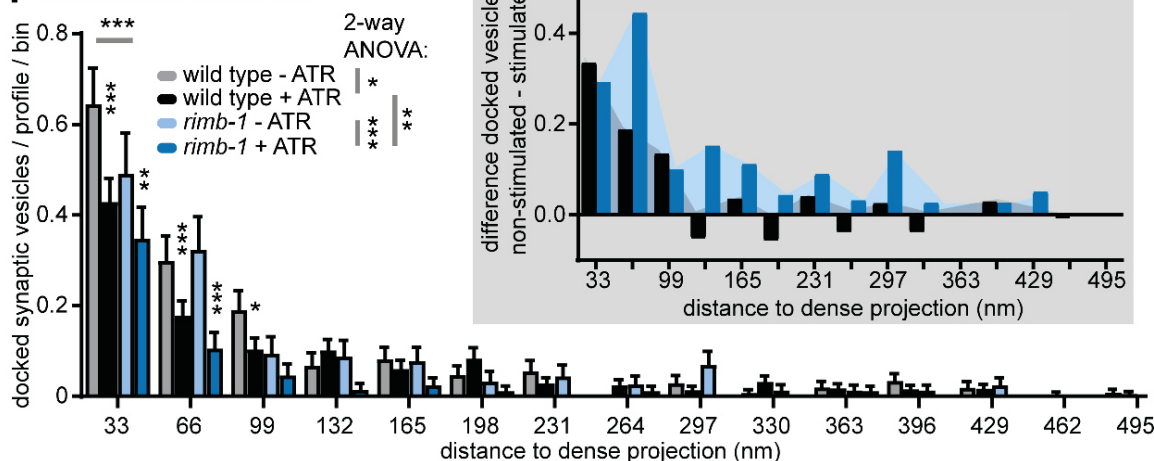
Figure 7: Electron microscopy analysis of photostimulated cholinergic *rimb-1* synapses. A) Transmission electron micrographs of cholinergic synapses expressing ChR2 (*zxIs6*), from animals that were high-pressure frozen following 30 s of photostimulation. 40 nm sections; genotype and ATR treatment indicated. Synaptic vesicles (SVs, closed arrowheads), docked SVs (open white arrowheads), dense core vesicles (DCVs, black arrows), large vesicles (LV, i.e. endosomes induced after photostimulation), and the dense projections (DP) are indicated. Scale bar is 200 nm. **B)** Quantification of all SVs, **C)** docked SVs, **D)** DCVs, and **E)** LVs, per profile. Data in B-E shown as median and 25/75 quartiles (thick and thin lines), min to max. One-way ANOVA with Kruskall-Wallis / Dunn's multiple comparison test. **F)** The distribution of distances of docked SVs to the DP (along the plasma membrane) was analyzed in 33 nm bins, for the genotypes indicated. Two-way ANOVA / Tukey test (within bins, between groups). Inset: Difference in the number of docked SVs (normalized to 33 nm bin, no ATR) in each bin without photostimulation, minus with photostimulation (i.e. showing where SVs disappeared). See also **Fig. S7B**. In B-F: Statistical significance given as *p<0.05; **p<0.01; ***p<0.001.

12

420 **Untethering P/Q type VGCCs affects transmission and counteracts the loss of RIMB-1**
421 CaV2 VGCCs are tethered to docked SVs by RIM and RIMB-1 via multiple interactions,
422 involving the SH3 and PDZ domains of RIMB-1 and RIM, respectively, which bind the UNC-
423 2/CaV2 C-terminus (**Fig. 1B, 8A**).
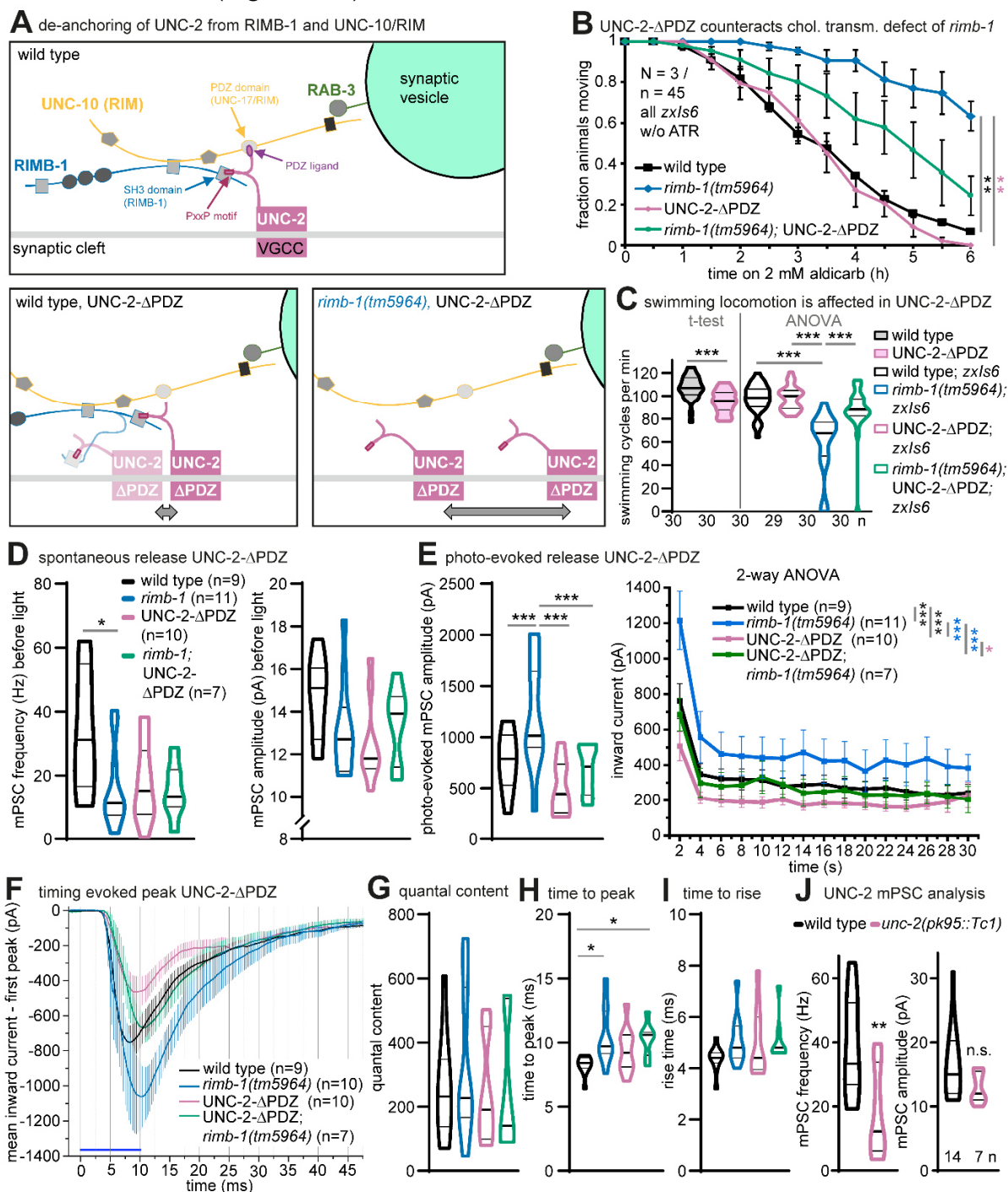
424
425 **Figure 8: Untethering the CaV2 VGCC alters synaptic transmission, exacerbated by *rimb-1* deletion. A)**
426 Upper panel: Protein-protein interactions involving the CaV2(UNC-2) VGCC and RIMB-1. UNC-2 is tethered by
427 interactions with RIMB-1 (PxxP motif bound by RIMB-1 SH3 domain) and RIM/UNC-10 (C-terminal PDZ ligand
428 bound by UNC-10 PDZ domain). Lower left panel: Removing the PDZ ligand might loosen UNC-2 tethering at the
429 docked SV site. Lower right panel: Removing RIMB-1 further untethers UNC-2-ΔPDZ. **B)** Aldicarb paralysis assay,
430 mean ± s.e.m., 3 replicates, n=15 animals each, genotypes indicated. Log rank test, Bonferroni correction. **C)**
431 Swimming assay, comparing locomotion rate in the indicated mutants, compared to wild type. Data shown as
432 median and 25/75 quartiles (thick and thin lines), min to max. T-test or one-way ANOVA with Tukey test. n = number
433 of animals tested. **D)** Electrophysiological analysis of UNC-2-ΔPDZ animals, compared to controls. mPSC frequency
434 and amplitudes, before photostimulation. One-way ANOVA, Tukey test. **E)** Photoevoked (cholinergic neurons,

435   transgene *zxIs6*) PSC amplitudes of first and consecutive stimuli. One-way ANOVA, Newman-Keuls test and two-
436   way ANOVA, Fisher test. n = number of animals tested. **F)** Time-course of first ePSC (mean ± s.e.m.) and analysis
437   of ePSC parameters **G-I)** quantal content, time to peak and time to rise. One-way ANOVA, Kruskall-Wallis test. **J)**
438   Analysis of mPSC frequency and amplitudes in *unc-2* l.o.f. mutant; T-test. One-way ANOVA, Newman-Keuls test.
439   n = number of animals. In B-E, G-J: Statistical significance given as *p<0.05; **p<0.01; ***p<0.001.

440   Thus far, we either analyzed the mild defect induced by the loss of RIMB-1 in the *tm5964* allele,
441   or the very strong defect induced by loss of UNC-10/RIM. Phenotypes of the latter are strong,
442   likely because they involve additional functions of RIM, not only UNC-2 tethering. We reasoned
443   that untethering the UNC-2 channel may achieve an intermediate phenotype and exacerbate
444   the *rimb-1* phenotype, when combined, allowing UNC-2 to diffuse even more (**Fig. 8A**). Thus
445   the UNC-2 PDZ ligand (its C-terminal 10 amino acids) was removed by CRISPR-mediated
446   genome editing; from now on we refer to this mutant as UNC-2-ΔPDZ. First, we analyzed
447   cholinergic transmission in UNC-2-ΔPDZ animals and in *rimb-1*; UNC-2-ΔPDZ double mutants
448   (**Fig. 8B**). UNC-2-ΔPDZ *per se* had no phenotype in the aldicarb assay, however, it appeared
449   to counteract rather than exacerbate the resistance phenotype of *rimb-1* mutants. UNC-2-
450   ΔPDZ animals were slightly, but significantly affected for swimming. Again, the *rimb-1*; UNC-
451   2-ΔPDZ double mutants were somewhat rescued when compared to the *rimb-1* mutants, and
452   this was similarly found for ChR2-evoked body contractions (**Fig. S7A**). Next, we analyzed
453   synaptic transmission by electrophysiology in UNC-2-ΔPDZ and *rimb-1*; UNC-2-ΔPDZ animals,
454   before and during photostimulation of cholinergic neurons (**Fig. 8D-I**). UNC-2-ΔPDZ did not
455   significantly reduce spontaneous release (mPSC rate), but it reverted the significantly reduced
456   mPSC rate of *rimb-1* animals (**Fig. 8D**), while mPSC amplitudes were not altered. Thus,
457   untethering of UNC-2 is not strongly deleterious for spontaneous activity, and it may allow the
458   VGCC to trigger SVs that it cannot efficiently reach in the *rimb-1* mutant, when it is still tethered
459   to UNC-10/RIM. However, upon photostimulation, UNC-2-ΔPDZ animals exhibited strongly
460   reduced ePSC amplitudes when compared to *rimb-1* mutants and to wild type (**Fig. 8E**). This
461   indicates that UNC-2-ΔPDZ supports spontaneous release, but fails to do so during evoked
462   activity. Possibly, the strong optogenetic stimulus requires tight coupling of UNC-2 and docked
463   SVs. UNC-2-ΔPDZ, and particularly *rimb-1*; UNC-2-ΔPDZ double mutants, were delayed in
464   their time to peak (**Fig. 8F, H**), in line with an increased distance of the VGCC to the docked
465   SV, while the rise time was unaffected (**Fig. 8I**). Quantal content was unaltered in this set of
466   mutants (**Fig. 8G**).

467   We compared effects of untethering vs. absence of UNC-2. In *unc-2(pk95::Tc1)* loss-
468   of-function mutants, mPSC frequency was largely reduced, but mPSC amplitude was
469   unaltered (**Fig. 8J**), similar to the UNC-2-ΔPDZ mutant and the *rimb-1*; UNC-2-ΔPDZ double
470   mutants (**Fig. 8D; S7B**). In contraction assays, *unc-2(pk95::Tc1)* mutants showed largely
471   reduced effects and were most similar to *rimb-1(tm5964)* mutants (**Fig. S7A, C**). Thus, the
472   absence of the channel is essentially comparable to the loss of its tethering.

473   **Acute degradation of the CaV2 channel β-subunit CCB-1 reduces synaptic transmission**
474   Because the *rimb-1* and *unc-2* mutations may induce long-lasting compensatory effects, we
475   wanted to acutely eliminate UNC-2 function, and to compare this to the completely untethered
476   UNC-2-ΔPDZ in *rimb-1* background. To this end, we used a photosensitive degron (PSD),
477   which can effectively degrade synaptic proteins within 45-60 min of mild blue illumination
478   (Hermann et al., 2015). The PSD was fused to the C-terminus of the essential VGCC β-subunit
479   CCB-1 by CRISPR-editing (**Fig. 9A**). CCB-1 is required for VGCC biogenesis and function
480   (Laine et al., 2011). Photodegradation is expected to disrupt the CCB-1 protein and to either
481   inactivate the VGCC complex, or to destabilize it and cause its disruption. 1 h photodegradation

14

482 of CCB-1::PSD caused aldicarb resistance, though only in the absence of GABAergic signaling
483 in *unc-47* mutants (likely because of an excitation-inhibition imbalance in the CCB-1::PSD
484 strain; **Fig. 9B**). Furthermore, it significantly reduced swimming, compared to illuminated wild
485 type animals, and this effect recovered after 24h (**Fig. 9C**). The mPSC frequency was
486 significantly decreased by about 75% in CCB-1::PSD animals after 1 h blue light illumination,
487 confirming acute degradation of CCB-1 (**Fig. 9D**), and was comparable to the UNC-2 deletion
488 (**Fig. 8J, S7B**). Likewise, it did not significantly affect mPSC amplitude. Thus, UNC-2 function
489 is affected by the acute degradation of the CCB-1 β-subunit, either through an effect on
490 channel properties, or by affecting stability of the channel in the plasma membrane, or both. In
491 sum, untethering of CaV2/UNC-2 could partially balance the absence of RIMB-1. Possibly, the
492 complete untethering allows diffusion of the CaV2 channel near docked SVs that are in the
493 periphery of the AZ. Since the deletion of UNC-2/CaV2 does not eliminate all transmission,
494 this implies that other VGCCs partially compensate for function at the NMJ, most likely EGL-
495 19/CaV1 L-type VGCCs, as was recently shown (Liu et al., 2018; Tong et al., 2017).

496
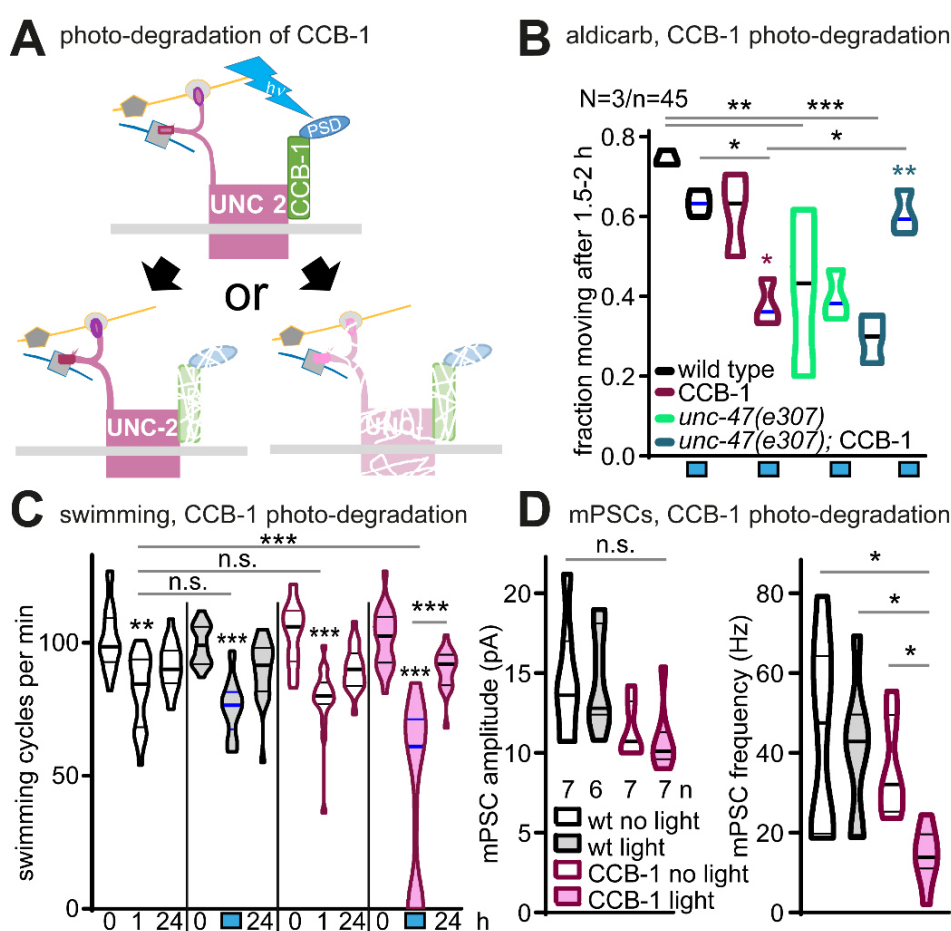
Figure 9: Acute photodegradation of the CaV2 β-subunit CCB-1 affects behavior and reduces synaptic transmission. A) Acutely inactivating (or destabilizing) UNC-2 by photodegradation of the β-subunit, CCB-1, tagged with a C-terminal photo-sensitive degron (PSD). **B)** Animals (genotype and/or treatment as indicated: CCB-1: PSD-tagged version; *unc-47* vGAT mutants; blue boxes: photostimulation for 1h) were analyzed in aldicarb (1 mM) paralysis assay. Data averaged from the 1.5-2 h time points. Two-way ANOVA with Tukey test. **C)** Swimming assay in CCB-1::PSD animals before and after photodegradation (blue bar, shaded data sets) and following 24 h recovery. Compared to wild type controls, and non-illuminated animals (non-shaded data sets). One way ANOVA with Bonferroni test within data sets (light and no light) and two-way ANOVA to compare datasets without and with illumination. **D)** mPSC analysis, frequency and amplitude, without and with CCB-1::PSD photo-degradation (1h), and wild type controls.

UNC-2/CaV2 synaptic density is reduced in the absence of RIMB-1 or the β-subunit

The de-anchoring of the UNC-2 channel via elimination of the RIMB-1 protein and the PDZ ligand at the UNC-2 C-terminus affect (i.e. increase) its mobility in the synapse, and thus likely diminish its location in vicinity of docked SVs (i.e. move it away, on average). Yet, it may also affect its overall amount in the active zone membrane. To address this, we imaged GFP::UNC-2 in nerve ring synapses (**Fig. 10A**; GFP was inserted by CRISPR in the N-terminal domain of UNC-2; strain kindly provided by Mei Zhen; Gao et al., 2018). Further, the UNC-2 PDZ ligand was deleted in this strain, and we compared both strains in wild type and *rimb-1(tm5964)* background, assessing overall nerve ring fluorescence level as well as synaptic puncta intensity and size (**Fig. 10B**). Fluorescence levels were significantly reduced in animals lacking both RIMB-1 and the UNC-2 PDZ ligand, compared to all other genotypes. This could be due to less clustering, or to overall reduction of the (synaptic) expression level of the CaV2/UNC-2. The fluorescence intensity of UNC-2 clusters was also significantly reduced without RIMB-1, and even more so by the additional deletion of the UNC-2 PDZ ligand. Cluster size was not significantly different. Thus, loss of RIMB-1 and UNC-2 anchoring reduces synaptic levels of the channel, explaining the reduced synaptic function. Alternatively, UNC-2 trafficking to the synapse is inhibited, or its localization is more diffuse.
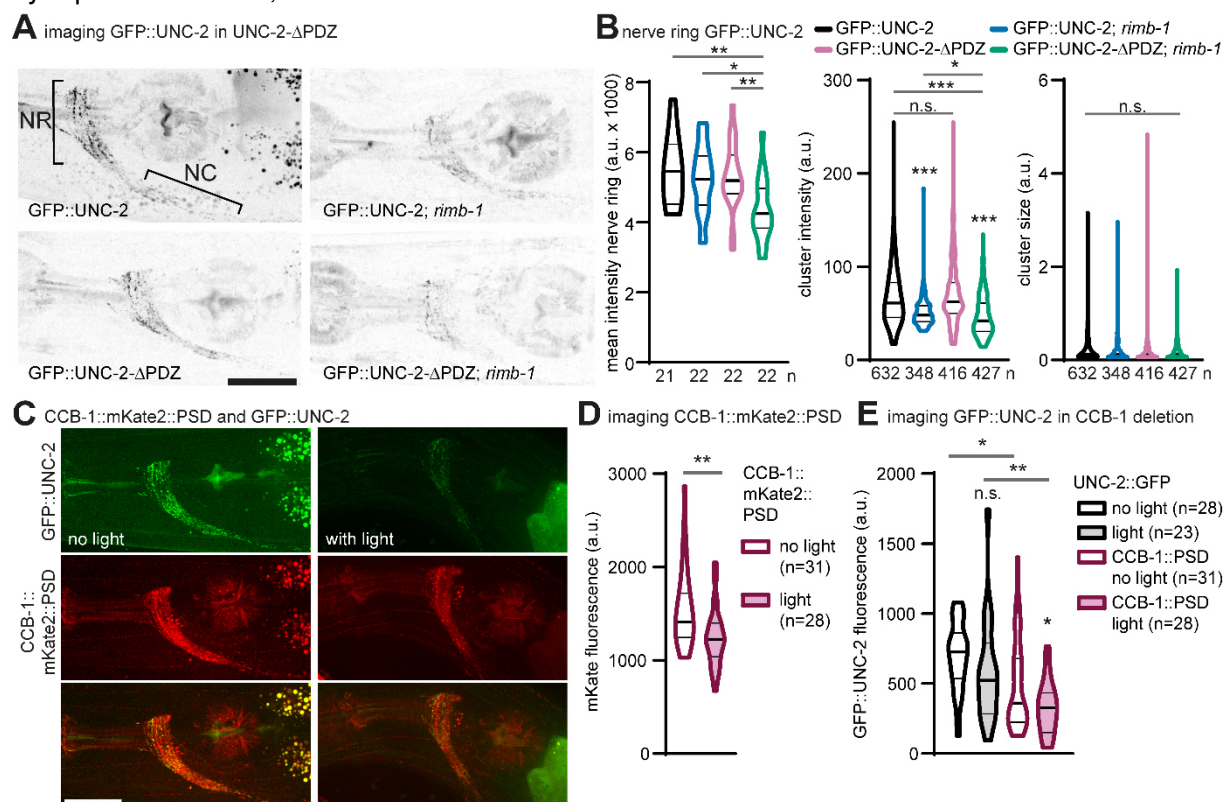
Figure 10: CaV2/UNC-2 channels are reduced at synapses in *rimb-1* mutants and after acute photodegradation of the CCB-1 β-subunit. A) Confocal z-projections of fluorescence of GFP::UNC-2 in the nerve ring (NR) and anterior ventral nerve cord (NC). Anterior is to the left, scale bar = 20 μm, genotypes as indicated. **B)** Quantification of fluorescent puncta (synaptic UNC-2 clusters) as shown in A, mean intensity of nerve ring (n= number of animals), mean cluster fluorescence and size (n= number of puncta). Data shown as median and 25/75 quartiles (thick and thin lines), min to max. One-way ANOVA with Tukey test or Kruskal-Wallis / Dunn's test. **C)** Confocal stacks of nerve ring fluorescence of GFP::UNC-2 (green) and CCB-1::mKate2::PSD (red), and overlay, before and after blue light activation of the PSD for 1 h; scale bar = 20 μm. **D)** CCB-1::mKate2::PSD fluorescence in the nerve ring, before and after blue light stimulation; n = number of animals analyzed. **E)** Quantification of GFP::UNC-2 in controls and in animals expressing CCB-1::mKate2::PSD, before and after 1 h blue illumination. Data shown as median and 25/75 quartiles (thick and thin lines), min to max. T-test or one-way ANOVA with Newman-Keuls test. In B, D: Statistical significance given as *p<0.05; **p<0.01; ***p<0.001.

537   We also assessed the effects of acute photodegradation of the CCB-1::PSD β-subunit on UNC-
538   2 abundance. GFP::UNC-2 and CCB-1::mKate2::PSD co-localized in synaptic puncta,
539   although CCB-1 was more abundant and present also at more peripheral synaptic regions
540   (**Fig. 10C**). Fluorescence of CCB-1::mKate2::PSD was significantly reduced after 1 h of blue
541   illumination (**Fig. 10D**), while GFP::UNC-2 signal was not affected by the same blue light
542   treatment (**Fig. 10E**). However, combination with CCB-1::PSD reduced GFP::UNC-2 levels in
543   the dark, and, even more, in response to blue light. Thus, absence of the β-subunit affected
544   UNC-2 function and synaptic density in a similar way as the absence of RIMB-1 and the UNC-
545   2 PDZ ligand, most likely affecting the close proximity of the P/Q-type VGCC to docked SVs.
546

Discussion

548   The fidelity and robustness of synaptic transmission depends on the precise morphology and
549   spatial organization of the active zone (Sudhof, 2013). Thus, mutations in proteins that
550   orchestrate the anchoring and tight apposition of docked SVs and CaV2 VGCCs are likely to
551   negatively affect this process. Also, such proteins are probable targets for regulation of
552   synaptic transmission, and could be utilized to set the excitation-inhibition balance also in
553   complex neural circuits (Huang et al., 2019; Liu et al., 2018). Here, we characterized in detail
554   the function of the *C. elegans* RIMB-1 protein, as well as its (functional) interaction with the
555   CaV2/UNC-2 VGCC, and determinants of VGCC localization at NMJ synapses, in cholinergic
556   and GABAergic neurons.
557   The lack of RIMB-1 function in *C. elegans* synapses had a mild phenotype on behavior
558   (swimming) and caused some resistance to the ACh esterase inhibitor aldicarb, demonstrating
559   cholinergic deficits. In response to optogenetic stimulation, the defect was also observable,
560   however, lack of UNC-10/RIM had much more severe defects. The phenotypes of the double
561   mutant were dominated by the *unc-10* defects, somewhat contradictory to an earlier report
562   (Kushibiki et al., 2019), that assessed UNC-2::GFP overexpressed from a transgene. The
563   situation in worms differs from that of the *Drosophila* NMJ, where *drbp* mutants had more
564   severe phenotypes than *rim* mutants, depending on whether baseline or plasticity inducing
565   conditions were studied (Liu et al., 2011; Muller et al., 2015).
566   Electrophysiology surprisingly showed increased transmission in *rimb-1* mutants in
567   response to cholinergic stimulation. However, voltage imaging demonstrated reduced
568   depolarization in *rimb-1* animals, in line with the behavioral defects. The likely reason for the
569   decreased depolarization in response to cholinergic neuron activation is the reduced
570   acuteness of release, which is delayed and likely not as synchronous as required to induce
571   muscular action potentials (Liu et al., 2013). Therefore, the neurons try to balance this by
572   increased output of ACh, leading to increased postsynaptic current. However, as this occurs
573   at the wrong time, it can only partially compensate the *rimb-1* mutant deficit. In support of this
574   hypothesis, we found that in mutants lacking GABA, the *rimb-1* mutant neurons performed
575   much worse. Likely, this is because the lack of inhibition leads to a lower homeostatic drive,
576   thus *rimb-1* cholinergic neurons do not upregulate their output as much. Overall, our findings
577   show a differential importance of RIMB-1 in cholinergic vs. GABAergic synapses. While
578   cholinergic synapses compensate the lack of RIMB-1 by increasing the ACh output,
579   GABAergic synapses are weakened without any obvious homeostatic response. Such
580   differential functions are also found in different central synapses in the mouse (Brockmann et
581   al., 2019). In *C. elegans*, a gain-of-function mutation in UNC-2/CaV2 can induce increased
582   cholinergic, but reduced GABA transmission, through effects on $GABA_A$ receptors, or rather,
583   GABA synapse numbers (Huang et al., 2019). Here, we probed post-synaptic nAChRs through

17

584 levamisole paralysis assays, which did not show a defect in *rimb-1* mutants. We probed
585 GABAergic synapses by direct ChR2-induced stimulation, which showed reduced currents in
586 *rimb-1* mutants. Spontaneous GABA transmission showed reduced frequency but unaltered
587 amplitudes in *rimb-1* animals. An additional layer of complexity at the *C. elegans* NMJ is given
588 by the feedback inhibition that GABAergic neurons can elicit to cholinergic motor neurons via
589 the AVA premotor interneurons (Liu et al., 2020). Also this way, reduced synaptic transmission
590 due to the lack of RIMB-1 may affect the summed outcome of NMJ transmission.
591   Mislocalization of CaV2/UNC-2 leads to lower ACh release as fewer SVs are accessed
592 by Ca^{2+}. This is supported by our analysis of spontaneous release (mPSCs), and in behavioral
593 assays. However, if CaV2/UNC-2 channels can rather freely diffuse in the synaptic membrane,
594 they may also affect SVs that are docked in regions where they would normally not fuse. When
595 optogenetic stimulation is used, which is much stronger than physiological activity during
596 spontaneous release (Liewald et al., 2008; Liu et al., 2009), the larger Ca^{2+} domains could
597 reach more docked SVs, distal to the active zone, where fusion events can still be observed
598 (Watanabe et al., 2013). This slows down transmission, as we show, but may at the same time
599 increase the amount of ACh released. The time from an optogenetic stimulus to reaching ePSC
600 peak was delayed in both cholinergic and GABAergic *rimb-1* mutant synapses; thus, as in
601 other systems (Acuna et al., 2016), RIMB-1 function is required for faithful and fast
602 transmission. Quantal content was not reduced in *rimb-1* mutants, thus even if fewer SVs were
603 released in a fast manner, overall the synapse was able to fuse normal numbers of SVs, only
604 over a prolonged time. This indicates that Ca^{2+} levels in the vicinity of SVs rise more slowly in
605 *rimb-1* mutants, but eventually reach sufficient levels to fuse SVs. As our ultrastructural
606 analysis showed, the site of release was more remote from the dense projection, likely because
607 CaV2/UNC-2 channels moved to more distal positions relative to the DP in the active zone
608 membrane.
609   The deletion of the C-terminal PDZ ligand of the UNC-2 channel, by which it is anchored
610 to RIM, had in part similar effects as the *rimb-1* mutation (mPSC frequency), in part it was less
611 (behavior), or more severe (ePSC amplitude, evoked body contraction). In combination, the
612 phenotypes of *rimb-1* and UNC-2-ΔPDZ were exacerbated or counteracted each other. This is
613 difficult to reconcile, but may again be explained by the different degree of UNC-2/CaV2 de-
614 anchoring, complex signaling in the motor circuit, spontaneous versus evoked activity and the
615 need for precise VGCC localization for the latter. The photodegradation of the CCB-1::PSD β-
616 subunit, which strongly reduced mPSC frequency and thus likely induced an acute functional
617 elimination of the CaV2 channel complex, had a similar effect as its de-anchoring. Both
618 manipulations led to a similar reduction in GFP::UNC-2 signal at nerve ring synapses, which
619 may be due to destabilization and partial loss of the channel; yet also a re-localization away
620 from synaptic regions into the axonal plasma membrane appears possible. To rigorously
621 distinguish these possibilities, further work is required. In a recent publication, RIMB-1 function
622 was assessed with respect to its role in building the synaptic cytomatrix/DP and in anchoring
623 CaV2 channels (Oh et al., 2021). These authors found a contribution of RIMB-1 and a larger
624 effect of UNC-10/RIM mutations on CaV2/UNC-2 abundance at synapses.
625   The effect of eliminating all CaV2 channels on synapse structure was analyzed in
626 mammalian synapses (Held et al., 2020). Overall synapse structure was not affected, although
627 the CaV2 β-subunit lost its localization to synaptic regions. This is in line with our findings,
628 where loss of CCB-1 also affected UNC-2 synaptic location and/or abundance, thus these
629 proteins may mutually influence each other. The authors also analyzed the deletion of the
630 entire C-terminus of murine CaV2.1, which demonstrated that it is required for channel
631 targeting to the synapse, and for triggering of efficient SV release. However, in mice, removing

18

632   only the C-terminal PDZ ligand had no functional effects on its own, apart from a slightly
633   lowered CaV2 abundance, but had to be combined with removal of the CaV2 RIM-BP binding
634   site to evoke effects. This latter situation resembles our combination of *rimb-1* and UNC-2-
635   ΔPDZ. Another study of the CaV2.1 C-terminus, however, does not observe alterations in
636   VGCC function in mice when the RIM and RIM-BP binding sites are simultaneously removed
637   (Lubbert et al., 2017). Thus, there may be species-specific differences in the regulation of the
638   CaV2 channel and its synaptic localization by binding partners.
639   Overall our work confirms the general evolutionary conservation of RIM-BP function in
640   *C. elegans*, and provides new information on how the protein regulates synaptic transmission
641   through accurate placing of CaV2 channels in the vicinity of docked SVs. It further provides
642   information on how loss of this protein affects excitation-inhibition balance in complex circuits,
643   implying that regulation of this balance may be achieved *via* RIMB-1 by differentially affecting
644   each synapse type, in this case cholinergic and GABAergic motor neurons. In the future, cell-
645   type specific determinants of RIMB-1 function, e.g. through posttranslational modification or
646   changes in expression level, will have to be revealed. Last, our work shows that de-anchoring
647   the CaV2 channel from the active zone dense projection has effects similar to its elimination.
648   The remaining transmission must be mediated by other VGCCs, most likely CaV1/EGL-19.

649

650

Materials and Methods

652   **Strains**
653   *C. elegans* wild type Bristol N2 and mutant strains were maintained on NGM plate seeded with *E. coli* OP50 as
654   described earlier (Brenner, 1974). Young adult hermaphrodites cultured at 20°C were used. Mutant alleles and
655   integrated transgenes used in this study:

656

657   *rimb-1(tm5964)*
658   **CB307**: *unc-47(e307)*
659   **KG4995:** *rimb-1(ce828)*
660   **NL735**: *unc-2(pk95::Tc1)X*
661   **NM1657**: *unc-10(md1117)*
662   **ZM9583**: *unc-2(hp858[GFP::UNC-2])* (GFP knock-in in genomic location of *unc-2*)
663   **ZX426**: *zxIs3[punc-47::ChR2(H134R)::yfp; lin-15+]*
664   **ZX460**: *zxIs6[punc-17::ChR2(H134R)::yfp; lin-15+]V*
665   **ZX531**: *unc-47(e307)III; zxIs6[punc-17::ChR2(H134R)::yfp; lin-15+]*
666   **ZX668:** *zxIs9[punc-47::ChR2(H134R)::YFP; unc-119+]*
667   **ZX1605**: *unc-2(pk95::Tc1); zxIs6[punc-17::ChR2(H134R)::yfp; lin-15+]*
668   **ZX1954**: *zxIs120[pmyo-3::Arch(D95N)::2xmyc; pmyo-3::CFP]; zxIs6[punc-17::ChR2(H134R)::yfp; lin-15+]*
669   **ZX2025**: *rimb-1(tm5964)III; zxIs6[punc-17::ChR2(H134R)::yfp; lin-15+]*
670   **ZX2271**: *ccb-1(zx3[ccb-1::mKate2::PSD])* (CRISPR knock-in of mKate2 with a photosensitive degron (PSD))
671   **ZX2320**: *ccb-1(zx3[ccb-1::mKate2::PSD]); zxIs5[punc-17::ChR2(H134R)::yfp; lin-15+]*
672   **ZX2321**: *ccb-1(zx3[ccb-1::mKate2::PSD]); unc-2(hp858[GFP::UNC-2])*
673   **ZX2340**: *unc-10(md1117); rimb-1(tm5964)*
674   **ZX2412**: *unc-10(md1117); rimb-1(tm5964); zxIs6[punc-17::ChR2(H134R)::yfp; lin-15+]*
675   **ZX2413**: *unc-10(md1117); zxIs6[punc-17::ChR2(H134R)::yfp; lin-15+]*
676   **ZX2474**: *zxEx1137[primb-1::GFP; punc-17::mCherry]*
677   **ZX2574**: *rimb-1(tm5964)III; zxIs3[punc-47::ChR2(H134R)::yfp; lin-15+]*
678   **ZX2562**: *rimb-1(tm5964)III; oxIs353[pmyo-3::ChR2::mCherry::unc-54 3'-UTR; lin15+]V*
679   **ZX2573**: *ccb-1(zx3[ccb-1::mKate2::PSD]); unc-47(e307) III.*
680   **ZX2584**: *rimb-1(tm5964); zxIs120[pmyo-3::Arch(D95N)::2xmyc; pmyo-3::CFP]; zxIs6[punc-17::ChR2(H134R)::yfp;*
681   *lin-15+]*
682   **ZX2623/PHX1749**: *unc-2(syb1749[UNC-2-ΔPDZ])* (UNC-2-ΔPDZ CRISPR deletion of 10 C-terminal amino acids)
683   **ZX2624**: *unc-2(syb1749[UNC-2-ΔPDZ]); zxIs6[punc-17::ChR2(H134R)::yfp; lin-15+]*
684   **ZX2625**:   *unc-2(syb1749[UNC-2-ΔPDZ]);   rimb-1(tm5964)III;   zxIs6[punc-*ZX2626:   *rimb-1(tm5964)III;   unc-*
685   *47(e307)III; zxIs6[punc-17::ChR2(H134R)::yfp; lin-15+]*
686   **ZX2627**: *snb-1(md247)V; oxIs353[pmyo-3::ChR2::mCherry::unc-54 3'-UTR; lin15+]V*

19

687 **ZX2691**: *unc-2(syb2088[UNC-2-ΔPDZ]); unc-2(hp858[GFP::UNC-2])*
688 **ZX2757**: *unc-2(syb1749[UNC-2-ΔPDZ])* 3x outcrossed
689 **ZX2758**: *unc-2(syb1749[UNC-2-ΔPDZ]); zxIs6[punc-17::ChR2(H134R)::yfp; lin-15+]*
690 **ZX2759**: *unc-2(syb1749[UNC-2-ΔPDZ]); rimb-1(tm5964)III; zxIs6[punc-17::ChR2(H134R)::yfp; lin-15+]*
691 **ZX2691/PHX2088**: *unc-2(syb2088[UNC-2-ΔPDZ]); unc-2(hp858[GFP::UNC-2])* (UNC-2-ΔPDZ CRISPR deletion of
692 10 C-terminal amino acids in GFP::UNC-2 insertion)
693 **ZX2824**: *rimb-1(tm5964) III; unc-2(syb2088[UNC-2-ΔPDZ]); unc-2(hp858[GFP::UNC-2])*
694 **ZX2825**: *rimb-1(tm5964) III; unc-2(hp858[GFP::UNC-2])*
695 **ZX3112**: *rimb-1(tm5964); zxIs9[punc-47::ChR2(H134R)::YFP; unc-119+]*

696 **Molecular biology**
697 To investigate the expression pattern of RIMB-1, we created *a rimb-1p::GFP* plasmid. The *rimb-1p* promoter (3 kb
698 upstream of ATG) was amplified by PCR from genomic DNA using primers oBJ76
699 (TAGCTCTTCCAGCGAGAGGACCTCCTCCTC) and oBJ77 (AGCGCTGTTGGTGACTAGGTGGTCC), was
700 inserted into vector pCS179 (*flp-1p(trc)::GFP*) containing GFP, described in (Oranth et al., 2018).
701 The strain ZX2271 *(ccb-1(zx3[ccb-1::mKate2::PSD]))* was generated using a CRISPR knock-in strategy (Dickinson
702 et al., 2015). The *C. elegans* germline was injected with a plasmid that serves as a template to transcribe a guide
703 RNA (gRNA) that targets the C-terminus-encoding sequence of *ccb-1.* The gRNA binding sequence
704 (AAGAGGTACGTACAGGTACT) was inserted into the vector pDD162 (from Addgene) using the NEB Q5 Site-
705 Directed Mutagenesis Kit. A second plasmid (pIA03) was co-injected in the germline to serve as a repair template,
706 which includes the sequences for fluorescent protein mKate2, PSD, and a self-excising cassette containing a
707 dominant visible marker for a rolling phenotype *(sqt-1(d))*, a heat shock-inducible Cre recombinase *(hs::Cre)*, and
708 hygromycin resistance gene *(hygR)*. The progeny of injected animals was selected for hygromycin resistance and
709 rolling phenotype. Animals were then heat shocked (34°C for 4 hours) to excise the cassette, thus ending up with
710 the *ccb-1::mKate2::PSD* sequence only. Successful knock-in was verified by PCR (forward primer:
711 GGGGGTACGCACATTACTG, reverse primer GGGGATGTCACAAAACGGGCTG) and Sanger sequencing
712 (primer: GCAGCAACCACAACAGCAACAAC).

713 **Behavioral assays**
714 Transgenic worms were cultivated in the dark at 20°C on nematode growth medium (NGM) with OP50-1 bacteria
715 (Brenner, 1974) without or with all-*trans* retinal (ATR; Liewald et al., 2008). Dishes containing ATR were prepared
716 by spreading 320 µl of OP50-1 culture, mixed with 0.64 µl of 100 mM ATR stock (dissolved in ethanol) onto 5.5-cm
717 dishes containing 8.2 ml of NGM. About 18 h prior to the experiments, L4 larvae, grown on ATR plates, were placed
718 on fresh ATR plates. Worms were illuminated with blue light (contraction-assay: 1.4 mW/mm^2, swimming-assay:
719 0.53 mW/mm^2) from a 50 W HBO mercury lamp, filtered through a GFP excitation filter (450–490 nm), on 5.5 cm
720 diameter dishes, under a 10× objective in a Zeiss Axiovert 40 microscope (Zeiss, Germany). The duration of
721 illumination was defined by a computer-controlled shutter (Sutter Instruments). Worms were filmed with a Powershot
722 G9 digital camera (Canon, Japan) at 640 × 480 resolution with 30 fps. The body length was determined as
723 previously described (Erbguth et al., 2012). The length values were normalized to the averaged values measured
724 before illumination (0–5 s; normalization was carried out for each animal). To exclude measurement errors (i.e.
725 when the animals body touches itself), all values below 80% were excluded and the length-profiles were averaged
726 for each strain. The experiments were repeated on 2–3 different days (worms were picked from different
727 populations); the final graphs show the average of all individual animals.
728 For analyzing swimming behavior, worms were placed into 96-well plates containing 100 µl NGM and 100 µl of M9
729 buffer per well. For analysis of the effect of CCB-1 photodegradation, animals were illuminated for 1h (470 nm, 400
730 µW, 20°C). Worms were left in M9 buffer for 15 min before the swimming-assay, then they were filmed for 60 s.
731 The swimming cycles (the animals' body bends twice per cycle), were counted manually. The swimming assays
732 were repeated on three different days, with 9–10 worms/group, picked from different populations.
733 Crawling speed was measured by the multi-worm tracker, as described previously (Swierczek et al., 2011).
734
735 **Pharmacological (Aldicarb and Levamisole) Assays**
736 To assay aldicarb sensitivity, 2 mM aldicarb dishes were prepared (Mahoney et al., 2006). After transferring the
737 animals (14–15 young adults/trial, in total three trials on three different days, with worms picked from different
738 populations) to the dishes, they were scored every 30 min by three gentle touches with a hair pick. The assays
739 were performed blinded and on the same day with the same batch of aldicarb dishes. For analysis of the effect of
740 CCB-1 photodegradation, animals were illuminated for 1h (470 nm, 100 µW, 1h, 20°C), and then incubated on 1
741 mM aldicarb plates. The data for the 1.5 and 2 h time points were averaged.
742 For levamisole assays, we used an agonist of the levamisole-sensitive nAChR of the neuromuscular junction, the
743 racemic mixture tetramisole, at 2 mM on NGM plates (corresponding to 1 mM levamisole). Animals were incubated
744 on these plates as described for the aldicarb assay, and assessed for paralysis every 30 min.

20

Electrophysiology

Electrophysiological recordings from body wall muscle cells were conducted in immobilized and dissected adult worms as described previously (Liewald et al., 2008). Animals were immobilized with Histoacryl glue (B. Braun Surgical, Spain) and a lateral incision was made to access neuromuscular junctions (NMJs) along the anterior ventral nerve cord. The basement membrane overlying body wall muscles was enzymatically removed by incubation in 0.5 mg/ml collagenase for 10 s (C5138, Sigma-Aldrich, Germany). Integrity of body wall muscle cells and nerve cord was visually examined via DIC microscopy. Recordings from body wall muscles were acquired in whole-cell patch-clamp mode at room temperature (20-22°C) using an EPC-10 amplifier equipped with Patchmaster software (HEKA, Germany). The head stage was connected to a standard HEKA pipette holder for fire-polished borosilicate pipettes (1B100F-4, Worcester Polytechnic Institute, Worcester, MA, USA) of 4-9 MΩ resistance and recordings were sampled at 3.33 kHz.

The extracellular bath solution consisted of 150 mM NaCl, 5 mM KCl, 5 mM $CaCl_2$, 1 mM $MgCl_2$, 10 mM glucose, 5 mM sucrose, and 15 mM HEPES (pH 7.3 with NaOH,~330 mOsm). The internal/patch pipette solution consisted of K-gluconate 115 mM, KCl 25 mM, $CaCl_2$ 0.1 mM, $MgCl_2$ 5 mM, BAPTA 1 mM, HEPES 10 mM, Na_2ATP 5 mM, Na_2GTP 0.5 mM, cAMP 0.5 mM, and cGMP 0.5 mM (pH 7.2 with KOH,~320 mOsm). With the solutions used, reversal potentials are about +20 mV for nicotinic ACh receptors (nAChRs) and -30 mV for $GABA_A$ receptors (Maro et al., 2015). For most experiments, recordings were conducted at a holding potential of –60 mV where nAChR-related currents (EPSCs) and $GABA_A$ receptor-related currents (IPSCs) both display as inward currents. At a holding potential of -10 mV (**Fig. S6A**), however, EPSCs and IPSCs are recorded as inward and outward currents, respectively.

Light activation was performed using an LED lamp (KSL-70, Rapp OptoElectronic, Hamburg, Germany; 470 nm, 8 mW/mm²) and controlled by the Patchmaster software. Subsequent analysis and graphing was performed using Patchmaster, and Origin (Originlabs). Analysis of mPSCs was conducted with MiniAnalysis (Synaptosoft, Decatur, GA, USA, version 6.0.7) to acquire parameters such as mPSC frequency, peak amplitude, time to peak (time from start of light stimulus until peak maximum), rise time (time from start of peak until peak maximum), decay time, and area under the curve. For the analysis of quantal content, the area under the curve of photo-evoked currents was divided by the mean area under the curve of respective mPSCs of the same animal measured before photostimulation.

Fluorescence Microscopy

For analyzing the fluorescence level of GFP::UNC-2 and CCB-1::mKate2::PSD in the nerve ring, animals were transferred onto 10% agarose pads in M9 buffer (K_2PO_4 20 mM; Na_2HPO_4 40 mM; NaCl 80 mM; $MgSO_4$ 1 mM) and immobilized with 1 µl 20 mM tetramisole hydrochloride. For the widefield fluorescence imaging of these animals, an Axiovert 200 or an Observer Z1 microscope (Zeiss, Germany) was used, equipped with a 40x/1.3 Zeiss oil objective, a 460 nm LED (Prior Scientific), a GFP filter cube (ex. 470/40 nm, em. 520/35 nm) and RFP filter cube (ex. 580/23 nm, em. 625/15). The nerve ring region was located using white transmission light. The fluorescence excitation light was turned on and a fluorescence image was captured using an EMCCD camera (Photometrics Evolve 512 Delta), gain (GFP: 68 (ZM9583), 4 (ZX2321); RFP: 20 (ZX2321, ZX2271), exposure time 50 ms (ZM9583) or 100 ms (ZX2321, ZX2271), controlled using Micro Manager software (Edelstein et al., 2014). Images were analysed using FIJI software (Schindelin et al., 2012). For quantification, a ROI was placed around the nerve ring and mean fluorescence intensity was measured. For background correction, a background value was measured in the worm's head close to the nerve ring.

Confocal Microscopy

The expression patterns of *rimb-1p*::GFP and *unc-17p::mCherry* (strain ZX2474) were analyzed using a spinning disc confocal microscope (Cell Observer SD, Zeiss, Germany), equipped with a 40x air objective (LD Plan-NEOFLUAR 40x/0.6 PH2 Kor ∞/0 1,5; Zeiss, Germany), an LED-based illumination system (excitation wavelengths 488 nm and 561 nm) and a double band pass emission filter (DBP 527/54 + 645/60, Zeiss). Micrographs were taken with an EMCCD camera (Rolera EM-C2, Teledyne QImaging). Animals were transferred onto 10% agarose pads in M9 buffer and immobilized with Polybead polystyrene 0.1 mm microspheres (Polysciences Inc., Warrington, PA, USA).

For analyzing the synaptic puncta intensity and size of GFP::UNC-2 in the nerve ring, animals were immobilized as described above (10% agarose pads in M9; 1 µl 20 mM tetramisole hydrochloride). In this case the spinning disc confocal microscope (Cell Observer SD, Zeiss, Germany), was equipped with a 63 x oil immersion objective (63 x/ 1.4 Oil DIC Plan apochromat), LED illumination (488 nm) and a 520/35 nm emission filter. Gain (150) and exposure time (1000 ms) were controlled by ZEN 2 blue software (Zeiss). Images were obtained with a Rolera EM-C2 EMCCD camera (Teledyne QImaging). After locating the nerve ring using only white light, z-stacks were acquired using a piezo focused stage (NanoScan Z, Prior Scientific). 40 images (0.5 µm spacing) were taken per animal, which were then z-projected (standard deviation) and analysed using FIJI software.

21

Electron Microscopy

Transgenic L4 worms were transferred from regular NGM dishes to freshly seeded E. coli OP50 –/+ (0.1 mM) ATR dishes 1 to 2 days before high-pressure freezing (HPF). Young adult animals were used for HPF fixation, based on methods previously described (Rostaing et al., 2004; Weimer, 2006; Kittelmann et al., 2013). Briefly, about 10–40 worms were loaded into a 100 μm deep aluminum planchette (Microscopy Services) filled with *E. coli* OP50 –/+ ATR, covered with a 0.16 mm sapphire disc and a 0.4 mm spacer ring (Engineering Office M. Wohlwend GmbH) for subsequent photostimulation. To prevent preactivation, all manipulations were done under red light. For light stimulation experiments, worms were continuously illuminated with a laser (~20 mW/mm^2) for 30 s, followed by HPF at –180°C under 2100 bar pressure in a Bal-Tec HPM010 HPF machine. A ~5 s period of manual insertion of the sample after photostimulation is required with this high pressure freezer.

After freezing, specimens were transferred under liquid nitrogen into a Reichert AFS machine (Leica) for freeze substitution. Tannic acid (0.1% in dry acetone) fixative was used to incubate samples at –90°C for 100 h. Then, a process of washing was performed, followed by an incubation of 2% OsO$_4$ for 39.5 h (in dry acetone) while slowly increasing the temperature up to room temperature. Afterwards, the process of embedding in Epoxy resin (Agar Scientific, AGAR 100 Premix kit hard) was executed with increasing concentration from 50% to 100% at room temperature and 100% at 60°C over 48 h.

For electron micrographs, cross sections were cut at a thickness of 40 nm, transferred to formvar-covered copper slot grids and counterstained in 2.5% aqueous uranyl acetate for 4 min, followed by washing with distilled water. Then, grids were carried onto Reynolds lead citrate solution for 2 min in a CO$_2$-free chamber and subsequently washed in distilled water again. Images of regions in the ventral nerve cord were taken with an Erlangshen ES500W CCD camera (Gatan) in a Philips CM12 transmission electron microscope operated at 80 kV. Images were scored blind for each condition and tagged in ImageJ (NIH). ImageJ ROIs were stored and then quantified based on methods described previously (Steuer Costa et al., 2017). The diameters of synapses from each stimulation condition vary due to the different extent of SV exocytosis or because different synapses were sampled. Thus, each value for the number of docked SVs was normalized and represents the number of docked SVs along a membrane whose perimeter is 1548 nm in a profile; the other organelles are represented as the numbers of SVs or LVs in a typical synaptic profile of 164,100 nm^2 (Steuer Costa et al., 2017). SV size was scored from 3 to 10 middle images of randomly selected synapses or from randomly selected single images per synapse for each mutant or stimulation protocol. 2–3 worms, and typically 10–19 synapses were analyzed per genotype and condition; 1–2 technical replicates were performed.

Voltage imaging

For voltage imaging experiments, ATR (Sigma-Aldrich, USA) had to be supplied to the animals. Therefore, one day prior to each experiment, transgenic L4 stage worms were transferred onto NGM plates, seeded with OP50 bacterial suspension supplemented with ATR (final ATR concentration: 0.01 mM). For imaging, animals were immobilized with polystyrene beads (0.1 μm diameter, at 2.5% w/v, Sigma-Aldrich) on top of 10 % agarose pads (in M9 buffer). Voltage-dependent fluorescence of Arch(D95N) was excited with a 637 nm red laser (OBIS FP 637LX, Coherent) at 1.8 W/mm^2 and imaged at 700 nm (700/75 ET bandpass filter, integrated in Cy5 filter cube, AHF Analysentechnik), while ChR2(H134R) was stimulated by a monochromator (Polychrome V) at 300 μW/mm^2. Imaging was performed on an inverted microscope (Zeiss Axio Observer Z1), equipped with a 40x oil immersion objective (Zeiss EC Plan-NEOFLUAR 40x/ N.A. 1.3, Oil DIC ∞ / 0.17), a laser beam splitter (HC BS R594 lambda/2 PV flat, AHF Analysentechnik), a galilean beam expander (BE02-05-A, Thorlabs) and an EMCCD Camera (Evolve 512 Delta, Photometrics).

Statistical Analysis

All quantitative data were reported as mean ± s.e.m., and n indicated the number of animals, N the number of replicates. Significance between data sets after two-tailed Student's t-test or after one-way or two-way ANOVA, with Bonferroni's multiple comparison test, Fisher test, or Tukey's post-hoc test, is given as p-value. If data was not distributed normally, we used Newman-Keuls test, or Kruskall-Wallis test with Dunn's multiple comparisons. For paralysis assays, we used the log rank test (with Bonferroni correction) to compare datasets across the duration of the experiment. The respective statistics used are indicated for each experiment in the figure legends. * signifies p<0.05, **p<0.01, and ***p<0.001. Data was analyzed and plotted in GraphPad Prism (GraphPad Software, Inc., La Jolla, CA, USA, version 8.02), Microsoft Excel 2016, or in OriginPro 2020b (OriginLab Corporation, Northampton, USA).

22

162

Acknowledgements

Author contributions

Experiments were conceived, designed, and analyzed by B.J., J.F.L., S.-c. Y., S.U., I.C.A., A.C.F.B., M.W.S., and A.G. Experiments were conducted by B.J., J.F.L., S.-c. Y., S.U., I.C.A., A.C.F.B., M.W.S., and J.S. The manuscript was written by B.J., J.F.L., and A.G. Funding was acquired by A.G.

Declaration of Interests

The authors declare no competing interests.

References

Ackermann, F., Waites, C.L., and Garner, C.C. (2015). Presynaptic active zones in invertebrates and vertebrates. EMBO Rep *16*, 923-938.

Acuna, C., Liu, X., Gonzalez, A., and Sudhof, T.C. (2015). RIM-BPs Mediate Tight Coupling of Action Potentials to Ca(2+)-Triggered Neurotransmitter Release. Neuron *87*, 1234-1247.

Acuna, C., Liu, X., and Sudhof, T.C. (2016). How to Make an Active Zone: Unexpected Universal Functional Redundancy between RIMs and RIM-BPs. Neuron *91*, 792-807.

Azimi Hashemi, N., Bergs, A.C.F., Schuler, C., Scheiwe, A.R., Steuer Costa, W., Bach, M., Liewald, J.F., and Gottschalk, A. (2019). Rhodopsin-based voltage imaging tools for use in muscles and neurons of Caenorhabditis elegans. Proc Natl Acad Sci U S A *116*, 17051-17060.

Brenner, S. (1974). The genetics of Caenorhabditis elegans. Genetics *77*, 71-94.

Brockmann, M.M., Maglione, M., Willmes, C.G., Stumpf, A., Bouazza, B.A., Velasquez, L.M., Grauel, M.K., Beed, P., Lehmann, M., Gimber, N.*, et al.* (2019). RIM-BP2 primes synaptic vesicles via recruitment of Munc13-1 at hippocampal mossy fiber synapses. eLife *8*.

Brockmann, M.M., Zarebidaki, F., Camacho, M., Grauel, M.K., Trimbuch, T., Sudhof, T.C., and Rosenmund, C. (2020). A Trio of Active Zone Proteins Comprised of RIM-BPs, RIMs, and Munc13s Governs Neurotransmitter Release. Cell reports *32*, 107960.

Brunger, A.T., Choi, U.B., Lai, Y., Leitz, J., and Zhou, Q. (2018). Molecular Mechanisms of Fast Neurotransmitter Release. Annual review of biophysics *47*, 469-497.

Dickinson, D.J., Pani, A.M., Heppert, J.K., Higgins, C.D., and Goldstein, B. (2015). Streamlined Genome Engineering with a Self-Excising Drug Selection Cassette. Genetics *200*, 1035-1049.

Edelstein, A.D., Tsuchida, M.A., Amodaj, N., Pinkard, H., Vale, R.D., and Stuurman, N. (2014). Advanced methods of microscope control using µManager software. 2014.

Edwards, S.L., Morrison, L.M., Manning, L., Stec, N., Richmond, J.E., and Miller, K.G. (2018). Sentryn Acts with a Subset of Active Zone Proteins To Optimize the Localization of Synaptic Vesicles in Caenorhabditis elegans. Genetics *210*, 947-968.

Erbguth, K., Prigge, M., Schneider, F., Hegemann, P., and Gottschalk, A. (2012). Bimodal activation of different neuron classes with the spectrally red-shifted channelrhodopsin chimera C1V1 in Caenorhabditis elegans. PLoS ONE *7*, e46827.

23

905 Gao, S., Guan, S.A., Fouad, A.D., Meng, J., Kawano, T., Huang, Y.C., Li, Y., Alcaire, S., Hung, W., Lu, Y., *et al.*
906   (2018). Excitatory motor neurons are local oscillators for backward locomotion. eLife *7*, e29915.
907 Han, Y., Kaeser, P.S., Sudhof, T.C., and Schneggenburger, R. (2011). RIM determines Ca(2)+ channel density and
908   vesicle docking at the presynaptic active zone. Neuron *69*, 304-316.
909 Held, R.G., Liu, C., Ma, K., Ramsey, A.M., Tarr, T.B., De Nola, G., Wang, S.H., Wang, J., van den Maagdenberg,
910   A.M., Schneider, T., *et al.* (2020). Synapse and Active Zone Assembly in the Absence of Presynaptic Ca2+
911   Channels and Ca2+ Entry. Neuron *107*, 1-17.
912 Hermann, A., Liewald, J.F., and Gottschalk, A. (2015). A photosensitive degron enables acute light-induced protein
913   degradation in the nervous system. Current Biology *25*, R749-R750.
914 Hibino, H., Pironkova, R., Onwumere, O., Vologodskaia, M., Hudspeth, A.J., and Lesage, F. (2002). RIM binding
915   proteins (RBPs) couple Rab3-interacting molecules (RIMs) to voltage-gated Ca(2+) channels. Neuron *34*, 411-
916   423.
917 Hochbaum, D.R., Zhao, Y., Farhi, S.L., Klapoetke, N., Werley, C.A., Kapoor, V., Zou, P., Kralj, J.M., Maclaurin, D.,
918   Smedemark-Margulies, N., *et al.* (2014). All-optical electrophysiology in mammalian neurons using engineered
919   microbial rhodopsins. Nat Methods *11*, 825-833.
920 Huang, Y.C., Pirri, J.K., Rayes, D., Gao, S., Mulcahy, B., Grant, J., Saheki, Y., Francis, M.M., Zhen, M., and Alkema,
921   M.J. (2019). Gain-of-function mutations in the UNC-2/CaV2alpha channel lead to excitation-dominant synaptic
922   transmission in Caenorhabditis elegans. eLife *8*.
923 Kaeser, P.S., Deng, L., Wang, Y., Dulubova, I., Liu, X., Rizo, J., and Sudhof, T.C. (2011). RIM proteins tether Ca2+
924   channels to presynaptic active zones via a direct PDZ-domain interaction. Cell *144*, 282-295.
925 Kittelmann, M., Liewald, J.F., Hegermann, J., Schultheis, C., Brauner, M., Steuer Costa, W., Wabnig, S., Eimer, S.,
926   and Gottschalk, A. (2013). In vivo synaptic recovery following optogenetic hyperstimulation. Proc Natl Acad Sci U
927   S A *110*, E3007-3016.
928 Koushika, S.P., Richmond, J.E., Hadwiger, G., Weimer, R.M., Jorgensen, E.M., and Nonet, M.L. (2001). A post-
929   docking role for active zone protein Rim. Nat Neurosci *4*, 997-1005.
930 Kralj, J.M., Douglass, A.D., Hochbaum, D.R., Maclaurin, D., and Cohen, A.E. (2012). Optical recording of action
931   potentials in mammalian neurons using a microbial rhodopsin. Nat Methods *9*, 90-95.
932 Kushibiki, Y., Suzuki, T., Jin, Y., and Taru, H. (2019). RIMB-1/RIM-Binding Protein and UNC-10/RIM Redundantly
933   Regulate Presynaptic Localization of the Voltage-Gated Calcium Channel in Caenorhabditis elegans. J Neurosci
934   *39*, 8617-8631.
935 Laine, V., Frokjaer-Jensen, C., Couchoux, H., and Jospin, M. (2011). The alpha1 subunit EGL-19, the alpha2/delta
936   subunit UNC-36, and the beta subunit CCB-1 underlie voltage-dependent calcium currents in Caenorhabditis
937   elegans striated muscle. J Biol Chem *286*, 36180-36187.
938 Liewald, J.F., Brauner, M., Stephens, G.J., Bouhours, M., Schultheis, C., Zhen, M., and Gottschalk, A. (2008).
939   Optogenetic analysis of synaptic function. Nat Methods *5*, 895-902.
940 Liu, H., Li, L., Wang, W., Gong, J., Yang, X., and Hu, Z. (2018). Spontaneous Vesicle Fusion Is Differentially
941   Regulated at Cholinergic and GABAergic Synapses. Cell reports *22*, 2334-2345.
942 Liu, K.S., Siebert, M., Mertel, S., Knoche, E., Wegener, S., Wichmann, C., Matkovic, T., Muhammad, K., Depner,
943   H., Mettke, C., *et al.* (2011). RIM-binding protein, a central part of the active zone, is essential for neurotransmitter
944   release. Science *334*, 1565-1569.
945 Liu, P., Chen, B., and Wang, Z.-W. (2020). GABAergic motor neurons bias locomotor decision-making in C. elegans.
946   Nature communications *11*, 5076.
947 Liu, P., Chen, B., and Wang, Z.W. (2013). Postsynaptic current bursts instruct action potential firing at a graded
948   synapse. Nature communications *4*, 1911.
949 Liu, Q., Hollopeter, G., and Jorgensen, E.M. (2009). Graded synaptic transmission at the Caenorhabditis elegans
950   neuromuscular junction. Proc Natl Acad Sci U S A *106*, 10823-10828.
951 Lubbert, M., Goral, R.O., Satterfield, R., Putzke, T., van den Maagdenberg, A.M., Kamasawa, N., and Young, S.M.,
952   Jr. (2017). A novel region in the CaV2.1 alpha1 subunit C-terminus regulates fast synaptic vesicle fusion and
953   vesicle docking at the mammalian presynaptic active zone. eLife *6*.
954 Mahoney, T.R., Luo, S., and Nonet, M.L. (2006). Analysis of synaptic transmission in Caenorhabditis elegans using
955   an aldicarb-sensitivity assay. Nat Protoc *1*, 1772-1777.
956 Maro, G.S., Gao, S., Olechwier, A.M., Hung, W.L., Liu, M., Ozkan, E., Zhen, M., and Shen, K. (2015). MADD-
957   4/Punctin and Neurexin Organize C. elegans GABAergic Postsynapses through Neuroligin. Neuron *86*, 1420-
958   1432.
959 Muller, M., and Davis, G.W. (2012). Transsynaptic control of presynaptic Ca(2)(+) influx achieves homeostatic
960   potentiation of neurotransmitter release. Curr Biol *22*, 1102-1108.
961 Muller, M., Genc, O., and Davis, G.W. (2015). RIM-binding protein links synaptic homeostasis to the stabilization
962   and replenishment of high release probability vesicles. Neuron *85*, 1056-1069.
963 Nanou, E., and Catterall, W.A. (2018). Calcium Channels, Synaptic Plasticity, and Neuropsychiatric Disease.
964   Neuron *98*, 466-481.
965 Oh, K.H., Krout, M.D., Richmond, J.E., and Kim, H. (2021). UNC-2 CaV2 Channel Localization at Presynaptic Active
966   Zones Depends on UNC-10/RIM and SYD-2/Liprin-alpha in Caenorhabditis elegans. J Neurosci *41*, 4782-4794.
967 Oranth, A., Schultheis, C., Tolstenkov, O., Erbguth, K., Nagpal, J., Hain, D., Brauner, M., Wabnig, S., Steuer Costa,
968   W., McWhirter, R.D., *et al.* (2018). Food Sensation Modulates Locomotion by Dopamine and Neuropeptide
969   Signaling in a Distributed Neuronal Network. Neuron *100*, 1414-1428 e1410.
970 Schindelin, J., Arganda-Carreras, I., Frise, E., Kaynig, V., Longair, M., Pietzsch, T., Preibisch, S., Rueden, C.,
971   Saalfeld, S., Schmid, B., *et al.* (2012). Fiji: an open-source platform for biological-image analysis. Nature Methods
972   *9*, 676-682.

24

973 Schultheis, C., Brauner, M., Liewald, J.F., and Gottschalk, A. (2011). Optogenetic analysis of GABAB receptor
974   signaling in Caenorhabditis elegans motor neurons. J Neurophysiol *106*, 817-827.
975 Steuer Costa, W., Yu, S.C., Liewald, J.F., and Gottschalk, A. (2017). Fast cAMP Modulation of Neurotransmission
976   via Neuropeptide Signals and Vesicle Loading. Curr Biol *27*, 495-507.
977 Sudhof, T.C. (2012). Calcium control of neurotransmitter release. Cold Spring Harb Perspect Biol *4*, a011353.
978 Sudhof, T.C. (2013). Neurotransmitter release: the last millisecond in the life of a synaptic vesicle. Neuron *80*, 675-
979   690.
980 Swierczek, N.A., Giles, A.C., Rankin, C.H., and Kerr, R.A. (2011). High-throughput behavioral analysis in C.
981   elegans. Nat Methods *8*, 592-598.
982 Tong, X.J., Lopez-Soto, E.J., Li, L., Liu, H., Nedelcu, D., Lipscombe, D., Hu, Z., and Kaplan, J.M. (2017). Retrograde
983   Synaptic Inhibition Is Mediated by alpha-Neurexin Binding to the alpha2delta Subunits of N-Type Calcium
984   Channels. Neuron *95*, 326-340 e325.
985 Wang, Y., Sugita, S., and Sudhof, T.C. (2000). The RIM/NIM family of neuronal C2 domain proteins. Interactions
986   with Rab3 and a new class of Src homology 3 domain proteins. J Biol Chem *275*, 20033-20044.
987 Watanabe, S., Liu, Q., Davis, M.W., Hollopeter, G., Thomas, N., Jorgensen, N.B., and Jorgensen, E.M. (2013).
988   Ultrafast endocytosis at Caenorhabditis elegans neuromuscular junctions. eLife *2*, e00723.
989 Wu, X., Cai, Q., Shen, Z., Chen, X., Zeng, M., Du, S., and Zhang, M. (2019). RIM and RIM-BP Form Presynaptic
990   Active-Zone-like Condensates via Phase Separation. Molecular Cell *73*, 971-984.e975.
991 Yu, S.C., Janosi, B., Liewald, J.F., Wabnig, S., and Gottschalk, A. (2018). Endophilin A and B Join Forces With
992   Clathrin to Mediate Synaptic Vesicle Recycling in Caenorhabditis elegans. Frontiers in molecular neuroscience
993   *11*, 196.

25

Supplemental Figures and Legends
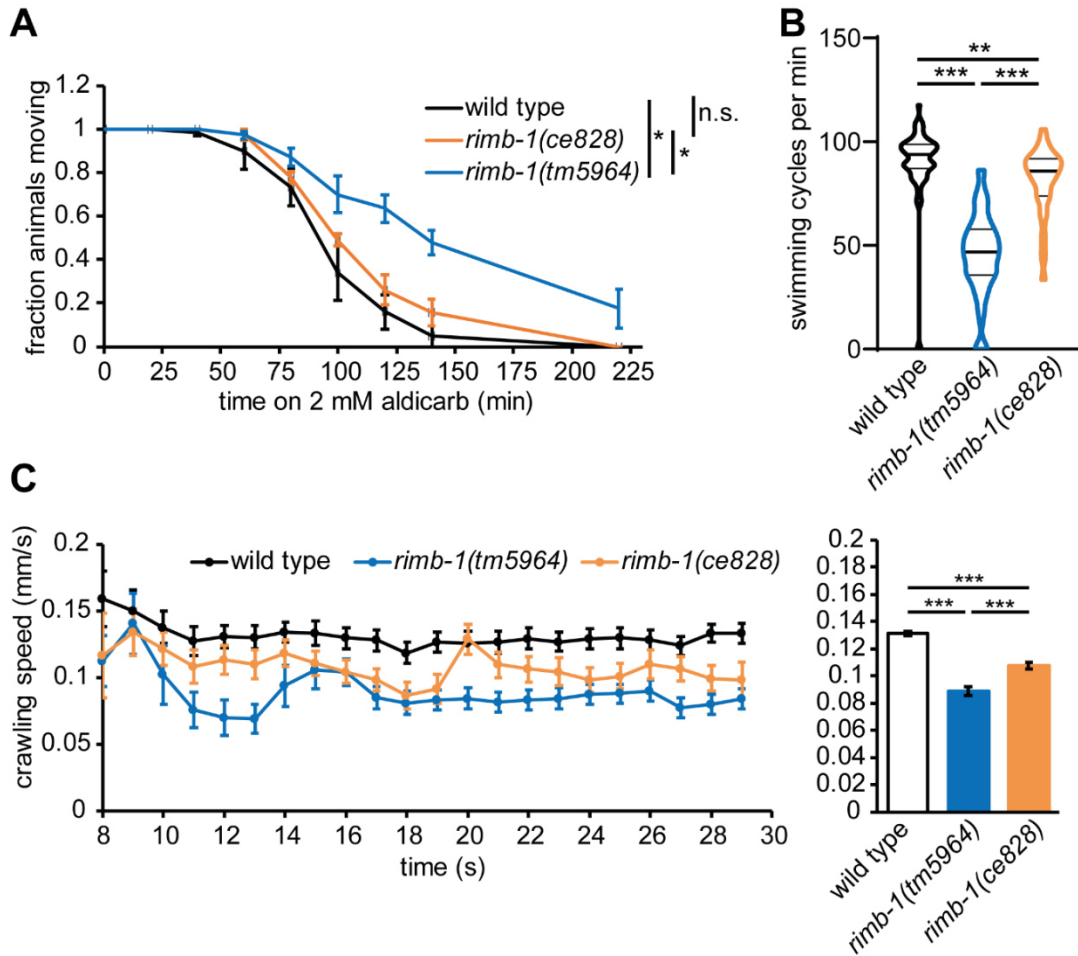
Figure S1: Comparing two *rimb-1* alleles. *rimb-1* mutants *tm5964* and *ce828* were compared by **A)** resistance to aldicarb, testing for cholinergic transmission (3 replicates, n=15 animals each; Log rank test, Bonferroni correction), **B)** swimming and **C)** crawling locomotion. In A and C, mean ± s.e.m. are shown, in B, median and 25/75 quartiles (thick and thin lines), min to max. One-way ANOVA with Tukey test. Statistical significance given as *p<0.05; **p<0.01; ***p<0.001.

26
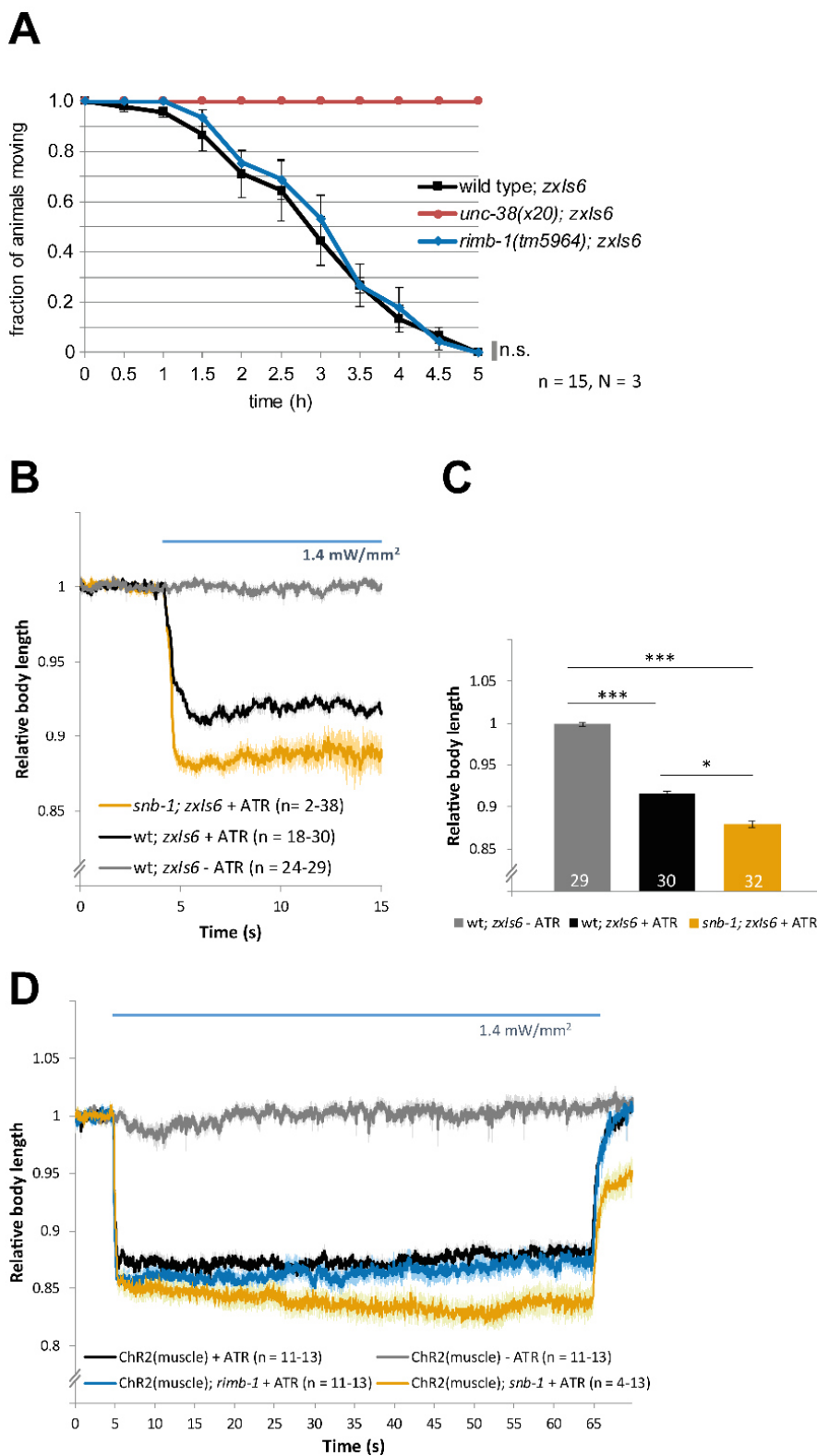
Figure S2: *rimb-1* mutants have no post-synaptic defect in muscular nAChRs, and normal muscle excitability. A) Levamisole-induced paralysis (1 mM, targeting muscular nAChRs), assessed over time, in three replicates, for the indicated number of animals of the indicated genotypes. Mean ± s.e.m. Log rank test. **B)** ChR2 expressed in cholinergic neurons, photoinduced muscle contraction (photostimulus indicated by blue bar). Shown is the mean (± s.e.m.) relative body length, n = number of animals. Synaptobrevin *snb-1(md247)* mutants show increased muscle contraction, despite reduced ACh release, due to compensatory excitability increase in post-synaptic muscle (Liewald et al., 2008). **C)** Statistical analysis of the data shown in B, one-way ANOVA, Bonferroni-corrected. **D)** Body contraction induced by ChR2 expressed in muscle, demonstrating increased contractions in *snb-1* mutants, but normal excitability in *rimb-1* mutants. Statistical significance given as ***p<0.001.

27

167
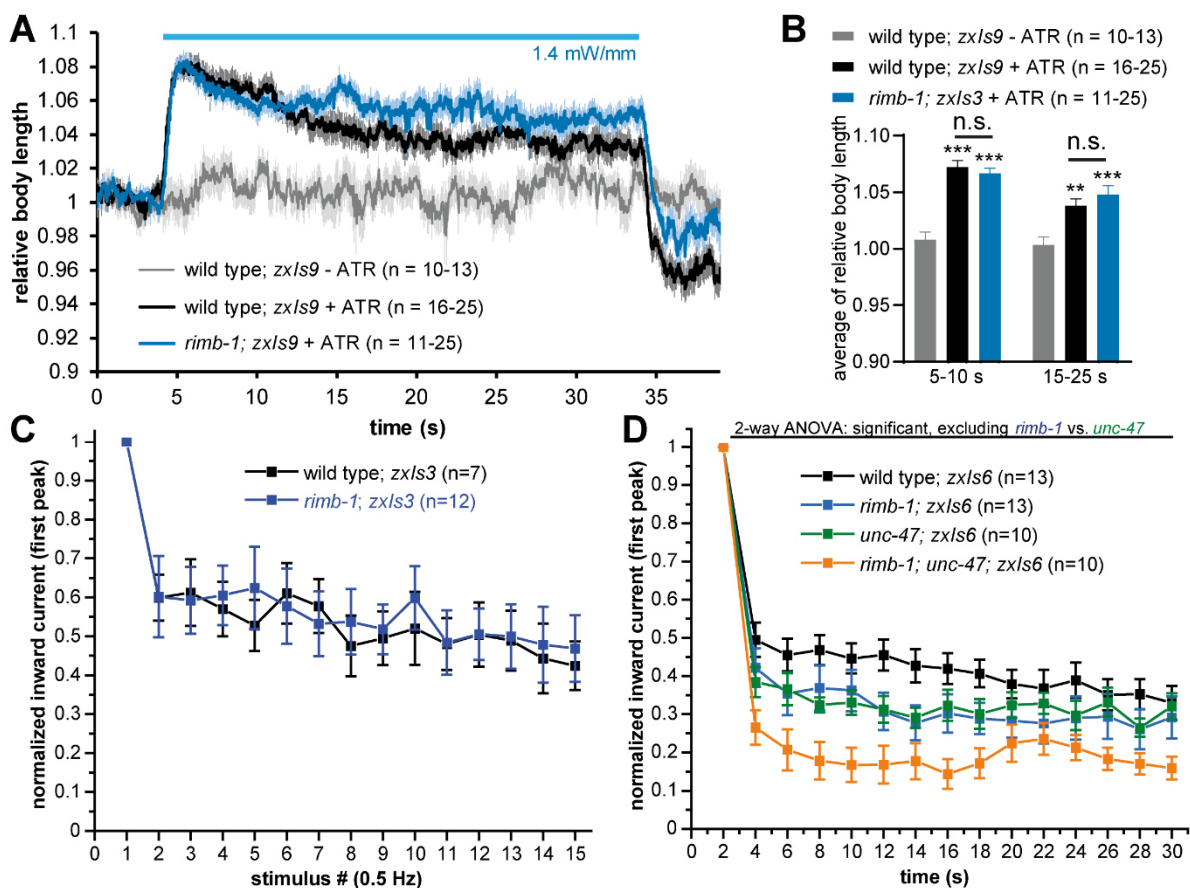
Figure S3: GABAergic transmission at the NMJ in *rimb-1* mutants. A) Photostimulation of GABAergic neurons (transgene *zxIs9*) causes body elongation. Genotypes and number of animals tested are indicated. **B)** Group data of the experiments shown in A, for the time period 1-5 s of the photostimulus; one-way ANOVA with Bonferroni correction. Statistical significance given as ***p<0.001. **C)** Photoevoked IPSCs for 15 consecutive stimuli, normalized to the first peak; means ± s.e.m. Related to **Fig. 5D**. No progressive change in the normalized amplitude is apparent. **D)** Indirectly probing the GABAergic NMJ using cholinergic stimulation of GABAergic neurons, comparing wild type, *rimb-1* and *unc-47* vGAT mutants, normalized to the first peak. Related to **Fig. 6E**. Two-way ANOVA with Fisher test.
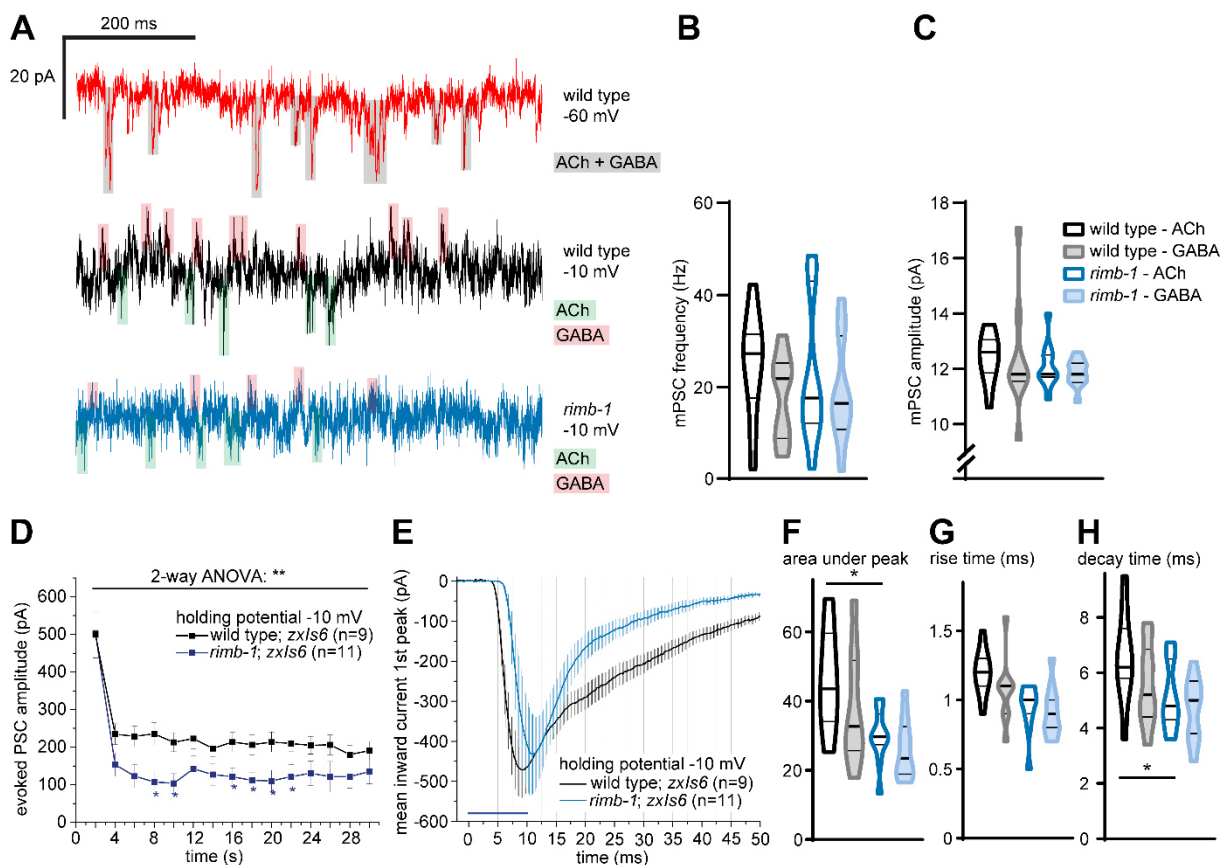
Figure S4: *rimb-1* defects in evoked NMJ transmission at -10 mV. A) mPSCs measured at different holding potentials (-60 mV or -10 mV), discerning cholinergic (green shade) and GABAergic (red shade) currents. Genotypes as noted. **B)** Frequency and **C)** amplitude, of cholinergic and GABAergic mPSCs, in wild type and *rimb-1(tm5964)* mutants. **D)** Mean (± s.e.m.) ePSCs for 15 consecutive cholinergic photo stimuli, measured at -10 mV. n = number of animals. **E)** Time course of first ePSC (mean ± s.e.m.), measured at -10 mV. Analysis of mPSC parameters **F)** area under peak, **G)** rise and **H)** decay time. One-way ANOVA with Tukey test. Data in B, C, F-H shown as median and 25/75 quartiles (thick and thin lines), min to max. Statistical significance in D, F given as *p<0.05; **p<0.01.
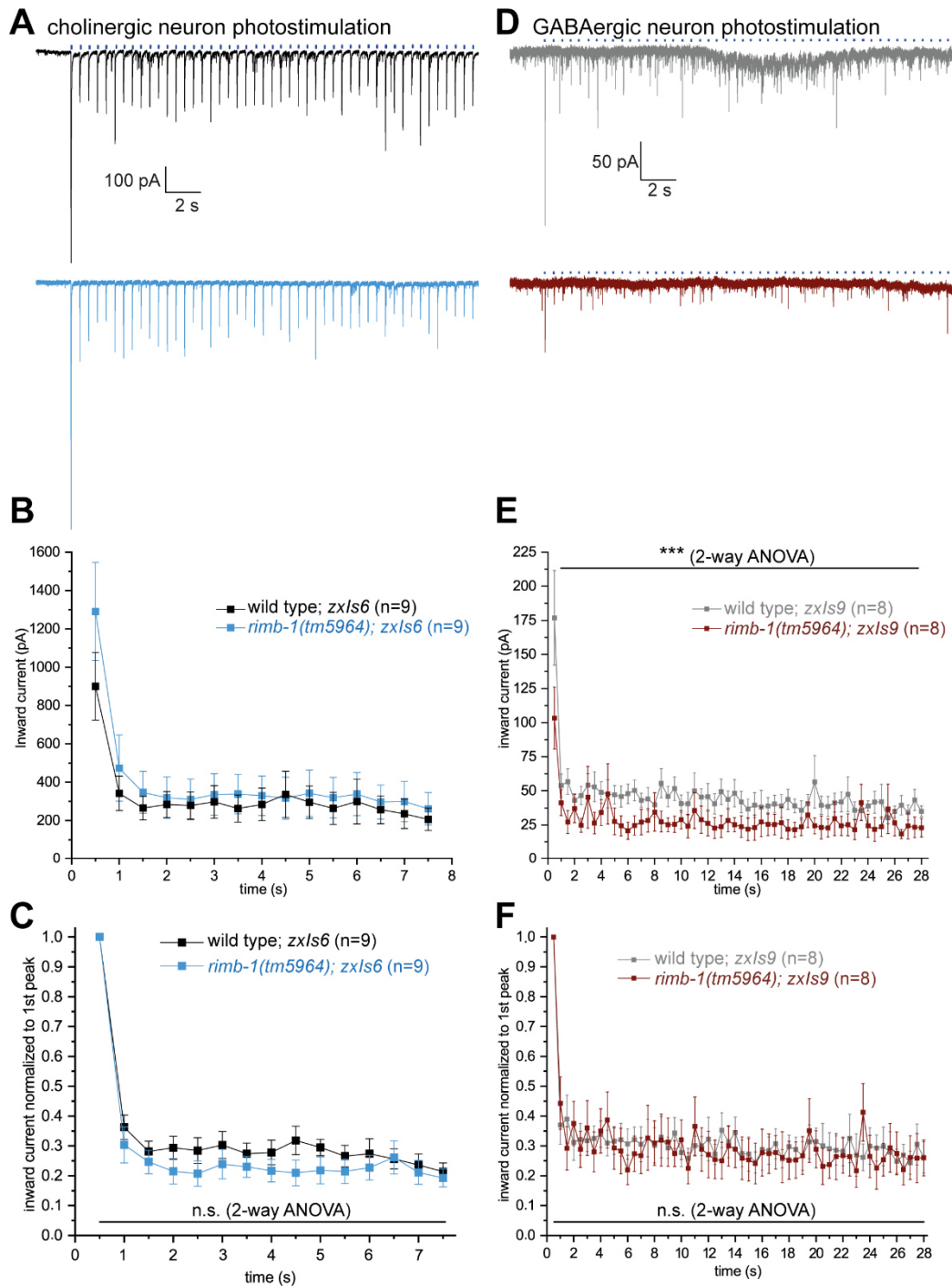
Figure S5: Repeated 2 Hz stimulation of cholinergic and GABAergic synapses reveals no effect on depression or facilitation. A-C) Cholinergic (transgene *zxIs6*) and **D-F)** GABAergic (transgene *zxIs9*) photostimulation, 2 Hz, 10 ms stimuli. Original records, mean (± s.e.m.) ePSCs, without or with normalization to the first peak. **D-F)** Cholinergic photostimulation, 2 Hz, 10 ms stimuli. Original records, mean (± s.e.m.) ePSCs, without or with normalization to the first peak.

30

170

A length of DP (nm)

B distribution of docked SVs along PM relative to DP
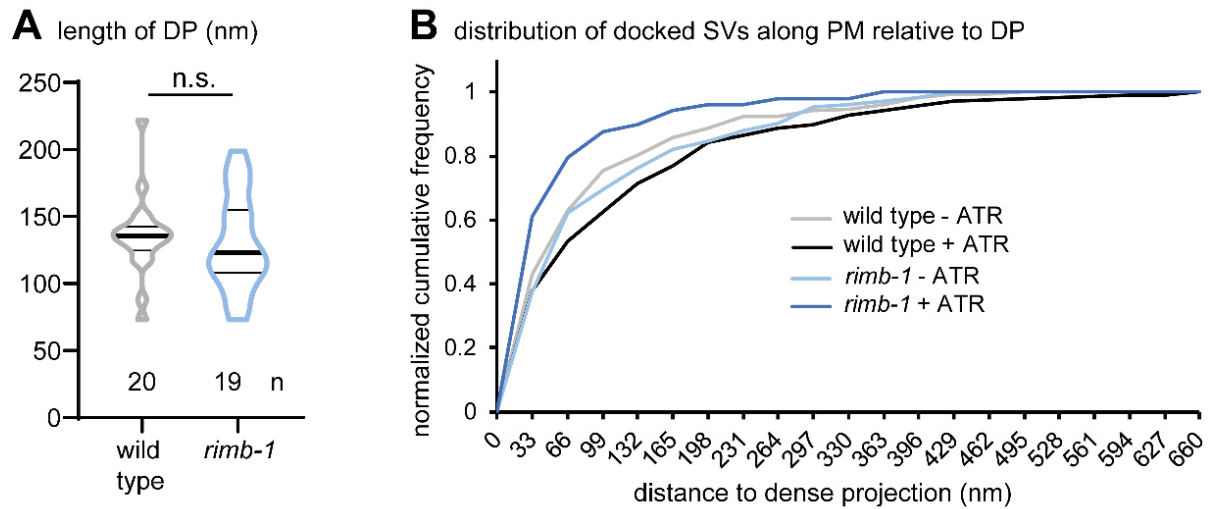
1036

Figure S6: Ultrastructural parameters of *rimb-1* mutant synapses. A) Length of the dense projection was not altered in *rimb-1* synapses. **B)** Cumulative distribution of docked SVs in illuminated wild type vs. *rimb-1* mutant synapses, with or without ATR. Docked SVs in silent synapses are not differently distributed in *rimb-1* mutants, but fuse more distal to the DP. Related to **Fig. 5F**.

31
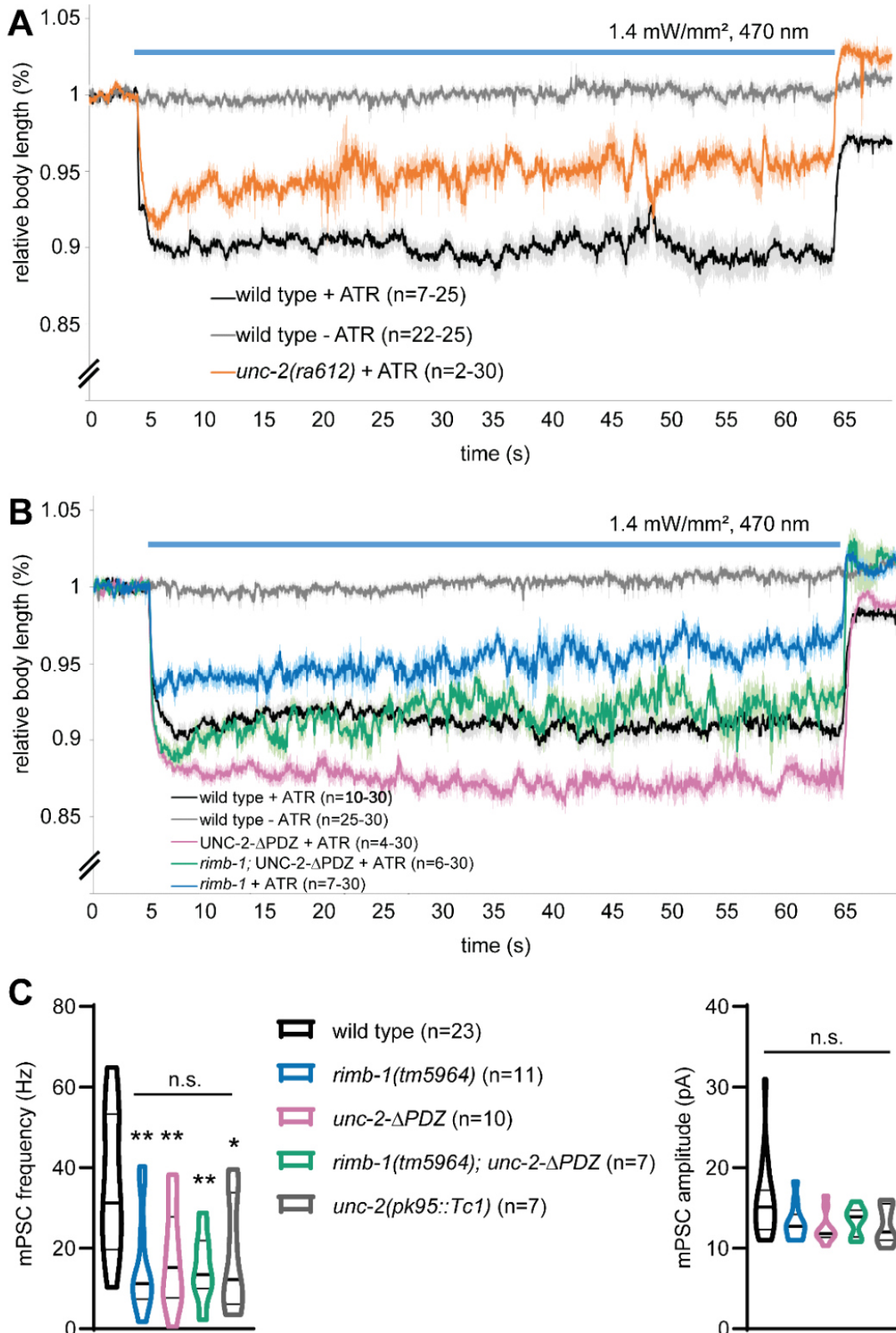
Figure S7: Differential effects of untethering and deleting CaV2/UNC-2 VGCCs on induced behavior and basal synaptic transmission. A, B) Photoinduced body contraction (transgene *zxIs6*) in *unc-2* deletion mutants, as well as *rimb-1*, UNC-2-ΔPDZ and *rimb-1*; UNC-2-ΔPDZ double mutants, compared to wild type controls. Mean ± s.e.m., light stimulus indicated by blue bar; n= number of animals analyzed. **C)** Spontaneous synaptic transmission, mPSC frequency and amplitude, compared in the indicated genotypes. n = number of animals, data shown as median and 25/75 quartiles (thick and thin lines), min to max. One-way ANOVA with Tukey test, *p<0.05, **p<0.01.

2.6 Rhodopsin-based voltage imaging tools for use in muscles and neurons of *Caenorhabditis elegans*

The following pages contain the published version of the research article "Rhodopsin-based voltage imaging tools for use in muscles and neurons of *Caenorhabditis elegans*"[15]. Material from: Azimi Hashemi, N. and Bergs, A. *et al.* Rhodopsin-based voltage imaging tools for use in muscles and neurons of *Caenorhabditis elegans*. *Proceedings of the National Academy of Sciences of the United States of America* **116**, 17051–17060; 10.1073/pnas.1902443116 (2019).

Rhodopsin-based voltage imaging tools for use in muscles and neurons of *Caenorhabditis elegans*

Negin Azimi Hashemi[a,b,1], Amelie C. F. Bergs[a,b,c,1], Christina Schüler[a,b], Anna Rebecca Scheiwe[a,b], Wagner Steuer Costa[a,b], Maximilian Bach[a,b], Jana F. Liewald[a,b], and Alexander Gottschalk[a,b,2]

[a]Buchmann Institute for Molecular Life Sciences, Goethe University, D-60438 Frankfurt, Germany; [b]Institute for Biophysical Chemistry, Goethe University, D-60438 Frankfurt, Germany; and [c]International Max Planck Research School in Structure and Function of Biological Membranes, Max Planck Institute of Biophysics, D-60438 Frankfurt, Germany

Genetically encoded voltage indicators (GEVIs) based on microbial rhodopsins utilize the voltage-sensitive fluorescence of all-*trans* retinal (ATR), while in electrochromic FRET (eFRET) sensors, donor fluorescence drops when the rhodopsin acts as depolarization-sensitive acceptor. In recent years, such tools have become widely used in mammalian cells but are less commonly used in invertebrate systems, mostly due to low fluorescence yields. We systematically assessed Arch(D95N), Archon, QuasAr, and the eFRET sensors MacQ-mCitrine and QuasAr-mOrange, in the nematode *Caenorhabditis elegans*. ATR-bearing rhodopsins reported on voltage changes in body wall muscles (BWMs), in the pharynx, the feeding organ [where Arch(D95N) showed approximately 128% ΔF/F increase per 100 mV], and in neurons, integrating circuit activity. ATR fluorescence is very dim, yet, using the retinal analog dimethylaminoretinal, it was boosted 250-fold. eFRET sensors provided sensitivities of 45 to 78% ΔF/F per 100 mV, induced by BWM action potentials, and in pharyngeal muscle, measured in simultaneous optical and sharp electrode recordings, MacQ-mCitrine showed approximately 20% ΔF/F per 100 mV. All sensors reported differences in muscle depolarization induced by a voltage-gated Ca²⁺-channel mutant. Optogenetically evoked de- or hyperpolarization of motor neurons increased or eliminated action potential activity and caused a rise or drop in BWM sensor fluorescence. Finally, we analyzed voltage dynamics across the entire pharynx, showing uniform depolarization but compartmentalized repolarization of anterior and posterior parts. Our work establishes all-optical, noninvasive electrophysiology in live, intact *C. elegans*.

voltage imaging | all-optical electrophysiology | microbial rhodopsin | electrochromic FRET | neuromuscular

Activity of excitable cells like muscles and neurons is assessed by electrophysiology, Ca²⁺ or voltage imaging (1–7). While electrical measurements provide the highest sensitivity and temporal accuracy, imaging methods are much more versatile for applications in live animals and for recording multiple cells simultaneously. Genetically encoded Ca²⁺ indicators (GECIs) today cover most of the visible spectrum with comparably narrow spectral width, thus enabling multiplexing with other optical tools (8–10). Furthermore, GECIs were improved immensely since their first reporting in the late 1990s, to provide several thousandfold of fluorescence increases upon Ca²⁺-binding (5). With differential kinetic properties, some GECIs enable detection of single action potentials (APs), and thus they are widely used in neuroscience. However, in many neuron types Ca²⁺ imaging fails to reflect spiking dynamics or subthreshold voltage fluctuations, or to assess high-frequency APs (11). Furthermore, Ca²⁺ measures neuronal activity indirectly, and neuronal depolarization is not always accompanied by a Ca²⁺ increase (12). Finally, GECIs are not well suited to detect hyperpolarization, as often Ca²⁺ does not decrease below basal cytosolic concentration. Thus, voltage imaging tools (GEVIs) are an important addition to the toolbox of sensors for excitable cell activity (11, 13–18).

The development of GEVIs lagged behind that of GECIs, and several different designs have been explored that couple voltage changes to fluorescence changes. These range from FRET sensors to circularly permuted GFP, similar as for GECIs (4, 5). However, such tools for a long time reached only a few percent in fluorescence change per 100 mV of membrane voltage change, making detection of single APs a challenge. More recently, microbial rhodopsins were found to exhibit a voltage-dependency of the fluorescence of their chromophore, retinal (17, 19). The fluorescence signal change was higher than for the other protein-based GEVIs (∼20 to 40% per 100 mV), and was improved by mutagenesis (13, 18). However, the absolute fluorescence of the rhodopsins is very small, and in particular, the voltage sensitivity of the fluorescence, due to the nature of the process requiring more than 1 photon to be absorbed (20), becomes appreciable only at very high excitation light intensities. Thus, electrochromic FRET (eFRET) sensors were developed that couple fluorescence of a normal fluorescent protein (FP) to the rhodopsin. Upon depolarization, the latter acts as FRET acceptor, thus quenching the (much stronger) fluorescence of the FP, which

Significance

Neuronal and other excitable cell activity is characterized by alteration in membrane voltage, while intracellular Ca²⁺ levels and transmitter release are affected downstream of electrical activity. Thus, the most direct way of monitoring neuronal activity is by membrane voltage. Electrophysiology is demanding for multiple cells or cell ensembles and difficult to use in live animals, thus imaging methods are desirable. Yet, genetically encoded voltage indicators fell behind Ca²⁺ indicators until recently, when microbial rhodopsins and derivatives were introduced as genetically encoded voltage indicators. We evaluated rhodopsin tools for voltage imaging in muscles and neurons of *Caenorhabditis elegans*, a prime animal model in neuro- and cell biology, showing robust performance and the ability to characterize genetic mutants.

acts as a FRET donor (14, 16). Several variants of eFRET sensors were developed, which are composed of modified archaerhodopsins [Arch(D95N), QuasAr (18), Archon (13)], or other proton pumps like Mac (from *Leptoshaeria maculans*) or Ace2N, derived from the *Acetabularia* rhodopsin proton pump (14, 21, 22). Each of these proteins is coupled with specific linkers to fluorescent proteins—like mOrange, mCitrine, mNeon, or mRuby3—depending on the absorption of the respective rhodopsin, to achieve maximal FRET efficiency and imaging at different wavelengths. An alternative to improve voltage-dependent rhodopsin fluorescence may be to change the chemical properties of the chromophore. We previously used retinal analogs to reconstitute function of microbial rhodopsin optogenetic tools, altering their characteristics (23), and observed that some retinal analogs conferred higher fluorescence to the rhodopsin.

Here, we surveyed a range of microbial rhodopsin GEVIs in excitable cells of the nematode *Caenorhabditis elegans*, an important model system in physiology, molecular, cellular, and behavioral neurobiology. We show that eFRET sensors are robust tools allowing us to analyze voltage signals with little experimental effort, and that the retinal analog dimethylaminoretinal (DMAR) strongly improves absolute fluorescence. Direct voltage-dependent retinal fluorescence can be measured in the infrared under excitation at high intensity, both in muscles and in neurons, and membrane voltage can be adjusted concomitantly with rhodopsin tools for de- or hyperpolarization. Alterations in AP amplitude and duration were robustly detected in gain-of-function (g.o.f.) mutants of the L-type Ca^{2+} channel EGL-19 in a muscular pump, the pharynx, allowing correlation with the timing of pump events. Finally, GEVIs enabled us to visualize the spatiotemporal compartmentalization of voltage changes in this muscular structure.

Results

Arch(D95N) Equipped with ATR Shows Dim, Fluctuating Fluorescence in Muscle That Is Enhanced by DMAR.

To explore the potential of analyzing muscle voltage changes via rhodopsin fluorescence, we expressed Arch(D95N) (17), QuasAr [an improved variant of Arch (18)], and Archon (13), a further evolved version, in body wall muscles (BWMs), or in pharyngeal muscles (PMs), and supplemented the animals with all-*trans* retinal (ATR). Under an epi-fluorescence microscope equipped with a 100 W HBO lamp for excitation and a sCMOS camera, very dim fluorescence was observable around 700 nm. Using a 637-nm laser and an EMCCD camera, fluorescence was more readily observable (Fig. 1 *A* and *B*). In comparison with Arch(D95N), QuasAr and Archon fluorescence was 2.4- and 2.1-fold more intense, respectively, showing 1.7-fold higher contrast over background fluorescence (in BWMs) (Fig. 1 *D* and *E*). In immobilized animals, BWM fluorescence intensity fluctuated in the range of 20 to 25% ΔF/F, likely representing voltage changes (*SI Appendix*, Fig. S1) that could correspond to APs, as recorded by patch clamp previously (24, 25).

When we supplemented animals with the retinal analog DMAR (23) (Fig. 1 *D*, *Inset*), we observed an approximately 250-fold higher absolute fluorescence (in PMs) (Fig. 1 *B* and *D*), and similarly, when we used retinal analog VI, fluorescence levels increased 81-fold [gain-corrected; note this was in Arch WT, in which analog VI does not mediate function, thus is not hyperpolarizing the cell; it could not be incorporated by Arch(D95N)]. This also led to higher contrast (138-fold and 44-fold for DMAR and analog VI, respectively) (Fig. 1*E*). Fluorescence yield of Arch(D95N) could also be increased by using 10× more ATR during animal cultivation, and 50× higher camera gain (Fig. 1 *B* and *D*). Increased fluorescence due to DMAR or increased ATR and gain was likewise observed in BWMs (Fig. 1*B*). Finally, we also expressed eFRET sensors, QuasAr-mOrange and MacQ-mCitrine,
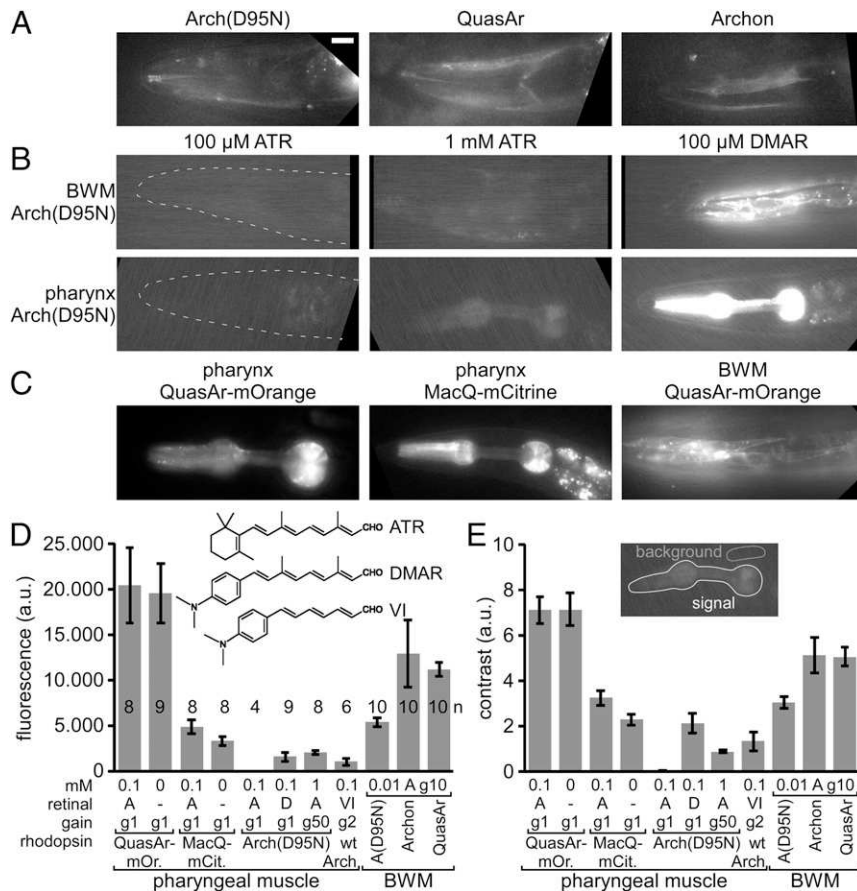
Fig. 1. Expression of rhodopsin voltage sensors in *C. elegans* muscle cells. (*A*) Expression and imaging of retinal fluorescence [Arch(D95N), QuasAr, Archon] in BWM cells in the head. (Scale bar, 10 μm. Scale for *B* and *C*, also 10 μm.) (*B*) Expression and imaging of Arch(D95N) in BWMs (*Upper*) and in PM (*Lower*), complemented with ATR (2 concentrations) and with the retinal analog DMAR (see *Inset* in *D* for chemical structures of ATR, DMAR and retinal analog VI). Dashed line indicates worm head. (*C*) Expression and imaging of eFRET voltage sensors (MacQ-mCitrine, QuasAr-mOrange) in PMs and BWMs. (*D* and *E*) Characteristics of basal fluorescence for the sensors expressed in PMs or BWMs, as indicated. Fluorescence intensity (*D*) as average gray values of an ROI enclosing the entire pharynx and contrast (*E*) as the ratio of signal over mean fluorescence of a control ROI were acquired (20-ms exposure) with different gain (indicated as "g" and a number). Rhodopsins were supplemented with ATR, DMAR, or analog VI ("A," "D," "VI"; concentrations in millimolars). Shown are means ± SEM. Number of animals imaged is indicated in *D*. In *A*–*C*, anterior is to the left.

Azimi Hashemi et al.

175

in PMs or BWMs (Fig. 1C). Since for those, fluorescence of canonical FPs is observed, their absolute fluorescence was much higher than for any of the rhodopsin-only sensors [∼3,000- and 800-fold higher fluorescence than Arch(D95N)-ATR, for QuasAr-mOrange and MacQ-mCitrine, respectively] (Fig. 1D). Moreover, their contrast level compared with background was 460- and 211-fold higher, respectively (Fig. 1E).

Intrinsic Activity in Muscle Is Accompanied by Fluorescence Changes of Rhodopsin GEVIs. To assess if the fluorescence of the sensors is also voltage-dependent, we observed it during intrinsic activity. For the pharynx, we immobilized animals such that pharyngeal pumping persists (i.e., treated with serotonin to mimic the presence of food). QuasAr-mOrange fluorescence changes were apparent upon PM contraction as a drop in intensity that was only observed when the protein was supplemented with ATR, thus yielding a functional eFRET acceptor (Fig. 2 A and B and Movie S1). The fluorescence of the terminal bulb (TB; "grinder" region) was further used to detect PM contractions.

For Arch(D95N) in BWMs, fluorescence fluctuations occurred at a rapid time scale (Fig. 2C), reminiscent of BWM APs appearing spontaneously in dissected animals, and which can be recorded by current-clamp electrophysiology (Fig. 2E). To explore whether fluorescence fluctuations occurred in response to muscular depolarization, we analyzed the muscle arms of QuasAr-expressing BWM cells in the head (Fig. 2D and Movie S2). Fluorescence fluctuated in a dorso-ventrally reciprocal fashion, as expected for the control of muscles during locomotion of the animal. As shown previously, such reciprocal activity is apparent in immobilized animals (26), even though at a slower pace than expected for freely moving animals. Fluctuations of 10 to 15% ΔF/F were found for all rhodopsin-based voltage sensors tested in BWMs [Arch(D95N), Archon, QuasAr] (Fig. 2 F–H, SI Appendix, Fig. S1, and Movies S3 and S4). These analyses were somewhat affected by movement: Animals were not anesthetized, thus photostimulation of cholinergic neurons led to muscle contraction and to a noisy baseline (SI Appendix, Fig. S1 B, C, E, and J). When we expressed and coactivated the hyperpolarizing anion-selective channelrhodopsin ACR2 (27, 28) in cholinergic motor neurons (MNs), fluorescence fluctuations in BWMs were absent and the baseline was less noisy, as inhibition of MNs paralyzes the animal (Fig. 2I and SI Appendix, Fig. S1 F and J). Thus, large fluctuations, most likely APs (see below), were evoked by presynaptic cholinergic MNs that depolarized BWM cells via acetylcholine (ACh) signaling, while noise was mostly due to movement.

QuasAr Enables Imaging of Electrical Activity in Neurons. To explore the possibility of imaging neuronal activity using QuasAr, we chose RIM neurons. These were previously shown to be active during locomotion, yet somewhat contradictory findings were reported (29–32): spontaneous reversals, or reversals evoked by mechanosensory neurons, reduced or increased RIM Ca^{2+} levels, which also show slow fluctuations; in addition, noxious stimuli evoked RIM hyperpolarization via glutamate signals. We thus attempted visualizing RIM voltage changes equivalent to these Ca^{2+} fluctuations, or in response to excitatory and inhibitory inputs. We expressed QuasAr in RIM neurons using the Ptdc-1 promoter. QuasAr::GFP could be readily observed in 2 neurons in the vicinity of the pharyngeal TB, which we identified as RIML and RIMR (Fig. 2J). When we imaged QuasAr fluorescence in immobilized animals, we observed phases lacking obvious activity (signals <1% ΔF/F) (Fig. 2L), that were interrupted by phases of activity: (i) the signal fluctuated rapidly for up to 4% ΔF/F, interrupted by (ii) short phases of increases or decreases of ΔF/F of up to 10%, and (iii) slow fluctuations either up- or downward of 5 to 15% (Fig. 2K and SI Appendix, Fig. S3 A and B). As a comparison, RIM Ca^{2+} signals showed similar slow fluctuations (SI Appendix, Fig. S3A), but no brief activity changes, likely as these electrical events are integrated to slower changes in Ca^{2+} concentration. When we measured (voltage-insensitive) RIM::GFP, we did not observe any rapid or

long-lasting changes, and signal fluctuation was <1% ΔF/F (Fig. 2K). The brief pulses of de- or hyperpolarizing activity in RIM were of average amplitude of 8% ΔF/F, and lasted ∼120 ms (SI Appendix, Fig. S2C). These events could correspond to inhibitory and excitatory inputs, evoking postsynaptic potentials. As a second example, we imaged cholinergic MNs. QuasAr expressed from the Punc-17 promoter in retrovesicular ganglion MNs showed rapid fluctuations of ∼4% ΔF/F, which were larger than the signals observed during inactive phases in RIM (Fig. 2L and SI Appendix, Fig. S3B). This indicated that these cells were active, but differed in their activity patterns from RIM. Cholinergic neurons have graded potentials, while RIM likely has a bistable membrane potential. These findings demonstrate that rhodopsin-based voltage imaging allows characterizing intrinsic neuronal and circuit activity, as previously shown in response to neuronal stimulation (13).

Optogenetic De- and Hyperpolarization of MNs Enables Calibration of Rhodopsin Voltage Signals in BWMs. To estimate how voltage-induced fluorescence changes compare with electrically measured voltages, we evoked BWM depolarization by optogenetic stimulation of cholinergic MNs. When recorded by current clamp, channelrhodopsin-2 (ChR2) stimulation evoked mean APs of 29.15 mV (n = 8) (Figs. 2E and 3 A, B, and I). We imaged BWM cell voltage using the 3 voltage sensors: Arch(D95N), QuasAr, and Archon. Imaging basal fluorescence signals with 637-nm laser excitation (Fig. 1A) (without actuator-mediated stimulation) revealed spontaneous brief increases of fluorescence of ∼15% ΔF/F for QuasAr, and ∼10% for Archon and for Arch(D95N) (Fig. 2 F–H and SI Appendix, Fig. S1). These lasted for ∼50 to 100 ms, and were reminiscent of APs measured by electrophysiology in BWM cells (Fig. 2E). During prolonged recordings (25 s), QuasAr and Archon showed APs that canceled out upon averaging, exhibiting only little change in baseline, while Arch(D95N) was photo bleaching (Fig. 2C and SI Appendix, Fig. S1 A, D, and H). When we used ChR2 stimulation of MNs, this led to increased ΔF/F signals, corresponding to depolarization: ∼22.7% for QuasAr and Arch(D95N), and ∼13.3% for Archon, for the first evoked peak (Fig. 3 C–F, and I and SI Appendix, Figs. S1 B, C, E, and H–J). Trains of APs could be observed that were overlaid on the overall increased fluorescence rise (SI Appendix, Fig. S1J). When averaged over the 5-s stimulus period, signals were ∼21.4%, 14.6%, and 17.0% for QuasAr, Archon, and Arch(D95N), respectively. When we photo-hyperpolarized cholinergic MNs using ACR2, the fluorescence of QuasAr dropped by about 14.6%, and no AP-like spikes were observable (Figs. 2I and 3 G–I and SI Appendix, Fig. S1 F–J). Our measurements allow a rough calibration of the observed fluorescence voltage signals: ∼78% ΔF/F per 100 mV for QuasAr and Arch(D95N), and approximately 46% for Archon, which resembles reported data [∼45% ΔF/F per 100 mV for Arch(D95N) (17), QuasAr (18), and Archon (13)].

Arch(D95N) Shows Robust Fluorescence Increases in PMs. We assessed voltage-dependent changes in rhodopsin fluorescence in the pharynx in more detail. This muscular feeding pump exhibits APs and contractions. Arch(D95N), despite showing dim fluorescence, displayed strong fluorescence changes upon pharynx activity, on average ∼122% ΔF/F (Fig. 4 A and D and Movie S5). The pharynx AP was previously reported to be between 80 and 115 mV (33–35), which we could confirm by our own sharp electrode recordings (Fig. 4C), on average 95.3 ± 3.6 mV (10 APs each from n = 7 animals). Thus, in PMs, 100-mV depolarization corresponds to ∼128% fluorescence increase for Arch(D95N). This is larger than reported for Arch(D95N) or QuasAr in mammalian cells and neurons (17, 18), and also largely exceeds the fluorescence increase observed in BWMs upon excitation (Fig. 3 C, D, and I), for unknown reasons. The signal-to-noise ratio (SNR) was ∼70 (Fig. 4D). Detecting Arch(D95N) fluorescence in BWMs requires a strong excitation laser (up to 1,800 mW/mm², 637 nm; in PMs, approximately one-tenth of this intensity was sufficient) and an EMCCD camera,

NEUROSCIENCE
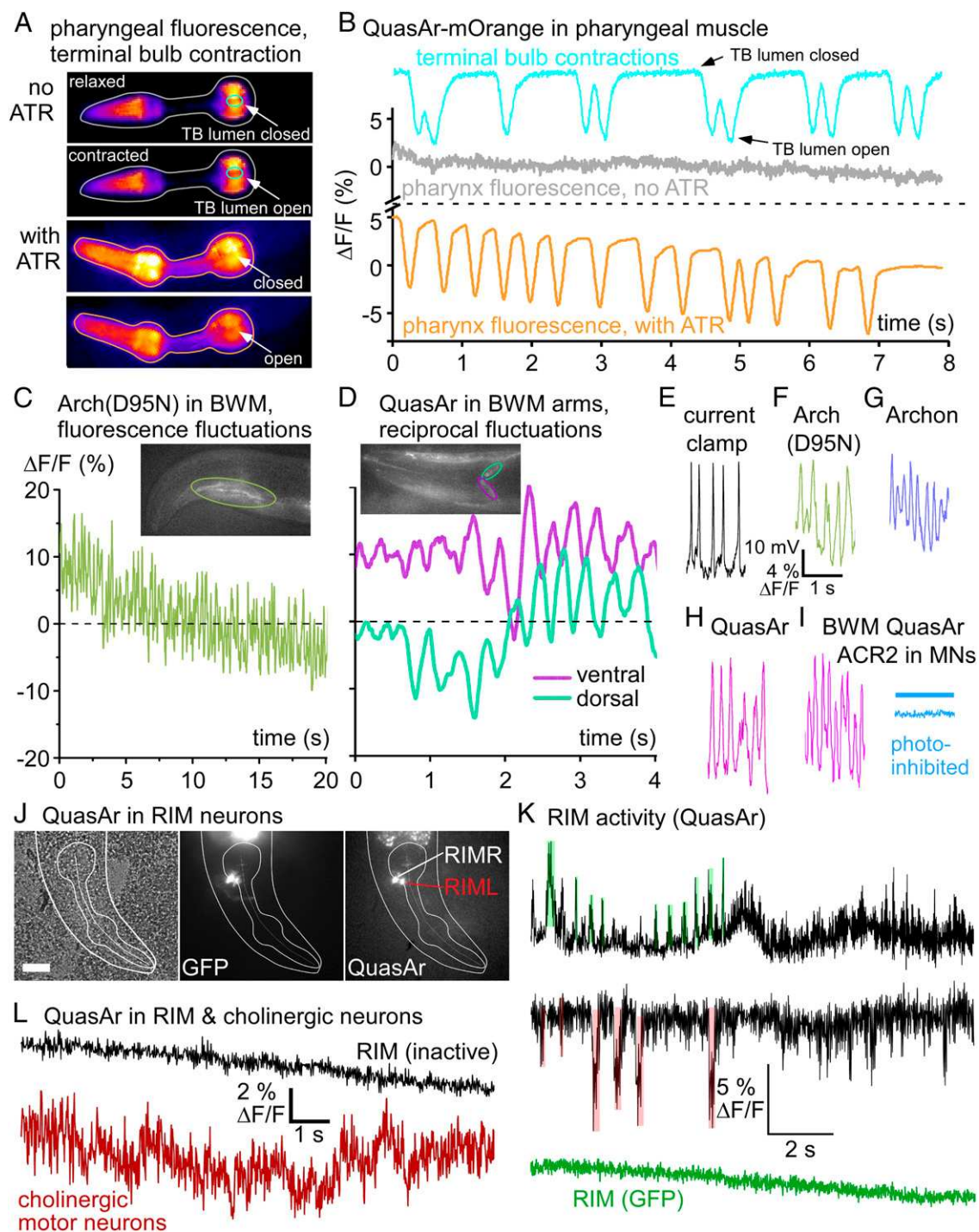
Fig. 2. Rhodopsin sensors detect intrinsic voltage changes in muscles and neurons. (*A*) Expression of QuasAr-mOrange in PMs, false-color representation of fluorescence intensity. *Upper* 2 images, animal raised without ATR; movie frames depict relaxed and contracted states. Time series of ROIs for fluorescence of the entire organ (gray) and for TB lumen (grinder region, cyan) are shown in *B*. *Lower* 2 images, animal supplemented with ATR (orange, voltage fluorescence ROI). Upon pharyngeal contraction fluorescence drops as TB lumen opens. (*B*) ΔF/F fluorescence time traces (acquired at 189 fps, 1-ms exposure) of ROIs indicated in *A*, in percent. Cyan graph: fluctuations of fluorescence signal due to opening and "darkening" of TB lumen, closed and open states. Without ATR, no change in fluorescence is observed despite pumping (gray trace; same movie as for TB contraction). Orange trace: Animal kept on ATR shows fluorescence drop upon PM depolarization; see also Movie S1. (*C*) Arch(D95N) fluorescence imaged in head BWM (ROI indicated in *Inset*; 158 fps, 2-ms exposure). (*D*) QuasAr imaging in BWM, dorsal, and ventral muscle arms in the nerve ring (ROIs indicated in turquoise and magenta), ΔF/F fluorescence shows dorso-ventral alternation. See also Movie S2. (*E*) APs recorded in dissected BWM, current clamp. (*F–H*) Fluorescence fluctuations of similar frequencies in BWM cells expressing Arch(D95N) (*F*), Archon (*G*), and QuasAr (*H*); each acquired at 158 fps, 2-ms exposure; see also Movies S3 and S4. (*I*) AP-like activity imaged in QuasAr-expressing BWM is stopped by ACR2-mediated photoinhibition of cholinergic motor neurons (blue trace, blue bar indicates illumination). (*J*) QuasAr::GFP expression in RIML and RIMR neurons. DIC (*Left*), GFP (*Center*), and QuasAr (*Right*) fluorescence in head region; outline of head and PM indicated. Scale bar, 20 μm. (*K*) QuasAr fluorescence fluctuations in RIM neurons (black traces), showing slow and fast inhibitory and excitatory events (shaded in red and green, respectively; for statistical analysis, see SI Appendix, Fig. S2C), while GFP (green trace) shows only photobleaching. (*L*) QuasAr fluorescence traces in RIM during inactive phase (black), and in cholinergic MNs (red). See also SI Appendix, Fig. S2.

Azimi Hashemi et al.

177
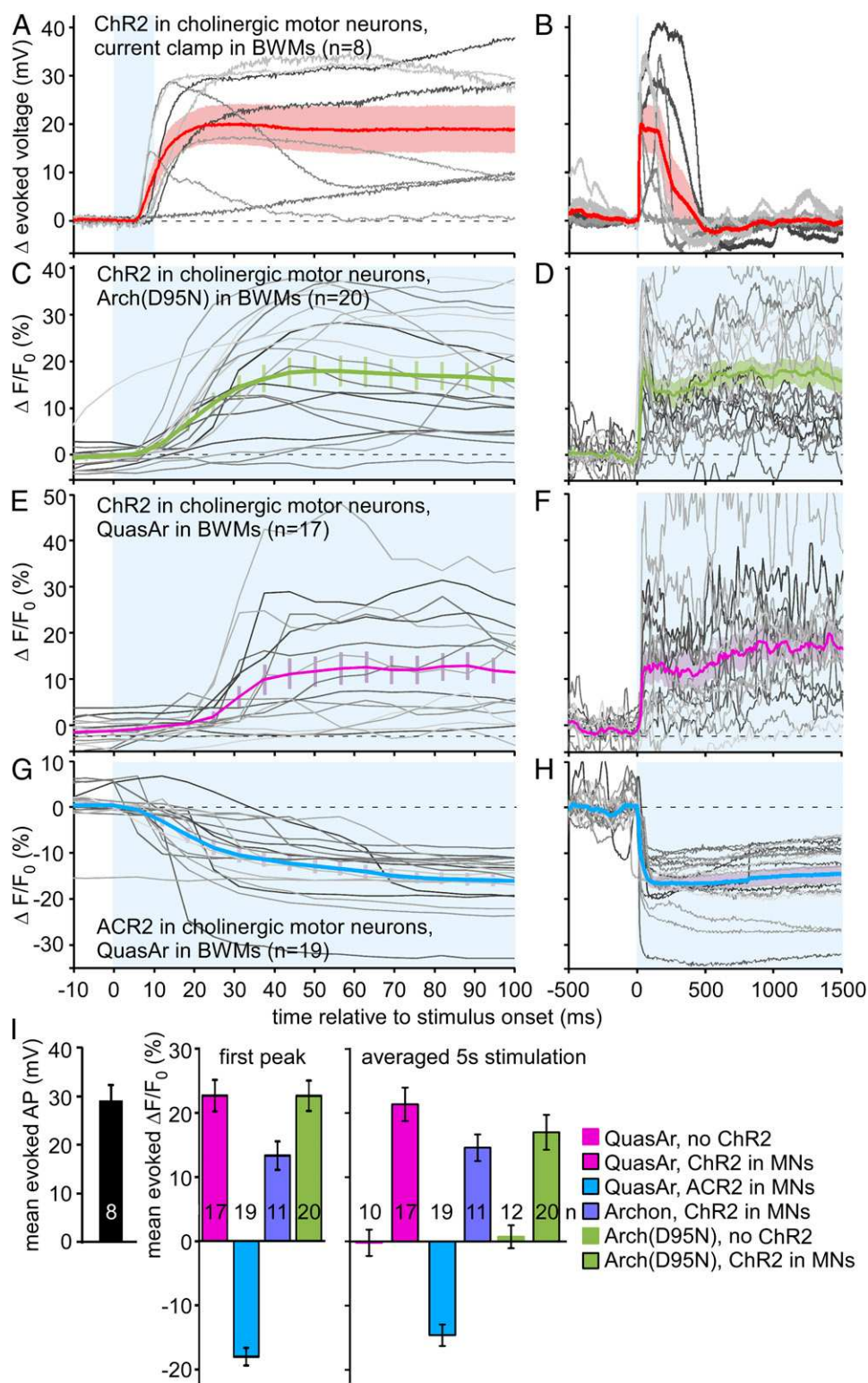
Fig. 3. Electrical and voltage-sensor signals in BWMs, induced by optogenetic manipulation of cholinergic MNs. (*A*) ChR2 mediated depolarization of cholinergic MNs (10-ms light pulse, indicated by blue shade) evokes APs in BWM cells, recorded under current clamp ($n = 8$ animals, single records in gray). Mean $\pm$ SEM voltage trace is shown in red and pink shade. (*B*) As in *A*, but extended time scale. (*C* and *D*) Arch(D95N) fluorescence voltage signals recorded in response to 5-s photo-depolarization of cholinergic MNs by ChR2. Mean $\pm$ SEM and single records from indicated number of animals. (*E* and *F*) As in *C* and *D*, using QuasAr in BWMs. (*G* and *H*) As in *E* and *F*, but using ACR2 anion channelrhodopsin for hyperpolarization of cholinergic MNs. (*I*) Mean $\pm$ SEM analysis of the data shown in *A*–*H*, for electrically measured AP amplitudes, and for the first fluorescence peak (assuming first AP) or during the entire 5-s light stimulus, for indicated combinations of sensors, actuators, controls. Frame rate in *C*–*H*: 158 fps, 2-ms exposure. *n*, number of animals. See also *SI Appendix*, Fig. S1.

equipment not available in every laboratory. Thus, we assessed whether DMAR-supplemented Arch(D95N) would simplify voltage imaging. Fluorescence was largely increased (Fig. 1*D*) and could be visualized with a common sCMOS camera and excitation through an HBO lamp (30 mW/mm², 620 nm); however, this did not allow recording APs. Possibly, DMAR must also be strongly excited to report voltage: using laser excitation ($\sim$180 mW/mm², 637 nm), Arch(D95N)-DMAR showed activity-dependent fluorescence in-

creases of $\sim$27% (i.e., $\sim$28.3%/100 mV), with an SNR of $\sim$35 (Fig. 4 *A* and *D* and Movie S6). Signals were very uniform within a pump train in the same animal, but varied more between animals (*Discussion* and *SI Appendix*, Fig. S3 *A* and *B*). Thus, while the signal change per millivolt is $\sim$5-fold lower for DMAR than for ATR, the increased detectability of the fluorescence makes this a valid alternative. We also tested analog VI in Arch WT; however, this retinal analog exhibited no voltage-dependence.

Azimi Hashemi et al.   PNAS | August 20, 2019 | vol. 116 | no. 34 | **17055**

178
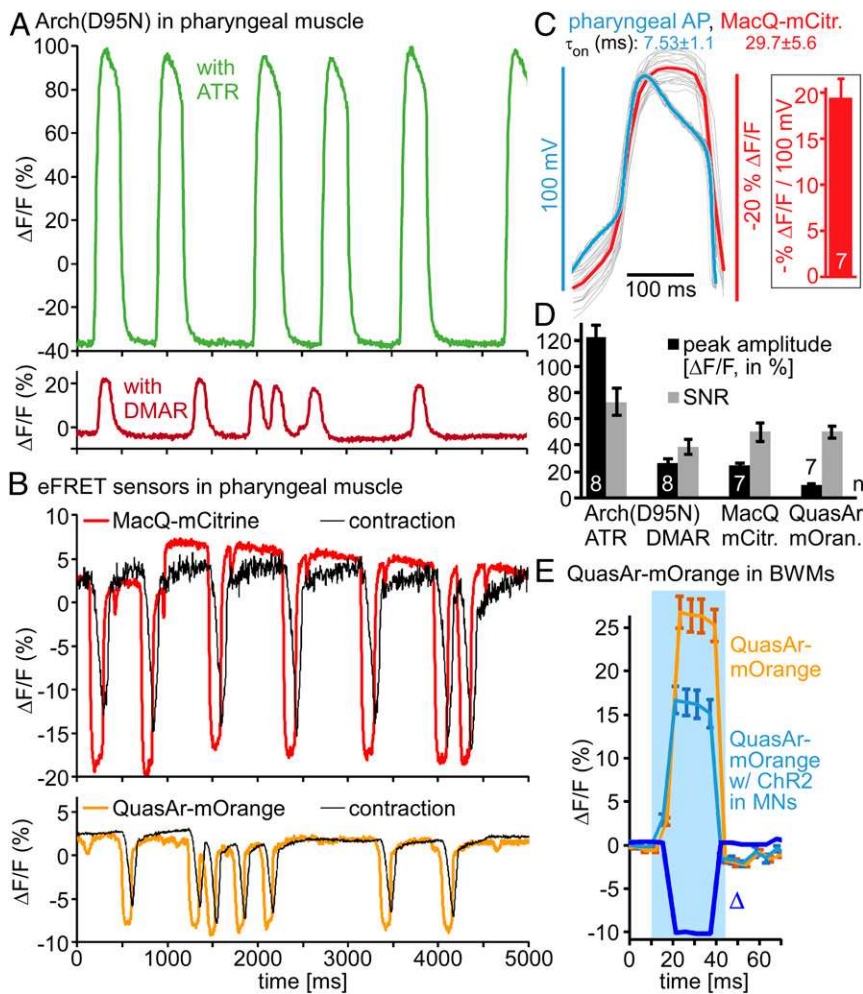
Fig. 4. Arch(D95N) and eFRET voltage-sensor signals quantified in PMs during pumping. (*A*) Arch(D95N) ΔF/F signals of PMs (entire organ) during pump trains, supplemented with ATR (above) or DMAR (below); see also Movies S5 and S6. (*B*) Pharyngeal APs, drop in fluorescence of eFRET sensors MacQ-mCitrine (*Upper*, red) (see also Movie S7) and QuasAr-mOrange (*Lower*, orange) (Movie S1). Corresponding TB contraction signal, black. (*C*, *Left*) Pharyngeal APs (overlay of 20 individual APs) and mean (blue), measured by sharp electrode recording (33), and concomitant ΔF/F signals measured from the same APs by MacQ-mCitrine (red, mean ΔF/F). (*Right*) Calibration ΔF/F per millivolt (each 10 APs from $n = 7$ animals). Also indicated are τ_{on} values for electrically and optically measured APs. (From ref. 33. Reprinted with permission from AAAS.) (*D*) Group data for sensors shown in *A* and *B*, mean ± SEM ΔF/F peak amplitudes, and SNR, defined as ratio of peak amplitude and SD of the noise (ΔF/F fluctuation between peaks). (*E*) QuasAr-mOrange signal in BWMs in response to photostimulation of ChR2 in cholinergic MNs (bright blue) or without ChR2 expression (orange), before and during a blue-light stimulus (blue shade). Both signals rise due to additional mOrange excitation. Difference graph (Δ, dark blue) shows drop in fluorescence upon ChR2-mediated stimulation. $n = 7$ to 8 animals, 3 to 15 APs each (or silent periods in between) were analyzed for *D*, and 12 to 13 animals in *E*. Frame rate in *A*, *B*, and *E*: 189 fps, 1-ms exposure.

eFRET Sensors Expressed in PMs Report on Voltage and Enable Concomitant Analysis of Muscle Contraction. As an alternative requiring no laser excitation, we analyzed the eFRET sensors QuasAr-mOrange and MacQ-mCitrine in PMs during pumping. A region of interest (ROI) encircling the entire pharynx was compared with an ROI outside the pharynx, but within the head of the animal (background). Fluorescence of both sensors was readily seen with standard epifluorescence microscope excitation intensities (HBO lamp or LEDs). MacQ-mCitrine and QuasAr-mOrange showed approximately −25 and approximately −10% reductions in the fluorescence upon pharyngeal pumping, respectively (Fig. 4*B*, *SI Appendix*, Fig. S3 *C–F*, and Movies S1 and S7). SNR was comparable for both sensors (~50) (Fig. 4*D*). Thus, despite lower overall fluorescence (Fig. 1*D*), MacQ-mCitrine is the more sensitive voltage reporter. Signals for both sensors were quite uniform in the same animal, while mean signal traces between animals varied (*SI Appendix*, Fig. S3 *C–F*). For rigorous calibration of MacQ-mCitrine fluorescence signals, we concomitantly recorded membrane voltage by sharp electrodes from the same dissected pharynxes. Measured APs were 95.3 ± 3.6 mV (10 APs each from $n = 7$ animals) (Fig. 4*C* and *SI Appendix*, Fig. S3 *G* and *H*), and the corresponding signals of MacQ-mCitrine were 19.49 ± 2.03% ΔF/F per 100 mV (Fig. 4*C*). Optically determined signals increased more slowly than the electrically determined voltages (time constants, electrical: τ_{on} = 7.53 ± 1.1 ms, τ_{off} = 5.02 ± 0.7 ms; ΔF/F: τ_{on} = 29.7 ± 5.6 ms, τ_{off} = 38.7 ± 9.4 ms). The protein-based measurement is thus ~4× "slower," which should be kept in mind when analyzing very fast events. QuasAr-mOrange signals corresponded to ~10.5% ΔF/F per 100 mV in PMs. In BWMs, we "calibrated" QuasAr-

mOrange signals following ChR2 stimulation in MNs, by comparing this to similarly illuminated animals lacking ChR2 (Fig. 4*E*): although mOrange excitation causes some ChR2 stimulation, a blue-light pulse resulted in different fluorescence increases in the 2 strains (~10% smaller for animals expressing ChR2). As photoevoked APs are 29 mV (Fig. 3*I*), this amounts to approximately −34% ΔF/F per 100 mV. Thus, QuasAr-mOrange appears to be more sensitive in BWMs than in PMs.

Analyzing a small ROI enclosing the pharyngeal TB grinder region allowed deriving the opening of the pharynx from the fluorescence signal (Figs. 2 *A* and *B* and 4*B*). Thus, we could correlate depolarization and contraction of the muscle. We wrote scripts to systematically analyze the measured fluorescence traces. These involved automatic detection of relevant events, aligning, synchronizing, and averaging. Then, parameters could be derived such as amplitude, area under the peak (corresponding to charge transfer), AP- and pump-duration (both defined as rise from and return to the baseline, or by using the full-width at half-maximum), delay of pump versus voltage, or rise and drop of the voltage as τ_{on} and τ_{off} values (Fig. 5*A*). Signals could be analyzed and compared for Arch(D95N) equipped with ATR and DMAR, MacQ-mCitrine, and QuasAr-mOrange (Fig. 5 *B–H*) (8 to 15 animals with 2 to 10 APs, each): pumps could not be deduced for Arch(D95N)-ATR as the basal fluorescence was too dim to detect TB opening. A comparison between signals observed by the tested sensor-retinal combinations showed, as deduced from manual analysis, different amplitudes of the pharyngeal AP [132, 22.6, −23.5, and −11.6% ΔF/F_0 for Arch(D95N)-ATR, Arch(D95N)-DMAR, MacQ-mCitrine, and QuasAr-mOrange, respectively], while the duration of the AP was

179
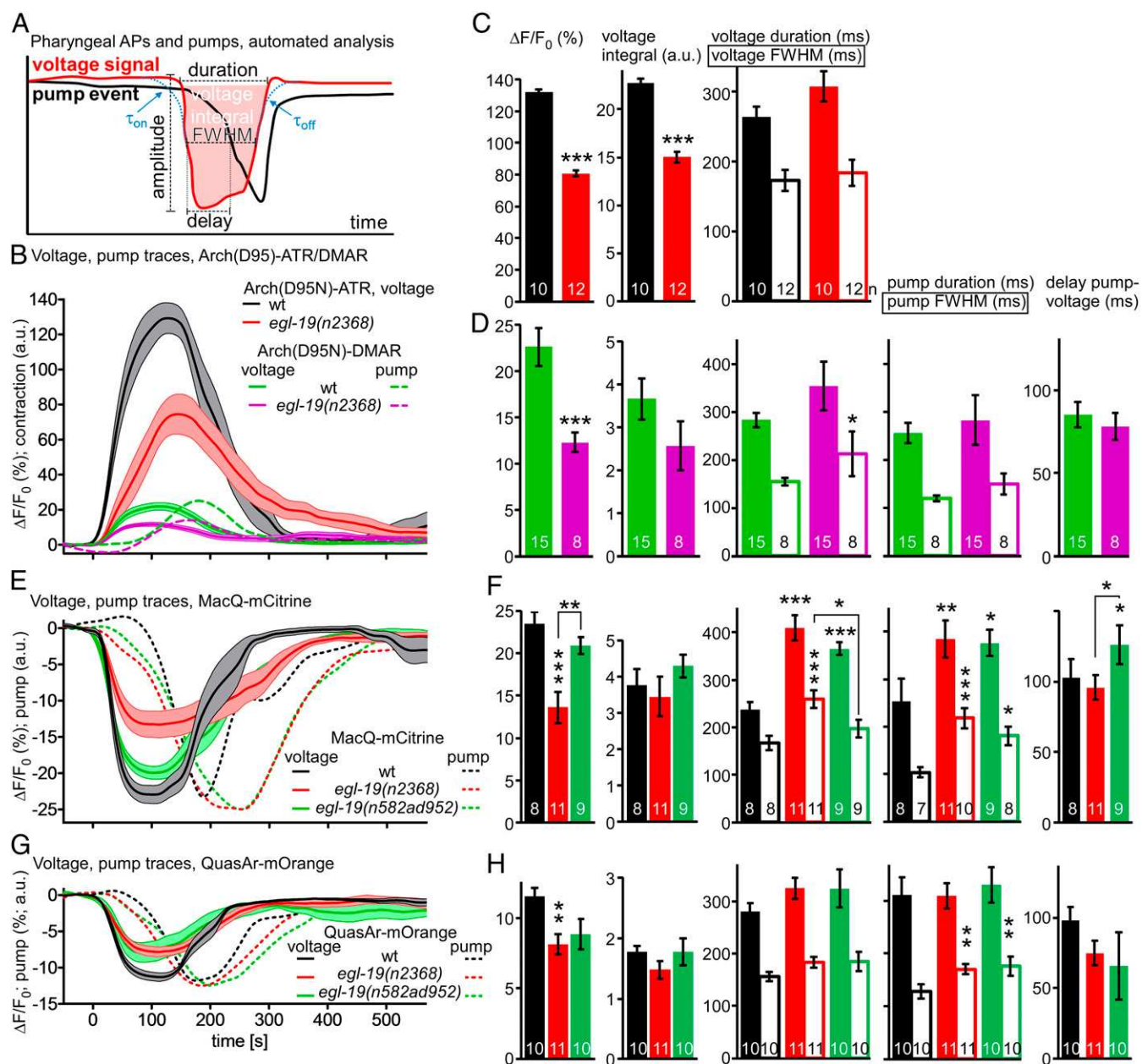
Fig. 5. Pharyngeal AP and pump parameters quantified by automated analysis in WT and L-type VGCC g.o.f. mutants. (*A*) Automated analysis of pharyngeal AP parameters and corresponding TB contraction, determined after extraction and alignment of AP and pump events from fluorescence traces (see *Materials and Methods* for details). (*B*) Mean ± SEM data obtained using Arch(D95N) equipped with ATR and DMAR, in WT and in *egl-19(n2368)* mutants. (*C* and *D*) Mean ± SEM of AP and pump parameters deduced from data in *B*. (*E–H*) Mean ± SEM data and parameters deduced from MacQ-mCitrine (*E* and *F*) or QuasAr-mOrange recordings (*G* and *H*). Frame rate in *B*, *E*, and *G*: 189 fps, 1-ms exposure. Data in *C*, *D*, *F*, and *H* were statistically analyzed by ANOVA, Bonferroni correction. ***$P \leq 0.001$, **$P \leq 0.01$, *$P \leq 0.05$.

very similar (264, 283, 238, and 281 ms, respectively; no significant difference, n.s.). For Arch(D95N)-DMAR, MacQ-mCitrine, and QuasAr-mOrange, we could also compare other parameters among the sensors: the pump duration was 255, 264, and 304 ms, respectively (n.s.); the delay from voltage rise to pump onset was 85, 103, and 98 ms, respectively (n.s.); voltage signal τ_{on} (~15 ms; i.e., smaller than measured in Fig. 4*C*, likely due to the cut worm preparation versus intact animals) and τ_{off} (~35 ms), as well as pump rise [erroneous for Arch(D95N), 23 to 39 ms for the eFRET sensors] and decay time constants (19 to 39 ms) (*SI Appendix*, Fig. S4) were not significantly different between sensors. This shows tight coupling of pharyngeal voltage and contraction kinetics, observable with each sensor, and

allows correlating these events. It should also allow characterizing aberrations in mutants affecting PM physiology, in ways not possible by electrophysiology, as muscle movement makes precise intracellular recordings demanding or even precludes them.

"Gain-of-Function" Mutations in L-Type Channels Prolong Pump Duration but Reduce Voltage Increases. We used the voltage sensors to quantitatively compare mutants affecting the L-type voltage-gated Ca^{2+} channel (VGCC) EGL-19. This channel carries currents shaping the plateau phase of the pharyngeal AP (36, 37). Loss-of-function mutants are lethal; however, several g.o.f. alleles were isolated and, due to EGL-19's additional

function in BWMs, characterized as affecting muscle tone. We analyzed 2 g.o.f. alleles, *n2368* and *n582ad952*. These affect amino acids close to the pore domain of the second VGCC module (*n2368* → G365R), or a double mutation in the pore of the first and the voltage sensor of the third module (*n582ad952* → S372L, R899H). We compared 8 to 15 animals per genotype, 2 to 10 APs per animal. Imaging PM activity with Arch(D95N)-ATR or -DMAR or the 2 eFRET voltage sensors showed a significantly reduced AP amplitude for *n2368* (to 52 to 65% of the WT) (Fig. 5 *B–H*), and a reduced signal (n.s.) for *n582ad952*. For MacQ-mCitrine, both alleles showed significantly prolonged AP and pump durations (Fig. 5 *E* and *F* [pump duration was also increased for QuasAr-mOrange] and Fig. 5 *G* and *H*). Thus, g.o.f. describes the effect of these alleles on PM contraction properties (i.e., prolonged pump). Respective the AP [which in BWMs is similarly reduced in amplitude, although also prolonged (24, 25)], these alleles are hypomorphic rather than g.o.f. The dihydropyridine analog nemadipine A (NemA) is a potent inhibitor/accelerates desensitization of EGL-19 (38, 39). We analyzed the influence of NemA on voltage-dependent PM fluorescence signals, compared with animals incubated in just the DMSO-containing vehicle (*SI Appendix*, Fig. S5). As expected, NemA decreased WT voltage signals, and essentially restored the *egl-19* g.o.f. alleles to DMSO-control levels in WT. This was true for all sensors tested [Arch(D95N)-DMAR, QuasAr-mOrange, and MacQ-mCitrine], although to different degrees. In sum, voltage imaging is a valuable method for characterization of ion channels, and more easily applied than electrophysiology.

Imaging Spatially Compartmentalized Voltage Signals in the Pharynx. Electrophysiology is difficult in electrically coupled cell systems, thus precluding analysis of compartmentalization of cell ensembles. This is expected to be the case for the pharynx, where anterior and posterior portions act differently, as implied by the different events visible in electropharyngeograms (EPGs i.e., extracellular recordings of pharyngeal electrical activity) (40–42). EPGs are current recordings with a complex, yet stereotypic structure (Fig. 6*C*), corresponding to PM depolarization and repolarization events, including currents due to inhibitory neurons that terminate the pharyngeal AP. These different events are not spatially resolvable by EPG recordings, and cannot be addressed by simultaneous sharp electrode recordings from different sections of the pharynx (33–36, 43). We thus assessed compartmentalized PM activity by voltage imaging. A MacQ-mCitrine recording of a pump train with uniform single events (Movie S7) was processed to represent changes in voltage, rather than absolute signals. We calculated difference movies, and after aligning and averaging, we could clearly observe depolarization and repolarization events (Fig. 6*A* and Movie S8). Spatiotemporal differences in voltage-change rate along the longitudinal axis of the pharynx were obvious (Fig. 6 *A* and *B*). All PMs synchronously depolarized, while repolarization, following approximately 144 ms later, occurred first in the anterior PMs (the corpus), and 50 ms later in the isthmus and TB. A small section connecting the corpus and isthmus showed additional depolarization between the 2 repolarization events (161 ms). This region could match the connection between pm5 and pm4 muscle cells, where multiple inputs from pharyngeal neurons occur that could underlie the minor signal. It will be interesting to visualize this region in more detail, ideally with markers for pharyngeal neuron cell types. The EPG measures currents from the extracellular medium into the PMs and thus represents changes in muscle polarization. We wondered if mean voltage-difference events, averaged across the whole pharynx, would correspond to the EPG. We simultaneously recorded EPGs and optical eFRET signals of MacQ-mCitrine. Optical signals only occurred when ATR was present, and matched the electrical recordings very well (*SI Appendix*, Fig. S6). When we calculated the inverse mean signal change of the entire pharynx, it fitted the EPG recording precisely (Fig. 6*C*). A single de-

polarization spike (corresponding to "E" or "E2") was followed by 2 repolarization spikes, corresponding to the anterior and posterior parts of the pharynx ("R1" and "R2") (40, 42–45). In sum, optical measurements match EPGs, yet outperform them with respect to spatial information.

Discussion

We surveyed microbial rhodopsin-based voltage sensors in different muscles and neurons of *C. elegans*. These include the rhodopsins Arch(D95N) (equipped with ATR and the retinal analog DMAR), QuasAr, and Archon, as well as the eFRET sensors MacQ-mCitrine and QuasAr-mOrange. We show that all of them detect APs with robust fluorescence changes of up to 128% per 100 mV in the pharynx, and 78% in BWMs. These values were larger than previously reported for other organisms. This may result from different lipid compositions of *C. elegans* membranes, beneficially influencing Arch' properties. Making these high $\Delta F/F_0$ values accessible, however, required high-power laser excitation (up to 1,800 mW/mm^2 637-nm light), achievable only in a small field-of-view, as well as an EMCCD camera, to enable recording at a high frame rate despite the low absolute fluorescence. Addition of ATR to the culture medium caused increased background fluorescence upon blue-light stimulation, thus low concentrations of ATR are recommended. Lower excitation light intensities (180 mW/mm^2) were sufficient when using DMAR as an alternative to ATR. DMAR strongly boosted the absolute fluorescence levels, yet reduced the fluorescence change per voltage change by a factor of 5. Possibly, a similar branched photocycle as in Arch(D95N)-ATR (20) is present with DMAR, requiring more than 1 photon to be absorbed. However, it was feasible to use this sensor/retinal analog combination to robustly measure parameters of pharyngeal pumping that were similar to those measured with the eFRET sensors, and to compare VGCC g.o.f. mutants to WT.

Despite 75% lower absolute fluorescence intensity, the MacQ-mCitrine eFRET sensor showed approximately 3-fold higher $\Delta F/F$ than QuasAr-mOrange. Parameters of pharyngeal APs and pumping were similar for all sensors, emphasizing that they did not alter the properties of the pharynx, and our sharp electrode recordings did not reveal PM properties different from previous reports (33–35). Electrophysiological measurements are demanding and do not allow concomitant analysis of muscular movement and contraction parameters, while our imaging approach does. Since the parameters we measured in WT and *egl-19* g.o.f. alleles were not altered by the 3 sensors, we expect that other mutations affecting pharyngeal physiology and pumping will also be accessible using the methods described here. Furthermore, we showed that NemA, a VGCC blocker, similarly affected—actually restored—pharyngeal AP characteristics in *egl-19* g.o.f. mutants, as shown earlier by electrophysiology (38). The signals we determined for pharyngeal voltage fluorescence fluctuations were quite comparable in pump trains of single animals, but differed across animals. This may be due to the differences in immobilization of each individual and might be improved by more reproducible immobilization conditions (e.g., in microfluidic devices).

Our imaging approach allows following fluorescence fluctuations in a spatiotemporally defined manner across an ensemble of electrically coupled cells. This confirmed earlier assumptions made from EPG recordings (i.e., that TB repolarization is delayed relative to corpus repolarization). Due to movement, this cannot be simultaneously measured by sharp electrodes in the 2 parts of the pharynx, emphasizing that optical measurements provide new possibilities. We observed not only the functional electrical compartmentalization of the 2 pharyngeal halves but also observed smaller subcompartments at their interface, with potentially distinct electrical activities during distinct phases of excitation-repolarization. This could be further assessed, for example, in gap junction mutants or cell-specific knockdown animals. Evaluating voltage change rates across the

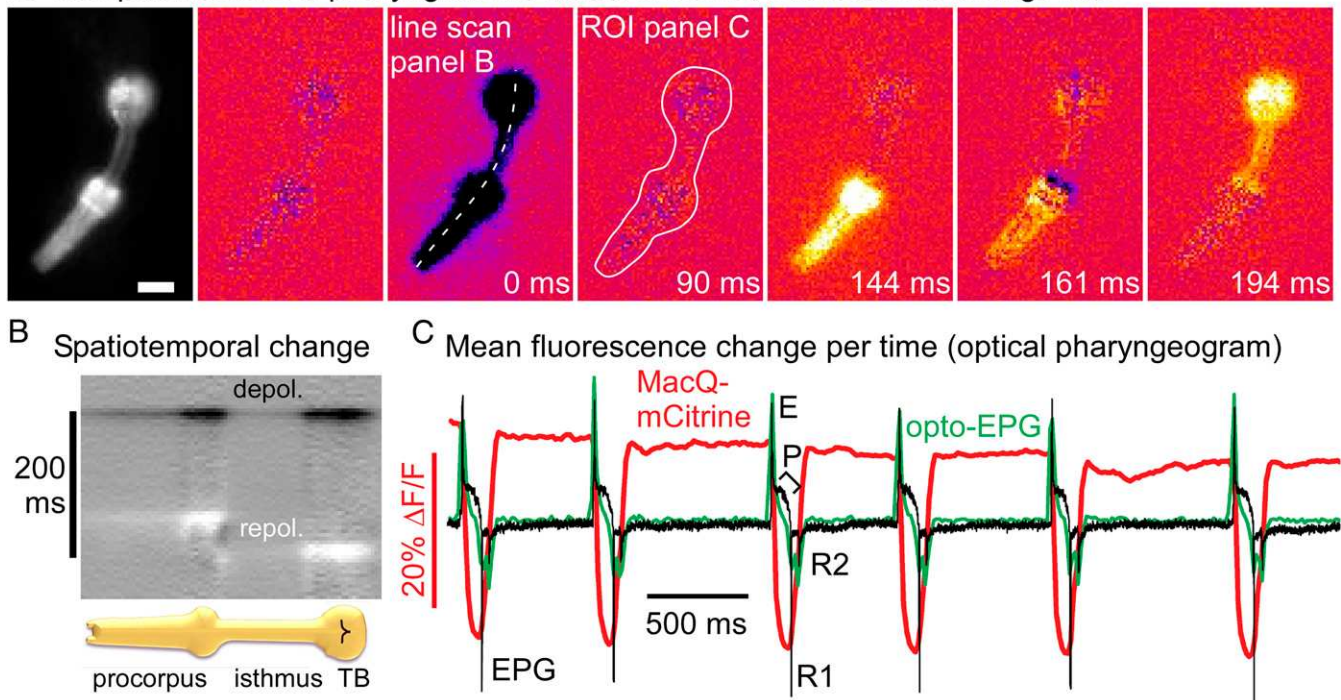## A Compartmentalized pharyngeal AP, MacQ-mCitrine, fluorescence change rate

B Spatiotemporal change

C Mean fluorescence change per time (optical pharyngeogram)

Fig. 6. Pharyngeal AP repolarization occurs in a spatiotemporally compartmentalized fashion. (*A*) A MacQ-mCitrine fluorescence movie (191 fps, 1-ms exposure) of a pharyngeal pump train was analyzed by measuring fluorescence differences from frame to frame and averaging 12 events, aligned to peak depolarization rate (0 ms, as indicated). (Scale bar, 20 μm.) Dark and bright colors represent high rates of depolarization and repolarization, respectively (Movie S8). Linear ROI along axis of the pharynx allows generating a kymograph (*B*) for analysis of spatiotemporal development of voltage; synchronous depolarization, consecutive repolarization of corpus and TB. An ROI around the entire pharynx allows generating an "optical EPG" (*C*) by plotting inverted mean values (green). The EPG (black) was measured simultaneously, showing (from left to right) typical spikes: E/E2 excitation, inhibitory P spikes, as well as R1 and R2 repolarization; eFRET signal is overlaid in red.

pharynx allowed us to generate an "optical EPG," recapitulating most of the characteristic features of the classical EPG. Simultaneous electrical and optical measurements enable optimal $\Delta F/F$ signal calibration.

Finally, neuronal activity was also measurable using QuasAr. We expected this to be difficult since *C. elegans* neurons often exhibit only small membrane-potential changes. Cholinergic neurons showed activity in line with the graded potentials previously described for these neurons (46). The locomotion interneuron RIM exhibited fast de- or hyperpolarizing events, possibly due to presynaptic input. In line with Ca^{2+} imaging, RIM voltage also showed slow fluctuations that could represent a bistable membrane potential, corresponding to forward and reverse locomotion states of this neuron, and which could result from the integration of many concomitant small inputs to RIM. Future work will use (optogenetic) activation or inhibition of neurons up- or downstream of RIM, to explore the circuit activity in an all-optical manner, in intact, possibly even freely moving animals.

The combination of voltage imaging in the infrared and blue-light stimulation of ChR2 enables all-optical electrophysiology approaches for *C. elegans*, and will greatly facilitate such measurements, bypassing complicated electrophysiological approaches (47). It should further enable analyzing mutants affecting neuromuscular junction function that are too small to allow dissection for patch-clamp electrophysiology. That voltage imaging is performed in intact animals is a distinct advantage over measurements in dissected animals, since the composition of extracellular and pipette solutions may alter the endogenous physiology. In sum, we compared a range of useful tools for all-optical interrogation of muscular tissues, cell ensembles, and neurons, in response to intrinsic activities, as well as

optogenetically evoked neurotransmission, and provide guidelines for their use in *C. elegans*.

Materials and Methods

An extended Materials and Methods section is provided in *SI Appendix*.

***C. elegans* Culture and Transgenic Animals and Molecular Biology.** *C. elegans* culture and transgenic animals and molecular biology were all according to standard methods and are described in detail in *SI Appendix*.

Voltage and Ca^{2+} Imaging of Immobilized Animals. Information on animal preparation and imaging conditions, as well as microscope setup, are mostly standard procedures and explained in *SI Appendix*.

Animals were cultivated in the presence of ATR or respective ATR-analogs [final ATR concentration: 0.01 mM for ChR2 or ACR2 blue-light stimulation, 1 mM for imaging Arch(D95N) in pharynx, and 0.1 mM for imaging eFRET sensors]. APs were observed clearly only with 637-nm laser excitation, 180 mW/mm² (in pharynx), and 1.8 W/mm² for imaging of QuasAr and Archon in BWMs. For imaging, worms were immobilized with polystyrene beads. Imaging was performed on an inverted microscope (Zeiss Axio Observer Z1), equipped with 40× oil immersion objective (Zeiss EC Plan-NEOFLUAR 40×/N.A. 1.3, Oil DIC ∞/0.17), LED light sources (KSL 70, Rapp OptoElectronic) or monochromator (PolychromeV, Till Photonics) for photostimulation, a 637-nm laser (OBIS FP 637LX, Coherent) for excitation of voltage sensors, a galilean beam expander (BE02-05-A, Thorlabs), and an EMCCD Camera (Evolve 512 Delta, Photometrics). Voltage sensor fluorescence was imaged at 700 or 747 nm for ATR, and at 780 nm for DMAR. eFRET sensors were imaged with 545/30- or 472/30-nm excitation and 610/75- or 520/35-nm emission, respectively.

Processing and Automated Data Analysis of Pharyngeal Voltage and Pump Events. Processing and automated data analysis of pharyngeal voltage and pump events were done with an automated custom workflow in KNIME 3.6.2 (KNIME AG) (48), which was used to synchronize pump and voltage events

182

across animals by calling an R (R 3.5.1, The R Foundation for Statistical Computing; ref. 49) script to process each of the Excel tables (script accessible via https://open.ag.bmls.uni-frankfurt.de/s/qmLbijczkxAogEE).

Electrophysiology. Recordings were conducted from dissected BWM cells on the ventral side of the body anterior to the vulva as described earlier (47). EPG recordings and cut-head preparation were performed as described previously (38). Intracellular recordings were performed following a previously described protocol (41).

Software and Statistics. Software used was Knime 3.6.2 (KNIME AG), R 3.5.1 (The R Foundation for Statistical Computing). Statistics used were ANOVA with Bonferroni correction, after verification of normal distribution of the data.

1. C. K. Kim, A. Adhikari, K. Deisseroth, Integration of optogenetics with complementary methodologies in systems neuroscience. *Nat. Rev. Neurosci.* **18**, 222–235 (2017).
2. T. Knöpfel, Genetically encoded optical indicators for the analysis of neuronal circuits. *Nat. Rev. Neurosci.* **13**, 687–700 (2012).
3. Y. Xu, P. Zou, A. E. Cohen, Voltage imaging with genetically encoded indicators. *Curr. Opin. Chem. Biol.* **39**, 1–10 (2017).
4. S. D. Antic, R. M. Empson, T. Knöpfel, Voltage imaging to understand connections and functions of neuronal circuits. *J. Neurophysiol.* **116**, 135–152 (2016).
5. M. Z. Lin, M. J. Schnitzer, Genetically encoded indicators of neuronal activity. *Nat. Neurosci.* **19**, 1142–1153 (2016).
6. J. H. Simpson, L. L. Looger, Functional imaging and optogenetics in *Drosophila*. *Genetics* **208**, 1291–1309 (2018).
7. J. R. Enterina, L. Wu, R. E. Campbell, Emerging fluorescent protein technologies. *Curr. Opin. Chem. Biol.* **27**, 10–17 (2015).
8. H. Dana *et al.*, Sensitive red protein calcium indicators for imaging neural activity. *eLife* **5**, e12727 (2016).
9. J. Akerboom *et al.*, Genetically encoded calcium indicators for multi-color neural activity imaging and combination with optogenetics. *Front. Mol. Neurosci.* **6**, 2 (2013).
10. T. W. Chen *et al.*, Ultrasensitive fluorescent proteins for imaging neuronal activity. *Nature* **499**, 295–300 (2013).
11. Y. Gong, J. Z. Li, M. J. Schnitzer, Enhanced archaerhodopsin fluorescent protein voltage indicators. *PLoS One* **8**, e66959 (2013).
12. P. D. E. Williams *et al.*, Serotonin disinhibits a *Caenorhabditis elegans* sensory neuron by suppressing Ca²⁺-dependent negative feedback. *J. Neurosci.* **38**, 2069–2080 (2018).
13. K. D. Piatkevich *et al.*, A robotic multidimensional directed evolution approach applied to fluorescent voltage reporters. *Nat. Chem. Biol.* **14**, 352–360 (2018).
14. Y. Gong, M. J. Wagner, J. Zhong Li, M. J. Schnitzer, Imaging neural spiking in brain tissue using FRET-opsin protein voltage sensors. *Nat. Commun.* **5**, 3674 (2014).
15. N. C. Flytzanis *et al.*, Archaerhodopsin variants with enhanced voltage-sensitive fluorescence in mammalian and Caenorhabditis elegans neurons. *Nat. Commun.* **5**, 4894 (2014).
16. P. Zou *et al.*, Bright and fast multicoloured voltage reporters via electrochromic FRET. *Nat. Commun.* **5**, 4625 (2014).
17. J. M. Kralj, A. D. Douglass, D. R. Hochbaum, D. Maclaurin, A. E. Cohen, Optical recording of action potentials in mammalian neurons using a microbial rhodopsin. *Nat. Methods* **9**, 90–95 (2011).
18. D. R. Hochbaum *et al.*, All-optical electrophysiology in mammalian neurons using engineered microbial rhodopsins. *Nat. Methods* **11**, 825–833 (2014).
19. J. M. Kralj, D. R. Hochbaum, A. D. Douglass, A. E. Cohen, Electrical spiking in Escherichia coli probed with a fluorescent voltage-indicating protein. *Science* **333**, 345–348 (2011).
20. D. Maclaurin, V. Venkatachalam, H. Lee, A. E. Cohen, Mechanism of voltage-sensitive fluorescence in a microbial rhodopsin. *Proc. Natl. Acad. Sci. U.S.A.* **110**, 5939–5944 (2013).
21. Y. Gong *et al.*, High-speed recording of neural spikes in awake mice and flies with a fluorescent voltage sensor. *Science* **350**, 1361–1366 (2015).
22. M. Kannan *et al.*, Fast, in vivo voltage imaging using a red fluorescent indicator. *Nat. Methods* **15**, 1108–1116 (2018).
23. N. AzimiHashemi *et al.*, Synthetic retinal analogues modify the spectral and kinetic characteristics of microbial rhodopsin optogenetic tools. *Nat. Commun.* **5**, 5810 (2014).
24. S. Gao, M. Zhen, Action potentials drive body wall muscle contractions in Caenorhabditis elegans. *Proc. Natl. Acad. Sci. U.S.A.* **108**, 2557–2562 (2011).
25. P. Liu *et al.*, Genetic dissection of ion currents underlying all-or-none action potentials in C. elegans body-wall muscle cells. *J. Physiol.* **589**, 101–117 (2011).
26. O. Tolstenkov *et al.*, Functionally asymmetric motor neurons contribute to coordinating locomotion of *Caenorhabditis elegans*. *eLife* **7**, e34997 (2018).
27. A. Bergs *et al.*, Rhodopsin optogenetic toolbox v2.0 for light-sensitive excitation and inhibition in Caenorhabditis elegans. *PLoS One* **13**, e0191802 (2018).
28. E. G. Govorunova, O. A. Sineshchekov, R. Janz, X. Liu, J. L. Spudich, Neuroscience. Natural light-gated anion channels: A family of microbial rhodopsins for advanced optogenetics. *Science* **349**, 647–650 (2015).
29. T. Kawano *et al.*, An imbalancing act: Gap junctions reduce the backward motor circuit activity to bias C. elegans for forward locomotion. *Neuron* **72**, 572–586 (2011).
30. B. J. Piggott, J. Liu, Z. Feng, S. A. Wescott, X. Z. S. Xu, The neural circuits and synaptic mechanisms underlying motor initiation in C. elegans. *Cell* **147**, 922–933 (2011).
31. V. Venkatachalam *et al.*, Pan-neuronal imaging in roaming Caenorhabditis elegans. *Proc. Natl. Acad. Sci. U.S.A.* **113**, E1082–E1088 (2016).
32. Y. Kagawa-Nagamura, K. Gengyo-Ando, M. Ohkura, J. Nakai, Role of tyramine in calcium dynamics of GABAergic neurons and escape behavior in *Caenorhabditis elegans*. *Zoological Lett.* **4**, 19 (2018).
33. M. W. Davis, R. Fleischhauer, J. A. Dent, R. H. Joho, L. Avery, A mutation in the C. elegans EXP-2 potassium channel that alters feeding behavior. *Science* **286**, 2501–2504 (1999).
34. K. A. Steger, B. B. Shtonda, C. Thacker, T. P. Snutch, L. Avery, The C. elegans T-type calcium channel CCA-1 boosts neuromuscular transmission. *J. Exp. Biol.* **208**, 2191–2203 (2005).
35. C. J. Franks *et al.*, Ionic basis of the resting membrane potential and action potential in the pharyngeal muscle of Caenorhabditis elegans. *J. Neurophysiol.* **87**, 954–961 (2002).
36. B. Shtonda, L. Avery, CCA-1, EGL-19 and EXP-2 currents shape action potentials in the Caenorhabditis elegans pharynx. *J. Exp. Biol.* **208**, 2177–2190 (2005).
37. R. Y. Lee, L. Lobel, M. Hengartner, H. R. Horvitz, L. Avery, Mutations in the alpha1 subunit of an L-type voltage-activated Ca2+ channel cause myotonia in Caenorhabditis elegans. *EMBO J.* **16**, 6066–6076 (1997).
38. C. Schüler, E. Fischer, L. Shaltiel, W. Steuer Costa, A. Gottschalk, Arrhythmogenic effects of mutated L-type Ca 2+-channels on an optogenetically paced muscular pump in Caenorhabditis elegans. *Sci. Rep.* **5**, 14427 (2015).
39. T. C. Kwok *et al.*, A small-molecule screen in C. elegans yields a new calcium channel antagonist. *Nature* **441**, 91–95 (2006).
40. D. M. Raizen, L. Avery, Electrical activity and behavior in the pharynx of Caenorhabditis elegans. *Neuron* **12**, 483–495 (1994).
41. A. Cook, C. J. Franks, L. Holden-Dye, Electrophysiological recordings from the pharynx. *WormBook* **100**, 1–7 (2006).
42. L. Avery, D. Raizen, S. Lockery, Electrophysiological methods. *Methods Cell Biol.* **48**, 251–269 (1995).
43. M. W. Davis *et al.*, Mutations in the Caenorhabditis elegans Na,K-ATPase alpha-subunit gene, eat-6, disrupt excitable cell function. *J. Neurosci.* **15**, 8408–8418 (1995).
44. K. A. Steger, L. Avery, The GAR-3 muscarinic receptor cooperates with calcium signals to regulate muscle contraction in the Caenorhabditis elegans pharynx. *Genetics* **167**, 633–643 (2004).
45. J. Dillon *et al.*, AutoEPG: Software for the analysis of electrical activity in the microcircuit underpinning feeding behaviour of Caenorhabditis elegans. *PLoS One* **4**, e8482 (2009).
46. Q. Liu, G. Hollopeter, E. M. Jorgensen, Graded synaptic transmission at the Caenorhabditis elegans neuromuscular junction. *Proc. Natl. Acad. Sci. U.S.A.* **106**, 10823–10828 (2009).
47. J. F. Liewald *et al.*, Optogenetic analysis of synaptic function. *Nat. Methods* **5**, 895–902 (2008).
48. M. Berthold *et al.*, "KNIME: The Konstanz information miner" in *Data Analysis, Machine Learning and Applications*, C. Preisach, H. Burkhardt, L. Schmidt-Thieme, R. Decker, Eds. (Studies in Classification, Data Analysis, and Knowledge Organization, Springer, 2008), pp. 319–326.
49. R Core Team, R: A language and environment for statistical computing (Version 3.5.1, R Foundation for Statistical Computing, Vienna, Austria, 2014).

183

PNAS

www.pnas.org

Supplementary Information for

Rhodopsin-based voltage imaging tools for use in muscles and neurons of *Caenorhabditis elegans*

Negin Azimi Hashemi, Amelie C. F. Bergs, Christina Schüler, Anna Rebecca Scheiwe, Wagner Steuer Costa, Maximilian Bach, Jana F. Liewald, Alexander Gottschalk

corresponding author: Alexander Gottschalk
Email: a.gottschalk@em.uni-frankfurt.de

This PDF file includes:

Supplementary Materials and Methods
Supplementary References
Figs. S1 to S6
Captions for movies S1 to S8
Captions for dataset S1

Other supplementary materials for this manuscript include the following:

Movies S1 to S8
Dataset S1

1

SUPPLEMENTARY MATERIALS AND METHODS

C. elegans culture and transgenic animals

Worms were cultivated on nematode growth medium (NGM) plates, seeded with *E. coli* OP50-1 strain (1). Generation of transgenic animals was performed by microinjection of plasmid DNA, at varying concentrations (2). For transgenic strains ZX1917, ZX1918 and ZX1958, 3 ng/µL of the respective voltage sensor DNA was injected into the gonads of mother animals. For strains ZX1920, ZX1953, ZX2476, ZX2479 and ZX2483, 10 ng/µL, for ZX2560, 30 ng/µL and for ZX2477, 40 ng/µL of the respective voltage sensor plasmids were used in combination with either 1.5 ng/µL of the co-expression marker p*myo-2*::CFP or 30 ng/µL of p*elt-2*::GFP or p*myo-3*::CFP. For ZX2483 50 ng/µL of p*unc-17*::ACR2::eYFP, and for ZX2543, 100 ng/µL of p*tdc-1s*::jRCaMP1b-opti were injected.

Transgenic C. elegans *strains*

The following strains were used or generated: **DA952:** *egl-19(n582ad952),* **MT6129**: *egl-19(n2368),* **ZX1907**: *zxEx922[pmyo2::Arch::2xMyc; pmyo-3::CFP],* **ZX1917**: *zxEx942[pmyo-2::QuasAr::mOrange; pmyo-3::CFP],* **ZX1918**: *zxEx943[pmyo-2::MacQ::mCitrine; pmyo-3::mCherry],* **ZX1920:** *zxIs121[pmyo-3::QuasAr::mOrange; pmyo-3::CFP],* **ZX1951**: *egl-19(n2368); zxEx942[pmyo-2::QuasAr::mOrange; pmyo-3::CFP],* **ZX1952**: *egl-19(n2368); zxEx942[pmyo-2::MacQ-mCitrine; pmyo-3::mCherry],* **ZX1953:** *zxIs120[pmyo-3::ArchD95N::2xmyc-tag; pmyo-3::CFP],* **ZX1954**: *zxIs6; zxIs120[pmyo-3::ArchD95N::2xmyc-tag; pmyo-3::CFP],* **ZX1955**: *egl-19(n582ad952); zxEx942[pmyo-2::QuasAr::mOrange; pmyo-3::CFP],* **ZX1956**: *egl-19(n582ad952); zxEx942[pmyo-2::MacQ-mCitrine; pmyo-3::mCherry],* **ZX1958**: *zxEx944[pmyo-2::ArchD95N::2xmyc-tag; pmyo3::CFP],* **ZX1959**: *egl-19(n582ad952); zxEx944[pmyo-2::ArchD95N; pmyo-3::CFP],* **ZX1960**: *zxIs5[punc-17::ChR2(H134R); lin-15+]; zxIs121[pmyo-3::QuasAr::mOrange; pmyo-3::CFP],* **ZX2476**: *zxEx1139[pmyo-3::QuasAr; pmyo-2::CFP],* **ZX2477**: *zxEx1140[punc-17::QuasAr; pmyo-3::CFP],* **ZX2479**: *zxIs5[punc-17::ChR2(H134R); lin-15+]; zxEx1142[pmyo-3::Archon::GFP; pmyo-2::CFP],* **ZX2482**: *zxIs5[punc-17::ChR2(H134R); lin-15+]; zxEx1145[pmyo-3::QuasAr; pmyo-2::CFP],* **ZX2483**: *zxEx1146[punc-17::ACR2::eYFP; pmyo-3::QuasAr; pelt-2::GFP],* **ZX2534**: *lite-1(ce314); zxEx1169[ptdc-1s::jRCaMP1b-opti; pggr-2::loxP::ChR2::mCherry::bc::GFP; pggr-1::Cre],* **ZX2560**: *zxEx1203[ptdc-1s::QuasAr::GFP; pelt-2::GFP].*

Molecular biology

Plasmid **pAB4** (*punc-17*::ACR2::eYFP) was described earlier (3). **pAB16** (p*myo-3*::QuasAr) was generated via Gibson Assembly based on p*myo-3*::QuasAr::mOrange and pPD96.52 (p*myo-3*, Addgene plasmid #1608), using restriction enzymes *Bam*HI and *Xba*I and primers QUASAR_fwd (5'-cccacgaccactagatccatATGGTAAGTATCGCTCTGCAG-3') and QUASAR_rev (5'-gtcctttggccaatcccgggCTCGGTGTCGCCCAGAATAG-3'). **pAB19** (p*myo-3*::Archon::GFP) was generated via subcloning from *rig-3*::wArchon1::GFP (a gift from Steven Flavell) into pPD96.52, using restriction enzymes *Kpn*I und *Sac*I. **pNH13** (p*myo-2*::QuasAr::mOrange) and **pNH12** (p*myo-2*::MacQ::mCitrine) were generated by subcloning of plasmids #59173 and #48762 (Addgene) into pPD132.102 (p*myo-2*, #1662, Addgene) via restriction with *Bam*HI and *Eco*RI. Site-directed mutagenesis of plasmid pNH10 (p*myo-2*::Arch::2xMycTag) resulted in plasmid **pNH11** (p*myo-2*::Arch(D95N)::2xMycTag), using primers oNH7 (5´TATGCCAGGTACGCC

AACTGGCTGTTTACCACC3´) and oNH8 (5´-GGTGGTAAACAGCCAGTCGGCGTACCTG GCATA-3´). **pAB17** (p*unc-17*::QuasAr) was generated via Gibson assembly based on p*myo-3*::QuasAr (pAB16) and RM#348p (p*unc-17*, a gift from Jim Rand), using NheI restriction and primers punc17_QuasAr_fwd (5'-attttcaggaggacccttggATGGTAAGTATCGCTCTGCAG-3') and punc17_QuasAr_rev (5'-ataccatggtaccgtcgacgCTCGGTGTCGCCCAGAATAG-3'). **pAB23** (p*tdc-1s*::QuasAr::GFP) was generated via Gibson assembly based on p*tdc-1s*::GFP and p*myo-3*::QuasAr (pAB16), using AgeI restriction and primers p*tdc-1s*_QuasAr_GFP_fwd (5'-catttttcaggaccgcccaaatggtaagtatcgctctgcagg-3') and ptdc-1s_QuasAr_GFP_rev (5'-tcctttactca tttttctagctcggtgtcgcccagaa-3'). **pXY10** (p*tdc-1s*::jRCaMP1b-opti) was generated by subcloning based on pXY09 (p*unc-17*::jRCaMPb-opti), cut with SphI & NheI (blunted) and pXY07 cut with SphI & AgeI (blunted). **pXY09** was generated from RM#348p (p*unc-17*; a gift from J. Rand), cut with KpnI & EcoRV, and insertion of a synthesized, codon-optimized version of jRCaMP1b (4). **pXY07** (ptdc-1s::GFP): The ptdc-1 promoter was amplified using primers oM010 5`-TCATgcatgcATTTCTGTATGAGCCGCCCG-3' & oM015 5`-TTGGACCGGTTGGGCGGTC CTGAAAAATGC-3' and subcloned with SphI & AgeI cuts.

Voltage and Ca²⁺ imaging of immobilized animals

One day prior to the experiments, transgenic animals at L4 stage were transferred onto NGM plates seeded with OP50-1 from bacterial suspensions supplemented with ATR (Sigma-Aldrich, USA) or the respective ATR-analogues DMAR or VI (final ATR concentration: 0.01 mM for experiments with ChR2 or ACR2 blue-light stimulation, 1 mM for imaging experiments or Arch(D95N) in the pharynx, and 0.1 mM for imaging eFRET sensors); note that for analog VI we used Arch wt, and an HBO lamp (30 mW/mm² excitation at 620 nm). DMAR could be visualized well with HBO illumination, however, APs were observed clearly only with 637 nm laser excitation, 180 mW/mm². For imaging, worms were placed onto 10 % agarose pads (M9 buffer) on microscope slides and immobilized with polystyrene beads (0.1 µm diameter, at 2.5% w/v, Sigma-Aldrich). Imaging was performed on an inverted microscope (Zeiss Axio Observer Z1), equipped with 40x oil immersion objective (Zeiss EC Plan-NEOFLUAR 40x/ N.A. 1.3, Oil DIC ∞ / 0.17), a 470 nm LED light source (KSL 70, Rapp OptoElectronic, Hamburg, Germany) or monochromator (PolychromeV, Till Photonics) for photostimulation, a 637 nm laser (OBIS FP 637LX, Coherent) for excitation of voltage sensors (1.8 W/mm² for imaging of QuasAr and Archon in BWMs and 180 mW/mm² for PM measurements or for imaging Arch(D95N)-DMAR in BWMs), a galilean beam expander (BE02-05-A, Thorlabs), and an EMCCD Camera (Evolve 512 Delta, Photometrics). Voltage sensor fluorescence was imaged at 700 or 747 nm emission (700/75 ET Bandpass filter, integrated in Cy5 filter cube, AHF Analysentechnik) for ATR, and at 780 nm (780 LP ET Longpass Filter) for DMAR. eFRET sensors were imaged with 545/30 or 472/30 nm excitation (HBO100 100 W mercury lamp, Zeiss, at 30 mW/mm² for 545/30 nm and 10 mW/mm² for 472/30 nm) and 610/75 or 520/35 nm emission (472/30 ET Bandpass, 610/75 ET Bandpass and 520/35 ET Bandpass Filters, AHF Analysentechnik), respectively. Stimulation of optogenetic actuators (ChR2 or ACR2) was performed with 300 µW/mm² at 470 nm. Acquisition times, frame rates and gain used for imaging rhodopsin voltage sensors were 1 or 2 ms, 158 or 190 fps and gain 1 (for DMAR) or gain 10 or 50 (for ATR). For eFRET sensors, it was 1 ms exposure, 190 fps and gain 10, or as stated.

3

To induce pumping under imaging conditions, animals were incubated in 3 µl serotonin (20 mM, in M9 buffer) for 3 min prior to the experiments. For drug assays, animals were exposed to 30 nM nemadipine A in 0.2 % DMSO in M9, or to the vehicle control.

For imaging neurons, animals were cultivated in the presence of 0.1 mM ATR, immobilized in polystyrene beads, and excited by 1.8 W/mm² 637 nm laser light. Exposure time was 5 ms, binning was 4x4, a 700/75 ET bandpass filter, integrated in Cy5 filter cube, was used to acquire images on an EMCCD camera (Evolve 512 Delta).

For imaging Ca^{2+} via jRCaM1b, a 590 nm LED (KSL 70, Rapp OptoElectronic, Hamburg, Germany; 0.6 mW/mm²) and an EMCCD Camera (Evolve 512 Delta; EM-gain: 50) were used, as well as these filters: GFP/mCherry Dualband ET Filter was combined with a 647/57 nm emission filter and a 605 nm longpass beamsplitter (F56-019, F37-647 and F38-605, respectively, all AHF Analysentechnik, Germany). RCaMP movies were acquired at 70 ms exposure, ca. 14 fps.

Processing and automated data analysis of pharyngeal voltage and pump events

Movie acquisition (with frame rates of 160 or ca. 190 fps, at 1 ms exposure time) was performed by using the *Photometrics PVCAM Device Adapter for µManager* (5). For BWM experiments, raw image sequences were analyzed via ROI selection of signal and background and *multi-measure* function in ImageJ (National Institutes of Health, USA; https://imagej.nih.gov/ij/index.html). Changes in fluorescence were calculated as $\Delta F/F_0$, or $\Delta F/F_{mean}$, where F_{mean} (or F, for simplicity) is the mean fluorescence (F_{mean}) of the ROI, calculated for the entire imaging period. Contrast was calculated as the ratio between mean fluorescence of a ROI across the pharyngeal or BWM tissue expressing the voltage sensor, and the mean fluorescence of a ROI within the animal, but chosen in tissue not expressing sensors and showing no autofluorescence. Signal to noise ratio (SNR) was calculated as the ratio of the mean fluorescence of all peaks (= APs) observed during a pump train, and the standard deviation of the fluorescence in the ROI during resting phases.

To register voltage signals in the PMs, a ROI was defined around the whole pharynx, whereas a smaller circular ROI was positioned over the terminal bulb lumen with the grinder, to track contractions via the accompanying lumen opening (lowering of the fluorescence in this ROI, as fluorescing tissue retracts radially). For background correction, another ROI was defined in an arbitrary dark region outside the worm, or, for contrast measurements, 'inside' the worm, but avoiding the gut or tissue expressing the respective voltage sensor. $\Delta F/F$ was calculated in Excel (Microsoft). A custom workflow in KNIME 3.6.2 (KNIME AG, Zurich, Switzerland (6)) was used to synchronize pump and voltage events across animals by calling an R (R 3.5.1, The R Foundation for Statistical Computing) script to process each of the Excel tables (the respective script will be provided on a publicly available server; see main manuscript). The R script (included in the KNIME workflow) proceeds to fit a spline curve to the input data with as many anchor points as data points present. The fit curve is sampled at constant 200 data points per second to account for the variable camera timing. Pumps are found as local minima with a centered time window of 625 ms. A manual input of indices can be used to correct this peak registration. The signals that passed manual control are synchronized first to the pump minimum. The voltage signal is then analyzed for the peak onset by searching for the minimum of the scaled difference with a lag of 50 ms of a centered moving average with window size of 105 ms. The events are subsequently synchronized to the onset of the voltage peak and grouped per animal, or

4

analyzed individually, where appropriate. The signals are further analyzed to extract start and end of peak by searching for the first and last data point to cross a line at 10 % of the distance from the baseline to the peak minimum, respectively. Analogously, the full width at half maximum (FWHM) is calculated by searching for the two data points that cross the 50 % line between baseline and peak minimum. Duration is defined as the time difference between start and end of a peak. The kinetic parameters τ_{ON} and τ_{OFF} are modelled each with a mono-exponential curve fit accounting only for the time frames from (-50 ms, $FWHM_{start}$) and ($FWHM_{end}$, 305 ms), respectively. The area (voltage integral) is calculated as the integral from start to end of the peak from the baseline. The amplitude is calculated as the peak minimum to the maximum value at negative time after synchronization in the depicted time frame. The delay is reported as the time difference between the $FWHM_{start}$ of the voltage and $FWHM_{start}$ of the pump peaks.

Electrophysiology

Recordings were conducted from dissected BWM cells on the ventral side of the body anterior to the vulva as described earlier (1). Animals were immobilized with Histoacryl glue (B. Braun Surgical, Spain) and a lateral incision was made to access neuromuscular junctions along the ventral nerve cord. The basement membrane overlying muscles was removed by incubation in 0.5 mg/ml collagenase for 10 s (C5138, Sigma-Aldrich, Germany). BWMs were patch-clamped in whole-cell mode at 22°C using an EPC10 amplifier with head stage connected to a standard HEKA pipette holder for fire-polished borosilicate pipettes (1B100F-4, WPI, USA) of 4-7 MΩ resistance. The extracellular (bath) solution contained: NaCl 150 mM; KCl 5 mM; CaCl$_2$ 5 mM; MgCl$_2$ 1 mM; glucose 10 mM; sucrose 5 mM; HEPES 15 mM, pH7.3 with NaOH, ≈330 mOsm. The pipette solution contained: K-gluconate 115 mM; KCl 25 mM; CaCl$_2$ 0.1 mM; MgCl$_2$ 5 mM; BAPTA 1 mM; Hepes 10 mM; Na$_2$ATP 5 mM; Na$_2$GTP 0.5 mM; cAMP 0.5 mM; cGMP 0.5 mM, pH7.2 with KOH, ≈320mOsm. Current clamp recordings were conducted using Patchmaster software (HEKA, Germany) (3). Light activation was performed using an LED (KSL-70, Rapp OptoElectronic, Hamburg, Germany; 470 nm, 1 mW/mm²) and controlled by the EPC10 amplifier. Data were analyzed by Patchmaster software.

For electropharyngeogram (EPG) recordings, L4 animals were placed for ca. 24 h on NGM plates seeded with OP50 and supplemented either with or without ATR; for PM intracellular recordings, this time was extended to 2-3 days. Animals were transferred into a recording chamber containing a Sylgard-coated coverslip and filled with 1.5 mL of EmD50 buffer (NaCl, 140 mM; KCl, 3 mM; CaCl$_2$, 3 mM; MgCl$_2$, 1 mM; Hepes, 10 mM; D-Mannitol, 50 mM; pH 7.3 adjusted with NaOH) containing 2-20 µM 5 Hydroxytryptamin to stimulate pumping. Cut-head preparation and EPG recording of strain ZX1918 were performed as described previously (7). Intracellular recordings were performed following a previously described protocol (8), also for the manufacturing of intracellular electrodes and the positioning of the holding and the intracellular electrodes. For combined voltage imaging an EMCCD Camera (Evolve 512 Delta) was used. Data were analyzed by OriginPro.

Software and statistics

Knime 3.6.2 (KNIME AG, Zurich, CH), R 3.5.1 (The R Foundation for Statistical Computing). Statistics used were ANOVA with Bonferroni correction, after verification of normal distribution of the data

SUPPLEMENTARY REFERENCES

1.   Liewald JF, *et al.* (2008) Optogenetic analysis of synaptic function. *Nat Methods* 5(10):895-902.
2.   Evans T (2006) Transformation and microinjection. *WormBook*.
3.   Bergs A, *et al.* (2018) Rhodopsin optogenetic toolbox v2.0 for light-sensitive excitation and inhibition in Caenorhabditis elegans. *PLoS One* 13(2):e0191802.
4.   Dana H, *et al.* (2016) Sensitive red protein calcium indicators for imaging neural activity. *eLife* 5.
5.   Edelstein A, Amodaj N, Hoover K, Vale R, & Stuurman N (2010) *Computer Control of Microscopes Using μManager* (John Wiley & Sons, Inc.).
6.   Berthold M, *et al.* (2008) KNIME: The Konstanz Information Miner. *Data Analysis, Machine Learning and Applications,* Studies in Classification, Data Analysis, and Knowledge Organization, eds Preisach C, Burkhardt H, Schmidt-Thieme L, & Decker R (Springer Berlin Heidelberg), pp 319-326.
7.   Schuler C, Fischer E, Shaltiel L, Steuer Costa W, & Gottschalk A (2015) Arrhythmogenic effects of mutated L-type Ca(2+)-channels on an optogenetically paced muscular pump in Caenorhabditis elegans. *Scientific reports* 5:14427.
8.   Cook A, Franks CJ, & Holden-Dye L (2006) Electrophysiological recordings from the pharynx. *WormBook* 17:1-7.

6
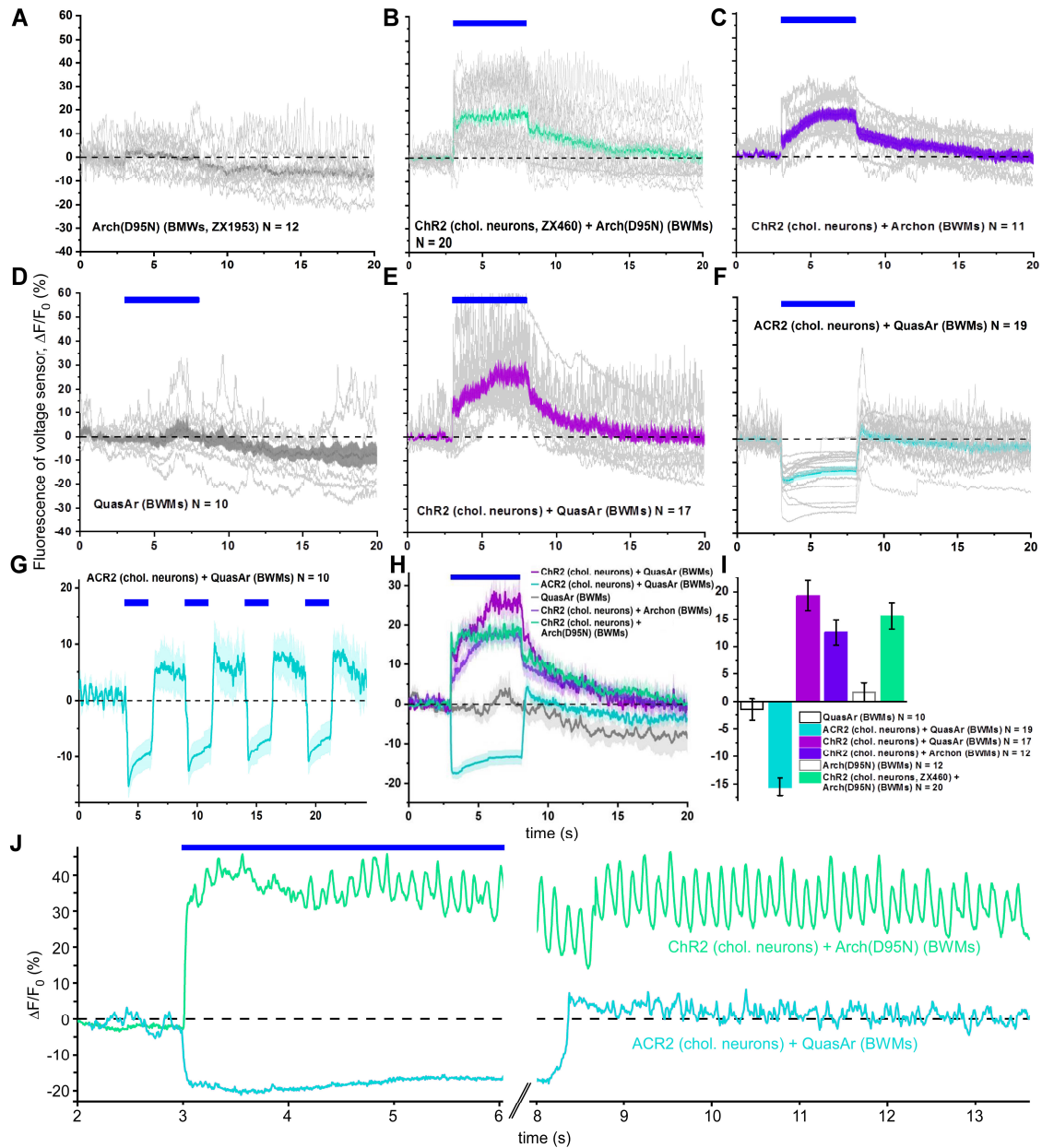
Fig. S1. Summary of individual and mean voltage fluorescence traces for various rhodopsin voltage sensors expressed in BWMs. Related to Figs. 1 and 3. A) Arch(D95N)-ATR, spontaneous activity. **B)** Arch(D95N)-ATR with ChR2 expressed in cholinergic neurons. **C)** Archon with ChR2 expressed in cholinergic neurons. **D)** QuasAr, spontaneous activity. **E)** QuasAr with ChR2 expressed in cholinergic neurons. **F, G)** QuasAr with ACR2 expressed in cholinergic neurons. **H)** Summary of mean fluorescence changes in (B, C, E, F). Blue bars in (A-H) indicate photo-stimulation periods. **I)** Statistical analysis of the mean±SEM fluorescence changes of data shown in H, averaged across the 5 s stimulation periods. **J)** Single traces of Arch(D95N) and QuasAr expressed in BWMs, before during (blue bar) and after photoactivation of ChR2 or ACR2 in cholinergic neurons, as indicated.

7

A RIM Ca²⁺ (RCaMP) and RIM voltage (QuasAr)

C RIM peak amplitudes and duration (QuasAr)

B RIM: intrinsic activity, hyperpolarization

RIM: intrinsic activity, depolarization

5% ΔF/F

500 ms

RIM: no obvious activity

cholinergic motor neurons
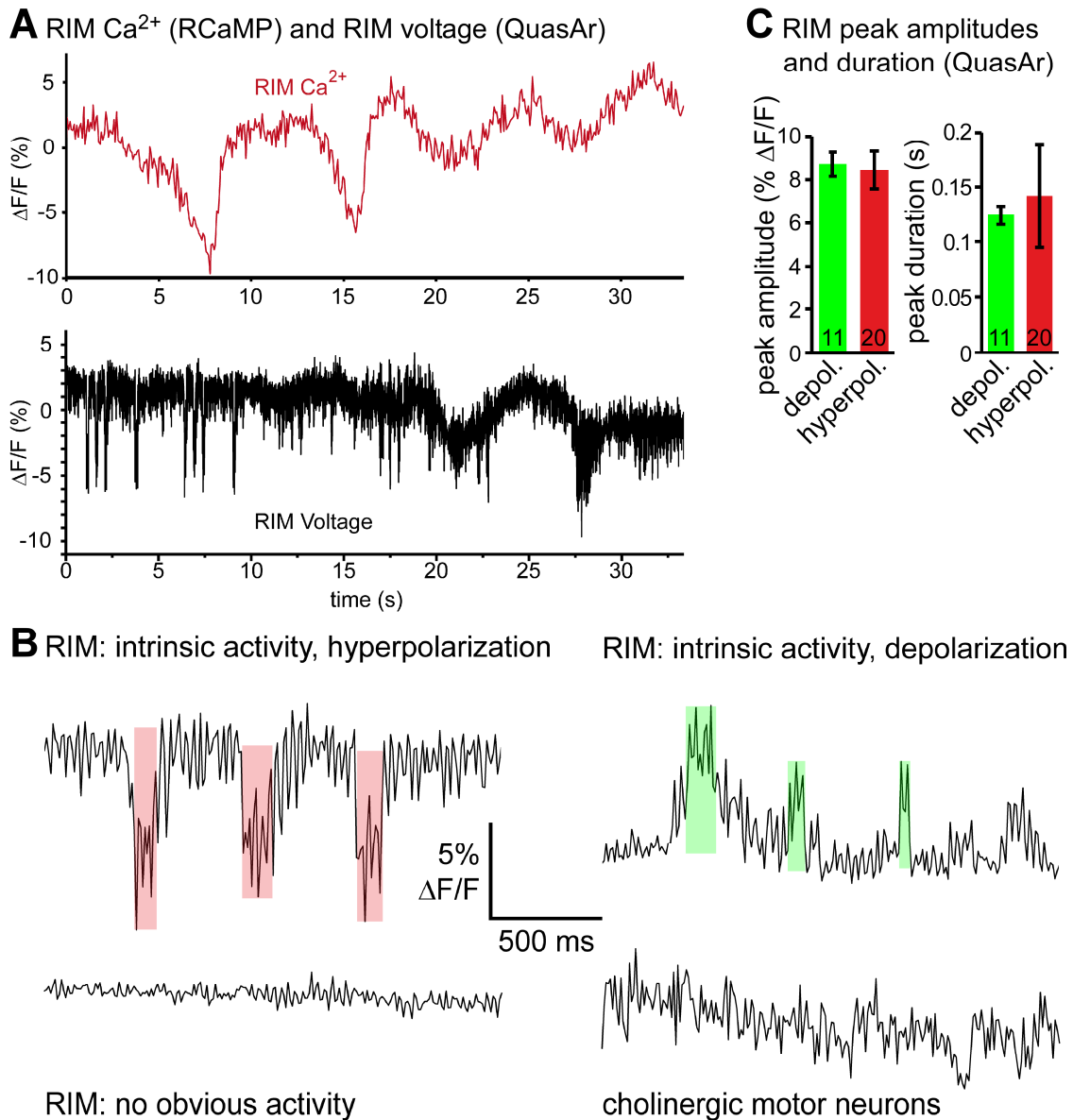
Fig. S2. Neuronal activity can be observed by Ca²⁺- and QuasAr voltage imaging: A) Comparison of activity in RIM, measured by jRCaMP1b Ca²⁺ imaging (red, upper panel) as well as by QuasAr (black, lower panel). Similar slow bouts of hyperpolarizing activity can be observed. **B)** RIM::QuasAr voltage traces show brief de- (green) and hyperpolarizing (red) spikes. **C)** Statistical analysis of representative de- and hyperpolarizing peaks in RIM::QuasAr recordings, as demarcated in B). Peak amplitude and peak durations, means±SEM, n, number of animals, is indicated.Type or paste caption here. Paste figure above the caption.
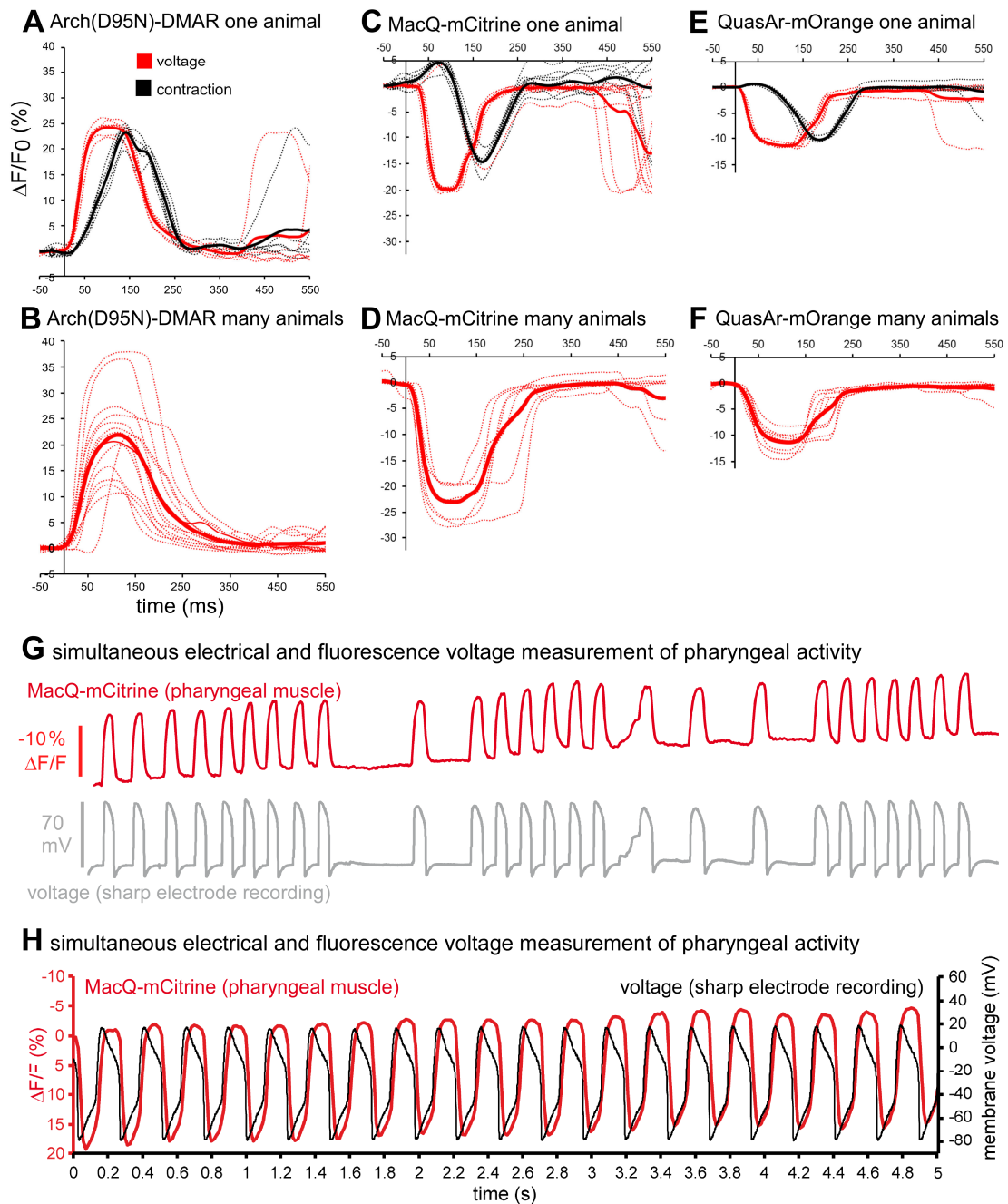
Fig. S3. Comparison of voltage traces recorded using rhodopsin and eFRET voltage sensors, as well as by sharp electrodes in the pharynx during pump trains in single animals, and across animals. Related to Fig. 4. A) Arch(D95N)-DMAR, voltage and pump fluorescence signals of a single animal, aligned and averaged. Red: voltage trace; black: pump trace. **B)** As in (A), but mean pump events of 11 animals. **C, D)** Single animal events measured with MacQ-mCitrine in the pharynx (C) and mean events observed in 7 animals (D). **E, F)** As in (C, D), but using QuasAr-mOrange (n=7 animals in F). **G, H)** Dissected pharynx, impaled by sharp electrode, allows for membrane potential recording (grey and black traces, in G, H, respectively) and simultaneous optical recording using MacQ-mCitrine (red traces in G, H).

9

192
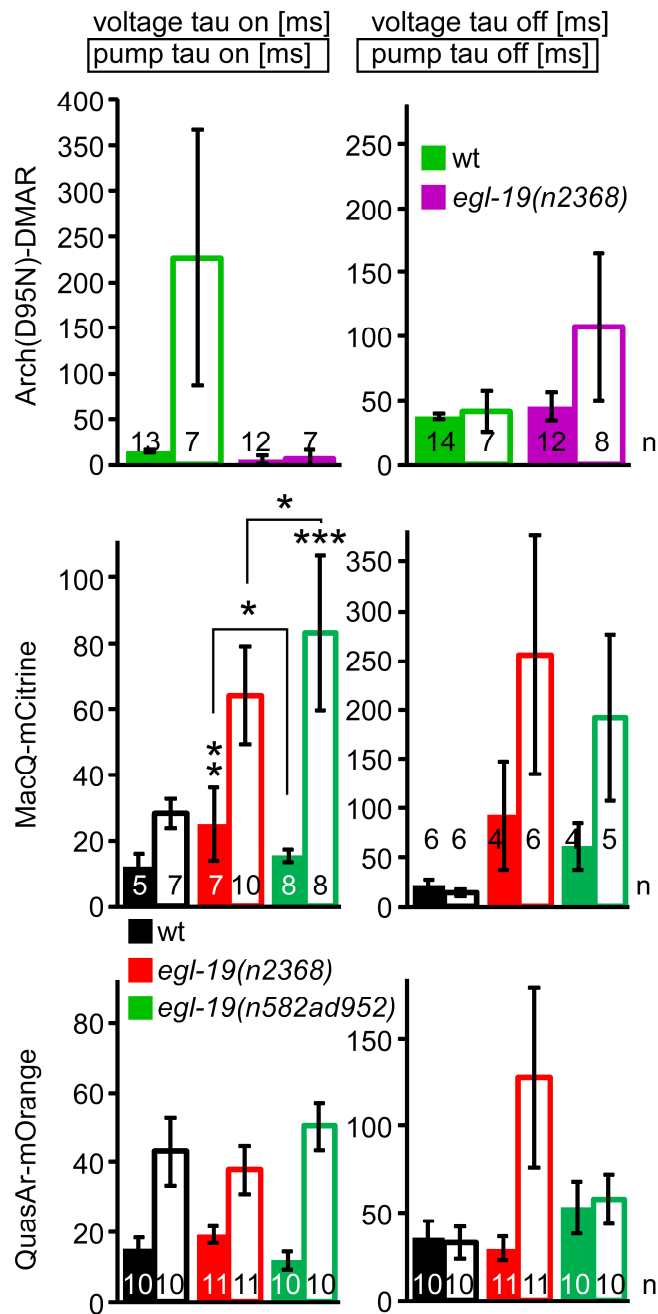
Fig. S4 Voltage and pump signal rise and decay times, automatically determined for pharyngeal APs and pump events measured with rhodopsin and eFRET sensors. Related to Fig. 5. Parameters, genotypes and number of animals as indicated, measured for animals expressing Arch(D95N), equipped with DMAR (top), MacQ-mCitrine (middle) and QuasAr-mOrange (lower panels). Means±SEM, ANOVA with Bonferroni correction, ***P≤0.001, **P≤0.01, *P≤0.05.

10
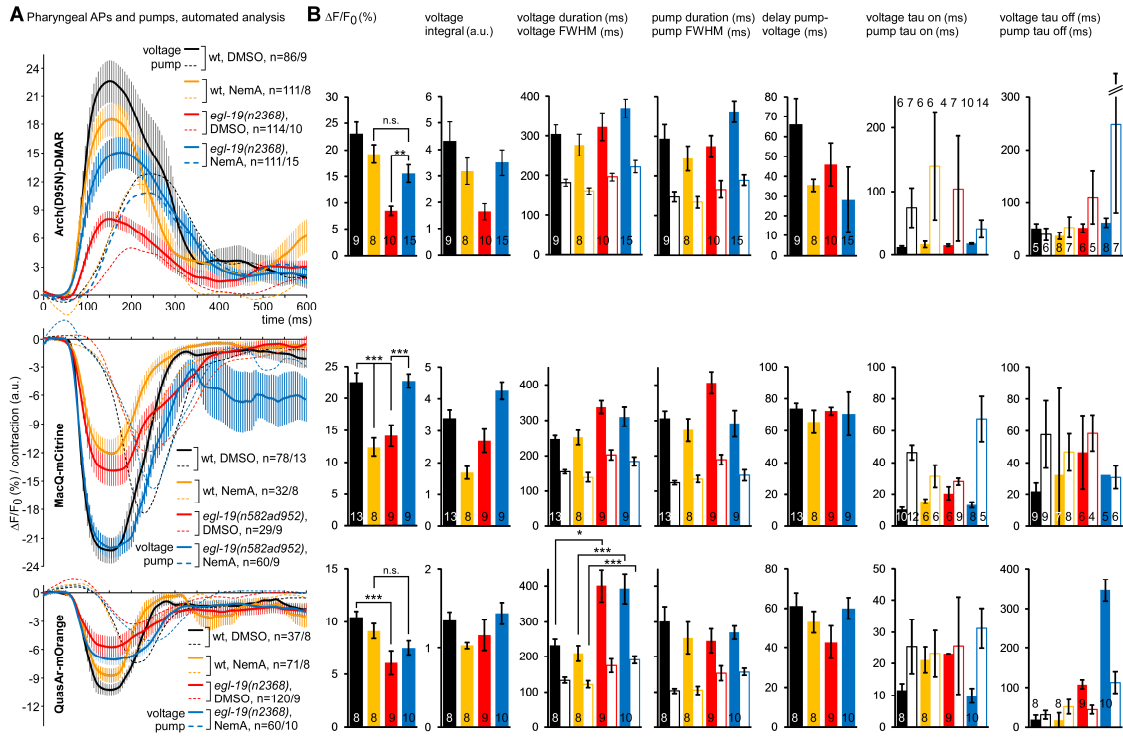
Fig. S5. Comparison of voltage and pump parameters measured in mutants and in response to nemadipine-A (NemA) in the pharynx. A) Mean±SEM values for the indicated genotypes and drug or vehicle treatments, as well as different rhodopsin voltage sensors, as indicated. Also indicated is the number of animals analyzed, as well as the number of APs and pump events. **B)** Group data of automated analysis of parameters extracted from the data shown in (A), as in Fig. 5. Frame rate in (A): 189 fps, 1 ms exposure. Means±SEM, ANOVA with Bonferroni correction, ***P≤0.001, **P≤0.01, *P≤0.05.

simultaneous EPG and voltage fluorescence measurement in pharynx
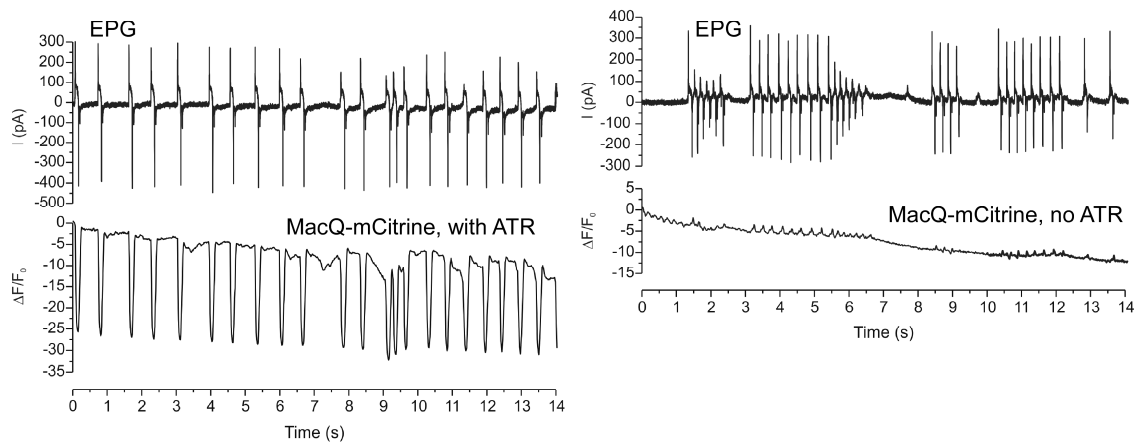
Fig. S6. Comparison of simultaneous EPG and MacQ-mCitrine fluorescence measurements in presence and absence of ATR. EPG traces (upper panels, measured as currents) and simultaneous MacQ-mCitrine voltage dependent fluorescence changes ($\Delta F/F_0$, lower panels) in the presence (left panels) or absence of ATR (right panels).

Movie S1. QuasAr-mOrange in pharynx, spontaneous pumping.

Movie S2. QuasAr in muscle arms, dorso-ventrally alternating intrinsic activity.

Movie S3. QuasAr in BWMs, intrinsic activity.

Movie S4. QuasAr in BWMs, intrinsic activity.

Movie S5. Arch(D95N)-ATR in pharynx, spontaneous pumping.

Movie S6. Arch(D95N)-DMAR in pharynx, spontaneous pumping.

Movie S7. MacQ-mCitrine in pharynx, spontaneous pumping.

Movie S8. MacQ-mCitrine in pharynx, spontaneous pumping, difference movie, 12 events aligned, averaged, 10x slowed.

Supplementary Dataset S1 (separate file)

Collected raw fluorescence traces (ROIs) and electrophysiology data of experiments underlying the data in the paper, Excel sheets, sorted by figure number and panel.

13

2.7   Optogenetischer Werkzeugkasten für neue experimentelle Ansätze

The following pages contain the published version of the review article "Optogenetischer Werkzeugkasten für neue experimentelle Ansätze"[12]. Material from: Bergs, A., Liewald, J. & Gottschalk, A. Optogenetischer Werkzeugkasten für neue experimentelle Ansätze. *Biospektrum* **25**, 398–401; 10.1007/s12268-019-1069-z (2019). Reproduced with permission from Springer Nature.

Rhodopsinbasierte Optogenetik

Optogenetischer Werkzeugkasten für neue experimentelle Ansätze

AMELIE BERGS, JANA LIEWALD, ALEXANDER GOTTSCHALK
UNIVERSITÄT FRANKFURT A. M.

In rhodopsin-based optogenetics the light-activatable cation channel ChR2 is employed to selectively gain control over single neurons. As arising experimental questions become more and more challenging, there is a strong need to further expand the optogenetic toolbox. Along with the discovery of various natural rhodopsins, molecular engineering facilitates the development of custom tools for a variety of applications, ranging from cell culture to light-control of whole organisms like *Caenorhabditis elegans*.

■ Im Laufe der Evolution entwickelten zahlreiche Organismen lichtempfindliche Proteine, unter anderem Rhodopsine, um sich an ihre Umgebung anpassen zu können. Eines davon, Channelrhodopsin-2 (ChR2), findet sich im Augenfleck der Alge *Chlamydomonas rein-hardtii* und fungiert als Licht-aktivierbarer Ionenkanal (**Abb. 1A**, [1]). ChR2 erlaubt es dem Einzeller, optimale Lichtverhältnisse aufzusuchen. Die Entdeckung von Channelrhodopsin im Jahr 2002 ermöglichte die Entwicklung der Optogenetik, also von Methoden, die mithilfe von Licht die Regulation der Aktivität von Zellen erlauben. Diese Anwendungen revolutionierten zunächst die Neurowissenschaften, inzwischen aber auch die Zellbiologie. Durch zellspezifische Expression in der Membran von Muskeln oder Neuronen, können diese mit hoher räumlicher und zeitlicher Präzision durch Licht aktiviert werden (**Abb. 1B**). Dies erlaubt eine zelltypspezifische, nicht-invasive Aktivierung, im Gegensatz zu den vormals verwendeten Mikroelektroden. Blaulichtanregung von ChR2 führt zu einer Isomerisierung des Kofaktors Retinal, der Öffnung des Kanals, einem Kationenstrom in das Zellinnere und damit zur Depolarisierung − also der Aktivierung − der Zelle. Zusammen mit Halorhodopsin, einer mit gelbem Licht aktivierbaren, hyperpolarisierenden (inaktivierenden) Chloridionenpumpe, können so einzelne Neurone über genetisch codierte Lichtschalter selektiv „ein-" oder „ausgeschaltet" und die sich daraus ergebenden Effekte (bis hin zu Verhaltensänderungen im intakten Tier) analysiert werden (**Abb. 1C**).

Erweiterung des Repertoires optogenetischer Werkzeuge

Um immer komplexeren Fragestellungen gerecht zu werden, besteht ein großer Bedarf, das Repertoire an optogenetischen Werkzeugen zu erweitern. Es wurden viele andere natürliche Rhodopsine entdeckt, darunter auch Anionen-Channelrhodopsine (ACRs), die gleichwertig effiziente hyperpolarisierende Rhodopsine darstellen [2]. Sie leiten negativ geladene Chloridionen in das Zellinnere, unterdrücken neuronale Aktivität und sind durch ihre Kanaleigenschaften um ein Vielfaches effizienter als die hyperpolarisierenden Ionenpumpen.

Außerdem werden gezielt künstliche Rhodopsine entwickelt. So konnten z. B. über
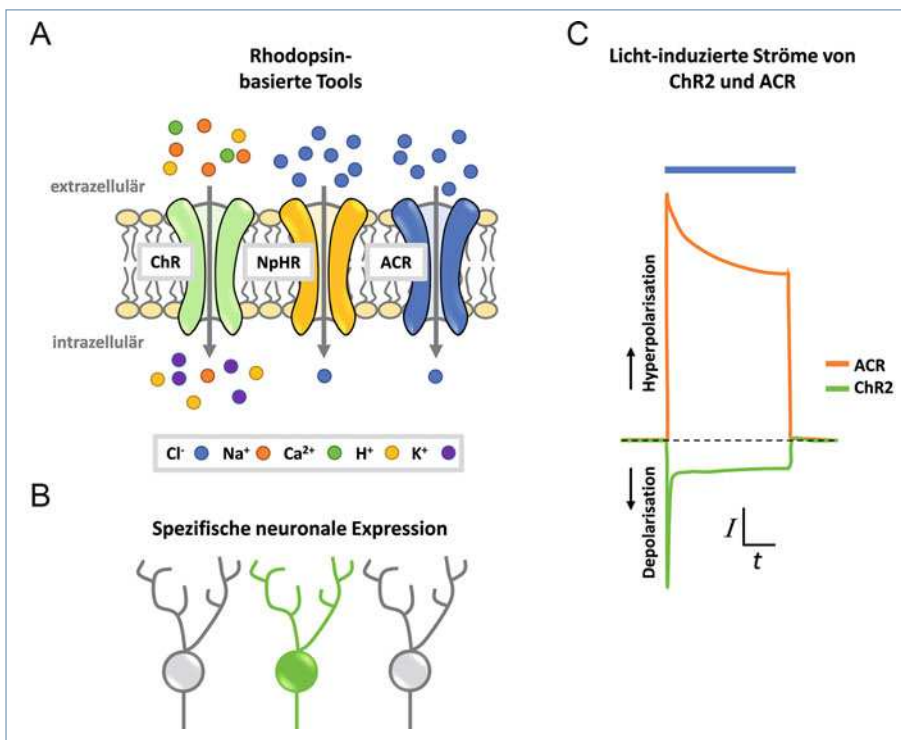
▲ **Abb. 1:** Rhodopsinbasierte Optogenetik. **A**, Ionenleitfähigkeit der am häufigsten verwendeten optogenetischen Werkzeuge ChR (Channelrhodopsin), NpHR (Halorhodopsin) und ACR (Anionenselektives Channelrhodopsin). **B**, Mit zellspezifischen Promotoren kann eine selektive Expression erzielt werden. **C**, Licht-induzierte Ströme in einem elektrophysiologischen *Patch-Clamp*-Experiment.
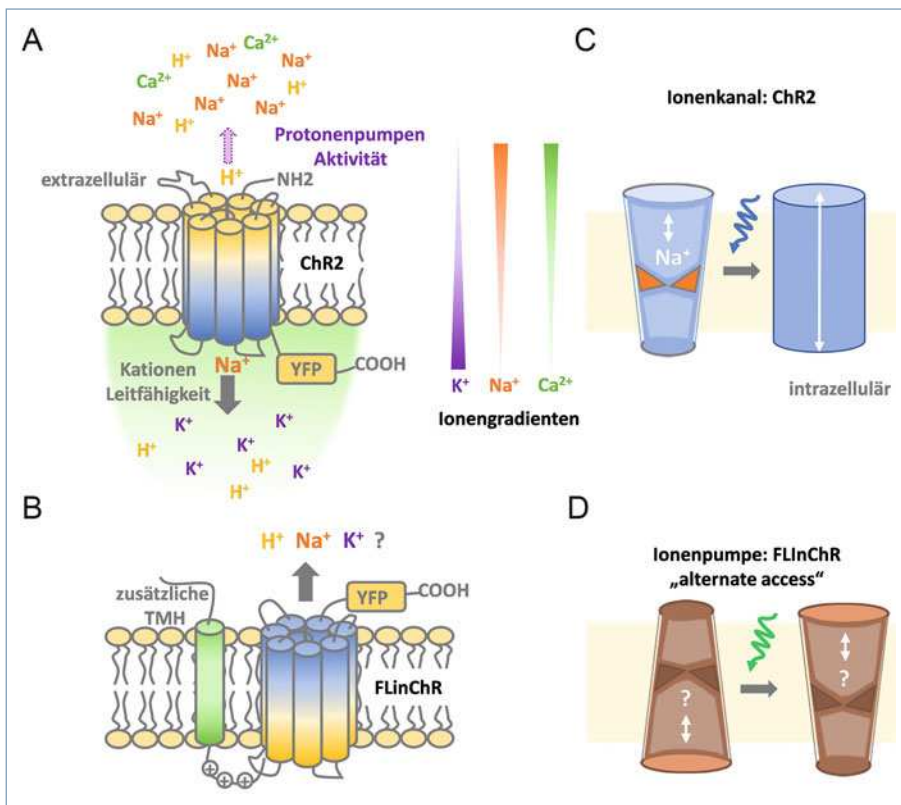
▲ **Abb. 2:** FLInChR (*full-length inversion of ChR*). **A**, Wildtyp-ChR2 leitet Kationen entlang deren Gradienten ins Zellinnere (Depolarisation), wohingegen das synthetisch durch Invertierung hergestellte Molekül FLInChR Kationen aus der Zelle herauspumpt (Hyperpolarisation). **B**, Eine Licht-induzierte Öffnung des ChR2-Kanals (**C**) steht dem Modell des *alternate access* bei Ionenpumpen gegenüber, bei welchem sich der cytoplasmatische und der extrazelluläre Halbkanal abwechselnd öffnet und schließt (**D**).

strukturbasierte Mutagenese nahe der Retinalbindungsstelle die elektrostatischen Wechselwirkungen im Protein verändert werden, was zu neuer Funktionalität im Hinblick auf Lichtsensitivität, Kinetik, Ionenselektivität und spektralen Eigenschaften führte [3]. Beispielsweise bleiben die *step-function*-Opsine, bei denen die zentrale Ionenpore im Protein mutiert wurde [4], einmal durch Licht aktiviert deutlich länger im geöffneten Zustand (Minuten bis Stunden). Sie können durch gelb-grünes Licht wieder „ausgeschaltet" werden. Die Stimulation ist somit nicht auf die Dauer des Lichtsignals begrenzt, was besonders Langzeitexperimenten zugutekommt.

Ein neuartiger Ansatz zur Erweiterung des optogenetischen Werkzeugkastens basiert auf der topologischen Inversion der Rhodopsine. Durch Fusion einer zusätzlichen Transmembranhelix an ChR2 und Einführung positiv geladener Aminosäuren konnte ein in seiner Topologie, aber auch Funktion inverses Protein generiert werden: FLInChR (*full-length inversion of ChR*) transportiert Kationen über

einen Pumpmechanismus aus der Zelle heraus und fungiert somit als Hyperpolarisator (**Abb. 2B**, [5]). Außerdem hat FLInChR ein rot-verschobenes Anregungsmaximum, was bei Experimenten, die zwei komplementär arbeitende Rhodopsine erfordern, hilfreich ist.

FLInChR – wie wird aus einem Ionenkanal eine Ionenpumpe?

FLInChR birgt auch das Potenzial, einen mechanistischen Einblick in die Funktion der Rhodopsine zu erhalten. Wie wird durch einfache Inversion eines Ionenkanals seine Funktionalität dermaßen umgestaltet? Wie bewirkt dies eine Veränderung des *gating*-Mechanismus? Die Strukturaufklärung und ein Vergleich mit der ChR2-Struktur könnten Hinweise auf die Unterschiede der beiden Rhodopsinklassen (Kanäle und Pumpen) geben.

Die passive Ionenleitfähigkeit von ChR2 erfordert die simultane Öffnung beider jeweils zur cytoplasmatischen oder extrazellulären Seite ausgerichteten Halbkanäle (**Abb. 2C**). Die Kanaleigenschaft entwickelte sich womöglich aus dem energieabhängigen *alternate access*-Mechanismus von Ionenpumpen, bei denen jeweils nur ein Halbkanal geöffnet ist und ein gerichteter Transport abläuft (**Abb. 2D**). Eine Studie, die die Umwandlung einer Pumpe zu einem Kanal zum Ziel hatte, fand einen Blockierungsmechanismus, der den passiven Ionendurchgang in der Ionenpumpe verhindert [6]. Womöglich wurde dieses Blockierungselement durch strukturelle Umgestaltung in FLInChR, z. B. durch asymmetrische Eigenschaften der Membran, wiederhergestellt. Auch ChR2 weist eine rudimentäre Protonenpumpfunktion auf (**Abb. 2A**, [7]). Haben Kanäle möglicherweise nie ganz ihre Pumpfähigkeit verloren? Und koexistieren beide Mechanismen in ChR2, während im invertierten FLInChR der Pumpaspekt überhandgenommen hat?

Laborspezifische Zielsetzungen

Auch ganze Organismen lassen sich nach der Expression von Rhodopsinen über Licht
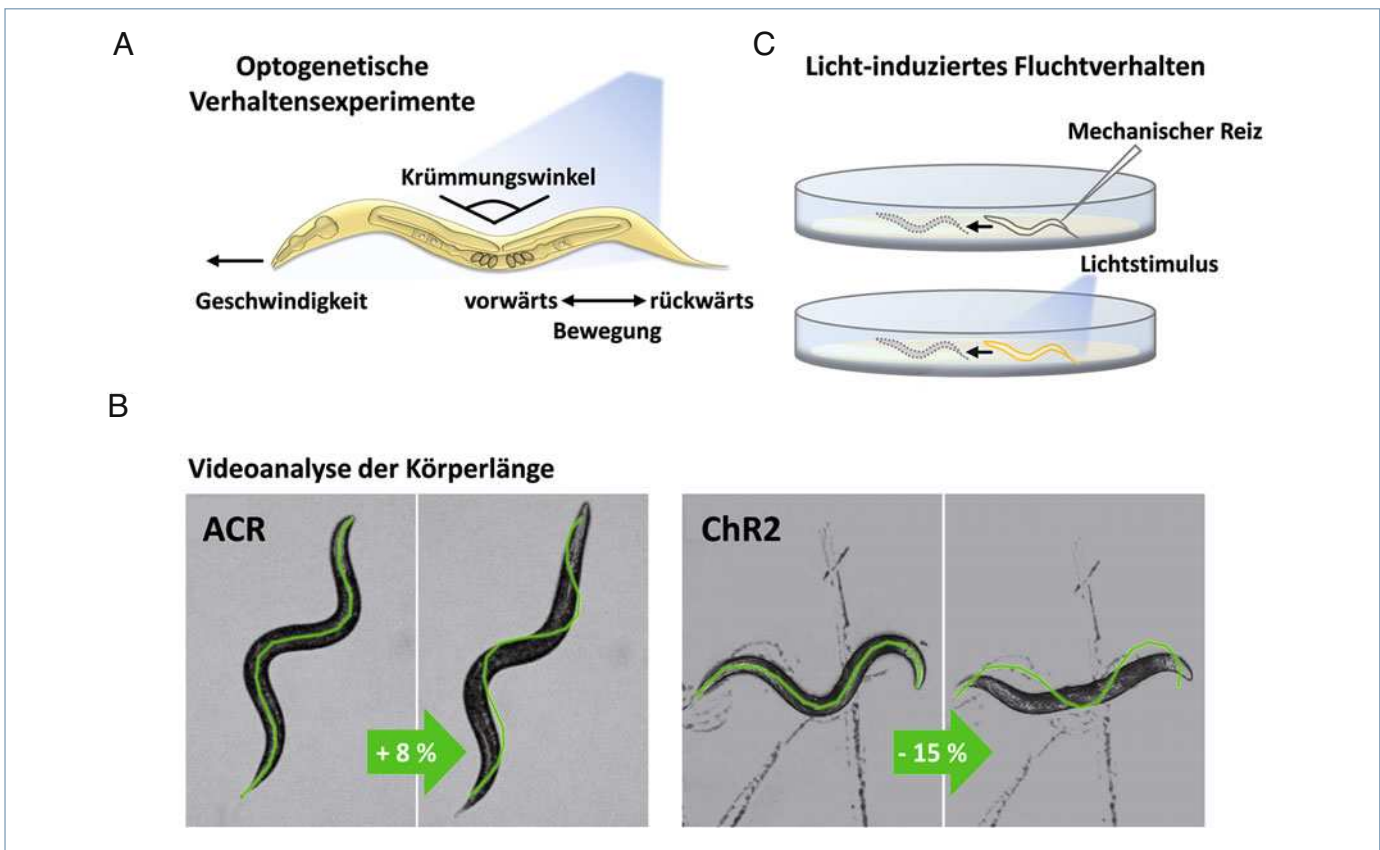
▲ **Abb. 3:** Optogenetik in *Caenorhabditis elegans*. **A**, Die Analyse der aus Videoaufzeichnungen optogenetischer Verhaltensexperimente gewonnenen Parameter (wie Körperlänge, Geschwindigkeit, Bewegungsrichtung, Biegungswinkel), die z. B. durch ChR2-Aktivierung von Neuronen des Bewegungsapparats beeinflusst werden, lassen Rückschlüsse auf die Funktionsweise des jeweiligen Neurons zu. **B**, Rhodopsinbasierte optogenetische Werkzeuge können auch über Videoanalyse der Körperlänge charakterisiert werden. **C**, Durch ChR2 im nozizeptiven Neuron PVD hervorgerufenes Fluchtverhalten, analog zum mechanischen Reiz.

beeinflussen. In unserem Tiermodell, dem Fadenwurm *Caenorhabditis elegans*, ergründen wir die neuronale Aktivität und das daraus resultierende Verhalten. Wegen der simplen Anatomie mit nur 302 Neuronen, einfachen Verhaltensweisen sowie seiner Transparenz ist *C. elegans* prädestiniert für optogenetische Untersuchungen. Daher war es auch das erste lebende Tier, an dem die Lichtsteuerbarkeit durch ChR2 gezeigt wurde [8].

Durch Licht hervorgerufenes Verhalten werten wir über Videoanalyse aus. Als Parameter dienen z. B. Geschwindigkeit und Richtung der Bewegung sowie Länge und Biegungswinkel des sich schlängelnden Tieres (**Abb. 3A**). Neue Rhodopsine lassen sich auf einfache Weise in Muskeln charakterisieren (**Abb. 3B**, [9]), sie bewirken entweder eine Muskelkontraktion oder -entspannung, was sich in einer geringeren oder vergrößerten Körperlänge widerspiegelt. Komplexere Fragen werden durch Ansteuerung einzelner Neurone adressiert: Zum Beispiel löst ChR2-Aktivierung in dem nozizeptiven Neuron PVD

eine fluchtartige Vorwärtsbewegung aus (**Abb. 3C**), so als wäre das Tier unsanft berührt worden. Durch Verknüpfung von neuronaler Aktivität und Verhalten war es möglich, die Interaktion von PVD mit anderen Neuronen zu verstehen und die beteiligten molekularen Komponenten zu identifizieren [10].

Neben der Ionenleitfähigkeit besitzen einige Rhodopsine auch die Eigenschaft, Veränderungen des Membranpotenzials in ein Fluoreszenzsignal zu übersetzen [11]. So kann die dynamische Aktivität von erregbaren Zellen nachverfolgt werden. Will man zusätzlich ein Neuron optogenetisch über weitere Rhodopsine stimulieren, wird klar, wie wichtig es ist, die Variabilität der Rhodopsin-Werkzeuge zu erweitern. Nur so können spektral gut separierte Moleküle kombiniert werden.

Ein weiteres Anwendungsfeld von Rhodopsinen ist die Untersuchung der Freisetzung von Neurotransmittern an chemischen Synapsen. Dieser Vorgang lässt sich anhand

der synaptischen Morphologie im Elektronenmikroskop untersuchen, wobei Veränderungen durch ChR2-Stimulation hervorgerufen werden. Dauerstimulation führt zur Bildung großer Endosomen, aus denen dann neue synaptische Vesikel gebildet werden. Zumeist kann man dabei nur „Endprodukte" beobachten, selten jedoch die Bildung der Endosomen. Hier helfen die *step-function*-Opsine. Die Verwendung von Channelrhodopsinen mit unterschiedlichen funktionalen Eigenschaften erlaubt es somit, verschiedenste Fragestellungen im Experiment zu adressieren. ∎

Literatur

[1] Nagel G, Ollig D, Fuhrmann M et al. (2002) Channelrhodopsin-1: a light-gated proton channel in green algae. Science 296:2395–2398
[2] Govorunova EG, Sineshchekov OA, Janz R et al. (2015) Natural light-gated anion channels: a family of microbial rhodopsins for advanced optogenetics. Science 349:647–650
[3] Hegemann P, Möglich A (2010) Channelrhodopsin engineering and exploration of new optogenetic tools. Nat Methods 8:39–42
[4] Berndt A, Yizhar O, Gunaydin LA et al. (2009) Bi-stable neural state switches. Nat Neurosci 12:229–234

[5] Brown J, Behnam R, Coddington L et al. (2018) Expanding the optogenetics toolkit by topological inversion of rhodopsins. Cell 175:1131–1140

[6] Vogt A, Guo Y, Tsunoda SP et al. (2015) Conversion of a light-driven proton pump into a light-gated ion channel. Sci Rep 5:553

[7] Feldbauer K, Zimmermann D, Pintschovius V et al. (2009) Channelrhodopsin-2 is a leaky proton pump. Proc Natl Acad Sci 106:12317–12322

[8] Nagel G, Brauner M, Liewald JF et al. (2005) Light activation of channelrhodopsin-2 in excitable cells of *Caenorhabditis elegans* triggers rapid behavioral responses. Curr Biol 15:2279–2284

[9] Bergs A, Schultheis C, Fischer E et al. (2018) Rhodopsin optogenetic toolbox v2.0 for light-sensitive excitation and inhibition in *Caenorhabditis elegans*. PLoS One 13:e0191802

[10] Husson SJ, Costa WS, Wabnig S et al. (2012) Optogenetic analysis of a nociceptor neuron and network reveals ion channels acting downstream of primary sensors. Curr Biol 22:743–752

[11] Kralj JM, Douglass AD, Hochbaum DR et al. (2011) Optical recording of action potentials in mammalian neurons using a microbial rhodopsin. Nat Methods 9:90–95

Korrespondenzadresse:
Amelie Bergs
Zelluläre und molekulare Neurobiologie
Institut für Biophysikalische Chemie
Goethe-Universität Frankfurt a. M.
Buchmann Institute for Molecular Life Sciences
Max-von-Laue-Straße 15
D-60438 Frankfurt a. M.
Tel.: 069-798-42713
amelie.bergs@stud.uni-frankfurt.de
www.bmls.de/Cellular_and_Molecular_
Neurobiology/aboutus.html

AUTOREN

Amelie Bergs
Jahrgang **1992**. **2011–2017** Biochemiestudium an der Universität Frankfurt a. M.; dort seit **2017** Promotionsstudentin (AG Gottschalk).

Jana Liewald
Jahrgang **1971**. **1990–1997** Biologiestudium an der Universität Mainz; dort **2002** Promotion (AG Wegener). **2002–2004** Postdoktorandin am Pharmakologischen Institut, Universität Mainz (AG Nawrath). Seit **2004** Postdoktorandin am Institut für Biochemie, Universität Frankfurt a. M. (AG Gottschalk).

Alexander Gottschalk
Jahrgang **1969**. **1990–1996** Chemiestudium an den Universitäten Frankfurt a. M., Edinburgh, UK, und Marburg. **1999** Promotion an der Universität Marburg (AG Lührmann). **2000–2003** Postdoktorand an der University of California, San Diego, Neurobiologie von *Caenorhabditis elegans*. **2004–2009** Juniorprofessor und seit **2010** Professor an der Universität Frankfurt a. M.

2.8 Expanding the Optogenetics Toolkit by Topological Inversion of Rhodopsins

The following pages contain the published version of the research article "Expanding the Optogenetics Toolkit by Topological Inversion of Rhodopsins"[10]. Material from: Brown, J. *et al.* Expanding the Optogenetics Toolkit by Topological Inversion of Rhodopsins. *Cell* **175**, 1131-1140.e11; 10.1016/j.cell.2018.09.026 (2018).

Cell

Expanding the Optogenetics Toolkit by Topological Inversion of Rhodopsins

Graphical Abstract

Highlights

- Transmembrane proteins can be inverted via recombination with N-terminal domains

- Topological inversion of rhodopsins yields new variants with unique properties

- Inversion of ChR$^{ET/TC}$ reverses cationic flux creating a potent inhibitor: FLInChR
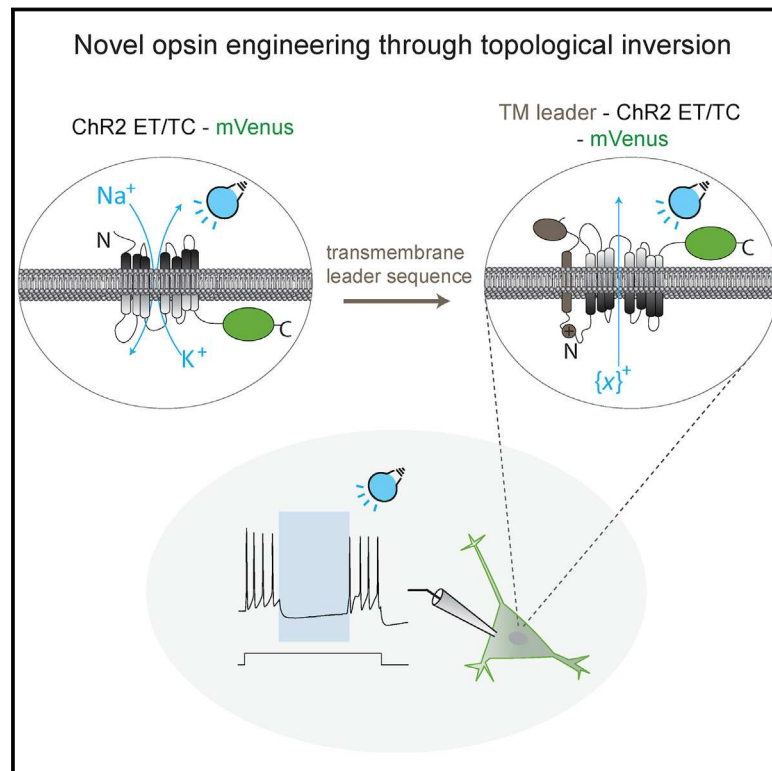
Authors

Jennifer Brown, Reza Behnam, Luke Coddington, ..., Alexander Gottschalk, Joshua T. Dudman, Alla Y. Karpova

Correspondence

dudmanj@janelia.hhmi.org (J.T.D.), alla@janelia.hhmi.org (A.Y.K.)

In Brief

By topologically inverting opsin proteins within the membrane, it may be possible to double the existing toolkit available for optogenetics

CellPress

Expanding the Optogenetics Toolkit by Topological Inversion of Rhodopsins

Jennifer Brown,[1,2,8,9] Reza Behnam,[1,8] Luke Coddington,[1,8] D.G.R. Tervo,[1,8] Kathleen Martin,[1,10] Mikhail Proskurin,[1,3] Elena Kuleshova,[1,4] Junchol Park,[1] James Phillips,[1,2] Amelie C.F. Bergs,[5,6,7] Alexander Gottschalk,[5,6] Joshua T. Dudman,[1,8,*] and Alla Y. Karpova[1,8,11,*]

[1]Janelia Research Campus, Howard Hughes Medical Institute, Ashburn, VA 20147, USA
[2]Department of Physiology, Development and Neuroscience, University of Cambridge, Cambridge CB2 3EG, UK
[3]Department of Neuroscience, Johns Hopkins University Medical School, Baltimore, MD 21205, USA
[4]Institute of Higher Nervous Activity and Neurophysiology of the Russian Academy of Sciences, Moscow 117485, Russia
[5]Buchmann Institute for Molecular Life Sciences, Goethe-University D-60438 Frankfurt, Germany
[6]Institute for Biophysical Chemistry, Goethe-University, D-60438 Frankfurt, Germany
[7]International Max-Planck Research School in Structure and Function of Biological Membranes, Max-Planck-Institute of Biophysics, D-60438 Frankfurt, Germany
[8]These authors contributed equally
[9]Present address: University of California, Berkeley, Berkeley, CA, USA
[10]Present address: New York University, New York, NY, USA
[11]Lead Contact
*Correspondence: dudmanj@janelia.hhmi.org (J.T.D.), alla@janelia.hhmi.org (A.Y.K.)
 https://doi.org/10.1016/j.cell.2018.09.026

SUMMARY

Targeted manipulation of activity in specific populations of neurons is important for investigating the neural circuit basis of behavior. Optogenetic approaches using light-sensitive microbial rhodopsins have permitted manipulations to reach a level of temporal precision that is enabling functional circuit dissection. As demand for more precise perturbations to serve specific experimental goals increases, a palette of opsins with diverse selectivity, kinetics, and spectral properties will be needed. Here, we introduce a novel approach of "topological engineering"—inversion of opsins in the plasma membrane—and demonstrate that it can produce variants with unique functional properties of interest for circuit neuroscience. In one striking example, inversion of a Channelrhodopsin variant converted it from a potent activator into a fast-acting inhibitor that operates as a cation pump. Our findings argue that membrane topology provides a useful orthogonal dimension of protein engineering that immediately permits as much as a doubling of the available toolkit.

INTRODUCTION

The discovery of a diversity of microbial rhodopsins (Béjà et al., 2000; Nagel et al., 2003; Oesterhelt and Stoeckenius, 1971) that convert light-dependent isomerization of a bound chromophore into conformational changes that enable transport of ions across the cellular membrane has led to the generation of an extensive toolkit for optogenetics (Fenno et al., 2011). Genome mining (Chuong et al., 2014; Klapoetke et al., 2014) has proven to be

the most productive avenue for finding variants with particularly useful properties by tapping into the changes that evolution imposed onto the general rhodopsin scaffold when adjusting its function for the specific niche of the individual microorganisms (Sharma et al., 2006). A complementary effort has focused on further enhancing this natural variation of the opsin backbone through directed molecular engineering (Berndt et al., 2014, 2016; Deisseroth and Hegemann, 2017). Structure-guided mutagenesis in the vicinity of the chromophore and along the presumed conduction pathway has led to some notable successes, with examples of interchanged functionality (Inoue et al., 2015), altered ion selectivity (Berndt et al., 2014), and improved photocycle kinetics (Gunaydin et al., 2010; Lin et al., 2009). The actual mechanism of conduction remains incompletely understood (Volkov et al., 2017), however, and the consequences of individual mutations do not seem to readily confer predictable functional changes to different opsin backbones (Lin et al., 2013). These factors limit the effectiveness of structure-guided mutagenesis and argue for diversification in the available approaches for further expanding the toolkit.

Although a major driving force for the evolutionary expansion of membrane protein families and refinement of their function may have come from relatively conservative point mutations, changes in membrane topology are also hypothesized to have contributed to this process (Rapp et al., 2007; Seppälä et al., 2010). While some membrane proteins can be induced to adopt a non-canonical orientation with a few mutations (Seppälä et al., 2010), evolution of altered topology would most easily arise through the introduction of large sequences by recombination. In one striking example, ionotropic glutamate receptors appear to have arisen following the insertion of a potassium channel gene in the middle of a periplasmic glutamate binding protein (Chen et al., 1999; Tikhonov and Magazanik, 2009; Turano et al., 2001; Wollmuth and Sobolevsky, 2004). The resulting addition of a large extracellularly targeted domain onto the previously intracellular N terminus of

the potassium channel is thought to have imposed a topological inversion of the channel portion, although direct tests of this proposal remain lacking. Perhaps surprisingly, the inverted channel domain in ionotropic glutamate receptors displays significantly greater permeability for Na^+ and Ca^{2+} (Sobolevsky et al., 2003) despite sharing the core residues important for K+ selectivity with their presumed evolutionary ancestors (Wood et al., 1995). If topological inversion of true channels significantly alters ion permeability, it may have even greater consequences for proteins that move ions across the membrane in a transporter-like fashion. Transporters are distinguished by intramolecular ion coordination and conformational changes that restrict and permit, in sequence, access to internal and external compartments. In addition to altering selectivity, their inversion thus has the potential of reversing the movement of ions independent of electrochemical gradients by altering which residues are exposed to the extra- and intracellular compartments. Rhodopsin family members that appear to behave like transporters have properties of both transporters and channels, reflecting a proposed functional continuum (Gadsby, 2009): their currents show strong dependence on electrochemical gradients, but the flux is markedly lower than that of diffusion-limited channels. We therefore hypothesized that inversion of rhodopsins could yield new variants with unexpected, and perhaps desirable, functional properties.

Here, we demonstrate that topological inversion can be robustly achieved by the introduction of strategically targeted N-terminal domains. When applied to rhodopsins, such "topological engineering" can lead to the generation of variants with unique functional properties of use in neuroscience research. We highlight two engineered variants that display properties that have not to date been engineered through structure-guided mutagenesis: a cation channel that displays markedly greater selectivity for K^+ over Na^+ (generated through an inversion of CsChrimson) and a non-specific cation pump (generated through an inversion of a Channelrhodopsin [ChR]). The latter, dubbed FLInChR (*f*ull-*l*ength *in*version of *ChR*), represents a novel light-gated inhibitor of neural activity, and we demonstrate that it is sufficiently potent for common optogenetic experiments such as *in vivo* circuit interrogation. Thus, topological inversion permits access to new functionalities without fundamentally impairing the ionic flux and therefore has the potential to rapidly produce new variants of use to the neuroscience community.

Our findings suggest that topological inversion is not energetically prohibitive and is robust to the nature of the N-terminal inversion domain, thus supporting the notion that domain recombination may indeed be sufficient to drive changes in membrane topology observed in the evolution of membrane protein families. Further, these data suggest that membrane topology is a useful, general, and unique dimension of protein engineering—in addition to immediately permitting as much as a doubling of the available toolkit, it may aid future structure-function studies of permeation in Channelrhodopsins.

RESULTS

To begin to evaluate the potential of topological engineering for generating novel rhodopsin variants, we designed a leader sequence that contains the signal sequence and the transmembrane (TM) domain of Neurexin 1B-delta—a type I integral membrane protein—that could, in principle, impose topological inversion on any membrane protein with an extracellular N terminus (Figure 1A). To impart further stability on the orientation of the N-terminal TM domain, we also included a short positively charged peptide into the presumed cytoplasmic portion of the leader sequence (Bernsel et al., 2008; Gafvelin and von Heijne, 1994; von Heijne, 1992). We chose a positively charged peptide that serves as the recognition sequence for a Golgi-bound protease, furin (Thomas, 2002), because establishing that the fusion protein is protected from furin-mediated cleavage would lend further support for the desired orientation of the leader sequence.

Fusion between the Neurexin (Nx)-based N-terminal domain and ChR2 E123T/T159C—a variant chosen because of its fast kinetics and robust membrane insertion (Berndt et al., 2011)—resulted in a protein that could be easily expressed at high levels, displayed efficient membrane targeting, and trafficked well down axons (Figure S1). Immunostaining for the N-terminal myc− epitope tag under non-permeabilized conditions and live-cell GFP florescence imaging in the presence of proteinase K verified that both N and C termini of the fusion protein are in the extracellular space, as predicted for successful topological inversion (Figures 1B and 1C). Pairing the Neurexin-based N-terminal domain with either CsChrimson or ArchT was equally effective at achieving inversion (Figure 1C), as was pairing ChR E123T/T159C with an alternative N-terminal domain that contained the transmembrane domain of Synaptobrevin (Syb) (Figure S2).

We also explored whether any naturally existing non-canonical orientation of a transmembrane protein may be attributed to its N-terminal domain. We focused on insect odorant receptors—a family of heptahelical proteins that have the opposite membrane orientation compared with their mammalian counterparts and function as odor-gated ion channels rather than G-protein-coupled receptors (Benton et al., 2006). Strikingly, fusion of the N-terminal leader sequence from the *Drosophila* OR 59D.1 gene to ChR E123T/T159C also resulted in an inversion (Figure 1D). This finding lends further credence to the notion that introduction of targeted N-terminal domains through recombination may have contributed during evolution to changes in membrane protein orientation and possibly to the emergence of new functionalities.

To evaluate the functional consequences of rhodopsin inversion, we next examined the current evoked by photoactivation of the inverted proteins in cultured hippocampal neurons (transfected at DIV7, evaluated at DIV 14-21). Flipping the orientation of CsChrimson in the membrane preserved the inward direction of the photocurrent at resting membrane potential and had no significant effect on the current's spectral sensitivity (Figure 2A). The photocurrent still reversed when the membrane was depolarized (Figure 2B). However, the reversal potential of the inverted CsChrimson was significantly lower than that of the original opsin (-35.3 ± 5.2 mV, n = 5 versus 4.7 ± 2.5 mV, n = 5, p < 0.0001). Decreasing the extracellular Na^+ concentration from 130 mM to 5 mM caused a further leftward shift in the reversal potential (to -62.7 ± 3.6 mV, n = 5 versus
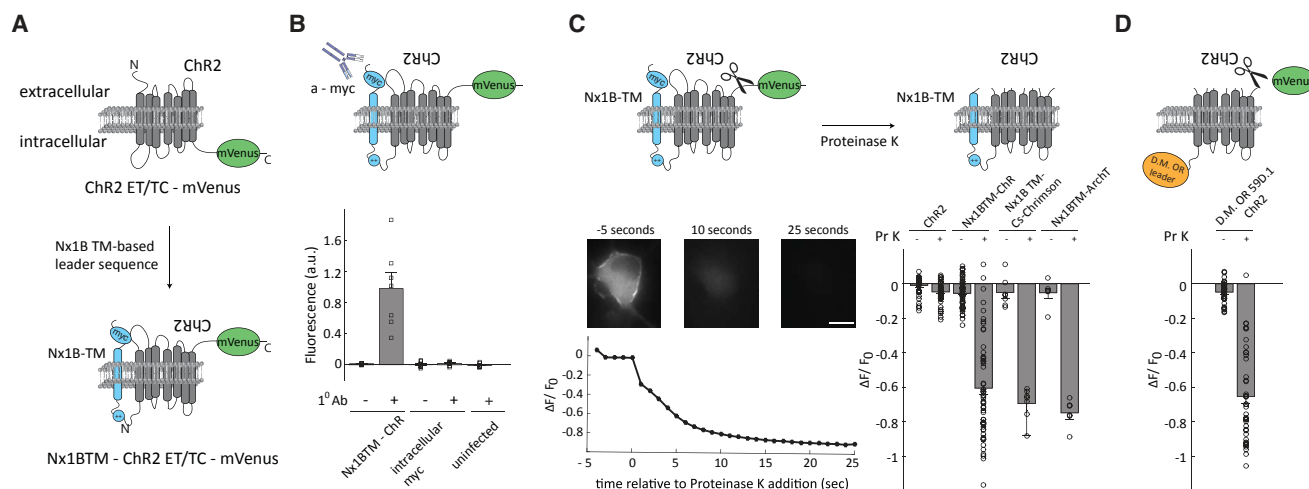
Figure 1. A Molecular Engineering Approach to Topological Inversion of Rhodopsins

(A) Schematic of the approach. Nx1B-TM denotes transmembrane domain of Neurexin 1B, ++ denotes positively charged furin cleavage site.

(B) Immunocytochemical evaluation of the location of the N-terminal-myc epitope tag. (Top) Schematic of the approach. (Bottom) Background-subtracted, bead fluorescence-normalized fluorescence intensity of regions of interest manually drawn over cell bodies. 1°Ab: primary anti-myc antibody.

(C) Proteinase K-based evaluation of the location of the C-terminal-mVenus domain in primary neuronal cultures. (Top) Schematic of the approach. Scissors depict action of extracellularly added Proteinase K. (Lower-left) Time-lapse live-cell imaging of four individual experiments. Scale bar, 1 μm. (Lower-right) Background-subtracted change in fluorescence at the end of the assay (normalized to the starting fluorescence) for native ChR ET/TC (n = 59), inverted ChR ET/TC (n = 47), inverted CsChrimson (n = 7), and inverted ArchT (n = 6).

(D) Proteinase K-based evaluation of the location of the C-terminal mVenus domain for the fusion of *Drosophila melanogaster* OR 59D.1 gene N-terminal leader sequence and ChR ET/TC (n = 42). (Top) Schematic of the approach. (Bottom) Background-subtracted change in fluorescence at the end of the assay.

Error bars represent standard error of the mean.

130 mM Na⁺), bringing it closer to the reversal potential for K⁺. Together, these results indicate that, for CsChrimson, topological inversion preserved the opsin's cation channel-like properties but led to a significantly (∼7- to 8-fold) increased K⁺ permeability—a sought-after functional change that has eluded other molecular engineering efforts (Grote et al., 2014).

Inversion of ChR E123T/T159C led to an even more dramatic change in opsin functionality. Cells expressing inverted ChR E123T/T159C variants—dubbed *full-length Inversion of ChR* (FLInChRs)—displayed robust outward currents, suggesting that inversion converted this opsin from a potent activator into an inhibitor (Figure 2C). Comparison of current amplitudes elicited by photostimulation at varying wavelengths revealed that the spectral response of FLInChR photocurrents was red-shifted with respect to its "topological isomer," peaking around 560 nm (Figure 2D). FLInChR photocurrents were outward at all tested membrane potentials and exhibited a very weak voltage dependence regardless of the internal solution used, implicating a pump-like mechanism for FLInChR conductance (mean increase of 18% ± 4% at +40 mV compared to −80 mV, n = 16, Figure 2C). Replacement of external ions with sucrose had no effect on FLInChR photocurrent amplitude (p = 0.5, n = 4, Figure 2E), indicating that FLInChR photocurrents result from transport of cations out of the cell. An ammonium pre-pulse protocol (Schwiening and Boron, 1994) designed to shift the cell's pH—first basic, and then acidic—had no effect on FLInChR current amplitude (Figure 2F, n = 5, p = 0.9), suggesting that protons are not the exclusive charge carrier of the FLInChR photocurrent. We did not detect any change in photocurrent amplitude when switching

between Na⁺- and K⁺-based internals (Figure 2G, n = 9 versus n = 22, p > 0.5). Nevertheless, increasing cation size further by substituting with TEA⁺-based internal resulted in a significant drop in the photocurrent (Figure 2G, 165 ± 22 pA for K+, n = 22 versus 106 ± 15 pA for TEA⁺, n = 20, p < 0.05, one-way ANOVA with a post hoc Tukey's test). Taken together, the above evidence is most consistent with the notion that inversion transformed ChR2 E123T/T159C into a potent optogenetic inhibitor that functions like a light-activated, non-selective cation pump. Thus, topological engineering can indeed be sufficient to produce marked changes in the functional properties of opsins. Moreover, similarly to the case of CsChrimson inversion, inversion of ChR E123T/T159C resulted in a functionality (cation pumping) distinct from those attained with previous molecular engineering efforts. This finding, together with the observation that inversion also markedly altered the action spectrum of ChR2 ET/TC (Figures 2D), suggests that topological engineering induces a significant rearrangement of side chains around the active site.

The efficiency of optogenetic-based manipulations of cell activity critically depends on both the properties of the opsin as well as the biophysics of the targeted cell type. Thus, it is desirable to have a range of opsin properties (different ions conducted, a continuum from pump-like to channel-like behavior, etc.) for specific use cases. However, to qualify as a viable optogenetic tool for neuroscience, a new reagent must be capable of dramatically perturbing activity in at least some cell types. We therefore next aimed to verify that the altered active site packing of the inverted configuration retains sufficient light-dependent
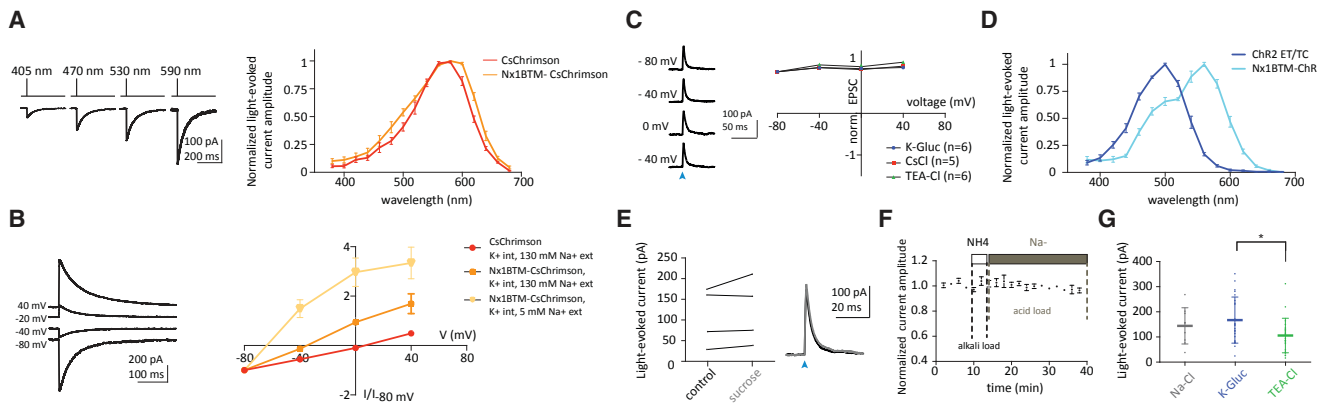
Figure 2. Opsin Inversion Generates Novel Functionality

(A) Action spectrum of native and inverted CsChrimson in hippocampal neuronal cultures.

(B) Current-voltage relationship for native (n = 5) and inverted (n = 5) CsChrimson. Note a shift of the reversal potential toward the reversal potential for potassium.

(C) Current amplitude as a function of holding potential in three different internal solutions for inverted ChR2 ET/TC. Note the lack of current reversal.

(D) Action spectrum for native (n = 4) and inverted (n = 4) ChR2 ET/TC and FLInChR.

(E) Amplitude of light-evoked current amplitude in physiological conditions and following wholesale replacement of external ions by sucrose.

(F) Current amplitude during bidirectional manipulation of internal pH (n = 5, see STAR Methods).

(G) Amplitude of light-evoked current following ion substitutions. Error bars represent standard error of the mean. *p < 0.05, one-way ANOVA with post hoc Tukey's test. All currents were characterized in response to 2 ms light pulses (wide-field illumination, 10 mW/mm^2 at the focal plane of the objective).

ion transport for robust circuit interrogation by evaluating the inhibitory potential of FLInChR variants in brain slices. We first chose to target substantia nigra *pars reticulata* (SNr) neurons due to extensive prior experience using the parent ChR2 variant in this experimental preparation (Brown et al., 2014) and the fact that tonically active neurons provide an ideal test case for evaluating inhibitory optogenetic actuators.

We prepared midbrain slices from adult GAD-Cre mice that had been injected into SNr with an adeno-associated virus carrying mVenus-tagged FLInChR or ArchT and targeted for whole-cell recordings SNr GABAergic neurons visually identified to express the opsin (Figure 3A). To further ascertain that inversion resulted in a marked change in the opsin function as well as to detect any contribution from potentially native, un-flipped ChR, we first chose conditions (wide-field illumination with a 1 ms pulse of 470 nm light; holding potential of −70 mV) that have previously been shown to elicit strong inward currents in ChR2-expressing SNr GABAergic cells (Brown et al., 2014). FLInChR-expressing cells displayed robust outward currents under these conditions (Figure 3B for FLInChR[Nx] and Figure 3C for FLInChR[Syb]). Consistent with our observations in dissociated cultures, FLInChR-mediated photocurrent was observed even when cells were stimulated with 590 nm light (Figures 3B and 3C)—conditions under which the parent ChR2 variant is not expected to display robust activity (Berndt et al., 2011). Evoked outward currents were on par with those mediated by ArchT—a commonly used and potent optogenetic inhibitor (Figure 3D). We observed a similarly rapid onset latency (FLInChR [Nx]: 0.33 ± 0.01 ms @ 470 nm; 0.30 ± 0.01 ms @ 590 nm, n = 4, Figure 3E, top; FLInChR[Syb] 0.24 ± 0.01 ms @ 470 nm; 0.24 ± 0.01 ms @590 nm, n = 4, Figure 3F, top; ArchT: 0.25 ± 0.04 ms @ 470 nm; 0.22 ± 0.03 ms @ 590 nm, n = 4, Figure 3G, top) and rapid decay time constants (FLInChR[Nx]: 2.51 ±

0.14 ms @ 470 nm; 2.60 ± 0.25 ms @ 590 nm, n = 4, Figure 3E, bottom; FLInChR[Syb] 3.07 ± 0.13 ms @ 470 nm; 3.31 ± 0.24 ms @590 nm, n = 4, Figure 3F, bottom; ArchT: 2.49 ± 0.04 ms @ 470 nm; 2.24 ± 0.03 ms @ 590 nm, n = 4, Figure 3G, bottom) for FLInChR- and ArchT-mediated currents. The comparable performance of Arch and FLInChR variants argues that the structural re-arrangements in the vicinity of the active site (a consequence of inversion) are compatible with efficient light-dependent ion transport.

We next took advantage of the fact that SNr GABAergic cells respond to depolarizing current *in vitro* with firing rates of > 150 Hz (Figure 4A) to examine the efficiency, with which FLInChR can inhibit evoked activity. In the absence of light stimulation, we were able to evoke progressively higher spiking frequency in FLInChR-expressing neurons by injecting increasing steps of depolarizing current in a whole-cell current clamp mode. Brief pulses (100 ms) of photostimulation induced significant hyperpolarization of the membrane voltage that was maintained even during depolarizing current injection steps. Evoked spiking was mostly eliminated during photostimulation and could only be partially recovered with very large (> 400 pA) current injections (Figures 4A and 4B). Similarly, efficient suppression of evoked spiking could be observed in FLInChR-expressing cortical neurons (Figure S3). The ability to sustain photoinhibition for prolonged periods (Figures 4A and 4C) was likely due to only moderate desensitization of FLInChR-mediated currents beyond the initial 100 ms (Figure S4, photocurrent amplitude normalized to peak: 0.8062 ± 0.0743 at 100 ms, 0.6333 ± 0.1131 ms at 1000 ms, n = 4). Combined, these results demonstrate that FLInChR is a robust optogenetic inhibitor that can suppress evoked activity even in fast-spiking neurons and may be sufficient for *in vivo* circuit interrogation experiments in behaving animals.
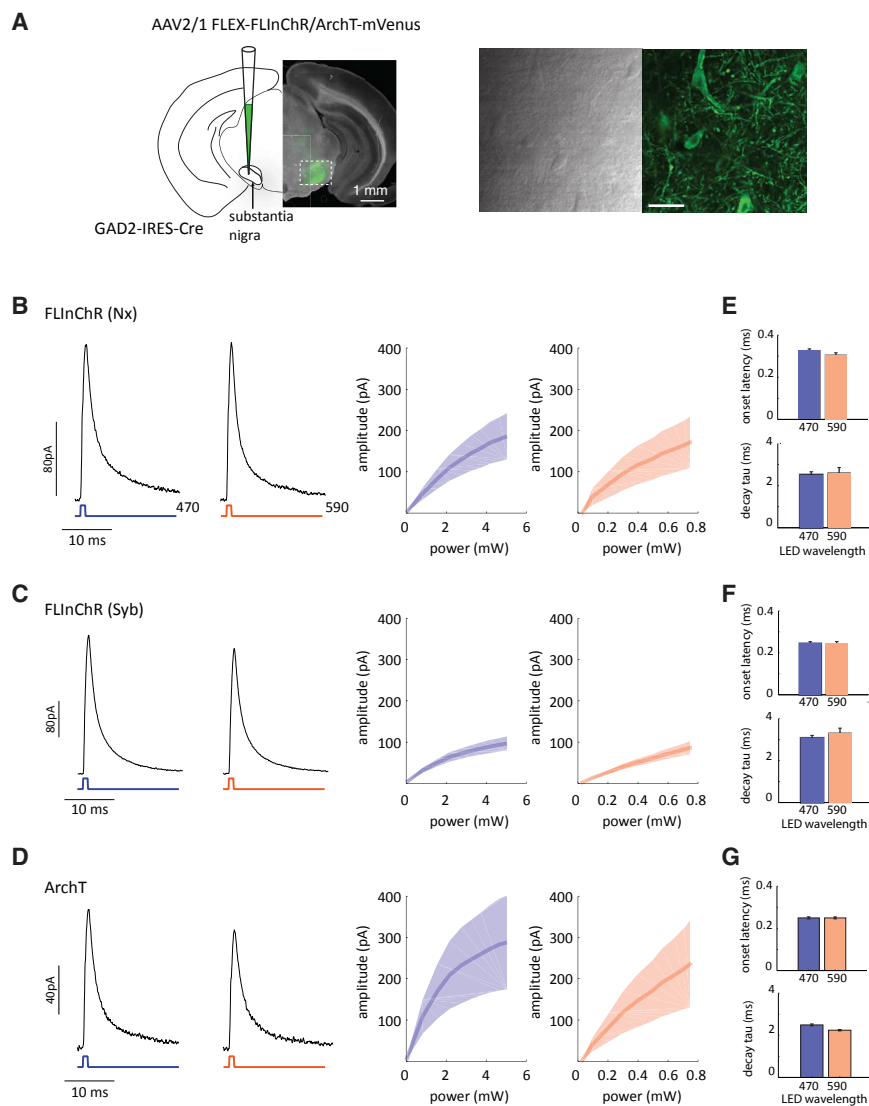
(A) (Left) Schematic of the experimental preparation. Brain slices were prepared from GAD2-IRES-Cre mice that had been previously injected into substantia nigra with AAV2/1 CAG FLEX FLInChR-mVenus or AAV2/1 CAG FLEX ArchT-mVenus. (Right) Representative differential interference contrast (DIC) and fluorescence images of FLInChR-expressing slices.

(B–D) (Left two panels) Representative whole-cell currents observed in SNr cells expressing either FLInChR(Nx) (B), FLInChR(Syb) (C), or ArchT (D) held at −70 mV in response to a 1 ms light pulse (10 mW/mm^2 at the focal point of the objective) at 470 nm and 590 nm. (Right two panels) Photocurrent amplitude as a function of light power at the objective (n = 4 cells each). Light shading represents standard error of the mean.

(E–G) (Top) Response latencies across cells for the two wavelengths. (Bottom) Decay constants for light-induced currents (n = 4 cells each).

Error bars represent standard error of the mean.

velocity of reaches in "light ON" trials (Figure 5C), which necessitated reaches of significantly longer reach duration for all mice (Figures 5D–5G). Importantly, the size of the observed behavioral effect for FLInChR-mediated perturbation of movement vigor was similar in magnitude to that observed in experiments in which basal ganglia activity was manipulated with ArchT (Panigrahi et al., 2015). Thus, although comparisons between different optogenetic tools are notoriously subject to the vagaries of the specific experimental preparation, the observed robust performance places FLInChR variants favorably among extant optogenetic tools for *in vivo* circuit perturbation experiments. Indeed, parallel sets of behavioral perturbation experiments in *Caenorhabditis elegans* nematodes expressing FLInChR in muscle cells (Video S1 and Figure S5), and in rats expressing FLInChR in prefrontal cortical neurons (data not shown), provided further support that this new opsin variant is a powerful new inhibitor suitable for *in vivo* manipulations.

The rapid kinetics of FLInChR-mediated photoinhibition evident in slice experiments (Figure 3) prompted us to investigate whether FLInChR might aid with optogenetic tagging efforts—a common method for identification of neuronal cell types in electrophysiological experiments. While simple in principle, such experiments can be notoriously difficult in awake, active animals because of pronounced network effects, especially in circuits with strong recurrent connectivity, e.g. neocortex. The depolarizing opsin ChR2 is by far the most frequently used optogenetic tag, but in excitatory neuronal populations, its use for optotagging can be problematic (Lima et al., 2009). As latencies of light-driven modulation are often on par with synaptic delays,

SNr neurons are the primary output of the basal ganglia—a brain structure thought to be central to the bi-directional control of the vigor of voluntary movement in rodents (Dudman and Krakauer, 2016; Panigrahi et al., 2015) and in primates (Anderson and Horak, 1985; Desmurget and Turner, 2010). Given the efficacy of FLInChR *in vitro*, we next asked whether focal optogenetic inhibition of SNr projection neurons could be used for behavioral circuit perturbation experiments. We trained mice expressing FLInChR in the SNr on a previously developed effort-based operant task that requires animals to adjust the vigor of a reaching movement to obtain reward (Figures 5A and 5B). Once animals attained expert performance, we suppressed activity in the SNr on 25% of randomly selected reaches by delivering light through bilaterally implanted optical fibers. Similar to the past study (Panigrahi et al., 2015), we applied the perturbation selectively during movement. Consistent with the efficient perturbation of spiking observed in FLInChR-expressing animals *in vitro*, we observed a specific and systematic reduction in peak
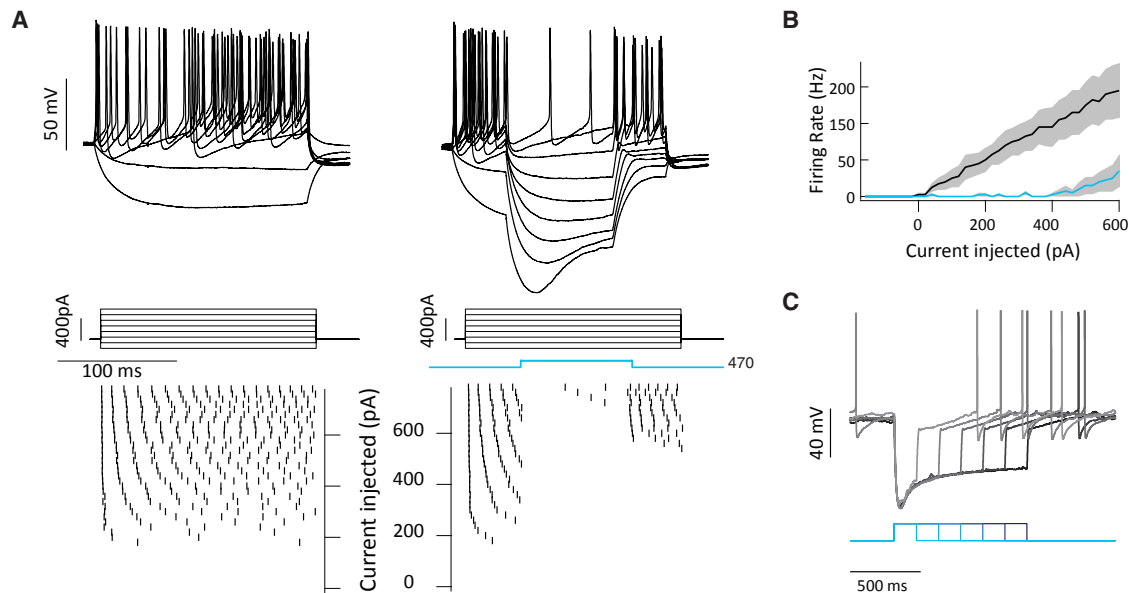
Figure 4. FLInChR Mediates Efficient Suppression of Spiking

(A) Example responses of a FLInChR-expressing SNr cell to step current injections with and without 470 nm light (10 mW/mm^2 at the focal point of the objective). (Top) Overlaid voltage traces. (Bottom) Raster plots of spiking activity.

(B) Population average of firing rates in response to injected current with (black) and without (blue) light exposure.

(C) Spiking activity of an example cell in the presence of progressively longer illumination at 470 nm.

light-dependent activation by neighboring ChR2$^+$ neurons driving a ChR2$^-$ cell over threshold can be indistinguishable from direct light activation of a ChR2$^+$ cell (Buzsáki et al., 2015). Inhibitory opsins, in principle, provide an alternative approach to opto-tagging populations of excitatory cells such as cortical projection neurons (PNs). Since PNs derive most of their excitatory drive from long-range inputs (Guo et al., 2017), short latencies to light-dependent inhibition are unlikely to result from removal of synaptic drive through local recurrent connections. We therefore used rAAV2-retro-mediated delivery (Tervo et al., 2016) to selectively target long-range PNs in layer 5 of sensorimotor cortex in awake, behaving mice and rats and analyzed the distribution of latencies to detectable photoinhibition through simultaneous extracellular recordings (Figure 5H).

Robust photoinhibition was easily observed even in large rat PNs after 2–3 weeks of expression (Figure 5I, significant responses detected in 19.5% of recorded units). When the optical fiber was advanced alongside the recording electrodes, the majority of light-sensitive units displayed latency to photoinhibition below three milliseconds (although latencies up to 10 milliseconds could be observed in some cases). The ease of finding units with very short photoinhibition latencies and their spatial distribution (nominal depths of 0.9–1.3 mm from the cortical surface, consistent with the location in the rat brain of retrogradely labeled striatal-projecting cortical neurons) strongly suggests that short-latency suppression is mediated by a direct effect. To verify the efficacy of direct FLInChR-mediated photo-inhibition in such settings, we used juxta-cellular recordings in an equivalent experiment in the mouse. Illumination through the

pipette (Coddington and Dudman, 2017) was sufficient to induce rapid suppression of activity that could be maintained for up to 5 s of constant illumination (Figure 5J), further arguing in favor of the direct nature of the observed photoinhibition. Moreover, when activity across all cortical layers was evaluated simultaneously with a large, high channel-density electrode array (Jun et al., 2017), units with rapid and robust suppression of firing (Figure 5K) were exclusively found at depths consistent with layer 5 PNs (Figure 5L). Notably, these high-density recordings revealed that targeted photoinhibition of targeted PNs is accompanied by disinhibition of other cortical neurons within the circuit (Figure 5L, units with positive change in activity during illumination). However, the observed positive modulation of activity was both systematically delayed compared to presumed direct photoinhibition (indicative of polysynaptic connectivity) and distributed across cortical layers. Collectively, these data suggest that FLInChR can be used *in vivo* in awake animals to effectively silence target populations of neurons. Moreover, the magnitude, speed, and duration of activity suppression attainable even in large, difficult-to-inhibit pyramidal neurons argue that FLInChR is a useful tool for a variety of perturbation and opto-tagging experiments.

DISCUSSION

The potential of the optogenetic approach for dissecting neural circuit function is widely appreciated, with an ongoing search for new rhodopsin variants with specific functions (Chuong et al., 2014; Deisseroth and Hegemann, 2017; Klapoetke et al., 2014). Despite extensive electrophysiological studies and the
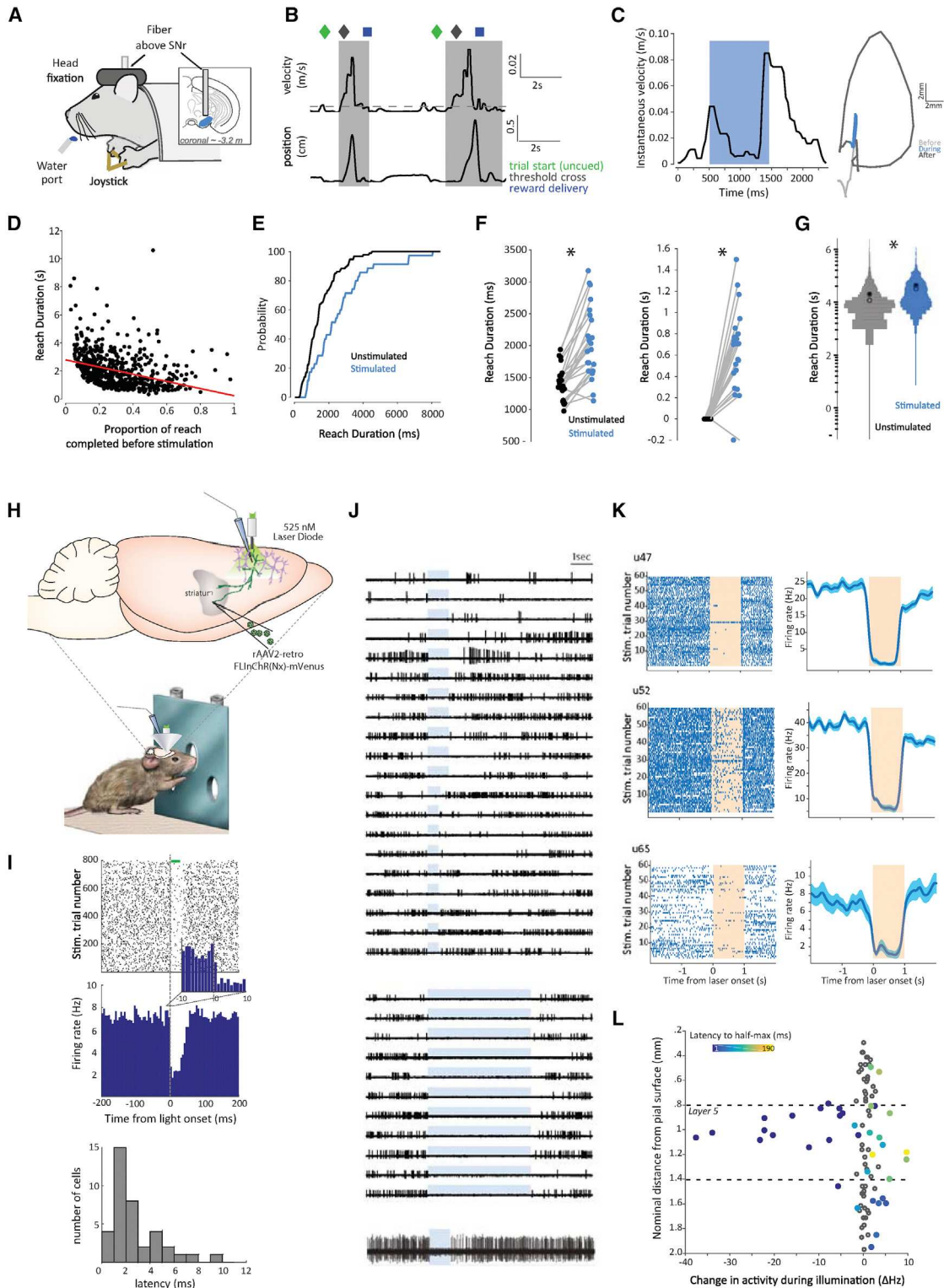
Figure 5. FLInChR Is an Effective Light-Dependent Inhibitor for Circuit Dissection

(A) Experimental paradigm used to evaluate the efficacy of FLInChR in awake behaving animals. Head-fixed mice were trained to manipulate a joystick, with responses above a certain threshold preferentially rewarded. Effect of FLInChR-based perturbation of neural ensemble activity in SNr on response vigor was then assessed. Selective expression of FLInChR in the GABA-ergic cells of the SNr was achieved through stereotaxic delivery of AVV2/1 FLEX-FLInChR in GAD2-IRES-Cre mice.

(legend continued on next page)

availability of high-resolution structural data for a number of rhodopsins (Kato et al., 2012; Volkov et al., 2017), the key processes governing opsin function—gating and permeation—remain incompletely understood, thus hampering molecular engineering efforts. The function-altering inversion of rhodopsin topology that we describe here adds an orthogonal dimension for opsin engineering that should permit further expansion of the toolkit and might help shed additional light on the mechanism of ion transport in the opsin family.

The relative ease with which we were able to invert Channelrhodopsins is surprising in light of the prevailing notion that most proteins tend to have a very strong preference for a specific topology (reviewed in von Heijne, 2006). Much evidence, particularly in prokaryotes, points to the "inside-positive" charge bias as a key guiding principle that determines protein orientation (von Heijne and Gavel, 1988; von Heijne, 1986, 1992). Most bacterial multi-spanning proteins display a prominent alternation in clusters of positive charges—enriched in cytoplasmic loops and sparse in periplasmic loops—and flipping their first helix is thought to be insufficient for altering the overall orientation because the topological information is present locally throughout the protein sequence (Gafvelin and von Heijne, 1994). However, the positive charge bias appears to have significantly weakened in the evolution of eukaryotes, raising the possibility that the specific orientation of the N-terminal helix may have begun to play a progressively larger role in determining the overall topology of transmembrane proteins, with the helices closer to the C-terminus free to follow either orientation once the N terminus is fixed (Hartmann et al., 1989; Heijne, 1994). Indeed, some evidence points to the positive charge bias being strongest across the first transmembrane helix in eukaryotic proteins, arguing in favor of such N-terminal regulation (Hartmann et al., 1989). If true, this would not only have constituted an efficient mechanism for ensuring a specific topology, but would also have paved an evolutionary path for the merging of modular transmembrane protein domains through the process of genetic recombination.

Our finding that topological inversion of Channelrhodopsins (ChRs) does not leave the ionic flux unaltered brings into focus the likely mixing of channel- and pump-like functionalities at the core of the conduction mechanism. Although ion channels and pumps are often presented as two distinct families, growing evidence suggests that they might be more appropriately viewed as representing two extremes of a continuum of proteins that allow passage of ions across lipid membranes (Accardi and Miller, 2004; Gadsby, 2009; Miller, 2006; Zifarelli and Pusch, 2007). Unlike channels, pumps require at least one conformational change associated with flux across the membrane, and at the extreme, true transporter pumps require multiple changes: one to eliminate exposure of the substrate to one side of the membrane and a second to expose it to the other side. These relatively slow conformational changes impose non-negligible delays on ion passage, significantly reducing the flux of pumps compared with those observed for channels. Strikingly, the flux of ChRs is also markedly lower than that of cation channels selective for similar monovalent ions—a finding that hints at the possibility that ChRs might embody examples of transmembrane proteins that blur the distinction between channels and pumps. Indeed, although the detailed mechanism of ion permeation through ChRs remains incompletely understood, the lack of a clearly identifiable pore in high-resolution structures of ChR variants has led to the suggestion that an obligate conformational change must accompany ion flux across the membrane (Volkov et al., 2017). Our ability to reverse the flux of ions by inverting a ChR variant in the membrane provides strong experimental support for the sequential exposure of the cytosolic and the extracellular cavities in ChR to ions and thus for an obligate conformational change. The ability of inversion to alter ion selectivity in CsChrimson also provides experimental support for the importance of charged residues near the membrane surface—and thus distant from the pore itself—in determining selectivity (Berndt et al., 2016; Roux and MacKinnon, 1999). Additional details about the mechanism of ion transfer may emerge in the future from comparisons of high-resolution structures for the "topological isomers," especially in cases in which such inversion leads to marked functional changes.

The observed spectral and mechanistic differences between "topological isomers" suggest that, while the core functionality of rhodopsins—light responsiveness and ion transport—is preserved following inversion, the surrounding electrostatic interactions are altered in the voltage environment of the inverted configuration. Indeed, the specific biophysical properties of individual rhodopsins are uniquely determined by the protein

(B) Schematic of the experimental protocol. Trial start (green diamond) was un-cued. Reaches had to pass variable threshold (gray diamond) for a delayed water reward (blue square). Reaches were extracted using both the Euclidean displacement and the velocity of the joystick. Light (473 nm, 1–5 mW at the fiber tip) was delivered on the first reach of ~20% of trials.

(C) Instantaneous velocity and trajectory in space for an example reach before (light gray), during (blue), and after (dark gray) light delivery.

(D) Duration of "stimulated" reaches as a function of the fraction of reach completed at the time of light onset (n = 627 reaches in six animals).

(E) Cumulative distribution of durations for "stimulated" (n = 25) and "unstimulated" (n = 94) reaches during one session.

(F) Mean reach durations for "stimulated" reaches than for "unstimulated" reaches across 23 sessions in six animals. *p < 0.01, paired t test.

(G) Distribution of reach durations for all 627 "stimulated" and 2254 "unstimulated" reaches. White dot indicates distribution median; black, distribution mean. *p < 0.01, Mann-Whitney test.

(H) Schematic of the experiment aimed to optogenetically tag projection neurons in behaving mice and rats.

(I) (Top two panels) Activity in an example rat cortico-striatal neuron for 800 repeated light presentations. Light power was 2 mW at the fiber tip. (Bottom panel) Distribution of latencies for light-dependent suppression of spiking across neurons.

(J) Repeated photoinhibition in an example juxta-cellular recording from a mouse layer 5 projection neuron. Note efficient suppression of spiking throughout the duration of illumination.

(K) Activity in three example mouse projection neurons for 60 repeated light presentations.

(L) Distribution of light-dependent modulation effects across cortical layers. Notice that robust short-latency inhibition is confined to layer 5.

environment in the vicinity of the chromophore and along the conduction pathway (Schneider et al., 2015). As the demand for more precise molecular tools to serve the specific experimental goals increases (Berndt et al., 2011) (Yizhar et al., 2011), a palette of opsins with diverse ion selectivity, kinetics, and spectral properties will be needed (Wietek and Prigge, 2016). Because neither non-specific cation pumping nor robust K$^+$ selectivity have been engineered through structure-guided mutagenesis to date, topological engineering may permit exploration of a subspace of variants uniquely accessible in the inverted configuration and may enable rapid diversification (as much as a doubling) of the available optogenetics toolkit.

STAR★METHODS

Detailed methods are provided in the online version of this paper and include the following:

- KEY RESOURCES TABLE
- CONTACT FOR REAGENT AND RESOURCE SHARING
- EXPERIMENTAL MODEL AND SUBJECT DETAILS
  - ○ Dissociated neuronal cultures
  - ○ Animal lines
- METHOD DETAILS
  - ○ Constructs and adeno associated virus
  - ○ Proteinase K assay
  - ○ Myc-tag assay
  - ○ *In vitro* whole-cell electrophysiology in dissociated neuronal cultures
  - ○ Internal solutions for whole cell-recordings
  - ○ Ammonium prepulse protocol
  - ○ *In vitro* whole-cell slice electrophysiology
  - ○ *In vivo* perturbation of SNr GABAergic activity during effort-based operant task
  - ○ Behavioral experiments in *C. elegans*
  - ○ Extracellular electrophysiological identification of FLInChR-expressing neurons in awake rats
  - ○ Extracellular electrophysiological identification of FLInChR-expressing neurons in awake rat
- QUANTIFICATION AND STATISTICAL ANALYSIS
- DATA AND SOFTWARE AVAILABILITY

SUPPLEMENTAL INFORMATION

Supplemental Information includes five figures and one video and can be found with this article online at https://doi.org/10.1016/j.cell.2018.09.026.

AUTHOR CONTRIBUTIONS

J.B., R.B., L.C., D.G.R.T., J.T.D., and A.Y.K. designed the study; J.B., R.B., L.C., D.G.R.T., J.T.D., K.M., M.P., E.K., J.P., and J.P. conducted the experiments. A.C.F.B. and A.G. designed and carried out screening of FLInChR(Nx) in *C. elegans*. J.B., R.B., L.C., D.G.R.T., J.T.D., and A.Y.K. wrote the manuscript.

REFERENCES

Accardi, A., and Miller, C. (2004). Secondary active transport mediated by a prokaryotic homologue of ClC Cl-channels. Nature *427*, 803–807.

Anderson, M.E., and Horak, F.B. (1985). Influence of the globus pallidus on arm movements in monkeys. III. Timing of movement-related information. J. Neurophysiol. *54*, 433–448.

Béjà, O., Aravind, L., Koonin, E.V., Suzuki, M.T., Hadd, A., Nguyen, L.P., Jovanovich, S.B., Gates, C.M., Feldman, R.A., Spudich, J.L., et al. (2000). Bacterial rhodopsin: evidence for a new type of phototrophy in the sea. Science *289*, 1902–1906.

Benton, R., Sachse, S., Michnick, S.W., and Vosshall, L.B. (2006). Atypical membrane topology and heteromeric function of Drosophila odorant receptors in vivo. PLoS Biol. *4*, e20.

Berndt, A., Schoenenberger, P., Mattis, J., Tye, K.M., Deisseroth, K., Hegemann, P., and Oertner, T.G. (2011). High-efficiency channelrhodopsins for fast neuronal stimulation at low light levels. Proc. Natl. Acad. Sci. USA *108*, 7595–7600.

Berndt, A., Lee, S.Y., Ramakrishnan, C., and Deisseroth, K. (2014). Structure-guided transformation of channelrhodopsin into a light-activated chloride channel. Science *344*, 420–424.

Berndt, A., Lee, S.Y., Wietek, J., Ramakrishnan, C., Steinberg, E.E., Rashid, A.J., Kim, H., Park, S., Santoro, A., Frankland, P.W., et al. (2016). Structural foundations of optogenetics: Determinants of channelrhodopsin ion selectivity. Proc. Natl. Acad. Sci. USA *113*, 822–829.

Bernsel, A., Viklund, H., Falk, J., Lindahl, E., von Heijne, G., and Elofsson, A. (2008). Prediction of membrane-protein topology from first principles. Proc. Natl. Acad. Sci. USA *105*, 7177–7181.

Brown, J., Pan, W.-X., and Dudman, J.T. (2014). The inhibitory microcircuit of the substantia nigra provides feedback gain control of the basal ganglia output. eLife *3*, e02397.

Buzsáki, G., Stark, E., Berényi, A., Khodagholy, D., Kipke, D.R., Yoon, E., and Wise, K.D. (2015). Tools for probing local circuits: high-density silicon probes combined with optogenetics. Neuron *86*, 92–105.

Chen, G.-Q., Cui, C., Mayer, M.L., and Gouaux, E. (1999). Functional characterization of a potassium-selective prokaryotic glutamate receptor. Nature *402*, 817–821.

Chuong, A.S., Miri, M.L., Busskamp, V., Matthews, G.A., Acker, L.C., Sørensen, A.T., Young, A., Klapoetke, N.C., Henninger, M.A., Kodandaramaiah, S.B., et al. (2014). Noninvasive optical inhibition with a red-shifted microbial rhodopsin. Nat. Neurosci. *17*, 1123–1129.

Coddington, L.T., and Dudman, J.T. (2017). Emergence of reward expectation signals in identified dopamine neurons. bioRxiv. https://doi.org/10.1101/238881.

Deisseroth, K., and Hegemann, P. (2017). The form and function of channelrhodopsin. Science *357*, eaan5544.

Desmurget, M., and Turner, R.S. (2010). Motor sequences and the basal ganglia: kinematics, not habits. J. Neurosci. *30*, 7685–7690.

Dudman, J.T., and Krakauer, J.W. (2016). The basal ganglia: from motor commands to the control of vigor. Curr. Opin. Neurobiol. *37*, 158–166.

Fenno, L., Yizhar, O., and Deisseroth, K. (2011). The development and application of optogenetics. Annu. Rev. Neurosci. *34*, 389–412.

Gadsby, D.C. (2009). Ion channels versus ion pumps: the principal difference, in principle. Nat. Rev. Mol. Cell Biol. *10*, 344–352.

Gafvelin, G., and von Heijne, G. (1994). Topological "frustration" in multispanning E. coli inner membrane proteins. Cell 77, 401–412.

Gallivan, J.P., and Chapman, C.S. (2014). Three-dimensional reach trajectories as a probe of real-time decision-making between multiple competing targets. Front. Neurosci. 8, 215.

Gerfen, C.R., Paletzki, R., and Heintz, N. (2013). GENSAT BAC cre-recombinase driver lines to study the functional organization of cerebral cortical and basal ganglia circuits. Neuron 80, 1368–1383.

Grote, M., Engelhard, M., and Hegemann, P. (2014). Of ion pumps, sensors and channels—Perspectives on microbial rhodopsins between science and history. Biochim. Biophys. Acta 1837, 533–545.

Gunaydin, L.A., Yizhar, O., Berndt, A., Sohal, V.S., Deisseroth, K., and Hegemann, P. (2010). Ultrafast optogenetic control. Nat. Neurosci. 13, 387–392.

Guo, Z.V., Inagaki, H.K., Daie, K., Druckmann, S., Gerfen, C.R., and Svoboda, K. (2017). Maintenance of persistent activity in a frontal thalamocortical loop. Nature 545, 181–186.

Hanks, T.D., Kopec, C.D., Brunton, B.W., Duan, C.A., Erlich, J.C., and Brody, C.D. (2015). Distinct relationships of parietal and prefrontal cortices to evidence accumulation. Nature 520, 220–223.

Hartmann, E., Rapoport, T.A., and Lodish, H.F. (1989). Predicting the orientation of eukaryotic membrane-spanning proteins. Proc. Natl. Acad. Sci. 86, 5786–5790.

Heijne, G. (1994). Membrane proteins: from sequence to structure. Annu. Rev. Biophys. Biomol. Struct. 23, 167–192.

Inoue, K., Tsukamoto, T., Shimono, K., Suzuki, Y., Miyauchi, S., Hayashi, S., Kandori, H., and Sudo, Y. (2015). Converting a light-driven proton pump into a light-gated proton channel. J. Am. Chem. Soc. 137, 3291–3299.

Jun, J.J., Steinmetz, N.A., Siegle, J.H., Denman, D.J., Bauza, M., Barbarits, B., Lee, A.K., Anastassiou, C.A., Andrei, A., and Aydın, Ç. (2017). Fully integrated silicon probes for high-density recording of neural activity. Nature 551, 232.

Karlsson, M.P., Tervo, D.G., and Karpova, A.Y. (2012). Network resets in medial prefrontal cortex mark the onset of behavioral uncertainty. Science 338, 135–139.

Kato, H.E., Zhang, F., Yizhar, O., Ramakrishnan, C., Nishizawa, T., Hirata, K., Ito, J., Aita, Y., Tsukazaki, T., and Hayashi, S. (2012). Crystal structure of the channelrhodopsin light-gated cation channel. Nature 482, 369–374.

Klapoetke, N.C., Murata, Y., Kim, S.S., Pulver, S.R., Birdsey-Benson, A., Cho, Y.K., Morimoto, T.K., Chuong, A.S., Carpenter, E.J., Tian, Z., et al. (2014). Independent optical excitation of distinct neural populations. Nat. Methods 11, 338–346.

Lima, S.Q., Hromádka, T., Znamenskiy, P., and Zador, A.M. (2009). PINP: a new method of tagging neuronal populations for identification during in vivo electrophysiological recording. PLoS ONE 4, e6099.

Lin, J.Y., Lin, M.Z., Steinbach, P., and Tsien, R.Y. (2009). Characterization of engineered channelrhodopsin variants with improved properties and kinetics. Biophys. J. 96, 1803–1814.

Lin, J.Y., Knutsen, P.M., Muller, A., Kleinfeld, D., and Tsien, R.Y. (2013). ReaChR: a red-shifted variant of channelrhodopsin enables deep transcranial optogenetic excitation. Nat. Neurosci. 16, 1499–1508.

Miller, C. (2006). ClC chloride channels viewed through a transporter lens. Nature 440, 484–489.

Nagel, G., Szellas, T., Huhn, W., Kateriya, S., Adeishvili, N., Berthold, P., Ollig, D., Hegemann, P., and Bamberg, E. (2003). Channelrhodopsin-2, a directly light-gated cation-selective membrane channel. Proc. Natl. Acad. Sci. USA 100, 13940–13945.

Oesterhelt, D., and Stoeckenius, W. (1971). Rhodopsin-like protein from the purple membrane of Halobacterium halobium. Nat. New Biol. 233, 149–152.

Osborne, J.E., and Dudman, J.T. (2014). RIVETS: a mechanical system for in vivo and in vitro electrophysiology and imaging. PLoS ONE 9, e89007.

Panigrahi, B., Martin, K.A., Li, Y., Graves, A.R., Vollmer, A., Olson, L., Mensh, B.D., Karpova, A.Y., and Dudman, J.T. (2015). Dopamine is required for the neural representation and control of movement vigor. Cell 162, 1418–1430.

Rapp, M., Seppälä, S., Granseth, E., and von Heijne, G. (2007). Emulating membrane protein evolution by rational design. Science 315, 1282–1284.

Roux, B., and MacKinnon, R. (1999). The cavity and pore helices in the KcsA K+ channel: electrostatic stabilization of monovalent cations. Science 285, 100–102.

Schneider, F., Grimm, C., and Hegemann, P. (2015). Biophysics of Channelrhodopsin. Annu. Rev. Biophys. 44, 167–186.

Schwiening, C.J., and Boron, W.F. (1994). Regulation of intracellular pH in pyramidal neurones from the rat hippocampus by Na(+)-dependent Cl(-)-HCO3- exchange. J. Physiol. 475, 59–67.

Seppälä, S., Slusky, J.S., Lloris-Garcerá, P., Rapp, M., and von Heijne, G. (2010). Control of membrane protein topology by a single C-terminal residue. Science 328, 1698–1700.

Sharma, A.K., Spudich, J.L., and Doolittle, W.F. (2006). Microbial rhodopsins: functional versatility and genetic mobility. Trends Microbiol. 14, 463–469.

Sobolevsky, A.I., Yelshansky, M.V., and Wollmuth, L.P. (2003). Different gating mechanisms in glutamate receptor and K+ channels. J. Neurosci. 23, 7559–7568.

Tervo, D.G.R., Hwang, B.-Y., Viswanathan, S., Gaj, T., Lavzin, M., Ritola, K.D., Lindo, S., Michael, S., Kuleshova, E., Ojala, D., et al. (2016). A designer AAV variant permits efficient retrograde access to projection neurons. Neuron 92, 372–382.

Thomas, G. (2002). Furin at the cutting edge: from protein traffic to embryogenesis and disease. Nat. Rev. Mol. Cell Biol. 3, 753–766.

Tikhonov, D.B., and Magazanik, L.G. (2009). Origin and molecular evolution of ionotropic glutamate receptors. Neurosci. Behav. Physiol. 39, 763–773.

Turano, F.J., Panta, G.R., Allard, M.W., and van Berkum, P. (2001). The putative glutamate receptors from plants are related to two superfamilies of animal neurotransmitter receptors via distinct evolutionary mechanisms. Mol. Biol. Evol. 18, 1417–1420.

Volkov, O., Kovalev, K., Polovinkin, V., Borshchevskiy, V., Bamann, C., Astashkin, R., Marin, E., Popov, A., Balandin, T., and Willbold, D. (2017). Structural insights into ion conduction by channelrhodopsin 2. Science 358, eaan8862.

von Heijne, G. (1986). The distribution of positively charged residues in bacterial inner membrane proteins correlates with the trans-membrane topology. EMBO J. 5, 3021.

von Heijne, G. (1992). Membrane protein structure prediction. Hydrophobicity analysis and the positive-inside rule. J. Mol. Biol. 225, 487–494.

von Heijne, G. (2006). Membrane-protein topology. Nat. Rev. Mol. Cell Biol. 7, 909–918.

von Heijne, G., and Gavel, Y. (1988). Topogenic signals in integral membrane proteins. Eur. J. Biochem. 174, 671–678.

Wietek, J., and Prigge, M. (2016). Enhancing channelrhodopsins: An overview. Methods Mol. Biol., 141–165.

Wollmuth, L.P., and Sobolevsky, A.I. (2004). Structure and gating of the glutamate receptor ion channel. Trends Neurosci. 27, 321–328.

Wood, M.W., VanDongen, H.M., and VanDongen, A.M. (1995). Structural conservation of ion conduction pathways in K channels and glutamate receptors. Proc. Natl. Acad. Sci. USA 92, 4882–4886.

Yizhar, O., Fenno, L.E., Prigge, M., Schneider, F., Davidson, T.J., O'Shea, D.J., Sohal, V.S., Goshen, I., Finkelstein, J., Paz, J.T., et al. (2011). Neocortical excitation/inhibition balance in information processing and social dysfunction. Nature 477, 171–178.

Zifarelli, G., and Pusch, M. (2007). CLC chloride channels and transporters: a biophysical and physiological perspective. In Reviews of physiology, biochemistry and pharmacology (Springer), pp. 23–76.

STAR★METHODS

KEY RESOURCES TABLE

REAGENT or RESOURCE	SOURCE	IDENTIFIER
Deposited Data		
FLInChR	this paper	GenBank accession # BankIt2158148 BSeq#1 MK046864
Antibodies		
Rabbit anti-c-myc	Sigma	Cat # C3956; RRID:AB_439680
Goat anti-Rabbit IgG secondary antibody Alexa Fluro 594	Abcam	Cat #150080; RRID:AB_2650602
Bacterial and Virus Strains		
AAV2/1 CAG-ChR2(ET/TC)-mVenus	this paper	N/A
AAV2/1 CAG-Cre	this paper	N/A
AAV2/1 CAG-Flex-CsChrimson-mVenus	this paper	N/A
AAV2/1 CAG-Flex-FLInChR(Syb)-mVenus	this paper	N/A
AAV2/1 CAG-FLInCHR (Nx)-mVenus	this paper	N/A
AAV2/1 CAG-FLInCHR (Syb)-mVenus	this paper	N/A
AAV2/1 CAG-Nx1B TM-ARCH(TR)-mVenus	this paper	N/A
AAV2/1 CAG-Nx1BTM-CsChrimson-mVenus	this paper	N/A
AAV2/1 CAG-OR 59D.1-ChR ET/TC-mVenus	this paper	N/A
rAAV2-retro CAG-Cre	this paper	N/A
Chemicals, Peptides, and Recombinant Proteins		
DPBS with Ca^{2+} and Mg2+	GIBCO	14040117
Proteinase K	Sigma	P4850
Ultra Rainbow Fluorescent Particles Beads; mean diameter: 3.80 um	Bangs Laboratories, Inc.	610
NBACTIV4	BrainBits	NBACTIV4
poly-D-Lysine	Corning	3524
Kynurenic acid	Sigma	K3375
SR95531	Tocris	1262
N-methyl-D-glucamine	Sigma	M2004
Experimental Models: Cell Lines		
primary neuronal cultures	this paper	N/A
Experimental Models: Organisms/Strains		
transgenic C. elegans strain ZX2282 (zxEx1105[pmyo-3::FLInChR::mVenus; pmyo-2::CFP] in N2)	this paper	N/A
GAD2-IRES-Cre mouse line	Jackson Laboratory	Stock #010802
Sim1-KJ18 mouse line	GENSAT	Stock # 031742-UCD
Long-Evans rat	Charles River Labs	Stock #006
Software and Algorithms		
AxoGraph X	https://axograph.com/	N/A
Cerebro	https://bitbucket.org/mkarlsso/trodes/src	N/A
Igor Pro	Wavemetrics	N/A
Igor Pro Scripts	http://dudmanlab.org/	N/A
Imaging, behavior, electrophysiology, optogenetics analysis code	this paper	N/A
JRCLUST	https://github.com/JaneliaSciComp/JRCLUST	N/A

(*Continued on next page*)

REAGENT or RESOURCE	SOURCE	IDENTIFIER
MATLAB	Mathworks	N/A
Slidebook 5.0-Innovatove Application	https://www.intelligent-imaging.com	N/A
SpikeGLX	https://github.com/billkarsh/SpikeGLX	N/A
Trodes	https://bitbucket.org/mkarlsso/trodes/src	N/A

CONTACT FOR REAGENT AND RESOURCE SHARING

Further information and requests for reagents should be directed to, and will be fulfilled by, the Lead Contact, Alla Y. Karpova (alla@janelia.hhmi.org).

EXPERIMENTAL MODEL AND SUBJECT DETAILS

Dissociated neuronal cultures

Mixed sex dissociated hippocampal cultures were prepared from Sprague-Dawley post-natal day 0 to 1 rat pups. Fourty-thousand neurons were plated on each poly-D-Lysine coated glass coverslips (Cat no. 3524; Corning) and cultured in in NBACTIVE4 (BrainBits).

Animal lines

In vivo experiments were performed either in male CAG-IRES-Cre mice, male Sim1-KJ18 mice, and male Long Evans rats. Experiments were conducted according to National Institutes of Health guidelines for animal research and were approved by the Institutional Animal Care and Use Committee at HHMI's Janelia Farm Research Campus.

METHOD DETAILS

Constructs and adeno associated virus

Serotype	Payload	Titer (GC/ml)
AAV2/1	CAG-ChR2(ET/TC)-mVenus	2.3E+12
AAV2/1	CAG-FLInCHR (Nx)-mVenus	1.9E+12
AAV2/1	CAG-Flex-CsChrimson-mVenus	8.8E+12
AAV2/1	CAG-Nx1BTM-CsChrimson-mVenus	2.8E+12
rAAV2-retro	CAG-Cre	7.1E+12
rAAV2-retro	CAG-Flex-FLInChR(Nx)-mVenus	3.0E+12
AAV2/1	CAG-Nx1B TM-ARCH(TR)-mVenus	1.6E+12
AAV2/1	CAG-Cre	1.1E+12
AAV2/1	CAG-FLInCHR (Syb)-mVenus	2.1E+12
AAV2/1	CAG-Flex-FLInChR(Syb)-mVenus	2.0E+12
AAV2/1	CAG-OR 59D.1-ChR ET/TC-mVenus	1.8E+12

Proteinase K assay

Coverslips of dissociated hippocampal neuronal cultures were infected with AAVs (see above) seven to ten days after plating. Seven to ten days after AAV infection, coverslips were transferred into a 24 well glass bottom plate (Cat No. P24G-1.0-13-F; Matek Corp) with 80 μL to 100 μL of DPBS with Ca^{2+} and Mg^{2+} (Cat No. 14040117; GIBCO) in each well. Epifluorescence imaging was performed using an Olympus x81 microscope equipped with a 40X objective (Olympus UplanFLN 40x/0.75) and FITC cube (FITC-2024B-000; Semrock) using Slidebook 5.0-Innovatove Application (www.intelligent-imaging.com). Images were acquired at a rate of 1 Hz for 30 s. Following the acquisition of five baseline images, either 40 μL of PBS (vehicle) or 40 μL of 2.3 mg/mL proteinase K (1:10 dilution of 1095 units/mL or 23 mg protein/mL, Sigma Cat No. P4850) was added to the well, and twenty-five additional images were acquired.

Time-lapsed images were analyzed using custom MATLAB and Python scripts. Regions of interest (ROI) and background regions were manually selected using the first image from each experiment, blind to the condition. The difference of the mean fluorescence of each ROI and the mean fluorescence from the background region in the same image was calculated, and the mean of these differences for the five baseline images (F_0) and the five final images (F_{final}) determined. Using these initial and final fluorescences, a

difference in fluorescence was found and normalized to the initial fluorescence to yield the normalized change in fluorescence ($\Delta F/F_0$).

Myc-tag assay

Neurons were infected five days after plating with AAV-CAG-FLInChR-mVenus and AAV-CAG-Myc-GFP. Ten days post-infection three wells in each group were stained with rabbit anti-c-*myc* primary antibody (C3956; Sigma) at 1:1000 dilution for 60 minutes. Wells were washed with PBS three times, and then fixed with 4% paraformaldehyde (PFA) in 0.1M phosphate buffer (PB). All of the wells were labeled with Goat anti-Rabbit IgG secondary antibody Alexa Fluro 594. Ultra Rainbow Fluorescent Particles Beads (Cat No. 610; mean diameter: 3.80 μm; Bangs Laboratories, Inc.) were diluted 1:500 for imaging. Images were acquired for a single time point using microscopy setup described above, with addition of imaging Alex Fluor 594 using a TRITC filter set (TRITC-B-OMF-Samrock).

Each image was analyzed blind to condition, by selecting regions of interest (ROI) for the soma, background and bead regions for each coverslip and the mean fluorescence for each ROI determined. The background ROI mean fluorescence was subtracted from the mean soma ROI fluorescence, and then normalized to the mean bead fluorescence to yield the arbitrary units (a.u.) in Figure 1.

In vitro whole-cell electrophysiology in dissociated neuronal cultures

In vitro electrophysiological characterization of opsins was done in hippocampal neurons cultured prepared as described above and infected with a virus carrying the payload of interest at 7 days *in vitro* (DIV). At 14-21 DIV, whole cell recordings were done using an extracellular solution of artificial cerebrospinal fluid (ACSF) that contained the following: 135 mM NaCl, 15 mM glucose, 3 mM KCl, 1.3 mM CaCl$_2$, 1 mM MgSO$_4$, 10 mM HEPES. For wholesale external ion replacement experiments (Figure 4C) and well as reductions in [Na$^+$] (Figure 5B), ions were replaced with equimolar amounts of sucrose. SR95531 (5 μM) and Kynurenic acid (0.1 mM) were added to all solutions to block ionotropic GABA and glutamate receptors, respectively. All experiments were done at room temperature, which was approximately 25°C. Glass recording pipettes were pulled to a resistance of 1-3 MΩ with a P-97 horizontal puller (Sutter Instruments), and access resistance–as measured by the instantaneous current response to a -5 mV step with pipette capacitance cancelled–was always less than 8 MΩ. Light-evoked currents were induced using 2 ms full field illumination through the microscope objective at 0.2 Hz using a 4-wavelength high power LED light source (Thorlabs LED4D067, with a DC4100 4-channel LED driver; power measured at objective focal plane was $\sim$1 mW), with the exception of the experiments measuring excitation spectra, in which case a Polychrome V monochromator (TILL Photonics) was used as the light source. Responses were measured with a Multiclamp 700B amplifier (Molecular Devices) and AxoGraph X acquisition software.

Internal solutions for whole cell-recordings

To evaluate the ionic basis of the light-evoked currents we used four different internal solutions: Cs-Cl, TEA-Cl, Na-Cl and K-Gluc. The Cs-Cl solution contained 5 mM CsCl, 130 mM CeMeSO$_4$, 10 mM HEPES, 0.5 mM EGTA, 0.4 mM Na-GTP, 4 mM Mg-ATP, 10 mM phosphocreatine, and was adjusted to pH 7.3. To replace cations, we used TEA-Cl containing 140 mM TEA-Cl, 10 mM HEPES, 0.5 mM EGTA, and 10 mM phosphocreatine, adjusted to pH 7.3. K-Gluc solution, in turn, contained 130 mM K-Gluconate, 5 mM KCl, 10 mM HEPES, 0.5 mM EGTA, 0.4 mM Na-GTP, 4 mM Mg-ATP, 10 mM phosphocreatine, adjusted to pH 7.3. Na-Cl based internal solution contained 135 mM NaCl, 3 mM KCl, 1.3 mM CaCl$_2$, 1 mM MgSO$_4$, 10 mM HEPES, 0.4 mM Na-GTP, 4 mM Mg-ATP, 10 mM phosphocreatine.

Ammonium prepulse protocol

To address the role of pH in the light-evoked FLInChR current, an ammonium prepulse protocol was used (Schwiening and Boron, 1994). Briefly, an ammonium challenge was used to shift internal pH basic and then acidic. The normal extracellular solution was first replaced with one in which 20 mM NH$_4$Cl was added and 20 mM NaCl was omitted. Subsequently, a sodium-free (Na-) extracellular solution containing an equimolar substitution of N-methyl-D-glucamine (NMDG) for NaCl was used to replace the ammonium challenge and used for the rest of the recording session. All solutions contained SR95531 (5 μM) and Kynurenic acid (0.1 mM).

In vitro whole-cell slice electrophysiology

Adult (6-8 weeks old) GAD2-IRES-Cre (Jackson Laboratory, Stock #010802) mice were injected with AAV2/1 CAG-FLEX FLInChR-mVenus; sections were taken 3-4 weeks post injection. Mice were deeply anaesthetized under isoflurane, decapitated, and the brains were removed. Coronal midbrain slices (300 μM thick) were sectioned (Leica VT1200S, Germany) in ice-cold modified artificial cerebral spinal fluid (ACSF) (52.5 mM NaCl, 100 mM sucrose, 26 mM NaHCO3, 25 mM glucose, 2.5 mM KCl, 1.25 mM NaH2PO4, 1 mM CaCl2, 5 mM MgCl2, and 100 μM kynurenic acid). Slices were transferred to a holding chamber and incubated at 35°C for 30 min in modified ACSF (119 mM NaCl, 25 mM NaHCO3, 28 mM glucose, 2.5 mM KCl, 1.25 mM NaH2PO4, 1.4 mM CaCl2, 1 mM MgCl2, 3 mM sodium pyruvate, 400 μM ascorbate, and 100 μM kynurenic acid, saturated with 95% O2/5% CO2) and then stored at 21°C.

For recordings, slices were transferred to a recording chamber perfused with modified ACSF (119 mM NaCl, 25 mM NaHCO3, 11 mM glucose, 2.5 mM KCl, 1.25 mM NaH2PO4, 1.4 mM CaCl2, 1 mM MgCl2, 3 mM sodium pyruvate, 400 μM ascorbate, saturated with 95% O2/5% CO2) and maintained at 32–34°C at a flow rate of 2–3 ml/min. Substantia nigra GABAergic neurons expressing the opsin were targeted for recordings. Voltage clamp recordings of evoked photocurrents were made using electrodes (5–8 MΩ)

containing a CeMeSO4-based intracellular solution (in mM) (114 mM CeMeSO4, 4 mM NaCl, 10 mM HEPES, 5 mM QX314.Cl, 0.3 mM GTP, 4 mM ATP, 10 mM phosphocreatine, pH 7.5). Recordings were made using a MultiClamp700B amplifier (Molecular Devices) interfaced to a computer using an analog to digital converter (PCI-6259; National Instruments) controlled by custom written scripts (to be made available at http://dudmanlab.org/) in Igor Pro (Wavemetrics). Photo-activation was carried out using a dual scan head raster scanning confocal microscope and control software developed by Prairie Systems and incorporated into a BX51 upright microscope (Olympus America). Individual neurons were patched under DIC optics with a water-immersion 40X objective. Cells were held at −70mV and evoked current measured following brief 1 ms wide field illumination (470mM or 590mM). To measure spiking activity, current-clamp recordings were made using a potassium gluconate-based intracellular solution (137.5 mM potassium gluconate, 2.5 mM KCl, 10 mM HEPES, 4 mM NaCl, 0.3 mM GTP, 4 mM ATP, 10 mM phosphocreatine, pH 7.5). Depolarizing current steps (200 ms) were used to evoke high frequency spiking of GABAergic neurons, while brief 100ms wide field illumination (470 mM, 1 mW at the focal plane of the objective) during the current step was used to assess the effectiveness of FLInChR to suppress evoked spiking. Progressively longer photostimulation was used to assess effect of duration on spiking suppression. Analysis of postsynaptic evoke currents and spiking was performed using custom written analysis code in Igor Pro (Wavemetrics). Rise time constants of postsynaptic currents were measured by finding the 20%–80% slope of the rising phase of the stimulus-evoked current. Decay time constant of postsynaptic currents were measured by fitting a single exponential to the decay phase of the stimulus-evoked currents. Spikes were detected at the threshold of maximum acceleration.

In vivo perturbation of SNr GABAergic activity during effort-based operant task

Adult GAD-IRES-Cre mice were individually housed in a temperature and humidity-controlled room maintained on a reversed 12 hr light/dark cycle. Following 1 week of recovery from surgery for targeted injection of AAV2/1-CAG-FLEX-FLInChR-mVenus into SNr and placement of the head fixation chamber (Osborne and Dudman, 2014), mice were put onto water restriction with water consumption limited to at least 1 ml per day. Mice underwent daily health checks and water restriction was eased if mice fell below 70% of their body weight at the beginning of deprivation.

Water deprived mice were trained on a head-fixed variable amplitude operant task as previously described (Osborne and Dudman, 2014; Panigrahi et al., 2015), undergoing at least 2 weeks of daily sessions of initial training prior to perturbation experiments. For training, mice were placed in a darkened chamber with both paws positioned on a small metal handle attached to a joystick with two degrees of freedom (as seen in Figure 5A). Movement of the joystick was detected by a Hall effect sensor with a linear voltage/displacement relationship. Voltage traces for each axis were recorded at 10 kHz and analysis of movements conducted offline. Movement threshold detection and triggering of water delivery were accomplished with a custom micro controller device. A session typically consisted of 120 trials within 7 blocks at different threshold amplitude requirements.

Individual forelimb movements, 'reaches', were extracted from voltage traces by thresholding the change in position and ensuring that movements were separated by at least 200 ms. To extract parameters of the outward component of the reach, we followed a technique described in detail previously (Gallivan and Chapman, 2014). Briefly, the outward component of the reach was determined by finding the end point of maximum displacement. A reach was defined as the trajectory from earliest detectable movement to reaching the maximum displacement (the most eccentric point on the convex hull that captured the trajectory). Movement velocity was computed with summary statistics of the trajectory (max, average).

Photostimulation was delivered via a fiber coupled solid state laser (488 nm; LaserGlow) coupled via a ferrule sleeve to an optical fiber (200 μm diameter) positioned just above the SNr. Laser pulses were gated through the analog modulation circuitry of the laser by modulating the pulse width (1-10ms). Pulse trains (16.7 Hz; 450 ms duration) were triggered by displacement of the joystick past a threshold lower in magnitude than the threshold required to elicit reward delivery. A randomly chosen 25% of all trial-initiating movements (as detected online) were allowed to trigger photo stimulation.

Behavioral experiments in C. elegans

For body-wall muscle expression in C. elegans, pmyo-3::FLInChR::mVenus was synthesized in a codon optimized manner, resulting in the plasmid pAB15. The respective transgenic strain ZX2282 (zxEx1105[pmyo-3::FLInChR::mVenus; pmyo-2::CFP] in N2), was generated via microinjection of 50 ng/μL plasmid DNA with 2 ng/μL of the co-injection marker pmyo-2::CFP. Animals were cultured on NGM plates, seeded with E. coli OP-50 strain, in 6 cm Petri dishes. For optogenetic experiments, OP-50 was supplemented with ATR (0.15 μL of stock (100 mM in ethanol) mixed with 300 μL OP-50 bacterial solution).

Video analysis of changes in body length upon light stimulation monitored the evoked effect and provided qualitative information, whether the expressed protein worked as a depolarizer (body contraction) or hyperpolarizer (body relaxation). For behavioral experiments, young adult transgenic animals were cultivated overnight on ATR supplemented plates. To guarantee for an artifact free video analysis, the worms were singled on plain NGM plates prior to the experiments. An Axiovert 40 CFL microscope (Zeiss, Germany) with 10x magnification and a Powershot G9 digital camera (Canon, USA) were used to record the animals' behavior. For photo-stimulation of FLInChR, transgenic animals were challenged by 5 s light pulses (HBO light source, 580 nm, 22 mW/mm), controlled via an Arduino-driven shutter (Sutter Instruments, USA). The body length analysis was performed based on a custom written script for MATLAB (Mathworks, USA). For the analysis of data, the animals' body length was normalized to the recording period prior to illumination.

217

Extracellular electrophysiological identification of FLInChR-expressing neurons in awake rats

Extracellular electrophysiology was performed using tetrode microdrives as previous described (Karlsson et al., 2012) in combination with viral delivery of FLInChR and fiber optic delivery of light. Corticostriatal neurons in the Anterior Congulate Cortex (Cg1) of adult Long Evans rats were labeled by combining injections of two viruses. rAAV2-retro-Cre (titer: 7.1E+12 GC/ml) was injected bilaterally into the striatal axonal field (ML: 1.94 mm, AP: 2.29 mm, DV: −4.57 mm; 600 nL per site) with the aim of achieving retrograde access to cortico-striatal neurons. A Cre-dependent FLInChR construct was delivered through localized viral injection in the cortex approximately 1.5 mm away from the recording site to minimize damage. To ensure sufficient spread of the virus, rAAV2-retro was chosen as the serotype for delivery, but with the aim of utilizing its enhanced local spread rather than retrograde functionality. rAAV2-retro-CAG-FLEX-FLInChR (titer: 9.2E+12 GC/ml) was thus injected into the dorsal medial prefrontal cortex (ML: −0.6 mm, 0.6 mm; AP: 1.2 mm, 1.2 mm; DV: −3.0/2.5 mm, −3.0/2.5 mm; 300 nL per site). Several week after virus injection, optical-fiber-containing microdrive was implanted over rostral ACC (ML: −0.6 mm; AP: 2-3 mm)

Light delivery was accomplished using a fiber optic lowered from one of the shuttles of the microdrive, where the fiber optic transmitted light from a laser diode, which was controlled using custom hardware triggered remotely by infrared light and custom software. The fiber optic (200 μm core, 0.5 NA hard polymer fiber optics, FP200URT; ThorLabs), was butt-coupled to a laser diode (520 nm; Cat No. PL520_B1; World Star Tech) bonded (Norlands 68).

Fibers were sharpened using chemical etching approach (Hanks et al., 2015). Specifically, the cable jacket, strengthening fibers, and outer plastic coating (typically white or orange) were fully removed, leaving 1 cm of fiber optic cable and inner plastic coating intact. Then 2 mm of the fiber tip (with final layer of plastic coating still attached) was submerged in 48% hydrofluoric acid topped with mineral oil for 85 min, followed by water for 5 min (submerging 5 mm), and acetone for 2 min (to soften the plastic). The plastic coating was then gently cut with a razor and pulled off with tweezers to reveal a 1 mm sharp-etched fiber tip. Light emitted from the fiber optic tip was ∼2 mW, leading to an estimated power density of ∼60 mW/mm^2. Manufacturing, parts information and detailed documentation are provided online at https://karpova-lab.github.io/cerebro/ (https://github.com/Karpova-Lab/cerebro; http://cerebro.readthedocs.io/en/1.0/). Light pulses of 20 ms duration were delivered at 0.5 Hz throughout the recording session, in order to inactivate spontaneous and behaviorally evoked activity.

After the electrophysiology experiments, single units were isolated and clustered as previously described (Karlsson et al., 2012). Peri-event histograms were used to examine the light-dependent inactivation of neuronal activity (Figure 5I). To discover single units that had light-dependent inactivation, we z-scored the neuronal activity and selected units that had a decrease of at least two standard deviations for at least 20% of 1 ms time bins during the 20 ms light pulse period. We constructed a histogram of the latency to inactivation of these selected units, where the latency was the time after light onset to the first bin that had an activity decrease of at least two standard deviations (Figure 5I).

Extracellular electrophysiological identification of FLInChR-expressing neurons in awake rat

For cell-type specific *in vivo* recordings from motor cortex, rAAV2-CAG-Flex-FLInChR-mVenus was injected to the pons bilaterally (relative to lambda: 0.4 mm anterior, 0.4 mm lateral, 5.5, 5.75, 6 mm deep, 70 nL/depth) in Sim1-KJ18 mice, selectively labeling a pyramidal type (PT) layer 5 population (Gerfen et al., 2013; Tervo et al., 2016). Mice were awake during recordings and were generally immobile, having been previously head restrained for behavioral training. Prior to recordings, a craniotomy was made over the recording site (from bregma: 0.5 mm anterior, 1.7 mm lateral) at least 4 hours prior to recording. Exposed brain tissue was kept moist with phosphate-buffered saline at all times, and craniotomy sites were covered with Kwik-Sil elastomer (WPI) outside of the recording session.

Juxta-cellular recordings were performed as described previously (Coddington and Dudman, 2017). Briefly, a small craniotomy (< 200 μm diameter) was made over the recording site (at least 4 hours prior to recording. Exposed brain tissue was kept moist with phosphate-buffered saline at all times, and craniotomy sites were covered with Kwik-Sil elastomer (WPI) outside of the recording session. Borosilicate glass pipettes (Sutter, BF165-120-10) were pulled to a long taper (resistance 5-8 mOhm) with a P-97 micropipette puller (Sutter). Pipettes were filled with 0.5 M NaCl solution and mounted in a holder with a side port (Warner, PE30W-T17P) to allow insertion of a fiber (105 μm core, 0.22 NA, Thorlabs) that was coupled to a 473 nm laser (OEM Laser Systems) to carry light to the pipette tip. Pipettes were lowered through the brain with a micromanipulator (Luigs and Neumann) while a small cycling current injection allowed monitoring of resistance changes across the pipette tip. Within the target region (700-1100 μm from pial surface), the pipette tip was advanced by 1-2 μm steps until a steep increase in resistance was detected. The pipette was then advanced 5-10 μm until positive-going spikes were resolved well above noise (> ∼0.5 mV). FLInChR expression and responses were assayed with single laser pulses of varying durations (0.5-5.0 s), with power measured out of the tip of an exposed pipette of 5 mW. Responses were amplified (Multiclamp 700B, Axon Instruments), then digitally recorded at a 30 kHz sample rate with a Cerebus Signal Processor (Blackrock Microsystems).

For neural population recording using the neuropixel probe, awake mice fully recovered from craniotomy were head-fixed in a RIVETS chamber (Osborne and Dudman, 2014, Plos One). A neuropixel probe (option 3 phase A) with 374 recording sites (Jun et al., 2017, Nature) was lowered through the craniotomy manually. After a smooth descent (200 μm/min), the probe sat still at the target depth for at least 5 min before initiation of recording to allow the electrodes to settle. An Ag wire was soldered onto the reference pad of the probe and shorted to ground. This reference wire was connected to an Ag/AgCl wire was positioned on the skull. The craniotomy and the Ag/AgCl wire were covered with a saline bath. Voltage signals are filtered (high-pass above 300 Hz), amplified

(200x gain), multiplexed and digitized (25 kHz) on the base, allowing the direct transmission of noise-free digital data from the probe, and were recorded using an open-source software SpikeGLX (https://github.com/billkarsh/SpikeGLX). Recorded data were pre-processed using an open-source software JRCLUST (https://github.com/JaneliaSciComp/JRCLUST) to identify single- or multi units in the primary motor cortex (M1). To assay FLInChR expression and responses, a fiber (200 μm core, 0.39 NA, Thorlabs) coupled to a 574 nm laser source (Omicron) was placed to deliver light onto the craniotomy. Single laser pulses of 1 s duration with power measured at the tip of the fiber of 8 mW were delivered 60 times with 8 s intervals.

QUANTIFICATION AND STATISTICAL ANALYSIS

All imaging, elecrophysiological and behavioral data were processed and analyzed using analysis routines custom-written in MATLAB. Statistical analyses were conducted using Wilcoxon signed ranksum tests followed by Bonferroni correction, Mann-Whitney U, 1-way paired ANOVA, 2-sampled t test or paired t test when appropriate. The n value, the mean values $\pm$ SEM for each dataset, and statistically significant effects are reported in figure legends and are summarized in the table below. The significance threshold was held at $\alpha = 0.05$.

FIGURE/ASSAY	TEST		F, t, U, W VALUE	p value	n
Figure 1B	Wilcoxon signed rank test	uninfected; 1° myc antibody	11	0.6120898801	7
Figure 1B	Wilcoxon signed rank test	AAV-CAG -Myc-GFP; no 1° myc antibody	17	0.8886378609	8
Figure 1B	Wilcoxon signed rank test	AAV-CAG -Myc-GFP; 1° myc antibody	6	0.1762963744	7
Figure 1B	Wilcoxon signed rank test	Nx1BTM-ChR2; no 1° myc antibody	3	0.1158514975	6
Figure 1B	Wilcoxon signed rank test	Nx1BTM-ChR2; 1° myc antibody	0	0.01796047753	7
Figure 1C	Wilcoxon signed rank test	ChR2		0.0042	47
Figure 1C	Wilcoxon signed rank test	Nx1BTM-ChR2		2.21E-15	59
Figure 1C	Wilcoxon signed rank test	Nx1BTM-CsChrimson		0.0035	7
Figure 1C	Wilcoxon signed rank test	Nx1BTM-ArchT		0.0022	6
Figure 1D	Wilcoxon signed rank test	fusion of OR 59D.1 N-terminal leader sequence and ChR ET/TC		5.15E-14	45
Figure 2B	1-way unpaired ANOVA		74.5	<0.0001	5 versus 5 versus 5
Figure 2C	Mann-Whitney U		130	0.0002	16.00
Figure 2E	Mann-Whitney U		4	0.5	4.00
Figure 2F	1-way paired ANOVA		0.006	0.97	5.00
Figure 2G	1-way unpaired ANOVA		3.4	0.04	9 versus 22 versus 20
Figure 3B					4 (2 mice)
Figure 3C					5 (2 mice)
Figure 3D					4 (2 mice)
Figure 3E.1(onset)	2-sampled t test			0.99	4 (2 mice)
Figure 3F.1	2-sampled t test			0.1	5 (2 mice)
Figure 3G.1	2-sampled t test			0.98	4 (2 mice)
Figure 3E.2 (decay)	2-sampled t test			0.37	4 (2 mice)
Figure 3F.2	2-sampled t test			0.76	5 (2 mice)
Figure 3G.2	2-sampled t test			0.00078	4 (2 mice)
Figure 4B	paired t test			2.33E-09	4 (2 mice)
Figure 5I	paired t test				

DATA AND SOFTWARE AVAILABILITY

The accession number for the FLINChR sequence reported in this paper is [GenBank]: BankIt2158148 BSeq#1 MK046864.
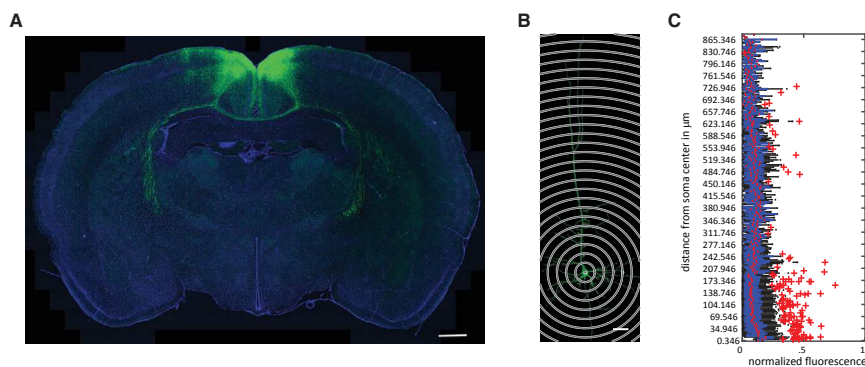
Figure S1. Inverted ChR ET/TC Displays Robust Intracellular Trafficking, Related to Figure 1

(A) Image of a coronal rat brain slice with neurons in the anterior cingulate cortex that project to supplementary motor cortex expressing FLInChR(Nx). Note the evident fiber tracts suggestive of robust axonal trafficking. (B) A maximum projection for a confocal image of rat laver 5 neuron expressing FLInChR with concentric circles at increasing radii describing the analysis of FLInChR expression as a function of distance from the soma center. (C) Fluorescence intensity normalized to peak intensity along the circumference of concentric circles relative to the center of the soma. Only pixels from intersections of these circum-ferences and the segmented neuron are used. The red line represents the median fluorescence, blue boxes mark the 25th and 75th percentiles, whiskers represent the extreme data points and, + represent outliers. Note that despite a modest increase in the median fluorescence at the soma, the dendritic expression remains consistent throughout the neuron.
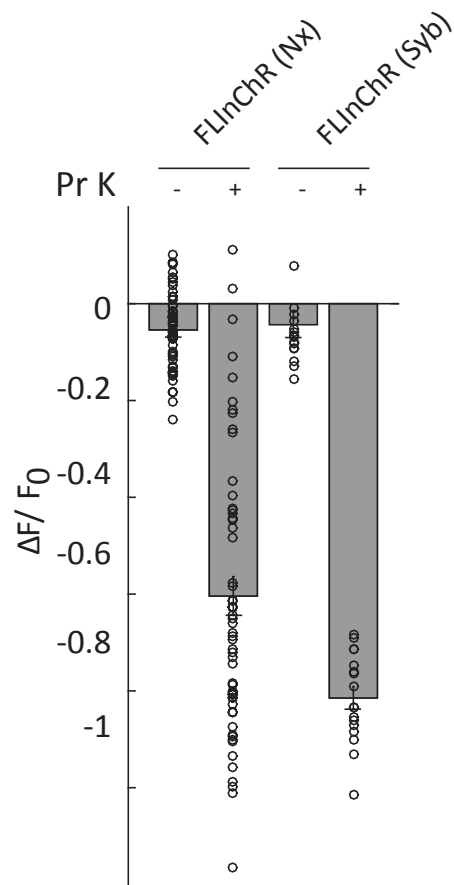
Figure S2. Inversion Is Robust to the Choice of N-Terminal Linker Domain, Related to Figure 1

Proteinase K-based evaluation of the location of the C-terminal-mVenus domain in primary neuronal cultures for FLInChR(Nx) (as in Figure 1) and FLInChR(Syb) (n = 16).
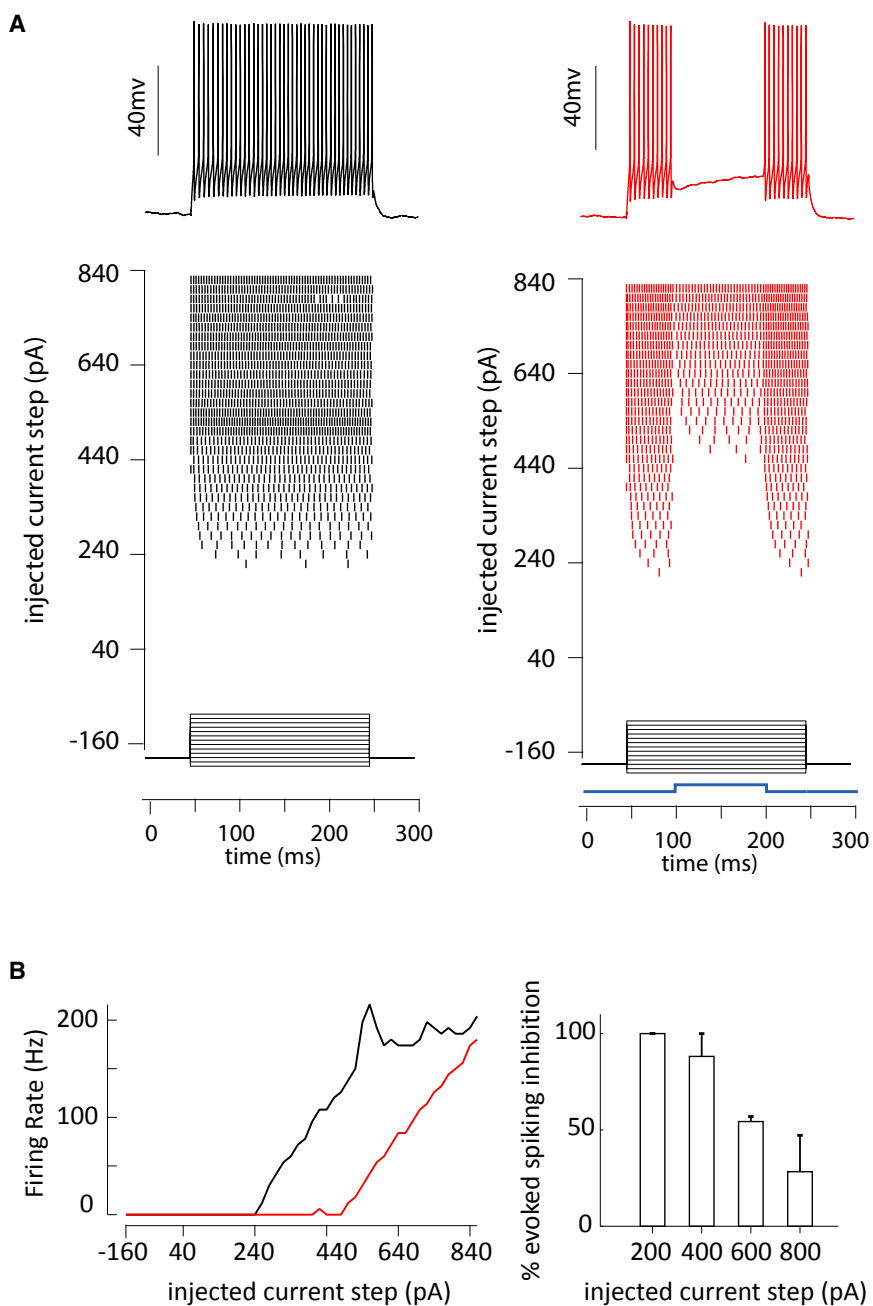
Figure S3. FLInChR Mediates Efficient Suppression of Spiking in Cortical Neurons, Related to Figure 4

(A) Responses of a FLInChR-expressing layer 4 stellate cell to step current injections with and without 470nm light. Top: overlaid voltage traces. Bottom: raster plots of spiking activity. (B) Left panel: Firing rate in response to injected current of different amplitude with (black) and without (blue) light exposure. Right panel: Percent inhibition for different levels of injected current.
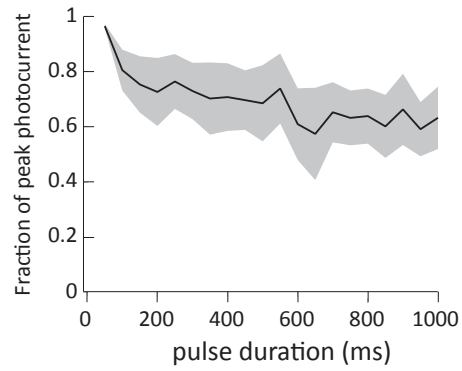
Figure S4. FLInChR-Mediated Photocurrent Shows Moderate Desensitization, Related to Figure 4

Voltage clamp recordings from FLInChR-expressing SNr neurons (n = 4) with long light pulses. Note only moderate decay of photocurrent after the initial 100 ms. Light shading represents standard error of the mean.

A

B
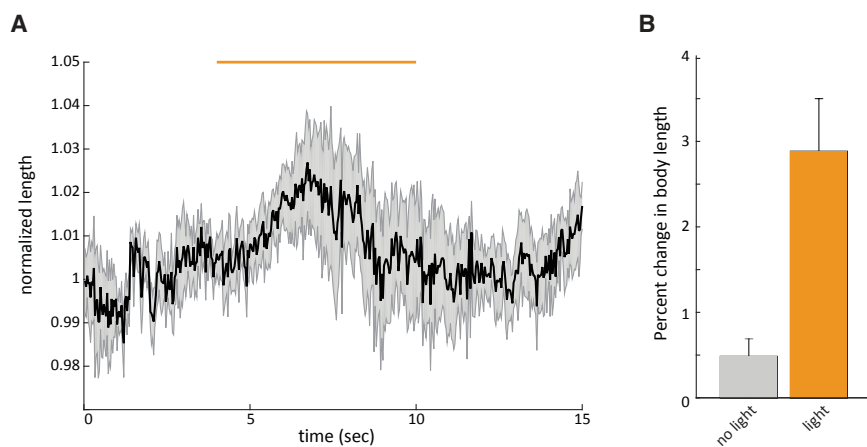
Figure S5. FLInChR-Mediated Hyperpolarization of Body Wall Muscles Induces Body Elongations in *C. Elegans*, Related to Figure 5

Mean normalized body length (±SEM) relative to the initial length in animals expressing FLInChR in body-wall muscles. Left panel: time course of muscle elongation. Right panel: average percent change in body length over a 5 s window before and after onset of illumination.

2.9 Functionally asymmetric motor neurons contribute to coordinating locomotion of *Caenorhabditis elegans*

The following pages contain the published version of the research article "Functionally asymmetric motor neurons contribute to coordinating locomotion of *Caenorhabditis elegans*"[14]. Material from: Tolstenkov, O. *et al*. Functionally asymmetric motor neurons contribute to coordinating locomotion of *Caenorhabditis elegans*. *eLife* **7**; 10.7554/eLife.34997 (2018).

Functionally asymmetric motor neurons contribute to coordinating locomotion of *Caenorhabditis elegans*

Oleg Tolstenkov[1,2,3], Petrus Van der Auwera[1,2,4], Wagner Steuer Costa[1,2], Olga Bazhanova[1], Tim M Gemeinhardt[1,2], Amelie CF Bergs[1,2,5], Alexander Gottschalk[1,2,3]*

[1]Buchmann Institute for Molecular Life Sciences, Goethe University, Frankfurt, Germany; [2]Institute for Biophysical Chemistry, Goethe University, Frankfurt, Germany; [3]Cluster of Excellence Frankfurt Macromolecular Complexes, Goethe University, Frankfurt, Germany; [4]Department of Biology, Functional Genomics and Proteomics Unit, Katholieke Universiteit Leuven, Leuven, Belgium; [5]International Max Planck Research School in Structure and Function of Biological Membranes, Frankfurt, Germany

Abstract Locomotion circuits developed in simple animals, and circuit motifs further evolved in higher animals. To understand locomotion circuit motifs, they must be characterized in many models. The nematode *Caenorhabditis elegans* possesses one of the best-studied circuits for undulatory movement. Yet, for 1/6th of the cholinergic motor neurons (MNs), the AS MNs, functional information is unavailable. Ventral nerve cord (VNC) MNs coordinate undulations, in small circuits of complementary neurons innervating opposing muscles. AS MNs differ, as they innervate muscles and other MNs asymmetrically, without complementary partners. We characterized AS MNs by optogenetic, behavioral and imaging analyses. They generate asymmetric muscle activation, enabling navigation, and contribute to coordination of dorso-ventral undulation as well as anterio-posterior bending wave propagation. AS MN activity correlated with forward and backward locomotion, and they functionally connect to premotor interneurons (PINs) for both locomotion regimes. Electrical feedback from AS MNs via gap junctions may affect only backward PINs.

DOI: https://doi.org/10.7554/eLife.34997.001

*For correspondence:
a.gottschalk@em.uni-frankfurt.de

Competing interests: The authors declare that no competing interests exist.

Introduction

Locomotion represents a basic component of many complex behaviors and is regulated by neuronal circuits that share similar properties in a wide variety of species, including humans (*Guertin, 2012*; *Kiehn, 2011*; *Mullins et al., 2011*). These circuits, as shown in virtually all model systems studied, can generate rhythmic motor patterns without sensory inputs, and therefore act as central pattern generators (CPGs; *Pearson, 1993*). In higher vertebrates CPGs are very complex systems and represent distributed networks made of multiple coupled oscillatory centers, grouping in pools as discrete operational units (*Fidelin et al., 2015*; *Kiehn et al., 2010*; *Rybak et al., 2015*). Motor neurons (MNs) within the pool are able to integrate convergent inputs; they are recruited and activated gradually, which underlies the variable changes in muscle tension that are necessary for movement. Overlaid on these circuits are interactions with (and among) premotor interneurons (PINs), which modulate the patterns of MN activity and coordinate the CPGs (*Goulding, 2009*). In mammals, it is particularly the commissural interneurons (CIN) which regulate activity of left and right CPGs, and which may therefore themselves act as rhythm generators. Such neurons are often excitatory (e.g.

CINei of the mouse; *Kiehn, 2016*), but can also be inhibitory (e.g. CINi), while others act as electrical connectors or activity 'sinks' for CPGs and motor neuron pools. Examples are ipsilateral V2a interneurons in zebrafish, which are retrogradely recruited by motor neurons (*Song et al., 2016*) to modulate their activity. A similar effect of motor neurons providing feedback to the CPG was recently shown for drug-induced locomotor-like activity in the neonatal mouse (*Falgairolle et al., 2017*).

Despite the difference in the forms of locomotion and anatomy of neural circuits between vertebrates and invertebrates, they share similar principles. Yet, how complex vertebrate locomotion circuits operate and how they developed from more simple ones is not understood, thus a comprehensive analysis of invertebrate circuits is a prerequisite to this goal. The relative simplicity of invertebrate nervous systems has helped to develop concepts that guide our understanding of how complex neuronal networks operate (*Marder et al., 2005*; *Selverston, 2010*). *C. elegans* is a nematode with only 302 neurons in the hermaphrodite. A largely reconstructed wiring diagram of its neural circuits (*Varshney et al., 2011*; *White et al., 1986*) and various tools for imaging and (opto) genetic interrogation of circuit activity (*Fang-Yen et al., 2015*; *Leifer et al., 2011*; *Nagel et al., 2005*; *Stirman et al., 2011*) render *C. elegans* a useful model to study fundamental principles of the neuronal control of behavior.

C. elegans moves by generating waves of dorso-ventral bends along its body. These predominantly lead to forward movement, which is occasionally interrupted by brief backing episodes, the frequency of which is modulated by sensory responses (*Cohen and Sanders, 2014*; *Gjorgjieva et al., 2014*; *Pierce-Shimomura et al., 2008*; *Zhen and Samuel, 2015*). The animal's undulations are controlled by neural circuits in the head and VNC. The core components of the motor circuits in *C. elegans* include head motor/interneurons that exhibit Ca^{2+} oscillations during alternating head bending (*Hendricks et al., 2012*; *Shen et al., 2016*). The bending motions may be transmitted to the remainder of the body in part by proprioceptive feedback (*Wen et al., 2012*), with contribution also by gap junctions (*Xu et al., 2018*). Furthermore, rhythm generators in the VNC were shown to play a role in oscillatory activity during locomotion of *C. elegans* (*Fouad et al., 2018*). In the body, motor neurons are found in ensembles or subcircuits, repeating 6 times from the 'neck' to the tail of the animal, containing one or two neurons of each class (6 – 13 neurons found in the individual classes, with 11 AS MNs; *Haspel and O'Donovan, 2011*; *White et al., 1986*). Upstream of the motor neurons are PINs which integrate inputs from sensory and other interneurons, and that relay their activity in a gating fashion: They are themselves not oscillatory, but set up- or down-states of the motor neurons, using gap junction and synaptic networks (*Kawano et al., 2011*), in a manner similar to the V2a interneurons of the fish (*Song et al., 2016*). The classes of MNs are distinguished by transmitter used (acetylcholine or GABA), ventral or dorsal innervation, and roles in forward or backward locomotion (*Von Stetina et al., 2005*; *Zhen and Samuel, 2015*). Functions of the different types of MNs are understood to various degrees. For example, the DA9 A-type MN was recently demonstrated to generate intrinsic rhythmic activity by P/Q/N-type Ca^{2+} channels, which is both attenuated and potentiated by activity of the reversal PIN AVA (*Kawano et al., 2011*; *Gao et al., 2018*). Thus, motor neurons, rather than interneurons, can be oscillators, demonstrating that different activities are compressed in the *C. elegans* motor circuit with its limited number of cells. To fully understand these circuits, all of the motor neurons need to be characterized. However, for the cholinergic AS MN class, representing one fifth of VNC cholinergic neurons, surprisingly no physiological data is available. Yet, these neurons are interesting in that they asymmetrically innervate only dorsal muscle and ventral inhibitory VD neurons. Further, in contrast to other MN types, the AS MNs are innervated extensively by chemical synapses from both forward and reverse PINs, and they also form gap junctions with these cells (*White et al., 1986*).

In this study, we investigated the role of AS MNs in the VNC locomotor circuit based on predictions made from the wiring diagram, using optogenetic tools, behavioral analysis, and Ca^{2+} imaging in immobilized and moving animals. We reveal important roles of AS MNs in dorso-ventral and antero-posterior coordination of undulations during locomotion, as stimulation of AS MNs distorts, and inhibition blocks, propagation of the body wave. We show that AS MNs act through excitation of dorsal muscles and inhibitory ventral VD motor neurons. The intrinsically evoked activity of AS MNs during crawling correlates with both forward and reverse locomotion. Functionally asymmetric electrical connections suggest AS MN feedback to the backward PIN AVA, a feature recently observed for locomotor circuits also in other animals (*Matsunaga et al., 2017*; *Song et al., 2016*).

227

Results

Selective expression and activation of optogenetic tools in AS MNs

Six classes of cholinergic MNs are involved in mediating the dorso-ventral sinusoidal wave observed during locomotion of *C. elegans*: DA, VA, DB, VB, VC and AS. Up to date, no promotor exclusively triggering expression in AS MNs is known. To achieve specific activation of AS MNs, we used a subtractive approach for expression combined with selective illumination. The p*unc-17* promoter (*unc-17* encodes the vesicular acetylcholine transporter) drives expression in all cholinergic neurons including the MNs in the VNC. In combination with p*acr-5* (expression in DB and VB MNs) and p*unc-4* (expression in DA, VA and VC MNs), we could restrict expression of optogenetic tools to the AS MNs (*Figure 1A,B*): Briefly, broad expression from p*unc-17* was suppressed in the DB, VB, DA, VA and VC neurons by expressing dsRNA constructs targeting the optogenetic tool using p*acr-5* and p*unc-4* promoters (*Figure 1AI*). Alternatively, we used the Q system (*Wei et al., 2012*): We placed the QF transcriptional activator under the p*unc-17* promoter, thus driving expression of the optogenetic tool from constructs harboring the QUAS QF binding motif. To restrict expression to AS MNs in the VNC, we additionally used the QS suppressor under the p*acr-5* and p*unc-4* promoters (*Figure 1AII*). We verified that expression along the VNC was restricted to AS MNs, by imaging many animals (*Figure 1B*; *Figure 1—figure supplement 1A*). Last, since these approaches still led to expression in additional cholinergic neurons in head and tail ganglia, we avoided activation of optogenetic tools in those cells by selective illumination of segments of the animals body that correspond to AS MNs (*Stirman et al., 2011*; *Stirman et al., 2012*; *Figure 1AIII*).

Depolarization of AS MNs activates body wall muscles (BWMs) and increases body bending during locomotion

C. elegans moves by propagating undulation waves along the body. Body bends are generated by cholinergic neurons mediating contraction of muscles on one side, and by GABAergic neurons mediating simultaneous relaxation of the contralateral side of the body (*Donnelly et al., 2013*; *McIntire et al., 1993*). According to the wiring diagram (*Chen et al., 2006*; *Varshney et al., 2011*; *White et al., 1986*) AS MNs send 68/144 documented synapses to the dorsal BWM cells (i.e. 47% of all presynaptic contacts made by the AS neurons) and 66/144 synapses to inhibitory ventral (GABAergic) VD MNs (i.e. 46% of all AS neuron synaptic terminals). We measured parameters of crawling in intact worms moving freely on agar substrate. Activation of ChR2 in all cholinergic neurons including VNC MNs leads to strong contraction of the worm body and coiling (*Zhang et al., 2007*; *Liewald et al., 2008*). AS MNs innervate only dorsal muscles, thus we wondered if their simultaneous depolarization would hinder propagation of the body bending wave. Animals in which ChR2 was activated in AS MNs kept the ability to propagate the undulation, yet they displayed a distorted wave, deeper bending (*Figure 1C,DI*), and transiently reduced speed (*Figure 1DII, III*). Furthermore, photo-depolarization of AS MNs evoked body contraction, though contraction was reduced when compared to ChR2 activation of all VNC cholinergic MNs (*Figure 1DIV,V*). These behavioral phenotypes were blue-light dependent, and absent in transgenic animals raised without all-*trans* retinal (ATR), the obligate ChR2 co-factor. As the forward locomotion bending wave propagates from head to tail, we probed how AS MN activity contributes to this propagation. We thus stimulated AS MNs in small segments of the body (anterior, midbody, posterior; *Figure 1EI*). These manipulations neither caused marked disruption of the wave (*Figure 1EII*), nor did they reduce speed. However, they led to a reduction of body length (*Figure 1—figure supplement 2A–C*), most pronounced after stimulation of the anterior segment. As we did not observe strong effects, particularly not on propagation of the undulation wave, we wondered if ChR2-mediated photostimulation may have been too weak to evoke robust AS MN activation. We thus used Chrimson as a more potent optogenetic tool for depolarization (*Klapoetke et al., 2014*; *Figure 1—figure supplement 3*; *Figure 1—video 2*). While effects on body length and bending angles were more pronounced than with ChR2 stimulation, the speed decrease remained transient, and the propagation of the bending wave was still not prominently disrupted or distorted by AS::Chrimson photostimulation. In sum, AS MN depolarization facilitates, but may not play an instructive role in generating the undulatory wave.
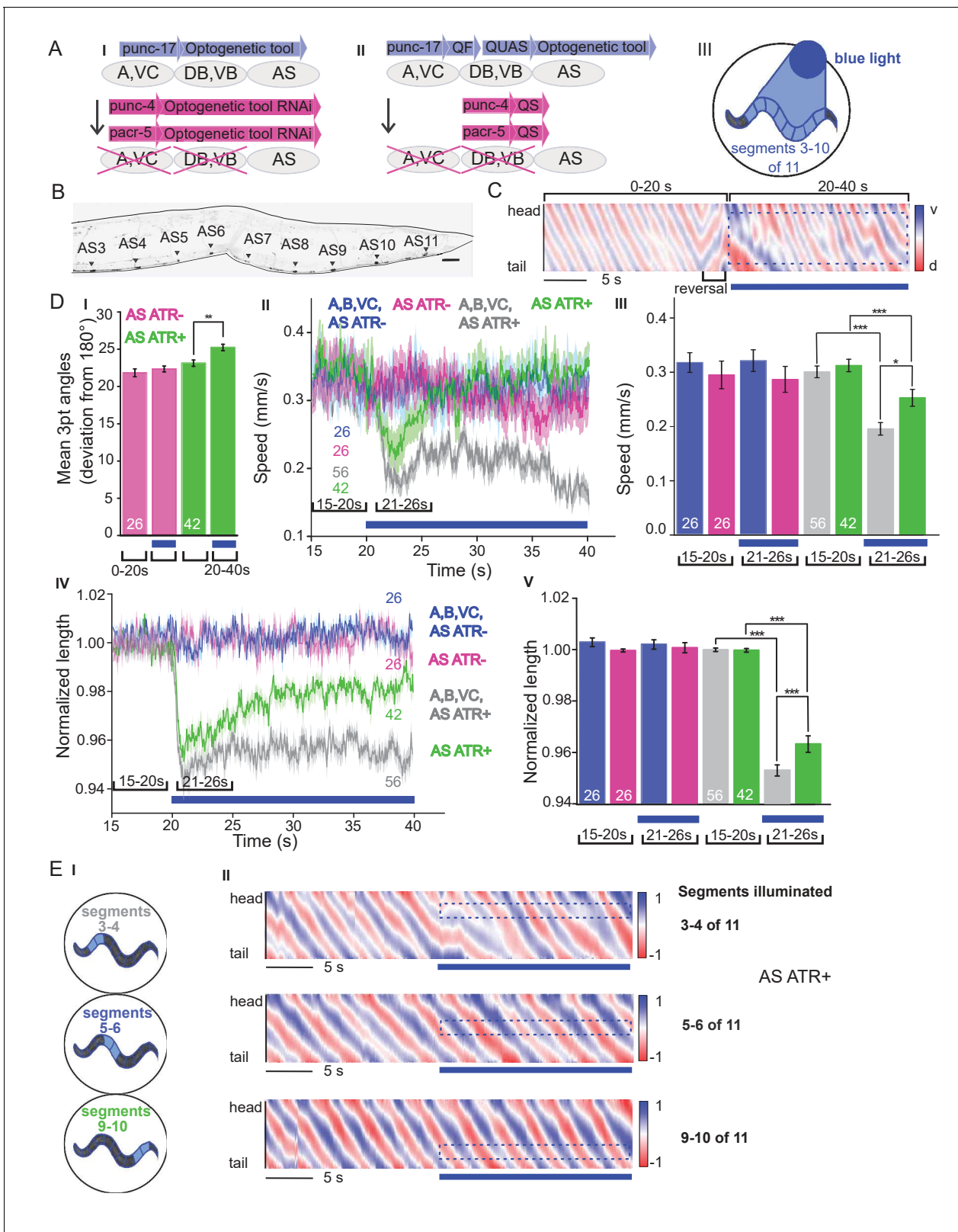
Figure 1. Specific photodepolarization of AS MNs via ChR2 leads to body contraction, increased bending angles and reduced speed in freely moving *C. elegans*. (**A**) 'Subtractive' expression and illumination strategy to achieve specific stimulation of AS MNs by optogenetic tools: (I) Silencing of optogenetic tool protein expression in the non-target subsets of MNs by dsRNA; (II) Using the Q system for conditional expression. The transcriptional activator QF binds to the QUAS sequence to induce optogenetic tool expression. The transcriptional inhibitor QS suppresses expression in unwanted

Figure 1 continued on next page

Figure 1 continued

cells by binding to QF; (III) Selective illumination of the VNC MNs by 470 nm blue light. The body of the worm was divided into 11 segments, of which 3 – 10 were illuminated in animals moving freely on agar plates. (B) Expression pattern of ChR2(H134R)::YFP in AS MNs by the dsRNA subtractive approach; scale bar, 20 μm. See also *Figure 1—figure supplement 1*. (C) Representative body postures kymograph (20 s) of normalized 2-point angles of a 100-point spine, calculated from head to tail of the animal. Positive and negative curvature is represented by blue and red color. Animal expressed ChR2 in AS MNs as in AI and was illuminated after 10 s as in AIII. Blue bar, period of 470 nm illumination. (D) Photodepolarization of AS MNs by ChR2 (in animals raised with ATR): I) Analysis of mean bending angles, before and during the blue light illumination period (as in C). (II, III) Locomotion speed: Mean ±SEM crawling speed of animals before and during blue illumination (blue bar), comparing animals expressing ChR2 in AS MNs or in all types of cholinergic MNs in the VNC, raised in the presence or absence of ATR (III: Group data of mean speed of the animals before (15–20 s) and during (21–26 s) ChR2 photoactivation; IV, (V) Mean ±SEM body length of the animals shown in I, II (V: Group data of the mean length before (15–20 s) and during (21–26 s) photoactivation). (E) Depolarization of subsets of AS MNs in body segments. (I) Scheme of anterior, midbody and posterior segmental illumination; II) Representative body posture kymographs of 2-point angles from head to tail before (20 s) and during ChR2 photoactivation by blue light in the segments of the worm body, corresponding to experiments as in E I). See also *Figure 1—video 1* and *Figure 1—figure supplement 2*. P values *≤0.05; **≤0.01; ***≤0.001. Number of animals is indicated in D. Statistical test in D III and V: ANOVA with Tukey's post hoc test.

The following video and figure supplements are available for figure 1:

Figure supplement 1. Expression of ChR2 can be restricted to AS MNs.
**Figure supplement 2.** Local AS neuron activation affects body length.
Figure supplement 3. Specific photodepolarization of AS MNs via Chrimson leads to body contraction, increased bending angles and reduced speed in freely moving C. elegans.
Figure 1—video 1. Freely moving animal before and during photodepolarization of AS MNs by ChR2 (in animal raised with ATR), blue light = 470 nm, 1.8 mW/mm^2.
Figure 1—video 2. Freely moving animal before and during photodepolarization of AS MNs by Chrimson (in animal raised with ATR), red light = 650 nm, 1.8 mW/mm^2.

AS MN depolarization causes dorsal bias during locomotion by asymmetric BWM activation

We next assessed general effects of AS MN activation on locomotion by analyzing animal tracks. As before, animals expressing ChR2 in all cholinergic neurons slowed (*Figure 1DII, III)* and almost stopped when illuminated (*Figure 2AI*). In contrast, during photostimulation of ChR2 just in AS MNs, animals crawled in circles (*Figure 2AII*; *Figure 1—video 1*), This was due to a bias of head bending towards the dorsal side (*Figure 2AIII–VI*; *Figure 1—figure supplement 3B*), which led to a mild, but significant increase in average bending along the entire body (*Figure 2AV, VI*; this was stronger for AS::Chrimson animals, *Figure 1—figure supplement 3E*), while stimulation of all VNC cholinergic neurons caused deep bending with no dorsal or ventral bias (*Figure 2AIV-VI*). In sum, depolarization of AS MNs contributes to dorso-ventral coordination. Thus, one function of AS MNs may be to facilitate navigation. Unlike the A and B class MNs, the AS MNs have no 'opposing' partner neurons (like VA/DA or VB/DB) and innervate (dorsal) BWMs and inhibitory VD neurons (that innervate ventral muscle). We wondered whether this functional asymmetry affected locomotion during AS MN photostimulation by evoking biased activation of dorsal BWMs. Thus, we used Ca^{2+} imaging (GCaMP3) in BMWs of immobilized animals (*Figure 2BI*). We observed intrinsically evoked activity in muscle cells, that was not synchronized across animals, but which uncovered alternating dorso-ventral activity when the traces of both sides of the animals were aligned to the first dorsal peak (*Figure 2BII, III, IV-VIII*). This activity is likely evoked by the motor nervous system, even in an immobilized animal. When we photostimulated (ChR2) AS MNs (*Figure 2BII, IV-VI,* and *Figure 2—video 1*) in animals raised with ATR, we observed asymmetric responses in the BWM: The Ca^{2+} signal in dorsal muscle cells increased, while it simultaneously decreased in the ventral muscles. Thus, the asymmetry in AS MNs anatomy is reflected also by asymmetry of their functional output.

Figure 2. Photodepolarization of AS MNs causes transient activation of dorsal and simultaneous inhibition of ventral BWMs, and a dorsal bias in freely crawling animals. **A)** (I, II) Representative locomotion tracks of freely moving animals (raised with ATR) with ChR2 expressed in all cholinergic MNs (I) or only in AS MNs (II) before (20 s) and during photostimulation (20 s) by 470 nm blue light (indicated by blue shaded area; tracks are aligned such that they cross the blue area at the time of light onset). (III) Schematic showing the thirteen points defining eleven 3-point angles along the spine of the animal. (IV) Mean (±SEM) ratio of dorsal to ventral bending at the 2nd 3-point bending angle in animals expressing AS::ChR2 or ChR2 in all VNC cholinergic neurons during photostimulation (animals raised with and without ATR). (V) Mean (±SEM) time traces of all 3-point bending angles (absolute values) before and during blue illumination (blue bar; ChR2 in AS MNs or in all cholinergic MNs; raised with and without ATR). (VI) Group data of

Figure 2 continued on next page

Figure 2 continued

experiments in (V), comparing 20 s blue light illumination (blue bar), to the 20 s before illumination. (B) I) AS MNs expressing ChR2 are illuminated by 470 nm blue light, Ca^{2+} signal is recorded in the BWM expressing GCaMP3 (arrows, chemical synapses). (II) Representative snapshots of Ca^{2+} signals in BWM cells during blue light illumination in animals cultivated with and without all-trans-retinal (ATR). Lines indicate regions used to generate kymographs. (III) Representative kymograph of spontaneous Ca^{2+} fluctuations in BWM cells of animal raised without ATR. (IV) Representative kymograph of Ca^{2+} signals in BWM cells in animals cultivated with ATR, in which AS MNs were photostimulated for the entire period. (V, VI) Mean Ca^{2+} signals ($\Delta F/F \pm$ SEM) in dorsal and ventral BWM during the first 10 s of illumination (V) in animals raised with and without ATR and group data (VI), quantified during the first 2 s of illumination. (VII) Transients of spontaneous Ca^{2+} signals in dorsal muscles in animal without ATR. VIII) Mean Ca^{2+} signals ($\Delta F/F \pm$ SEM) in dorsal and ventral BWM in animals raised without ATR, but aligned to the first dorsal Ca^{2+} spike, showing reciprocity of spontaneous dorso-ventral muscle activity. See also *Figure 2—video 1*. P values *$\leq$0.05; **$\leq$0.01; ***$\leq$0.001; number of animals is indicated. Statistical test: ANOVA with Tukey's post-hoc test.

DOI: https://doi.org/10.7554/eLife.34997.008

The following video is available for figure 2:

Figure 2—video 1. Ca^{2+} signal in the BWM expressing GCaMP3 during photodepolarization of AS MNs by ChR2 (in animal raised with ATR), blue light = 470 nm, 1.2 mW/mm^2.

DOI: https://doi.org/10.7554/eLife.34997.009

AS MN ablation disrupts the locomotion pattern

The observed effects indicated an ability of AS MNs to evoke the bending wave during forward locomotion. We can exclude that this was due to ineffective optogenetic stimulation, as even during AS MN stimulation *via* Chrimson, animals performed undulatory forward locomotion (*Figure 1*, *Figure 1—figure supplement 3*; *Figure 1—video 2*). However, given the effects on bending, the AS MNs nonetheless may play an important role in generating locomotion patterns and in navigation. We probed the necessity of AS MNs for locomotion by ablation, as described earlier for other MNs and PINs (*Chalfie et al., 1985*; *Gao et al., 2018*; *McIntire et al., 1993*; *Piggott et al., 2011*). To this end, we used the genetically encoded, membrane targeted (*via* a pleckstrin homology -PH-domain) blue light activated m̲iniature S̲inglet O̲xygen G̲enerator (PH-miniSOG; *Xu and Chisholm, 2016*) and targeted illumination (*Figure 3AI*). Brief illumination of the AS MNs with 470 nm light (2 mW/mm^2, 2.5 min) led to visible and quantifiable locomotion defects: Animals with ablated AS MNs retained the ability to move, but crawled with lower speed, increased bending angles and an overall distorted undulation wave along the body, with a highly irregular pattern (*Figure 3AII-IV, Figure 3—figure supplement 1A; Figure 3—video 1). Thus, ablation of AS MNs disrupted coordination of the bending wave.*

To further explore how AS MN ablation affects bending, we performed Ca^{2+} imaging in muscle cells of immobilized AS::PH-miniSOG expressing animals, using the red fluorescent Ca^{2+} indicator RCaMP (*Akerboom et al., 2013*), analyzing spontaneous Ca^{2+} signals in ventral and dorsal muscles. Ventral muscles showed Ca^{2+} fluctuations that led to intermediate fluorescence when averaged over many animals, both in the presence, or after the ablation of AS MNs. In contrast, the dorsal muscle on average showed higher fluorescence that, upon AS MN ablation, was significantly reduced compared to ventral muscle (*Figure 3AV-VII*). This emphasizes that AS MNs provide biased dorsal muscle drive.

Chronic hyperpolarization of AS MNs eliminates Ca^{2+} activity in dorsal BWMs

Photodepolarization of AS MNs caused reciprocal effects on Ca^{2+} signals in dorsal and ventral muscles (*Figure 2*). We wondered whether hyperpolarization of AS MNs may have opposite effects. AS MNs form excitatory chemical synapses to dorsal muscle and to VD MNs (the latter inhibit ventral muscle), but also gap-junctions (to VA MNs, possibly exciting ventral muscle). Thus, several outcomes are conceivable: (1) Decrease of Ca^{2+} levels in dorsal, and increase in ventral muscles; (2) AS MN hyperpolarization may reduce ventral muscle activity via gap junctions to VA MNs; (3) A mixture of both, possibly even causing oscillations. We thus used the *Drosophila* histamine-gated Cl$^-$-channel HisCl1 (*Pokala et al., 2014*), as a hyperpolarizing tool (*Figure 3BI*). Since *C. elegans* has no endogenous histamine receptors, HisCl1 can be specifically activated using histamine. First, we incubated animals expressing HisCl1 in AS MNs with histamine, and compared them to controls not incubated with histamine (*Figure 3BII*; *Figure 3—figure supplement 1B*; *Figure 3—video 2*). Animals on
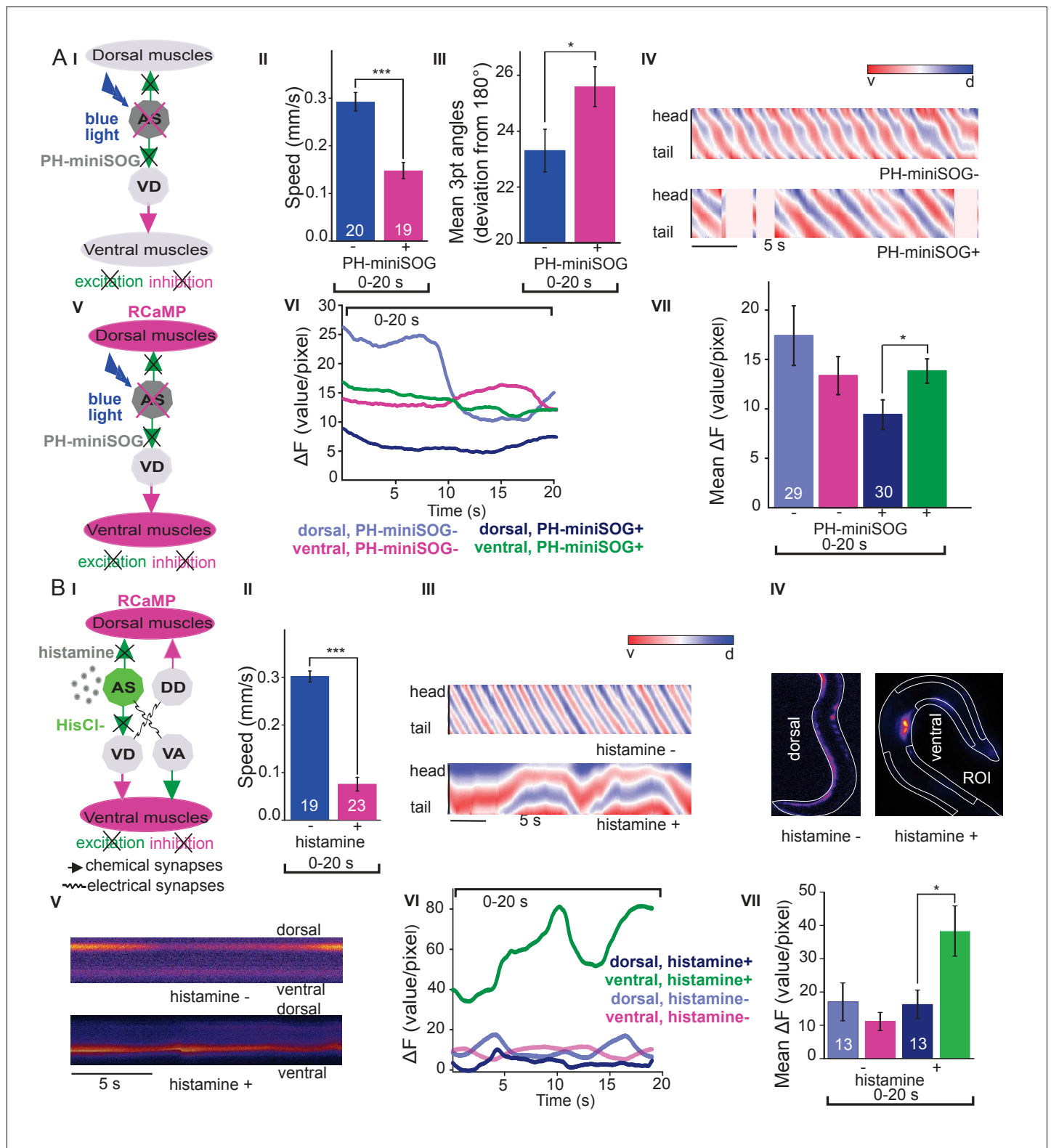
232

Figure 3. Optogenetic ablation and chronic hyperpolarization of AS MNs disrupts the locomotion pattern. (**A**) I) Schematic of optogenetic ablation of AS MNs by PH-miniSOG and connectivity to relevant cell types (arrows, chemical synapses; curved lines, electrical synapses). Quantification of mean ±SEM speed (II) and bending angles (III) of animals without or with expression of PH-miniSOG (*via* the Q system) in AS MNs, following 150 s of blue light exposure and 2 hr resting period. IV) Representative body posture kymographs (as in *Figure 1C*) of wild type animal (upper panel) and animal expressing PH-miniSOG after photoactivation (lower panel). V) Schematic of Ca²⁺ imaging in BWM (RCaMP fluorescence) during PH-miniSOG ablation. *Figure 3 continued on next page*

233

Figure 3 continued

VI) Representative transients of Ca²⁺ signaling in dorsal and ventral muscles after AS MN ablation by PH-miniSOG. VII) Mean Ca²⁺ signals (ΔF/F ± SEM) in dorsal and ventral BWM of animals without or with expression of PH-miniSOG. See also *Figure 3—figure supplement 1A* and *Figure 3—video 1*. (B) I) Schematic of Ca²⁺ imaging in BWM (RCaMP fluorescence) during hyperpolarization of AS MNs by HisCl1 (expressed in AS MNs *via* the Q system), and connectivity to relevant cell types (see also AI; note that this simplified diagram reflects cell type connectivity but does not accurately reflect connections between individual cells). (II) Mean ±SEM speed of freely moving animals on agar dishes without and with 10 mM histamine. (III) Representative body posture kymographs of animals freely moving on agar without (upper) or with 10 mM histamine (after 240 s incubation; lower panel). (IV) Representative fluorescent micrographs of Ca²⁺ activity in the BWM of animals mounted on agar slides without (left) or with 10 mM histamine (after 240 s incubation; right panel). (V) Representative kymographs (20 s) of Ca²⁺ activity in dorsal and ventral BWM of animals as in IV. (VI) Representative Ca²⁺ activity in dorsal and ventral BWM from animals as (shown in IV, V. VII) Mean ±SEM fluorescence of dorsal and ventral BWM as in VI. See also *Figure 3—figure supplement 1B* and *Figure 3—video 2*. P values *$\leq$0.05, ***$\leq$0.001; number of animals indicated in AII, VII; BII, VII. Statistics: T-test for AII, III and B II; ANOVA with Tukey's post-hoc test for A VII and BVII.

DOI: https://doi.org/10.7554/eLife.34997.010

The following video and figure supplement are available for figure 3:

Figure supplement 1. Optogenetic inactivation and HisCl1-induced hyperpolarization of AS MNs affects locomotion speed and bending angles.
DOI: https://doi.org/10.7554/eLife.34997.011

Figure 3—video 1. Freely moving animal, 2 hr after optogenetic ablation (150 s) of AS MNs by PH-miniSOG.
DOI: https://doi.org/10.7554/eLife.34997.012

Figure 3—video 2. Freely moving animal expressing HisCl1 after 4 min exposure on 10 mM histamine.
DOI: https://doi.org/10.7554/eLife.34997.013

histamine plates moved significantly slower (ca. 75% reduction) than animals without histamine, demonstrating that AS MNs are actively involved in promoting locomotion (however, this manipulation also affects other cholinergic neurons outside the VNC; see below). To analyze the possible reason for the reduced speed, we analyzed the crawling body postures (*Figure 3BIII*). Histamine exposure strongly disturbed the propagation of the body wave, leading to very slow and irregular movement and frequent directional changes. We assessed the effects of constant AS MN hyperpolarization on muscle physiology and activity again via RCaMP, in immobilized animals (*Figure 3BIV*), either without or with histamine. Consistent with the dorsal innervation of muscles by AS MNs, intrinsically evoked Ca²⁺ activity in animals with hyperpolarized AS MNs was observed only in ventral BWM, and animals showed ventral bending. Over time, on histamine, ventral Ca²⁺ fluctuations had much higher amplitude than those in dorsal muscle, while animals without histamine showed comparable fluctuations in both dorsal and ventral muscles, which were of the same low amplitude as in dorsal muscle with histamine (*Figure 3BV-VII*). In sum, hyperpolarization of AS MNs inhibits their excitatory signaling to dorsal muscles, and blocks their activation of GABAergic VD motor neurons, which leads to ventral muscle disinhibition. Similar effects are found upon ablation of AS MNs, and both types of manipulation cause a strong bias to uniform ventral muscle activation, which is likely to disrupt propagation of the body wave.

Acute hyperpolarization of AS MNs induces ventral muscle contraction through disinhibition

Chronic hyperpolarization of AS MNs by HisCl1 lacks temporal resolution, and, due to the expression from the *unc-17* promoter, despite our 'subtractive' expression, hyperpolarization of head and tail neurons could affect the outcome of these experiments. To avoid inhibition of these neurons, we looked for a potent hyperpolarizing optogenetic tool, enabling to use selective illumination for specific AS MN inhibition. We thus used the natural Cl⁻-conducting anion channelrhodopsin (ACR1), which causes strong (shunting) inhibition upon illumination (*Sineshchekov et al., 2015*; *Bergs et al., 2018*) *Figure 4A*).

Acute, ACR1-induced photo-hyperpolarization of all cholinergic neurons in freely moving animals strongly reduced crawling speed (to below 20%) and essentially stopped locomotion (*Figure 4B,C*). When we restricted expression of ACR1 and illumination to the AS MNs, we observed a similar reduction of speed, though not as pronounced (to ca. 35% of the initial speed; *Figure 4B*). Controls (animals raised without ATR) showed no change in locomotion speed. These results, together with the HisCl1 experiments may suggest that the speed reduction was caused by a lack of ACh release from AS MNs to dorsal muscles. As this should cause partial relaxation of the body, we analyzed
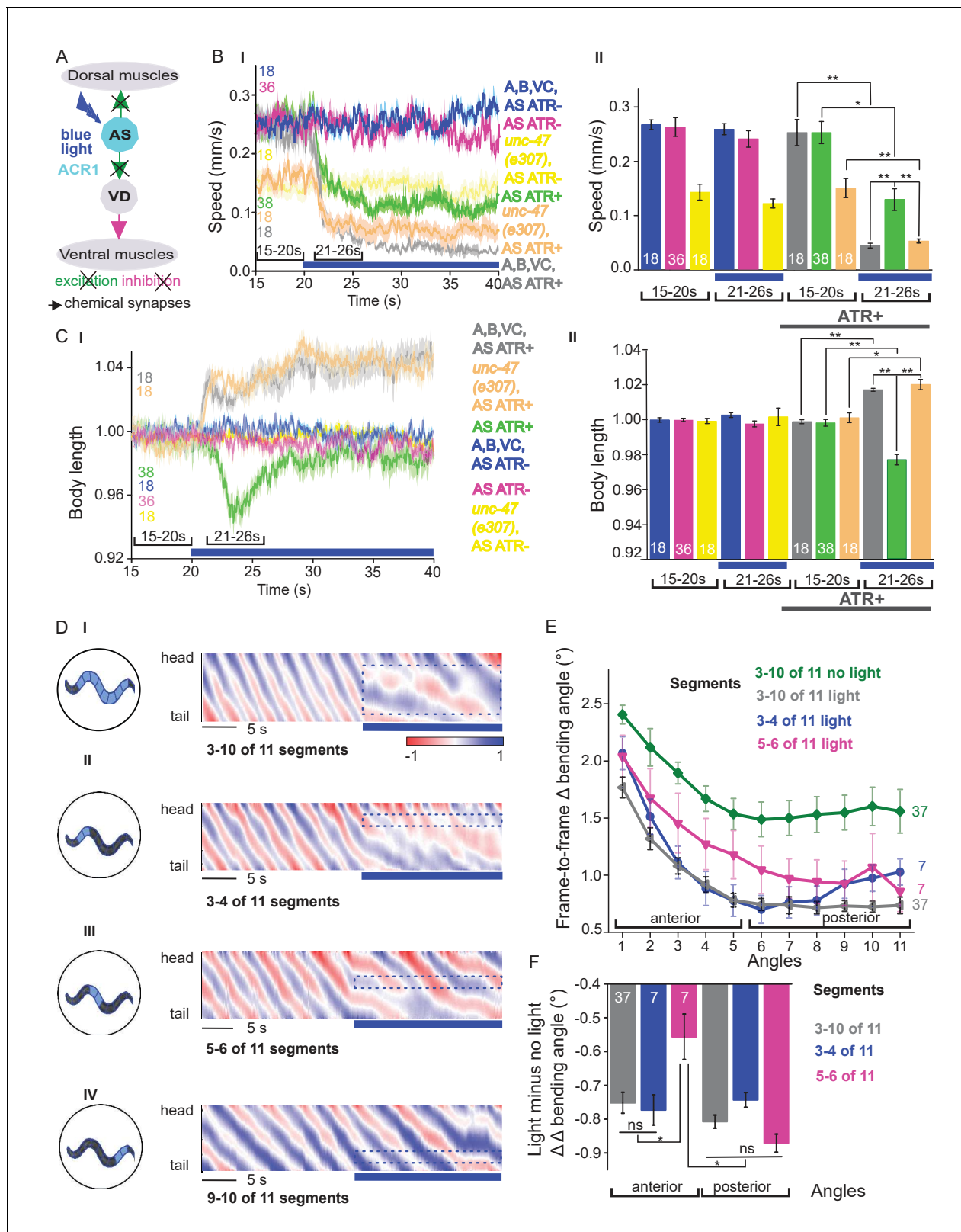
234

Figure 4. Acute optogenetic hyperpolarization of AS MNs ceases locomotion, causes disinhibition of ventral BWM via GABAergic VD MNs, and blocks propagation of the locomotion body wave. (**A**) Schematic of experiment; hyperpolarization of AS MNs by the ACR1 anion channel rhodopsin activated by 470 nm blue light (arrows, chemical synapses). (**B**) Time traces (I) and group data quantification (II) of mean ±SEM speed before (15 – 20 s) and during (21 – 26 s) blue illumination (indicated by blue bar). Compared are strains expressing ACR1 in all VNC cholinergic neurons, or in AS MNs only

Figure 4 continued on next page

Figure 4 continued

(*via* the Q system), in wild type or *unc-47(e307)* mutant background, raised in the presence or absence of ATR, as indicated. (**C**) Time traces (I) and group data quantification (II) of mean ±SEM body length of the animals shown in B. (**D**) Hyperpolarization of AS MNs in all (I), in the anterior (II), middle (III) and posterior (IV) segments of the worm body. Representative body postures kymographs of normalized 2-point angles from head to tail in animal expressing ACR1 in AS MNs before and during illumination by blue light in the indicated body segments. (**E**) Mean, absolute difference of bending angles, from one video frame to the next (25 Hz), at each of eleven 3-point angles, for experiments as in (**D**). (**F**) Mean difference of the differential bending angles between dark and illuminated conditions, for the analyses shown in (**E**). Data were averaged for the anterior five or the posterior 6 3-pt bending angles. See also *Figure 4—figure supplement 1* and *Figure 4—videos 2-4*. P values *≤0.05; **≤0.01; number of animals is indicated. Statistics: ANOVA with Tukey's post hoc test.

The following video and figure supplement are available for figure 4:

Figure supplement 1. Local stimulation of AS MNs in different body segments.

Figure 4—video 1. Freely moving animal expressing ACR1 in AS MNs before (20 s) and during ACR1 photoactivation by 470 nm 1.8 mW/mm^2 blue light.

Figure 4—video 2. Selective illumination of anterior segment.

Figure 4—video 3. Selective illumination of midbody segment.

Figure 4—video 4. Selective illumination of posterior segment.

body length: For animals expressing ACR1 in all cholinergic neurons, we observed a prominent body elongation, in line with the absence of all excitatory (cholinergic) transmission to muscle (*Figure 4C*). However, hyperpolarization of only the AS MNs led to partial and transient body contraction (*Figure 4C*; *Figure 4—video 1*). This might be explained by synaptic connections of AS MNs to the GABAergic VD MNs: Hyperpolarization of AS MNs would reduce excitation of VD MNs, which in turn would cause dis-inhibition of muscle cells, and thus contraction. To test this, we repeated the experiment in *unc-47(e307)* mutants, lacking the vesicular GABA transporter, and thus GABAergic transmission. Consistently, *unc-47* mutants showed relaxation instead of contraction of BWMs (*Figure 4C*). Body wave propagation was strongly attenuated, as for the analogous experiment using HisCl1 in AS MNs; however, using ACR1, this was induced within 2 – 3 s of illumination. Last, we probed if local AS MN inhibition (i.e. in anterior, midbody or posterior neurons) would block the propagation of the wave posterior from this point (*Figure 4D*). This was the case: In about half of the animals tested, inhibition of anterior and midbody AS neurons hindered propagation of the wave to the posterior part of the body, leading to dragging behind of the tail region (*Figure 4D*; *Figure 4—video 2-4*). Analyses of the extent of movement in individual body segments showed that a reduction of movement was also found in the head region, however, this was more pronounced toward the posterior, particularly when the midbody AS neurons were inhibited (*Figure 4E*; *Figure 4—figure supplement 1A* shows how the eleven 3-point angles analyzed correspond to illuminated body segments): The extent of reduction in body movement in the anterior part of the animal was significantly smaller than the change in posterior body movement (*Figure 4F*). Animals also showed a reduction of speed, though not as pronounced as when all AS MNs were hyperpolarized, and length was not affected (*Figure 4—figure supplement 1A*). When the posterior segment was hyperpolarized, no obvious effects were observed. In sum, AS MNs are required for antero-posterior propagation of the body wave.

AS MN activity oscillates during crawling, and correlates with body bends

Measuring Ca^{2+} transients in the ventral cord MNs during locomotion revealed higher activity states for B- and A-type MNs during forward and backward locomotion, respectively (*Haspel et al., 2010*; *Kawano et al., 2011*; *Qi et al., 2013*). Correlation of Ca^{2+} traces in AS MNs with dorsal body bends was previously shown in freely crawling animals (*Faumont et al., 2011*). Considering the unique situation of AS MNs, i.e. coupling with both forward and backward command interneurons, we

wondered if AS MNs would maintain equal activity during both locomotion states. Thus, we measured Ca^{2+} transients in AS6 and AS7 in moving animals.

AS6 and AS7 showed oscillatory activity during locomotion, which was correlated with the change of body bends. During forward crawling, (anterior) AS6 activity preceded (posterior) AS7 activity by about 1–2 s (*Figure 5A,B*; *Figure 5—video 1*). To understand if AS MN Ca^{2+} transients are related to the locomotion body wave, we measured the angle defined by the position of AS6, the vulva, and AS7. We then performed cross-correlation analysis (for individual undulations, i.e. full periods of the bending wave) of the Ca^{2+} signal in AS6 or AS7 and the respective bending angle at the given time (*Figure 5D*; *Figure 5—video 1*). Here, the Ca^{2+} signal in AS6 preceded the maximal bending at the vulva by about 2 s, while the signal in AS7 coincided (correlation coefficients were ~0.30–0.35). Thus, the wave of activity in AS MNs appears to travel antero-posteriorly at the time scale of the undulatory wave. Note the animals crawl under a cover slip, slowing down locomotion; in animals moving freely on agar, the wave oscillates with ca. 0.5 Hz (*Gao et al., 2018*), while here, the delay of two maxima of undulation is ca. 3 – 4 s (*Figure 5B*). We also measured cross-correlation between the Ca^{2+} signals in the AS6 and AS7 neurons (coefficient ~0.28). During reversal periods (we only included reversals of at least 10 s; *Figure 5C*), there was weaker correlation (coefficient ~0.15–0.3) of AS6 and AS7 Ca^{2+} signals with the vulva bending angles, or with each other, and there was a smaller time lag between these signals (~1 s, *Figure 5E*). The cross-correlation of Ca^{2+} signals of the neurons and the bending angle were not different between forward and reversal locomotion (*Figure 5F*). The peaks of AS6 and AS7 Ca^{2+} signals did not reveal any difference between forward and reverse movements (*Figure 5G*). In sum, AS MNs showed oscillatory activity that was correlated with body bends during both forward and backward crawling.

AS MNs integrate signaling from both forward and backward PINs

The PINs AVA, AVD, and AVE connect to the DA and VA MNs, and induce reversals and backward locomotion. Conversely, the PINs AVB and PVC are connected to the DB and VB forward MNs and mediate forward locomotion (*Chalfie et al., 1985*; *Chronis et al., 2007*; *Kawano et al., 2011*; *Piggott et al., 2011*; *Qi et al., 2013*; *Wicks et al., 1996*). Endogenous (*Kawano et al., 2011*) as well as stimulated activity of the PINs modulates activity of A- and B-type MNs (*Gao et al., 2015*; *Gao et al., 2018*; *Liu et al., 2017*).

The AS MNs are postsynaptic to both backward (synapse number: AVA - 63, AVE - 7) and forward PINs (AVB - 13, PVC - 2). This may suggest a bias of AS MNs for backward locomotion; however, synapse number is not the only determinant of synaptic weight. No chemical synapses are known from AS MNs towards the PINs, yet, there are 37 gap junctions reported between AVA and the AS MNs as well as five gap junctions between AVB and the AS MNs. Electrical synapses could mediate anterograde as well as retrograde signaling between AS MNs and PINs (*Chen et al., 2006*; *Varshney et al., 2011*; *White et al., 1986*). To assess whether depolarization of AVA and AVB would lead to observable and/or different Ca^{2+} responses in the AS MNs, we generated strains expressing ChR2 in the PINs and GCaMP6 in AS MNs (*Figure 6AI*): One strain specifically expressed ChR2 in AVA (*Schmitt et al., 2012*) and another strain expressed ChR2 from the *sra-11* promoter in AIA, AIY, and AVB neurons, of which only AVB has direct synaptic connections to AS MNs. The respective animals were photostimulated and Ca^{2+} transients were measured in AS3 (anterior) and AS8 (posterior) MNs of immobilized animals, raised either in absence or presence of ATR (i.e. without and with functional ChR2). Stimulation of AVA or AVB both resulted in a steady, synchronous increase of the Ca^{2+} signal in the AS3 neuron; however, no increase was observed in animals raised without ATR (*Figure 6AII-IV; Figure 6—video 1, 2*). A similar increase was found in the AS8 neuron, and both AS3 and AS8 showed a synchronized increase of activity (*Figure 6—figure supplement 1A,B*). Thus, signaling from both forward and backward PINs is excitatory to the AS MNs. While AVA depolarization evoked a response of comparably low, and AVB depolarization caused a response of significantly higher amplitude (20 vs. 40% ΔF/F after 3 s, respectively; *Figure 6AIV*), this difference is probably not meaningful, as expression levels of ChR2 in AVA vs. in AVB likely differ.

Inequality in regulated behavior based on imbalances in wiring has been observed for the PINs and A- and B-class MNs (*Kawano et al., 2011*; *Roberts et al., 2016*), where AVA coupling to A-type MNs via gap junctions is rectifying towards AVA (*Liu et al., 2017*). We thus assessed the role of the electrical synapses between the PINs and the AS MNs. AS MNs express UNC-7 and INX-3 as the sole innexins. INX-3 is widely expressed in multiple tissues, and AVA and AVB also express UNC-
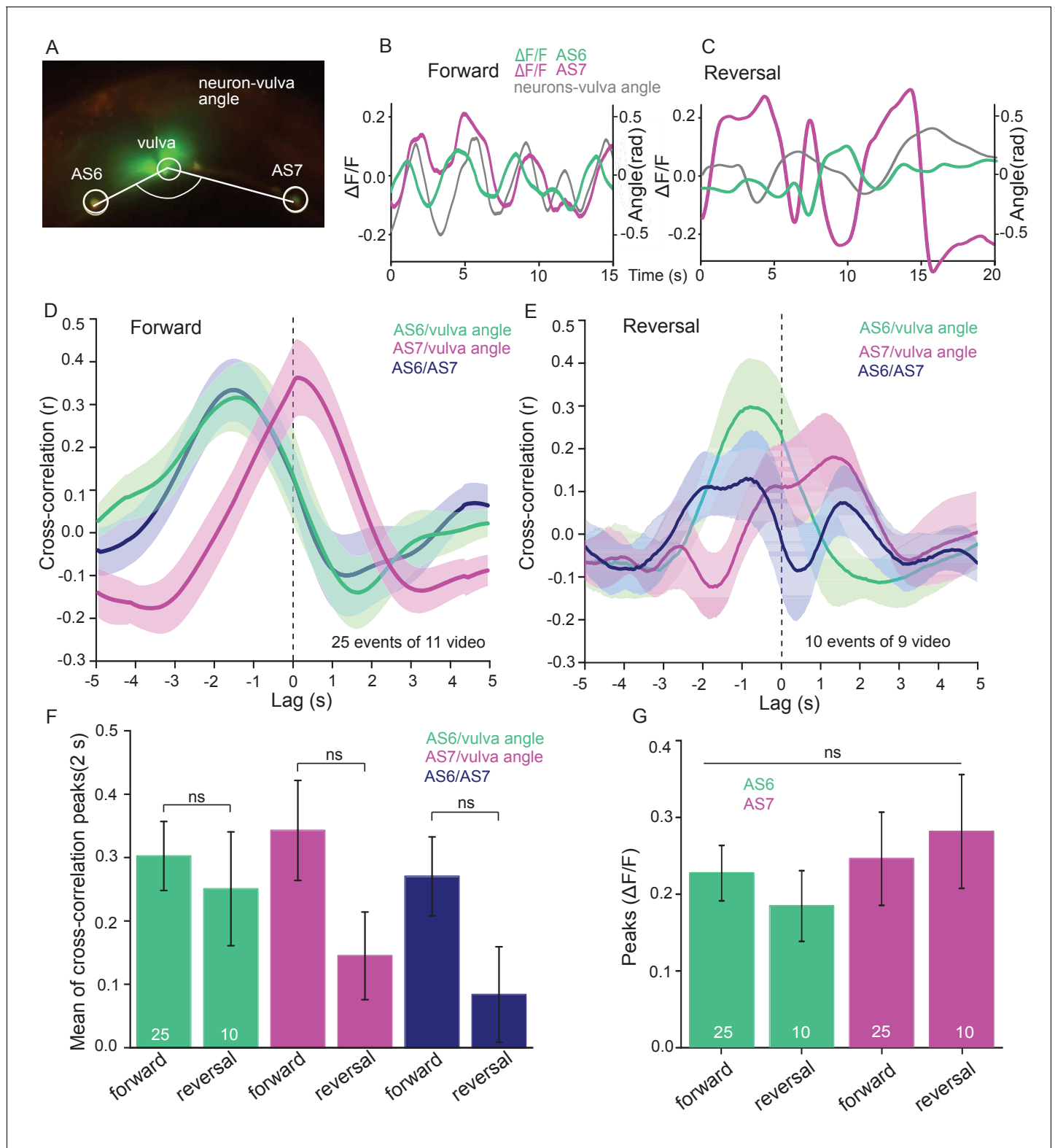
237

Figure 5. AS MNs show oscillatory Ca^{2+} activity in moving animals. (**A**) Fluorescent micrograph (merged channels) of the vulva region, showing red (mCherry) and green (GCaMP6), expressed in AS MNs (with the use of the Q system), and GFP, expressed in vulva muscles. Angle between vulva and the two flanking AS6 and AS7 neurons is indicated. (**B, C**) Representative analysis of time traces of Ca^{2+} signals (ΔF/F) in AS6 and AS7, as well as the angle defined by the vulva and the two neurons during crawling (B, 15 s, forward; C, 20 s, reverse). (**D, E**) Cross-correlation analysis (mean ± SEM) of single periods of the body wave (5 s each) for each of the AS6 and AS7 GCaMP6 signals with the vulva angle, as well as for the two Ca^{2+} signals, during
Figure 5 continued on next page

7 (*Altun et al., 2009*; *Starich et al., 2009*). Thus, we used an *unc-7(e5)* null mutant, in which no electrical coupling should occur between AS MNs and AVA or AVB, and repeated the above experiments (*Figure 6BI-IV*). This showed similar depolarization of AS MNs following AVB stimulation, while activity of the AS MNs did not increase significantly with ATR. Thus, gap junctions may contribute particularly to AVA-AS MN signaling.

Retrograde electrical signaling from AS MNs depolarizes AVA but not AVB interneurons

To explore whether there is also retrograde signaling from AS MNs to PINs via gap junctions, we perfomed the reciprocal experiment, i.e. we tested if AS MN photostimulation could lead to depolarization of the PINs. We crossed a transgene expressing ChR2 in the AS MNs with strains expressing the ratiometric Ca^{2+} indicator cameleon (bearing CFP and YFP moieties; *Miyawaki et al., 1997*) in the PINs (driven by *sra-11* and *nmr-1* promoters, for expression in AVB and AVA, respectively, a kind gift by M. Zhen; *Figure 6CI*). Both promoters express in several head neurons, yet we could identify AVB and AVA by their position with respect to anatomical landmarks and with respect to other (known) fluorescent neurons. Photodepolarization of the AS MNs (in animals raised in the presence of ATR) caused Ca^{2+} transients in AVA ($\Delta R/R \sim 18\%$), but had no significant effect on Ca^{2+}-activity in AVB interneurons (*Figure 6CII-IV*). The latter is in line with the much smaller number of gap junctions between AS MNs and AVB. A small ($\Delta R/R \sim 9$–10%), insignificant increase of the ratio of the CFP/YFP signal was observed in the control animals raised without ATR, in both AVA and AVB (likely due to uneven bleaching of CFP vs. YFP). In the *unc-7* gap junction mutant background, the Ca^{2+} signal ($\Delta R/R \sim 11\%$) was now comparable to the signal observed in the control without ATR, indicating that UNC-7 electrical synapses are responsible for transmission between AS MNs and AVA. For AVB, we did not observe any significant effect in the *unc-7(e5)* mutant. Similar observations were made in L4 larvae, which we tested to rule out any differences caused by altered expression levels due to developmental changes (data not shown).

Discussion

Movement by undulations is remarkably effective across scales and in a variety of environments (*Cohen and Sanders, 2014*). Despite the diversity of their anatomy, the nervous systems of distantly related organisms may adopt similar strategies to control locomotion by undulations. Based on physiological data we revealed several features of the AS MNs highlighting their function in one of the most studied locomotion circuits, the VNC of *C. elegans*. The main findings of this work are: (1) Depolarization of AS MNs does not disrupt locomotion, but causes a dorsal bias. (2) AS MN hyperpolarization inhibits locomotion and prevents generation and propagation of the undulatory wave. (3) AS MN activity oscillates during both forward and reverse locomotion. (4) AS MNs are stimulated by forward as well as reverse premotor interneurons. (5) AS MNs have functional electrical connections to the backward PIN AVA. Our findings for AS MNs in the *C. elegans* locomotor circuit have parallels in several animal models (see below).

Figure 6. Reciprocal and asymmetric mutual activation of AS MNs and forward and reverse PINs, AVB and AVA. (A) (I) Schematic of the experiment for measurement of AS MN Ca²⁺ signals (GCaMP6) during AVB or AVA photodepolarization *via* ChR2 with 470 nm blue illumination (arrows, chemical synapses; curved lines, electrical synapses). (II, III) Time traces of mean (±SEM) Ca²⁺ transients (ΔF/F) in AS MNs during depolarization of AVA (II) and AVB (III) by ChR2, in animals raised in absence or presence of ATR. Brackets indicate time periods used for statistical analysis in IV. (IV) Group data quantification of experiments shown in II and III (for the 1–3 s time period). See also *Figure 6—figure supplement 1* and *Figure 6—video 1, 2*. (B) (I-IV), as in A (I-IV), but in the *unc-7(e5)* gap junction mutant background. (C) (I) Schematic of the experiment for measurement of Ca²⁺ signals (cameleon) in AVB or AVA PINs during AS MN photodepolarization *via* ChR2. (II, III) Mean (±SEM) of Ca²⁺ transients (ΔR/R YFP/CFP ratios) in AVA (II) and AVB (III) during AS MN depolarization, in wild type or *unc-7(e5)* mutant animals, raised in absence or presence of ATR. IV) Group data quantification of experiments in II and III (for the 0–1 s time period). P values *≤0.05; **≤0.01; ***≤0.001; number of animals is indicated. Statistical test: Mann-Whitney U test.

The following video and figure supplement are available for figure 6:

Figure supplement 1. AS MNs are simultaneously activated by photostimulation of the AVA and AVB PINs.

Figure 6—video 1. Ca²⁺ signal in the AS MNs expressing GCaMP6 during photodepolarization of the AVA PIN by ChR2 (in animal raised with ATR), 470 nm blue light, 1.2 mW/mm².

Figure 6 continued on next page

AS MNs act in coordination of dorso-ventral bends, antero-posterior wave propagation and possibly forward-backward states

AS MNs occupy a significant part of the VNC circuit (11 of 75 neurons) and two AS MNs are present in each functional segment of the circuit (*Haspel and O'Donovan, 2011*). Yet, in absence of physiological information, they were missing in many models representing the locomotor circuit function in *C. elegans* (*Von Stetina et al., 2005*; *Zhen and Samuel, 2015*). We showed that AS MNs are important for several aspects of locomotion, among them dorso-ventral coordination: Their depolarization activates dorsal BWMs leading to contraction and dorsal bias in freely moving animals, while AS MN hyperpolarization eliminates activity in dorsal BWMs and induces contraction of ventral BWMs through disinhibition. Thus, it is likely that AS MNs counteract neurons providing a ventral bias, e.g. the VA and VB MNs, or even the VC neurons (*Faumont et al., 2011*; *White et al., 1986*). This corresponds to recent computational studies, which predicted a significant role of AS MNs in coordinating dorso-ventral bending (*Olivares et al., 2017*) and in the control of BWMs (*Yan et al., 2017*). Furthermore, AS MNs are active both during forward and reverse locomotion. In line with this, AS MN hyperpolarization disrupts propagation of the antero-posterior body wave. Since the AS MNs connect to both forward and backward PINs, they could play a role in integrating forward and backward locomotion motifs, e.g. by providing an electrical sink (or source; this is more likely for AS-to-AVA signaling, due to the higher number of gap junctions, and in line with our results) for the PINs of the respective opposite direction (*Figure 7A,B*). Similar functions were shown for A-type MNs and AVA (*Kawano et al., 2011*; *Liu et al., 2017*) as well as for V2a interneurons and MNs in zebrafish (*Song et al., 2016*).

AS MNs, as other MN types, innervate only one side of the BWMs (dorsal). However, unlike other MN classes, AS MNs have no obvious class of 'partner' neurons innervating only ventrally. However, there are the VC neurons, which innervate ventral muscle. Yet, there are only six VC neurons, and two of them mainly innervate vulval muscle. AS MNs thus provide asymmetric excitation, which may be required to enable complex regulatory tasks like gradual changing of direction during navigation. Indeed, optogenetic depolarization of AS MNs, resulting in curved locomotion tracks, mimicked the 'weathervane' mode of navigation towards a source of attractive salt (*Iino and Yoshida, 2009*). During locomotion, higher order neurons, that integrate sensory information, might influence the AS MNs to generate this bias to the dorsal side. In the lamprey, lateral bends were caused by asymmetry in stimulation of the mesencephalic locomotor region (*Sirota et al., 2000*), and in the freely moving lamprey even comparatively small left or right asymmetries in activity of the reticulospinal system correspond to lateral turning (*Deliagina et al., 2000*).

Asymmetry in contralateral motifs of complex locomotor circuits is also known from vertebrate spinal cord CPGs in flexor-extensor coordination (*Grillner and Wallén, 2002*). In mice, flexor motor neurons are predominantly active and inhibit extensor motor neurons, which in turn show intervals of tonic activity between inhibitory states, corresponding to flexor bursts (*Machado et al., 2015*; *Rybak et al., 2015*). When comparing numbers of synaptic inputs from *C. elegans* cholinergic MNs to BWM (*Varshney et al., 2011*; *White et al., 1986*), predominance is apparent in excitatory neuromuscular junctions from A- and B-type MNs to ventral muscles (number of synapses: A-type to ventral muscle: 225, to dorsal muscle: 111, B-type to ventral muscle: 228, to dorsal muscle: 58), as well as in the corresponding contralateral synapses to inhibitory DD MNs, which innervate dorsal muscle (VA and VB to DD: 180 and 194 synapses, DA and DB to DD: 8 and 29 synapses). Therefore, tonic activity of B- or A-type MNs would be expected to generate a bias towards ventral bending, and this could be balanced by excitation of AS MNs. In addition, VC neurons may contribute in counteracting AS MN function (see above). However, the compressed nature of the *C. elegans* nervous system, in which single neurons fulfill multiple tasks that in higher animals are executed by layers of different cells, may not always allow for the direct comparison to vertebrate systems.
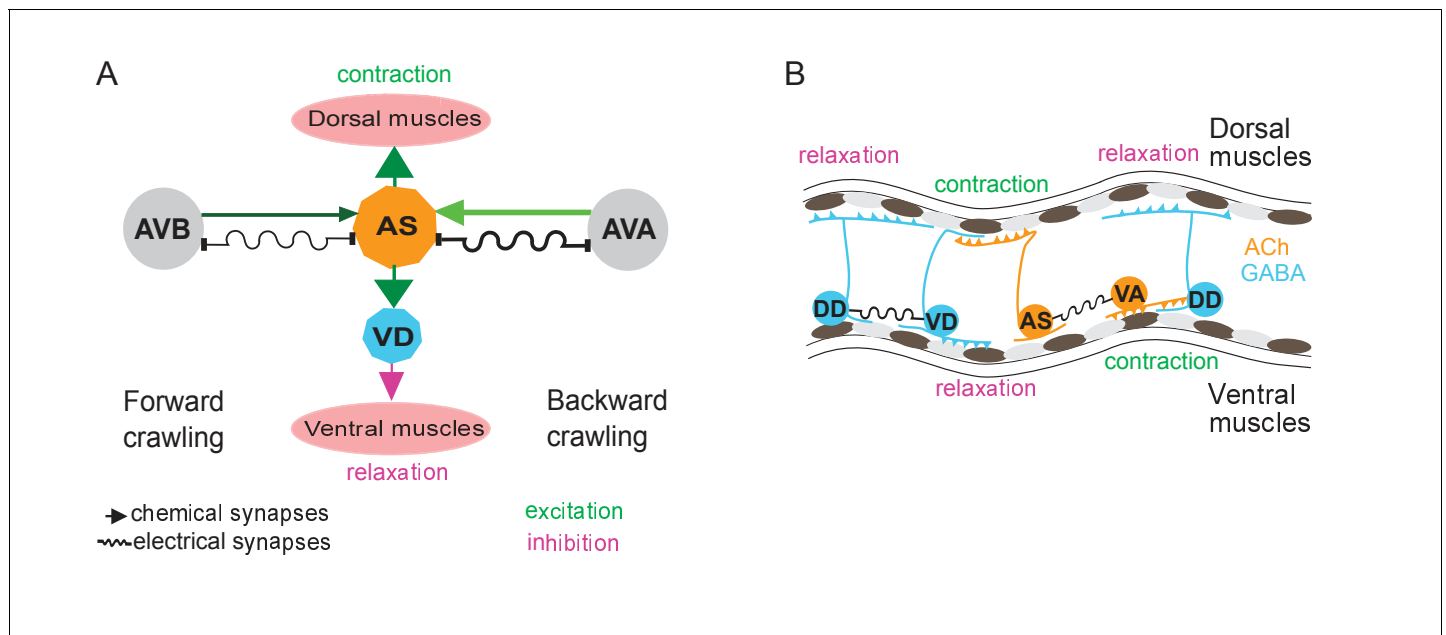
Figure 7. Models summarizing findings of this work. (**A**) AS MNs asymmetrically regulate dorso-ventral bending during forward and backward locomotion, by excitatory chemical transmission to dorsal muscles and ventral GABAergic VD MNs, thus causing ventral inhibition. Interconnections (arrows, chemical synapses; curved lines, electrical synapses; thickness of lines indicates relative synapse number as an approximation of synaptic strength; color shade represents strength of functional connections measured in this work) of AS MNs and their other synaptic partners, that is the PINs AVB and AVA, via both chemical synapses from the PINs and (reciprocal) electrical synapses from AS MNs are also shown. Data in this work suggest (chemical) excitatory regulation of AS MNs by AVA and AVB during forward and backward locomotion, respectively, and reciprocal electrical regulation of AVA by AS MNs. (**B**) Interconnections and functional roles of AS MNs and other VNC MNs during the propagation of the undulatory wave along the body. Depolarization (which could be initiated by AVB, not shown here, or by proprioceptive feedback from the adjacent body segment) of AS MNs causes contraction of the dorsal BWMs and simultaneous relaxation of ventral BWMs through the excitation of VD MNs. This phase is followed by contraction of ventral BWMs, e.g. through the electric coupling of AS and VA MNs, and relaxation of the dorsal BWMs through VD-DD electrical coupling or VA-DD chemical synapses. Cholinergic (orange) and GABAergic (blue) cell types are indicated. Antero-posterior localization of cell bodies and connectivity to other cell types are arbitrary.

DOI: https://doi.org/10.7554/eLife.34997.026

The groups of forward (AVB, PVC) and backward PINs (AVA, AVD, AVE), respectively, are synchronized (*Prevedel et al., 2014*), inhibit each other and change their state stochastically (*Pierce-Shimomura et al., 2008*; *Roberts et al., 2016*). Recently, ability of MNs to modulate activity of PINs was shown in several animal models: for B-type MNs changing the inhibitory chemical transmission of AVB to AVA in *C. elegans* (*Kawano et al., 2011*; *Liu et al., 2017*), for MNs regulating the frequency of crawling in *Drosophila* (*Matsunaga et al., 2017*), for MNs affecting activity of the excitatory V2a neurons in zebrafish (*Song et al., 2016*), and, in mice, such activity was suggested for MNs, changing the frequency of rhythmic CPG activity after stimulation by rhodopsins (*Falgairolle et al., 2017*). Positive feedback from MNs required the function of gap junctions, coupling between MNs and PINs in all these systems. Our data suggest that AS MNs have electrical feedback to the backward PIN AVA. No signal was seen in AVB, yet expression of the Ca²⁺ indicator cameleon was less in AVB, which may have influenced the outcome (see also *Kawano et al., 2011*). If the AS neurons would provide inhibition in the context of the free moving animal, e.g. as an electrical sink for AVA, AS MN activity may exert a bias to promote the forward locomotion state.

AS MNs as part of CPGs in the ventral nerve cord?

CPGs are dedicated neural circuits with intrinsic rhythmic activities (*Grillner, 2006*; *Guertin, 2012*). In many organisms including those showing undulatory movement (e.g. leech, lamprey), series of CPGs are distributed along the length of the body in locomotor neural circuits (*Kristan et al., 2005*; *Mullins et al., 2011*). In *C. elegans*, the bending wave can be generated even in the absence of all PINs (*Gao et al., 2018*; *Kawano et al., 2011*; *Zheng et al., 1999*) as well as in absence of

GABAergic MNs (*Donnelly et al., 2013*; *McIntire et al., 1993*). The existence of series of CPGs in the *C. elegans* VNC was discussed for a long time, and single neurons or small groups of neurons were suggested (*Cohen and Sanders, 2014*; *Gjorgjieva et al., 2014*; *Zhen and Samuel, 2015*). B-type MNs are able to propagate the bending wave posteriorly. The bending may originate from a possible head CPG that generates head oscillations (*Hendricks et al., 2012*; *Shen et al., 2016*), simply by proprioceptive coupling (*Wen et al., 2012*), though recent work showed that also gap junctions are involved (*Xu et al., 2018*). Recently, pacemaker properties of the posterior A-type MN, DA9, were revealed during backward locomotion, that are based on the activity of a P/Q/N-type Ca^{2+} channel (*Gao et al., 2018*), and local oscillators were shown to function in the VNC also for forward locomotion (*Fouad et al., 2018*). Computational modelling of repeating units of the VNC (*Haspel and O'Donovan, 2011*), based on connectome data, identified a dorsally oriented sub-circuit consisting of AS, DA, and DB MNs, which could act as a potential CPG (*Olivares et al., 2017*). Our data on recording dorso-ventral and temporally coordinated oscillatory muscle Ca^{2+} transients in immobilized animals may be a consequence of rhythmic activity in the motor nervous system. Yet, whether AS MNs are part of this activity is currently unknown. The oscillations of AS MN Ca^{2+} levels we observed both during forward and reverse locomotion are not per se an indication of pacemaker activity, as they may be affected by proprioceptive feedback or through other motor neurons. We did not observe them in immobilized animals, which would have been a stronger indication of autonomous CPG activity.

Potential gating properties of AS MNs

Among PINs, AVB and AVA are most important for enabling forward and backward locomotion, respectively (*Chalfie et al., 1985*; *Kato et al., 2015*; *Roberts et al., 2016*). Bistable states with two distinct membrane potentials, i.e. up and down states, that 'gate' activity of the downstream target neurons, were shown for several interneurons including AVA and AVB (*Gordus et al., 2015*; *Kato et al., 2015*; *Mellem et al., 2008*). For MNs, bistability was inferred for the A-, B- and D- types of MNs from direct recordings (*Liu et al., 2014*) as well as from the graded responses in muscles, corresponding to shorter or longer activity bursts in MNs (*Liu et al., 2017*). Further, all-or-none responses in BWM cells, corresponding to spiking neurons as well as to mammalian skeletal muscles, that result from integrating graded excitatory and inhibitory input from MNs, were demonstrated (*Gao and Zhen, 2011*; *Liu et al., 2009*). AS MNs may similarly integrate inputs from forward and backward PINs, or themselves influence the PINs via UNC-7 and/or INX-3 gap junctions, to gate signal propagation in the VNC during forward locomotion, or to couple to A-type MN oscillators (DA9), via the AVA PIN during backward locomotion (*Gao et al., 2018*). In line with this hypothesis, we found ceasing of locomotion when AS MNs were hyperpolarized. Gating neurons that affect rhythmic properties of CPGs are also known for the leech locomotor circuit (*Friesen and Kristan, 2007*; *Mullins et al., 2011*; *Taylor et al., 2000*).

Conclusions

The previously uncharacterized class of AS motor neurons is specialized in coordination of dorso-ventral undulation bends during wave propagation, a feature maintained by asymmetry in both synaptic input and output. Moreover AS neurons integrate signals for forward and reverse locomotion from premotor interneurons and potentially gate ventral nerve cord circuits and PINs via gap junctions.

Materials and methods

Strains and genetics

C. elegans strains were maintained under standard conditions on nematode growth medium (NGM) and fed by *E. coli* strain OP50-1 (*Brenner, 1974*). Transgenic lines were generated using standard procedures (*Fire and Pelham, 1986*) by injecting young adult hermaphrodites with the (plasmid-encoded) transgene of interest and a marker plasmid that expresses a fluorescent protein. In some cases, empty vector was included to increase the overall DNA concentration to 150 –200 ng/µl.

The following strains were used or generated for this study: N2 (wild type isolate, Bristol strain), CB5: *unc-7(e5)X*, CB307: *unc-47(e307)III*, CZ16469: *acr-2(n2420)X; juEx4768[psra-11::ChR2::yfp]*

243

(*Qi et al., 2013*), PD4665: *wt; ccls4655[pes-10::GFP;dpy-20+]*, RM2558: *wt; ls[punc-17::GFP-NLS]*, ZM5091: *wt; hpIs190[pnmr-1(short2)-D3cpv; lin-15+]*, ZM5089: *unc-7(e5)X; hpIs190*, ZM5132: *wt; hpIs179[psra-11-D3cpv]*, ZM5136: *unc-7(e5)X; hpIs179* (all ZM strains are kind gift from Mei Zhen), ZX460: *wt; zxls6[punc-17::ChR2(H134R)::yfp; lin-15+]V*, ZX499: *wt; zxls5[punc-17::ChR2(H134R)::yfp; lin-15+]X*, ZX1023: *lite-1(ce314)X; zxls30[pflp-18::flox::ChR2mCherry::SL2::GFP; pgpa-14::nCre; lin-15+]*, ZX1396: *wt; zxls51[pmyo-3::RCaMP1h]*, ZX2002: *lite-1(ce314)X; zxls6*, ZX2004: *lite-1(ce314)X; zxEx1016 [punc-4::ChR2_RNAi_{sense & antisense} pmyo-2::mCherry]; zxEx1017[pacr-5::ChR2_RNAi_{sense & antisense}; pmyo-3::mCherry]*, ZX2007: *wt; zxls5; zxEx1016; zxEx1017*, ZX2008: *wt; zxEx1023[punc-17::QF; pacr-5::QS::mCherry; punc-4::QS::mCherry; QUAS::ACR1::YFP; pmyo-2::mCherry]*, ZX2011: *wt; zxEx1020[punc-17::QF; pacr-5::QS::mCherry; punc-4::QS::mCherry; QUAS::HisCl1::GFP; pmyo-2::mCherry]*, ZX2012: *lite-1(ce314)X; ccls4655[pes-10::GFP; dpy-20+]; zxEx1021[punc-17::QF; pacr-5::QS::mCherry; punc-4::QS::mCherry; QUAS::GCaMP6::SL2::mCherry; pmyo-2::mCherry]*, ZX2110: *wt; mdls[punc-17::GFP-NLS;] zxEx1024[punc-17::QF; pacr-5::QS::mCherry; punc-4::QS::mCherry; QUAS::PH-miniSOG; pmyo-2::mCherry]*, ZX2113: *unc-47(e307)III; zxEx1029[punc-17::QF; pacr-5::QS::mCherry; punc-4::QS::mCherry; QUAS::ACR1::YFP; pmyo-2::mCherry]*, ZX2114: *wt; zxls51; zxEx1020*, ZX2127: *lite-1(ce314)X; zxls30; zxEx1021*, ZX2128: *lite-1(ce314)X; juEx4768; zxEx1021*, ZX2132: *wt; zxls5; zxEx1016, zxEx1017; zxEx1028[pmyo-3::GCaMP3]*, ZX2212: *lite-1(ce314)X; hpIs179; zxls6; zxEx1016, zxEx1017*, ZX2213: *lite-1(ce314)X; hpIs190; zxls6; zxEx1016, zxEx1017*, ZX2217: *unc-7(e5)X; hpIs190; zxls6; zxEx1016, zxEx1017*; ZX2220: *unc-7(e5); hpIs179; zxls6; zxEx1016, zxEx1017*, ZX2221: *unc-7(e5)X; zxls6; zxEx1016, zxEx1017*,ZX2427: *unc-7(e5); juEx4768; zxEx1021*; ZX2428: *unc-7(e5); zxls30; zxEx1021*; ZX2429: *wt; zxls51; zxEx1111[punc-17::QF; pacr-5::QS::mCherry; punc-4::QS::mCherry; QUAS::PH-miniSOG; pmyo-2::mCherry]*; ZX2434: *wt; zxEx1112 [punc-17::QF; pacr-5::QS::mCherry; punc-4::QS::mCherry; QUAS::Chrimson::GFP; pmyo-2::mCherry]* (Schild, Glauser, 2015; pdg274[QUAS::Chrimson::GFP] is a kind gift from Dominique Glauser), ZX2435: *zxEx432[pglr-1::ChR2(C128S)::YFP; lin-15]; zxEx1021*.

Molecular biology

We used the following promoters:3.5 kb *punc-17* (*Sieburth et al., 2005*), 2.5 kb *punc-4* (*Miller et al., 1992*) and 4.3 kb *pacr-5* (*Winnier et al., 1999*), genomic DNA sequence upstream of the ATG start codon of each gene, respectively. The *punc-4*::ChR2 sense and antisense construct was generated as follows: The p*unc-4* promoter from plasmid pCS139 was subcloned into pCS57 (*Schultheis et al., 2011*) by *Sph*I and *Nhe*I, 1 kb antisense sequence was amplified from the ligated construct pOT1 *punc-4*::ChR2::YFP using primers (5'-GGGGTTTAAACAGCTAGCGTCGATCCATGG-3' and 5'-CCCGCGGCCGCCCAGCGTCTCGACCTCAATC-3') and subcloned into the same construct by *Not*I and *Pme*I to get pOT2. To silence ChR2 expression under the *pacr-5* promoter we used a sense and antisense strands approach (*Esposito et al., 2007*) as follows: The *pacr-5* promoter was amplified from genomic DNA using primers (5'-TTATGATGCGAAAGCTGAATCGAGAAAGAG-3', 5'-CCATGCTTACTGCACTTGCTTCCCATACTTC-3', nested 5'-GGGGCATGCATCGAGAAAGA-GAAGCGGCG-3', 5'-CCCGCTAGCAAAGCATTGAAACTGGTGAC-3') and subcloned into pCS57 with *Sph*I and *Nhe*I to yield pOT3 (*pacr-5*::ChR2::YFP). The sense and antisense strands were amplified from this construct using primers (for the coding region of ChR2: 5'-ATGGATTATGGAGGCGCCC-3', 5'-CCAGCGTCTCGACCTCAATC-3'; for the promoter sense: 5'-GGCGGA-GAGTAGTGTGTAGTG-3' and 5'-GGGCGCCTCCATAATCCATCAAAGCATTGAAACTGGTGAC-GAG-3'; for the promoter antisense: 5'-GGCGGAGAGTAGTGTGTAGTG-3' and 5'-GATTGAGG TCGAGACGCTGGCAAAGCATTGAAACTGGTGAC GAG-3'; for fusion of sense strand: 5'-GCGG TTTCACGCTCTGATGAT-3' and 5'-CTCAGTGCCACCAATGTTCAA-3'; and for fusion of the antisense strand: 5'-GCGGTTTCACGCTCTGATGAT-3' and 5'-GCGCGAGCTGCTATTTGTAA-3').

The pOT6 *punc-17*::QF construct was generated as follows: QF::SL2::mCherry sequence was amplified from plasmid XW08 (a kind gift from Kang Shen and Xing Wei) using primers 5'-CAGGAG-GACCCTTGGATG CCGCCTAAACGCAAGAC-3' and 5'-AGTAGAACTCAGTTTTCTGATGA-CAGCGGCCGATG-3', and subcloned into pCS57 (*Schultheis et al., 2011*) using In-Fusion cloning (Takara/Clontech). The SL2::mCherry fragment was cut out by *Sal*I and *Bbv*CI and 5'-overhangs were filled in with Klenow polymerase (NEB). The pOT8 *pacr-5*::QS::mCherry construct was generated by subcloning the *pacr-5* promoter from pOT3 into vector XW09 (*Wei et al., 2012*) (a gift from Kang Shen and Xing Wei) with *Sph*I and *Nhe*I. The pOT7 *punc-4*::QS::mCherry construct was generated by subcloning the *punc-4* promoter from the pOT1 plasmid into XW09 vector with *Sph*I and *Nhe*I. The

244

pOT10 pQUAS::Δpes-10::HisCl1::GFP construct was generated by subcloning the sequence encoding HisCl1::GFP from plasmid pNP403 (*Pokala et al., 2014*) (kind gift from Navin Pokala and Cori Bargmann) into the XW12 vector (a gift from Kang Shen and Xing Wei) with *Asc*I and *Psp*OMI. The pOT11 pQUAS::Δpes-10::GCamP6::SL2::mCherry construct was generated as follows: pQUAS::Δpes-10 sequence was amplified from plasmid XW12 using primers 5'-ACAGCTATGACCATGATTACGC-CAAG-3' and 5'-CCCCGCGGCCGCCCAATCCCGGGGATCCTCTA-3', and subcloned into plasmid p*lin-11*::GCaMP6::SL2::mCherry with *Sph*I and *Not*I. The pOT13 pQUAS::Δpes-10::ACR1::YFP construct was generated as follows: ACR1::YFP sequence was amplified from plasmid pAB03 (*punc-17*:: ACR1::YFP; *Bergs et al., 2018*) using primers 5'-CCCCGGCGCGCCATCCATGAGCAGCATCACC-3' and 5'-CCCCGAATTCCTTACTTGTACAGCTCGTCCAT-3', and subcloned into vector XW12 with *Asc*I and *Eco*RI. Plasmid pOT17 (pQUAS::Δpes-10::PH-miniSOG(Q103L)) was generated as follows: PH-miniSOG(Q103L) sequence was amplified from plasmid pCZGY2849 (a gift from Andrew Chisholm: Addgene plasmid 74112) using primers 5'-CCCCGGCGCGCCCTTCGGATCCAGATCTA TGCAC-3' and 5'-TGTACAAGAAAGCTGGGTCG-3') and subcloned into vector XW12 using *Asc*I and *Eco*RI restriction sites. The construct details are available on request.

Animal tracking and behavioral analysis

For worms moving freely on NGM, locomotion parameters were acquired with a previously described worm tracker (*Stirman et al., 2011*) allowing to precisely target illumination of identified segments of the worm body by a modified off-the-shelf liquid crystal display (LCD) projector, integrated with an inverted epifluorescence microscope. Light power was measured with a powermeter (PM100, Thorlabs, Newton, NY, USA) at the specimen focal plane. Animals used in all the optogenetics experiments were raised in the dark at 20 °C on NGM plates with *E. coli* OP50-1 and all-*trans*-retinal. The OP50-retinal plates were prepared 1–2 days in advance by seeding a 6 cm NGM-agar plate with 250 µl of OP50 culture and 0.25 µl of 100 mM retinal dissolved in ethanol. Young adults were transferred individually on plain NGM plates under red light (>600 nm) in a dark room and kept for 5 min in the dark before transfer to the tracker.

For experiments with ChR2 depolarizing MNs (*Figures 1* and *2*), blue light of 470 nm and 1.8 mW/mm^2 intensity was used with the following light protocol: 20 s' dark' (referring to no blue light illumination) control, 20 s of illumination, followed again by 20 s dark. The animals' body was divided into 11 segments, of which 3 – 10, 3 – 4, 5 – 6 or 9 – 10 were illuminated, depending on the experiment.

For optogenetic ablation experiments (*Figure 3A*; *Figure 3—figure supplement 1*), AS MNs were ablated in animals expressing PH-miniSOG by 2.5 min exposure to 470 nm light of 1.8 mW/mm^2 intensity; segments 3 – 10 out of 11 were illuminated. Animals were analyzed after a 2 hr resting period for 60 s without illumination. Wild type worms were used as a control with the same illumination protocol. Ablation was verified by fluorescence microscopy in strain ZX2110 expressing green fluorescent protein (GFP) in all cholinergic neurons, in addition to PH-miniSOG in AS MNs.

For experiments of AS MN hyperpolarization using the histamine-gated Cl⁻-channel HisCl1 (*Figure 3B*; *Figure 3—figure supplement 1*), worm locomotion was measured on NGM plates with 10 mM histamine 4 min after transfer from plates without histamine, for 60 s without illumination. The same strain on NGM without histamine served as a control.

For experiments in which MNs were hyperpolarized with natural Cl⁻-conducting anion channel rhodopsin (ACR1; *Figure 4*), due to the high operational light sensitivity of the channel, the system was modified as described (*Steuer Costa et al., 2017*). An additional band pass filter (650 ± 25 nm) was inserted in the background light path and a mechanical shutter (Sutter Instrument Company, Novato, USA), synchronized to the light stimulation, was placed between projector and microscope. Control animals were tested for the background light stimulation and showed no response. The light stimulation protocol was 20 s without illumination, 20 s in 70 µW/mm^2 470 nm light and 20 s without illumination. The worms' body was divided into 11 segments, and segments 3 – 10, 3 – 4, 5 – 6 or 9 – 10 were illuminated, respectively. As the experiment in *unc-47(e307)* background was performed with a different transgene injected into *unc-47(e307)* mutants, we tested the extrachromosomal array after outcrossing into wild type background, where it evoked contraction of the animals, as expected (*Figure 4—figure supplement 1*).

For experiments in which MNs were depolarized with Chrimson (*Figure 1—figure supplement 1*) red light of 650 nm and 1.8 mW/mm^2 intensity was used with the following light protocol: 20

s 'dark' (referring to no red light illumination) control, 20 s of illumination, followed again by 20 s dark).

Tracks were automatically filtered to exclude data points from erroneously evaluated movie frames with a custom-made workflow in KNIME (KNIME Desktop version 3.5, KNIME.com AG, Zurich, Switzerland; *Warr, 2012*). Our constraints were that animals do not move faster than 1.25 mm/s and their length does not show a discrepancy above 25% to the mean first five seconds of the video. Videos were excluded from analysis when more than 15% of the data points had to be discarded by our constraints. Behavior data passed the Shapiro-Wilk normality test.

For determination of the ratio of dorso-/ventral angles (*Figure 1BIII, IV*), the second out of 11 three point angles, measured from head to tail, was registered for animals for which the vulva position was previously indicated by manually indicating this to the software. For each track, values of the second three-point angle were averaged for dorsal and ventral bends individually, and the ratio was calculated.

To calculate the frame-to-frame difference of bending angles (*Figure 4E*), data on each of eleven 3-point angles were extracted, smoothed by running an average of 15 frames, and the Δ of absolute values between two subsequent frames were calculated and averaged for before and during illumination conditions for each angle. The light – no light Δ Δ of bending angles (*Figure 4F*) were calculated by subtracting the value of the no light from the light condition. They were then averaged for the bending angles 1–5 (anterior) and 6–11 (posterior).

Body posture analysis

Binarized videos of freely crawling animals were used to segment the animals' body, and analyzed as described earlier (*Hums et al., 2016*; *Stephens et al., 2008*), using a custom MATLAB script (MathWorks, Natick, Massachusetts). Briefly, grey scale worm images were binarized with a global image threshold using Otsu's method (*Otsu, 1979*). Objects encompassing border pixels were ignored and only the largest object was assumed to be the worm. The binary image was further processed (by thickening, removing spur pixels, flipping pixels by majority and filling holes). Worm skeletonization was achieved by thinning to produce an ordered vector of 100 body points and corresponding tangent angles (theta) from head to tail. Images that could not be analyzed or where the skeleton of the animal was unusually small were considered as missing data points. Head and tail assignment was checked manually. The theta angles were smoothened by a simple moving average with a window of 15 centered data points. The mean of these angles was then compared to the Eigenworms computed from previously published data on N2 videos (*Stephens et al., 2008*). The Eigen projections obtained were taken as a measure of worm posture and plotted.

Fluorescence microscopy

Animals were immobilized in M9 saline with 50 mM NaN_3 and mounted on 10% agar pads with polystyrene beads. Images were recorded under 40x magnification on an inverted fluorescence microscope (Axiovert 200, Zeiss, Germany) or with a Zeiss Cell Observer SD, 488 nm excitation laser at 40% power and a Rolera EM-C2 with EM gain of 100, full resolution and 100 ms exposure time. ImageJ tools were used to obtain maximum projections, image straightening and aligning.

Ca^{2+} imaging

Microscope setup: Fluorescence measurements were carried out on an inverted fluorescence microscope (Axiovert 200, Zeiss, Germany) equipped with motorized stage MS 2000 (Applied Scientific Instrumentation, USA) and the PhotoTrack quadrant photomultiplier tube (PMT; Applied Scientific Instrumentation, USA). Two high-power light emitting diodes (LEDs; 470 and 590 nm wavelength, KSL 70, Rapp Optoelektronik, Germany) or a 100 W HBO mercury lamp were used as light sources. A Photometrics DualView-Λ beam splitter was used to obtain simultaneous dual-wavelength acquisition; these were coupled to a Hamamatsu Orca Flash 4.0 sCMOS camera operated by HCImage Live (Hamamatsu) or MicroManager (http://micro-manager.org). Light illumination protocols (temporal sequences) were programmed on, and generated by, a Lambda SC Smart shutter controller unit (Sutter Instruments, USA), using its TTL output to drive the LED power supply or to open a shutter when using the HBO lamp.

246

Measurement of Ca^{2+} in muscles and AS MNs in immobilized worms

For measurements of GCaMP3 (*Figure 2*) and RCaMP (*Figure 3B*) in muscles and GCaMP6 in AS MNs (*Figures 5* and *6*), the following light settings were used: GFP/mCherry Dualband ET Filterset (F56-019, AHF Analysentechnik, Germany), was combined with 532/18 nm and 625/15 nm emission filters and a 565 longpass beamsplitter (F39-833, F39-624 and F48-567, respectively, all AHF). ChR2 stimulation was performed using 1.0 – 1.2 mW/mm^2 blue light, unless otherwise stated. To measure RCaMP or mCherry fluorescence, 590 nm, 0.6 mW/mm^2 yellow light was used. The 2x binned images were acquired at 50 ms exposure time and 20 fps. Animals were immobilized on 2 or 4% M9 agar pads with polystyrene beads (Polysciences, USA) and imaged by means of 25x or 40x oil objective lenses. 5 s of yellow light illumination and 15 s of blue light illumination protocols were used. For RCaMP imaging 20 s yellow light illuminations were used. Measurements of control animals (i.e. raised without ATR, or without histamine) were conducted the same way as for animals kept in the presence of ATR, or exposed to histamine.

Image analysis was performed in ImageJ (NIH). For Ca^{2+}-imaging in muscles, regions of interest (ROIs) were selected for half of the BWM cells in the field of view, or around the neuron of interest for Ca^{2+}-imaging in AS MNs. Separate ROIs were selected for background fluorescence with the same size. Mean intensity values for each video frame were obtained and background fluorescence values were subtracted from the fluorescence values derived for GCaMP or RCaMP. Subtracted data was normalized to $\Delta F/F = (F_i-F)/F$, where F_i represents the intensity at the given time point and F represents the average fluorescence of the entire trace.

Measurement of Ca^{2+} in muscles and AS motor neurons in moving animals

Measurements of GCaMP6 and mCherry were performed using the same filter and microscope settings as for immobilized worms. Moving worms were assayed on 1% agar pads in M9 buffer. Tracking was based on the PhotoTrack system (Applied Scientific Instrumentation, USA) that uses the signals from a 4-quadrant photomultiplier tube (PMT) sensor for automated repositioning of a motorized XY stage to keep a moving fluorescent marker signal in the field of view (*Faumont et al., 2011*). For this purpose, an oblique 80% transmission filter was inserted in the light path to divert 20% of the light to the PMT quadrants. A 535/30 bandpass filter (F47-535, AHF) was used to narrow the emission spectrum prior to detection for improved tracking performance. A fluorescent marker GFP was expressed in vulval muscle cells, strains PD4665 and ZX2012. Video files containing data of both fluorescent channels (for GCaMP6 and mCherry) were processed with custom written Wolfram Mathematica notebooks. Both color channels were virtually overlaid to accurately correct the spatial alignment. Images were first binarized to identify the centroid of the moving neuronal cell bodies throughout all frames. Mean intensity values of a circular ROI (18 pixel radius) centered on this centroid were measured and subtracted with the mean intensity values of a surrounding donut shaped background ROI (five pixel width). Coordinates of two AS neurons of interest were recorded relative to the vulva and to each other to obtain their relative distance and the angle between the vulva and the two neurons of interest. The traces were normalized to $\Delta F/F = (F_i- F)/F$, where F represents the average of the entire trace, and were used for correlation analysis. We used strain ZX2435, raised on ATR, to initiate long reversals. This strain expresses the step-function opsin ChR2(C128S) in the backward PINs including AVA (*Schultheis et al., 2011*).

Measurement of Ca^{2+} signals in PINs

Ca^{2+} imaging with cameleon D3cpv (*Palmer et al., 2006*) was performed on 5% agar pads as described (*Kawano et al., 2011*) on an Axiovert 200 microscope (Zeiss), using a 100x/1.30 EC Plan-Neofluar Oil M27 oil immersion objective. ChR2 stimulation was performed using 8 mW/mm^2 blue light delivered by a 100 W HBO mercury lamp. The excitation light path was split using a dual-view (Photometrics) beam splitter with a CFP/YFP filter set. The YFP/CFP ratio after background subtraction was normalized to the $\Delta R/R=(R_i-R)/R$, where R_i represents the YFP/CFP ratio at the given time point and R represents the average of the entire trace during blue light stimulation. YFP/CFP ratios without normalization were used for quantification and statistics (*Figure 6BIV*). This data did not pass the Shapiro-Wilk normality test.

247

Correlation analysis

Cross-correlation analyses were performed with built-in MATLAB functions. Ca^{2+} transients in AS6 and AS7 and vulva angles were smoothed for 10 frames. Individual bending events identified as segment of the trace between two minima were used for cross-correlation with 100 time lags (10 s). For comparison of peak correlations, the maximum correlation (positive or negative) in a 5 s time window centered on the peak of the control mean correlation was used.

Statistics

Data is given as means ± SEM. Significance between data sets after two-tailed Student's t-test or after Mann-Whitney U-test or after ANOVA is given as p-value (*$p \leq 0.05$; **$p \leq 0.01$; ***$p \leq 0.001$), the latter was given following Tukey's post-hoc test. Data was analyzed and plotted in Excel (Microsoft, USA), in OriginPro 2016 (OriginLab Corporation, Northampton, USA) or in MATLAB (MathWorks, Natick, Massachusetts, USA).

Additional information

Author contributions

Oleg Tolstenkov, Conceptualization, Resources, Data curation, Formal analysis, Funding acquisition, Validation, Investigation, Visualization, Methodology, Writing—original draft, Writing—review and editing; Petrus Van der Auwera, Resources, Software, Supervision, Methodology; Wagner Steuer Costa, Software, Formal analysis, Methodology; Olga Bazhanova, Data curation, Formal analysis; Tim M Gemeinhardt, Resources, Data curation, Formal analysis, Methodology; Amelie CF Bergs, Resources; Alexander Gottschalk, Conceptualization, Formal analysis, Supervision, Funding acquisition, Validation, Visualization, Project administration, Writing—review and editing

Author ORCIDs
Oleg Tolstenkov http://orcid.org/0000-0002-6484-9965
Petrus Van der Auwera http://orcid.org/0000-0001-7540-4788
Wagner Steuer Costa http://orcid.org/0000-0001-7707-2596
Alexander Gottschalk http://orcid.org/0000-0002-1197-6119

Additional files

Supplementary files
• Transparent reporting form
DOI: https://doi.org/10.7554/eLife.34997.027

Data availability
All data generated or analysed during this study are included in the manuscript and supporting files. Source data files are videos from live cell imaging and behavioral experiments. Due to their size, they are provided via the following link (sorted by main figure of the paper): https://open.ag.bmls.uni-frankfurt.de/s/x2ixrBokXazi6wQ.

The following dataset was generated:

Author(s)	Year	Dataset title	Dataset URL	Database, license, and accessibility information
Oleg Tolstenkov, Petrus Van der Auwera, Wagner Steuer Costa, Olga Bazhanova, Tim M Gemeinhardt, Amelie CF Bergs, Alexander Gottschalk	2018	Behavior and imaging videos from which data in this paper was generated, sorted by figure number	https://open.ag.bmls.uni-frankfurt.de/s/x2ixr-BokXazi6wQ	Publicly available at institutional server: open.ag.bmls.uni-frankfurt.de

References

Akerboom J, Carreras Calderón N, Tian L, Wabnig S, Prigge M, Tolö J, Gordus A, Orger MB, Severi KE, Macklin JJ, Patel R, Pulver SR, Wardill TJ, Fischer E, Schüler C, Chen TW, Sarkisyan KS, Marvin JS, Bargmann CI, Kim DS, et al. 2013. Genetically encoded calcium indicators for multi-color neural activity imaging and combination with optogenetics. *Frontiers in Molecular Neuroscience* **6**:1–29. DOI: https://doi.org/10.3389/fnmol.2013.00002, PMID: 23459413

Altun ZF, Chen B, Wang ZW, Hall DH. 2009. High resolution map of Caenorhabditis elegans gap junction proteins. *Developmental Dynamics* **238**:1936–1950. DOI: https://doi.org/10.1002/dvdy.22025, PMID: 19621339

Bergs A, Schultheis C, Fischer E, Tsunoda SP, Erbguth K, Husson SJ, Govorunova E, Spudich JL, Nagel G, Gottschalk A, Liewald JF. 2018. Rhodopsin optogenetic toolbox v2.0 for light-sensitive excitation and inhibition in Caenorhabditis elegans. *PLoS One* **13**:e0191802. DOI: https://doi.org/10.1371/journal.pone.0191802, PMID: 29389997

Brenner S. 1974. The genetics of Caenorhabditis elegans. *Genetics* **77**:71–94. PMID: 4366476

Chalfie M, Sulston JE, White JG, Southgate E, Thomson JN, Brenner S, White G. 1985. The neural circuit for touch sensitivity in Caenorhabditis elegans. *The Journal of Neuroscience* **5**:956–964. DOI: https://doi.org/10.1523/JNEUROSCI.05-04-00956.1985, PMID: 3981252

Chen BL, Hall DH, Chklovskii DB. 2006. Wiring optimization can relate neuronal structure and function. *PNAS* **103**:4723–4728. DOI: https://doi.org/10.1073/pnas.0506806103, PMID: 16537428

Chronis N, Zimmer M, Bargmann CI. 2007. Microfluidics for in vivo imaging of neuronal and behavioral activity in Caenorhabditis elegans. *Nature Methods* **4**:727–731. DOI: https://doi.org/10.1038/nmeth1075, PMID: 17704783

Cohen N, Sanders T. 2014. Nematode locomotion: dissecting the neuronal-environmental loop. *Current Opinion in Neurobiology* **25**:99–106. DOI: https://doi.org/10.1016/j.conb.2013.12.003, PMID: 24709607

Deliagina TG, Zelenin PV, Fagerstedt P, Grillner S, Orlovsky GN. 2000. Activity of reticulospinal neurons during locomotion in the freely behaving lamprey. *Journal of Neurophysiology* **83**:853–863. DOI: https://doi.org/10.1152/jn.2000.83.2.853, PMID: 10669499

Donnelly JL, Clark CM, Leifer AM, Pirri JK, Haburcak M, Francis MM, Samuel AD, Alkema MJ. 2013. Monoaminergic orchestration of motor programs in a complex C. elegans behavior. *PLoS Biology* **11**: e1001529. DOI: https://doi.org/10.1371/journal.pbio.1001529, PMID: 23565061

Esposito G, Di Schiavi E, Bergamasco C, Bazzicalupo P. 2007. Efficient and cell specific knock-down of gene function in targeted C. elegans neurons. *Gene* **395**:170–176. DOI: https://doi.org/10.1016/j.gene.2007.03.002, PMID: 17459615

Falgairolle M, Puhl JG, Pujala A, Liu W, O'Donovan MJ. 2017. Motoneurons regulate the central pattern generator during drug-induced locomotor-like activity in the neonatal mouse. *eLife* **6**:e26622. DOI: https://doi.org/10.7554/eLife.26622, PMID: 28671548

Fang-Yen C, Alkema MJ, Samuel AD. 2015. Illuminating neural circuits and behaviour in *Caenorhabditis elegans* with optogenetics. *Philosophical Transactions of the Royal Society B: Biological Sciences* **370**:20140212. DOI: https://doi.org/10.1098/rstb.2014.0212, PMID: 26240427

Faumont S, Rondeau G, Thiele TR, Lawton KJ, McCormick KE, Sottile M, Griesbeck O, Heckscher ES, Roberts WM, Doe CQ, Lockery SR. 2011. An image-free opto-mechanical system for creating virtual environments and imaging neuronal activity in freely moving Caenorhabditis elegans. *PLoS One* **6**:e24666. DOI: https://doi.org/10.1371/journal.pone.0024666, PMID: 21969859

Fidelin K, Djenoune L, Stokes C, Prendergast A, Gomez J, Baradel A, Del Bene F, Wyart C. 2015. State-Dependent Modulation of Locomotion by GABAergic Spinal Sensory Neurons. *Current Biology* **25**:3035–3047. DOI: https://doi.org/10.1016/j.cub.2015.09.070, PMID: 26752076

Fire A, Pelham H. 1986. Integrative transformation of Caenorhabditis elegans. *The EMBO Journal* **5**:2673–2680. DOI: https://doi.org/10.1002/j.1460-2075.1986.tb04550.x, PMID: 16453714

Fouad AD, Teng S, Mark JR, Liu A, Alvarez-Illera P, Ji H, Du A, Bhirgoo PD, Cornblath E, Guan SA, Fang-Yen C. 2018. Distributed rhythm generators underlie *Caenorhabditis elegans* forward locomotion. *eLife* **7**:e29913. DOI: https://doi.org/10.7554/eLife.29913, PMID: 29360037

Friesen WO, Kristan WB. 2007. Leech locomotion: swimming, crawling, and decisions. *Current Opinion in Neurobiology* **17**:704–711. DOI: https://doi.org/10.1016/j.conb.2008.01.006, PMID: 18339544

Gao S, Zhen M. 2011. Action potentials drive body wall muscle contractions in Caenorhabditis elegans. *PNAS* **108**:2557–2562. DOI: https://doi.org/10.1073/pnas.1012346108, PMID: 21248227

Gao S, Xie L, Kawano T, Po MD, Guan S, Zhen M, Pirri JK, Alkema MJ. 2015. The NCA sodium leak channel is required for persistent motor circuit activity that sustains locomotion. *Nature Communications* **6**:6323. DOI: https://doi.org/10.1038/ncomms7323, PMID: 25716181

Gao S, Guan SA, Fouad AD, Meng J, Kawano T, Huang YC, Li Y, Alcaire S, Hung W, Lu Y, Qi YB, Jin Y, Alkema M, Fang-Yen C, Zhen M. 2018. Excitatory motor neurons are local oscillators for backward locomotion. *eLife* **7**: e29915. DOI: https://doi.org/10.7554/eLife.29915, PMID: 29360035

Gjorgjieva J, Biron D, Haspel G. 2014. Neurobiology of *Caenorhabditis elegans* locomotion: where do we stand? *BioScience* **64**:476–486. DOI: https://doi.org/10.1093/biosci/biu058, PMID: 26955070

Gordus A, Pokala N, Levy S, Flavell SW, Bargmann CI. 2015. Feedback from network states generates variability in a probabilistic olfactory circuit. *Cell* **161**:215–227. DOI: https://doi.org/10.1016/j.cell.2015.02.018, PMID: 25772698

Goulding M. 2009. Circuits controlling vertebrate locomotion: moving in a new direction. *Nature Reviews Neuroscience* **10**:507–518. DOI: https://doi.org/10.1038/nrn2608, PMID: 19543221

Grillner S, Wallén P. 2002. Cellular bases of a vertebrate locomotor system-steering, intersegmental and segmental co-ordination and sensory control. *Brain Research Reviews* **40**:92–106. DOI: https://doi.org/10.1016/S0165-0173(02)00193-5, PMID: 12589909

Grillner S. 2006. Biological pattern generation: the cellular and computational logic of networks in motion. *Neuron* **52**:751–766. DOI: https://doi.org/10.1016/j.neuron.2006.11.008, PMID: 17145498

Guertin PA. 2012. Central pattern generator for locomotion: anatomical, physiological, and pathophysiological considerations. *Frontiers in Neurology* **3**:1–15. DOI: https://doi.org/10.3389/fneur.2012.00183, PMID: 23403923

Haspel G, O'Donovan MJ, Hart AC. 2010. Motoneurons dedicated to either forward or backward locomotion in the nematode Caenorhabditis elegans. *Journal of Neuroscience* **30**:11151–11156. DOI: https://doi.org/10.1523/JNEUROSCI.2244-10.2010, PMID: 20720122

Haspel G, O'Donovan MJ. 2011. A perimotor framework reveals functional segmentation in the motoneuronal network controlling locomotion in Caenorhabditis elegans. *Journal of Neuroscience* **31**:14611–14623. DOI: https://doi.org/10.1523/JNEUROSCI.2186-11.2011, PMID: 21994377

Hendricks M, Ha H, Maffey N, Zhang Y. 2012. Compartmentalized calcium dynamics in a C. elegans interneuron encode head movement. *Nature* **487**:99–103. DOI: https://doi.org/10.1038/nature11081, PMID: 22722842

Hums I, Riedl J, Mende F, Kato S, Kaplan HS, Latham R, Sonntag M, Traunmüller L, Zimmer M. 2016. Regulation of two motor patterns enables the gradual adjustment of locomotion strategy in *Caenorhabditis elegans*. *eLife* **5**:e14116. DOI: https://doi.org/10.7554/eLife.14116, PMID: 27222228

Iino Y, Yoshida K. 2009. Parallel use of two behavioral mechanisms for chemotaxis in Caenorhabditis elegans. *Journal of Neuroscience* **29**:5370–5380. DOI: https://doi.org/10.1523/JNEUROSCI.3633-08.2009, PMID: 19403805

Kato S, Kaplan HS, Schrödel T, Skora S, Lindsay TH, Yemini E, Lockery S, Zimmer M. 2015. Global brain dynamics embed the motor command sequence of Caenorhabditis elegans. *Cell* **163**:656–669. DOI: https://doi.org/10.1016/j.cell.2015.09.034, PMID: 26478179

Kawano T, Po MD, Gao S, Leung G, Ryu WS, Zhen M. 2011. An imbalancing act: gap junctions reduce the backward motor circuit activity to bias C. elegans for forward locomotion. *Neuron* **72**:572–586. DOI: https://doi.org/10.1016/j.neuron.2011.09.005, PMID: 22099460

Kiehn O, Dougherty KJ, Hägglund M, Borgius L, Talpalar A, Restrepo CE. 2010. Probing spinal circuits controlling walking in mammals. *Biochemical and Biophysical Research Communications* **396**:11–18. DOI: https://doi.org/10.1016/j.bbrc.2010.02.107, PMID: 20494103

Kiehn O. 2011. Development and functional organization of spinal locomotor circuits. *Current Opinion in Neurobiology* **21**:100–109. DOI: https://doi.org/10.1016/j.conb.2010.09.004, PMID: 20889331

Kiehn O. 2016. Decoding the organization of spinal circuits that control locomotion. *Nature Reviews Neuroscience* **17**:224–238. DOI: https://doi.org/10.1038/nrn.2016.9, PMID: 26935168

Klapoetke NC, Murata Y, Kim SS, Pulver SR, Birdsey-Benson A, Cho YK, Morimoto TK, Chuong AS, Carpenter EJ, Tian Z, Wang J, Xie Y, Yan Z, Zhang Y, Chow BY, Surek B, Melkonian M, Jayaraman V, Constantine-Paton M, Wong GK, et al. 2014. Independent optical excitation of distinct neural populations. *Nature Methods* **11**:338–346. DOI: https://doi.org/10.1038/nmeth.2836, PMID: 24509633

Kristan WB, Calabrese RL, Friesen WO. 2005. Neuronal control of leech behavior. *Progress in Neurobiology* **76**:279–327. DOI: https://doi.org/10.1016/j.pneurobio.2005.09.004, PMID: 16260077

Leifer AM, Fang-Yen C, Gershow M, Alkema MJ, Samuel AD. 2011. Optogenetic manipulation of neural activity in freely moving Caenorhabditis elegans. *Nature Methods* **8**:147–152. DOI: https://doi.org/10.1038/nmeth.1554, PMID: 21240279

Liewald JF, Brauner M, Stephens GJ, Bouhours M, Schultheis C, Zhen M, Gottschalk A. 2008. Optogenetic analysis of synaptic function. *Nature Methods* **5**:895–902. DOI: https://doi.org/10.1038/nmeth.1252, PMID: 18794862

Liu Q, Hollopeter G, Jorgensen EM. 2009. Graded synaptic transmission at the Caenorhabditis elegans neuromuscular junction. *PNAS* **106**:10823–10828. DOI: https://doi.org/10.1073/pnas.0903570106, PMID: 19528650

Liu P, Chen B, Wang ZW. 2014. SLO-2 potassium channel is an important regulator of neurotransmitter release in Caenorhabditis elegans. *Nature Communications* **5**:5155. DOI: https://doi.org/10.1038/ncomms6155, PMID: 25300429

Liu P, Chen B, Mailler R, Wang ZW. 2017. Antidromic-rectifying gap junctions amplify chemical transmission at functionally mixed electrical-chemical synapses. *Nature Communications* **8**:14818. DOI: https://doi.org/10.1038/ncomms14818, PMID: 28317880

Machado TA, Pnevmatikakis E, Paninski L, Jessell TM, Miri A. 2015. Primacy of flexor locomotor pattern revealed by ancestral reversion of motor neuron identity. *Cell* **162**:338–350. DOI: https://doi.org/10.1016/j.cell.2015.06.036, PMID: 26186188

Marder E, Bucher D, Schulz DJ, Taylor AL. 2005. Invertebrate central pattern generation moves along. *Current Biology* **15**:R685–R699. DOI: https://doi.org/10.1016/j.cub.2005.08.022, PMID: 16139202

Matsunaga T, Kohsaka H, Nose A, Goodman CS, Looger L, Budnik V, Griffith L, Wyman RJ, Lee T. 2017. Gap Junction-Mediated Signaling from Motor Neurons Regulates Motor Generation in the Central Circuits of Larval Drosophila. *The Journal of Neuroscience* **37**:2045–2060. DOI: https://doi.org/10.1523/JNEUROSCI.1453-16.2017, PMID: 28115483

McIntire SL, Jorgensen E, Kaplan J, Horvitz HR. 1993. The GABAergic nervous system of Caenorhabditis elegans. *Nature* **364**:337–341. DOI: https://doi.org/10.1038/364337a0, PMID: 8332191

Mellem JE, Brockie PJ, Madsen DM, Maricq AV. 2008. Action potentials contribute to neuronal signaling in C. elegans. *Nature Neuroscience* **11**:865–867. DOI: https://doi.org/10.1038/nn.2131, PMID: 18587393

Miller DM, Shen MM, Shamu CE, Bürglin TR, Ruvkun G, Dubois ML, Ghee M, Wilson L. 1992. C. elegans unc-4 gene encodes a homeodomain protein that determines the pattern of synaptic input to specific motor neurons. *Nature* **355**:841–845. DOI: https://doi.org/10.1038/355841a0, PMID: 1347150

Miyawaki A, Llopis J, Heim R, McCaffery JM, Adams JA, Ikura M, Tsien RY. 1997. Fluorescent indicators for Ca2+ based on green fluorescent proteins and calmodulin. *Nature* **388**:882–887. DOI: https://doi.org/10.1038/42264, PMID: 9278050

Mullins OJ, Hackett JT, Buchanan JT, Friesen WO. 2011. Neuronal control of swimming behavior: comparison of vertebrate and invertebrate model systems. *Progress in Neurobiology* **93**:244–269. DOI: https://doi.org/10.1016/j.pneurobio.2010.11.001, PMID: 21093529

Nagel G, Brauner M, Liewald JF, Adeishvili N, Bamberg E, Gottschalk A. 2005. Light activation of channelrhodopsin-2 in excitable cells of Caenorhabditis elegans triggers rapid behavioral responses. *Current Biology* **15**:2279–2284. DOI: https://doi.org/10.1016/j.cub.2005.11.032, PMID: 16360690

Olivares E, Izquierdo EJ, Beer RD. 2017. A ventral nerve cord CPG may underlie locomotion in C. elegans. arXiv1705.02301v2 [Q-bio. NC] 18 June.

Otsu N. 1979. A Threshold Selection Method from Gray-Level Histograms. *IEEE Transactions on Systems, Man, and Cybernetics* **9**:62–66. DOI: https://doi.org/10.1109/TSMC.1979.4310076

Palmer AE, Giacomello M, Kortemme T, Hires SA, Lev-Ram V, Baker D, Tsien RY. 2006. Ca2+ indicators based on computationally redesigned calmodulin-peptide pairs. *Chemistry & Biology* **13**:521–530. DOI: https://doi.org/10.1016/j.chembiol.2006.03.007, PMID: 16720273

251

Pearson KG. 1993. Common principles of motor control in vertebrates and invertebrates. *Annual Review of Neuroscience* **16**:265–297. DOI: https://doi.org/10.1146/annurev.ne.16.030193.001405, PMID: 8460894

Pierce-Shimomura JT, Chen BL, Mun JJ, Ho R, Sarkis R, McIntire SL. 2008. Genetic analysis of crawling and swimming locomotory patterns in C. elegans. *PNAS* **105**:20982–20987. DOI: https://doi.org/10.1073/pnas.0810359105, PMID: 19074276

Piggott BJ, Liu J, Feng Z, Wescott SA, Xu XZ. 2011. The neural circuits and synaptic mechanisms underlying motor initiation in C. elegans. *Cell* **147**:922–933. DOI: https://doi.org/10.1016/j.cell.2011.08.053, PMID: 22078887

Pokala N, Liu Q, Gordus A, Bargmann CI. 2014. Inducible and titratable silencing of Caenorhabditis elegans neurons in vivo with histamine-gated chloride channels. *PNAS* **111**:2770–2775. DOI: https://doi.org/10.1073/pnas.1400615111, PMID: 24550306

Prevedel R, Yoon YG, Hoffmann M, Pak N, Wetzstein G, Kato S, Schrödel T, Raskar R, Zimmer M, Boyden ES, Vaziri A. 2014. Simultaneous whole-animal 3D imaging of neuronal activity using light-field microscopy. *Nature Methods* **11**:727–730. DOI: https://doi.org/10.1038/nmeth.2964, PMID: 24836920

Qi YB, Po MD, Mac P, Kawano T, Jorgensen EM, Zhen M, Jin Y. 2013. Hyperactivation of B-type motor neurons results in aberrant synchrony of the Caenorhabditis elegans motor circuit. *Journal of Neuroscience* **33**:5319–5325. DOI: https://doi.org/10.1523/JNEUROSCI.4017-12.2013, PMID: 23516296

Roberts WM, Augustine SB, Lawton KJ, Lindsay TH, Thiele TR, Izquierdo EJ, Faumont S, Lindsay RA, Britton MC, Pokala N, Bargmann CI, Lockery SR. 2016. A stochastic neuronal model predicts random search behaviors at multiple spatial scales in *C. elegans*. *eLife* **5**:e12572. DOI: https://doi.org/10.7554/eLife.12572, PMID: 26824391

Rybak IA, Dougherty KJ, Shevtsova NA. 2015. Organization of the Mammalian Locomotor CPG: Review of Computational Model and Circuit Architectures Based on Genetically Identified Spinal Interneurons(1,2,3). *eNeuro* **2**:1–21. DOI: https://doi.org/10.1523/ENEURO.0069-15.2015, PMID: 26478909

Schmitt C, Schultheis C, Pokala N, Husson SJ, Liewald JF, Bargmann CI, Gottschalk A. 2012. Specific expression of channelrhodopsin-2 in single neurons of Caenorhabditis elegans. *PLoS One* **7**:e43164. DOI: https://doi.org/10.1371/journal.pone.0043164, PMID: 22952643

Schrödel T, Prevedel R, Aumayr K, Zimmer M, Vaziri A. 2013. Brain-wide 3D imaging of neuronal activity in Caenorhabditis elegans with sculpted light. *Nature Methods* **10**:1013–1020. DOI: https://doi.org/10.1038/nmeth.2637, PMID: 24013820

Schultheis C, Liewald JF, Bamberg E, Nagel G, Gottschalk A. 2011. Optogenetic long-term manipulation of behavior and animal development. *PLoS One* **6**:e18766. DOI: https://doi.org/10.1371/journal.pone.0018766, PMID: 21533086

Selverston AI. 2010. Invertebrate central pattern generator circuits. *Philosophical Transactions of the Royal Society B: Biological Sciences* **365**:2329–2345. DOI: https://doi.org/10.1098/rstb.2009.0270, PMID: 20603355

Shen Y, Wen Q, Liu H, Zhong C, Qin Y, Harris G, Kawano T, Wu M, Xu T, Samuel AD, Zhang Y. 2016. An extrasynaptic GABAergic signal modulates a pattern of forward movement in *Caenorhabditis elegans*. *eLife* **5**:e14197. DOI: https://doi.org/10.7554/eLife.14197, PMID: 27138642

Sieburth D, Ch'ng Q, Dybbs M, Tavazoie M, Kennedy S, Wang D, Dupuy D, Rual JF, Hill DE, Vidal M, Ruvkun G, Kaplan JM. 2005. Systematic analysis of genes required for synapse structure and function. *Nature* **436**:510–517. DOI: https://doi.org/10.1038/nature03809, PMID: 16049479

Sineshchekov OA, Govorunova EG, Li H, Spudich JL. 2015. Gating mechanisms of a natural anion channelrhodopsin. *PNAS* **112**:14236–14241. DOI: https://doi.org/10.1073/pnas.1513602112, PMID: 26578767

Sirota MG, Di Prisco GV, Dubuc R. 2000. Stimulation of the mesencephalic locomotor region elicits controlled swimming in semi-intact lampreys. *European Journal of Neuroscience* **12**:4081–4092. DOI: https://doi.org/10.1046/j.1460-9568.2000.00301.x, PMID: 11069605

Song J, Ampatzis K, Björnfors ER, El Manira A. 2016. Motor neurons control locomotor circuit function retrogradely via gap junctions. *Nature* **529**:399–402. DOI: https://doi.org/10.1038/nature16497, PMID: 26760208

Starich TA, Xu J, Skerrett IM, Nicholson BJ, Shaw JE. 2009. Interactions between innexins UNC-7 and UNC-9 mediate electrical synapse specificity in the Caenorhabditis elegans locomotory nervous system. *Neural Development* **4**:16. DOI: https://doi.org/10.1186/1749-8104-4-16, PMID: 19432959

Stephens GJ, Johnson-Kerner B, Bialek W, Ryu WS. 2008. Dimensionality and dynamics in the behavior of C. elegans. *PLoS Computational Biology* **4**:e1000028. DOI: https://doi.org/10.1371/journal.pcbi.1000028, PMID: 18389066

Steuer Costa W, Yu SC, Liewald JF, Gottschalk A. 2017. Fast cAMP Modulation of Neurotransmission via Neuropeptide Signals and Vesicle Loading. *Current Biology* **27**:495–507. DOI: https://doi.org/10.1016/j.cub.2016.12.055, PMID: 28162892

Stirman JN, Crane MM, Husson SJ, Wabnig S, Schultheis C, Gottschalk A, Lu H. 2011. Real-time multimodal optical control of neurons and muscles in freely behaving Caenorhabditis elegans. *Nature Methods* **8**:153–158. DOI: https://doi.org/10.1038/nmeth.1555, PMID: 21240278

Stirman JN, Crane MM, Husson SJ, Gottschalk A, Lu H. 2012. A multispectral optical illumination system with precise spatiotemporal control for the manipulation of optogenetic reagents. *Nature Protocols* **7**:207–220. DOI: https://doi.org/10.1038/nprot.2011.433, PMID: 22240583

Taylor A, Cottrell GW, Kristan WB. 2000. A model of the leech segmental swim central pattern generator. *Neurocomputing* **32-33**:573–584. DOI: https://doi.org/10.1016/S0925-2312(00)00214-9

Varshney LR, Chen BL, Paniagua E, Hall DH, Chklovskii DB. 2011. Structural properties of the Caenorhabditis elegans neuronal network. *PLoS Computational Biology* **7**:e1001066. DOI: https://doi.org/10.1371/journal.pcbi.1001066, PMID: 21304930

Von Stetina SE, Treinin M, Miller DM. 2005. The motor circuit. *International Review of Neurobiology* **69**:125–167. DOI: https://doi.org/10.1016/S0074-7742(05)69005-8

Warr WA. 2012. Scientific workflow systems: Pipeline Pilot and KNIME. *Journal of Computer-Aided Molecular Design* **26**:801–804. DOI: https://doi.org/10.1007/s10822-012-9577-7, PMID: 22644661

Wei X, Potter CJ, Luo L, Shen K. 2012. Controlling gene expression with the Q repressible binary expression system in Caenorhabditis elegans. *Nature Methods* **9**:391–395. DOI: https://doi.org/10.1038/nmeth.1929, PMID: 22406855

Wen Q, Po MD, Hulme E, Chen S, Liu X, Kwok SW, Gershow M, Leifer AM, Butler V, Fang-Yen C, Kawano T, Schafer WR, Whitesides G, Wyart M, Chklovskii DB, Zhen M, Samuel AD. 2012. Proprioceptive coupling within motor neurons drives C. elegans forward locomotion. *Neuron* **76**:750–761. DOI: https://doi.org/10.1016/j.neuron.2012.08.039, PMID: 23177960

White JG, Southgate E, Thomson JN, Brenner S. 1986. The mind of a worm. *Philosophical Transactions of the Royal Society of London. Series B, Biological Sciences* **314**:1–340. DOI: https://doi.org/10.1098/rstb.1986.0056

Wicks SR, Roehrig CJ, Rankin CH. 1996. A dynamic network simulation of the nematode tap withdrawal circuit: predictions concerning synaptic function using behavioral criteria. *The Journal of Neuroscience* **16**:4017–4031. DOI: https://doi.org/10.1523/JNEUROSCI.16-12-04017.1996, PMID: 8656295

Winnier AR, Meir JY, Ross JM, Tavernarakis N, Driscoll M, Ishihara T, Katsura I, Miller DM. 1999. UNC-4/UNC-37-dependent repression of motor neuron-specific genes controls synaptic choice in Caenorhabditis elegans. *Genes & Development* **13**:2774–2786. DOI: https://doi.org/10.1101/gad.13.21.2774, PMID: 10557206

Xu S, Chisholm AD. 2016. Highly efficient optogenetic cell ablation in C. elegans using membrane-targeted miniSOG. *Scientific Reports* **6**:21271. DOI: https://doi.org/10.1038/srep21271, PMID: 26861262

Xu T, Huo J, Shao S, Po M, Kawano T, Lu Y, Wu M, Zhen M, Wen Q. 2018. Descending pathway facilitates undulatory wave propagation in *Caenorhabditis elegans* through gap junctions. *PNAS* **115**:E4493–E4502. DOI: https://doi.org/10.1073/pnas.1717022115, PMID: 29686107

Yan G, Vértes PE, Towlson EK, Chew YL, Walker DS, Schafer WR, Barabási AL. 2017. Network control principles predict neuron function in the Caenorhabditis elegans connectome. *Nature* **550**:519–523. DOI: https://doi.org/10.1038/nature24056, PMID: 29045391

Zhang F, Wang LP, Brauner M, Liewald JF, Kay K, Watzke N, Wood PG, Bamberg E, Nagel G, Gottschalk A, Deisseroth K. 2007. Multimodal fast optical interrogation of neural circuitry. *Nature* **446**:633–639. DOI: https://doi.org/10.1038/nature05744, PMID: 17410168

Zhen M, Samuel AD. 2015. C. elegans locomotion: small circuits, complex functions. *Current Opinion in Neurobiology* **33**:117–126. DOI: https://doi.org/10.1016/j.conb.2015.03.009, PMID: 25845627

Zheng Y, Brockie PJ, Mellem JE, Madsen DM, Maricq AV. 1999. Neuronal control of locomotion in C. elegans is modified by a dominant mutation in the GLR-1 ionotropic glutamate receptor. *Neuron* **24**:347–361. DOI: https://doi.org/10.1016/S0896-6273(00)80849-1, PMID: 10571229

Figures and figure supplements

Functionally asymmetric motor neurons contribute to coordinating locomotion of *Caenorhabditis elegans*
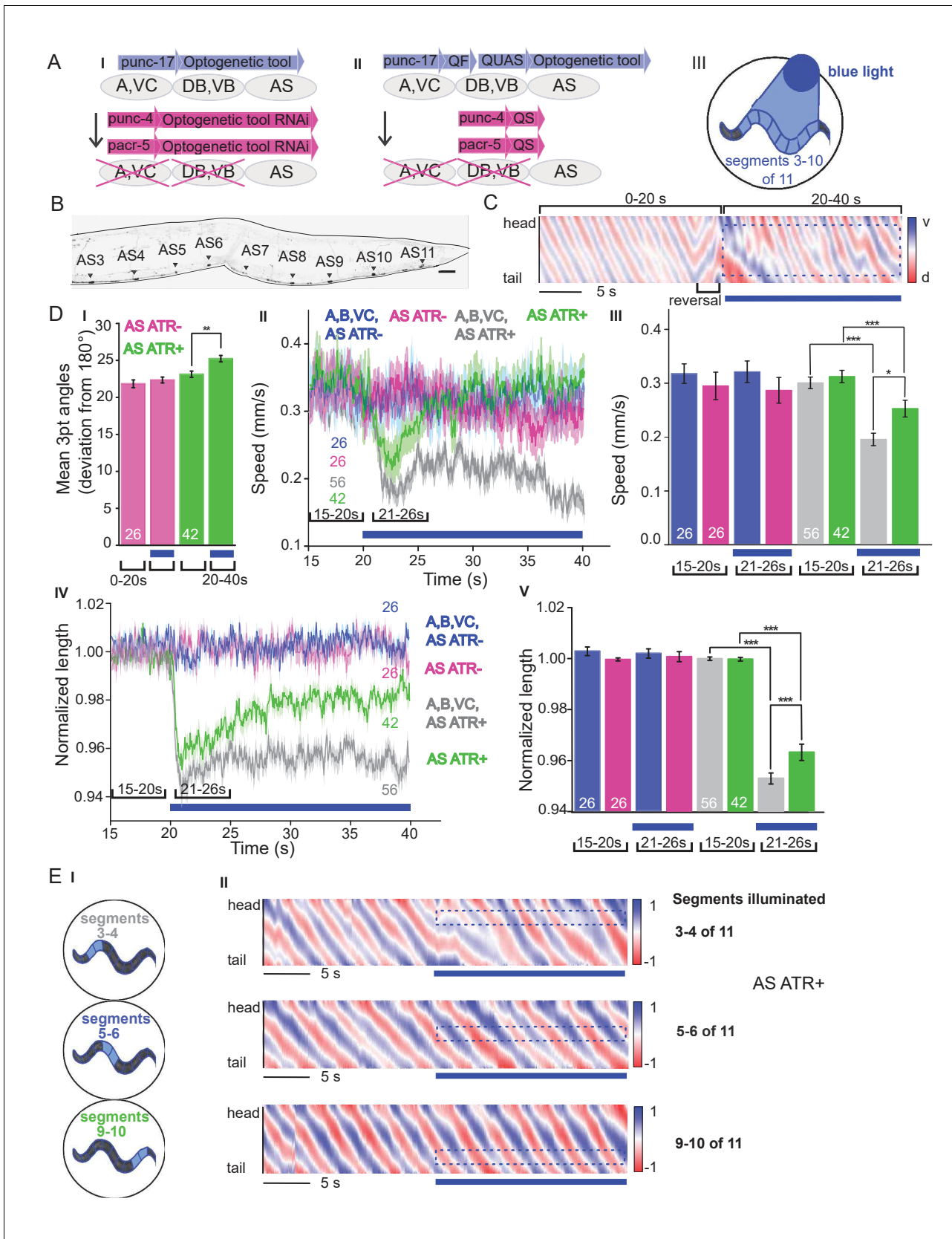
Oleg Tolstenkov *et al*

254

Figure 1. Specific photodepolarization of AS MNs via ChR2 leads to body contraction, increased bending angles and reduced speed in freely moving *C. elegans*. (**A**) 'Subtractive' expression and illumination strategy to achieve specific stimulation of AS MNs by optogenetic tools: (I) Silencing of

Figure 1 continued on next page

255

Figure 1 continued

optogenetic tool protein expression in the non-target subsets of MNs by dsRNA; (II) Using the Q system for conditional expression. The transcriptional activator QF binds to the QUAS sequence to induce optogenetic tool expression. The transcriptional inhibitor QS suppresses expression in unwanted cells by binding to QF; (III) Selective illumination of the VNC MNs by 470 nm blue light. The body of the worm was divided into 11 segments, of which 3 – 10 were illuminated in animals moving freely on agar plates. (**B**) Expression pattern of ChR2(H134R)::YFP in AS MNs by the dsRNA subtractive approach; scale bar, 20 μm. See also *Figure 1—figure supplement 1*. (**C**) Representative body postures kymograph (20 s) of normalized 2-point angles of a 100-point spine, calculated from head to tail of the animal. Positive and negative curvature is represented by blue and red color. Animal expressed ChR2 in AS MNs as in AI and was illuminated after 10 s as in AIII. Blue bar, period of 470 nm illumination. (**D**) Photodepolarization of AS MNs by ChR2 (in animals raised with ATR): I) Analysis of mean bending angles, before and during the blue light illumination period (as in C). (II, III) Locomotion speed: Mean ±SEM crawling speed of animals before and during blue illumination (blue bar), comparing animals expressing ChR2 in AS MNs or in all types of cholinergic MNs in the VNC, raised in the presence or absence of ATR (III: Group data of mean speed of the animals before (15–20 s) and during (21–26 s) ChR2 photoactivation); IV, (**V**) Mean ±SEM body length of the animals shown in I, II (V: Group data of the mean length before (15–20 s) and during (21–26 s) photoactivation). (**E**) Depolarization of subsets of AS MNs in body segments. (**I**) Scheme of anterior, midbody and posterior segmental illumination; II) Representative body posture kymographs of 2-point angles from head to tail before (20 s) and during ChR2 photoactivation by blue light in the segments of the worm body, corresponding to experiments as in E I). See also *Figure 1—video 1* and *Figure 1—figure supplement 2*. P values *$\leq$0.05; **$\leq$0.01; ***$\leq$0.001. Number of animals is indicated in D. Statistical test in D III and V: ANOVA with Tukey's post hoc test.

256

Figure 1—figure supplement 1. Expression of ChR2 can be restricted to AS MNs. (A) Expression of ChR2::YFP in the VNC MNs, either in all cholinergic neurons (upper panel), or restricted in AS MNs using the RNAi approach (middle panel), or the Q system for conditional expression (lower panel). Arrow heads point to AS MNs. Note that in the top panel, many more MN cell bodies are visible in addition to the AS MNs. Animals were photographed, then the VNCs were cut from the resulting composite images, virtually straightened and aligned at the vulva. (B) Quantification of the visible MNs in the VNC for each of the three expression approaches. P value **≤0.01. Number of animals is indicated. Statistical test: ANOVA with Tukey's post hoc test.
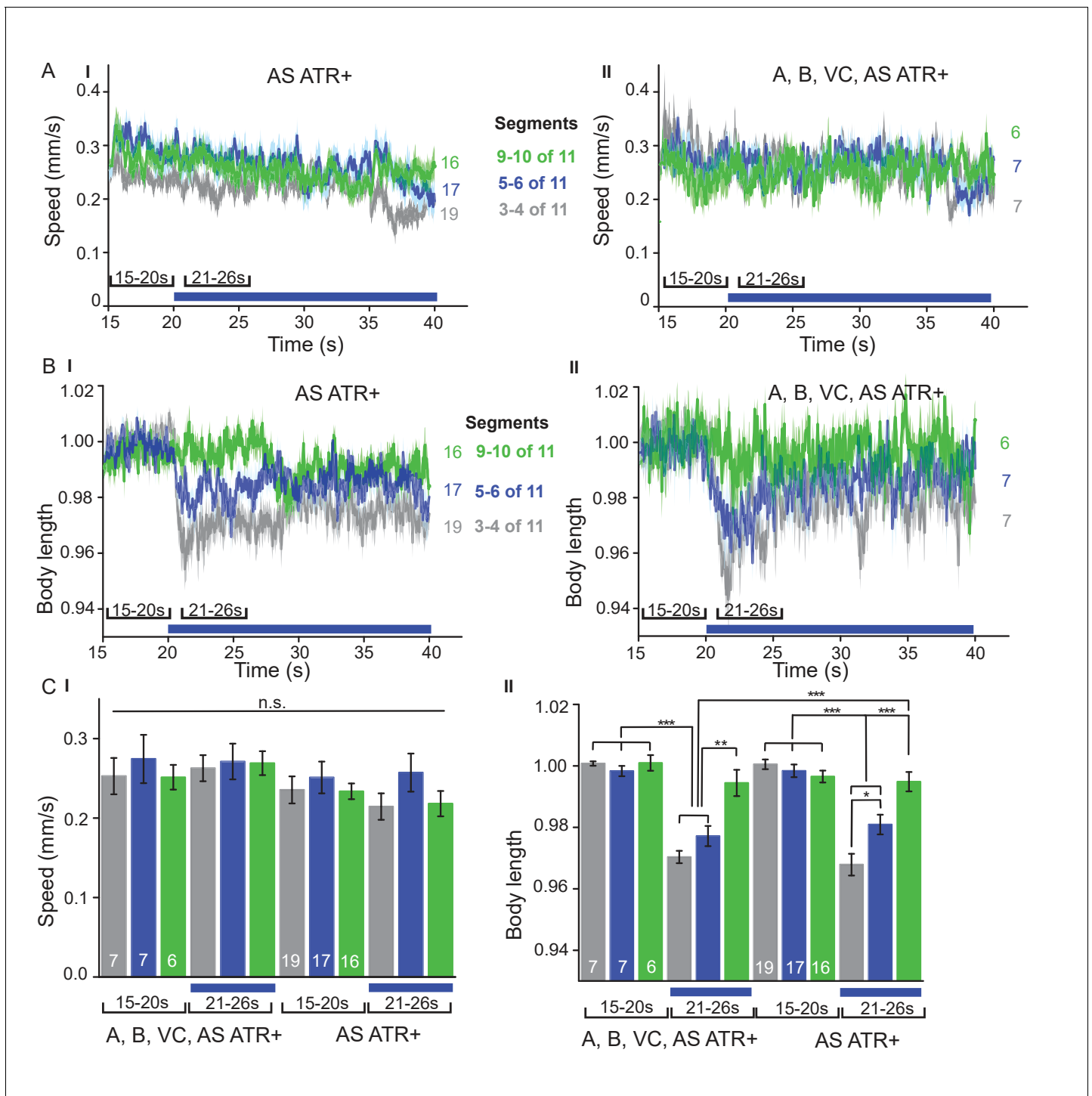
Figure 1—figure supplement 2. Local AS neuron activation affects body length. (**A** I, II) **C** I) Speed and (**B** I, II) (**C** II) body length (time traces, A, B, and group data, C) before and during photodepolarization of AS MNs or of all cholinergic MNs in the anterior, middle and posterior segments of the worm body by ChR2 (in animals raised with ATR). P value *≤0.05, **≤0.01, ***≤0.001; number of animals is indicated. Statistical test: ANOVA with Tukey's post-hoc test.

DOI: https://doi.org/10.7554/eLife.34997.004

258
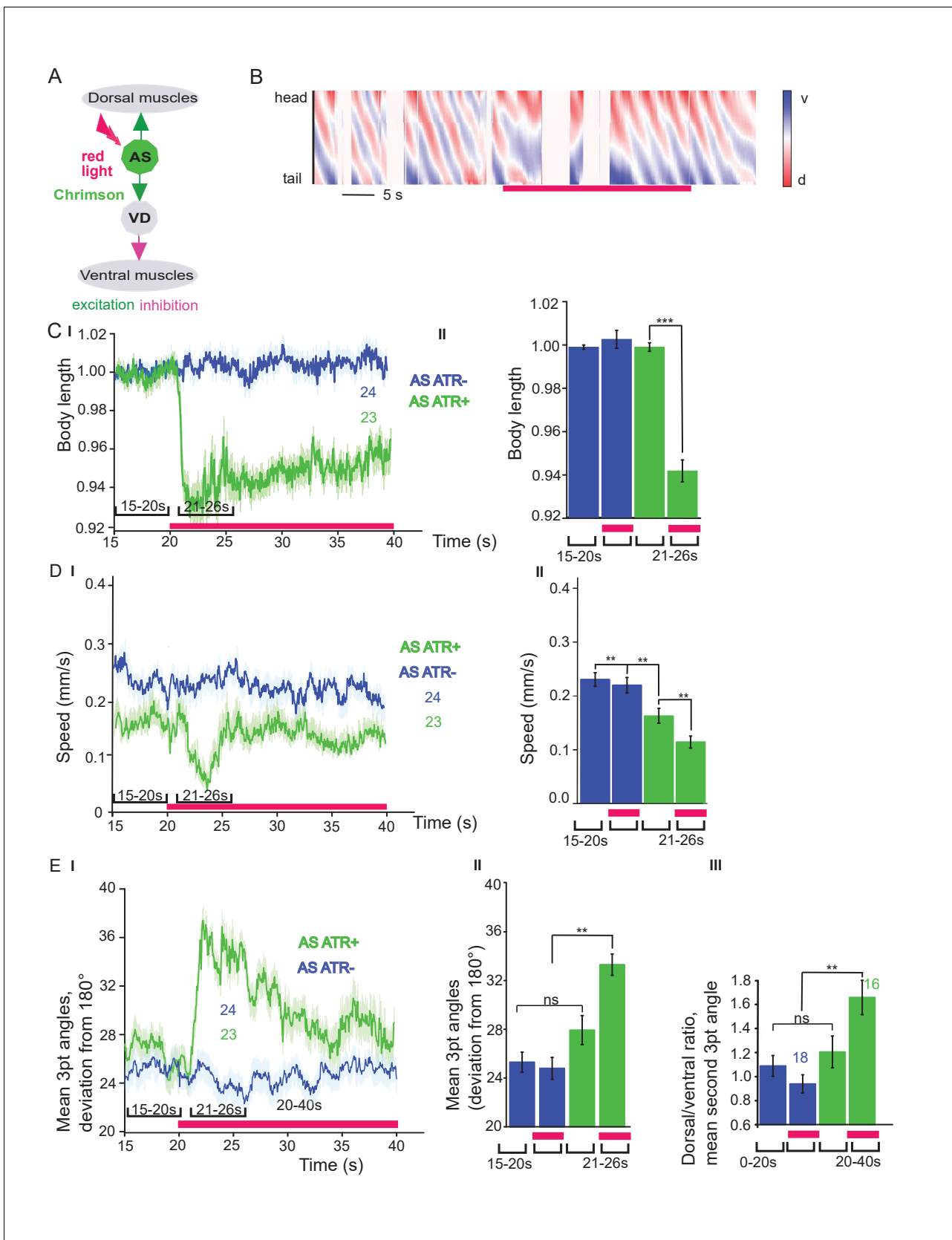
Figure 1—figure supplement 3. Specific photodepolarization of AS MNs via Chrimson leads to body contraction, increased bending angles and reduced speed in freely moving *C. elegans*. (**A**) AS MNs expressing Chrimson were illuminated by 650 nm red light. (**B**) Representative body postures

Figure 1—figure supplement 3 continued on next page

259

Figure 1—figure supplement 3 continued

kymograph (40 s) of normalized 2-point angles of a 100-point spine, calculated from head to tail of the animal. Dorsal and ventral curvature is represented by blue and red color. The animal expressing Chrimson in AS MNs was illuminated after 20 s. Red bar, period of 650 nm illumination. Interruptions in the analysis are due to inability of the analysis script to assign periods of strong body bends when anterior and posterior body touched. (**C**) Photodepolarization of AS MNs by Chrimson (in animals raised with ATR): I, II) Body length and group data (II) of mean length of the animals before (15–20 s) and during (21–26 s) Chrimson photoactivation. (**D**) I, II) Locomotion speed: Mean ±SEM crawling speed of animals before and during blue illumination (red bar), comparing animals expressing Chrimson in AS MNs, raised in the presence or absence of ATR, and group data (II) of mean speed of the animals before (15–20 s) and during (21–26 s) Chrimson photoactivation. (**E**) I) Mean (±SEM) time traces of all 3-point bending angles before and during red illumination (red bar; animals raised with and without ATR). II) Group data as in I, comparing 5 s red light illumination (red bar), to the 5 s before illumination. III) Mean (±SEM) ratio of dorsal to ventral bending at the 2nd 3-point bending angle in animals expressing AS::Chrimson during photostimulation (animals raised with and without ATR). See also *Figure 1—video 2*. P values **$\leq$0.01; ***$\leq$0.001. Number of animals is indicated. Statistical test: ANOVA with Tukey's post hoc test.

DOI: https://doi.org/10.7554/eLife.34997.005
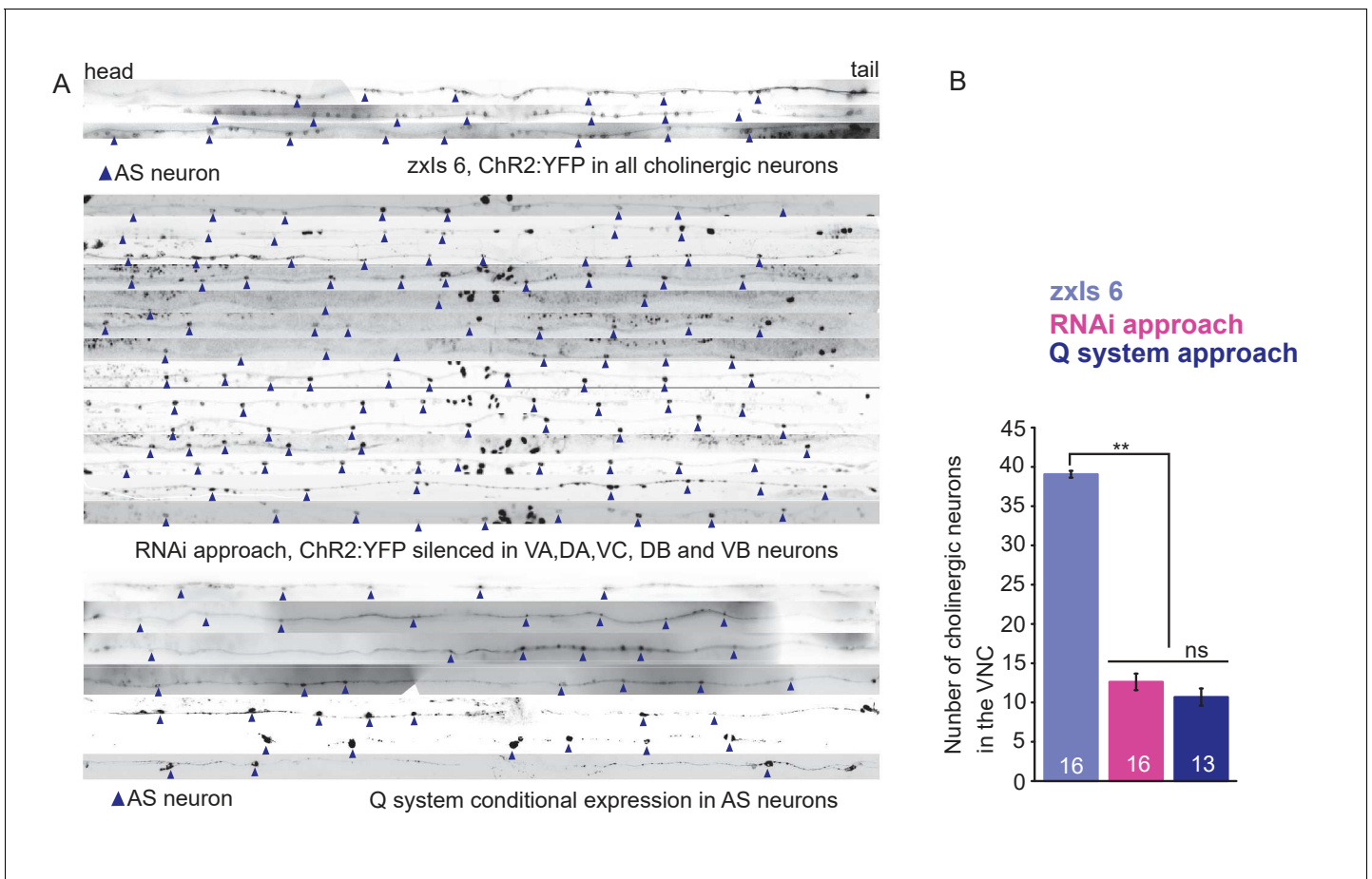
260

Figure 2. Photodepolarization of AS MNs causes transient activation of dorsal and simultaneous inhibition of ventral BWMs, and a dorsal bias in freely crawling animals. A) (I, II) Representative locomotion tracks of freely moving animals (raised with ATR) with ChR2 expressed in all cholinergic MNs (I) or only in AS MNs (II) before (20 s) and during photostimulation (20 s) by 470 nm blue light (indicated by blue shaded area; tracks are aligned such that they cross the blue area at the time of light onset). (III) Schematic showing the thirteen points defining eleven 3-point angles along the spine of the animal. (IV) Mean (±SEM) ratio of dorsal to ventral bending at the 2nd 3-point bending angle in animals expressing AS::ChR2 or ChR2 in all VNC cholinergic neurons during photostimulation (animals raised with and without ATR). (V) Mean (±SEM) time traces of all 3-point bending angles (absolute

Figure 2 continued on next page

261

Figure 2 continued

values) before and during blue illumination (blue bar; ChR2 in AS MNs or in all cholinergic MNs; raised with and without ATR). (VI) Group data of experiments in (V), comparing 20 s blue light illumination (blue bar), to the 20 s before illumination. (B) I) AS MNs expressing ChR2 are illuminated by 470 nm blue light, Ca^{2+} signal is recorded in the BWM expressing GCaMP3 (arrows, chemical synapses). (II) Representative snapshots of Ca^{2+} signals in BWM cells during blue light illumination in animals cultivated with and without all-trans-retinal (ATR). Lines indicate regions used to generate kymographs. (III) Representative kymograph of spontaneous Ca^{2+} fluctuations in BWM cells of animal raised without ATR. (IV) Representative kymograph of Ca^{2+} signals in BWM cells in animals cultivated with ATR, in which AS MNs were photostimulated for the entire period. (V, VI) Mean Ca^{2+} signals ($\Delta F/F \pm SEM$) in dorsal and ventral BWM during the first 10 s of illumination (V) in animals raised with and without ATR and group data (VI), quantified during the first 2 s of illumination. (VII) Transients of spontaneous Ca^{2+} signals in dorsal muscles in animal without ATR. VIII) Mean Ca^{2+} signals ($\Delta F/F \pm SEM$) in dorsal and ventral BWM in animals raised without ATR, but aligned to the first dorsal Ca^{2+} spike, showing reciprocity of spontaneous dorso-ventral muscle activity. See also *Figure 2—video 1*. P values *$\leq$0.05; **$\leq$0.01; ***$\leq$0.001; number of animals is indicated. Statistical test: ANOVA with Tukey's post-hoc test.

DOI: https://doi.org/10.7554/eLife.34997.008

262

Figure 3. Optogenetic ablation and chronic hyperpolarization of AS MNs disrupts the locomotion pattern. (**A**) I) Schematic of optogenetic ablation of AS MNs by PH-miniSOG and connectivity to relevant cell types (arrows, chemical synapses; curved lines, electrical synapses). Quantification of mean ±SEM speed (II) and bending angles (III) of animals without or with expression of PH-miniSOG (*via* the Q system) in AS MNs, following 150 s of blue light exposure and 2 hr resting period. IV) Representative body posture kymographs (as in *Figure 1C*) of wild type animal (upper panel) and animal

Figure 3 continued on next page

263

Figure 3 continued

expressing PH-miniSOG after photoactivation (lower panel). V) Schematic of Ca^{2+} imaging in BWM (RCaMP fluorescence) during PH-miniSOG ablation. VI) Representative transients of Ca^{2+} signaling in dorsal and ventral muscles after AS MN ablation by PH-miniSOG. VII) Mean Ca^{2+} signals (ΔF/F ± SEM) in dorsal and ventral BWM of animals without or with expression of PH-miniSOG. See also *Figure 3—figure supplement 1A* and *Figure 3—video 1*. (**B**) I) Schematic of Ca^{2+} imaging in BWM (RCaMP fluorescence) during hyperpolarization of AS MNs by HisCl1 (expressed in AS MNs *via* the Q system), and connectivity to relevant cell types (see also AI; note that this simplified diagram reflects cell type connectivity but does not accurately reflect connections between individual cells). (II) Mean ±SEM speed of freely moving animals on agar dishes without and with 10 mM histamine. (III) Representative body posture kymographs of animals freely moving on agar without (upper) or with 10 mM histamine (after 240 s incubation; lower panel). (IV) Representative fluorescent micrographs of Ca^{2+} activity in the BWM of animals mounted on agar slides without (left) or with 10 mM histamine (after 240 s incubation; right panel). (V) Representative kymographs (20 s) of Ca^{2+} activity in dorsal and ventral BWM of animals as in IV. (VI) Representative Ca^{2+} activity in dorsal and ventral BWM from animals as (shown in IV, V. VII) Mean ±SEM fluorescence of dorsal and ventral BWM as in VI. See also *Figure 3—figure supplement 1B* and *Figure 3—video 2*. P values *$\leq$0.05, ***$\leq$0.001; number of animals indicated in AII, VII; BII, VII. Statistics: T-test for AII, III and B II; ANOVA with Tukey's post-hoc test for A VII and BVII.

DOI: https://doi.org/10.7554/eLife.34997.010

264

Figure 3—figure supplement 1. Optogenetic inactivation and HisCl1-induced hyperpolarization of AS MNs affects locomotion speed and bending angles. (A) Time traces of mean (±SEM) speed (I) and bending angles (II) of freely moving wild type animals, or animals expressing PH-miniSOG in AS MNs, 2 hr after 150 s of blue light exposure. (B) Time traces of mean (±SEM) speed of freely moving animals expressing HisCl1in AS MNs, comparing animals on plates without and with 10 mM histamine. Number of animals tested is indicated.

DOI: https://doi.org/10.7554/eLife.34997.011
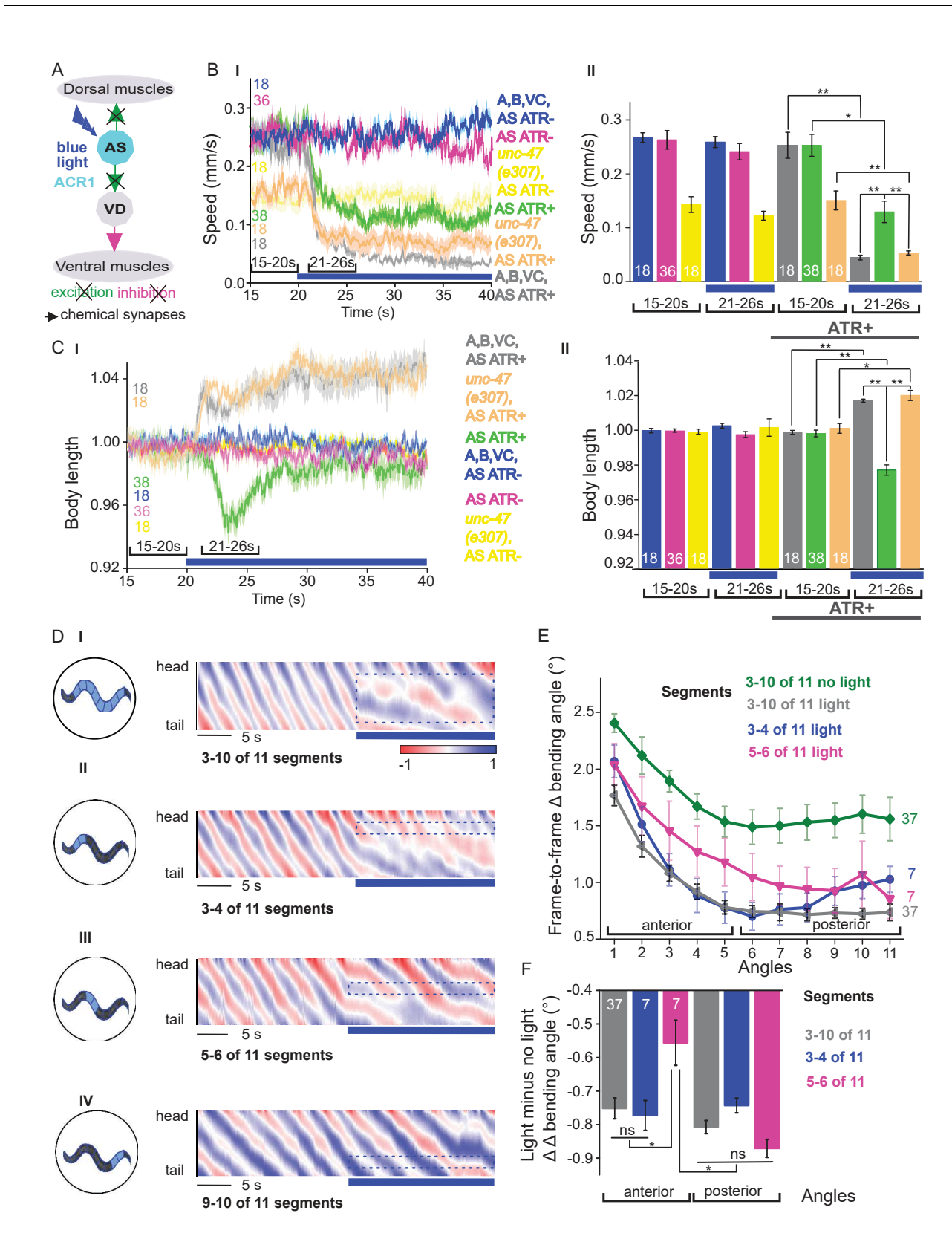
Figure 4. Acute optogenetic hyperpolarization of AS MNs ceases locomotion, causes disinhibition of ventral BWM via GABAergic VD MNs, and blocks propagation of the locomotion body wave. (**A**) Schematic of experiment; hyperpolarization of AS MNs by the ACR1 anion channel rhodopsin activated

Figure 4 continued on next page

266

Figure 4 continued

by 470 nm blue light (arrows, chemical synapses). (**B**) Time traces (I) and group data quantification (II) of mean ±SEM speed before (15 – 20 s) and during (21 – 26 s) blue illumination (indicated by blue bar). Compared are strains expressing ACR1 in all VNC cholinergic neurons, or in AS MNs only (*via* the Q system), in wild type or *unc-47(e307)* mutant background, raised in the presence or absence of ATR, as indicated. (**C**) Time traces (I) and group data quantification (II) of mean ±SEM body length of the animals shown in B. (**D**) Hyperpolarization of AS MNs in all (I), in the anterior (II), middle (III) and posterior (IV) segments of the worm body. Representative body postures kymographs of normalized 2-point angles from head to tail in animal expressing ACR1 in AS MNs before and during illumination by blue light in the indicated body segments. (**E**) Mean, absolute difference of bending angles, from one video frame to the next (25 Hz), at each of eleven 3-point angles, for experiments as in (**D**). (**F**) Mean difference of the differential bending angles between dark and illuminated conditions, for the analyses shown in (**E**). Data were averaged for the anterior five or the posterior 6 3-pt bending angles. See also *Figure 4—figure supplement 1* and *Figure 4—videos 2-4*. P values *$\leq$0.05; **$\leq$0.01; number of animals is indicated. Statistics: ANOVA with Tukey's post hoc test.

DOI: https://doi.org/10.7554/eLife.34997.014

Figure 4—figure supplement 1. Local stimulation of AS MNs in different body segments. (**A**) Schematic showing how the 13 points defining 11 3-point angles correspond to the 11 body segments that were individually illuminated. (**B**) Mean speed (I, II) and body length (III, IV) of animals expressing ACR1 in AS MNs, in which the indicated body segments were illuminated. Group data shown in II, IV. (**C**) The extrachromosomal array expressing ACR1 in the *unc-47(e307)* mutant as shown in main *Figure 4B,C* functions as expected in wt background. P value *≤0.05; number of animals is indicated. Statistical test in B: ANOVA with Tukey's post-hoc test.
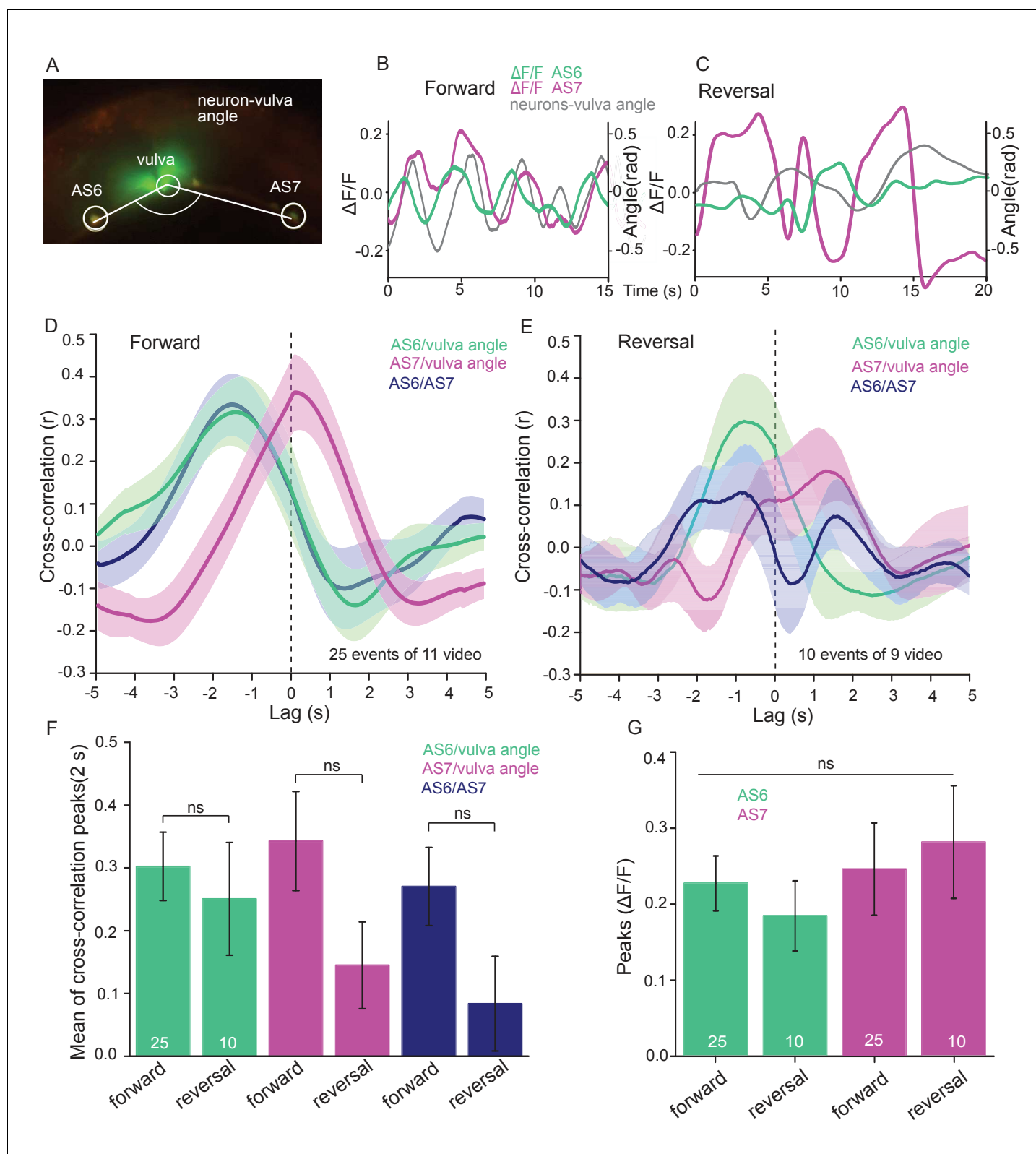
Figure 5. AS MNs show oscillatory Ca^{2+} activity in moving animals. (**A**) Fluorescent micrograph (merged channels) of the vulva region, showing red (mCherry) and green (GCaMP6), expressed in AS MNs (with the use of the Q system), and GFP, expressed in vulva muscles. Angle between vulva and the two flanking AS6 and AS7 neurons is indicated. (**B, C**) Representative analysis of time traces of Ca^{2+} signals (ΔF/F) in AS6 and AS7, as well as the angle defined by the vulva and the two neurons during crawling (B, 15 s, forward; C, 20 s, reverse). (**D, E**) Cross-correlation analysis (mean ± SEM) of

Figure 5 continued on next page

Figure 5 continued

single periods of the body wave (5 s each) for each of the AS6 and AS7 GCaMP6 signals with the vulva angle, as well as for the two Ca^{2+} signals, during forward (D) or backward (E) locomotion. (F) Comparison of the mean cross-correlation peaks (during the 2 s centered on the peak) of the fluorescence of AS6 or AS7 and the neuron/vulva angle, or between AS6 and AS7 neurons, for forward or reverse locomotion. (G) Comparison of the peak Ca^{2+} signals (mean ± SEM) in AS6 and AS7, during forward or reverse locomotion, respectively. See also *Figure 5—video 1*. Number of animals is indicated in D-G. Statistical test: ANOVA with Tukey's post-hoc test.

270

Figure 6. Reciprocal and asymmetric mutual activation of AS MNs and forward and reverse PINs, AVB and AVA. (**A**) (I) Schematic of the experiment for measurement of AS MN Ca²⁺ signals (GCaMP6) during AVB or AVA photodepolarization *via* ChR2 with 470 nm blue illumination (arrows, chemical synapses; curved lines, electrical synapses). (II, III) Time traces of mean (±SEM) Ca²⁺ transients (*ΔF/F*) in AS MNs during depolarization of AVA (II) and AVB (III) by ChR2, in animals raised in absence or presence of ATR. Brackets indicate time periods used for statistical analysis in IV. (IV) Group data quantification of experiments shown in II and III (for the 1–3 s time period). See also *Figure 6—figure supplement 1* and *Figure 6—video 1, 2*. (**B**) (I-IV), as in A (I-IV), but in the *unc-7(e5)* gap junction mutant background. (**C**) (I) Schematic of the experiment for measurement of Ca²⁺ signals (cameleon) in AVB or AVA PINs during AS MN photodepolarization *via* ChR2. (II, III) Mean (±SEM) of Ca²⁺ transients (*ΔR/R* YFP/CFP ratios) in AVA (II) and AVB (III) during AS MN depolarization, in wild type or *unc-7(e5)* mutant animals, raised in absence or presence of ATR. IV) Group data quantification of experiments in II and III (for the 0–1 s time period). P values *≤0.05; **≤0.01; ***≤0.001; number of animals is indicated. Statistical test: Mann-Whitney U test.

DOI: https://doi.org/10.7554/eLife.34997.022

Figure 6—figure supplement 1. AS MNs are simultaneously activated by photostimulation of the AVA and AVB PINs. (**A,B**) Cross-correlation analysis of GCaMP6 fluorescence signals (ΔF/F) in AS3 and AS8 neurons, during photodepolarization of AVA (A) or AVB (B), expressing ChR2, respectively, in animals raised in the presence of ATR.

Figure 7. Models summarizing findings of this work. (**A**) AS MNs asymmetrically regulate dorso-ventral bending during forward and backward locomotion, by excitatory chemical transmission to dorsal muscles and ventral GABAergic VD MNs, thus causing ventral inhibition. Interconnections (arrows, chemical synapses; curved lines, electrical synapses; thickness of lines indicates relative synapse number as an approximation of synaptic strength; color shade represents strength of functional connections measured in this work) of AS MNs and their other synaptic partners,that is the PINs AVB and AVA, via both chemical synapses from the PINs and (reciprocal) electrical synapses from AS MNs are also shown. Data in this work suggest (chemical) excitatory regulation of AS MNs by AVA and AVB during forward and backward locomotion, respectively, and reciprocal electrical regulation of AVA by AS MNs. (**B**) Interconnections and functional roles of AS MNs and other VNC MNs during the propagation of the undulatory wave along the body. Depolarization (which could be initiated by AVB, not shown here, or by proprioceptive feedback from the adjacent body segment) of AS MNs causes contraction of the dorsal BWMs and simultaneous relaxation of ventral BWMs through the excitation of VD MNs. This phase is followed by contraction of ventral BWMs, e.g. through the electric coupling of AS and VA MNs, and relaxation of the dorsal BWMs through VD-DD electrical coupling or VA-DD chemical synapses. Cholinergic (orange) and GABAergic (blue) cell types are indicated. Antero-posterior localization of cell bodies and connectivity to other cell types are arbitrary.

DOI: https://doi.org/10.7554/eLife.34997.026

2.10 Rhodopsin optogenetic toolbox v2.0 for light-sensitive excitation and inhibition in *Caenorhabditis elegans*

The following pages contain the published version of the research article "Rhodopsin optogenetic toolbox v2.0 for light-sensitive excitation and inhibition in *Caenorhabditis elegans*"[9]. Material from: Bergs, A. *et al*. Rhodopsin optogenetic toolbox v2.0 for light-sensitive excitation and inhibition in *Caenorhabditis elegans*. *PloS one* **13**, e0191802; 10.1371/journal.pone.0191802 (2018).

Rhodopsin optogenetic toolbox v2.0 for light-sensitive excitation and inhibition in *Caenorhabditis elegans*

Amelie Bergs[1,2,3], **Christian Schultheis**[1,2¤a], **Elisabeth Fischer**[1,2¤b], **Satoshi P. Tsunoda**[1,2¤c], **Karen Erbguth**[1,2], **Steven J. Husson**[4], **Elena Govorunova**[5], **John L. Spudich**[5], **Georg Nagel**[6], **Alexander Gottschalk**[1,2,7]*, **Jana F. Liewald**[1,2]*

1 Buchmann Institute for Molecular Life Sciences, Goethe-University, Frankfurt, Germany, **2** Department of Biochemistry, Chemistry and Pharmacy, Institute of Biophysical Chemistry, Goethe-University, Frankfurt, Germany, **3** International Max Planck Research School in Structure and Function of Biological Membranes, Frankfurt, Germany, **4** Systemic Physiological & Ecotoxicological Research (SPHERE), University of Antwerp, Antwerp, Belgium, **5** Center for Membrane Biology, Department of Biochemistry and Molecular Biology, University of Texas Health Science Center at Houston, McGovern Medical School, Houston, Texas, United States of America, **6** Department of Biology, Institute for Molecular Plant Physiology and Biophysics, Julius-Maximilians-University of Würzburg, Würzburg, Germany, **7** Cluster of Excellence Frankfurt - Macromolecular Complexes (CEF-MC), Goethe University, Frankfurt, Germany

¤a Current address: Boehringer-Ingelheim Pharma GmbH & Co KG, Biberach, Germany
¤b Current address: University of Edinburgh, Centre for Integrative Physiology, Hugh Robson Building, George Square, Edinburgh, United Kingdom
¤c Current address: JST Presto, 4-1-8 Honcho, Kawaguchi, Saitama, Japan
* a.gottschalk@em.uni-frankfurt.de (AG); liewald@biochem.uni-frankfurt.de (JFL)

Abstract

In optogenetics, rhodopsins were established as light-driven tools to manipulate neuronal activity. However, during long-term photostimulation using channelrhodopsin (ChR), desensitization can reduce effects. Furthermore, requirement for continuous presence of the chromophore all-*trans* retinal (ATR) in model systems lacking sufficient endogenous concentrations limits its applicability. We tested known, and engineered and characterized new variants of de- and hyperpolarizing rhodopsins in *Caenorhabditis elegans*. ChR2 variants combined previously described point mutations that may synergize to enable prolonged stimulation. Following brief light pulses ChR2(C128S;H134R) induced muscle activation for minutes or even for hours ('Quint': ChR2(C128S;L132C;H134R;D156A;T159C)), thus featuring longer open state lifetime than previously described variants. Furthermore, stability after ATR removal was increased compared to the step-function opsin ChR2(C128S). The double mutants C128S;H134R and H134R;D156C enabled increased effects during repetitive stimulation. We also tested new hyperpolarizers (ACR1, ACR2, ACR1(C102A), ZipACR). Particularly ACR1 and ACR2 showed strong effects in behavioral assays and very large currents with fast kinetics. In sum, we introduce highly light-sensitive optogenetic tools, bypassing previous shortcomings, and thus constituting new tools that feature high effectiveness and fast kinetics, allowing better repetitive stimulation or investigating prolonged neuronal activity states in *C. elegans* and, possibly, other systems.

Introduction

Optogenetics allows versatile modulation of the activity of cells with high spatiotemporal resolution using light [1, 2]. Many optogenetic tools have been developed in the past decade. Most numerous are the microbial opsins, which mediate ionic currents across the plasma membrane [3]. Following heterologous expression, they can be used to gain control over excitable cells in living tissue or freely behaving animals, and even patterns of neuronal activity can be mimicked [4]. Rhodopsin optogenetic tools are used in various model organisms, from the nematode *C. elegans* [5–9] to non-human primates like the macaque [10, 11], to study basic mechanisms of synaptic transmission but also the function of neuronal circuits generating complex behaviors.

A range of optogenetic tools is available for activation–i.e. depolarization (e.g. ChR2)—or inhibition—i.e. hyperpolarization (e.g. NpHR) of excitable cells [12–21]. Nevertheless, current tools are still limited in their applicability, mostly as temporal control (e.g. repetitive or long-term excitation) or effectiveness are often not sufficient for more complex protocols, particularly in invertebrate models where ATR supplementation is required. Thus, there is a continuous interest to expand the toolbox in order to allow for a broader range of precise applications. Novel rhodopsins are either identified by screening sequenced genomes or by site-directed mutagenesis of established proteins [17, 22–26]. In case of ChR2, point mutations were identified that affect its membrane expression, ion selectivity, conductivity, kinetics, or action spectrum [27, 28]. The H134R mutation increases plasma membrane expression [29] as well as steady-state photocurrents, and data from *C. elegans* and other expression hosts suggest that H134R stabilizes incorporation of all-*trans* retinal (ATR) [7, 8, 27, 30]. ChR2(T159C) exhibits improved plasma membrane expression and increased channel conductivity, leading to larger photocurrents [21, 31]. The CatCh (calcium translocating channelrhodopsin; L132C) variant increases Ca^{2+} conductivity and apparent light sensitivity, presumably due to charge effects of Ca^{2+} at the cytosolic leaflet of the plasma membrane improving activation of voltage-gated Na^+ channels [32]. Thus, even very low light intensities can trigger action potentials.

Other ChR2 mutants affect photocycle kinetics and are useful for particularly fast or long-lasting depolarization. ChETA (E123T) accelerates channel closing and recovery from the desensitized state and can trigger exceptionally fast depolarizations, allowing elicitation of action potentials with high frequency (up to 200 Hz) [33]. Likewise, Chronos and Chrimson enable fast spiking [19]. In contrast, mutation of ChR2-Cys128 to Thr, Ala, or Ser, or of Asp156 to Cys were shown to decelerate closing kinetics [8, 34, 35]. Following brief photoactivation, the open channel is stabilized, allowing depolarizations from seconds to minutes. Consequently, the operational light sensitivity is increased. Subsequent inactivation using a different wavelength enables a step-like switching. This 'step-function' property enables to mimick ongoing neuronal activity or reducing action potential thresholds. Yet, several properties limit the utility of such 'slow' variants for long-term depolarization in the range of hours, as could be of interest in developmental biology [8]. First, with closing kinetics in the range of seconds to minutes, they require repetitive stimulation to induce sustained depolarization for longer time periods. However, ChR2(C128S) and ChR2(C128T) enter long-lived desensitized states after channel closing, impeding immediate reactivation [34]. Furthermore, ChR2 (C128S) requires continuous supplementation of ATR to maintain sustained excitability [8]. The mutation may lead to loss of ATR, as indicated in resonance Raman spectroscopy measurements: The P353 photo-intermediate exhibited a signature of hydrolysis and reformation of the Schiff base, and transient formation of free ATR [30]. This affects ChR2(C128S) utility in organisms that require addition of ATR, like *C. elegans*, *Drosophila*, and to some extent,

276

Xenopus oocytes. Thus, ChR2 variants with further delayed closing kinetics combined with enhanced off-ATR excitability would be highly desirable.

Optically triggered hyperpolarization, leading to transient inactivation of excitable cells, is a potent means to gather information on the function of specific neurons. Commonly, light-driven ion pumps (e.g. NpHR) are agents of choice for membrane hyperpolarization [6, 15, 16, 18]. However, the active transport of pumps restricts the utility of these tools. At least under certain conditions, e.g. at high depolarization where the driving force for Cl$^-$ influx is high, ion channels would yield much higher current. Since only one ion is moved per photocycle, pumps require continuous stimulation, and they cannot take advantage of photocycle-affecting mutations [16]. Yet, as their action is usually independent of the membrane potential, pumps are also advantageous over channels, particularly at hyperpolarized potentials.

In search for a light-gated Cl$^-$-channel ChR2 was modified by site-directed mutagenesis: iC1C2, a ninefold mutated version of the C1C2 chimera [26], or ChloC (Chloride-conducting ChR2 [17]). As the latter retained some proton conductance, causing small, yet significant depolarization, two additional amino acids in the proton pathway were substituted, generating improved ChloC (iChloC) [36]. iC1C2 was improved to iC++, with 15x higher currents [37]. Even more effective are the natural anion channel rhodopsins which were identified in cryptophyte algae (ACR1, ACR2; here used for *Gt*ACR1 and *Gt*ACR2 from *Guillardia theta*)[24], and in additional species a whole range of channels was analyzed [38]. Their peak currents are larger than those of iChloC, iC1C2 or iC++ (ACR2 conducts ≈3-fold higher current than iC++ [24, 37]). While ACR2 exhibits particularly fast kinetics, ACR1 shows larger plateau currents and has a slightly red-shifted action spectrum (515 nm peak compared to 470 nm for ACR1). Being fast, exhibiting a ≈1000-fold higher operational light sensitivity (ACR2; Ref. [24]) than previously used hyperpolarizers and showing a very high conductance, ACRs are particularly interesting for optogenetic inhibition, as was recently demonstrated in *Drosophila* [39].

In a screening study for ACR homologues, ZipACR was identified as another promising tool for optogenetic silencing. In HEK293 cells, it induced even larger currents than ACR1, and featured an unprecedentedly fast conductance cycle. In cultured mouse hippocampal neurons, it enabled inhibition of individual spikes up to 50 Hz [38]. Searching for tools with slow closing kinetics, Cys102 in ACR1 was identified as the corresponding residue to Cys128 in ChR2. Accordingly, mutation in ACR1(C102A) resulted in decreased current amplitudes but also in dramatically prolonged current decay, making it 100-fold slower than wild-type ACR1 [40, 41].

In the present study, we explored the use of novel de- and hyperpolarizing optogenetic tools in *C. elegans*, with a focus on the utility in this important model system in behavioral, cellular and molecular neurosciences [13, 42–45]. Because of its small, well-defined nervous system [46] and its transparency, it is ideally suited for optogenetics. Tools affecting membrane potential can be tested in body-wall muscles (or cholinergic neurons), causing muscle contraction or relaxation (measured by video microscopy), and electrophysiologically accessible currents. For depolarizers, we combined several single mutations already known for ChR2 [7, 8, 21, 27, 29, 31, 32, 35], aiming to generate variants that unify favorable attributes of these mutations, particularly for long-term depolarization. Additionally, we examined some known variants that had not previously been tested in *C. elegans*. We analyzed the extent, duration, and repeatability of activation, operational light-sensitivity, and excitability after removing the animals from of ATR. The very efficient quintuple mutant 'Quint' allows depolarization for 8–10 h following a single light pulse, while ChR2(H134R;D156C) exhibited highest operational light sensitivity. For hyperpolarizers, we probed the potential of ACR1, ACR2, ACR1(C102A), and ZipACR as alternatives to the commonly used light-driven pumps. Particularly ACR1 and

277

ACR2 led to stable effects with fast kinetics and (at depolarized membrane potentials) higher photocurrents compared to NpHR.

Materials and methods

C. elegans culture and transgenic animals

Nematodes were cultivated on NGM plates seeded with *E. coli* OP-50 bacteria, optionally supplemented with ATR (Sigma-Aldrich, Germany) [13]. Transgenic animals were obtained by microinjection using varying concentrations of plasmid DNA. Strains ZX1788, ZX2022, ZX2023, ZX2024, ZX2026, ZX2206, and ZX2207 were generated via injection of 30ng/µl plasmid DNA each, combined with 5ng/µl of the co-marker pmyo-3::mCherry (ZX2024, ZX2026), 10ng/µl of pmyo-2::mCherry (ZX2022, ZX2023, ZX2206, ZX2207), or 10ng/µl of pelt-2:: mCherry (ZX1788) into gonads of N2 by standard procedures [47]. The reason for using different DNA amounts was that some constructs did not yield healthy strains when expressed at higher levels or that different amounts of plasma membrane expression were achieved. Since it is virtually impossible to control the precise amount of plasma membrane content of heterologously expressed membrane proteins, we rather generated several transgenic lines for each construct, choosing lines with similar transgene transmittance, mosaicism and membrane expression. Strains expressing pmyo-3::ChR2(C128S;H134R)::YFP and pmyo-3::ChR2-Quint:: YFP were produced by injection of 100ng/µl (ZX1295, ZX1299), 40ng/µl (ZX1296, ZX1300), 10ng/µl (ZX1297, ZX1301), or 2ng/µl (ZX1298, ZX1302) plasmid DNA. CatCh-related animals were obtained by microinjection of 80ng/µl plasmid DNA combined with 1.5ng/µl of pmyo-2:: mCherry (ZX1826, ZX1827, ZX1830).

The following transgenic strains were used or generated: **ZX299**: *lin-15(n765ts-);zxEx22 [pmyo-3::ChR2(H134R)::YFP;lin-15+]*, **ZX444**: *lin-15(n765ts-);zxEx301[pmyo-3::NpHR::ecfp; lin-15+]*, **ZX838**: *lin-15(n765ts-);zxEx423[pmyo-3::ChR2(C128S)::YFP;lin-15+]*, **ZX954**: *lin-15 (n765ts-);zxEx468[pmyo-3::ChR2(C128S;H134R)::YFP;lin-15+]*, **ZX1166**: N2;*zxEx536[pmyo-3:: ChR2(T159C)::YFP;pmyo-2::mCherry]*, **ZX1167**: N2;*zxEx537[pmyo-3::ChR2(H134R;T159C):: YFP;pmyo-2::mCherry]*, **ZX1295**: *lin-15(n765ts-);zxEx477[pmyo-3::ChR2(C128S;H134R)::YFP (100ng/µl);lin-15+]*, **ZX1296**: *lin-15(n765ts-);zxEx478[pmyo-3::ChR2(C128S;H134R)::YFP (40ng/µl);lin-15+]*, **ZX1297**: *lin-15(n765ts-);zxEx479[pmyo-3::ChR2(C128S;H134R)::YFP(10ng/ µl);lin-15+]*, **ZX1298**: *lin-15(n765ts-);zxEx480[pmyo-3::ChR2(C128S;H134R)::YFP(2ng/µl);lin-15+]*, **ZX1299**: *lin-15(n765ts-);zxEx477[pmyo-3::ChR2-Quint::YFP(100ng/µl);lin-15+]*, **ZX1300**: *lin-15(n765ts-);zxEx478[pmyo-3::ChR2-Quint::YFP(40ng/µl); lin-15+]*, **ZX1301**: *lin-15(n765ts-); zxEx479[pmyo-3::ChR2-Quint::YFP(10ng/µl);lin-15+]*, **ZX1302**: *lin-15(n765ts-);zxEx480[pmyo-3::ChR2-Quint::YFP(2ng/µl);lin-15+]*, **ZX1788**: N2;*zxEx1036[pmyo-3::ChR2(H134R;D156C):: YFP(30ng/µl);pELT-2::mCherry]*, **ZX1826**: N2;*zxEx740[pmyo-3::ChR2(C128S;L132C;H134R):: YFP;pmyo-2::mCherry]*, **ZX1827**: N2;*zxEx741[pmyo-3::ChR2(L132C)::YFP(80ng/µl);pmyo-2:: mCherry]*, **ZX1830**: N2;*zxEx744[pmyo-3::ChR2(L132C;H134R;T159C)::YFP(80ng/µl);pmyo-2:: mCherry]*, **ZX2022**: N2;*zxEx1031[pmyo-3::ACR1::eYFP(30ng/µl);pmyo-2::mCherry]*, **ZX2023**: N2;*zxEx1032[pmyo-3::ACR2::eYFP(30ng/µl);pmyo-2::mCherry]*, **ZX2024**: N2;*zxEx1033[punc-17::ACR1::eYFP(30ng/µl);pmyo-3::mCherry]*, **ZX2026**: N2;*zxEx1034[punc-17::ACR2::eYFP (30ng/µl);pmyo-3::mCherry]*, **ZX2206**: N2;*zxEx1073[pmyo-3::ACR1(C102A)::eYFP(30ng/µl); pmyo-2::mCherry]*, **ZX2207**: *N2;zxEx1074[pmyo-3::ZipACR::eYFP(30ng/µl);pmyo-2::mCherry]*.

All experiments were done using young adult hermaphrodites (picking L4 animals the evening before the experiment).

Animals expressing tools with enhanced light sensitivity (particularly Quint) were cultivated under zero light conditions to avoid stimulation. This included wrapping of NGM plates

with aluminum foil and keeping them in a closed incubator. Handling of animals was done under low-level red light using appropriate filter glass.

Molecular biology

Plasmids pAG54 (pmyo-3::ChR2(H134R)::YFP) [7], pCoS6 (pglr-1::loxP::LacZ::STOP::loxP:: ChR2(H134R)::mCherry::SL2::GFP) [48], pCS86 (pmyo-3::ChR2(C128S)::YFP) [8], pCS106 (pglr-1::ChR2(C128S)::YFP) [8], pCS126 (punc-47::ChR2(C128S)::YFP) [8], and pNP259 (pgpa-14::Cre) [48] were described earlier. The plasmid pCS116 (pmyo-3::ChR2(C128S; H134R)::YFP) was generated from pCS86 (pmyo-3::ChR2(C128S)::YFP) by site-directed mutagenesis using the primers oCS222 (5′-GGTCATTCTCATTCGCCTGTCAAACCTGAC-3′) and oCS223 (5′-GTCAGGTTTGACAGGCGAATGAGAATGACC-3′).

A PCR fragment amplified from pCS116 using primers oCS305 (5′-CACCTCACCGGTCATTTGCATTCGCC-3′) and oCS306 (5′-CCGGTGGCCATGGCGGAAGTGGCGCCCCACACAATGCAGCCAATAGCAG-3′) was cloned into pCS126 using the restriction enzymes *Age*I and *Msc*I, resulting in pCS172 (punc-47::ChR2(C128S;L132C;H134R;D156A;T159C)::YFP). A fragment of ChR2 including the five point mutations was subcloned into pCS116 with *Age*I and *Pvu*II to generate pCS173 (pmyo-3::ChR2(C128S;L132C;H134R;D156A;T159C)::YFP).

To construct pKE34 (pmyo-3::ChR2(T159C)::YFP) a PCR product was amplified from pChR2(T159C), using primers oKE79 (5`-GTCGTCAATGGCTCTGTACTTGTG-3`) and oKE80 (5`-AGAGCCAAGCCATGCCAGTC-3`) and inserted into pmyo-3::ChR2::YFP with *Bsu*36I and *Dra*III restriction sites.

To generate pKE35 (pmyo-3::ChR2(H134R;T159C)::YFP) two PCRs were performed with oKE79+81 (5`-GCCAATATCAGACACAAGCAGACC-3`) and oKE80+82 (5`-GGGTCTGCTTGTGTCTGATATTGG-3`) from pmyo-3::ChR2(H134R)::YFP and pKE34, respectively, leading to fragments carrying H134R and T159C separately, that were fused and inserted in the pmyo-3::ChR2(H134R)::YFP vector.

To construct pEF 11 (pmyo-3::ChR2(L132C)::YFP) pChR2(L132C) (a gift from E. Bamberg) and pmyo-3::ChR2(H134R)::YFP were restricted with *Dra*III and *Xho*I and the ChR2 (L132C) fragment was inserted into the pmyo-3::ChR2(H134R)::YFP backbone. pEF 14 (pmyo-3::ChR2(L132C_H134R_T159C)::YFP) was contructed by fusion PCR amplification generating fragments from pEF 11 with primer pairs oKE79 (5`-GTCGTCAATGGCTCTGTACTTGTG-3`), oAD22rev (5`-GACAGGCGAATGCAAATGACC-3`), and oAD22fw (5`-GGTCATTTGCATTCGCCTGTC-3`), oKE81 (5`-GCCAATATCAGACACAAGCAGACC-3`) and then fused with primer pair oKE79/81 and inserted into pEF11 with *Bsu*36I and *Dra*III restriction sites. pEF15 (pmyo-3::ChR2(C128S;L132C;H134R)::YFP) was generated by fusion PCR with fragments from pEF11 amplified with primer pairs oKE79 (5`-GTCGTCAATGGCTCTGTACTTGTG-3`), oAD23rev (5`-GACAGGCGAATGCAAATGACCGGTGAGGTG-3`), and oAD23fw (5`-CACCTCACCGGTCATTTGCATTCGCCTGTC-3`), oKE81 (5`-GCCAATATCAGACACAAGCAGACC-3`), fused with primer pair oKE79/81 and followed by restriction with *Bsu*36I and *Dra*III and insertion into pEF11.

The plasmid pAB05 (pmyo-3::ChR2(H134R;D156C)::YFP), was generated from plasmid pmyo3::CHOP-2(H134R-g.o.f.)::YFP, by site-directed mutagenesis using primers oST56 (5′-CATGGGTCTGCTTGTGTCTTGTATTGGCACAATTGTGTG-3′) and oST57 (5′-ACACAATTGTGCCAATACAAGACACAAGCAGACCCATG-3′). The constructs pAB01 (pmyo-3::ACR1::eYFP) and pAB02 (pmyo-3::ACR2::eYFP) were generated via subcloning of ACR1 (pFUGW-hGtACR1-eYFP) and ACR2 (pFUGW-hGtACR2-eYFP) [24] into pmyo-3 vector pDD96.52 (Fire Lab Vector Kit), using restriction enzymes *Eco*RI and *Xba*I. Subloning into the punc-17 vector RM#348p (gift from J. Rand) with restriction enzymes *Hinc*II and *Nhe*I for RM#348p

279

and *Eco*RI and *Xba*I for pFUGW-hGtACR1-EYFP and pFUGW-hGtACR2-EYFP resulted in plasmids pAB03 (punc-17::ACR1::eYFP) and pAB04 (punc-17::ACR2::eYFP).

The plasmid pAB09 (pmyo-3::ACR1(C102A)::eYFP) was generated from plasmid pAB01 (pmyo-3::ACR1::eYFP) by site-directed mutagenesis using primers ACR1_Q5_fwd (5′-GGTGT GCACCGCCCCTATCATGCTGG-3') and ACR1_Q5_rev (5′-CAGCTGGCCATTCTGGCC-3′).

The construct pAB10 (pmyo-3::ZipACR::eYFP) was generated via subcloning of ZipACR (pFUGW-ZipACR-eYFP) [38] into the pmyo-3 vector pDD96.52 (Fire Lab Vector Kit), using the restriction enzymes *Bam*HI and *Eco*RI.

For plasmid maps of all optogenetic tools see S3–S15 Data.

Fluorescence microscopy

Transgenic animals were transferred on 2% agarose pads in M9 buffer (K_2PO_4 20mM; Na_2HPO_4 40mM; NaCl 80mM; $MgSO_4$ 1mM) and immobilized with 1μl 50mM NaN_3 solution (Sigma-Aldrich, Germany) in M9. Expression was analysed using a Zeiss Axiovert 200 or Observer microscope, equipped with a 100W HBO mercury lamp, and a YFP or GFP filterset (AHF Analysentechnik, Germany). Images were obtained with a Axiocam MRm and Axiovi-sion software (Zeiss, Germany), with CoolSNAP HQ2 camera (Photometrics, USA) and Meta-Vue software (Molecular Devices, USA), or with OrcaFlash 4.0 (Hamamatsu, Germany) and μ-Manager software [49].

Behavioral experiments

Transgenic animals were cultivated overnight on ATR-supplemented NGM plates: 0.15μl of stock (100mM in ethanol) mixed with 300μl OP-50 bacterial solution and spread on 6cm dishes containing 10ml NGM. Prior to experiments, animals were transferred to unseeded NGM plates, enabling video analysis free from artefacts. Light intensity was adjusted by neutral density filters (AHF Analysetechnik, Germany) and monitored using an optical power meter (PM100, Thorlabs, USA). Recording of body length changes was performed on an Axiovert 40 CFL microscope (Zeiss, Germany) with 10x magnification using a Powershot G9 camera (Canon, USA). For photoactivation, transgenic animals were exposed to light pulses of the respective wavelength (HBO50 light source), controlled via a computer- or Arduino (https://www.arduino.cc)-driven shutter (Sutter Instruments, USA).

For analysis, videos were extracted and individual frames were processed with custom writ-ten scripts for ImageJ (National Institutes of Health, USA; https://imagej.nih.gov/ij/index.html [8]) or Matlab (Mathworks, USA) to yield bodylength [13]. Frames yielding false values (e.g. animals coiled) were excluded. For raw data of contraction assays please see S1 Data (depolar-izers) and S2 Data (hyperpolarizer). For evaluation of data, bodylength was normalized to recording period prior to illumination. Light pulse protocols, wavelengths, and intensities were specifically adjusted for each experiment as indicated in the figure legends.

For analysis of off-ATR excitability, animals were cultivated in presence of ATR until young adulthood and then transferred to freshly seeded plates without ATR. At specific time points after transfer, body contractions evoked by light stimulation were analyzed.

Electrophysiology in *C. elegans*

For recordings from BWMs animals were immobilized with Histoacryl glue (B. Braun Surgi-cal, Spain) and a lateral incision was made to access neuromuscular junctions along the ventral nerve cord. The basement membrane overlying muscles was enzymatically removed by incu-bation in 0.5mg/ml collagenase for 10s (C5138, Sigma-Aldrich, Germany). Muscles were patch-clamped in whole-cell mode at 22˚C using an EPC10 amplifier with head stage

280

connected to a standard HEKA pipette holder for fire-polished borosilicate pipettes (1B100F-4, WPI, USA) of 4-7-MΩ resistance. For all tools, the bath solution contained: NaCl 150mM; KCl 5mM; CaCl$_2$ 5mM; MgCl$_2$ 1mM; glucose 10mM; sucrose 5mM; HEPES 15mM, pH7.3 with NaOH, $\approx$330mOsm. For all depolarizing tools, the pipette solution contained: KCl 120mM; KOH 20mM; MgCl$_2$ 4mM; N-tris[Hydroxymethyl]methyl-2-aminoethane-sulfonic acid 5mM; CaCl$_2$ 0.25mM; sucrose 36mM; EGTA 5mM; Na$_2$ATP 4mM, pH7.2 with KOH, $\approx$315mOsm. Recordings were conducted at a holding potential of -60mV. For all hyperpolarizing tools, the pipette solution contained Potassium-gluconate 115mM; KCl 25mM; CaCl$_2$ 0.1mM; BAPTA 1mM; HEPES 50mM, pH7.3 with 1M KOH, $\approx$330mOsm. Recordings were conducted at a holding potential of 0mV. Light activation was performed using a LED lamp (KSL-70, Rapp OptoElectronic, Germany; 8mW/mm^2) and controlled by Patchmaster software (HEKA, Germany). Data were analyzed by Patchmaster software (HEKA, Germany).

Electrophysiology in HEK293 cells

HEK293 cells were transfected using the ScreenFectA transfection reagent (Waco Chemicals, USA). ATR (Sigma) was added as a stock solution in ethanol at the final concentration of 4µM. Photocurrents from the ACR(C102A) mutant expressed in HEK293 cells (S5i Fig) were recorded 48h after transfection with an Axopatch 200B amplifier (Molecular Devices, USA) using the 2kHz low-pass Bessel filter. The signals were digitized at 5kHz with a Digidata 1440A using pClamp 10 software (both Molecular Devices). Patch pipettes with resistances of 2-5MΩ were fabricated from borosilicate glass. The pipette solution contained (in mM): K-gluconate 135, MgCl$_2$ 2, HEPES 20, pH7.2. The bath solution contained (in mM): NaCl 150, CaCl$_2$ 1.8, MgCl$_2$ 1, glucose 5, HEPES 10, pH7.4. Continuous light pulses were provided by a Polychrome V light source (T.I.L.L. Photonics GMBH, Germany) at the half-bandwidth 15nm in combination with a mechanical shutter (Uniblitz Model LS6, Vincent Associates, USA; half-opening time 0.5ms). The quantum density at the focal plane of the 40x objective lens was 7.7mW/mm^2. All measurements were carried out at room temperature (25˚C).

Statistics

Data were analyzed in OriginPro 2015G (OriginLab Corporation, USA). Data are given as means±SEM. Significance between data sets after two-tailed Student's t-test or ANOVA is given as p-value (* p $\leq$ 0.05; ** p $\leq$ 0.01; *** p $\leq$ 0.001), the latter after Bonferroni′s multiple comparison test, or Tukey's post-hoc test.

Results

Characterization of ChR2 variants for long-term depolarization

Several ChR2 variants have been established for long-term depolarization, exhibiting a sloweddown photocycle due to modifications within the DC gate. We attempted to overcome limitations such as desensitized states after channel-closing [8] and dependence on continuous presence of ATR by combining known point mutations. In *C. elegans*, ChR2(H134R) had shown improved expression, reduced desensitization, and sustained excitability after removal of ATR [27, 50]. Thus, we included the H134R mutation in all tools generated. In double, triple, and quintuple mutants we combined H134R with C128S, D156A or D156C, all slowing down kinetics to various degrees [35, 51, 52], with L132C for increased Ca^{2+} conductance [32], and with T159C for increased plasma membrane insertion or conductivity [21] (Table 1; values for Mac and Arch were calculated from experiments published in [6]).

281

Table 1. Summary of results.

Tool		Change in body length (tool expressed in BWM) [%]	τ_{relax} [s]	Light sensitivity	Repeatability of stimulation	off-ATR excitability	Advantages of the most significant opsins screened
DEPOLARIZERS							
ChR2(H134R)		-14.9	1.1	-		++	
ChR2(C128S)		-14.6	181.7	++	-	-	
ChR2(L132C)	CatCh	-13.5	0.7	o			
ChR2(T159C)		-6.4	0.3				
ChR2(C128S;H134R)		-14.6	841.3	++	+	++	
ChR2(H134R;D156C)		-14.3	527.8	++++	++		
ChR2(H134R;T159C)		-14.7	0.6				
ChR2(C128S;L132C;H134R)		-10.7	1253.9	+++			
ChR2(L132C;H134R;T159C)		-16.3	2.3	+++			
ChR2(C128S;L132C;H134R;D156A;T159C)	Quint	-12.8	45370.1	+++		+	very slow closing kinetics high operational light sensitivity good off-ATR excitability
HYPERPOLARIZERS							
ACR1		+6.1	0.57	+++++	+		high photocurrents high operational light sensitivity red-shifted action spectrum
ACR2		+4.8	0.14	+++++	+		high photocurrents high operational light sensitivity high temporal precision
ACR1(C102A)		+3.4	26.04	+++++			
ZipACR	PsuACR_973	+4.5	0.15	+	+		
NpHR		+3.5	0.16	-	+		
Mac		+3.9	0.09		+		
Arch		+4.2	0.24		+		

YFP-tagged versions of the proteins were expressed in body-wall muscles (BWMs), and after screening numerous transgenic lines, those with low-mosaic, robust and (mostly) plasma membrane localized expression were chosen for experiments (see Methods / *C. elegans* culture and transgenic animals), aiming to provide a comparison and quantification of light-evoked effects: ChR2(C128S;H134R), ChR2(H134R;D156C), ChR2(H134R;T159C), ChR2(C128S; L132C;H134R), ChR2(L132C;H134R;T159C), and Quint (ChR2(C128S;L132C;H134R;D156A; T159C)) all localized to the plasma membrane (Fig 1), including muscle arm protrusions (S1 Fig), with some localization in intracellular membranes to variable degrees. Expression levels, as judged by fluorescence, were comparable to those of the single-mutation variants ChR2 (H134R), ChR2(C128S), ChR2(L132C), or ChR2(T159C) (Fig 1).

Photo-triggered body contractions (S2 Fig) were compared to ChR2(C128S) as the previous benchmark for long-term depolarization in *C. elegans* [8]. All strains were illuminated with blue light (1 or 2s; 450-490nm) and contractions were recorded as an indirect measure for the extent of muscle depolarization, while their duration reported on closing kinetics. Illumination of the double mutants ChR2(H134R;T159C), ChR2(H134R;D156C), and ChR2(C128S; H134R) resulted in strong body contractions of -14.7±0.6%, -14.3±0.5%, and -14.6±0.6%, respectively (Fig 2a and 2b). The triple mutant ChR2(C128S;L132C;H134R) led to the smallest contractions of all variants with multiple mutations (-10.8±1.5%; S1 Video), while ChR2

282

ChR2(H134R)::YFP

ChR2(C128S)::YFP

ChR2(L132C)::YFP

ChR2(T159C)::YFP

ChR2(C128S;H134R)::YFP

ChR2(H134R;D156C)::YFP

ChR2(H134R;T159C)::YFP

ChR2(C128S;L132C;H134R)::YFP

ChR2(L132C;H134R;T159C)::YFP

Quint::YFP
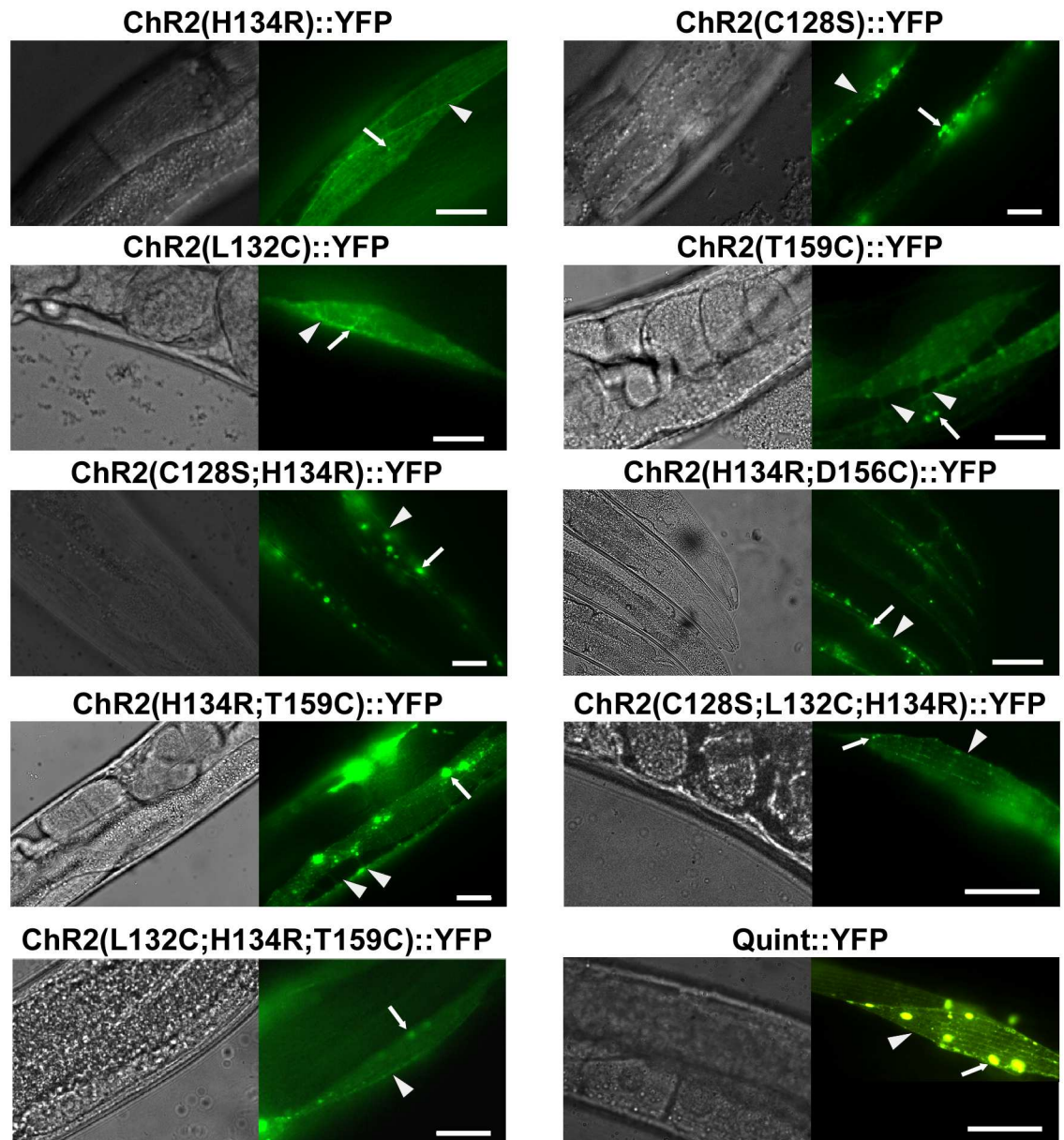
Fig 1. ChR2 variants expressed in body-wall muscle cells localize to membranes. DIC images (left panels) and fluorescence micrographs (right panels) showing expression of ChR2(H134R)::YFP, ChR2(C128S)::YFP, ChR2(L132C)::YFP, ChR2(T159C)::YFP ChR2(C128S;H134R)::YFP, ChR2(H134R;D156C)::YFP, ChR2(H134R;T159C)::YFP, ChR2(C128S;L132C;H134R)::YFP, ChR2 (L132C;H134R;T159C)::YFP, and Quint::YFP in body-wall muscle cells of *C. elegans*, as indicated. Arrows mark aggregates, arrowheads mark plasma membrane. Scale bar is 10 μm.

(L132C;H134R;T159C) led to the strongest contractions (-16.3±0.4%), featuring a distinct increase compared to the single mutant ChR2(L132C) (-13.5±1.4%). Finally, Quint evoked notable contractions of -12.8±0.8%. Generally, peak contractions were comparable to those evoked by ChR2(H134R) (-14.9±1.0%) and ChR2(C128S) (-14.6±0.7%).

After light was turned off animals expressing the triple mutant ChR2(L132C;H134R; T159C) relaxed their body with a slight delay (τ_{relax} value of 2.31±0.10s, compared to 1.08 ±0.06s in ChR2(H134R); Fig 2a; Table 1). In all other mutant combinations, with the exception
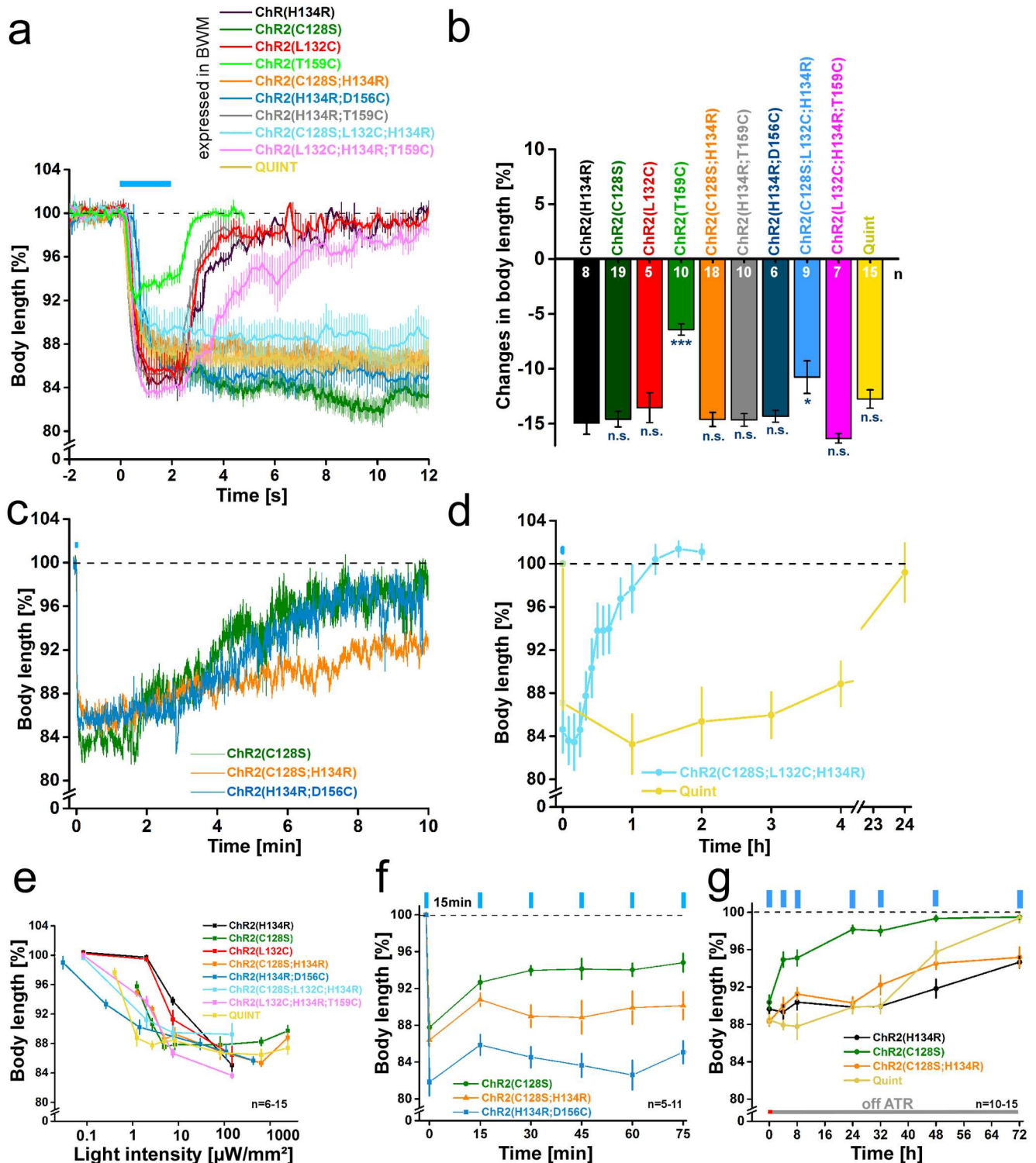
Fig 2. ChR2 variants expressed in body-wall muscle cells enable prolonged depolarization and body contractions. (a) Body length of animals expressing ChR2(H134R)::YFP, ChR2(C128S)::YFP, ChR2(L132C)::YFP, ChR2(T159C)::YFP ChR2(C128S;H134R)::YFP, ChR2(H134R;D156C)::YFP, ChR2(H134R; T159C)::YFP, ChR2(C128S;L132C;H134R)::YFP, ChR2(L132C;H134R;T159C)::YFP, and Quint::YFP in body-wall muscle cells of *C. elegans* during and after a blue light stimulus (0.2 mW/mm^2; 1 or 2 s; 450–490 nm; n = 5–19). **b)** Maximal changes in body length of all depolarizers tested. Shown is the mean normalized change in body length (± SEM) relative to the initial length of the animal. Significance given refers to ChR2(H134R): *p$<$0.05, ***p$<$0.001. **(c)** Same as in a) but displayed over 600 s for ChR2(C128S)::YFP, ChR2(C128S;H134R)::YFP, and ChR2(H134R;D156C)::YFP (n = 7–19). **(d)** Body length of

284

animals expressing ChR2(C128S;L132C;H134R) (n = 5–6; 2 s illumination; 470 nm; 1 mW/mm^2) or Quint (n = 8–14; 5 s illumination; 450–490 nm; 2.4 mW/mm^2) up to 24h after a blue light stimulus (450–490 nm). **(e)** Dependence of body contractions on light intensity in strains listed in (a). Reductions in body length were recorded in response to 1, 2 or 5 s light stimuli (450–490 nm) of light intensities in the range of 0.03–2.41 mW/mm^2 (n = 6–15). **(f)** Repeated stimulation of animals expressing ChR2(C128S)::YFP, ChR2(C128S;H134R)::YFP, and ChR2(H134R;D156C)::YFP. 2 s blue light pulses (0.2 mW/mm^2 ((C128S), (C128S;H134R)) or 1 mW/mm^2 (H134R;D156C); 450–490 nm; n = 5–11) were presented with ISI of 15 min. **(g)** Off-ATR excitability of animals up to 72 h after placing them on fresh NGM plates in absence of ATR (5s; 2.4 mW/mm^2; 450–490 nm; n = 10–15). Shown is the mean normalized body length (± SEM) calculated relative to the initial length of the animal; n = number of animals. Blue bar indicates illumination period.

of ChR2(H134R;T159C) (τ_{relax}: 0.57±0.03s), the delay in channel closing was much more pronounced and they showed long-lasting contractions. For ChR2(C128S;H134R), ChR2(H134R;D156C) and ChR2(C128S;L132C;H134R), time-dependent recovery was detectable in the minute-range (Fig 2c and 2d). Compared to ChR2(C128S) (τ_{relax}: 182±1.5s) contractions lasted considerably longer for ChR2(H134R;D156C) (528±12s), ChR2(C128S;H134R) (841±35s), and ChR2(C128S;L132C;H134R) (1254±292s), indicating further decelerated closing kinetics. Thus, effects that delay channel closing in H134R and C128S single mutants may partly add up, or even influence each other in a synergistic manner. Extremely delayed relaxation was obtained for Quint (τ_{relax}: ≈45,000 ± 25,000 s). Here, body contractions began to cease only after ≈4 hours (Fig 2d) and it took 24 hours until return to baseline. In fact, Quint may not be closing at all, and the recovery from contraction could simply be caused by turnover of the protein. Closing of Quint with yellow or red light, as is possible for C128S [8], was not achievable (data not shown). Due to high light sensitivity and slow recovery complementary electrophysiological recordings could not be performed since the ambient light required for dissection of the animals, even when we worked under minimal red-light conditions, already pre-activated these rhodopsins (for an action spectrum of Quint and in particular in response to red light of intensities used also for dissection of animals for electrophysiology, see S4 Fig). Animals showed increasing contraction (12%) already after 15 s of illumination, i.e. after a much briefer period than would be required for dissection.

The delayed closing kinetics should indirectly also increase the operational light sensitivity of these ChR2 variants, respectively the minimal light intensity required to evoke full contractions *in vivo*: As the proteins accumulate in the open state, reduced light intensities suffice to photoactivate a larger fraction of ChR2 molecules, the slower the photocycle (transition from P520 state to P480 state [53, 54]). To analyze this, we illuminated at different light intensities (0.03μW/mm^2–2.41mW/mm^2). While ChR2(H134R) requires intensities of 147μW/mm^2 to elicit maximal contractions (Fig 2e; S3a Fig), ChR2(C128S;H134R) still evoked full effects at just 4.9μW/mm^2, similar to ChR2(C128S) (S3b and S3d Fig). ChR2(H134R;D156C) turned out to be particularly useful for low-light applications: 0.26μW/mm^2 sufficed to evoke relevant contractions (Fig 2e; S3e Fig) and it was ≈3x more light sensitive than ChR2(C128S;H134R). For Quint, the minimum light intensity to evoke relevant contractions was 1.22μW/mm^2, making it ≈120x more light-sensitive than ChR2(H134R) (Fig 2e; S3h Fig).

In HEK293 cells, ChR2(L132C) had shown an increased light sensitivity [32], presumably due to enhanced activation of voltage-gated Na$^+$ channels. However, in *C. elegans* L132C only led to a minor increase in light sensitivity compared to ChR2(H134R) (Fig 2e). This may be due to the lack of Na$^+$ channels in *C. elegans*. Both (H134R) and (L132C) required light intensities of 7.5μW/mm^2 before showing substantial contractions. Maximal effects were reached at 147μW/mm^2 with body length decreases by -14.9±1.0% (H134R) and -13.5±1.4% (L132C) (S3a and S3c Fig). In contrast, the triple mutants ChR2(C128S;L132C;H134R) and ChR2(L132C;H134R;T159C) achieved substantial contractions already at 2μW/mm^2, also reaching a maximum at 147μW/mm^2 (Fig 2e; S3f and S3g Fig).

285

ChR2(C128S) and other 'slow' ChR2 variants enter long-lived desensitized states after channel closing, which limits their utility for repetitive photostimulation. This allows ongoing depolarization only at reduced light intensity, thus reducing efficiency [55]. As desensitized states were reduced for ChR2(H134R), we wondered if the desensitization would be less prominent for the (C128S;H134R) and (H134R;D156C) double mutants. Therefore, we presented repeated light stimuli (2s; 450-490nm; 200µW/mm^2) at interstimulus intervals (ISIs) of 15 minutes (Fig 2f). Starting with contractions of -12.2±0.7%, ChR2(C128S) reached a 50% reduced plateau activity with the third stimulus (-6.0±0.5%). In contrast, photostimulation of ChR2(C128S;H134R) caused an initial contraction of -13.6±0.7%, that was reduced by only 19% (-11.0±1.2%) at the third stimulus. A similar decrease of 15% was observed with ChR2 (H134R;D156C) (-18.2±1.5% initial contraction, reduced to -15.5±1.1% at third stimulus). These results demonstrate that H134R indeed confers a reduced tendency for desensitization, also when combined with other mutations. Thus, ChR2 variants for long-term depolarization are potentiated by the H134R mutation.

Finally, we analyzed the off-ATR excitability. Use of ChR2(C128S) for long-term depolarization requires ongoing supplementation of ATR [8]. This property limits applicability specifically in organisms that do not provide sufficient endogenous amounts of ATR, or which do not allow sufficient uptake of exogenous ATR (e.g. in eggs, or in certain developmental stages like the non-feeding dauer larva of *C. elegans*, and in experiments where depolarization needs to be achieved for hours or days). ATR removal reduced contractions of ChR2(C128S)-expressing animals within four hours (and even earlier with more frequent repeated stimulation [8]), while in ChR2(H134R)-expressing animals effects only started to decay slightly after 32 hours (Fig 2g). Similarly, full contraction effects were found until 24 and 32 hours post ATR removal for ChR2(C128S;H134R) (83% of initial effect) and Quint (87% of initial effect). Quint stopped responding within 72 hours while ChR2(C128S;H134R) still evoked significant contractions (-4.8±1.1%) at this timepoint, as did ChR2(H134R) (-5.3±0.7%). Hence, it appears likely that the augmenting effects of the H134R mutation are in part due to stabilization of the ATR-Schiff base. Consequently, such double mutants are likely preferable tools for optogenetic long-term depolarization when ATR supplementation is limited.

Photoinhibition of excitable cells by ACRs leads to strong behavioural effects and photocurrents

Next, we turned to new rhodopsin tools for neuronal inhibition, namely the natural anion channel rhodopsins ACR1, ACR2, and ZipACR, as well as the ACR1(C102A) step-function variant. All variants were expressed as eYFP fusion proteins in BWMs. Fluorescence was visible in the plasma membrane of BWMs (Fig 3a–3d). Illumination of ACR1 and ACR2 (5s; 470nm; 1mW/mm^2) resulted in the strongest body relaxation that we have ever observed, with maxima of 6.1±0.4% for ACR1 (Fig 3e and 3g), while ACR2 let to maximal elongations of 4.8±0.3% (Fig 3e and 3g). For comparison, Arch mediated maximal effects of 4.2±0.3% (at 568 nm) at saturating light levels [6]. Elongations ended right after termination of illumination and body length returned to baseline levels within 1-2s (τ_{relax}: 0.57±0.03s (ACR1), 0.14±0.02s (ACR2)). Values are similar to $\tau_{relax'}$ values that we previously observed for NpHR ($\tau_{relax'}$: 0.16±0.05s), Mac ($\tau_{relax'}$: 0.09±0.03s), and Arch ($\tau_{relax'}$: 0.24±0.04s; all expressed in BWMs) [6].

Illumination of ACR1(C102A) (2s, 470nm, 1mW/mm^2) and ZipACR (5s, 520nm, 1mW/mm^2) expressed in BWMs led to body elongations of 3.4±0.5% and 4.5±0.7%, respectively (Fig 3f and 3g; S2 Video). In contrast to the large currents reported for expression in HEK293 cells [38], ZipACR did not induce stronger behavioral effects than other ACRs in *C. elegans*. Its faster kinetics [38] did not obviously shorten the time BWMs require to contract after light-off

286
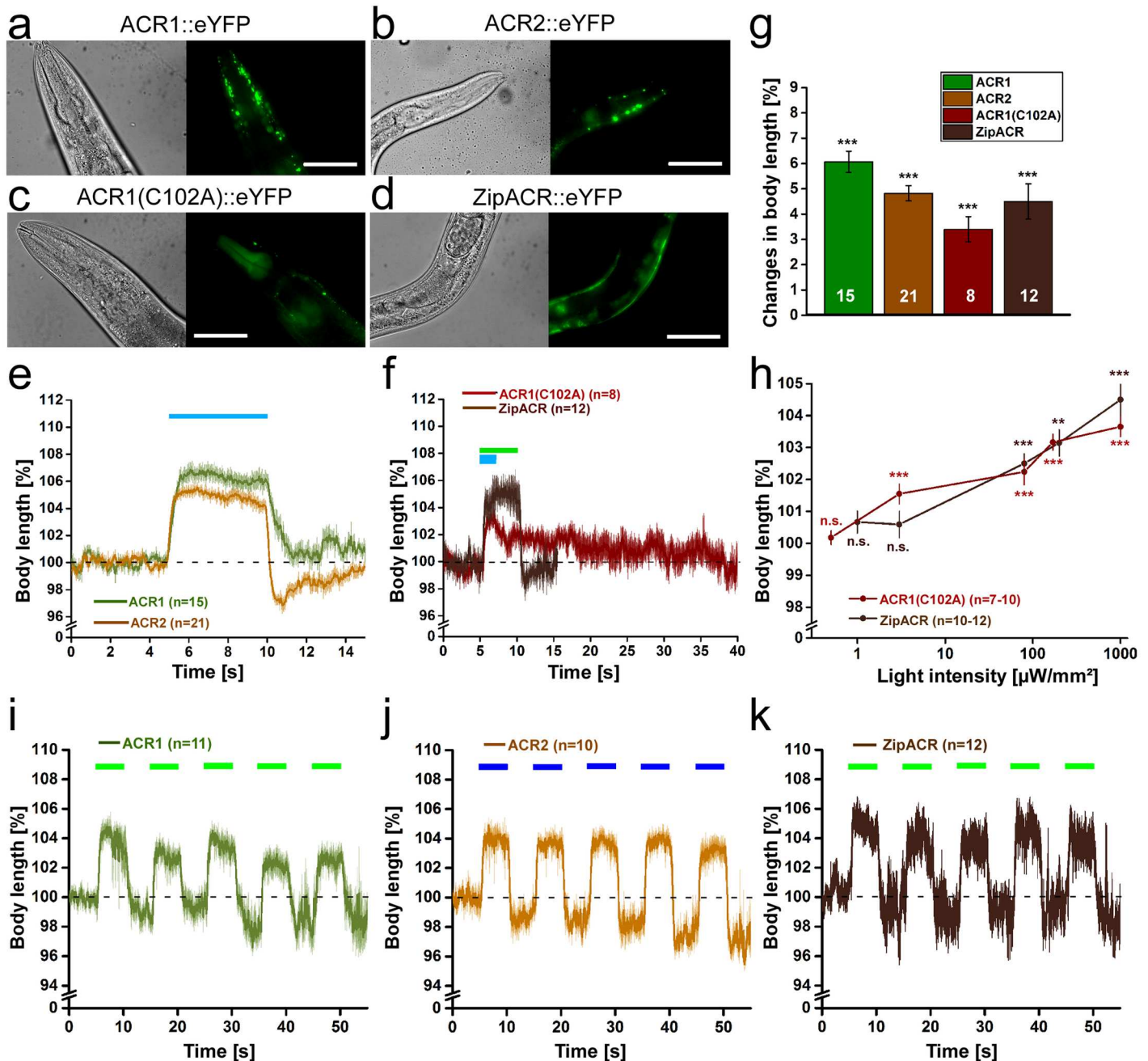
Fig 3. ACRs mediate strong hyperpolarization and body elongation. Expression of ACR1::eYFP (**a**), ACR2::eYFP (**b**), as well as ACR1(C102A)::eYFP (**c**) and ZipACR::eYFP (**d**) in body-wall muscle cells of *C. elegans*. Scale bar is 50 μm. (**e**) Body length of animals expressing ACR1 or ACR2 during and after a 5 s light stimulus (1 mW/mm^2; 470 nm). Shown is the mean normalized body length (± SEM) relative to the initial length of the animal. (**f**) Body length during and after a light stimulus (1 mW/mm^2) of animals expressing ACR1(C102A) (470 nm, 2 s) or ZipACR (520 nm, 5 s). (**g**) Maximal changes in body length induced by the tested hyperpolarizers. Shown is the mean normalized change in body length (± SEM) relative to the initial length of the animal. (**h**) Light intensity dependence of the body elongation of animals expressing ACR1(C102A) or ZipACR in body-wall muscle cells. (**i**) Body length in response to repetitive photostimulation (5 s, 5 s ISI, 80 μW/mm^2, 470 or 520 nm) of ACR1, ACR2 (**j**) or ZipACR (**k**) in animals expressing the respective channel in body-wall muscles; n = number of animals. Blue and green bars indicate illumination period. *p<0.05, **p<0.01, ***p<0.001.

($\tau_{relax'}$: 0.15±0.03s) compared to ACR2. ACR1(C102A) led to the expected dramatic decrease in channel closing ($\tau_{relax'}$: 26.04±4.62s), however, the maximal elongation was reduced by 56% compared to ACR1. Interestingly, animals expressing ACR2 or ZipACR often exhibited a slight body contraction right after cessation of the photostimulation (Fig 3e and 3f). This might represent the action of Cl^--pumps extruding negative charge from cells or indicate a depolarizing effect as a rebound reaction. The slight contraction might also be provoked by the fast speed of the response in ACR2 and ZipACR while it seems to be independent of its strength, since the effect was not observed with ACR1 which evoked strong body elongations just like ACR2.

Experiments at low light intensities revealed a high operational light sensitivity for ACR1 and ACR2, showing about half-maximal elongations at $75\mu W/mm^2$ when ACR1 (43% of maximum at $1mW/mm^2$) and ACR2 (56% of maximum at $1mW/mm^2$) were expressed in cholinergic neurons (S5d, S5e and S5f Fig). In agreement with the action spectrum of ACR1 being slightly red-shifted [24], ACR1- (but not ACR2-) expressing animals could also be stimulated with green light (520nm) at low light intensities ($3.6\mu W/mm^2$; S5d Fig). At $80\mu W/mm^2$ about half-maximal elongations were also reached for ZipACR (55%) and ACR1(C102A) (62%) (Fig 3h; S5g and S5h Fig). However, in contrast to ACR1 and ACR2, ZipACR caused no obvious relaxation effects at lower light intensities. One interesting feature of step-function opsins is the ability of channel closure by red-shifted light. Indeed, ACR1(C102A) expressed in HEK293 cells showed a partial and rather slow reduction in currents after red light exposure (620-660nm; maximum: 640nm) following activation at 515nm (S5i Fig).

Repeated photostimulation of ACR1 (520nm; Fig 3i; S5j Fig), ACR2 (470nm; Fig 3j; S5k Fig), or ZipACR (520nm; Fig 3k) (5s; $80\mu W/mm^2$, ISI 5s) demonstrated stability during recurrent activation and no obvious desensitization. During dark intervals, we noted a trend to lower baseline body length. Possibly this was due to alterations in cellular Cl^--concentration that could not immediately be balanced by intrinsic Cl^--pumps. For expression and functional analysis of ACR1 and ACR2 in cholinergic neurons, see S5 Fig and S3 Video.

A more recently generated, improved ChloC (iChloC [36]) was not tested, and neither were iC1C2 and iC++, as we could estimate from the literature that the currents they generate fall behind those of the ACRs [24, 37]; this does not imply that these proteins may not work well in *C. elegans*.

To investigate function of the most promising hyperpolarizers more precisely, we measured photocurrents of ACR1 and ACR2 and for comparison NpHR by patch-clamp recordings from BWMs. Photostimulation with blue light (470nm, 5s, $1mW/mm^2$) evoked large outward peak currents of 1083±264pA (τ_{off}: 0.23±0.05s) and 1530±204pA (τ_{off}: 0.10±0.02s) for ACR1 and ACR2, respectively (Fig 4a and 4b). These currents were about 10-fold larger than those obtained for NpHR at its excitation maximum of 590nm (143±41pA; $5.3mW/mm^2$). Ratios of currents at the end of the photostimulation and the initial peak currents were almost identical for all three hyperpolarizers ($\approx$64%). In case of the pump NpHR, the decrease in currents is most likely caused by a progressive increase of inactivated proteins. In case of the channels (ACRs) it may be a combination of desensitization and, due to the strong conductivity, also a drop in the electrochemical potential driving Cl^--influx. To test the influence of stimulus length and repeated stimulation, we conducted a protocol starting with light stimuli of 5, 10, and 20s separated by ISIs of 10s, followed by longer ISIs of 60 and 120s with 5s of stimulation each. All three rhodopsins could be repetitively stimulated. The last peak current in the sequence reached 94, 79, and 88% of the initial peak for ACR1, ACR2, and NpHR, respectively (Fig 4b). For ACRs, the currents continued to decay even after 20s of photostimulation, but depending on the duration of the ISI, the next peak current recovered towards initial values. This is in line with dissipation of the Cl^--gradient during the light stimulus, and implies that it

288
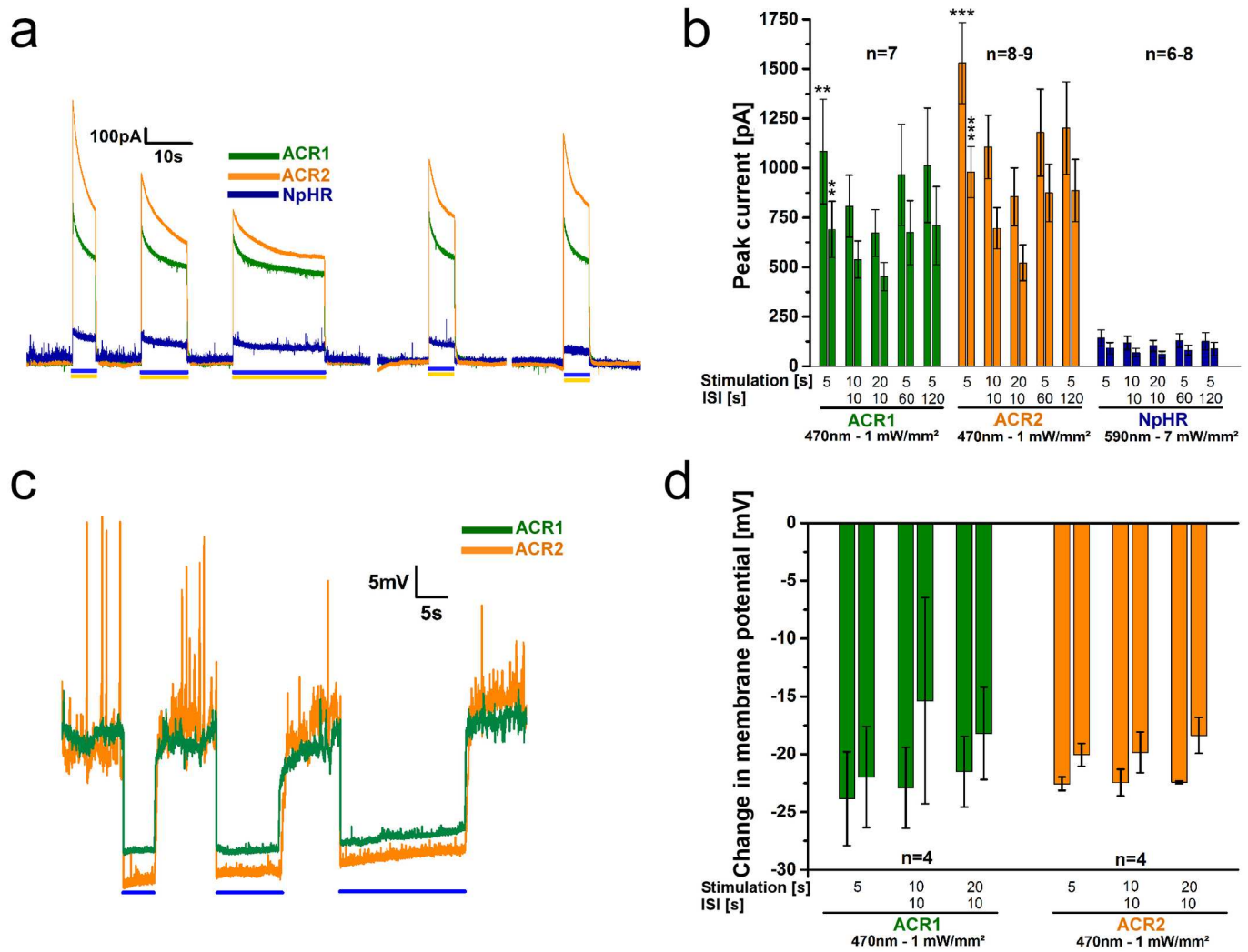
Fig 4. ACR1 and ACR2 mediate large photocurrents and hyperpolarization in patch-clamped BWMs. (a) Example current traces of body-wall muscle cells expressing ACR1, ACR2, or NpHR during 5 s, 10 s, and 20 s photostimulation (blue or yellow light, as indicated by bars) with 10 s ISIs. **(b)** Group data of experiments described in a). The paired bars at each time point represent peak currents (1st bar) and plateau currents (2nd bar). Significance refers to NpHR. **(c)** As in a), but showing voltage traces, before, during and after 5 s, 10 s, and 20 s photostimulation with 10 s ISI. **(d)** Group data for experiments shown in c). The paired bars at each time point represent peak (1st bar) and plateau (2nd bar) changes in the membrane potential. ACRs were illuminated at 470 nm (1 mW/mm^2), NpHR at 590 nm (7 mW/mm^2); n = number of animals. Displayed are mean ± SEM of currents or voltage in b) and c). $^{**}p<0.01$, $^{***}p<0.001$.

is counteracted by Cl$^-$-pumps (with net efflux during dark periods). As this should affect membrane voltage, we also recorded the membrane potential (Fig 4c and 4d). Spontaneous action potential bursts [56, 57] were suppressed by ACR activation. Also here we observed a hint of the action of Cl$^-$-efflux pumps, particularly during dark intervals, as the baseline potential gradually increased (see S6 Fig for averaged, filtered traces, showing baseline depolarization more obviously), as expected for extrusion of negative charge.

Our behavioral and electrophysiological results support previous reports for HEK293 cells [40], suggesting stable effects and high photocurrents mediated by ACRs, making them very effective for optogenetic (shunting) hyperpolarization, at least at depolarized potentials. For action near the Cl$^-$ equilibrium potential, NpHR (as a pump) can provide further activity, as it operates mostly independent of the membrane potential.

Discussion

Due to its reliability and relatively fast kinetics, H134R –the 'standard' ChR2 –is widely used as an optogenetic tool for depolarization of excitable cells. However, the demanding light requirements and progressive inactivation prevent its use for long-term experiments. ChR2(C128S) was established as a variant with slowed closing kinetics that allows prolonged depolarization over several minutes following a single short photostimulus. Yet, the requirement of continuous supplementation of the cofactor ATR and reduced effects during repetitive stimulation, as a consequence of the accumulation of desensitized states, limited its applicability. To bypass these limitations, we combined previously known mutations and characterized the resulting ChR2 variants for favorable properties in long-term depolarization (Fig 5a; Table 1).

Compared to ChR2(C128S), contractions evoked by ChR2(C128S;H134R) lasted slightly longer, while exhibiting similar operational light sensitivity. Yet, ChR2(C128S;H134R) exhibited superior off-ATR excitability, allowing to elicit strong contraction in BWMs for at least 24h after ATR removal, while effects for ChR2(C128S) ceased within 4h. Repetitive stimulation of ChR2(C128S;H134R) elicited higher contractions, indicating that it is less likely to be lost to desensitized states. Even higher effects during repetitive stimulation were found for ChR2 (H134R;D156C). Given that H134R remains fully activatable after 32h off ATR, we expect that H134R;D156C will show similar stability.

The different properties of ChR2(C128S) and ChR2(C128S;H134R) likely result from the H134R mutation. The open state life time in ChR2(H134R) is increased compared to ChR2 (wt) (17.9 vs. 13.5ms; [58]). Slowing effects on channel closing by C128S and H134R may thus add up (in a non-linear manner) in the double mutant. In a previous study it was proposed that mutants of C128 are more likely to lose their ATR from the chromophore binding pocket after channel closing, i.e. in specific states reached from the P480 state [30]. Reloading the apoprotein with ATR may be time-consuming or may be hampered after an initial photoactivation, which could explain the longevity of the 'lost' states. However, the need for reloading in C128S would also explain the need for ongoing presence of ATR. Why H134R affects the stability of the ChR2-ATR Schiff base can only be speculated. Nonetheless, charge/polarization effects may be involved. Yet, this hypothesis requires more direct biophysical analyses of this ChR2 variant. With its improved off-ATR excitability and response to repetitive stimulations, ChR2(C128S;H134R) might be favored over C128S, at least when ATR supplementation is a limiting factor, like in *D. melanogaster* or *C. elegans*, and when strong depolarizations are to be induced for more than a single photocycle. ChR2(H134R;D156C) may be even more useful in this context, given the stronger depolarization induced during the first 75 minutes.

The quintuple mutant Quint exhibited the slowest closing kinetics of all ChR2 variants known so far (including ChR2-XXL), causing depolarization of BWMs for many hours following a single 1s light stimulus and only returning to baseline values after about 24 hours. Unlike for the step-function opsins, we could not close the channel by using yellow light (data not shown), and it cannot be excluded that the behavioral effects seized only when the protein was degraded. Nonetheless, Quint extends temporal limits for minimal light-invasive, optogenetic depolarization. In line with drastically slowed closing kinetics, the operational light sensitivity was increased, evoking full contractions in BWMs at light intensities as low as $1.22\mu W/mm^2$ (ca. 1/10th light intensity of the sun on an overcast day, while light intensities used for ChR2 (H134R) experiments correspond to a sunny summer day [59]), i.e. ≈4-fold lower than for ChR2(C128S) and ≈120-fold lower than for ChR2(H134R). When stimulation of excitable cells for hours or days is intended and at low expression levels, Quint would be a good choice, possibly also in other model systems.

290
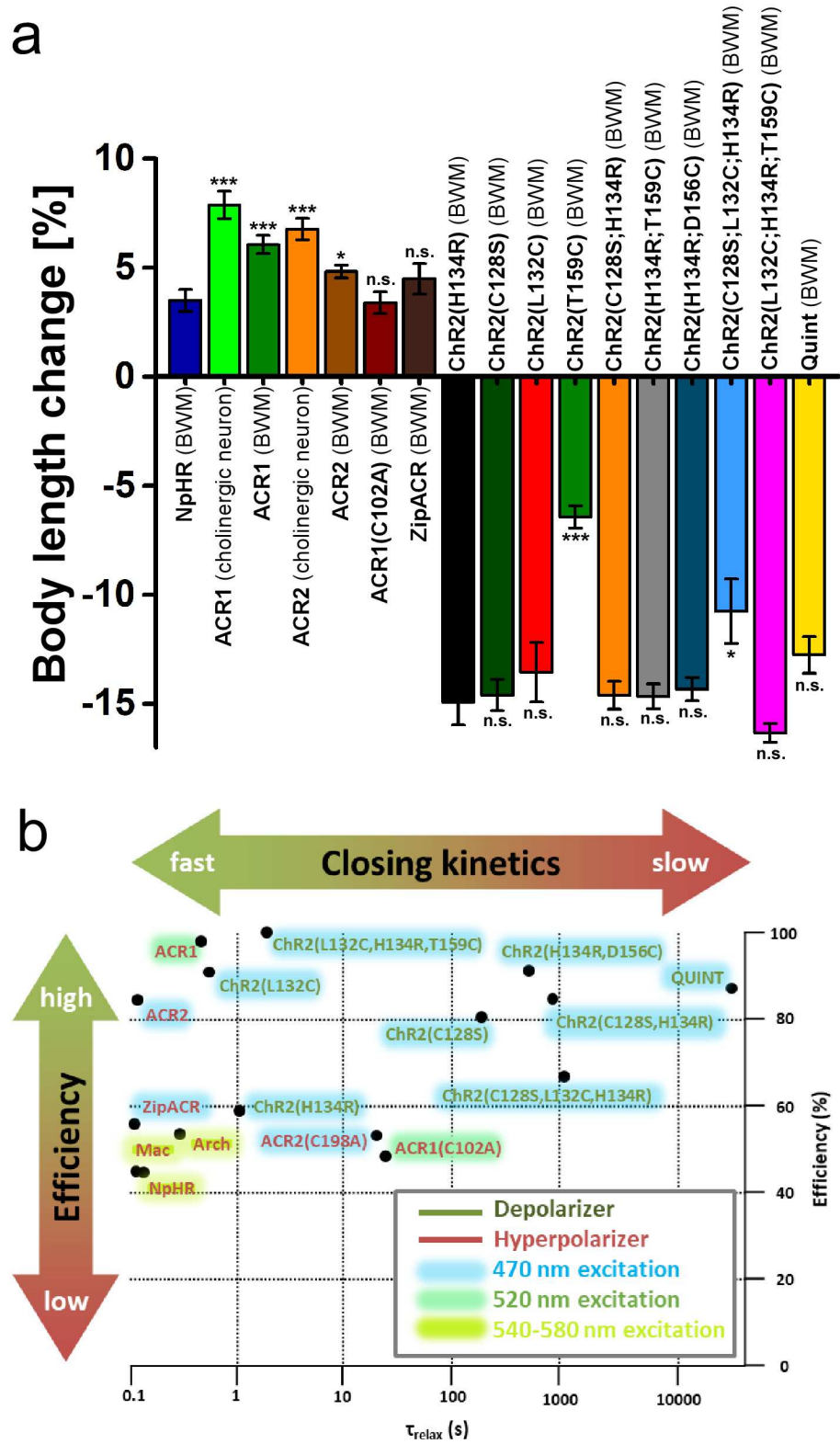
Fig 5. Evaluation of de- and hyperpolarizers characterized in this paper. a) Changes in body length induced by de- and hyperpolarizers. Shown is the mean normalized change in body length (± SEM) relative to the initial length of the animal; n = number of animals. Statistical differences for hyperpolarizers are referring to NpHR, statistical differences for depolarizers are referring to ChR2(H134R). **b)** Scheme of optogenetic de- and hyperpolarizers expressed in BWMs

291

of *C. elegans* classified by closing kinetics (τ_{relax}) and efficiency. The efficiency was determined as follows: Depolarizers —Relative comparison of contractions, induced by the respective tool, at 200 µW/mm^2 to the maximum possible contraction; Hyperpolarizers—Relative comparison of relaxations, induced by the respective tool, at 1 mW/mm^2 to the maximum possible relaxation. Hence, efficiency not only refers to the maximum possible changes in body length upon light saturation, but also includes information about the tool's light sensitivity. Therefore, some tools receive lower efficiencies, though they exhibit comparable maximum effects. Color shades indicate the light color of the respective tool's excitation wavelength.

The ACRs are an important extension to the repertoire of inhibitory optogenetic tools in *C. elegans*, because they combine channel properties and fast action. They feature extraordinarily high photocurrents in BWMs at low light intensities, even if this necessitates keeping in mind the corresponding alterations in cellular Cl⁻ concentrations. Their anion selectivity and high temporal precision make ACRs very efficient tools to inhibit neuronal activity with light. Furthermore, the red-shifted action spectrum of ACR1 facilitates a selective combination with blue-light activated optical tools. ACR1(C102A) demonstrated sustained and long-lasting effects in *C. elegans*, resembling those of the common depolarizing step-function mutants. This is a useful feature for long-term hyperpolarization applications.

In sum, we generated and characterized several new ChR2 variants and ACRs in *C. elegans* for either depolarization or hyperpolarization, complementing the optogenetic toolbox (for an overview, see Fig 5b). Particularily ChR2(C128S;H134R), ChR2(H134R;D156C), and Quint bypass limitations of optogenetic long-term and repetitive depolarization, particularly in animals lacking endogenous ATR. Furthermore, we could establish ACRs as powerful tools for fast optogenetic inhibition in the nematode. Together, these optogenetic tools allow a straightforward, easy and efficient manipulation of neuronal activity, likely also in other systems (however, we emphasize that this will have to be re-tested in the system of interest, as opsin expression is not universally similar in all hosts). They are particularly useful when only low light intensities can be achieved, or where long-term effects are desired. Our work also emphasizes that *C. elegans* may serve as an additional testbed for novel rhodopsin optogenetic tools.

Supporting information

S1 Fig. ChR2 variants expressed in body-wall muscle cells. Expression of ChR2(L132C):: YFP, ChR2(C128S;L132C;H134R)::YFP, and ChR2(L132C;H134R;T159C). Arrowheads indicate muscle arms which body-wall muscle cells extend towards the neuronal processes to form neuromuscular junctions. Scale bar is 10 µm.
(JPG)

S2 Fig. Description of behavioral assays in *C. elegans* expressing de- or hyperpolarizing rhodopsin-based tools in body-wall muscle cells. Photostimulation leads to either contraction or elongation of the body. Changes in body length are analyzed in videos of free moving animals (for further details see Materials and methods).
(JPG)

S3 Fig. ChR2 variants expressed in body-wall muscle cells induce body contractions depending on the light intensity used. Dependence of body contractions on light intensity in animals expressing **(a)** ChR2(H134R)::YFP, **(b)** ChR2(C128S)::YFP, **(c)** ChR2(L132C)::YFP, **(d)** ChR2(C128S;H134R)::YFP, **(e)** ChR2(H134R;D156C)::YFP, **(f)** ChR2(C128S;L132C; H134R)::YFP, **(g)** ChR2(L132C;H134R;T159C), and **(h)** Quint::YFP in body-wall muscle cells of *C. elegans*. Reductions in body length were recorded in response to light stimuli (1, 2, or 5 s, 450–490 nm) of intensities in the range of 0.03 µW/mm^2 to 2.41 mW/mm^2. Shown is the mean normalized body length (± SEM) calculated relative to the initial length of the animal;

292

n = number of animals.
(JPG)

S4 Fig. Quint induces body contractions over a broad wavelength spectrum. (a) Dependence of body contractions on wavelength (430–620 nm) in animals expressing Quint::YFP in body-wall muscle cells of *C. elegans*. Reductions in body length were recorded in response to light stimuli (5 s; 300 μW/mm^2). Shown is the mean normalized body length ($\pm$ SEM) calculated relative to the initial length of the animal. **(b)** Change in body length of animals expressing Quint::YFP (430–620 nm) or ChR2(H134R)::YFP (580 and 620 nm) following photostimulation (5 s; 300 μW/mm^2) at different wavelengths. **(c)** Body contractions of animals expressing Quint::YFP in response to prolonged stimulation with red light (15 s; 620 nm; 300 μW/mm^2). Shown is the mean normalized body length ($\pm$ SEM) calculated relative to the initial length of the animal; n = number of animals. **p$<$0.01, ***p$<$0.001.
(JPG)

S5 Fig. ACR variants induce body elongations depending on the used light intensity. Expression of ACR1::eYFP and ACR2::eYFP in cholinergic neurons of *C. elegans*. Scale bar is 50 μm. **b)** Body length calculated of animals expressing ACR1 or ACR2 expressed in cholinergic neurons during and after a 5 s light stimulus (1 mW/mm^2; 470 nm). Shown is the mean normalized body length ($\pm$ SEM) relative to the initial length of the animal. **(c)** Maximal changes in body length induced by the tested hyperpolarizers. Shown is the mean normalized change in body length ($\pm$ SEM) relative to the initial length of the animal. **(d)** Light wavelength and intensity dependence of the body elongation of transgenic animals expressing ACR1 or ACR2 in cholinergic neurons. Dependence of body elongations on light intensity in animals expressing ACR1 (cholinergic neuron) **(e)**, ACR2 (cholinergic neuron) **(f)**, ZipACR (BWM) **(g)** or ACR1(C102A) (BWM) **(h)**. Elongations in body length were recorded in response to light stimuli (2 or 5 s, 470 or 520 nm) of intensities in the range of 0.5 μW/mm^2 to 1 mW/mm^2. Shown is the mean normalized body length ($\pm$ SEM) calculated relative to the initial length of the animal. **(i)** Partial closing of ACR1(C102A) channel with red light (620–660 nm). The photocurrents were recorded from a HEK293 cell held at -40 mV at the amplifier output. The duration of the activating 515-nm light pulse was 10 ms (for further details see Methods section). **(j)** Body length in response to repetitive photostimulation (5 s, 5 s ISI, 80 μW/mm^2, 470 or 520 nm) of ACR1 or ACR2 **(k)** in animals expressing the respective channel in body-wall muscles or cholinergic neurons. Blue and green bars indicate illumination period. n = number of animals. Significance is given relative to body length before illumination: *p$<$0.05, **p$<$0.01, ***p$<$0.001. For easier comparison of effects in BWMs and cholinergic neurons results from BWMs presented in Fig 3g, 3i and 3j have been included in S5c,j,k Fig.
(JPG)

S6 Fig. Membrane potential shift following ACR-mediated hyperpolarization may indicate action of Cl$^-$ efflux pumps. Shown are the mean voltage traces of four experiments each, filtered as a sliding average (2000 frame window at 5 kHz sampling). Two consecutive dark and light stimulation periods from Fig 5c are shown (ACR1 and ACR2, as indicated). The upward (depolarizing) trend in the baseline is visualized by graphical regression.
(JPG)

S1 Video. A representative video obtained from animals expressing ChR2(C128S;L132C; H134R) in body-wall muscle, before and during the light stimulus phase. A body contraction is seen when the stimulation light is turned on.
(MP4)

293

S2 Video. A representative video obtained from animals expressing ACR1(C102) in body-wall muscle, before and during the light stimulus phase. A body elongation and reduction in locomotion is seen when the stimulation light is turned on.
(MP4)

S3 Video. A representative video obtained from animals expressing ACR1 in cholinergic neurons, before and during the light stimulus phase. A body elongation and stop of locomotion is seen when the stimulation light is turned on.
(MP4)

S1 Data. This file contains raw data of contractions assays related to depolarizers presented in this paper.
(XLSX)

S2 Data. This file contains raw data of contractions assays and electrophysiological recordings related to hyperpolarizers presented in this paper.
(XLSX)

S3 Data. This file contains plasmid maps of transgenic animals presented in this paper.
(DOCX)

S4 Data. This file contains the plasmid map of pmyo-3::ChR2(H134R).
(GBK)

S5 Data. This file contains the plasmid map of pmyo-3::ChR2(C128S).
(GBK)

S6 Data. This file contains the plasmid map of pmyo-3::ChR2(L132C).
(GBK)

S7 Data. This file contains the plasmid map of pmyo-3::ChR2(T159C).
(GBK)

S8 Data. This file contains the plasmid map of pmyo-3::ChR2(C128S;H134R).
(GBK)

S9 Data. This file contains the plasmid map of pmyo-3::ChR2(H134R;D156C).
(GBK)

S10 Data. This file contains the plasmid map of pmyo-3::ChR2(T159C).
(GBK)

S11 Data. This file contains the plasmid map of pmyo-3::ChR2(C128S;L132C;H134R).
(GBK)

S12 Data. This file contains the plasmid map of pmyo-3::ChR2(L132C;H134R;T159C).
(GBK)

S13 Data. This file contains the plasmid map of pmyo-3::Quint.
(GBK)

S14 Data. This file contains the plasmid map of pmyo-3::ACR1.
(GBK)

S15 Data. This file contains the plasmid map of punc-17::ACR1.
(GBK)

294

S16 Data. This file contains the plasmid map of pmyo-3::ACR2.
(GBK)

S17 Data. This file contains the plasmid map of punc-17::ACR2.
(GBK)

S18 Data. This file contains the plasmid map of pmyo-3::ACR1(C102A).
(GBK)

S19 Data. This file contains the plasmid map of pmyo-3::ZipACR.
(GBK)

S20 Data. This file contains the plasmid map of pmyo-3::NpHR.
(GBK)

Acknowledgments

Author Contributions

Conceptualization: Christian Schultheis, Alexander Gottschalk, Jana F. Liewald.

Data curation: Amelie Bergs, Christian Schultheis, Elisabeth Fischer, Satoshi P. Tsunoda, Karen Erbguth, Steven J. Husson, Elena Govorunova, Jana F. Liewald.

Formal analysis: Alexander Gottschalk.

Funding acquisition: Alexander Gottschalk.

Investigation: Amelie Bergs, Christian Schultheis, Elisabeth Fischer, Satoshi P. Tsunoda, Karen Erbguth, Steven J. Husson, Elena Govorunova, Jana F. Liewald.

Methodology: Amelie Bergs, Christian Schultheis, Jana F. Liewald.

Project administration: Alexander Gottschalk, Jana F. Liewald.

Resources: Elena Govorunova, John L. Spudich, Georg Nagel.

Software: Christian Schultheis.

Supervision: Alexander Gottschalk, Jana F. Liewald.

Visualization: Alexander Gottschalk, Jana F. Liewald.

Writing – original draft: Amelie Bergs, Christian Schultheis, Jana F. Liewald.

**Writing – review & editing:** Alexander Gottschalk.

References

1. Knöpfel T, Lin MZ, Levskaya A, Tian L, Lin JY, Boyden ES. Toward the second generation of optogenetic tools. J Neurosci. 2010; 30(45):14998–5004. https://doi.org/10.1523/JNEUROSCI.4190-10.2010 PMID: 21068304

2. Yizhar O, Fenno LE, Davidson TJ, Mogri M, Deisseroth K. Optogenetics in neural systems. Neuron. 2011; 71(1):9–34. https://doi.org/10.1016/j.neuron.2011.06.004 PMID: 21745635

3. Deisseroth K. Optogenetics: 10 years of microbial opsins in neuroscience. Nat Neurosci. 2015; 18 (9):1213–25. https://doi.org/10.1038/nn.4091 PMID: 26308982

4. Kocabas A, Shen CH, Guo ZV, Ramanathan S. Controlling interneuron activity in *Caenorhabditis elegans* to evoke chemotactic behaviour. Nature. 2012; 490(7419):273–7. https://doi.org/10.1038/nature11431 PMID: 23000898

5. Erbguth K, Prigge M, Schneider F, Hegemann P, Gottschalk A. Bimodal activation of different neuron classes with the spectrally red-shifted channelrhodopsin chimera C1V1 in *Caenorhabditis elegans*. PLoS ONE. 2012; 7(10):e46827. https://doi.org/10.1371/journal.pone.0046827 PMID: 23056472

6. Husson SJ, Liewald JF, Schultheis C, Stirman JN, Lu H, Gottschalk A. Microbial Light-Activatable Proton Pumps as Neuronal Inhibitors to Functionally Dissect Neuronal Networks in *C. elegans*. PLoS ONE. 2012; 7(7):e40937. https://doi.org/10.1371/journal.pone.0040937 PMID: 22815873

7. Nagel G, Brauner M, Liewald JF, Adeishvili N, Bamberg E, Gottschalk A. Light activation of channelrhodopsin-2 in excitable cells of *Caenorhabditis elegans* triggers rapid behavioral responses. Curr Biol. 2005; 15(24):2279–84. https://doi.org/10.1016/j.cub.2005.11.032 PMID: 16360690

8. Schultheis C, Liewald JF, Bamberg E, Nagel G, Gottschalk A. Optogenetic long-term manipulation of behavior and animal development. PLoS One. 2011; 6(4):e18766. https://doi.org/10.1371/journal.pone.0018766 PMID: 21533086

9. Schild LC, Glauser DA. Dual Color Neural Activation and Behavior Control with Chrimson and *Co*ChR in *Caenorhabditis elegans*. Genetics. 2015; 200(4):1029–34. https://doi.org/10.1534/genetics.115.177956 PMID: 26022242

10. Han X, Qian X, Bernstein JG, Zhou HH, Franzesi GT, Stern P, et al. Millisecond-timescale optical control of neural dynamics in the nonhuman primate brain. Neuron. 2009; 62(2):191–8. https://doi.org/10.1016/j.neuron.2009.03.011 PMID: 19409264

11. Stauffer WR, Lak A, Yang A, Borel M, Paulsen O, Boyden ES, et al. Dopamine Neuron-Specific Optogenetic Stimulation in Rhesus Macaques. Cell. 2016; 166(6):1564–71. https://doi.org/10.1016/j.cell.2016.08.024 PMID: 27610576

12. Boyden ES, Zhang F, Bamberg E, Nagel G, Deisseroth K. Millisecond-timescale, genetically targeted optical control of neural activity. Nat Neurosci. 2005; 8(9):1263–8. https://doi.org/10.1038/nn1525 PMID: 16116447

13. Liewald JF, Brauner M, Stephens GJ, Bouhours M, Schultheis C, Zhen M, et al. Optogenetic analysis of synaptic function. Nat Methods. 2008; 5(10):895–902. https://doi.org/10.1038/nmeth.1252 PMID: 18794862

14. Nagel G, Szellas T, Huhn W, Kateriya S, Adeishvili N, Berthold P, et al. Channelrhodopsin-2, a directly light-gated cation-selective membrane channel. Proc Natl Acad Sci U S A. 2003; 100(24):13940–5. https://doi.org/10.1073/pnas.1936192100 PMID: 14615590

15. Zhang F, Wang LP, Brauner M, Liewald JF, Kay K, Watzke N, et al. Multimodal fast optical interrogation of neural circuitry. Nature. 2007; 446(7136):633–9. https://doi.org/10.1038/nature05744 PMID: 17410168

16. Chow BY, Han X, Dobry AS, Qian X, Chuong AS, Li M, et al. High-performance genetically targetable optical neural silencing by light-driven proton pumps. Nature. 2010; 463(7277):98–102. https://doi.org/10.1038/nature08652 PMID: 20054397

17. Wietek J, Wiegert JS, Adeishvili N, Schneider F, Watanabe H, Tsunoda SP, et al. Conversion of channelrhodopsin into a light-gated chloride channel. Science. 2014; 344(6182):409–12. https://doi.org/10.1126/science.1249375 PMID: 24674867

18. Chuong AS, Miri ML, Busskamp V, Matthews GA, Acker LC, Sørensen AT, et al. Noninvasive optical inhibition with a red-shifted microbial rhodopsin. Nat Neurosci. 2014; 17(8):1123–9. https://doi.org/10.1038/nn.3752 PMID: 24997763

19. Klapoetke NC, Murata Y, Kim SS, Pulver SR, Birdsey-Benson A, Cho YK, et al. Independent optical excitation of distinct neural populations. Nat Methods. 2014; 11(3):338–46. https://doi.org/10.1038/nmeth.2836 PMID: 24509633

20. Prigge M, Schneider F, Tsunoda SP, Shilyansky C, Wietek J, Deisseroth K, et al. Color-tuned channelrhodopsins for multiwavelength optogenetics. J Biol Chem. 2012; 287(38):31804–12. https://doi.org/10.1074/jbc.M112.391185 PMID: 22843694

296

21. Berndt A, Schoenenberger P, Mattis J, Tye KM, Deisseroth K, Hegemann P, et al. High-efficiency channelrhodopsins for fast neuronal stimulation at low light levels. Proc Natl Acad Sci U S A. 2011; 108 (18):7595–600. https://doi.org/10.1073/pnas.1017210108 PMID: 21504945

22. Kato HE, Inoue K, Abe-Yoshizumi R, Kato Y, Ono H, Konno M, et al. Structural basis for Na(+) transport mechanism by a light-driven Na(+) pump. Nature. 2015; 521(7550):48–53. https://doi.org/10.1038/nature14322 PMID: 25849775

23. Gushchin I, Shevchenko V, Polovinkin V, Kovalev K, Alekseev A, Round E, et al. Crystal structure of a light-driven sodium pump. Nat Struct Mol Biol. 2015; 22(5):390–5. https://doi.org/10.1038/nsmb.3002 PMID: 25849142

24. Govorunova EG, Sineshchekov OA, Janz R, Liu X, Spudich JL. NEUROSCIENCE. Natural light-gated anion channels: A family of microbial rhodopsins for advanced optogenetics. Science. 2015; 349 (6248):647–50. https://doi.org/10.1126/science.aaa7484 PMID: 26113638

25. Govorunova EG, Spudich EN, Lane CE, Sineshchekov OA, Spudich JL. New Channelrhodopsin with a Red-Shifted Spectrum and Rapid Kinetics from Mesostigma viride. mBio. 2011; 2(3):e00115–11. https://doi.org/10.1128/mBio.00115-11 PMID: 21693637

26. Berndt A, Lee SY, Ramakrishnan C, Deisseroth K. Structure-guided transformation of channelrhodopsin into a light-activated chloride channel. Science. 2014; 344(6182):420–4. https://doi.org/10.1126/science.1252367 PMID: 24763591

27. Lin JY, Lin MZ, Steinbach P, Tsien RY. Characterization of engineered channelrhodopsin variants with improved properties and kinetics. Biophys J. 2009; 96(5):1803–14. https://doi.org/10.1016/j.bpj.2008.11.034 PMID: 19254539

28. Schneider F, Grimm C, Hegemann P. Biophysics of Channelrhodopsin. Annual review of biophysics. 2015; 44:167–86. https://doi.org/10.1146/annurev-biophys-060414-034014 PMID: 26098512

29. Ullrich S, Gueta R, Nagel G. Degradation of channelopsin-2 in the absence of retinal and degradation resistance in certain mutants. Biol Chem. 2013; 394(2):271–80. https://doi.org/10.1515/hsz-2012-0256 PMID: 23134970

30. Bruun S, Naumann H, Kuhlmann U, Schulz C, Stehfest K, Hegemann P, et al. The chromophore structure of the long-lived intermediate of the C128T channelrhodopsin-2 variant. FEBS Lett. 2011; 585 (24):3998–4001. https://doi.org/10.1016/j.febslet.2011.11.007 PMID: 22094167

31. Gradmann D, Berndt A, Schneider F, Hegemann P. Rectification of the channelrhodopsin early conductance. Biophys J. 2011; 101(5):1057–68. https://doi.org/10.1016/j.bpj.2011.07.040 PMID: 21889442

32. Kleinlogel S, Feldbauer K, Dempski RE, Fotis H, Wood PG, Bamann C, et al. Ultra light-sensitive and fast neuronal activation with the Ca(2)+-permeable channelrhodopsin CatCh. Nat Neurosci. 2011; 14 (4):513–8. https://doi.org/10.1038/nn.2776 PMID: 21399632

33. Gunaydin LA, Yizhar O, Berndt A, Sohal VS, Deisseroth K, Hegemann P. Ultrafast optogenetic control. Nat Neurosci. 2010; 13(3):387–92. https://doi.org/10.1038/nn.2495 PMID: 20081849

34. Berndt A, Yizhar O, Gunaydin LA, Hegemann P, Deisseroth K. Bi-stable neural state switches. Nat Neurosci. 2009; 12(2):229–34. https://doi.org/10.1038/nn.2247 PMID: 19079251

35. Dawydow A, Gueta R, Ljaschenko D, Ullrich S, Hermann M, Ehmann N, et al. Channelrhodopsin-2-XXL, a powerful optogenetic tool for low-light applications. Proc Natl Acad Sci U S A. 2014.

36. Wietek J, Beltramo R, Scanziani M, Hegemann P, Oertner TG, Simon Wiegert J. An improved chloride-conducting channelrhodopsin for light-induced inhibition of neuronal activity *in vivo*. Scientific reports. 2015; 5:14807. https://doi.org/10.1038/srep14807 PMID: 26443033

37. Berndt A, Lee SY, Wietek J, Ramakrishnan C, Steinberg EE, Rashid AJ, et al. Structural foundations of optogenetics: Determinants of channelrhodopsin ion selectivity. Proceedings of the National Academy of Sciences of the United States of America. 2016; 113(4):822–9. https://doi.org/10.1073/pnas.1523341113 PMID: 26699459

38. Govorunova EG, Sineshchekov OA, Rodarte EM, Janz R, Morelle O, Melkonian M, et al. The Expanding Family of Natural Anion Channelrhodopsins Reveals Large Variations in Kinetics, Conductance, and Spectral Sensitivity. Scientific reports. 2017; 7:43358. https://doi.org/10.1038/srep43358 PMID: 28256618

39. Mohammad F, Stewart JC, Ott S, Chlebikova K, Chua JY, Koh TW, et al. Optogenetic inhibition of behavior with anion channelrhodopsins. Nature methods. 2017; 14(3):271–4. https://doi.org/10.1038/nmeth.4148 PMID: 28114289

40. Sineshchekov OA, Li H, Govorunova EG, Spudich JL. Photochemical reaction cycle transitions during anion channelrhodopsin gating. Proceedings of the National Academy of Sciences of the United States of America. 2016; 113(14):E1993–2000. https://doi.org/10.1073/pnas.1525269113 PMID: 27001860

41. Sineshchekov OA, Govorunova EG, Li H, Spudich JL. Gating mechanisms of a natural anion channel-rhodopsin. Proc Natl Acad Sci U S A. 2015; 112(46):14236–41. https://doi.org/10.1073/pnas.1513602112 PMID: 26578767

42. Husson SJ, Gottschalk A, Leifer AM. Optogenetic manipulation of neural activity in *C. elegans*: From synapse to circuits and behaviour. Biology of the cell. 2013; 105(6):235–50. https://doi.org/10.1111/boc.201200069 PMID: 23458457

43. Kittelmann M, Liewald JF, Hegermann J, Schultheis C, Brauner M, Steuer Costa W, et al. *In vivo* synaptic recovery following optogenetic hyperstimulation. Proc Natl Acad Sci U S A. 2013; 110(32):E3007–16. https://doi.org/10.1073/pnas.1305679110 PMID: 23878262

44. Steuer Costa W, Yu S-c, Liewald J, Gottschalk A. Fast cAMP modulation of neurotransmission via neuropeptide signals and vesicle loading. Curr Biol. 2017; 27:495–507. https://doi.org/10.1016/j.cub.2016.12.055 PMID: 28162892

45. Watanabe S, Liu Q, Davis MW, Hollopeter G, Thomas N, Jorgensen NB, et al. Ultrafast endocytosis at *Caenorhabditis elegans* neuromuscular junctions. eLife. 2013; 2:e00723. https://doi.org/10.7554/eLife.00723 PMID: 24015355

46. White JG, Southgate E, Thomson JN, Brenner S. The Structure of the Nervous System of the Nematode *Caenorhabditis elegans*. Philos Trans R Soc Lond B Biol Sci. 1986; 314(1165):1–340. PMID: 22462104

47. Fire A. Integrative transformation of *Caenorhabditis elegans*. Embo J. 1986; 5(10):2673–80. PMID: 16453714

48. Schmitt C, Schultheis C, Pokala N, Husson SJ, Liewald JF, Bargmann CI, et al. Specific expression of channelrhodopsin-2 in single neurons of *Caenorhabditis elegans*. PLoS ONE. 2012; 7(8):e43164. https://doi.org/10.1371/journal.pone.0043164 PMID: 22952643

49. Edelstein AD, Tsuchida MA, Amodaj N, Pinkard H, Vale RD, Stuurman N. Advanced methods of microscope control using µManager software. J Biol Methods. 1(2).

50. Nagel G, Szellas T, Kateriya S, Adeishvili N, Hegemann P, Bamberg E. Channelrhodopsins: directly light-gated cation channels. Biochem Soc Trans. 2005; 33(Pt 4):863–6. https://doi.org/10.1042/BST0330863 PMID: 16042615

51. Bamann C, Gueta R, Kleinlogel S, Nagel G, Bamberg E. Structural guidance of the photocycle of channelrhodopsin-2 by an interhelical hydrogen bond. Biochemistry. 2010; 49(2):267–78. https://doi.org/10.1021/bi901634p PMID: 20000562

52. Yizhar O, Fenno LE, Prigge M, Schneider F, Davidson TJ, O'Shea DJ, et al. Neocortical excitation/inhibition balance in information processing and social dysfunction. Nature. 2011; 477(7363):171–8. https://doi.org/10.1038/nature10360 PMID: 21796121

53. Bamann C, Kirsch T, Nagel G, Bamberg E. Spectral characteristics of the photocycle of channelrhodopsin-2 and its implication for channel function. J Mol Biol. 2008; 375(3):686–94. https://doi.org/10.1016/j.jmb.2007.10.072 PMID: 18037436

54. Stehfest K, Ritter E, Berndt A, Bartl F, Hegemann P. The branched photocycle of the slow-cycling channelrhodopsin-2 mutant C128T. J Mol Biol. 2010; 398(5):690–702. https://doi.org/10.1016/j.jmb.2010.03.031 PMID: 20346954

55. Schoenenberger P, Gerosa D, Oertner TG. Temporal control of immediate early gene induction by light. PLoS One. 2009; 4(12):e8185. https://doi.org/10.1371/journal.pone.0008185 PMID: 19997631

56. Liu P, Chen B, Wang ZW. Postsynaptic current bursts instruct action potential firing at a graded synapse. Nature communications. 2013; 4:1911. https://doi.org/10.1038/ncomms2925 PMID: 23715270

57. Gao S, Zhen M. Action potentials drive body wall muscle contractions in *Caenorhabditis elegans*. Proc Natl Acad Sci U S A. 2011; 108(6):2557–62. https://doi.org/10.1073/pnas.1012346108 PMID: 21248227

58. Lin JY. A user's guide to channelrhodopsin variants: features, limitations and future developments. Exp Physiol. 2011; 96(1):19–25. https://doi.org/10.1113/expphysiol.2009.051961 PMID: 20621963

59. Burgess P. Variation in light intensity at different latitudes and seasons, effects of cloud cover, and the amounts of direct and diffused sun light. Continuous Cover Forestry Group (CCFG) Scientific Meeting Westonbirt Arboretum, Gloucestershire, UK2009.

Figure S1

ChR2(L132C)::YFP
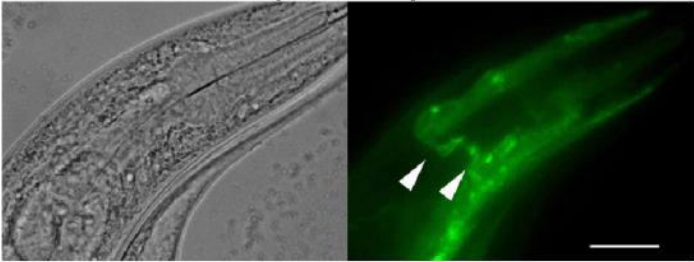
ChR2(C128S;L132C;H134R)::YFP
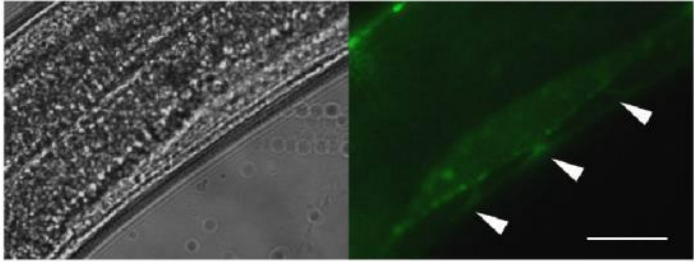
ChR2(L132C;H134R;T159C)::YFP
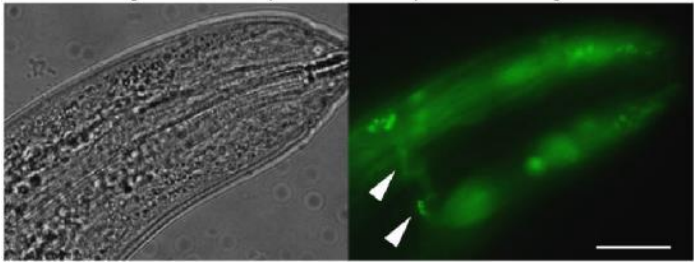
Figure S2
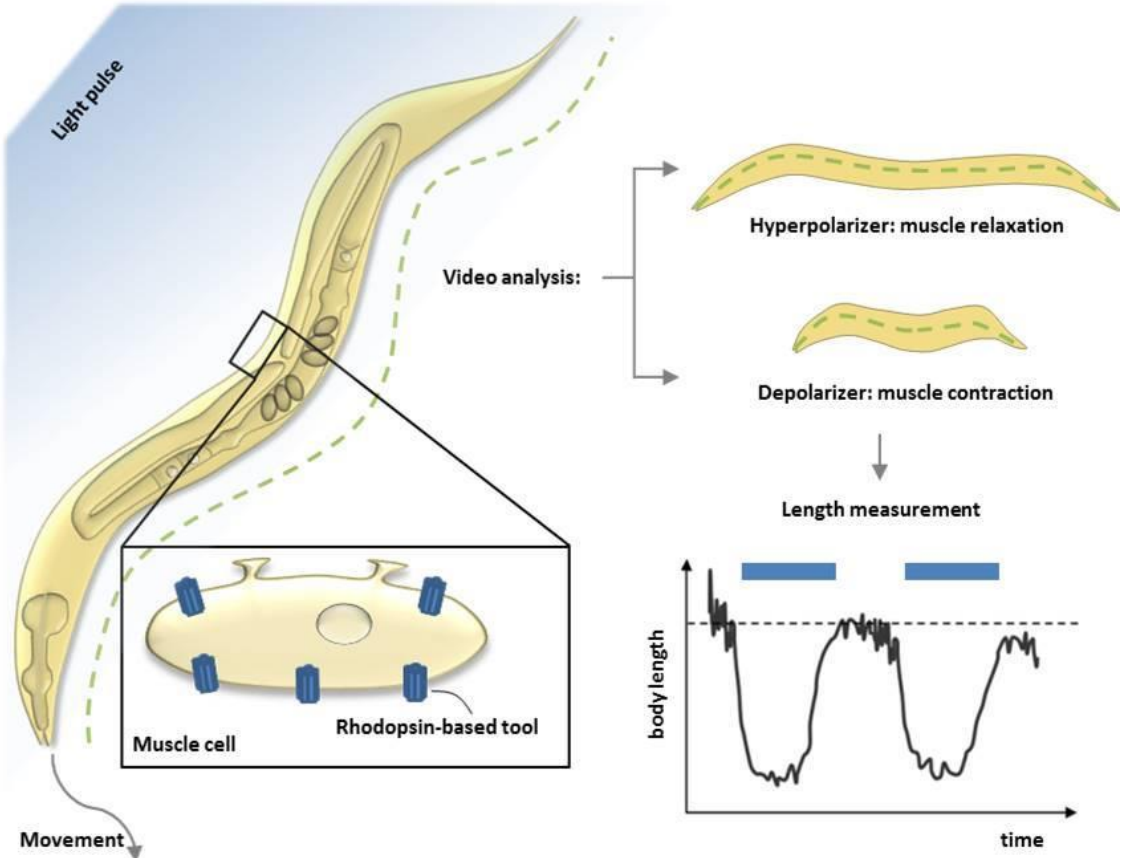
Figure S3

Figure S4

Figure S5

303

sliding average of normalized voltage traces
ACR2
ACR1
Time [s]
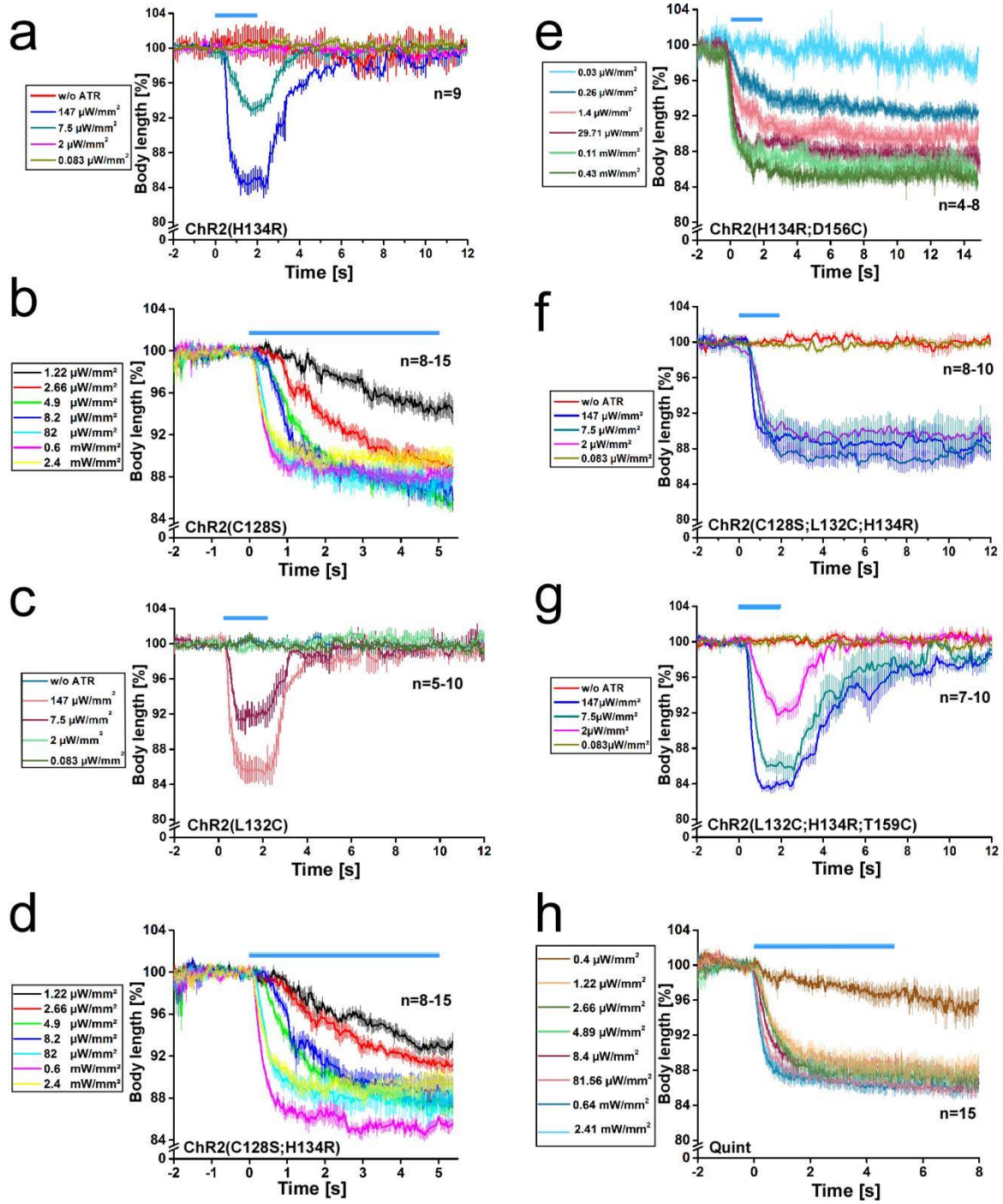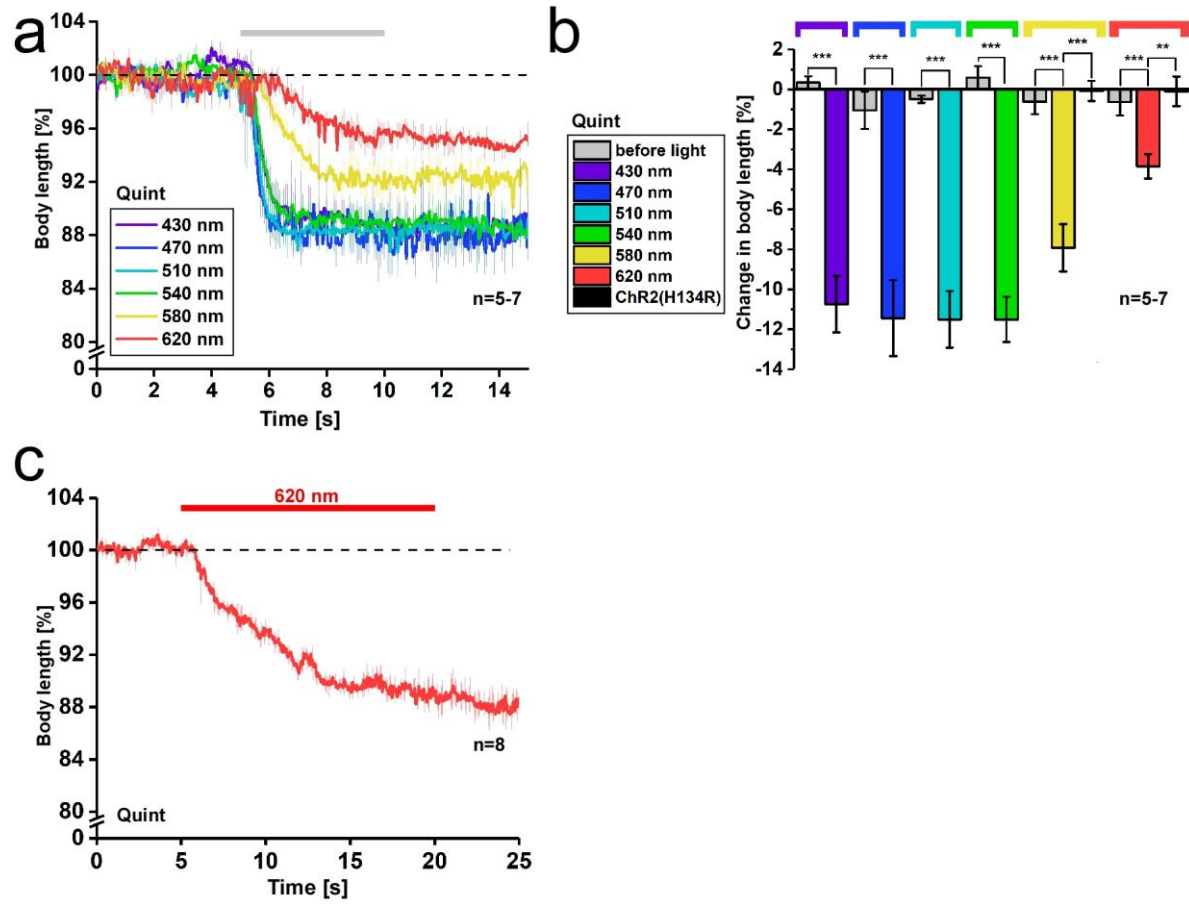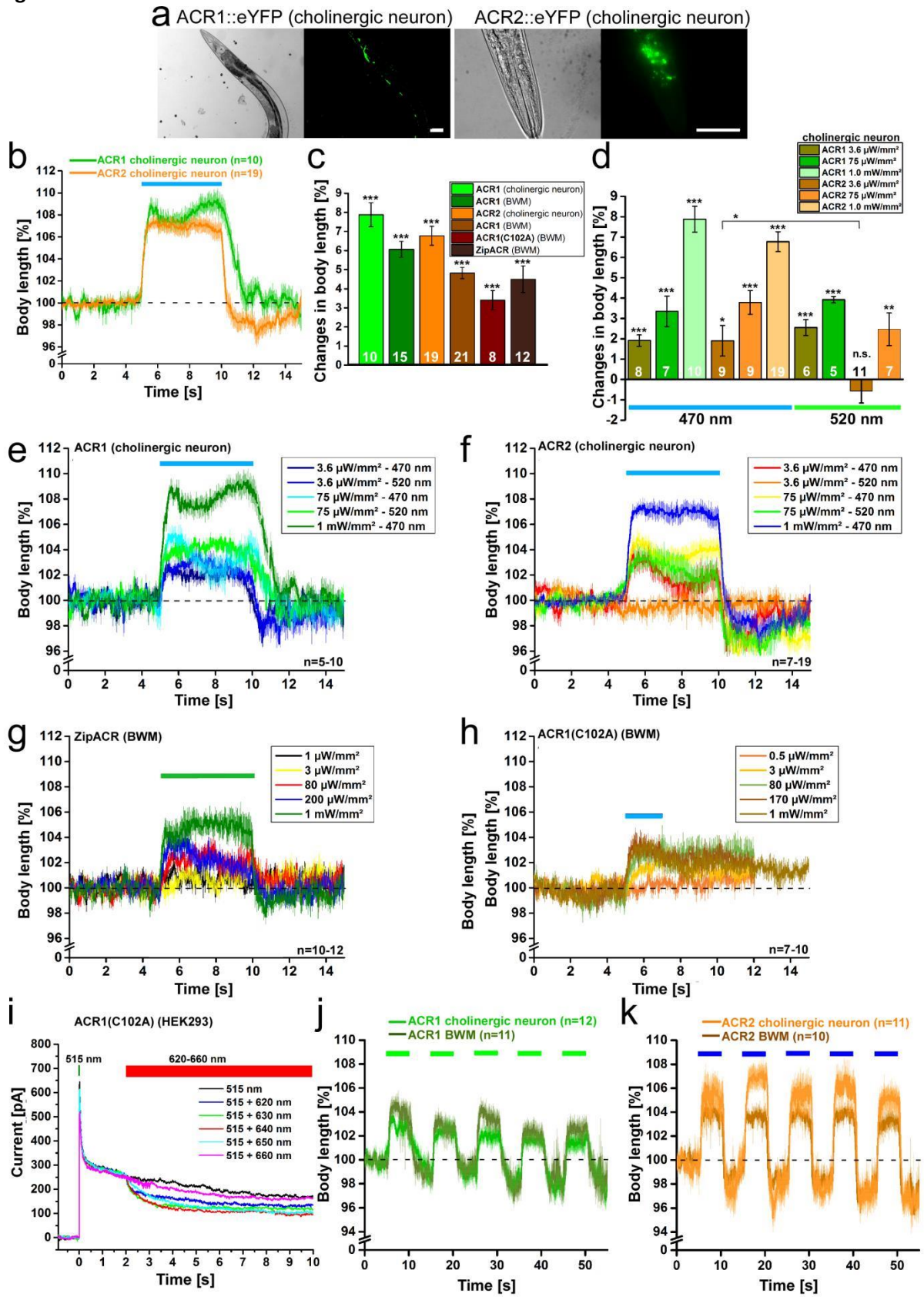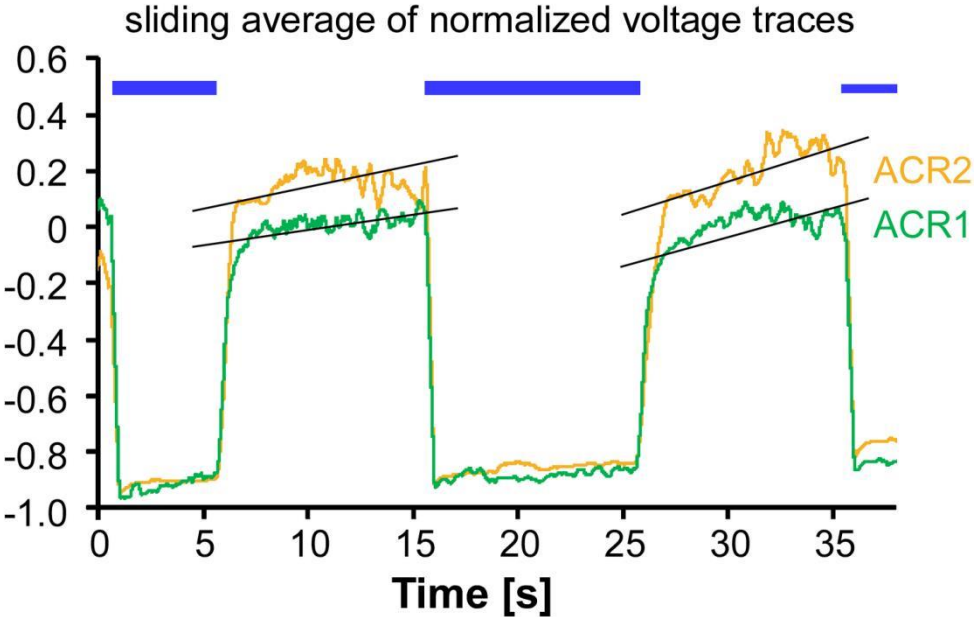
3. Discussion and future perspectives

3.1. Potential of all-optical electrophysiology and the OVC

As a result of this sequence of research studies, the first all-optical voltage clamp was developed and established in living animals[8]. Initial comparative studies of different rhodopsin-based optogenetic tools allowed the selection of appropriate actuators to meet the requirements of pure optical electrophysiology in *C. elegans*[9,15]. Eventually, reliable optical clamping of membrane voltage was accomplished in various muscular and neuronal tissues of the nematode, namely BWMs, the pharynx, cholinergic, and GABAergic neurons. Besides detection of altered cell physiology in *unc-13* mutants and generation of all-optical I-V-relationships to assess altered functionality of the L-type voltage-gated calcium channel EGL-19 (g.o.f.), the technique provided dynamic clamping of distinct APs in pharyngeal muscle and the enteric motor neuron DVB that could be aligned with accompanying behavior.

Voltage imaging as such and especially the OVC may now be used to shed light on various neuroscientific issues, which so far relied on labor-intensive patch clamp experiments. In addition to its ease of application, there are several direct benefits associated with the optical implementation of the voltage clamp technique and account for its great potential[23]: While classical patch clamp recordings are typically limited to one cell at a time, voltage imaging provides wide-field recordings of multiple cells simultaneously[109,110]. In this regard, OVC control could be restricted to one cell of interest, while observing the effects of various neighboring cells simultaneously, or even to expand the system's hard- and software to allow recording from independently OVC-controlled cells. To enable the measurement of cell ensembles in tissue, the development of new GEVIs in the red spectral range, but with lower required excitation intensity, would be desirable, as the high excitation intensity required for QuasAr2 can lead to phototoxic effects and photobleaching. In this regard, fluorophore degradation through interaction with oxygen generates reactive oxygen species that lead to cell damage, but also excited endogenous molecules may contribute to illumination-induced phototoxicity[79]. Moreover, illumination heats up the tissue, undesirably exerting influence on temperature-dependent

physiological processes. Already existing eFRET-based sensors exhibit much higher absolute fluorescence and require much lower excitation intensities, but at the expense of voltage sensitivity[70]. Further, imaging-based methods like the OVC allow to evaluate voltage dynamics at a subcellular level[80,111], e.g., to capture complex compartmental structures or fragile neuronal processes that are otherwise inaccessible to classical electrophysiology. As shown in this project, GEVI-based voltage imaging resolved electrical compartmentalization of the pharynx in *C. elegans* via generation of purely optical EPGs (electropharyngeogram) that visualized the temporally delayed de- and repolarization events in the subcompartments of this organ[15]. In addition, voltage imaging allows sequential measurements of the same cell in independent single acquisitions[111], unlike electrode-based applications that are limited as an acute technique. This has been particularly useful for the study of learning and memory[112]; by using the OVC, neurons of interest may not only be monitored but placed under genuine control in consecutive recordings with arbitrary temporal interruptions. In small animals such as *C. elegans*, where patch clamp experiments are limited to a few minutes and can only be applied to immobilized and dissected animals[5–7], the OVC may enable voltage clamping also in freely behaving animals. Here, the OVC opens up the opportunity to fine-tune behavioral aspects and to conclude on single cell driven activity patterns. Likewise, behavior-based feedback (velocity, direction of movement, body bending angles etc.) could be used in turn to control behavioral states dynamically.

3.2. OVC: Technical and molecular challenges

As the first proof-of-concept technology for optical voltage clamping, the OVC faces several challenges, currently limiting its applicability. With a maximum sampling rate of 100 Hz and system time constants of around 20 ms (50 Hz system frequency respectively), the feedback system performs fast enough for relatively slow voltage dynamics in *C. elegans* but would inevitably fail to control fast spiking in mammalian neurons. System speed is dependent on time constants of the used actuators and voltage sensors, determining the system frequency and eventually the maximum possible sampling rates. Likewise, photon capture at shorter exposure times, signal-to-noise of the expressed voltage indicator as well as computing time restricts the system's speed. The kinetics of the GEVIs are limited mainly by their off-kinetics: QuasAr2 exhibits a biexponential step response consisting of a fast 1.2 ms and a slow 11.8 ms time constant[35], where the fast contribution dominates with 68 % for a depolarizing step. Replacing QuasAr2 by a (future) faster GEVI, such as QuasAr1, may increase the inherent maximum system frequency, albeit potentially at the expense of voltage sensitivity. Likewise slow off-kinetics of the actuators are of less significance because of the bidirectional character that compensates for lagging channel closure. Since the OVC's current 10 ms exposure time provides photon counts of 1.8 million

per ROI (region of interest) and per frame with a respective accuracy of 0.08 % (shot-noise floor of the total signal power), a theoretical 1 kHz sampling would still reach an appropriate shot-noise floor-limited accuracy of less than 0.4 % (approximate photon capture of 185,000).

Next to the system's speed, the current OVC tool configuration requires a compensatory element to eliminate optical crosstalk to a minimum. Even if this performs well, the goal will be to keep the system as simple as possible and reduce potentially error-prone approximations. Since there is currently no further red-shifted equivalent to QuasAr2, it would be worth considering an alternative actuator combination that includes far blue and yellow/green activatable tools, to avoid spectral overlap with QuasAr2 stimulation. A tandem tool comprising bReaChES as depolarizing counterpart to ACR2 could reduce, though not entirely prevent cross-stimulation (**Figure 10**).
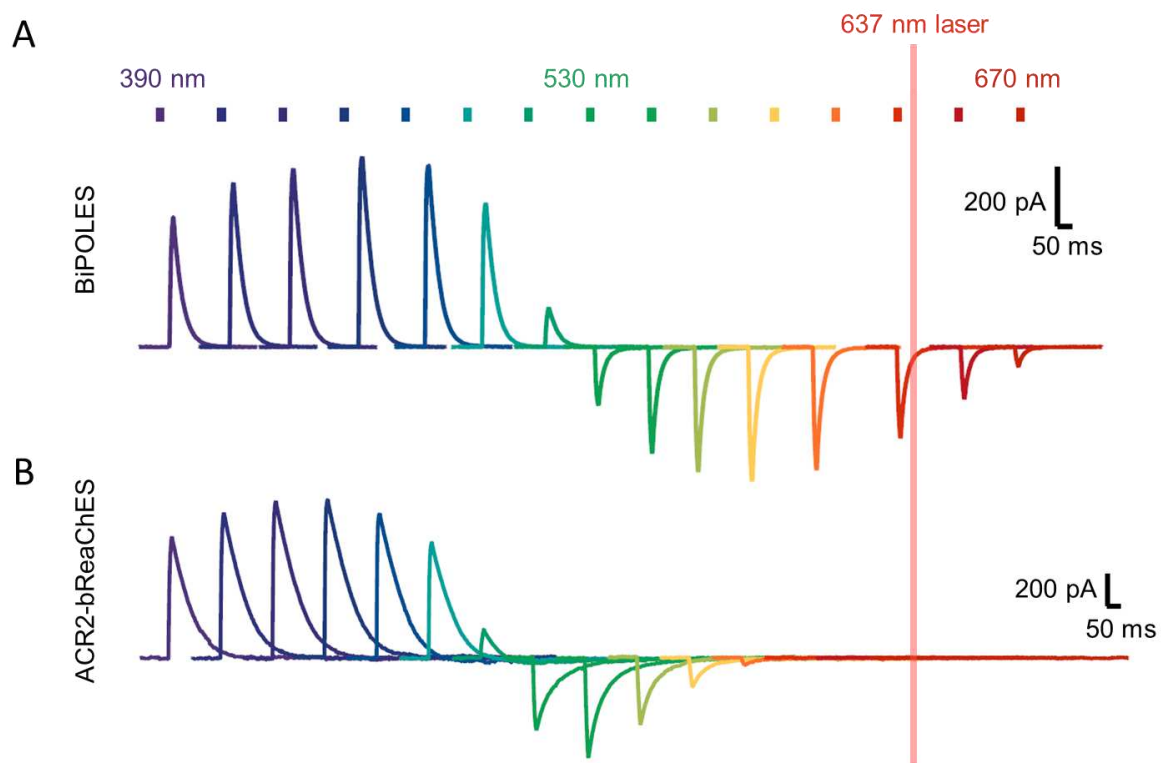
Figure 10. Photocurrents of two different tandem tools in HEK293 cells. (A) BiPOLES. **(B)** ACR2-bReaChES. Whole-cell patch clamp recordings at -60 mV with 10 ms light pulses. Theoretical QuasAr2 stimulation with laser as indicated. Data provided by Johannes Vierock[11].

A pair of actuators with two spectrally close elements (e.g., blue and green) but clear separation from the sensor excitation might bypass the detour via the compensation wavelength but would probably have a lower dynamic range and a very narrow excitation band, which could hamper voltage fine-tuning. Hence, future optogenetic tools with shifted and narrower absorption bands would be desirable. Regarding the selectable range of voltage sensors, the newest Arch-based variants QuasAr3, paQuasAr3, NovArch, and

QuasAr6a/b lag behind QuasAr2 in terms of voltage sensitivity and showed no further redshift in excitation spectra, though these newest engineering strategies yielded higher SNRs, improved localization, kinetics, and absolute brightness[111,113,114]. In addition, the higher SNR of the photoactivated variants is based on the additional illumination with blue light, which would interfere with excitation of OVC actuators. Considering the high photon count, achieved with QuasAr2 in the current experimental setup, it would be reasonable to investigate a red laser beyond 637 nm to reduce the excitation of Chrimson. Moreover, a factor that also depends on tool selection is the achievable dynamic range of the bidirectional voltage modulation. Although channels are superior to their pump equivalents in terms of efficiency and light sensitivity and are therefore applied in the OVC, there is one major drawback: Unlike with ion pumps, voltage modulation with channelrhodopsins relies on passive ion flow along their respective gradients and is therefore limited by the physiology of the cell type, especially by their reversal potentials for the corresponding ions. Although it generates robust data in the relevant physiological range and the dynamic range achieved is obviously sufficient to produce significant behavioral effects in the worm, it falls far short of conventional electrophysiology. In the attempt to transfer the OVC to the mammalian system[8], this becomes even more substantial: Optical modulation of membrane voltage was limited to a few millivolts, since here, unlike in *C. elegans*, the resting potential is close to the chloride reversal potential relevant to ACR2-driven hyperpolarization. The dynamic range also suffered from strong membrane leakage in the mammalian system compared to the nematode, probably caused by high expression levels. Powerful ion pumps would be ideal to extend the dynamic range and use the system independently of the model organism, but these are not yet available.

Another challenge compared to conventional electrophysiology is the indirect measurement of voltage via the relative change in fluorescence. These relative changes in fluorescence originate from subtly varying resting potentials. Therefore, all set clamp values are inevitably subject to a slight corresponding fluctuation and averaged data needs to be obtained for analysis – which is, however, also true for electrophysiology. Particularly for small animals as *C. elegans*, the required dissection is demanding and highly variable and so is the resulting data. Regarding accuracy and in agreement with earlier patch clamp recordings in BWMs, the cells investigated exhibit a normal distribution in resting potential (ca. -23 mV to -27 mV[8]), which stays constant during the calibration phase. This low variance along with the highly significant estimation parameters of the calibration regressions, however, allows a reliable conversion into absolute voltages despite the method's relative character. Nevertheless, the development of powerful probes that can directly detect absolute membrane voltage would be desirable. This typically involves a more sophisticated imaging regime, relying on ratiometric or time-resolved techniques and insensitivity to protein expression levels, bleaching, and background fluorescence[115]. For instance, in a previous study, the absolute membrane voltage was observed via a

complex illumination setup with a accuracy of 10 mV, where the wavelength-dependent time-domain response of the photocycle topology of Arch(D95H) was evaluated[115].

Last, a further challenge constitutes the adaptation and ongoing development of the control software. The current setup includes an I-controller to regulate the relative change in fluorescence by adjusting the wavelength. A shortcoming of this control variant is the inertia that arises when integration takes place over a long period of time. This is reflected in the increased reaction time, which makes it an accurate but slow controller[116]. Since system identification is crucial to set up any control application, the use of a PID controller along with a Kalman filter seemed reasonable but did not improve the control deviation or speed of the OVC system. Since biological systems are highly complex, the associated poor system knowledge limits the options in the choice of the control type to model-free approaches such as PID-control[86]. To improve control quality, several more advanced techniques are available. These include, for example, the fuzzy controller, adaptive controllers, and controllers based on neural networks – all being powerful approaches for handling non-linear, time-varying, adaptive systems[117,118].

3.3. Optical electrophysiology and the OVC: Future therapeutic and commercial potential

Next to immediate applications discussed above (chapter 3.1), all-optical electrophysiology and especially the OVC also possesses a promising commercial and maybe even therapeutic potential. Future neural and cardiac modulation therapies will most likely require closed-loop control, thus providing responsiveness to the current needs and (pathological) state of the targeted cells or tissues[119,120]. Implantable devices are already available to perform electrophysiological studies with the temporal and spatial precision of optogenetics[121]. These are used in basic cardiac and neuroscientific research as well as in pioneering studies of optogenetic pacing, optogenetic interruption of arrhythmias, and optogenetic adaptation of deep brain stimulation[122–124]. Recent developments in wireless technologies provide miniaturized optoelectronic devices with wireless power delivery and high flexibility, being well adaptable to the respective tissue or organ[86,121].

For example, in cardiac research, optogenetic pacing might be an advantageous alternative compared to the conventional electronic pacemakers[121]: Since the light stimulus must be confined only to the opsin-expressing group of cardiomyocytes, less energy is required than with an external electrical pulse. Optical stimulation via ion channels is also more physiological, as it resembles native activation of excitable cells. Moreover, and due to the low energy input, optogenetic defibrillators would be appealing

as this could bypass the need of high energy shocks. Recently developed three-dimensional elastic membranes, precisely fitting to the geometry of the heart, allow for both optical stimulation and usage of genetically encoded optical reporters, of which fluorescence is detected via photodetector arrays[121]. Assuming that gene delivery and clinical optogenetics can be realized and new highly sensitive and low intensity GEVIs will be developed, the use of the OVC technique would be conceivable within the scope of an adequate, less invasive alternative to conventional pacemakers. For neural application, conditional optogenetic stimulation based on online measurements and closed-loop feedback control is crucial for effective timing of therapeutically relevant stimulation interventions. This was for instance demonstrated for animal models of epilepsy, where real-time evaluation of seizures allowed to effectively hyperpolarize relevant neurons with NpHR-mediated hyperpolarization[125], unlike electrode-based approaches that lack spatial precision leading to unwanted side effects. By extending this approach to the true control nature of all-optical electrophysiology such as the OVC, pathological patterns could be detected without the need for additional electrodes and desired activity levels could be fine-tuned rather than shunting inhibition on a simple on-off principle.

In addition to the potential therapeutic use of the OVC, further development into a high-throughput screening platform is also an appealing option (see patent application: "AN OPTOGENETIC VOLTAGE CLAMP (OVC) AND USES THEREOf"[1] [126,127]). Thus, theoretically, the OVC could contribute to investigate ion channels of interest in a mutagenesis screen or compound libraries in a drug screening approach. The first step involves the generation of a stably transfected cell line, expressing all relevant molecular OVC components. When expressed in optimized amounts, the summed conductance of the OVC tools might be sufficient to compensate the currents of an additional ion channel under investigation. For the mutagenesis screening, the next step would be to transfect cells of the generated OVC cell line with randomly mutated versions of an ion channel, resulting in single cells, each expressing a unique mutant. Individual cells could be distributed into the wells of a microtiter plate via FACS and further expanded. An adapted and automated OVC device, equipped with either a camera or photomultiplier and the required light sources (**Figure 11**), could then be used to scan these
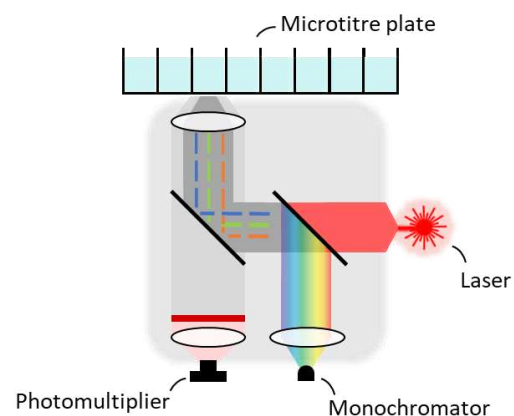
Figure 11. Model of a future HTS-OVC platform. The automated system is equipped with a photomultiplier, a monochromatic light source, and a laser for fluorescence recording or stimulation, respectively. A microtiter plate is moved automatically for each brief OVC recording (**Movie 5**).

---

[1] application number: EP 21162331.9; EP 4 056 681 A1; PCT/EP2022/056030

cells within the microtiter wells, moving from well to well and performing a brief OVC measurement (**Movie 5**). Comparable devices for fluorescence-based high-throughput screening already exist for calcium imaging[128]. To reduce the experiment duration and total scanning time per microtiter plate, the initial calibration time to counteract photobleaching could be bypassed by a preliminary test series to determine the bleaching parameters beforehand. This consideration is promising, since the measurement of many cells per well might allow an averaging of potential deviations.

Based on the aforementioned application, the second conceivable advancement of the OVC method could be high-throughput drug screening. Several pharmaceutical companies already have large substance libraries that could be potential target substances for interactions with specific ion channels. To identify relevant substances within these libraries, cells of the pre-generated OVC cell line mentioned above would first have to be transfected with a corresponding ion channel and cultured in a microtiter plate. The next step would be to add different test substances to each well and subsequently perform brief OVC measurements by using a high-throughput plate reader in 384-well format. Assuming a measurement time of a few seconds, the expected screening duration is in the range of a few minutes. Due to the purely optical nature of the OVC technique, the applicability may be considerably less complicated and most likely more cost-efficient than automated patch clamp systems, as the contactless procedure works without the need for pipettes and smaller volumes would be required. In addition, cell-to-cell variability would be more irrelevant with the OVC method, as the optical measurement can average the effect of hundreds of cells per compound, in contrast to the patch clamp method, where only a single cell can be observed. Eventually, for both potential applications, the evaluation of the feedback wavelength or related optical I-V-relations could allow to isolate mutants or substances of interest by exerting an influence on the respective channel. Depending on its characteristics (e.g., voltage-gated or constitutively open), modified conductivity or gating properties of the channel should occur at a specific membrane potential, reflected by a deviating wavelength output.

In conclusion, the OVC technology that has resulted from the present series of research works further extends the applicability of optogenetics and allows better adaptation to the highly complex and variable activity patterns of living organisms.

References

1. Bargmann, C. I. & Marder, E. From the connectome to brain function. *Nature methods* **10,** 483–490; 10.1038/nmeth.2451 (2013).

2. Anderson, D. J. Circuit modules linking internal states and social behaviour in flies and mice. *Nature reviews. Neuroscience* **17,** 692–704; 10.1038/nrn.2016.125 (2016).

3. MARMONT, G. Studies on the axon membrane; a new method. *Journal of cellular and comparative physiology* **34,** 351–382; 10.1002/jcp.1030340303 (1949).

4. HODGKIN, A. L. & HUXLEY, A. F. A quantitative description of membrane current and its application to conduction and excitation in nerve. *The Journal of physiology* **117,** 500–544; 10.1113/jphysiol.1952.sp004764 (1952).

5. Francis, M. M., Mellem, J. E. & Maricq, A. V. Bridging the gap between genes and behavior: recent advances in the electrophysiological analysis of neural function in Caenorhabditis elegans. *Trends in Neurosciences* **26,** 90–99; 10.1016/S0166-2236(02)00041-3 (2003).

6. Liu, P., Chen, B. & Wang, Z.-W. GABAergic motor neurons bias locomotor decision-making in C. elegans. *Nature communications* **11,** 5076; 10.1038/s41467-020-18893-9 (2020).

7. Noguchi, A., Ikegaya, Y. & Matsumoto, N. In Vivo Whole-Cell Patch-Clamp Methods: Recent Technical Progress and Future Perspectives. *Sensors (Basel, Switzerland)* **21**; 10.3390/s21041448 (2021).

8. Bergs, A. C. F. *et al.* All-optical closed-loop voltage clamp for precise control of muscles and neurons in live animals. *Nature communications* **14,** 1939; 10.1038/s41467-023-37622-6 (2023).

9. Bergs, A. *et al.* Rhodopsin optogenetic toolbox v2.0 for light-sensitive excitation and inhibition in Caenorhabditis elegans. *PloS one* **13,** e0191802; 10.1371/journal.pone.0191802 (2018).

10. Brown, J. *et al.* Expanding the Optogenetics Toolkit by Topological Inversion of Rhodopsins. *Cell* **175,** 1131-1140.e11; 10.1016/j.cell.2018.09.026 (2018).

11. Vierock, J. *et al.* BiPOLES is an optogenetic tool developed for bidirectional dual-color control of neurons. *Nature communications* **12**; 10.1038/s41467-021-24759-5 (2021).

12. Bergs, A., Liewald, J. & Gottschalk, A. Optogenetischer Werkzeugkasten für neue experimentelle Ansätze. *Biospektrum* **25,** 398–401; 10.1007/s12268-019-1069-z (2019).

13. Bergs, A., Henss, T., Glock, C., Nagpal, J. & Gottschalk, A. Microbial Rhodopsin Optogenetic Tools: Application for Analyses of Synaptic Transmission and of Neuronal Network Activity in Behavior. *Methods in molecular biology (Clifton, N.J.)* **2468,** 89–115; 10.1007/978-1-0716-2181-3_6 (2022).

14. Tolstenkov, O. *et al.* Functionally asymmetric motor neurons contribute to coordinating locomotion of Caenorhabditis elegans. *eLife* **7**; 10.7554/eLife.34997 (2018).

15. Azimi Hashemi, N. *et al.* Rhodopsin-based voltage imaging tools for use in muscles and neurons of Caenorhabditis elegans. *Proceedings of the National Academy of Sciences of the United States of America* **116,** 17051–17060; 10.1073/pnas.1902443116 (2019).

16. Jánosi, B. *et al. RIM and RIM-binding protein localize synaptic CaV2 channels to differentially regulate transmission in neuronal circuits* (2021).

17. Berndt, A., Yizhar, O., Gunaydin, L. A., Hegemann, P. & Deisseroth, K. Bi-stable neural state switches. *Nature neuroscience* **12,** 229–234; 10.1038/nn.2247 (2009).

18. Dawydow, A. *et al.* Channelrhodopsin-2-XXL, a powerful optogenetic tool for low-light applications. *Proceedings of the National Academy of Sciences of the United States of America* **111,** 13972–13977; 10.1073/pnas.1408269111 (2014).

19. Schultheis, C., Liewald, J. F., Bamberg, E., Nagel, G. & Gottschalk, A. Optogenetic long-term manipulation of behavior and animal development. *PloS one* **6,** e18766; 10.1371/journal.pone.0018766 (2011).

20. Wietek, J. *et al.* Conversion of channelrhodopsin into a light-gated chloride channel. *Science (New York, N.Y.)* **344,** 409–412; 10.1126/science.1249375 (2014).

21. Govorunova, E. G., Sineshchekov, O. A., Janz, R., Liu, X. & Spudich, J. L. NEUROSCIENCE. Natural light-gated anion channels: A family of microbial rhodopsins for advanced optogenetics. *Science (New York, N.Y.)* **349,** 647–650; 10.1126/science.aaa7484 (2015).

22. Gong, Y., Wagner, M. J., Zhong Li, J. & Schnitzer, M. J. Imaging neural spiking in brain tissue using FRET-opsin protein voltage sensors. *Nature communications* **5,** 3674; 10.1038/ncomms4674 (2014).

23. Adam, Y. All-optical electrophysiology in behaving animals. *Journal of neuroscience methods* **353,** 109101; 10.1016/j.jneumeth.2021.109101 (2021).

24. Rajasethupathy, P., Ferenczi, E. & Deisseroth, K. Targeting Neural Circuits. *Cell* **165,** 524–534; 10.1016/j.cell.2016.03.047 (2016).

25. Kleinlogel, S. *et al.* Ultra light-sensitive and fast neuronal activation with the $Ca^{2}+$-permeable channelrhodopsin CatCh. *Nature neuroscience* **14,** 513–518; 10.1038/nn.2776 (2011).

26. Gunaydin, L. A. *et al.* Ultrafast optogenetic control. *Nature neuroscience* **13,** 387–392; 10.1038/nn.2495 (2010).

27. Lin, J. Y., Knutsen, P. M., Muller, A., Kleinfeld, D. & Tsien, R. Y. ReaChR: a red-shifted variant of channelrhodopsin enables deep transcranial optogenetic excitation. *Nature neuroscience* **16,** 1499–1508; 10.1038/nn.3502 (2013).

28. Klapoetke, N. C. *et al.* Independent optical excitation of distinct neural populations. *Nature methods* **11,** 338–346; 10.1038/nmeth.2836 (2014).

29. Deisseroth, K. Optogenetics: 10 years of microbial opsins in neuroscience. *Nature neuroscience* **18,** 1213–1225; 10.1038/nn.4091 (2015).

30. Yizhar, O., Fenno, L. E., Davidson, T. J., Mogri, M. & Deisseroth, K. Optogenetics in neural systems. *Neuron* **71,** 9–34; 10.1016/j.neuron.2011.06.004 (2011).

31. Knöpfel, T. *et al.* Toward the second generation of optogenetic tools. *The Journal of neuroscience : the official journal of the Society for Neuroscience* **30,** 14998–15004; 10.1523/JNEUROSCI.4190-10.2010 (2010).

32. Emiliani, V. *et al.* Optogenetics for light control of biological systems. *Nat Rev Methods Primers* **2**; 10.1038/s43586-022-00136-4 (2022).

33. Deisseroth, K. Optogenetics. *Nature methods* **8,** 26–29; 10.1038/nmeth.f.324 (2011).

34. Kralj, J. M., Douglass, A. D., Hochbaum, D. R., Maclaurin, D. & Cohen, A. E. Optical recording of action potentials in mammalian neurons using a microbial rhodopsin. *Nature methods* **9,** 90–95; 10.1038/nmeth.1782 (2011).

35. Hochbaum, D. R. *et al.* All-optical electrophysiology in mammalian neurons using engineered microbial rhodopsins. *Nature methods* **11,** 825–833; 10.1038/nmeth.3000 (2014).

36. Fan, L. Z. *et al.* All-Optical Electrophysiology Reveals the Role of Lateral Inhibition in Sensory Processing in Cortical Layer 1. *Cell* **180,** 521-535.e18; 10.1016/j.cell.2020.01.001 (2020).

37. Piatkevich, K. D. *et al.* A robotic multidimensional directed evolution approach applied to fluorescent voltage reporters. *Nature chemical biology* **14,** 352–360; 10.1038/s41589-018-0004-9 (2018).

38. Knöpfel, T. & Song, C. Optical voltage imaging in neurons: moving from technology development to practical tool. *Nature reviews. Neuroscience* **20,** 719–727; 10.1038/s41583-019-0231-4 (2019).

39. Gong, Y., Li, J. Z. & Schnitzer, M. J. Enhanced Archaerhodopsin Fluorescent Protein Voltage Indicators. *PloS one* **8,** e66959; 10.1371/journal.pone.0066959 (2013).

40. Maclaurin, D., Venkatachalam, V., Lee, H. & Cohen, A. E. Mechanism of voltage-sensitive fluorescence in a microbial rhodopsin. *Proceedings of the National Academy of Sciences of the United States of America* **110,** 5939–5944; 10.1073/pnas.1215595110 (2013).

41. Béjà, O. *et al.* Bacterial rhodopsin: evidence for a new type of phototrophy in the sea. *Science (New York, N.Y.)* **289,** 1902–1906; 10.1126/science.289.5486.1902 (2000).

42. Litvin, F. F., Sineshchekov, O. A. & Sineshchekov, V. A. Photoreceptor electric potential in the phototaxis of the alga Haematococcus pluvialis. *Nature* **271,** 476–478; 10.1038/271476a0 (1978).

43. Harz, H. & Hegemann, P. Rhodopsin-regulated calcium currents in Chlamydomonas. *Nature* **351,** 489–491; 10.1038/351489a0 (1991).

44. Ernst, O. P. *et al.* Microbial and animal rhodopsins: structures, functions, and molecular mechanisms. *Chemical reviews* **114,** 126–163; 10.1021/cr4003769 (2014).

45. Zhang, F. *et al.* The microbial opsin family of optogenetic tools. *Cell* **147,** 1446–1457; 10.1016/j.cell.2011.12.004 (2011).

46. Kato, H. E. *et al.* Crystal structure of the channelrhodopsin light-gated cation channel. *Nature* **482,** 369–374; 10.1038/nature10870 (2012).

47. Nagel, G. *et al.* Channelrhodopsin-1: a light-gated proton channel in green algae. *Science (New York, N.Y.)* **296,** 2395–2398; 10.1126/science.1072068 (2002).

48. Nagel, G. *et al.* Channelrhodopsin-2, a directly light-gated cation-selective membrane channel. *Proceedings of the National Academy of Sciences of the United States of America* **100,** 13940–13945; 10.1073/pnas.1936192100 (2003).

49. Kuhne, J. *et al.* Unifying photocycle model for light adaptation and temporal evolution of cation conductance in channelrhodopsin-2. *Proceedings of the National Academy of Sciences of the United States of America* **116,** 9380–9389; 10.1073/pnas.1818707116 (2019).

50. Ritter, E., Stehfest, K., Berndt, A., Hegemann, P. & Bartl, F. J. Monitoring Light-induced Structural Changes of Channelrhodopsin-2 by UV-visible and Fourier Transform Infrared Spectroscopy*. *The Journal of Biological Chemistry* **283,** 35033–35041; 10.1074/jbc.M806353200 (2008).

51. Bamann, C., Kirsch, T., Nagel, G. & Bamberg, E. Spectral characteristics of the photocycle of channelrhodopsin-2 and its implication for channel function. *Journal of molecular biology* **375,** 686–694; 10.1016/j.jmb.2007.10.072 (2008).

52. Deisseroth, K. & Hegemann, P. The form and function of channelrhodopsin. *Science (New York, N.Y.)* **357**; 10.1126/science.aan5544 (2017).

53. Mattis, J. *et al.* Principles for applying optogenetic tools derived from direct comparative analysis of microbial opsins. *Nature methods* **9,** 159–172; 10.1038/nmeth.1808 (2011).

54. Govorunova, E. G., Sineshchekov, O. A. & Spudich, J. L. Emerging Diversity of Channelrhodopsins and Their Structure-Function Relationships. *Frontiers in cellular neuroscience* **15,** 800313; 10.3389/fncel.2021.800313 (2021).

55. Yizhar, O. *et al.* Neocortical excitation/inhibition balance in information processing and social dysfunction. *Nature* **477,** 171–178; 10.1038/nature10360 (2011).

56. Han, X. & Boyden, E. S. Multiple-color optical activation, silencing, and desynchronization of neural activity, with single-spike temporal resolution. *PloS one* **2,** e299; 10.1371/journal.pone.0000299 (2007).

57. Zhang, F. *et al.* Multimodal fast optical interrogation of neural circuitry. *Nature* **446,** 633–639; 10.1038/nature05744 (2007).

58. Mukohata, Y., Sugiyama, Y., Ihara, K. & Yoshida, M. An Australian halobacterium contains a novel proton pump retinal protein: archaerhodopsin. *Biochemical and biophysical research communications* **151,** 1339–1345; 10.1016/S0006-291X(88)80509-6 (1988).

59. Chow, B. Y. *et al.* High-performance genetically targetable optical neural silencing by light-driven proton pumps. *Nature* **463,** 98–102; 10.1038/nature08652 (2010).

60. Berndt, A., Lee, S. Y., Ramakrishnan, C. & Deisseroth, K. Structure-guided transformation of channelrhodopsin into a light-activated chloride channel. *Science (New York, N.Y.)* **344,** 420–424; 10.1126/science.1252367 (2014).

61. Berndt, A. *et al.* Structural foundations of optogenetics: Determinants of channelrhodopsin ion selectivity. *Proceedings of the National Academy of Sciences of the United States of America* **113,** 822–829; 10.1073/pnas.1523341113. (2016).

62. Govorunova, E. G. *et al.* The Expanding Family of Natural Anion Channelrhodopsins Reveals Large Variations in Kinetics, Conductance, and Spectral Sensitivity. *Scientific reports* **7,** 43358; 10.1038/srep43358 (2017).

63. Govorunova, E. G. *et al.* Extending the Time Domain of Neuronal Silencing with Cryptophyte Anion Channelrhodopsins. *eNeuro* **5**; 10.1523/ENEURO.0174-18.2018 (2018).

64. Ruffert, K. *et al.* Glutamate residue 90 in the predicted transmembrane domain 2 is crucial for cation flux through channelrhodopsin 2. *Biochemical and biophysical research communications* **410,** 737–743; 10.1016/j.bbrc.2011.06.024 (2011).

65. Baker, B. J. *et al.* Imaging brain activity with voltage- and calcium-sensitive dyes. *Cellular and molecular neurobiology* **25,** 245–282; 10.1007/s10571-005-3059-6 (2005).

66. Akerboom, J. *et al.* Genetically encoded calcium indicators for multi-color neural activity imaging and combination with optogenetics. *Frontiers in molecular neuroscience* **6,** 2; 10.3389/fnmol.2013.00002. (2013).

67. Chen, T.-W. *et al.* Ultrasensitive fluorescent proteins for imaging neuronal activity. *Nature* **499,** 295–300; 10.1038/nature12354 (2013).

68. Lin, M. Z. & Schnitzer, M. J. Genetically encoded indicators of neuronal activity. *Nature neuroscience* **19,** 1142–1153; 10.1038/nn.4359 (2016).

69. Williams, P. D. E. *et al.* Serotonin Disinhibits a Caenorhabditis elegans Sensory Neuron by Suppressing Ca2+-Dependent Negative Feedback. *The Journal of neuroscience : the official journal of the Society for Neuroscience* **38,** 2069–2080; 10.1523/JNEUROSCI.1908-17.2018 (2018).

70. Zou, P. *et al.* Bright and fast multicoloured voltage reporters via electrochromic FRET. *Nature communications* **5,** 4625; 10.1038/ncomms5625 (2014).

71. Flytzanis, N. C. *et al.* Archaerhodopsin variants with enhanced voltage-sensitive fluorescence in mammalian and Caenorhabditis elegans neurons. *Nature communications* **5,** 4894; 10.1038/ncomms5894 (2014).

72. Zhang, X. M., Yokoyama, T. & Sakamoto, M. Imaging Voltage with Microbial Rhodopsins. *Frontiers in molecular biosciences* **8,** 738829; 10.3389/fmolb.2021.738829 (2021).

73. Bando, Y., Grimm, C., Cornejo, V. H. & Yuste, R. Genetic voltage indicators. *BMC biology* **17,** 71; 10.1186/s12915-019-0682-0 (2019).

74. Kralj, J. M., Hochbaum, D. R., Douglass, A. D. & Cohen, A. E. Electrical spiking in Escherichia coli probed with a fluorescent voltage-indicating protein. *Science (New York, N.Y.)* **333,** 345–348; 10.1126/science.1204763 (2011).

75. Silapetere, A. *et al.* QuasAr Odyssey: the origin of fluorescence and its voltage sensitivity in microbial rhodopsins. *Nature communications* **13,** 5501; 10.1038/s41467-022-33084-4 (2022).

76. Lanyi, J. K. Proton transfers in the bacteriorhodopsin photocycle. *Biochimica et biophysica acta* **1757,** 1012–1018; 10.1016/j.bbabio.2005.11.003 (2006).

77. Abdelfattah, A. S. *et al.* A general approach to engineer positive-going eFRET voltage indicators. *Nature communications* **11**; 10.1038/s41467-020-17322-1 (2020).

78. Clemens, M., Phatak, P., Cui, Q., Bondar, A.-N. & Elstner, M. Role of Arg82 in the early steps of the bacteriorhodopsin proton-pumping cycle. *The journal of physical chemistry. B* **115,** 7129–7135; 10.1021/jp201865k (2011).

79. Rhee, J. K. *et al.* Biophysical Parameters of GEVIs: Considerations for Imaging Voltage. *Biophysical journal* **119,** 1–8; 10.1016/j.bpj.2020.05.019 (2020).

80. Gong, Y. *et al.* High-speed recording of neural spikes in awake mice and flies with a fluorescent voltage sensor. *Science (New York, N.Y.)* **350,** 1361–1366; 10.1126/science.aab0810 (2015).

81. Kannan, M. *et al.* Fast, in vivo voltage imaging using a red fluorescent indicator. *Nature methods* **15,** 1108–1116; 10.1038/s41592-018-0188-7 (2018).

82. Xu, Y. *et al.* Hybrid Indicators for Fast and Sensitive Voltage Imaging. *Angewandte Chemie (International ed. in English)* **57,** 3949–3953; 10.1002/anie.201712614 (2018).

83. Beck, C. & Gong, Y. A high-speed, bright, red fluorescent voltage sensor to detect neural activity. *Scientific reports* **9,** 15878; 10.1038/s41598-019-52370-8 (2019).

84. Mayr, O. *The origins of feedback control* (M.I.T. Press, Cambridge, 1970).

85. DiStefano, J. J., Stubberud, A. R. & Williams, I. J. *Feedback and control systems* (McGraw Hill Education, New York, 2014).

86. Grosenick, L., Marshel, J. H. & Deisseroth, K. Closed-loop and activity-guided optogenetic control. *Neuron* **86,** 106–139; 10.1016/j.neuron.2015.03.034 (2015).

87. Aström, K. J. & Murray, R. M. *Feedback Systems. An Introduction for Scientists and Engineers* (Princeton University Press, Princeton, NJ, USA, 2010).

88. Kalman, R. E. A New Approach to Linear Filtering and Prediction Problems. *Journal of Basic Engineering* **82,** 35–45; 10.1115/1.3662552 (1960).

89. *Advanced PID Control* (ISA, 2006).

90. Ogata, K. *Modern control engineering.* 3rd ed. (Prentice-Hall, Upper Saddle River, NJ, 1997).

91. Newman, J. P. *et al.* Optogenetic feedback control of neural activity. *eLife* **4,** e07192; 10.7554/eLife.07192 (2015).

92. Streit, J. & Kleinlogel, S. Dynamic all-optical drug screening on cardiac voltage-gated ion channels. *Scientific reports* **8,** 1153; 10.1038/s41598-018-19412-z (2018).

93. Quach, B., Krogh-Madsen, T., Entcheva, E. & Christini, D. J. Light-Activated Dynamic Clamp Using iPSC-Derived Cardiomyocytes. *Biophysical journal* **115,** 2206–2217; 10.1016/j.bpj.2018.10.018 (2018).

94. Kiskinis, E. *et al.* All-Optical Electrophysiology for High-Throughput Functional Characterization of a Human iPSC-Derived Motor Neuron Model of ALS. *Stem cell reports* **10,** 1991–2004; 10.1016/j.stemcr.2018.04.020 (2018).

95. HODGKIN, A. L., HUXLEY, A. F. & KATZ, B. Measurement of current-voltage relations in the membrane of the giant axon of Loligo. *The Journal of physiology* **116,** 424–448; 10.1113/jphysiol.1952.sp004716 (1952).

96. Wallach, A. The response clamp: functional characterization of neural systems using closed-loop control. *Frontiers in neural circuits* **7,** 5; 10.3389/fncir.2013.00005 (2013).

97. Kenyon, C. The nematode Caenorhabditis elegans. *Science (New York, N.Y.)* **240,** 1448–1453; 10.1126/science.3287621 (1988).

98. Brenner, S. The genetics of Caenorhabditis elegans. *Genetics* **77,** 71–94; 10.1093/genetics/77.1.71 (1974).

99. Husson, S. J., Gottschalk, A. & Leifer, A. M. Optogenetic manipulation of neural activity in C. elegans: from synapse to circuits and behaviour. *Biology of the cell* **105,** 235–250; 10.1111/boc.201200069 (2013).

100. Cook, S. J. *et al.* Whole-animal connectomes of both Caenorhabditis elegans sexes. *Nature* **571,** 63–71; 10.1038/s41586-019-1352-7 (2019).

101. Genome sequence of the nematode C. elegans: a platform for investigating biology. *Science (New York, N.Y.)* **282,** 2012–2018; 10.1126/science.282.5396.2012 (1998).

102. Amelie Bergs. *Characterization of novel Anion Channelrhodopsins and inverted Channelrhodopsin. Master thesis* (Frankfurt a.M., 2017).

103. David Zarkower. Somatic sex determination. Available at http://www.wormbook.org/chapters/www_somaticsexdeterm/somaticsexdeterm.html (2006).

104. Schüler, C., Fischer, E., Shaltiel, L., Steuer Costa, W. & Gottschalk, A. Arrhythmogenic effects of mutated L-type Ca2+-channels on an optogenetically paced muscular pump in Caenorhabditis elegans. *Scientific reports* **5**; 10.1038/srep14427 (2015).

105. Avery, L. & You, Y.-J. C. elegans feeding. *WormBook,* 1–23; 10.1895/wormbook.1.150.1 (2012).

106. Liu, Q., Kidd, P. B., Dobosiewicz, M. & Bargmann, C. I. C. elegans AWA Olfactory Neurons Fire Calcium-Mediated All-or-None Action Potentials. *Cell* **175,** 57-70.e17; 10.1016/j.cell.2018.08.018 (2018).

107. Jiang, J. *et al. C. elegans enteric motor neurons fire synchronized action potentials underlying the defecation motor program* (2021).

108. Gao, S. & Zhen, M. Action potentials drive body wall muscle contractions in Caenorhabditis elegans. *Proceedings of the National Academy of Sciences of the United States of America* **108,** 2557–2562; 10.1073/pnas.1012346108 (2011).

109. Abdelfattah, A. S. *et al.* Bright and photostable chemigenetic indicators for extended in vivo voltage imaging. *Science (New York, N.Y.)* **365,** 699–704; 10.1126/science.aav6416 (2019).

110. Piatkevich, K. D. *et al.* Population imaging of neural activity in awake behaving mice. *Nature* **574,** 413–417; 10.1038/s41586-019-1641-1 (2019).

111. Adam, Y. *et al.* Voltage imaging and optogenetics reveal behaviour-dependent changes in hippocampal dynamics. *Nature* **569,** 413–417; 10.1038/s41586-019-1166-7 (2019).

112. Villette, V. *et al.* Ultrafast Two-Photon Imaging of a High-Gain Voltage Indicator in Awake Behaving Mice. *Cell* **179,** 1590-1608.e23; 10.1016/j.cell.2019.11.004 (2019).

113. Tian, H. *et al.* Video-based pooled screening yields improved far-red genetically encoded voltage indicators. *Nature methods* **20,** 1082–1094; 10.1038/s41592-022-01743-5 (2023).

114. Chien, M.-P. *et al.* Photoactivated voltage imaging in tissue with an archaerhodopsin-derived reporter. *Science advances* **7**; 10.1126/sciadv.abe3216 (2021).

115. Hou, J. H., Venkatachalam, V. & Cohen, A. E. Temporal dynamics of microbial rhodopsin fluorescence reports absolute membrane voltage. *Biophysical journal* **106,** 639–648; 10.1016/j.bpj.2013.11.4493 (2014).

116. Lunze, J. *Regelungstechnik.* 6th ed. (Springer Verlag, Heidelberg, 2010).

117. Lutz, H. & Wendt, W. *Taschenbuch der Regelungstechnik. Mit MATLAB und Simulink.* 12th ed. (Verlag Europa-Lehrmittel, Nourney, Vollmer GmbH & Co. KG, Haan-Gruiten, 2021).

118. Cao, C., Ma, L. & Xu, Y. Adaptive Control Theory and Applications. *Journal of Control Science and Engineering* **2012,** 1–2; 10.1155/2012/827353 (2012).

119. Mickle, A. D. *et al.* A wireless closed-loop system for optogenetic peripheral neuromodulation. *Nature* **565,** 361–365; 10.1038/s41586-018-0823-6 (2019).

120. Krook-Magnuson, E., Szabo, G. G., Armstrong, C., Oijala, M. & Soltesz, I. Cerebellar Directed Optogenetic Intervention Inhibits Spontaneous Hippocampal Seizures in a Mouse Model of Temporal Lobe Epilepsy12. *eNeuro* **1**; 10.1523/ENEURO.0005-14.2014 (2014).

121. Madrid, M. K., Brennan, J. A., Yin, R. T., Knight, H. S. & Efimov, I. R. Advances in Implantable Optogenetic Technology for Cardiovascular Research and Medicine. *Frontiers in physiology* **12,** 720190; 10.3389/fphys.2021.720190 (2021).

122. Hsueh, B. *et al.* Cardiogenic control of affective behavioural state. *Nature* **615,** 292–299; 10.1038/s41586-023-05748-8 (2023).

123. Kim, T. *et al.* Injectable, cellular-scale optoelectronics with applications for wireless optogenetics. *Science (New York, N.Y.)* **340,** 211–216; 10.1126/science.1232437 (2013).

124. Gunaydin, L. A. *et al.* Natural neural projection dynamics underlying social behavior. *Cell* **157,** 1535–1551; 10.1016/j.cell.2014.05.017 (2014).

125. Paz, J. T. *et al.* Closed-loop optogenetic control of thalamus as a tool for interrupting seizures after cortical injury. *Nature neuroscience* **16,** 64–70; 10.1038/nn.3269 (2013).

126. Gottschalk, A. & Bergs, A. *AN OPTOGENETIC VOLTAGE CLAMP (OVC) AND USES THEREOF.* EP20210162331, C12N5/077;G01N21/64;G01N33/487 (2021).

127. Gottschalk, A. & Bergs, A. *AN OPTOGENETIC VOLTAGE CLAMP (OVC) AND USES THEREOF.* EP20210162331, A61K49/00;G01N21/64;G01N33/487 (2022).

128.   Monteith, G. R. & Bird, G. S. J. Techniques: high-throughput measurement of intracellular Ca(2+) -- back to basics. *Trends in pharmacological sciences* **26,** 218–223; 10.1016/j.tips.2005.02.002 (2005).

129.   Edelstein, A., Amodaj, N., Hoover, K., Vale, R. & Stuurman, N. Computer control of microscopes using µManager. *Current protocols in molecular biology* **Chapter 14,** Unit14.20; 10.1002/0471142727.mb1420s92. (2010).

Software manual

Preparation

To run the OVC software, the microscope control software µManager[129] must first be installed. The current OVC scripts are compatible with version v.1.4.22, which requires Windows XP, or 7-10. All scripts were tested with Windows 10. The execution of the programs requires the connection of a PolychromeV (TILL Photonics) device to the computer (software automatically detects the right USB port). Furthermore, the JAR file "TILLPolychrome.jar" must be placed in the µManager "MMPlugins" folder and the program library "TILLPolychromeJ.dll" in the Windows Sys32 folder.

Program execution

First, a rectangular ROI can be selected via the µManager user interface to limit the camera section to the size of the ROI. Then open the desired BSH file in the µManager script panel and press "Run". After all desired parameters for the OVC experiment have been selected, "OK" must be pressed to start the OVC experiment (**Figure 11**).
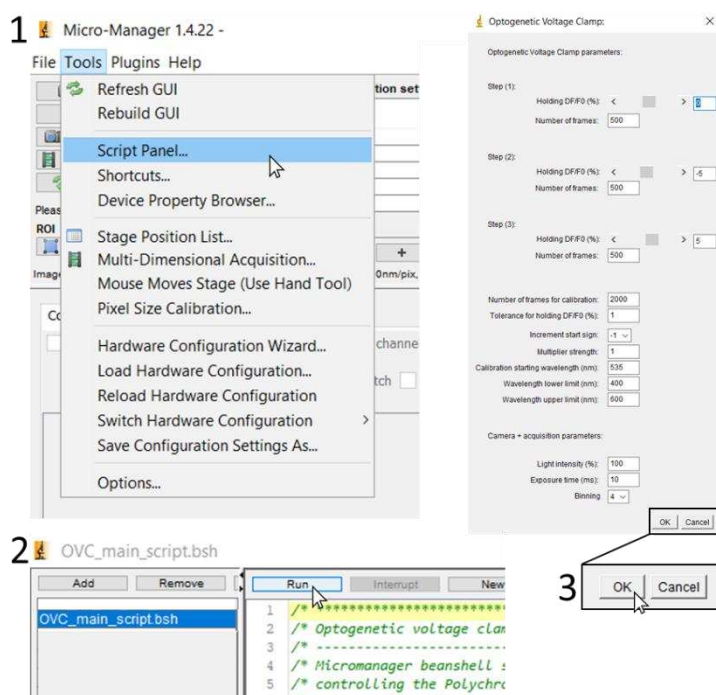
Figure 12. Execution of the OVC scripts in the µManager[129] script panel. Shown are screenshots of the µManager user interface (step 1 and 2).

Code

Readme file

```
Operating systems:
- µManager v.1.4.22 requires Windows XP, or 7-10. Windows 7 is recommended.
- Software tested on Windows 10.

Required non-standard hardware:
- Polychrome V (TILL Photonics).

Instruction / Installation:
- Install µManager v 1.4.22 (µManager 2.0 is not supported).
- Place a copy of TILLPolychrome.jar into MMPlugins folder and the TILLPolychromeJ.dll (Windows 64) into
Windows Sys32 folder.
- Set rectangular ROI in µManager live image mode (-> press crop to ROI button / reduce window to size
of ROI).
- Open BSH file via µManager script panel and press "Run".
- Select desired holding DF/F0 (%) and number of frames for each step, calibration and control
parameters, as well as camera settings.
- Press "OK" to run the script.

Demo:
- To test the script without a PolychromeV device and / or camera connected, comment out all
PolychromeV-specific commands (e.g. Start.setBandwidth(15, 1)) and open MicroManager with the demo
camera configuration file (MMConfg_demo.cfg).

-OVC on-the-run mode-

- In this mode, a window opens (while the script is running) to set the desired value (slider bar).
- A live status (system on hold, adapting or exceeding limits) is shown, enabling adjustment.

-OVC pseudo-IV mode-

- This mode enables to clamp relative fluorescence in 11 consecutive steps based on previously selected
upper and lower limits, resulting in an output of the average DF/F0 value and associated wavelength
achieved for each step (calculated as a mean of the last 25 % of each step).
- An optical wavelength / DF/F0 curve is produced and can be translated into an estimated I/V-diagram
using the calibration functions provided in the paper.

-Optical current clamp mode-

-The experimenter has the choice to set single pulses of certain wavelength and duration or to select
step-like or continuous wavelength ramps prior to the experiment.
-Similar to the main OVC script, this software provides bleaching correction and live DF/F0 readout.
```

OVC_main_script[3]

---

[3] Only the main script is listed as an example. All other scripts can be found in the section "digital content".

```
1    /* ************************************************************************ */
2    /* Optogenetic voltage clamp with online bleach correction - Camera and PolychromeV Control  */
3    /* ------------------------------------------------------------------------ */
4    /* Micromanager beanshell script to perform online fluorescence imaging, while in parallel  */
5    /* controlling the PolychromeV monochromator. Requires expression of a voltage sensor and  */
6    /* optogenetic tools for activation and inhibition. Compares measured F value with desired  */
7    /* DF/F0 holding value online and adapts PolychromeV wavelength accordingly. Once the  */
8    /* current F value is in desired tolerance range, wavelength will be hold.  */
9    /* ------------------------------------------------------------------------ */
10   /* To run the script, place a copy of TILLPolychrome.jar into MMPlugins folder and the  */
11   /* TILLPolychromeJ.dll (Windows 64) into Windows Sys32 folder. Runs on Micromanager 1.4.22.  */
12   /* ------------------------------------------------------------------------ */
13   /* Amelie Bergs  */
14   /* ************************************************************************ */
15
16   // Imports for Camera Control and Image Processing:
17   import ij.*;
18   import ij.process.*;
19   import org.micromanager.api.AcquisitionOptions;
20   import java.lang.Math;
21   import ij.measure.*;
22   package ij.process;
23   import java.awt.*;
24   import *;
25   import ij.text.*;
26   import ij.measure.ResultsTable;
27   import java.util.ArrayList;
28   import java.lang.String;
29   import ij.ImagePlus;
30   import ij.gui.Roi;
31   import ij.measure.CurveFitter;
32   import ij.plugin.frame.Fitter;
33   import ij.process.ImageProcessor;
34   import ij.process.ImageStatistics;
35   import bsh.Interpreter;
36   import bsh.EvalError;
37   import org.micromanager.utils.ImageUtils;
38   // Imports for PolychromeV Control:
39   import java.lang.reflect.Field;
40   import java.lang.*;
41   import java.io;
42   import java.net;
43   import com.bruxton.polychrome.*;  // Place copy of TILLPolychrome.jar into MMPlugins folder
44   // Imports for save data as file:
45   import java.io.FileWriter;
46   import java.io.PrintWriter;
47   // Variables for PolychromeV:
48   long handle;
49   int index;
50   double wavelength;
51   double duration;
52   boolean returnToRestingWavelength;
53   // Function feedback-loop algorithm:
54   double feedbackloop(a, b, c, frame, F, F0, F_correct_List, change_correct_List, holding_dF_F0,
55   wavelengths_List, increment, multiplier_strength) { // Corrects gray values based on exponential fitting
56   function, calculates corrected DF/F0 and adapts wavelength accordingly (with weighted increment)
57       exp_offset = a*Math.exp(-b*frame)+c; // calculates exp. offset with variables from exponential fit
58       ratio = (a*Math.exp(-b*0)+c)/ (a*Math.exp(-b*frame)+c); // calculates ratio: current and first
59   offset
60       F_correct = F * ratio;  // multiplies current F value to get corrected value
61       F_correct_List.add(frame, F_correct);
62       dF_F0_correct = ((F_correct - F0) / F0) * 100;  // calculates corrected DF/F0 value
63       change_correct_List.add(frame, dF_F0_correct); // calculates multiplier variable to weight
64   difference between set and current DF/F0 value
65       int multiplier = Math.abs(holding_dF_F0 - dF_F0_correct)*multiplier_strength;
66       new_wavelength = (wavelengths_List.get(frame)) + multiplier*increment; // Wavelength is calculated
67   based on last wavelength plus weighted multiplier
68       Start.setWavelength(new_wavelength, 1, false); // Sets PolychromeV to new wavelength
```

```
69          return new_wavelength;
70      }
71      // Lists:
72      ArrayList wavelengths_List = new ArrayList();
73      ArrayList dF_F0_List = new ArrayList();
74      ArrayList F_raw_List = new ArrayList();
75      ArrayList info_List = new ArrayList();
76      ArrayList F_correct_List = new ArrayList();
77      ArrayList dF_F0_correct_List = new ArrayList();
78      ArrayList step_List = new ArrayList();
79      ArrayList time_List = new ArrayList();
80      // Decimal formats:
81      DecimalFormat f = new DecimalFormat("#0.00");
82      DecimalFormat f2 = new DecimalFormat("#0.0000");
83      // *******************************************************************************************
84      // ----------------
85      // (1) Preparation:
86      // ----------------
87          gui.clearMessageWindow();
88          gui.message("Optogenetic voltage clamp: Camera + PolychromeV Control");
89          // Open PolychromeV (any USB port):
90          Polychrome Start = new Polychrome(0);
91
92          Start.setBandwidth(15, 1);
93          Start.setWavelength(690, 1, false);
94          // User dialog to select desired parameters:
95              int min = -40;
96              int max = 40;
97              String[] binningtable = {"1","2","4","8"};
98              String[] incrementtable = {"1","-1"};
99          //Input:
100             gd = new ij.gui.GenericDialog("Optogenetic Voltage Clamp:");
101             gd.addMessage("Optogenetic Voltage Clamp parameters:");
102             gd.addMessage("");
103             gd.addMessage("Step (1):");
104             gd.addSlider("Holding DF/F0 (%):",min,max,0);
105             gd.addNumericField("Number of frames: ", 500, 0);
106             gd.addMessage("");
107             gd.addMessage("Step (2):");
108             gd.addSlider("Holding DF/F0 (%):",min,max,-5);
109             gd.addNumericField("Number of frames: ", 500, 0);
110             gd.addMessage("");
111             gd.addMessage("Step (3):");
112             gd.addSlider("Holding DF/F0 (%):",min,max,5);
113             gd.addNumericField("Number of frames: ", 500, 0);
114             gd.addMessage("");
115             gd.addMessage("");
116             gd.addNumericField("Number of frames for calibration: ", 2000, 0);
117             gd.addNumericField("Tolerance for holding DF/F0 (%): ", 1, 0);
118             gd.addChoice("Increment start sign: ", incrementtable, incrementtable[1]);
119             gd.addNumericField("Multiplier strength: ", 1, 0);
120             gd.addNumericField("Calibration starting wavelength (nm): ", 535, 0);
121             gd.addNumericField("Wavelength lower limit (nm): ", 400, 0);
122             gd.addNumericField("Wavelength upper limit (nm): ", 600, 0);
123             gd.addMessage("");
124             gd.addMessage("Camera + acquisition parameters:");
125             gd.addMessage("");
126             gd.addNumericField("Light intensity (%): ", 100, 0);
127             gd.addNumericField("Exposure time (ms): ", 10, 0);
128             gd.addChoice("Binning", binningtable, binningtable[2]);
129             gd.showDialog();
130             if (gd.wasCanceled())
131                     return;
132         //Get output:
133             double holding_dF_F0 = gd.getNextNumber();
134             int nrFrames_1 = gd.getNextNumber();
135             double holding_dF_F0_2 = gd.getNextNumber();
136             int nrFrames_2 = gd.getNextNumber();
```

325

```java
137            double holding_dF_F0_3 = gd.getNextNumber();
138            int nrFrames_3 = gd.getNextNumber();
139            int nrFrames_cal = gd.getNextNumber();
140            double tolerance = gd.getNextNumber();
141            String incrementstartsign = gd.getNextChoice();
142            double multiplier_strength = gd.getNextNumber();
143            double start_wavelength = gd.getNextNumber();
144            double wllow = gd.getNextNumber();
145            double wlup = gd.getNextNumber();
146            int intensity = gd.getNextNumber();
147            int exposure = gd.getNextNumber();
148            String binning = gd.getNextChoice();
149            int binning_int = Integer.parseInt(binning);
150            int incrementstartsign_int = Integer.parseInt(incrementstartsign);
151
152            int nrFrames = nrFrames_1 + nrFrames_2 + nrFrames_3 + nrFrames_cal;
153            double intensitydez = intensity/100;
154
155            gui.message("Acquisition is running... Calibration...");
156            gui.message("multiplier strength: " + multiplier_strength);
157  // *******************************************************************************
158  // ----------------
159  // (2) Acquisition:
160  // ----------------
161      // clear all previous acquisitions:
162            gui.closeAllAcquisitions();
163      // Preparation of acquisition:
164            mmc.setExposure(exposure);
165            cameraName = mmc.getCameraDevice();
166            mmc.setProperty(cameraName, "Binning", binning);
167            gui.refreshGUI();
168      // file locations:
169            OVC = gui.getUniqueAcquisitionName("Live optical voltage clamp");
170            rootDirName = "C:/AcquisitionData";
171      // # of frames:
172            nrChannels = nrSlices = nrPositions = 1;
173            gui.openAcquisition(OVC, rootDirName,
174            nrFrames, nrChannels, nrSlices, nrPositions,
175              true,
176              false);
177
178            width = (int) mmc.getImageWidth();
179            height = (int) mmc.getImageHeight();
180            bytesPerPixel = (int) mmc.getBytesPerPixel();
181            bitDepth = (int) mmc.getImageBitDepth();
182      // Variables for feedbackloop:
183            double tolerance_max = holding_dF_F0 + tolerance;
184            double tolerance_min = holding_dF_F0 - tolerance;
185            double tolerance_max_step2 = holding_dF_F0_2 + tolerance;
186            double tolerance_min_step2 = holding_dF_F0_2 - tolerance;
187            double tolerance_max_step3 = holding_dF_F0_3 + tolerance;
188            double tolerance_min_step3 = holding_dF_F0_3 - tolerance;
189            double increment = incrementstartsign_int;
190            double new_wavelength = start_wavelength;
191            double dF_F0;
192            double F0 = 0;
193            dF_F0_correct = 0;
194            F_correct = 0;
195            wavelengths_List.add(0,start_wavelength);
196
197            gui.initializeAcquisition(OVC, width, height, bytesPerPixel, bitDepth);
198
199            mmc.startSequenceAcquisition(nrFrames, 0, true);
200            frame = 0;
201
202            exposureMs = mmc.getExposure();
203            now = System.currentTimeMillis();
204            while (mmc.getRemainingImageCount() > 0 || mmc.isSequenceRunning(mmc.getCameraDevice())) {
```

```
205                 if (mmc.getRemainingImageCount() > 0) {
206                     img = mmc.popNextTaggedImage();
207                     ImageProcessor proc = ImageUtils.makeProcessor(img);
208                     double F = proc.getStatistics().mean;
209                     gui.addImageToAcquisition(OVC, frame, 0, 0, 0, img);
210                     dF_F0 = ((F - F0) / F0) * 100;
211
212                       if (frame < nrFrames_cal && frame != (nrFrames_cal-1)) {
213                             F_correct_List.add(frame, 0);
214                             dF_F0_correct_List.add(frame, 0);
215                             Start.setWavelength(start_wavelength, 1, false);
216                             Info = ("Calibration");
217
218                         }   else if  (frame == (nrFrames_cal-1)){
219
220                         n = F_raw_List.size();
221                             double[] x = new double [n];
222                             double[] y = new double [n];
223
224                                 for (int i=2;i<n;i++){
225                                         x[i]=Double.valueOf(i);
226                                         y[i]=Double.valueOf(F_raw_List.get(i));
227                                     }
228
229                         y[0] = Double.valueOf(F_raw_List.get(4));
230                         y[1] = Double.valueOf(F_raw_List.get(4));
231                         y[2] = Double.valueOf(F_raw_List.get(4));
232
233                         CurveFitter fitter=new CurveFitter(x, y);
234
235                         fitter.doFit(11);
236
237                             double[] respara = fitter.getParams();
238                             a = respara[0];
239                             b = respara[1];
240                             c = respara[2];
241
242                             R = fitter.getRSquared();
243
244                             F_correct_List.add(frame, 0);
245                             dF_F0_correct_List.add(frame, 0);
246
247                             gui.message("Exponential fit for bleaching correction done.");
248                         gui.message("Bleach correction function: exp. offset = " + a + " * exp(-" + b + " *
249     x) + " + c);
250                             Info = ("Bleach correction function: exp. offset = " + a + " * exp(-" + b + " * x) +
251     " + c);
252
253                         } else if (frame == nrFrames_cal){
254
255                             MeanSum = 0;
256                                 for (int i=5;i<55;i++){
257                                         MeanSum = Double.valueOf(F_raw_List.get(i)*(a*Math.exp(-b*0)+c)/
258     (a*Math.exp(-b*i)+c)) + MeanSum;
259
260                                 }
261                             F0 = MeanSum/50;
262
263                             Info = ("Calculating F0: " + F0);
264
265                             F_correct_List.add(frame, 0);
266                             dF_F0_correct_List.add(frame, 0);
267     //Step 1:
268                         } else if (dF_F0_correct > tolerance_max && wllow <= new_wavelength &&
269     new_wavelength <= wlup && frame > nrFrames_cal && frame <= (nrFrames_cal + nrFrames_1)) {
270                             new_wavelength = feedbackloop(a, b, c, frame, F, F0, F_correct_List,
271     dF_F0_correct_List, holding_dF_F0, wavelengths_List, increment, multiplier_strength);
272
```

327

```java
273                                Info = ("Current dF/F0 greater than holding dF/F0 (" + holding_dF_F0 +" %). -->
274     Change wavelength by " + Math.abs(wavelengths_List.get(frame)-new_wavelength) + " nm");
275
276                         } else if (dF_F0_correct < tolerance_min && wllow <= new_wavelength &&
277     new_wavelength <= wlup && frame > nrFrames_cal && frame <= (nrFrames_cal + nrFrames_1)) {
278                                new_wavelength = feedbackloop(a, b, c, frame, F, F0, F_correct_List,
279     dF_F0_correct_List, holding_dF_F0, wavelengths_List, -increment, multiplier_strength);
280
281                                Info = ("Current dF/F0 smaller than holding dF/F0 (" + holding_dF_F0 +" %). -->
282     Change wavelength by " + Math.abs(wavelengths_List.get(frame)-new_wavelength) + " nm");
283     //Step 2:
284                         }  else if (steps = true && dF_F0_correct > tolerance_max_step2 && wllow <=
285     new_wavelength && new_wavelength <= wlup && frame > (nrFrames_cal + nrFrames_1) && frame <=
286     (nrFrames_cal + nrFrames_1 + nrFrames_2)) {
287                                new_wavelength = feedbackloop(a, b, c, frame, F, F0, F_correct_List,
288     dF_F0_correct_List, holding_dF_F0_2, wavelengths_List, increment, multiplier_strength);
289
290                                Info = ("Current dF/F0 greater than holding dF/F0 (" + holding_dF_F0_2 +" %). --
291     > Change wavelength by " + Math.abs(wavelengths_List.get(frame)-new_wavelength) + " nm");
292                         }  else if (steps = true && dF_F0_correct < tolerance_min_step2 && wllow <=
293     new_wavelength && new_wavelength <= wlup && frame > (nrFrames_cal + nrFrames_1) && frame <=
294     (nrFrames_cal + nrFrames_1 + nrFrames_2)) {
295                                new_wavelength = feedbackloop(a, b, c, frame, F, F0, F_correct_List,
296     dF_F0_correct_List, holding_dF_F0_2, wavelengths_List, -increment, multiplier_strength);
297     //Step 3:
298                                Info = ("Current dF/F0 smaller than holding dF/F0 (" + holding_dF_F0_2 +" %). --
299     > Change wavelength by " + Math.abs(wavelengths_List.get(frame)-new_wavelength) + " nm");
300
301                         }  else if (steps = true && dF_F0_correct > tolerance_max_step3 && wllow <=
302     new_wavelength && new_wavelength <= wlup && frame > (nrFrames_cal + nrFrames_1 + nrFrames_2)
303                         && frame <= (nrFrames_cal + nrFrames_1 + nrFrames_2 + nrFrames_3)) {
304                                new_wavelength = feedbackloop(a, b, c, frame, F, F0, F_correct_List,
305     dF_F0_correct_List, holding_dF_F0_3, wavelengths_List, increment, multiplier_strength);
306
307                                Info = ("Current dF/F0 greater than holding dF/F0 (" + holding_dF_F0_3 +" %). --
308     > Change wavelength by " + Math.abs(wavelengths_List.get(frame)-new_wavelength) + " nm");}  else if
309     (steps = true && dF_F0_correct < tolerance_min_step3 && wllow <= new_wavelength && new_wavelength <=
310     wlup && frame > (nrFrames_cal + nrFrames_1) && frame > (nrFrames_cal + nrFrames_1 + nrFrames_2)
311
312                         && frame <= (nrFrames_cal + nrFrames_1 + nrFrames_2 + nrFrames_3)) {
313                                new_wavelength = feedbackloop(a, b, c, frame, F, F0, F_correct_List,
314     dF_F0_correct_List, holding_dF_F0_3, wavelengths_List, -increment, multiplier_strength);
315
316                                Info = ("Current dF/F0 smaller than holding dF/F0 (" + holding_dF_F0_3 +" %). --
317     > Change wavelength by " + Math.abs(wavelengths_List.get(frame)-new_wavelength) + " nm");
318
319                         } else  {
320                             exp_offset = a*Math.exp(-b*frame)+c;
321                             ratio = (a*Math.exp(-b*0)+c)/ (a*Math.exp(-b*frame)+c);
322                             F_correct = F * ratio;
323                             F_correct_List.add(frame, F_correct);
324                            dF_F0_correct = ((F_correct - F0) / F0) * 100;
325                             dF_F0_correct_List.add(frame, dF_F0_correct);
326                             new_wavelength = (wavelengths_List.get(frame));
327                             Start.setWavelength(new_wavelength, 1, false);
328                             Info = "Hold. Current dF/F0 in tolerance range.";
329                         }
330
331                             if (new_wavelength < wllow) {
332                                 new_wavelength = new_wavelength + (wllow-new_wavelength);
333                                 Info = ("Lower wavelength limit (" + wllow + "nm) reached --> Correction.");
334
335                             } else if (new_wavelength > wlup) {
336                                 new_wavelength = new_wavelength + (wlup-new_wavelength);
337                                 Info = ("Upper wavelength limit (" + wlup + "nm) reached --> Correction.");
338                             }
339
340                         wavelengths_List.add(frame+1, new_wavelength);
```

```
341                         dF_F0_List.add(frame, dF_F0);
342                         F_raw_List.add(frame, F);
343                         info_List.add(frame, Info);
344
345                 frame++;
346
347                     }
348             else {
349                 mmc.sleep(Math.min(0.5 * exposureMs, 20));
350             }
351         }
352
353     double t = System.currentTimeMillis() - now;
354     mmc.stopSequenceAcquisition();
355     fps = nrFrames*1.0 / t * 1000;
356     double t_sec = t/1000;
357
358     gui.message("Acquisition finished. Elapsed time:  " + t + " ms (" + fps + " fps)");
359     // *****************************************************************************
360     // ----------------------
361     // (3) Write data to file:
362     // ----------------------
363     for (int i = 0; i < nrFrames_cal; i++){
364         step_List.add(i, "-");
365     }
366     for (int i = nrFrames_cal; i < nrFrames_cal+nrFrames_1; i++){
367         step_List.add(i, "Step 1: "+holding_dF_F0 + " %");
368     }
369     for (int i = nrFrames_cal+nrFrames_1; i < nrFrames_cal+nrFrames_1+nrFrames_2; i++){
370         step_List.add(i, "Step 2: "+ holding_dF_F0_2 + " %");
371     }
372     for (int i = nrFrames_cal+nrFrames_1+nrFrames_2; i < nrFrames_cal+nrFrames_1+nrFrames_2+nrFrames_3;
373     i++){
374         step_List.add(i, "Step 3: "+ holding_dF_F0_3 + " %");
375     }
376     for (int i = 0; i < nrFrames; i++){
377         time_List.add(i, (t_sec/nrFrames)+i*( t_sec/nrFrames));
378     }
379
380     DirectoryChooser dr = new DirectoryChooser("Choose directory");
381     dr.setDefaultDirectory("D:\temp");
382     acqDir = dr.getDirectory();
383
384     gd = new ij.gui.GenericDialog("Save files:");
385     gd.addStringField("File name: ", "");
386     gd.showDialog();
387     if (gd.wasCanceled())
388             return;
389     title = gd.getNextString();
390
391     timeStamp = new SimpleDateFormat("yyyy/MM/dd HH:mm").format(Calendar.getInstance().getTime());
392     timeStamp_title = new SimpleDateFormat("_yyyy_MM_dd").format(Calendar.getInstance().getTime());
393
394     File file = new File(acqDir + title + timeStamp_title + ".txt");
395     FileWriter fileWriter = new FileWriter(file, true);
396     PrintWriter writer = new PrintWriter(fileWriter);
397     writer.println("Title: " + title + " Date: " + timeStamp);
398     writer.println("Parameters for step (1): Holding dF/F0: " + holding_dF_F0 + " % Tolerance range: " +
399     tolerance_min + " - " + tolerance_max + " % Exposure time: " + exposure + " ms Binning: " + binning +"x"
400     + binning);
401     writer.println("Parameters for step (2): Holding dF/F0: " + holding_dF_F0_2 + " % Tolerance range: " +
402     tolerance_min_step2 + " - " + tolerance_max_step2 + " %");
403     writer.println("Parameters for step (3): Holding dF/F0: " + holding_dF_F0_3 + " % Tolerance range: " +
404     tolerance_min_step3 + " - " + tolerance_max_step3 + " %");
405     writer.println("Bleaching correction function: exp. offset = " + f.format(a) + " * exp(-" + f2.format(b)
406     + " * x) + " + f.format(c) + " R^2: " + f2.format(R) +" Video duration: " + f.format(t_sec) + " s
407     Framerate: " + f.format(fps));
408     writer.println("");
```

```java
409    writer.println("# Measurement"  + " \t " + "Time" + " \t " + "F" + " \t " + "F_bleach_correct" + " \t "
410    + "dF/F0" + " \t " + "dF/F0_bleach_correct" + " \t " + "Wavelength" + " \t "+ "Info"+ " \t "+ "Step");
411
412        for (int i = 0; i < nrFrames; i++){
413            writer.println(i + " \t " + f2.format(time_List.get(i)) + " \t " + f.format(F_raw_List.get(i)) +
414    " \t " + f.format(F_correct_List.get(i)) + " \t "
415            + f.format(dF_F0_List.get(i))+ " \t " + f.format(dF_F0_correct_List.get(i)) + " \t "+
416    f.format(wavelengths_List.get(i)) + " \t "+ info_List.get(i) + " \t "+ step_List.get(i));
417        }
418
419    writer.close();
420
421    gui.getAcquisition("Live optical voltage clamp");
422    ij.IJ.saveAs("TIFF", acqDir + title + "_clamp_movie" + timeStamp_title + ".tif");
423    gui.getAcquisition("Live optical voltage clamp").promptToSave(false);
424    ij.IJ.run("Close");
425
426    Desktop desktop = Desktop.getDesktop();
427    if(file.exists()) desktop.open(file);
428
429    Start.close();
```

Digital content

- This dissertation as PDF file
- Software code[*] (OVC_main_script, OVC_4_step_script, OVC_on_the_run_script, OVC_pseudo-IV_script, optical_current_clamp_script)
- Movie 1[*]: Body length analysis of animals expressing BiPOLES in cholinergic neurons. Wavelength ramp from 400 to 600 nm.
- Movie 2[**]: QuasAr2 in BWMs, intrinsic activity.
- Movie 3[*]: OVC/dynamic suppression of action potentials in the pharynx.
- Movie 4[*]: OVC on-the-run mode/live selection of clamp values.
- Movie 5: Scheme of a potential implementation of an HTS-OVC system.

---

[*] Material from: Bergs, A.C.F., Liewald, J.F., Rodriguez-Rozada, S. *et al.* All-optical closed-loop voltage clamp for precise control of muscles and neurons in live animals. *Nat Commun* **14**, 1939 (2023). https://doi.org/10.1038/s41467-023-37622-6. Reproduced with permission from Springer Nature.

[**] Material from: Azimi Hashemi, N. and Bergs, A. *et al.* Rhodopsin-based voltage imaging tools for use in muscles and neurons of *Caenorhabditis elegans*. *Proceedings of the National Academy of Sciences of the United States of America* **116**, 17051–17060; 10.1073/pnas.1902443116 (2019).

List of figures

Figure 1. Timeline of publications in the scope of this dissertation. Publications are listed according to their year of publication and content (optogenetic actuators, voltage sensors, application in C. elegans). Arrows indicate which publications are based on each other (first submission of OVC paper in 2021).

Figure 2. Overview of the most relevant channelrhodopsin-based tools listed by their initial description and spectral properties. Color coding further subdivides the tools shown by de- or hyperpolarizing characteristics (orange or blue outline respectively) and the purpose of the genetic manipulation (purple: enhanced photocurrents, red: modified kinetics, green: shift in absorption spectra, and yellow: ion selectivity resp. channel topology). * Tools covered by this project.

Figure 3. Mechanism of membrane voltage-dependent fluorescence of Arch. (A) Theoretical mechanism of proton transport. Protons are depicted as yellow spheres, proton donor (PD), proton acceptor (PA) and proton release (PR) sites are highlighted. (B) Scheme of Arch's voltage sensitivity and fluorescence. Figure prepared by the author according to 38,77.

Figure 4. Overview of the most relevant rhodopsin-based GEVIs listed by their initial description and voltage sensitivity. Color coding further subdivides the tools shown by direct readout (fluorophore: retinal) or eFRET sensors (fluorophore: FP; continuous or dotted outline respectively) and absorption maxima. Tools with fast kinetics are highlighted in purple. * Tools covered by this project.

Figure 5. Open- vs. closed-loop optogenetics. (A) Open-loop optogenetic experiments achieve only perturbation of the system since the control signal is independent of the output variable. Therefore, the stimulus is static and triggered effects on the system are subject to high variability. (B) Control signals are modulated online with respect to the output variable. Feedback occurs via readout of either electrophysiologically or optically derived data or based on macroscopic behavior.

Figure 6. Methods of (all-)optical electrophysiology listed in chronological order of their first description. The technologies are specified according to the choice of actuation and voltage tracking tools and then evaluated in terms of the level of pure optical control achieved. One + was scored each for the use of a GEVI instead of an electrode-based approach, the use of two counteracting tools instead of unidirectional modulation (indicated by one or two arrows; directed up- and downwards for de- and hyperpolarizing respectively), and lastly for the presence of real-time feedback control (indicated by cycle symbol).

Figure 7. Molecular OVC components and their spectral properties. (A) The OVC17 involves two counteracting optogenetic tools (BiPOLES – consisting of the hyperpolarizer ACR2 and the depolarizer Chrimson) for bidirectional modulation of the membrane potential, as well as a voltage sensor (QuasAr2). QuasAr2's voltage-dependent fluorescence is stimulated via a 637 nm laser and BiPOLES activity is modulated over a wavelength spectrum from 400 to 600 nm via a monochromatic light source. Blue star: mCerulean. (B) Absorption spectra of all components7,11,32. Wavelengths of the light sources used as specified.

Figure 8. Electrophysiological vs. optical approach of the voltage clamp technique. (A) Electrophysiology: The voltage clamp operates by a negative feedback mechanism. The membrane voltage is detected by the membrane potential amplifier and passed on to the feedback amplifier. The feedback amplifier subtracts the observed membrane voltage from the command voltage received from the signal generator that was selected by the experimenter beforehand. Finally, the signal is amplified and returned to the cell of interest via the current passing electrode (scheme generated by author according to https://tinyurl.com/bdfvh7ra). (B) All-optical adaption of the voltage clamp (OVC approach17): The function of the electrodes was taken over by applying optical elements. A sensitive camera records the fluorescence of the GEVI QuasAr2, while a live control software processes incoming grey values, calculates error signals and adapts the output variable wavelength accordingly. Eventually, feedback of light is generated and sent back to the optogenetic actuation pair BiPOLES to keep the membrane potential at a desired level.

Figure 9. Anatomy of C. elegans. (A) General anatomy. (B) Nervous system. Figure by the author according to [Masterarbeit] and Zarkower 2006.

Figure 10. Photocurrents of two different tandem tools in HEK293 cells. (A) BiPOLES. (B) ACR2-bReaChES. Whole-cell patch clamp recordings at -60 mV with 10 ms light pulses. Theoretical QuasAr2 stimulation with laser as indicated. Data provided by Johannes Vierock19.

Figure 11. Model of a future HTS-OVC platform. The automated system is equipped with a photomultiplier, a monochromatic light source and a laser for fluorescence recording or stimulation, respectively. A microtiter plate is moved automatically for each brief OVC recording.

Figure 12. Execution of the OVC scripts in the µManager script panel.

List of tables

Table 1. List of figures and detailed breakdown of the author's contribution. Publication: "All-optical closed-loop voltage clamp for precise control of muscles and neurons in live animals"[17].

Table 2. List of figures and detailed breakdown of the author's contribution. Book chapter: "Microbial Rhodopsin Optogenetic Tools: Application for Analyses of Synaptic Transmission and of Neuronal Network Activity in Behavior"[22].

Table 3. List of figures and detailed breakdown of the author's contribution. Publication: "BiPOLES is an optogenetic tool developed for bidirectional dual-color control of neurons"[19].

Table 4. List of figures and detailed breakdown of the author's contribution. Publication: "RIM and RIM-binding protein localize synaptic CaV2 channels to differentially regulate transmission in neuronal circuits"[25].

Table 5. List of figures and detailed breakdown of the author's contribution. Publication: "Rhodopsin-based voltage imaging tools for use in muscles and neurons of Caenorhabditis elegans"[24].

Table 6. List of figures and detailed breakdown of the author's contribution. Review article: "Optogenetischer Werkzeugkasten für neue experimentelle Ansätze"[21].

Table 7. List of figures and detailed breakdown of the author's contribution. Publication: "Expanding the Optogenetics Toolkit by Topological Inversion of Rhodopsins"[20].

Table 8. List of figures and detailed breakdown of the author's contribution. Publication: "Functionally asymmetric motor neurons contribute to coordinating locomotion of Caenorhabditis elegans"[23].

Table 9. List of figures and detailed breakdown of the author's contribution. Publication: "Rhodopsin optogenetic toolbox v2.0 for light-sensitive excitation and inhibition in Caenorhabditis elegans"[18].

Eidesstattliche Versicherung[4]

Ich versichere hiermit an Eides statt, dass ich die vorliegende kumulative Doktorarbeit mit dem Titel „From optical perturbation to true control: All-optical voltage clamp in live animals" selbstständig und ohne unzulässige fremde Hilfe erbracht habe. Alle beschriebenen Daten und Ergebnisse wurden von mir in dem für die Arbeit offiziell zur Verfügung stehenden Zeitraum erhalten und sind in Laborjournalen dokumentiert. Ich habe keine anderen als die angegebenen Quellen und Hilfsmittel benutzt sowie wörtliche und sinngemäße Zitate kenntlich gemacht. Die Arbeit hat in gleicher oder ähnlicher Form noch keiner Prüfungsbehörde vorgelegen. Ich versichere außerdem, dass ich in der vorliegenden Arbeit die Grundsätze guter wissenschaftlicher Praxis beachtet habe.

Frankfurt am Main,

_____
Amelie Bergs

---

[4] Statutory declaration

Curriculum vitae

Amelie Bergs

Work experience

Education and training

Publications

2023:

- Bergs, A. C. F. *et al.* All-optical closed-loop voltage clamp for precise control of muscles and neurons in live animals. *Nature communications* **14**, 1939; 10.1038/s41467-023-37622-6 (2023).

2022:

- Bergs, A., Henss, T., Glock, C., Nagpal, J. & Gottschalk, A. Microbial Rhodopsin optogenetic Tools: Application for Analyses of Synaptic Transmission and of Neuronal Network Activity in Behavior. *Methods in molecular biology* (Clifton, N.J.) **2468**, 89–115; 10.1007/978-1-0716-2181-3_6 (2022).

2021:
- Vierock, J. *et al.* BiPOLES is an optogenetic tool developed for bidirectional dual-color control of neurons. Nature communications **12**; 10.1038/s41467-021-24759-5 (2021).
- Janosi, B. *et al.* RIM and RIM-binding protein localize synaptic Cav2 channels in a differential manner to regulate transmission in neuronal circuits. *bioRxiv.* doi: https://doi.org/10.1101/2021.02.01.429206 (2021).

2019:
- Azimi Hashemi, N. and Bergs, A. *et al.* Rhodopsin-based voltage imaging tools for use in muscles and neurons of Caenorhabditis elegans. *Proceedings of the National Academy of Sciences of the United States of America* **116**, 17051–17060; 10.1073/pnas.1902443116 (2019).
- Bergs, A., Liewald, J. & Gottschalk, A. Optogenetischer Werkzeugkasten für neue experimentelle Ansätze. *Biospektrum* **25**, 398–401; 10.1007/s12268-019-1069-z (2019).

2018:
- Brown, J. *et al.* Expanding the Optogenetics Toolkit by Topological Inversion of Rhodopsins. *Cell* **175**, 1131-1140.e11; 10.1016/j.cell.2018.09.026 (2018).
- Tolstenkov, O. *et al.* Functionally asymmetric motor neurons contribute to coordinating locomotion of Caenorhabditis elegans. *eLife* **7**; 10.7554/eLife.34997 (2018).
- Bergs, A. *et al.* Rhodopsin optogenetic toolbox v2.0 for light-sensitive excitation and inhibition in Caenorhabditis elegans. *PloS one* **13**, e0191802; 10.1371/journal.pone.0191802 (2018).

Conferences and presentations

21/06/2021 – 24/06/2021 – virtual
Genetics Society of America: 23rd International C. elegans Conference Talk: "The optogenetic voltage clamp (OVC) – A closed-loop all-optical approach for true optogenetic control of muscles and neurons in live animals."

22/03/2021 – 30/03/2021 – virtual
German Neuroscience Society:14th Göttingen Neuroscience Meeting Talk: "Introducing the optogenetic voltage clamp – A closed-loop all-optical voltage clamp approach."

25/06/2018 – 28/06/2018 – Madison, Wisconsin, USA
CeNeuro: C. elegans neuroscience topic meeting Talk: "Actuation and Imaging of

Excitable Cell Activity Using Microbial Rhodopsins as Genetically Encoded Voltage Sensors."

01/06/2016 – 03/06/2016 – Max Delbrück Communications Center, Berlin, Germany
European Worm Meeting (EWM)

28/09/2014 – 01/10/2014 – Julius-Maximilians-Universität, Würzburg, Germany
Channelrhodopsin et al. - Optogenetic Tools and Applications conference

Patents

07/10/2021
An optogenetic voltage clamp (OVC) and uses thereof
Application number: EP 21162331.9; EP 4 056 681 A1; PCT/EP2022/056030